Strasser, M., Dugan, B., Kanagawa, K., Moore, G.F., Toczko, S., Maeda, L., and the Expedition 338 Scientists
Proceedings of the Integrated Ocean Drilling Program, Volume 338

Site C0002[1]

M. Strasser, B. Dugan, K. Kanagawa, G.F. Moore, S. Toczko, L. Maeda, Y. Kido, K.T. Moe, Y. Sanada, L. Esteban, O. Fabbri, J. Geersen, S. Hammerschmidt, H. Hayashi, K. Heirman, A. Hüpers, M.J. Jurado Rodriguez, K. Kameo, T. Kanamatsu, H. Kitajima, H. Masuda, K. Milliken, R. Mishra, I. Motoyama, K. Olcott, K. Oohashi, K.T. Pickering, S.G. Ramirez, H. Rashid, D. Sawyer, A. Schleicher, Y. Shan, R. Skarbek, I. Song, T. Takeshita, T. Toki, J. Tudge, S. Webb, D.J. Wilson, H.-Y. Wu, and A. Yamaguchi[2]

Chapter contents

Background and objectives

Integrated Ocean Drilling Program (IODP) Site C0002 (proposed Site NT3-01B; Fig. **F1**) is the centerpiece of the Nankai Trough Seismogenic Zone Experiment (NanTroSEIZE) project (Tobin and Kinoshita, 2006). Planned scientific and technical targets for IODP Expedition 338 included collecting logging-while-drilling (LWD), cuttings, and core data in the lower Kumano forearc basin and in the inner wedge of the Nankai accretionary complex and extending riser Hole C0002F to 3600 meters below seafloor (mbsf). This would extend the hole beyond the 20 inch casing point (860 mbsf), which was cemented in place during IODP Expedition 326 in 2010 (Expedition 326 Scientists, 2011) (Fig. **F2**). Riser drilling with the D/V *Chikyu* during Expedition 338 was to sample the interior of the accretionary complex in the midslope region beneath the Kumano forearc basin with both cores and drilling cuttings and to collect an extensive suite of LWD and mud-gas data to characterize the formation. Through the installation of two casing strings (16 inch casing from 860 to 2300 mbsf and 13⅜ inch casing from 2300 to 3600 mbsf), Expedition 338 was to prepare Hole C0002F for deeper drilling expected to reach the megasplay target during the 2014 and 2015 International Ocean Discovery Program riser drilling seasons. Because of weather and current conditions that caused the suspension of riser drilling operations (see below), LWD data and cuttings were only obtained from 860 to 2005 mbsf (Figs. **F2, F3**), and additional riserless coring (200–500, 900–940, and 1100–1120 mbsf) (Fig. **F3**) was completed at Site C0002 as part of contingency operations.

The uppermost 1400 m section at Site C0002 was characterized with a comprehensive LWD program during IODP Expedition 314 (Hole C0002A) (Fig. **F4**) (Expedition 314 Scientists, 2009). The intervals 0–204 and 475–1057 mbsf were cored during IODP Expedition 315 (Holes C0002D and C0002B) (Expedition 315 Scientists, 2009b). The Kumano forearc basin sedimentary package extends from the seafloor to ~940 mbsf and is underlain by the deformed inner wedge of the accretionary package. The seismic reflection character of the entire zone from ~940 mbsf to the megasplay reflection at ~5200 mbsf exhibits virtually no coherent reflections that would indicate intact stratal packages, which is in contrast to the outer accretionary wedge seaward of the megasplay fault system (Fig. **F2;** also see Moore et al., 2009). This seismic character is

[1] Strasser, M., Dugan, B., Kanagawa, K., Moore, G.F., Toczko, S., Maeda, L., Kido, Y., Moe, K.T., Sanada, Y., Esteban, L., Fabbri, O., Geersen, J., Hammerschmidt, S., Hayashi, H., Heirman, K., Hüpers, A., Jurado Rodriguez, M.J., Kameo, K., Kanamatsu, T., Kitajima, H., Masuda, H., Milliken, K., Mishra, R., Motoyama, I., Olcott, K., Oohashi, K., Pickering, K.T., Ramirez, S.G., Rashid, H., Sawyer, D., Schleicher, A., Shan, Y., Skarbek, R., Song, I., Takeshita, T., Toki, T., Tudge, J., Webb, S., Wilson, D.J., Wu, H.-Y., and Yamaguchi, A., 2014. Site C0002. *In* Strasser, M., Dugan, B., Kanagawa, K., Moore, G.F., Toczko, S., Maeda, L., and the Expedition 338 Scientists, *Proc. IODP,* 338: Yokohama (Integrated Ocean Drilling Program). doi:10.2204/iodp.proc.338.103.2014
[2] **Expedition 338 Scientists' addresses.**

thought to indicate complex deformation within the inner wedge of the Nankai accretionary prism.

The primary research objectives for the interval drilled during Expedition 338 were

1. Determination of the composition, age, stratigraphy, and internal style of deformation of the upper forearc basin section, the basin-to-prism transition, and the presumably Miocene accretionary complex;
2. Reconstruction of the accretionary complex's thermal, diagenetic, and metamorphic histories and comparison with present pressure and temperature conditions;
3. Determination of horizontal stress within the deep interior of the inner wedge;
4. Investigation of the mechanical state and behavior of the formation; and
5. Characterization of the overall structural evolution of the Nankai accretionary prism and the current state of the upper plate above the seismogenic plate boundary thrust.

Cuttings and core samples were collected for geomechanical experiments to be completed at inferred in situ conditions, which will help constrain mechanical and hydrological properties of the inner wedge materials. Continuous cuttings analyses provided information on the lithologic constituents and their variation with depth in the inner accretionary wedge. Cuttings help ground-truth properties estimated by LWD. Careful consideration must be made with cuttings, however, as there is known mixing because of the reaming-while-drilling (RWD) process (see **"Operations"**).

Initial riser drilling plans required modification when, because of a newly found risk of riser operations during a quick change in wind direction (e.g., weather front passing) with the fast Kuroshio Current, riser operations were suspended and we were unable to extend Hole C0002F to 3600 mbsf or set any casing strings (see **"Operations"**). The revised operations plan included LWD with cuttings collection from 872.5 to 2005.5 mbsf (Hole C0002F) and riserless coring of the intervals 200–505 mbsf (Holes C0002K and C0002L), 900–940 mbsf (Hole C0002J), and 1100.5–1120 mbsf (Hole C0002H) (Fig. **F3**). Relative locations of all Site C0002 holes are shown in Figure **F4.** This revised plan provided LWD data and cuttings samples from the previously unsampled deeper part of the accretionary prism and core samples across the unresolved unconformity between the Kumano Basin sediment and underlying accretionary prism sediment and across the gas hydrate zone, which was not cored during Expedition 315. Thus, the revised plan enabled us not only to newly explore the inner accretionary wedge to 2005.5 mbsf but also to complement our knowledge of this site.

Operations

Shimizu, Japan, port call

Expedition 338 officially began at 0000 h on 1 October 2012 while the *Chikyu* was north of Izu-Oshima, Japan, as part of the evacuation procedures for Typhoon Jelawat. The evacuation ended at 0400 h on 1 October when the vessel began to return to port call in Shimizu, Japan. Port call began at 0550 h on 2 October, with all loading operations concluded by 2400 h on 3 October. The vessel departed Shimizu, Japan, for Site C0002 at 1035 h on 4 October.

Site C0002

Hole C0002F

Seabed survey and transponder deployment began at 1230 h on 5 October 2012 and were completed on 7 October. After calibrating transponders, the *Chikyu* sailed to the blowout preventer (BOP) and riser running point 20.8 nmi northwest of Site C0002. The BOP and riser joints were set up in the moonpool and prepared for running, which began at 0400 h on 8 October. By 0400 h on 9 October, the BOP reached 490 m drilling depth below rig floor (DRF); however, because of the development of Typhoon Prapiroon, a decision was made to wait on weather (WOW) and to monitor the typhoon track at 0900 h on 9 October; subsequently, BOP and riser recovery began for evacuation standby at 1300 h on 11 October. Recovery was completed at 0600 h on 12 October. The vessel moved 21 nmi northwest of Site C0002 to facilitate the arrival of the first scientists by helicopter transfer on 13 October and to avoid the strengthening current. We continued to monitor developing typhoon tracks and remained in WOW status until 0700 h on 19 October, when preparations to begin running the BOP into the moonpool commenced. Once the BOP was in the moonpool at ~1700 h, BOP pressure tests were run, ending at 1800 h, and the BOP was run into the water. Careful attention was paid to the auxiliary (AUX) line and buoyant riser joints, all the while conducting regular AUX pressure tests (six pressure tests in total). AUX line troubleshooting and buoyancy riser joint replacement was required on 21 October when one joint was replaced.

While running the BOP, several function tests and pressure tests found failures on the AUX line, the conduit line, and the hot line, which were subsequently repaired. The BOP finally landed on the wellhead at 2130 h on 26 October. All function tests, repairs, and maintenance were complete by 1045 h on 29 October. The tests included a pickup test by increasing tensioner tension, slump tests by decreasing drawworks tension, function tests of the diverter, pressure tests of the wellhead connector and the 20 inch casing, function tests of the BOP from both the Blue Pod (driller's control panel) and the Yellow Pod (toolpusher's control panel), a pressure test of the BOP, a pressure test of the BOP with 20 inch casing and inside drill pipe, a function test of the remaining valves in block position, and confirmation of working time and flow rate of the BOP.

The bottom-hole assembly (BHA) for drill-out cement (DOC) was run into the hole at 1900 h on 30 October and tagged the top of the cement/bottom of the hole (842 mbsf) at 1415 h on 31 October. DOC with the 17 inch bit reached 872.5 mbsf, with an extension into the formation (to 875.5 mbsf) to confirm the cement plug was completely drilled through that ended at 2045 h. After DOC was complete, the hole was swept with Hi-Vis mud, then seawater, and then KNPP mud. Methane (15.5%) was found in the drilling mud, and after monitoring, it was decided to move ahead with two leak-off tests (LOTs) of the 20 inch casing shoe starting at ~1100 h on 1 November.

The DOC BHA was recovered and laid down, after which the LWD/measurement-while-drilling (MWD) underreamer BHA (see **"Introduction"** in the "Methods" chapter [Strasser et al., 2014a]) was made up and run into the hole (Table **T1**) and tested at 0430 h on 2 November. All function tests (n = 4: shallow, 50 meters below sea level [mbsl], and 132.5 and 778.5 mbsf) were successfully completed by 0100 h on 3 November, after which drilling began. The BHA was picked up to 905.8 mbsf after drilling ahead to 915.19 mbsf at 0745 h on 4 November to activate the underreamer (total of six attempts made), which took ~2 h.

Drilling with the underreamer BHA began at 1000 h on 4 November. Rate of penetration (ROP) was controlled at 40 m/h from 914.5 mbsf and changed to 20–26 m/h below 923.8 mbsf. Concerns with the large volume of cuttings, more than the waste mud control system could handle, required careful control, sweeping, and sometimes suspension of drilling. Repeat logging was carried out three times using these periods (~30 m/h): uplogging from 1432.40 to 1494.25 mbsf, downlogging from 1480.86 to 1538.77 mbsf, and downlogging from 1557.82 to 1615.58 mbsf. Expected rough weather caused drilling to be suspended at 1538.5 mbsf (2200 h on 5 November), and the BHA was pulled out of the hole above the BOP. Drilling resumed (ROP = 15 m/h) at 2100 h on 6 November but stopped again when 1604.5 mbsf was reached because dispersed sediment was observed coming from one port on the 36 inch conductor pipe with subsequent hydrate accumulation around the wellhead (1230 h on 7 November). Observation for 6 h showed stable flow, so drilling was resumed (ROP = 10–15 m/h) at 2300 h on 7 November. From 1604.5 to 2005.5 mbsf (2300 h on 7 November to 0800 h on 11 November), drilling continued with some interruptions, mainly because of waste mud control system issues (e.g., mud pump problems, screw conveyer for mud transfer issues, and strong currents interfering with supply boats). Drilling was stopped again to standby for rough weather, and the BHA was pulled out of the hole above the BOP at 1515 h on 12 November.

During WOW, a critical function failure of the Double V Shear (DVS) ram (a key component of the BOP designed to close the hole while maintaining annular pressure after the BOP disconnects) was found. It was decided at 0530 h on 13 November to spot cement and suspend the hole until the failure was resolved. Fortunately, the root cause of the failure was determined, and a mitigation plan was enacted for the BOP; therefore, at 0230 h on 14 November, the BOP disconnection plan was canceled. DOC began at 0115 h on 15 November and completed at 1630 h when the DOC BHA was pulled out of the hole to the surface. Subsequently, the underreamer BHA for reaming and enlarging the hole from 12¼ to 20 inches was run into the hole at 0000 h on 16 November. The underreamer was activated at 2848 m DRF at 0300 h; reaming was conducted from 0300 to 2300 h on 16 November. When bit depth reached 3955 m DRF (1990 mbsf) and the underreamer depth and 20 inch hole was at 3949 m DRF (1984 mbsf), an approaching weather system caused another WOW. Reaming and backreaming down to the final bit depth were performed over the next 5 h until the BHA was pulled out of the hole to 1576 m DRF by 1430 h on 17 November after performing backreaming in the hole and spotting with high-viscosity mud. As a standby operation, the kill line was flushed and the DVS ram was closed.

At 1730 h on 17 November, the vessel went into an emergency disconnect because of the high current speed of ~4.5 kt from the west and a sudden change in wind direction and speed (Fig. **F5**), the combination of which forced the vessel 40 m from the well center, and control of the vessel was lost. The emergency disconnect was conducted safely and efficiently and then the vessel drifted 1300 m east of the wellhead at 4 kt. However, while this was happening, the riser pipe hit the hull of the vessel and the intermediate flex joint sustained damage because of significant flexure. Pulling out of the hole to the surface continued, ending at 0415 h on 18 November; whereupon the vessel recovered the remotely operated vehicle (ROV) and moved to the low-current area (LCA) 13 nmi northwest of Hole C0002F to begin riser recovery. The tensioner ring was removed, and electrical cable connections were also removed.

Riser pull out began at 2300 h and termination joints were checked. The diverter was laid out from 0000 h on 19 November, and the riser termination joint was pulled out of the moonpool at 0430 h. The hot line was reterminated in the moonpool, and a pressure check from 1400 to 1800 h confirmed the BOP status was still good. The gooseneck was inspected, including welding points on the slip joint with magnetic particle inspection (MPI) for cracks from 2100 to 0030 h on 20 November. Riser sections continued to be pulled, stopping to perform pressure tests on the choke and kill lines for 3 h from 0315 h. After the intermediate flex joint was pulled up, the termination joint weld was inspected via MPI, whereupon four cracks were found; advice on repair was sought from the manufacturer. The results of careful inspection and manufacturer advice led to the conclusion that the repairs needed could only be conducted on shore; accordingly, it was decided to end riser operations as the time needed for repairs would exceed the planned expedition duration.

Meanwhile, the conduit and kill lines on the gooseneck passed inspection by 2315 h on 21 November after several tests and leakage troubleshooting. Once passed, the gooseneck was removed so that the intermediate flex joint could be installed, finishing at 0600 h on 22 November. Once installed, the gooseneck and choke, booster, and kill moonpool hoses were made up, pressure tested, and installed by 1515 h. The landing and riser joints were also picked up, connected, and lowered to the moonpool, where work began to couple the riser tensioners to the landing ring, finishing by 0330 h on 23 November.

After the ROV was launched, a dummy-landing test 50 m from the well center was conducted successfully at 1730 h, and by 2030 h the lower marine riser package was landed on the lower BOP stack and locked in place. Riser running components were laid down by 0600 h on 24 November. The diverter assembly was made up and run into the hole to 2987 m DRF by 1700 h and then slowly pulled out of the hole to 2878 m DRF. The first cement plug was set at 2200 h and then pulled out of the hole to 2460 m DRF while waiting for cement. At 0445 h on 25 November, the BHA was run into the hole back to 2805 m DRF to confirm the top of cement and to begin the first cement plug pressure test. After confirming the cement plug, the BHA was pulled out of the hole to 2367 m DRF to set the second cement plug, pulled out of the hole to 2120 m DRF, and then pulled out of the hole to the surface by 1745 h.

The Hydralift Power Swivel (HPS) was parked and the riser running tool and riser guide head were installed, finishing at 2245 h. Once complete, the master bushing was removed while the ROV removed the hydrate build-up around the wellhead connector. The diverter and upper flex joint were picked up and laid down by 0400 h on 26 November, whereupon the BOP was disconnected, the wellhead was examined by the ROV, and the ROV was recovered to the surface by 0730 h.

The vessel moved to the LCA ~15 nmi from Hole C0002F and began recovering riser joints and the BOP at 1200 h on 27 November. The intermediate flex joint was recovered at 0200 h on 28 November, after which riser joint and BOP recovery continued. Recovery was briefly halted on 30 November to load the guide horn from the supply boat *Shincho-Maru* and resumed at 1000 h. The riser joints were all recovered and laid down by 0930 h on 1 December, after which the BOP was pulled out to the surface, landed on the BOP cart, and moved to its storage position aft of the moonpool by 1815 h.

Once the BOP was loaded on the cart, the HPS was rigged up again, and the vessel returned to Site C0002, arriving at 0630 h on 1 December. At Site C0002, the ROV dove at 0745 h, and the vessel shifted to the Hole C0002G long-term borehole monitoring system (LTBMS) so that the ROV could inspect the LTBMS. The vessel shifted back to Hole C0002F, and the ROV set the corrosion cap and checked the bull's eyes, finishing by 1145 h. Once complete, the ROV began recovering and deploying transponders; 4 transponders were deployed and 10 were recovered, all completed by 0330 h on 2 December. The lower and middle guide horn sections were set on the BOP cart and connected by 0415 h; once connected, the vessel moved to Site C0012.

Hole C0002H

On 8 December 2012 at 0130 h, the ship moved 7 nmi north-northwest of Hole C0002H after preparations for coring began with the make up of the rotary core barrel (RCB) BHA. A short WOW period lasted until 1600 h, after which the vessel moved to within 5 nmi west of the well center. Drifting in began at 1800 h while the BHA was run into the hole, with a 1 h standby as an internal BOP ball valve malfunction was resolved. We continued to drift in to the well center, dropping the center bit at 0300 h on 9 December. The seafloor was tagged and confirmed at 1965 m DRF (1936.5 mbsl) at 0345 h, as indicated by an increase in weight on bit (WOB). We washed down the first 36 m then began drilling a 10⅝ inch hole at 0430 h, reaching 752 mbsf by 2000 h. The sinker bar was run down to recover the center bit for a wear check at 2145 h and dropped again at 2330 h, landing 13 min later. We then drilled to 1055 mbsf by 0730 h on 10 December. After a series of sweeping out the hole, drilling ahead, and sweeping again, the sinker bar was run at 1100 mbsf to recover the center bit in preparation for dropping the inner core barrel. At 1430 h, coring began, advancing 9.5 m to 1110 mbsf with recovery on deck at 1545 h. The BHA was stuck for the next 45 min, but after working and sweeping, the core barrel was dropped at 1845 h for the next coring advance. Coring to 1120 mbsf (9.5 m coring advance) began and the core barrel was recovered on deck at 2105 h. After the core barrel was recovered, the drill pipe was stuck in the hole again, but constant work freed the pipe at 0145 h on 11 December. The BHA was pulled out of the hole with reaming and laid down on deck by 0715 h. No obvious overpull or packoff indication was seen on the drill string, so preparations to return to RCB coring began. The vessel was moved 2 nmi from Hole C0002I for preparation for running the RCB BHA into Hole C0002I.

Hole C0002I

Hole C0002I operations began with drifting in at 1100 h on 11 December 2012 and dropping the center bit at 1630 h prior to spudding in at 1964.5 m DRF (1936 mbsl) 9 min later. The first 33.5 m was washed down and drilling ahead began from 1800 h, reaching 818.5 mbsf at 0600 h on 12 December. Another series of drilling ahead, sweeping, and hole cleaning began once past 905 mbsf. On 13 December, the bit reached 1360 mbsf at 0430 h, continuing until 0445 h on 13 December, when the 4S azimuth thruster shut down and dynamic positioning (DP) status changed to "yellow." Once this occurred, the BHA was pulled out of the hole to 900 mbsf in preparation for emergency pulling out of the hole to the seafloor. The 4S azimuth thruster was restarted at 0600 h, and DP status returned to "green." Circulation and hole cleaning began once green DP status was established and drilling back to 1105.5 mbsf began.

Drilling stopped at 1005 mbsf, whereupon the BHA became stuck at 1030 h on 13 December. Operations to free the stuck pipe began immediately. Attempts to recover the center bit at 1400 h on 14 December were unsuccessful; therefore, rig up of the Schlumberger wireline tool, the Free-Point Indicator Tool (FPIT), began at 1645 h. The stuck position was confirmed at 853 and 915 mbsf, after which the FPIT was rigged down for running the colliding tool to free the drill pipe at 0300 h on 15 December. The colliding tool was set and the explosive primed at 0700 h, when operations to install the colliding tool were suspended because of bad weather conditions, specifically high winds. The lower connection of the drill pipe on the rig floor was broken to run the colliding tool directly from the rig floor by 0745 h when the Schlumberger wireline winch failed. Troubleshooting began immediately and finished at 2130 h. The colliding tool was rigged up and the explosive was reset by 2315 h. The tool was run at 0300 h on 16 December, and the drill pipe was cut at 0345 h. The colliding tool was rigged down by 0515 h, and pulling out of the hole began. After the tools were laid down, the *Chikyu* moved to the LCA to load equipment and to perform maintenance on the HPS top drive, ending on 17 December. After pressure tests confirmed the integrity of the HPS repairs, we began making up and testing the RCB BHA for Hole C0002J.

Hole C0002J

The vessel moved to a position 3 nmi west of Hole C0002J, while the RCB BHA was made up and run into the hole from 1830 h on 17 December 2012. Spudding in Hole C0002J was confirmed at 1966 m DRF (1937.5 mbsl) at 0830 h on 18 December. The BHA was immediately jetted to 35 mbsf before drilling began. By 2330 h, the bit reached 872.5 mbsf before stopping to space out a single joint. Drilling continued until reaching 902 mbsf at 0045 h on 19 December. After sweeping out the hole, coring began at 0430 h. A total of seven RCB cores were collected, finishing at a total depth (TD) of 940 mbsf at 1930 h. Once coring was completed, kill mud was spotted and the RCB BHA was pulled out of the hole to the surface, and tool lay down was completed by 0545 h on 20 December. The vessel moved upstream 2 nmi to Hole C0002K and began preparations for coring in Hole C0002K.

Hole C0002K

Preparations for hydraulic piston coring system (HPCS)/extended shoe coring system (ESCS) coring started at 0545 h on 20 December 2012, and the BHA was run into the hole to 1966 m DRF (estimated water depth = 1937.5 mbsl) by 1645 h. The 11⁷⁄₁₆ inch BHA washed down the first 30 mbsf by 1700 h and then began drilling ahead to 200 mbsf. At 2230 h, coring began with the HPCS, ending after reaching 205.5 mbsf because of technical considerations. Switching to the extended punch coring system (EPCS) was completed by 0215 h on 21 December; four cores from 205.5 to 239 mbsf were cut by the EPCS. The low recovery of the last EPCS cores (n = 2) caused the switch to the ESCS from 239 mbsf. Five ESCS cores were collected from 239 to 286.5 mbsf, and the last core was cut at 2315 h on 21 December.

Once coring was completed, the ESCS BHA was pulled out of the hole to 1780 m DRF by 0100 h on 22 December. Two stands of S-150 drill pipe were added, and then the BHA was run down to 1800 m DRF to WOW from 0300 to 0830 h on 22 December. Once the cold front had passed, the *Chikyu* was shifted to the Hole C0002L well center for more coring.

Hole C0002L

The ESCS BHA was run down from 1800 to 1960 m DRF by 1030 h, just above the seafloor. Spudding in Hole C0002L began at 1045 h (water depth = 1937.5 mbsl) and washing down proceeded to 42 mbsf, after which drilling to 277 mbsf was completed by 1830 h. ESCS coring began at 277 mbsf at 2000 h on 22 December 2012. Coring finished at a TD of 505.0 mbsf at 0215 h on 25 December. Once coring operations were completed, 35 m^3 of kill mud was spotted in the hole and the BHA was pulled out of the hole to 1932 m DRF (above the seabed) by 0400 h. The BHA was laid down by 1030 h, after which the transponders were released and recovered (by 1230 h) by the watch boat, ending Hole C0002L operations. The *Chikyu* shifted to 2 nmi upstream of Site C0018 in preparation for LWD drilling.

Logging while drilling

Log data acquisition and quality control

LWD data, including gamma ray, azimuthal resistivity, resistivity images, and sonic slowness, were collected from 852.33 to 2005.5 mbsf (2819.83 to 3973.00 m DRF) in Hole C0002F (Table T2). MWD data were also collected. Details of the tool configurations and parameters of acquisition are provided in "Logging while drilling" in the "Methods" chapter (Strasser et al., 2014a).

Data acquisition

During LWD acquisition, the target ROP was <35 m/h but >10 m/h to optimize data acquisition and quality. The ROP was close to 35 m/h until ~1006 mbsf, below which it dropped to an average of ~20 m/h (Fig. F6). The ROP decreased to an average of ~12 m/h at 1483 mbsf and a low ROP of ~5 m/h was maintained between 1835 and 2005.5 mbsf. Three sections were relogged while reaming: 1432.40–1494.25 mbsf (ream Up 1); 1480.86–1538.77 mbsf (ream Down 2); and 1557.82–1615.58 mbsf (ream Down 3).

Annular temperature and pressure were monitored for safety analysis and to understand downhole conditions. Annular temperature increased with depth from 20° to 30°C (Fig. F6). Annular temperature has many negative spikes of ~1°C, only some of which correlate with changes in the other MWD logs. Annular pressure increased from 31,143 to 44,353 kPa from the top of the logged section to the bottom. WOB stayed fairly constant from 20 to 45 kN to 1500 mbsf. Between 1500 and 1550 mbsf, WOB markedly increased with peaks higher than 100 kN. From 1600 to 1835 mbsf, WOB increased, reaching maximum values of 179.5 kN. Downhole torque was relatively constant (1–4 kN·m) with one excursion where it increased to a maximum of 8.6 kN·m at ~1635.5 mbsf near the logging Unit IV/V boundary.

Data quality

Real-time drilling parameters and log responses were monitored for any indications of poor borehole conditions or degraded tool quality. The quality of the original data was also assessed by comparison with three repeat sections (see "Analysis of relogged sections").

The overall quality of the processed logging data is good, although the effects of heave, stick-slip, and drilling corkscrew are present and cannot be removed by data processing. Drilling corkscrew can be recognized from the resistivity images in the following intervals: 892–907, 923–932, 1087–1097, 1241–1250, and 1485–1492 mbsf. Irregular changes in borehole diameter, potentially due to cave-ins and preferential erosion of the borehole wall, could also have reduced data quality; however, this cannot be quantified, as direct caliper data were not collected. Future analyses of the resistivity log data may provide additional constraints on borehole diameter.

The Schlumberger engineers applied a correction of –2.18% to the gamma ray data because the drilling mud was potassium rich. Quality checks on the sonic data indicate good performance of the tool and good quality of the measurements. No shear wave velocities were picked, as formation shear velocities lower than the compressional velocity of the drilling mud cannot be independently determined from the recorded waveform data.

Additional impacts on data quality arose from delays in drilling (e.g., during WOW or cuttings backlog). Long off-bottom times might have disturbed the log quality (e.g., resistivity influenced by invasion features) or borehole environment (e.g., change in annular pressure). In order to evaluate these effects, depths when the bit was off bottom and the duration of time off bottom were extracted from the time series data (Fig. F6; Table T3).

Logging units and lithostratigraphy

LWD data were used to investigate and to interpret the geological, petrophysical, and geomechanical properties of the section drilled in Hole C0002F to provide an initial interpretation of

- Lithologic and sedimentological features,
- Structural features, and
- Geomechanical and physical properties.

The upper 872.5 m of Hole C0002F was drilled and cased during Expedition 326, and the sediment of this interval is assumed to be consistent with the sediment observed in Hole C0002A (logging Units I–III; Expedition 314 Scientists, 2009) (Fig. **F7**). The first unit encountered in Hole C0002F was therefore identified as logging Unit III. A gamma ray baseline value of 75 gAPI was used as a reference to define sand-bearing zones (gamma ray values < 75 gAPI) and clay-rich zones (gamma ray values > 75 gAPI). The sonic log can be used to indicate variations in bulk lithology and was used in conjunction with gamma ray and resistivity data to help identify logging units and subunits. Overall, three logging units (III, IV, and V) were defined based on changes in the character and trends of gamma ray, resistivity, and sonic velocity logs (Fig. **F8**). In addition, five subunits were identified in logging Unit IV and two subunits were identified in logging Unit V (Table **T4;** Fig. **F8**).

Unit III (875.5–918.5 mbsf)

Analysis of logging Unit III during Expedition 338 was complicated by the presence of cement cuttings generated while drilling out the cement plug emplaced during Expedition 326. Although the bottom of the cement plug emplaced during Expedition 326 was at 872.5 mbsf, the interpretation of the top of Unit III was complicated by operations in the hole (e.g., DOC and LOTs) prior to drilling forward into the formation during primary drilling and LWD operations. Thus, the top of Unit III is not clearly established in LWD data until 875.5 mbsf. Logging Unit III is characterized by relatively consistent responses in gamma ray values (~75 gAPI), resistivity (~1.4 Ωm), and sonic slowness (~134.6 µs/ft) (Fig. **F8**). Gamma ray values fluctuate around the 75 gAPI baseline and are interpreted to represent alternating thin (<2 m) clay-rich layers interbedded with thin silty to sandy layers. The shallow, medium, and deep resistivity logs are coincident, suggesting little-to-no mud invasion into the formation. The lack of mud invasion could indicate a low-permeability formation or balanced conditions in the hole.

The base of logging Unit III (918.5 mbsf) is defined where gamma ray values drop from ~79 to ~68 gAPI and slowness increases from ~130 to ~142 µs/ft. This is interpreted as a subtle compositional change from silty clay–dominated hemipelagic sediment (gamma ray values > 75 gAPI) to sand-bearing hemipelagic sediment (gamma ray values < 75 gAPI). In LWD Holes C0002A and C0002G, the logging Unit III/IV boundary is also placed where a clear change in lithology from clay to sand is observed (Expedition 314 Scientists, 2009; Expedition 332 Scientists, 2011).

In Hole C0002A, the Unit III/IV boundary is interpreted as an angular unconformity (Expedition 314 Scientists, 2009). Changes in bedding dip angle and direction across the logging Unit III/IV boundary in Hole C0002F support this interpretation (Fig. **F8**).

Unit IV (918.5–1638.0 mbsf)

Gamma ray, resistivity, and sonic slowness data exhibit more variability in logging Unit IV than in the other logging units and allow definition of five subunits (Table **T4;** Fig. **F8**).

Immediately below the logging Unit III/IV boundary, gamma ray values gradually increase from 68 to 86 gAPI with a corresponding decrease in resistivity (1.4–1.2 Ωm) and an increase in sonic slowness (130–142 µs/ft). At 932.4 mbsf, the gamma ray log reaches 89 gAPI and fluctuates (±20 gAPI) around this value through logging Subunit IVA (918.5–1033 mbsf). Prominent lows in gamma ray values occur at 984.5, 1003.0, and 1031.0 mbsf (59, 58, and 55 gAPI, respectively) (Fig. **F8**). From 929.0 to 962.5 mbsf, resistivity gradually increases to 1.7 Ωm with two prominent spikes at 962.1 and 975.4 mbsf (2.49 and 2.18 Ωm, respectively). Over the same depth interval, the slowness decreases from 139 to 117 µs/ft and then remains fairly constant at ~130 µs/ft to 989.0 mbsf; slowness then sharply increases to 136 µs/ft for ~30 m before returning to ~130 µs/ft. At 962.5 mbsf, resistivity decreases gradually to 1.4 Ωm at 992.5 mbsf before increasing to ~2.1 Ωm, with some high-value spikes, and reaching a local high of 3.4 Ωm at 1031.5 mbsf, which corresponds to a sharp drop in gamma ray values from 78 to 59 gAPI. This marks the basal boundary of logging Subunit IVA.

Between 1033.0 and 1080.0 mbsf (logging Subunit IVB), gamma ray values are generally >75 gAPI and resistivity remains relatively constant with minor fluctuations around 1.5–1.7 Ωm (Fig. **F8**). Through this subunit, sonic slowness has repeated gradual increases and sharp decreases to 1075 mbsf, where it fluctuates around ~125 µs/ft. A sharp resistivity spike at 1100 mbsf to ~2.4 Ωm marks the base of logging Subunit IVB.

Logging Subunit IVC (1100.0–1348.0 mbsf) exhibits large variations in slowness and resistivity with only minor variations in gamma radiation compared to the rest of logging Unit IV (Fig. F8). With the exception of a broad gamma ray low (~60 gAPI) and downhole decrease from 1109.7 to 1134.7 mbsf, gamma ray values fluctuate (±25–30 gAPI) around ~85 gAPI. Resistivity shows a series of step changes through this subunit. The resistivity log exhibits minor fluctuations around 1.7 Ωm and then increases to ~2.1 Ωm at 1153.4 mbsf before gradually decreasing to 1.7 Ωm at 1212.5 mbsf. Resistivity shows another step increase at 1212.5 mbsf to 2.8 Ωm, which is maintained until a drop at 1291 mbsf and a gradual decrease to the base of the subunit. Three prominent thin (<5 m) resistivity spikes are observed at 1213 mbsf (2.4 Ωm), 1232 mbsf (2.8 Ωm), and 1249.3 mbsf (3.05 Ωm). The spikes at 1232 and 1249.3 mbsf correlate with low spikes in slowness (125 and 98.2 µs/ft). There is also a corresponding sharp increase in the slowness at 1291 mbsf to 120 µs/ft, and slowness then remains constant to the base of the subunit (1348.0 mbsf).

At the logging Subunit IVC/IVD boundary, resistivity increases from 2.0 to 2.7 Ωm and slowness sharply decreases from 120 to 105 µs/ft. These correlate with a change in gamma ray values from 65 to 85 gAPI, and there is also a reversal in dip direction (see "Structural image analysis") (Fig. F8). Through logging Subunit IVD (1348.0–1500.0 mbsf), gamma ray values exhibit a series of alternating thick lows (~65 gAPI) and thin highs (95 gAPI), which are interpreted as interbedded sandstones and mudstones up to 5 m thick. Through logging Subunit IVD, slowness remains fairly constant with only minor fluctuations (±15 µs/ft) around an average of 103 µs/ft. The resistivity log exhibits an increasing and decreasing cycle from 1348 to 1431 mbsf, where it drops to ~2.2 Ωm and begins a gradually increasing trend with minor fluctuations. This increasing trend in resistivity continues through logging Subunit IVE to the base of logging Unit IV.

A sharp increase in gamma ray values to ~98 gAPI and a decrease in slowness from 107 to 94 µs/ft at 1500.0 mbsf marks the top of logging Subunit IVE (Fig. F8; Table T4). Through logging Subunit IVE, slowness gradually decreases from 107 to 82 µs/ft with only minor fluctuations. The upper ~10 m of Subunit IVE exhibits consistently high gamma ray values near 95 gAPI, and from 1512.9 to 1638.0 mbsf, the gamma ray log exhibits repeated, small-scale, increasing–decreasing cycles. Resistivity gradually increases through logging Subunit IVE but with increasingly prominent high-value spikes. The most prominent spike occurs at 1603.3 mbsf, where resistivity reaches 4.0 Ωm before dropping sharply back to 3.1 Ωm and continuing to gradually increase to the base of the subunit. At 1634.2 mbsf, resistivity reaches a maximum of 4.8 Ωm before sharply dropping back to 2.7 Ωm at 1638.0 mbsf. Also at 1638.0 mbsf, slowness sharply increases from 82 to 99 µs/ft and gamma ray values sharply increase from 72 to 95 gAPI. This prominent change in all the logs defines the logging Unit IV/V boundary.

Overall, logging Unit IV is characterized by alternating layers of thick sand-rich and clay-rich packages (lower to higher gamma ray values) with increasing compaction downhole. The resistivity images of these sand-rich packages, which range in thickness from 0.5 to 1 m, indicate that they are conductive (dark) and therefore permeable.

Unit V (1638.0–2005.5 mbsf)

Logging Unit V exhibits the least variability of the section logged during Expedition 338, especially in gamma ray values and slowness (Fig. F8). Variations in the resistivity data are used to define two subunits (Table T4). The gamma ray data start at ~95 gAPI at 1638.0 mbsf and have an overall gradual increase to 102 gAPI at 1946.0 mbsf. Below this, gamma ray values stay almost constant with small variations. Slowness maintains a near-constant value, with minor fluctuations (±10 µs/ft), through logging Unit V. There is a small change in slowness of 10 µs/ft at 1946.0 mbsf, the logging Subunit VA/VB boundary (Fig. F8). Through logging Subunit VA (1638.0–1946.0 mbsf), the resistivity log exhibits a series of increasing and decreasing cycles around 2.2 Ωm, with several prominent spikes. At 1752.6, 1778.0, 1795.0, and 1829.6 mbsf, resistivity drops to 1.8, 1.6, 1.8, and 2.2 Ωm, respectively. At 1946.0 mbsf, resistivity sharply decreases from 2.4 to 2.0 Ωm, marking the logging Subunit VA/VB boundary. Below 1946.0 mbsf, resistivity gradually increases, with only minor fluctuations, to 2.5 Ωm at the base of the hole.

Overall, logging Unit V is interpreted as a homogeneous clay-rich section, based on the overall gamma ray values (>95 gAPI) and low variability. The mottled appearance on resistivity images (Fig. F9C, F9D) could be caused by local disturbance to the layering and/or the presence of conductive minerals (possibly pyrite, see "Lithology").

Structural image analysis

In Hole C0002F, the main structural features were identified from the azimuthal resistivity images. Large-scale features are most clearly observed in the static images, whereas smaller scale features are highlighted in the dynamic images. In the absence of a direct caliper measurement, the bit diameter was used as the borehole diameter and assumed to be constant.

Bedding, fractures, faults, and folds were picked and structural zones were defined on the basis of interpreted faults, folds, and fracture zones (Table T5). Fractures were classified as conductive, resistive, or undefined based on the relative contrast with the resistivity of the surrounding formation (Fig. F10). In areas where the resistivity images were of poor quality (see "Data quality"), fracture picking was not possible. A summary of the total fracture counts for the hole and logging units is shown in Table T5.

Folds were defined as locations in the borehole where a change in bedding and fracture orientation was observed in the resistivity images (Fig. F8; Table T5). In some instances, the fold can be seen in the images, as demonstrated in Figure F9A, but the bedding dips also change in areas with poor image quality, preventing the actual fold hinge itself from being observed.

Bedding and fractures

Overall, bedding is high angle (~30°–80°) and exhibits variability with depth and with logging units (Fig. F8). Because of poor image quality in logging Unit III, very few bedding planes can be identified; those that can be identified dip <30° toward the southeast. Across the logging Unit III/IV boundary at 918.5 mbsf, a change in bedding dip is observed: dips are higher angle (>50°) and beds predominantly dip toward the southeast. This change in dip angle is interpreted as an angular unconformity.

Within logging Unit IV another bedding dip reversal is observed at the logging Subunit IVC/IVD boundary (Fig. F8), switching from dominantly southeast dipping above to northwest dipping below. In addition, several folds are identified within logging Unit IV (Table T5). At 1099, 1281, and 1648 mbsf, the folds can be clearly seen, and an intensely folded zone exists from 1500 to 1550 mbsf. In addition, strong changes in dip are present around 1063 and 1682 mbsf, although the areas immediately around the potential fold hinges are not clearly imaged.

There is no observed change in bedding dip direction across the logging Unit IV/V boundary, where beds dominantly dip toward the northwest (Fig. F8). However, within logging Unit V, bedding gradually decreases in angle (from >70° to <40°) with depth. Below ~1850 mbsf, no bedding planes can be identified clearly.

Fractures exhibit more variability in terms of dip angle and direction than bedding (Fig. F8). In general, high-angle fractures (60°–80°) dominate with bimodal dip direction to the northwest and southeast. Almost no low-angle fractures are observed, with the exception of two intervals: ~1090–1125 and ~1740–1800 mbsf, where dips range between ~30° and 50° (Fig. F10).

Because of poor image quality, no fractures could be identified above 918.5 mbsf. The variation of fracture dip orientation and angle between logging Units IV and V as well as within the subunits is summarized in Figure F10. Logging Unit IV is dominated by resistive fractures, which are concentrated in logging Subunits IVC and IVE and exhibit a bimodal distribution, dipping to the northwest and southeast. The increase in resistive fractures observed in logging Subunit IVE could be related to the increase in carbonate veins identified from cuttings (see "Structural geology"). A probable fault exists at 1360 mbsf, coinciding with a high-angle fracture that dips to the northwest (Fig. F10; Table T5).

Another fault is interpreted at the logging Unit IV/V boundary (1638 mbsf), but the image quality immediately above this boundary is poor, making it hard to distinguish fractures from bedding. Within logging Unit V there is an increase in the occurrence of conductive fractures (Fig. F10), although the low image quality throughout this section makes it difficult to confidently identify bedding or fractures. The observed fractures maintain the bimodal northwest–southeast dip direction, and there is no differentiation in dip direction between the conductive and resistive fractures.

Fracture dip changes from southeast above to northwest below the fold identified at 1682 mbsf, although the fold hinge itself is not immediately surrounded by any visible fractures. A concentration of high-angle conductive fractures around 1946.0 mbsf corresponds to the logging Subunit VA/VB boundary (Fig. F10). Despite deteriorating image quality, several lower angle (32°–45°) resistive fractures are observed in logging Subunit IVB, exhibiting a dominant southward dip direction.

Borehole breakouts and drilling-induced tensile fractures

In Hole C0002F, intervals with clear evidence for breakouts are sparse. Borehole breakouts occur only in three narrow depth ranges of 0.25–1 m around 916.0, 1617.0, and 1861.5 mbsf (Fig. F11) and are 34°–63° wide (Fig. F12). An example of a well-developed breakout from 1861.5 to 1862.5 mbsf is shown in Figure F13. Each of these depths is associated with significant time off bottom and an associated decrease in equivalent circulating density (ECD) (Fig. F6). A drop in ECD indicates a decrease in annular pressure in the borehole, which could lead to the initiation of borehole breakouts as stress at the borehole wall exceeds the formation strength. Drilling-induced tensile fractures (DITFs) were more common (Fig. F11) but were not continuous. This could be due to bad data coverage, localized changes in mechanical properties, or, less likely, localized changes in far-field stress. Examples of DITFs are shown in Figure F14.

In contrast to Hole C0002F, Hole C0002A was drilled and logged in riserless mode to 1401 mbsf (Expedition 314 Scientists, 2009). Based on interpretation of resistivity images, Hole C0002A contained numerous well-developed breakouts and few DITFs throughout the entire section, including the portion overlapping with Hole C0002F (~875–1400 mbsf) (Fig. F15). In both holes, breakouts indicate that the maximum horizontal compressive stress (S_{HMAX}) is trench-parallel. The difference in breakout and DITF abundance in Holes C0002F and C0002A is probably due to differences in annular pressure because Hole C0002F was drilled as a riser hole (mud-controlled pressure) and Hole C0002A was drilled as a riserless hole (hydrostatic pressure). Borehole breakouts and DITFs are controlled largely by hoop stress (see the "Methods" chapter [Strasser et al., 2014a]), and increasing annular pressure through mud control (i.e., riser drilling) makes breakout initiation less likely and DITFs more likely.

Physical properties

Changes in resistivity logs can reflect changes in formation porosity, as formations containing more fluid in pore space are less resistive and can also reflect changes in fluid type. Separation of resistivity at the bit (RAB) and shallow, medium, and deep button resistivity can be a result of mud invasion into the formation and therefore indicate formation permeability (Ellis and Singer, 2007). Analysis of resistivity logging data was complicated by operations in Hole C0002F, as the generation of large volumes of cuttings required frequent 10–60 min periods of hole cleaning and circulation (Table T3; Fig. F6). In addition, low ROP increased the amount of time for mud invasion to occur between when RAB and button resistivity tools passed through formation.

Porosity and bulk density from resistivity logs

In the absence of direct measurements using a neutron density tool, porosity and bulk density can be calculated from RAB (see "Logging while drilling" in the "Methods" chapter [Strasser et al., 2014a]). Resistivity-derived porosity and bulk density (Fig. F16) were used to evaluate relative change in lithology, compaction, and deformation.

Resistivity-derived porosity generally decreases with increasing depth. A significant decrease occurs below the logging Unit III/IV boundary moving from the Kumano Basin into the accretionary prism, and in logging Subunits IVD and IVE, the porosity is lower than the surrounding subunits. A slight increase in porosity occurs at the logging Subunit VA/VB boundary.

Resistivity-derived bulk density increases with depth (Fig. F16). At 1550 mbsf within logging Subunit IVE, there is a step increase in resistivity-derived bulk density that is caused by a change in the grain density (from 2.516 g/cm³ above to 2.662 g/cm³ below) used to calculate the bulk density.

Analysis of relogged sections

Frequent off-bottom periods during drilling (Table T3; Fig. F6) provided an opportunity to relog portions of the borehole between the bit and underreamer assembly. Relogging provided the opportunity to improve data quality because stick-slip is reduced while reaming up and down and to examine time evolution of borehole breakouts in resistivity images. Three intervals were relogged: 1432.40–1494.63 (ream up), 1480.86–1538.48 (ream down), and 1557.82–1615.47 mbsf (ream down). Whereas the intervals covering 1432.40–1494.63 and 1480.86–1538.48 mbsf show no evidence of borehole breakouts in resistivity images, the 1557.82–1615.47 mbsf relogged section indicates areas with breakouts ranging from 0.5 to 1.5 m high and 35°–123° wide. No breakouts were imaged in the original run over the intervals 1594–1601, 1587–1592.5, and 1607–1613 mbsf, yet there appear to be breakouts in the same intervals during the ream down (Fig. F17). It is not clear whether this is due to differences in data quality, changes in annular pressure during off-bottom periods, or development of breakouts over time.

Lithology

Hole C0002F

Based on integration of data available from cuttings and LWD, we identified three lithologic units and five subunits in Hole C0002F (Fig. F18; Table T6), differentiated using geological, geophysical, and geochemical characteristics, as described in "Lithology" in the "Methods" chapter (Strasser et al., 2014a).

The lithologic unit and subunit boundaries are defined primarily using the percent sandstone versus percent silty claystone supplemented by the quartz index (Q-index) (Figs. F18, F19, F20, F21, F22; Tables T6, T7, T8). Figures F23, F24, F25, and F26 show representative lithologies and rock components as seen in rock chips and smear slides.

Between ~875.5 and 890.5 mbsf (Samples 338-C0002F-1-SMW though 14-SMW), cuttings consisted of 100% fragments of cement derived from the earlier well completion (Expedition 326) and no lithology was observed (Fig. F18). The first observations of formation in cuttings were present at 890.5 mbsf (Sample 338-C0002F-14-SMW). However, although formation cuttings were present from 890.5 to 930.5 mbsf (Samples 14-SMW through 22-SMW), cement remained the dominant constituent in the cuttings mix. From 930.5 to 965.5 mbsf (Samples 22-SMW through 30-SMW), there is a progressive increase in the proportion of formation relative to cement, up to 100% silty claystone. See "Physical properties" for a more detailed description of cement contamination and cuttings.

Lithologic Unit III (lower part of Kumano forearc basin)

Interval: cuttings Samples 338-C0002F-7-SMW to 45-SMW

Depth: ~875.5–1025.5 mbsf

Lithology: greenish gray silty claystone

Hole C0002F drilling began within lithologic Unit III below the previously cemented 20 inch casing shoe at ~860 mbsf (Sample 338-C0002F-1-SMW). The base of lithologic Unit III was previously defined at 918.5 mbsf from LWD data (see "Logging while drilling") and by core and seismic integration in Hole C0002B (Expedition 315 Scientists, 2009b; including detailed descriptions and interpretations). The lithologic boundary in Hole C0002F is identified at 1025.5 mbsf (Sample 45-SMW) (Table T6) with the first occurrence of sand and changes in mineralogy.

Within the upper part of lithologic Unit III in Hole C0002F, ~70%–90% of the sampled cuttings consist of cement. As previously mentioned, samples contain 100% cement above 890.5 mbsf (Sample 14-SMW), which is consistent with other shipboard data (e.g., see "Physical properties" and discussion about mixing of cement). In cuttings from the formation, the lithology is greenish gray silty claystone (Figs. F18, F19). Locally, trace amounts of loose sand occur, some of which could also be disaggregated cement pieces. The silty claystone is semi-indurated (compact, but mechanically weak). In terms of accessory mineralogy (Fig. F20), glauconite grains are present (Fig. F23B–F23D) and fossils are absent to rare and some are pyritized (Fig. F25F).

Lithologic Unit IV (upper accretionary prism)

Interval: cuttings Samples 338-C0002F-45-SMW to 215-SMW

Depth: 1025.5–1740.5 mbsf

Lithology: dominant—greenish gray silty claystone; minor—sandstone

In Hole C0002B (Expedition 315 Scientists, 2009b), the lithologic Unit III/IV boundary is defined by an abrupt change in structural style and a shift in lithology from condensed silty claystone above to underlying interbeds of silty claystone, siltstone, and sandstone. In Hole C0002F, the lithologic Unit III/IV boundary is defined by the first occurrence of sandstone, albeit in very small amounts at 1025.5 mbsf (Sample 338-C0002F-45-SMW). In general, the macroscopic observation of cuttings was difficult because of the mixing of cuttings caused by the underreamer (see "Lithologic Unit III (lower part of Kumano forearc basin)" and "Physical properties"). Based on calcite mineralogy analyzed by X-ray diffraction (XRD), the boundary is smeared by ~50–70 m because of simultaneous cutting by the bit and the underreamer (see "X-ray diffraction mineralogy" and "Operations").

Within lithologic Unit IV, five subunits are defined on the basis of the occurrence of sandstone (Fig. F18; Table T6). These subunits are characterized by increasing and decreasing sand content:

- Lithologic Subunit IVA: 1025.5–1140.5 mbsf (Samples 338-C0002F-45-SMW to 71-SMW).
- Lithologic Subunit IVB: 1140.5–1270.5 mbsf (Samples 71-SMW to 100-SMW).
- Lithologic Subunit IVC: 1270.5–1420.5 mbsf (Samples 100-SMW to 134-SMW).
- Lithologic Subunit IVD: 1420.5–1600.5 mbsf (Samples 134-SMW to 182-SMW).
- Lithologic Subunit IVE: 1600.5–1740.5 mbsf (Samples 182-SMW to 215-SMW).

The dominant lithology in the subunits is greenish gray silty claystone with sandstone as a minor lithology (Figs. F18, F19). The silty claystone is semi-indurated, and the cuttings shape is subangular to angular (Table T7). Sandstone cuttings are generally loose or very weakly indurated (i.e., soft). Their typical shape is rounded. Loose quartz grains are the dominant component in the dispersed >63 µm sand-size fraction.

In lithologic Unit IV, the Q-index shows overall increased grain sizes compared with the surrounding lithologic Units III and V, ranging from ~700 to 1800 µm in diameter (Fig. F22). At 1485.5 mbsf (Sample 338-C0002F-148-SMW), the Q-index shifts to higher values, with an average of ~1300 µm, and also shows greater fluctuations when compared with surrounding units.

The main mineralogy in lithologic Subunit IVA can be summarized as follows (Fig. F20):

Quartz = dominant.
Feldspar = few.
Lithic fragments = few to common.
Mica = absent.
Volcanic glass = rare to common (but mostly as a few grains).
Pyrite = common.
Organics (including wood) = common.
Fossils = rare.

Smear slides show the high-temperature metamorphic mineral corundum at 1125.5 mbsf (Sample 338-C0002F-66-SMW) (Fig. F25A, F25B). Corundum is characteristic of contact-metamorphism of limestones and metamorphosed shales (e.g., schists). In lithologic Subunit IVA, the Q-index increases then decreases, in general showing relatively small grain sizes between 200 and 1200 µm (Fig. F22).

In lithologic Subunit IVB (1140.5–1270.5 mbsf; Samples 338-C0002F-71-SMW to 100-SMW), the major lithology is greenish gray silty claystone (average ~70%). In lithologic Subunit IVC (1270.5–1420.5 mbsf; Samples 100-SMW to 134-SMW), the major lithology is greenish gray silty claystone (average ~70%). In lithologic Subunit IVD (1420.5–1600.5 mbsf; Samples 134-SMW to 182-SMW), the major lithology is greenish gray silty claystone (average ~65%). In lithologic Subunit IVE (1600.5–1740.5 mbsf; Samples 182-SMW to 215-SMW), the major lithology is greenish gray silty claystone, showing a progressive increase in amount with depth (average ~70%). In comparison to the overlying units and subunits, the sandstone in lithologic Subunit IVE appears to be more indurated.

The mineralogy of lithologic Subunits IVB–IVE for the >63 µm sieved size fraction can be summarized as follows (Fig. F20; see Site C0002 smear slides in "Core descriptions"):

- Quartz is the dominant mineral.
- Feldspar increases from lithologic Subunit IVB (few) through lithologic Subunits IVC and IVD to lithologic Subunit IVE (common and locally abundant).
- Lithic fragments decrease from lithologic Subunit IVB (common) to lithologic Subunit IVE (few).
- Mica occurs only in lithologic Subunit IVE (few).
- Volcanic glass decreases from few to rare in lithologic Subunit IVB, few in lithologic Subunits IVC and IVD, and rare in lithologic Subunit IVE.
- Pyrite decreases from few in lithologic Subunits IVB–IVD to rare in lithologic Subunit IVE.
- Organic material/wood/lignite is common to locally abundant in lithologic Subunits IVB–IVD and decreases in lithologic Subunit IVE (few).
- Fossils are rare in all subunits.
- Glauconite is mostly absent in lithologic Subunits IVB and IVC and increases in lithologic Subunits IVD and IVE (rare).

Examples of some of these minerals are shown in Figures F23, F24, F25, and F26. Lithologic Subunit IVD locally contains high organic matter content (1535.5 mbsf; Sample 338-C0002F-161-SMW).

Lithologic Unit V (trench or Shikoku Basin hemipelagic deposits)

Interval: cuttings Samples 338-C0002F-215-SMW to 289-SMW
Depth: 1740.5–2004.5 mbsf
Lithology: dominant—greenish gray silty claystone; minor—sandstone

In Hole C0002F, the lithologic Unit IV/V boundary shows a gradual decrease of sand between 1680.5 and 1740.5 mbsf (Samples 338-C0002F-202-SMW through 214-SMW), with the complete disappearance of sandstone at the base of this interval (Figs. F18, F19). Lithologic Unit V is composed almost entirely of greenish gray silty claystone. The silty claystone is semi-indurated, and cuttings shape is subrounded to angular. The >63 µm sand-size fraction (Fig. F20) shows quartz as the dominant mineral, feldspar decreases from common to few with depth, lithic fragments are few, mica is rare to absent, volcanic glass is always rare, pyrite is common at the top of lithologic Unit V and then decreases to few, wood is mostly few and only locally common, and fossils are rare and become few at 1955.5 mbsf (Sample 274-SMW). Where present, fossils are commonly pyritized (Fig. F25F). Glauconite is always rare.

The Q-index in lithologic Unit V shows overall increased grain sizes compared with the surrounding lithologic Units IV and V, ranging from ~500 to 1800 µm in diameter (Fig. F22). At 1485.5 mbsf (Sample 338-C0002F-148-SMW), the Q-index shifts to both higher values (average ~1300 µm) and greater fluctuations. Although the Q-index in lithologic Unit V shows the lowest values (250–950 µm) compared with lithologic Unit IV, it also suggests that some very fine sandstone layers may be present.

Limitations using sediment cuttings

Even though the cuttings data correlate reasonably well with LWD and other data (see "Logging while

drilling," "Physical properties," "Structural geology," and **"Geochemistry"**), with depth shifts of ~50–70 m compared to LWD data, specific lithologic variations that are normally observed and documented in cores cannot be recognized in cuttings.

An important limiting factor on the reliability of cuttings is the amount of their stratigraphic mixing. For example, the collapse of wall rock into the drilling mud (cavings) results in vertical mixing of lithologies that makes it difficult to accurately reconstruct stratigraphic relationships. As sand was recovered in cuttings and drilling fluid as mostly unconsolidated material, the >63 µm sand fraction was separated during washing and sieving. Because of temperature, drilling mud circulation speed and viscosity, pH values, and chemical supplements added to the drilling mud, the lithified sediment is partly disaggregated. This makes it difficult to differentiate the drilling mud and disaggregated mud from mudstone or sand from sandstone.

In Hole C0002F, defining units and subunits by the first occurrence of a change in cuttings lithology (e.g., the first appearance of sandstone) is the most reasonable approach. Because of smearing effects created by the first cut by the drill bit and the last cut by the underreamer, as well as by general circulation of cuttings fragments, the base of a unit or subunit can be defined only in an imprecise way by the last common occurrence or the last occurrence of a lithology such as sandstone. In effect, the upper boundaries are clearly defined, whereas the lower boundaries are more arbitrary. Because of this complexity and for consistency, lithologic upper boundaries are defined by the first occurrence of a lithology (i.e., sandstone) and lower boundaries are defined by the first appearance of the lithology of the immediately subjacent unit. This approach only allows discrimination of units that have contrasting lithology.

Mineralogical and geochemical analyses

X-ray diffraction mineralogy

Bulk powder XRD results show the relative abundance of total clay minerals, quartz, feldspar, and calcite. As a measure of how accurate the XRD estimates are relative to absolute percentages, regression analysis of percent calcite from XRD versus percent calcium carbonate from coulometric analysis is shown in Figure **F27** (see also **"Organic geochemistry"**). The linear regression coefficient (R^2) shows a very good correlation of 0.97. The comparison also shows a slight shift in the coulometric data above ~10 wt%, which is to be expected if the concentration of $CaCO_3$ is expressed as a percentage of the total solid mass (weight percent) and calcite measured by XRD is normalized to 100 wt%.

Figure **F28** and Table **T9** show XRD data of cuttings from the 1–4 mm and >4 mm size fractions. No significant differences are apparent between cuttings size fractions; consequently, we continued to only analyze cuttings from the 1–4 mm size fraction (also in line with standard oil industry cuttings routines). Regularly spaced >4 mm samples were analyzed for quality control. Because of the mixing of cement and formation in the upper part of the hole (see **"Physical properties"**), XRD data were routinely measured starting at 920.5 mbsf (Sample 338-C0002F-20-SMW). The uppermost few measurements still show contamination with cement, especially in the >4 mm size fraction. Because of drilling with the underreamer, we observe a gradual increase between 920 and 1025.5 mbsf (Samples 20-SMW through 45-SMW) in total clay from ~32 to 58 wt% and in feldspar from ~12 to 28 wt% as well as a large decrease in calcite from ~28 to 5 wt%. Because of this gradual decrease in calcite, together with the first occurrence of sandstone, the lithologic Unit III/IV boundary is defined at 1025.5 mbsf (Sample 45-SMW). This boundary is defined by LWD data at ~918.5 mbsf (see **"Logging while drilling"**), whereas Expedition 315 observed an abrupt reduction in calcite content at the discordance at 922 mbsf (Expedition 315 Scientists, 2009b). This shift was explained during Expedition 315 as the abrupt change of the depositional site from below (lithologic Unit IV) to above the carbonate compensation depth (CCD) (lithologic Unit III). Similar but more gradual shifts in calcite content were also recorded from Ocean Drilling Program (ODP) Sites 1175 and 1176 (Shipboard Scientific Party, 2001a, 2001b; Underwood et al., 2003).

Lithologic Unit IV, which is divided into five subunits (IVA–IVE), shows five cycles of increasing then decreasing total clay content that correspond reasonably well with the subunit boundaries (Fig. **F28**). The amount of quartz (weight percent) remains relatively constant with a slight but not significant increase and then decrease within the subunits. Feldspar shows a broad distribution throughout lithologic Unit IV with no clear trend but some subtle changes at the subunit boundaries. Calcite content remains low with a more substantial decrease to ~1–2 wt% in lithologic Subunits IVB and IVC followed by an increase in lithologic Subunit IVE. More detailed observations can be summarized as follows. In lithologic Subunit IVA, total clay mineral content shows little variation with an average of ~58 wt%, quartz averages ~20 wt%, feldspar slightly increases from ~20 to 22 wt%, and calcite is low at ~3 wt%. At the lithologic Subunit IVA/IVB boundary (1140.5 mbsf; Sample 338-C0002F-71-SMW), total clay, quartz, feldspar, and calcite show more scatter in the data but no significant downhole changes or trends.

In lithologic Subunit IVB, total clay and quartz show similar values to those in lithologic Subunit IVA, but feldspar shows a slight increase and greater scatter. Calcite values remain similarly low (average = 3 wt%). In lithologic Subunit IVC at 1270 mbsf (Sample 338-C0002F-SMW-100), total clay content increases from an average of 44 wt% to 58 wt%, quartz increases slightly, and feldspar shows considerable scatter in the data. Calcite content drops to an average ~1 wt%.

In lithologic Subunit IVD from 1420.5 to 1600.5 mbsf (Samples 338-C0002F-134-SMW to 182-SMW), total clay increases and then decreases slightly, quartz content increases slightly, feldspar content decreases, and calcite values remain low.

In lithologic Subunit IVE between 1600.5 and 1740.5 mbsf (Samples 338-C0002F-182-SMW to 215-SMW), when compared with lithologic Subunit IVD data, total clay content decreases then increases, quartz content increases then decreases, feldspar values remain essentially constant, and calcite increases slightly. The lithologic Unit IV/V boundary at 1740.5 mbsf (Sample 215-SMW) is associated with an increase in total clay content. Within lithologic Unit V there is a further increase in clay mineral content at 1930.5 mbsf (Sample 269-SMW). Quartz content slightly increases at the Unit IV/V boundary and then decreases at 1860.5 mbsf (Sample 253-SMW). Feldspar decreases throughout lithologic Unit V to an average of ~12 wt%. Calcite decreases from 5 to 1 wt% until 1855.5 mbsf (Sample 254-SMW), where it increases again to an average of ~8 wt% before decreasing at 1930.5 mbsf (Sample 269-SMW) to an average of ~2 wt%.

All mineral data taken from cuttings in Hole C0002F correlate well with the core data from Site C0002B (450–1050 mbsf) (Fig. **F29**). In comparison with core data, the XRD data from cuttings are relatively homogeneous because of the preferential preservation of the fine-grained (more indurated) sediment in the silty claystone (1–4 mm size fraction) with respect to coarse-grained (less indurated) sandy sediment. Among the major minerals, calcite (XRD) shows the greatest amount of scatter. This is similar to observations made from Site C0002B (Expedition 315 Scientists, 2009b), where calcite abundance ranges from 0.63% (trace) to 27.16% with an average of 14.21%.

X-ray fluorescence

In order to characterize compositional trends with depth and/or lithologic characteristics of the sediments from Hole C0002F, X-ray fluorescence (XRF) analysis was undertaken for ~150 samples (Fig. **F30;** Table **T10**). Major and minor element contents (SiO_2, Al_2O_3, CaO, K_2O, Na_2O, Fe_2O_3, MgO, TiO_2, P_2O_5, and MnO) were analyzed and complemented by loss on ignition (LOI) measurements. To compare the composition of cuttings sizes, initially both 1–4 mm and >4 mm cuttings size fractions were analyzed. A comparison shows no significant differences for cuttings size fractions; therefore, further analysis only involved the 1–4 mm cuttings size fraction. The compositional spikes observed in the upper interval in Hole C0002F for the >4 mm cuttings size fraction are mainly due to the mixing of cement and formation (Fig. **F30**).

LOI within the zone of 100% cement ranges up to 25.4 wt%, and such samples are not plotted or used in assessing averages. Elemental compositions are described based on the results of the 1–4 mm cuttings size fraction. LOI averages 9.0 wt% with a maximum of 13 wt% at 920.5 mbsf (Sample 338-C0002F-20-SMW) and a minimum of 6.7 wt% at 1670.5 mbsf (Sample 201-SMW).

The abundance of SiO_2 is high throughout Hole C0002F with an average of 64.1 wt% and varying from a minimum of 58.5 wt% at 920.5 mbsf (Sample 338-C0002F-20-SMW) to a maximum of 67.84 wt% at 1330.5 mbsf (Sample 112-SMW). SiO_2 shows a reasonably good correlation with the other element oxides, such as Al_2O_3, Na_2O, K_2O, and CaO (Fig. **F31**).

Al_2O_3 averages 15.9 wt% with a minimum of 13.7 wt% at 925.5 mbsf (Sample 338-C0002F-21-SMW) and a maximum of 17.11 wt% at 1025.5 mbsf (Sample 45-SMW). CaO averages 4.30 wt% with a minimum of 2.10 wt% at 1870.5 mbsf (Sample 255-SMW) and a maximum of 12.0 wt% at 920.5 mbsf (Sample 20-SMW). K_2O averages 3.3 wt% with a minimum of 2.60 wt% at 920.5 mbsf (Sample 20-SMW) and a maximum of 3.6 wt% at 1990.5 mbsf (Sample 286-SMW). Na_2O averages 2.5 wt% with a minimum of 2.1% at 1970.5 mbsf (Sample 282-SMW) and a maximum of 2.8% at 1010.5 mbsf (Sample 42-SMW).

In common with the other element oxides, Fe_2O_3 shows no clear trend with depth and averages 5.3 wt% with a minimum of 4.5 wt% at 1430.5 mbsf (Sample 338-C0002F-136-SMW) and a maximum of 5.9 wt% at 1110.5 mbsf (Sample 64-SMW). MgO averages 2.2 wt% with a minimum of 1.85% at 1670.5 mbsf (Sample 201-SMW) and a maximum of 2.60% at 1010.5 mbsf (Sample 42-SMW). TiO_2 averages 0.64 wt% with a minimum of 0.58 wt% at 1430.5 mbsf (Sample 136-SMW) and a maximum of 0.71 wt% at 1000.5 mbsf (Sample 41-SMW).

MnO averages 0.065 wt% with a minimum of 0.05 wt% at 1890.5 mbsf (Sample 338-C0002F-260-SMW) and a maximum of 0.09 wt% at 1040.5 mbsf (Sample 49-SMW). P_2O_5 averages 0.09 wt% with a minimum of 0.06 wt% at 1910.5 mbsf (Sample 265-SMW) and a maximum of 0.13 wt% at 1040.5 mbsf (Sample 48-SMW).

Figure **F31** shows cross-plots for various element oxides. These graphs contain two distinct, nonoverlapping populations of data (labeled "Population 1" and "Population 2"). Population 1 consists of the data from 920.5 to 990.5 mbsf (Samples 338-C0002F-20-SMW through 36-SMW), and Population 2 contains all data from 995.5 to 1990.5 mbsf (Samples 37-SMW through 286-SMW). It is likely that Population 1 represents contamination from the cement, whereas Population 2 reflects essentially formation geochemical data.

SiO_2 shows a positive correlation with Al_2O_3 (Fig. **F31A**). CaO shows a negative correlation with both SiO_2 (Fig. **F31B**) and Al_2O_3 (Fig. **F31C**). Al_2O_3 shows a negative correlation with K_2O (Fig. **F31D**). LOI shows a positive correlation with CaO (Fig. **F31E**).

Interpretation of drilled stratigraphy

Lithologic Unit III, consisting of silty claystone with trace amounts of sandy material, is interpreted as the fill of the lower part of the Kumano forearc basin and potentially prism slope basins (Expedition 315 Scientists, 2009b). The composition of detrital grains is consistent with sediment supply from erosion of the exposed sedimentary and metasedimentary rock units within the Outer Zone of Japan, including the Shimanto Belt (e.g., Taira et al., 1988; Isozaki and Itaya, 1990). Lithologic Unit IV represents the uppermost part of the older accretionary prism sediment with silty claystone as the major lithology. Sandstone tends to consist of mainly quartzo-feldspathic material, including metamorphic rock fragments, common heavy-mineral assemblages, relatively rare ferromagnesian minerals, variable but generally small amounts of organic/wood material, and traces of volcanic glass. This assemblage is consistent with proximity to a volcanic source.

Expedition 315 interpreted lithologic Unit III as forearc or supra-accretionary prism slope deposits that accumulated above the CCD, both prior to and during the early stages of formation of the Kumano Basin (Expedition 315 Scientists, 2009b). Sediment-starved conditions were accompanied by a diverse assemblage of infauna. Local cementation of the sediment surface (by glauconite, possibly with phosphates and carbonates) was favored by slow sediment accumulation rates and exposure to oxygenated seawater.

Expedition 315 proposed that the base of lithologic Unit III is a depositional contact between accreted trench-wedge sediment and the initial deposits of hemipelagic silty claystone on the lowermost trench slope (Expedition 315 Scientists, 2009b). Seismic reflection profiles show complicated geometries with angular discordances and contrasts in structural style across the boundary. Expedition 315 Scientists interpreted the pronounced unconformity at ~922 mbsf (Expedition 315 Scientists, 2009b; their figure F4) as a manifestation of uplift along a system of out-of-sequence (splay) faults that occurred at ~5 Ma. Whether the uplift triggered erosion of accreted strata or favored slow sediment accumulation above the prism cannot be resolved without higher resolution biostratigraphy. This phase of tectonic activity led to bathymetric blockage along the seaward edge of an incipient Kumano Basin, creating a large sediment depocenter. It is noteworthy that the depositional environment remained starved of significant terrigenous influx for >3 m.y. As discussed above, delivery of silt and sand turbidites into the basin began at ~1.6 Ma, signaling the inception of lithologic Unit II deposits (Expedition 315 Scientists, 2009b).

During Expedition 315, the depositional environment of lithologic Unit IV was difficult to interpret because of poor core recovery and a strong tectonic overprint characterized by intense fracturing, scaly fabric in mudstone, and fragmentation of sandstone beds (Expedition 315 Scientists, 2009b). Seismic reflection data indicate that the contact between lithologic Units III and IV is a boundary between the forearc basin and the older accretionary prism, which means that the most likely depositional environment for lithologic Unit IV is older accretionary prism slope basin or trench wedge. Low concentrations of calcareous nannofossils suggest deposition below the CCD in a slope basin near the base of the trench slope. The Quaternary trench-wedge environment of the Nankai Trough is sandy (Pickering et al., 1993; Moore, Taira, Klaus, et al., 2001).

Lithologic Unit IV consists of the most sandstone-rich deposits recovered in Hole C0002F. The most likely depositional environment is that of older accretionary prism slope basin fill or accreted submarine-fan deposits that accumulated in either a paleotrench or the Shikoku Basin. In lithologic Unit IV, the presence of the high-temperature metamorphic mineral corundum at 1125.5 mbsf (Sample 338-C0002F-66-SMW) (Fig. F25A, F25B), a characteristic mineral of contact metamorphism of limestones and metamorphosed shales (e.g., schists), likely came from the Jurassic low-pressure/high-temperature Ryoke Metamorphic Belt. If correct, then its presence may indicate a sequential unroofing history from the Shimanto Belt to the older and more deeply buried Ryoke Belt.

The lithologic Unit IV/V boundary at 1740.5 mbsf (Sample 338-C0002F-215-SMW) is identified as an important candidate thrust zone (see "Logging while drilling"). XRD and XRF analyses show a significant shift in mineralogy and element oxides at this interface. For XRF analyses (Fig. F30), the shift to increased values for LOI, CaO, MgO, and P_2O_5, with an opposite shift for SiO_2, Al_2O_3, K_2O, Na_2O, Fe_2O_2, MgO, and TiO_2, can be explained by ion-rich fluid migrating along the thrust zone to precipitate Ca-Mg clay minerals.

Lithologic Unit V consists essentially of silty claystone as the finest grained deposits within any unit in Hole C0002F, also associated with the highest gamma radiation values (see "Logging while drilling"). Its thickness, several hundred meters, suggests that it is a candidate correlative unit to the hemipelagic lithologic Unit III drilled at subduction inputs Sites C0011 and C0012 (Expedition 322 Scientists, 2010a, 2010b), albeit possibly internally thrust duplicated and folded.

Hole C0002H

Two cores were recovered in Hole C0002H (Table T11). Core recovery was limited: ~18.4% in Core 338-C0002H-1R and 22.7% in Core 2R (see "Background and objectives"). Despite the difficulty with recovery and the consequent expectation of the preferential loss of unconsolidated sandy materials, ~27% of the recovered interval is weakly consolidated sandstone. The small amount of core recovered precludes identification of stratigraphically meaningful units and subunits, so we focus here on a detailed description of the two cores. The depth interval cored is situated in Subunit IVA (Hole C0002F; 1025.5–1140.5 mbsf) and suggests that these materials were obtained close to the lithologic Subunit IVA/IVB boundary as shown on Figure F18. Further comparison to Hole C0002F is discussed below.

Lithologic variation

The dominant lithology in both cores is dark greenish gray silty claystone (Figs. F32, F33). Minor lithologies include sandstone, sandy siltstone, and calcareous claystone. Silty claystones are consolidated to the point that they cannot be fully disaggregated by standard smear slide methodology (Fig. F34A). However, coherent fragments are sufficiently small that they can be usefully examined in transmitted light.

All the lithologies are dominated by a siliciclastic grain assemblage of clay, quartz, and feldspar (see Hole C0002H smear slides in "Core descriptions"). Lithic fragments are comparatively minor and consist mostly of sedimentary (fine-grained siliciclastic lithics and chert) and low-rank metamorphic clasts such as slate and phyllite. Minor mineral grains include micas (mostly biotite and chlorite) and a diverse assemblage of dense minerals. Examples of carbonate-bearing silty claystone are observed in intervals 338-C0002H-1R-1, 42–46 cm, 51–56 cm, and 96–103 cm. Carbonate is primarily present in the form of nannofossils (Fig. F34B) and as silt-size anhedral calcite and ranges from a trace in the dominant silty claystone to 30% in the more calcareous lithology, based on smear slide observations (see Hole C0002H smear slides in "Core descriptions"), XRD measurements (Table T12), and carbonate analyses (Table T13). A localized detrital component, concentrated fragments of terrestrial organic matter (Fig. F34C), occurs as sequences of laminae of 2–3 mm thickness in intervals 1R-1, 48–50 cm; 2R-3, 70–75 cm; and 2R-3, 103–107 cm (Figs. F32, F33).

Biological features

The above-noted nannofossils are dominantly moderately well preserved coccoliths and minor discoasters. Only a trace of highly fragmented siliceous bioclasts, including sponge spicules and radiolarians, was observed. Skeletal fragments of any type are rare. Agglutinated tubes of a possible large foraminifer are observed (~0.5 cm diameter) scattered throughout both cores.

Generalized bioturbation is observed throughout both cores, but particular ichnotaxa were not identified. Small (millimeter-scale) pyritized burrows are especially visible in the X-ray computed tomography (CT) images. Zones of intense burrowing are particularly well developed beneath the calcareous layers, which are themselves highly bioturbated. The X-ray CT image (Fig. F35) reveals that some burrows within noncalcareous silty claystone are filled with calcareous silty claystone from the overlying calcareous layer and also that some burrows appear to cross the lithologic boundary.

Authigenic components

Few authigenic components can be recognized in silty claystone using light microscopy. Pyrite framboids (Fig. F34C) are widely distributed through both cores. Possible microdolomite (Fig. F34D) of very uniform crystal size (1–3 µm) observed in the calcareous silty claystone at Section 338-C0002H-1R-1, 105 cm, possibly contributes to the high X-ray CT density that is observed for that lithology (Figs. F32, F35). The only macroscopically apparent authigenic feature is a drilling-deformed fragment of calcite-cemented sandstone surrounded by unconsolidated sand in interval 2R-1, 40–44 cm, that also displays high density on the X-ray CT image.

Comparison to Hole C0002H and other sites on the Nankai margin

Lithologies observed in Cores 338-C0002H-1R and 2R are consistent with the range of lithologies observed in Hole C0002F, and specifically, the sand-rich lithologic Subunit IVB (Fig. F18). The sandstone proportion recovered in Hole C0002H is most likely less than the actual stratigraphic percentage of sand as a consequence of sand loss during core recovery; there also may be some influence from underreamer mixing. XRD and XRF compositions (Figs. F36, F37; Tables T12, T14) are generally similar to those observed in cuttings in Hole C0002F but show far more scatter, as expected for discrete samples versus cuttings, because of the homogenization from mixing of different lithologies in the cuttings.

On a broader scale, lithologies recovered in Cores 338-C0002H-1R and 2R are similar to lithologies reported at IODP Site C0001 in lithologic Subunit IC (basal slope apron) and Unit II (accretionary prism) and in Hole C0002B in lithologic Unit IV (accretionary prism) (Expedition 315 Scientists, 2009a, 2009b) with the exception that the sand percentage recovered is somewhat higher in Hole C0002H, more similar to the sand-rich character observed in Hole C0002F lithologic Subunit IVB. Lithologies, major and minor grain components, and biologic components are all consistent with the features described more widely on the Nankai margin (e.g., Kinoshita, Tobin, Ashi, Kimura, Lallemant, Screaton, Curewitz, Masago, Moe, and the Expedition 314/315/316 Scientists, 2009) with the notable exception that volcanogenic material (volcanic lithic fragments, pumice, and volcanic glass) is very minor to absent in Hole C0002H. The loss of sand during drilling and coring and the general high level of drilling-induced core disturbance and structural deformation (see "Structural geology") prevent clear recognition of the characteristic sedimentary depositional successions in these cores. A few fining-upward sequences, capped by calcareous silty claystone (intervals 338-C0002H-1R-1, 52–54 cm; 1R-2, 3–11 cm; 2R-1, 16 cm; 2R-3, 42 cm; 2R-3, 68 cm; 2R-3, 69–72 cm; 2R-3, 85–89 cm; and 2R-3, 105–114 cm) suggest the presence of turbidites a few centimeters or tens of centimeters thick, with most now missing their sand (presumably lost during core recovery), that grade from fine sand or coarse silt at the base to more nannofossil rich silty claystone that has been greatly obscured by bioturbation. The ratio of siliciclastic debris to pelagic components suggests a relatively higher rate of sedimentation compared to the condensed mudrock succession in lithologic Unit III (Hole C0002B, Expedition 315 Scientists, 2009b). The abundant bioturbation in the silty claystones suggests deposition under conditions of normal seafloor oxygenation.

Hole C0002J

Seven cores were recovered in Hole C0002J (Table T15) with an average recovery of ~60% (see "Background and objectives"). The depth interval cored (902–940 mbsf), based on comparisons to logs from Hole C0002A (Expedition 314 Scientists, 2009), logs and cuttings from Hole C0002F (Fig. F18), and cores from Hole C0002B (Expedition 315 Scientists, 2009b), suggests that these materials were obtained close to the lithologic Unit III/IV boundary. Given the relatively short interval cored and the limited recovery, we focus on description of Hole C0002J cores and possible stratigraphic correlations of the cored interval and sediments observed in Holes C0002B and C0002F. Specifically, we focus on characterization of a possible unit boundary (lithologic Unit III/IV) in Section 338-C0002J-5R-8. Conclusions on the nature and exact position of this boundary will be further refined though postexpedition research.

Lithologic variation

The dominant lithology in Hole C0002J is dark olive-gray silty claystone (Fig. F38) (see Hole C0002J smear slides in "Core descriptions"). Minor lithologies include sandstone, sandy siltstone, silty claystone, calcareous claystone, and fine ash. XRD and XRF data show that bulk mineralogical and bulk elemental compositions are broadly similar to those observed at this depth interval in Hole C0002B (Figs. F39, F40), with a relatively sharp drop in carbonate content at the possible lithologic Unit III/IV boundary (see further discussion below).

All the lithologies are dominated by a siliciclastic grain assemblage of clay, quartz, and feldspar with variable amounts of pelagic carbonate (Tables T13, T16, T17). Lithic fragments consist mostly of sedimentary (fine-grained siliciclastic lithics and chert) and low-rank metamorphic clasts such as slate and phyllite (Fig. F41). Minor mineral grains include micas (mostly biotite and chlorite) and a diverse assemblage of dense minerals. Volcanic glass is widely distributed in the silty claystone and also in the coarser lithologies. Vitric material is mostly silt-size clear glass, but subordinate amounts of brown glass, microlitic volcanic rock fragments, and pumice (Fig. F42) are present locally. Carbonate is primarily present in the form of nannofossils and also as silt-size anhedral calcite and ranges from trace in the dominant silty claystone to 20% in the more calcareous lithology, based on smear slide observations (see Hole C0002J smear slides in "Core descriptions"), XRD measurements (Table T16), and carbonate analyses (Table T13). Minor amounts of terrestrial organic matter (red-brown color) are observed in the coarser lithologies.

Biological features

The above-noted nannofossils are dominantly moderately well preserved coccoliths and minor discoasters. Samples generally contain trace to minor amounts of highly fragmented siliceous bioclasts, including sponge spicules and radiolarians. Skeletal fragments of any type are rare. Agglutinated tubes of a possible large foraminifer are observed (~0.5 cm in diameter) scattered through the core.

Generalized bioturbation is pervasive and most readily appreciated in X-ray CT images. Small (millimeter-scale) pyritized burrows similar to *Trichichnus* (McBride and Picard, 1991) are the most common type of discrete burrow, but *Chondrites*, *Zoophycos*, and other discrete burrows are well preserved in local zones, most especially in Cores 338-C0002J-1R through 5R (Fig. F43).

Numerous occurrences of possible syndepositional erosion are observed in Cores 338-C002J-4R through 7R (Fig. F44), including angular mud clasts and scoured bedding surfaces that display a range of inclinations.

Authigenic components

Few authigenic components can be recognized in silty claystone using light microscopy. Pyrite framboids are widely distributed through all the cores and are most notably developed within and around burrows as noted above. Glauconite is also notable in Cores 338-C002J-1R to 5R and occurs in a variety of forms (Fig. F45). Slightly wavy greenish bands 1–3 cm thick are most likely slightly glauconized silty claystone, although the specific form of the glauconite is not discernible in smear slides. Glauconite also occurs as discrete grains of silt to granule size (Fig. F45C, F45E) that appear in smear slides as grass-green claystone and silty claystone (Fig. F45D).

The interval 338-C0002J-6R-1, 15–23 cm, has a zone of calcareous sandy mudstone composed of very uniform anhedral calcite microcrystals that form a matrix around sand grains (Fig. F46). This material is similar to possible authigenic calcite (microbial precipitate?) encountered in Sample 315-C0002B-59R-1, 45–52 cm (see "Core descriptions"), within the upper part of lithologic Unit IV (Expedition 315 Scientists, 2009b). This lithology is the source of the rare carbonate-rich material observed locally within lithologic Unit IV.

Possible unit boundary

A possible unit boundary (lithologic Unit III/IV; Kumano Basin/prism) is identified within a zone ~18 cm thick, beginning at ~926.66 mbsf in Section 338-C0002J-5R-8 (Fig. F47). Interpretation as a unit boundary is based on lithologic evidence, compared for reference to core observations made in Hole C0002B (Expedition 315 Scientists, 2009b), together with the proximity to the boundary depth observed by sampling and logging in Holes C0002A, C0002B, and C0002F. Lithologic evidence for the boundary includes the following:

- A relatively sharp boundary between calcareous glauconitic sandy silty claystone and less calcareous nonglauconitic silty claystone (Fig. F47),
- An abrupt and substantial increase in sand abundance below this boundary,
- A change in sand composition from glauconite rich with an admixture of volcanic glass to a more quartzo-feldspathic composition with abundant metamorphic rock fragments, and
- A substantial decrease in the amount of carbonate in silty claystone (see Hole C0002J smear slides in "Core descriptions") (Table T16; Fig. F39).

Ash occurs both above and below the boundary. Although ash is a persistent component of silty claystones above the boundary, the ash occurrence in both silty claystone and sandstone below the boundary is more variable, ranging from abundant in zones adjacent to ash beds to near absent in beds farther from the ash. In Section 338-C0002J-5R-8, immediately above and within the boundary zone, evidence for erosion, as described above and depicted in Figure F44, becomes pronounced (Fig. F47).

Bulk elemental compositional variation across the possible unit boundary in Section 338-C0002J-5R-8 was examined using XRF core scanning (Fig. F47; Table T18). The lithologic Unit III/IV boundary may not be a single sharp contact (as in Hole C0002B). Instead, it may occur as a zone of heterogeneous lithology, containing alternations of materials from lithologic Units III and IV. This variety is also reflected in the XRF core scanning results. The peaks in Fe_2O_3 correspond to levels rich in glauconite. Al_2O_3 yields a noisy signal, but greater Al_2O_3 clearly corresponds to carbonate-poor claystone.

Biostratigraphic data for Holes C0002B, C0002F, and C0002J results indicate the presence of middle Pliocene sediment at 925.48 mbsf (see **"Biostratigraphy"**; Tables **T19, T20, T21**), indicating that indeed the transition to prism sediment of likely late Miocene age occurs below this depth. Sediment below our proposed boundary at 926.7 mbsf have not, to date, yielded datable nannofossil material. It remains possible that coring in Hole C0002J did not penetrate the lithologic Unit III/IV boundary, as glauconitic materials (possibly affiliated with lithologic Unit III) are observed in the deepest section cored (Section 7). Carbonate content, however, provides stronger evidence that lithologies from Unit IV have been encountered. Although minor amounts of carbonate-bearing silty claystone have been observed in the upper part of lithologic Unit IV (mentioned in **"Authigenic components"**), claystones as calcite poor as the interval 338-C0002J-5R-8, 102–106 cm, have not been previously reported in lithologic Unit III (this chapter and Expedition 315 Scientists, 2009b).

Comparison to other data on the basin/prism boundary

Placement of the lithologic Unit III/IV boundary in Section 338-C0002J-5R-8 (Fig. **F47**) can be examined in the context of previous observations of the contact between basinal sediment and the prism (Table **T22**). A transition from calcareous mudstone in the basinal sediment to carbonate-poor mudstone in the prism is a theme that recurs across all the sampled holes at Site C0002 (Holes C0002B, C0002F, C002H, and C0002J) as well as at Site C0001. The depth of the tentative boundary placement in Hole C0002J is consistent with lithologic differences observed in silty claystones across this boundary in both Holes C0001H and C0002B, although the amount of sand observed below the boundary in Hole C0002J is greater. An increase in the amount of sand below the boundary is, however, consistent with observations made in logs and cuttings in Hole C0002F. The depth of the boundary tentatively identified in Hole C0002J, however, matches the log-identified boundary in Hole C0002F more closely than the boundary identified based on lithology. Biostratigraphic and paleomagnetic evidence indicate that the boundary as observed in Holes C0001H and C0002B is a significant unconformity. These observations are consistent with the evidence for syndepositional erosion documented here and are also consistent with the possibility that the boundary is variable in terms of the character of the lithologic transitions and the topography at the contact.

Holes C0002K and C0002L

The coring interval in Holes C0002K and C0002L was chosen to provide data within a gap (200–500 mbsf) that was not cored during Expedition 315. Based on comparisons to logs for Hole C0002A (Expedition 314 Scientists, 2009) and cores from Hole C0002B (Expedition 315 Scientists, 2009b), materials in this interval are within lithologic Unit II. A total of 35 cores comprising 265 sections were recovered in Holes C0002K and C0002L (Table **T23**) with an average recovery of ~69% and 79%, respectively (see **"Background and objectives"**).

Lithologic variation

The dominant lithology in Holes C0002K and C0002L is dark olive-gray silty claystone (Fig. **F48**) (see Hole C0002K and C0002L smear slides in **"Core descriptions"**). Minor lithologies include sandstone, sandy siltstone, silty claystone, calcareous claystone, and fine ash.

Most samples are dominated by a siliciclastic grain assemblage of clay, quartz, and feldspar with variable amounts of pelagic carbonate (Figs. **F49, F50;** Tables **T24, T13, T25**) and a minor but persistent component of volcanic glass. Total carbonate content ranges from <1% to ~15% in the dominant silty claystone and up to 30% in the more calcareous silty claystone in the pelagic-influenced upper parts of the turbidite cycles, based on smear slide observations (see Hole C0002K and C0002L smear slides in **"Core descriptions"**), XRD measurements (Table **T24**), and carbonate analyses (Table **T13**).

The feldspar is dominantly plagioclase; much of it is untwinned and highly vacuolized. Lithic fragments consist mostly of fine-grained siliciclastic lithics and chert and low-rank metamorphic clasts such as slate and phyllite (Fig. **F51**). Minor mineral grains include micas (mostly biotite and chlorite) and a diverse assemblage of dense minerals. Volcanic glass is widely distributed in silty claystones and also in coarser lithologies. Vitric material is mostly silt-size clear glass. Carbonate is primarily present in the form of nannofossils and also as foraminifers and silt-size anhedral calcite. Minor amounts of terrestrial organic matter are present.

The typical occurrence of sand in these cores takes the form of thin turbidite cycles that vary in sand thickness (Fig. **F52;** Table **T26**). Thicker turbidites range from decimeter to meters thick cycles with sand sitting above a scoured base; fining upward into sandy silt, clayey silt, and silty claystone; and capped by a somewhat calcareous silty claystone rich in pelagic debris (coccoliths) (Fig. **F52A**). Thinner turbidites begin with centimeter-scale silty sand or clayey silt (Fig. F52B), and the smallest ones are represented only by slightly coarser silty claystones at subtly scoured contacts above calcareous silty claystone (Fig. F52C). Across the depth interval sampled, turbidite sand has an uneven distribution (Fig. F53), being more abundant in the zones above 300 mbsf and below 450 mbsf. The thickest sand observed is ~1 m thick.

Biological features

The above-noted nannofossils are dominantly moderately well preserved coccoliths and minor discoasters. Samples generally contain a trace to minor amounts of highly fragmented siliceous bioclasts, including sponge spicules and radiolarians. A few core sections that are poor in sand (e.g., Cores 338-C0002K-1H and 2H and Sections 338-C0002L-4X-1 through 4X-6) contain biosiliceous components at amounts of a few percent. Generalized bioturbation and discrete burrows are not generally evident, either in core or CT images.

Authigenic components

Pyrite framboids are the only commonly observed authigenic component.

Interpretation

Expedition 315 Scientists (2009b), working from cores with poor recovery of the sand, interpreted lithologic Unit II as the lower forearc basin succession, dominated by the hemipelagic mud of distal turbidites. The somewhat better core recovery achieved in Holes C0002K and C0002L allows us to confirm this interpretation for the upper part of lithologic Unit II. Patterns of sand occurrence are suggestive of the presence of a coarsening-upward package of generally thin turbidites from ~460 mbsf to the top of lithologic Unit II, possibly underlain by a second similar cycle that begins at the top of Core 338-C0002L-22X at ~480 mbsf. Poor core recovery in Hole C0002B precludes immediate assessment of this possibility of large-scale turbidite packages within lithologic Unit II; additional work with core-log integration in postexpedition studies may further elucidate the depth trends of sand in lithologic Unit II.

Structural geology

Structural studies at Site C0002 consist of (1) analyses of cuttings from 865.5 to 2004.5 mbsf in Hole C0002F and (2) analyses of cores from 200–280.5, 277–502.8, 902–933.8, and 1100.5–1112.8 mbsf in Holes C0002K, C0002L, C0002J, and C0002H, respectively.

Structures in cuttings from Hole C0002F

In Hole C0002F, deformation structures in cuttings from the 1–4 and >4 mm size fractions were investigated from 865.5 to 2004.5 mbsf (see **"Structural geology"** in the "Methods" chapter [Strasser et al., 2014a]). In addition to natural deformation structures such as vein structures, carbonate veins, slickenlined surfaces, and minor faults, a high number of drilling-induced deformation structures were observed. Orientations of structures could not be measured because all information on orientation is lost during recovery of cuttings through the riser. All observed deformation structures that are not drilling induced are summarized in CUTTINGS STRUCTURE.XLSX in STRUCTURE in **"Supplementary material."** Figure F54 shows the percentage of deformed grains obtained from dividing the number of grains that show deformation structures by the total number of investigated grains.

Vein structures

Vein structures in cuttings are thin clay- or silty clay–filled extensional cracks or veins (Fig. F55) (Ogawa, 1980; Cowan, 1982; Brothers et al., 1996). The occurrence of vein structures is limited to between 860 and 1050 mbsf (Fig. F54). Maximum concentrations form a sharp peak of 5% at 900 mbsf. Considering cuttings from the drill bit and the underreamer, the depth range of these vein structures corresponds to lithologic Unit III observed in Hole C0002B, which is a clay-rich hemipelagic mud sandwiched between accreted sediments below and silty-clay rich hemipelagic sediments above (Expedition 315 Scientists, 2009b).

Mineral veins

Narrow mineral veins that exclusively consist of carbonate (most probably calcite) occur throughout the entire section below 1050 mbsf (Fig. F54). The veins have widths of less than a few millimeters and are present in mudstone, sandstone, and rare limestone cuttings. Carbonate veins are often exposed at the surfaces of clastic rock cuttings, which are, in most cases, planar and lineated (Fig. F56A, F56B). This suggests shear deformation during vein formation. The lineated surface is also sometimes associated with steps. Fiber growth of carbonate veins (Fig. F56C), where the growth direction is perpendicular to the vein wall, is locally observed, indicating repeated extensional fracturing and vein growth from solution (also see Fig. F56D, where calcite grains in veins grew from very fine calcite grains of the limestone wall rock). Observation of thin sections under optical microscope shows that carbonate veins consist of abundant, very fine calcite grains; a small fraction of larger grains (up to 100 µm) show mechanical twins (Fig. F56E). Also, the wall rocks were fractured during vein formation and incorporated into veins (i.e., selvages; Fig. F56F). Maximum concentrations of cuttings with carbonate veins of up to 2.5% occur between 1050 and 1150 mbsf (Fig. F54). It may be noted that from 1800 to 2000 mbsf the frequency of cuttings with carbonate veins is higher in the 1–4 mm size fraction compared to the >4 mm size fraction. This may indicate that cuttings with carbonate veins can be easily broken into smaller pieces with a diameter of <4 mm.

Slickenlined surfaces

Similar to mineral veins, cuttings with slickenlined surfaces occur throughout the entire section below 1050.5 mbsf. A slickenlined surface is the polished surface of a cutting that shows striations (Fig. F57A, F57B). Under the optical microscope, clay minerals are observed along incipient slickenlined surfaces, where they build a clay mineral–rich zone up to 100 µm in width on both sides of the incipient surface (Fig. F57B, F57C). Slickenlines are commonly associated with steps (Fig. F57D) from which the sense of shear can be inferred (e.g., Petit, 1987; Angelier, 1994; also see Expedition 319 Scientists, 2010, for detailed explanation of steps on faults). The degree of the preferred alignment of clay minerals seems to increase with depth, but this requires more detailed investigation. Depths or depth intervals for which the proportion of cuttings showing slickenlined surfaces exceeds 3% are found at 1060.5, 1215.5–1285.5, 1345.5–1375.5, 1550.5–1675.5, and 1895.5–1985.5 mbsf (Fig. F54). Among these depths, the 1550.5–1675.5 mbsf interval shows anomalously high concentrations of slickenlined surface–bearing cuttings of up to 10%. Also at these depths, a high number of lens-shaped cuttings, which are completely surrounded by slickenlined surfaces, are observed. In the shallower intervals of Hole C0002F (1010.5–1635.5 mbsf depth, mostly 1010.5–1235.5 mbsf), grains with a shiny surface but without slickenlines are commonly observed. These grains could be related to fracture surfaces coated by clay minerals, but the relationships with shear deformation are unclear. The abundance of grains with a shiny surface is listed in CUTTINGS STRUCTURE.XLSX in STRUCTURE in "Supplementary material" but not included in Figures F54 and F58.

Minor faults

Only two minor faults were observed within the cuttings. One is in a calcareous siltstone chip from cuttings Sample 338-C0002F-169-SMW, >4 mm (1565.5 mbsf bit depth) (Fig. F59A–F59D), and the other is in a laminated sandstone from cuttings Sample 238-SMW, >4 mm (1835.5 mbsf bit depth) (Fig. F59E, F59F). The first fault is characterized by two thin, black-colored parallel zones with thicknesses of up to 100 µm (Fig. F59A–F59C). Although the displacement along the faults is unclear, they are distinguished from other structures (e.g., stylolites) because of their planar shape and stepovers (Fig. F59C). Under the optical microscope, the fault slip zones are composed of dark-colored clay minerals with no preferred orientation (Fig. F59C, F59D). Inspection of thin sections shows that detrital quartz grains and foraminifer fossils adjacent to the fault do not show any deformation (Fig. F59D). In the case of the second fault (Sample 238-SMW, >4 mm; 1835.5 mbsf), laminations in the sandstone are displaced ~0.6 mm along the observed plane (Fig. F59E). The fault plane is accompanied by a very thin zone (<100 µm) in which neither comminuted material nor concentration of clay minerals is observed (Fig. F59F). The nature of both faults suggests that cataclastic flow, characterized by grain comminution or crushing, was not dominant during faulting.

Diagenesis and lithification processes of sediment

In the shallow part of Hole C0002F (above 1100 mbsf), sandstone is not observed in 1–4 mm and >4 mm cuttings. Between 1100 and 1500 mbsf, sandstone commonly occurs as rounded clasts that easily disaggregate. Under the optical microscope, such clasts appear to be composed of loosely packed sand grains surrounded by clay minerals (Fig. F60A). Because of the low degree of induration, large amounts of unconsolidated sandstone may have been dispersed during riser drilling. Below ~1500 mbsf, the sand becomes indurated enough to produce sandstone cuttings that remain intact during drilling, recovery, and sieving. At these depths, sedimentary structures such as graded bedding and laminations are commonly observed in cuttings (Fig. F60B). Quartz cement fills the gaps between the closely packed detrital grains (Fig. F60C, F60D). Compaction and cementation seem to have played important roles in the lithification process of sandstone.

Angular-shaped silty claystone cuttings gradually appear near 1600 mbsf. On a microscopic scale, the degree of parallel alignment of clay minerals increases with depth (compare Fig. F61A–F61F, retrieved from 1215.5, 1475.5, 1565.5, 1625.5, 1875.5, and 2004.5 mbsf). This increase could be caused by growth of clay minerals that became more significant with increasing depth, corresponding to increases in temperature, time, or tectonic compaction (Milliken and Reed, 2011; Day-Stirrat et al., 2011).

Drilling-induced deformation

Cuttings generally show severe drilling-induced disturbance. The most common drilling-induced structure is a characteristic sawtooth shape that is observed in many cuttings samples (Fig. F62A). This shape is likely formed by the drill bit or the underreamer. Because of their characteristic shape, those drilling-induced structures could be easily distinguished from natural deformation structures.

At shallow depths (above 1400 mbsf), drilling mud invasion is commonly observed in cuttings. Figure F62B shows a typical microscopic example of such an invasion. Under an optical microscope, drilling mud is characterized by a low birefringence matrix that contains angular grains of minerals with a wide range of grain sizes. Also, some of the original silty claystone shows embayed surfaces, suggesting that drilling mud with high fluid pressure invaded less cohesive formations.

In addition to those cuttings that were deformed by drilling mud injection, some cuttings are likely to be artificially formed during drilling and recovery operations. Such drilling-induced cohesive aggregates (DICAs), which occur in the 1–4 mm and >4 mm size fractions, contain less sorted angular mineral grains and fragments of small cuttings from the formation in a low-birefringence drilling mud matrix (Fig. F62C). Matrix-supported texture, scattered grain-size distribution, and low birefringence of matrix suggest that the DICAs are in fact aggregates of dispersed sand and small fragments of the formation that formed when mixed with drilling mud and remained intact during subsequent recovery, washing, and sieving.

In the deeper part of this hole (especially below 1800 mbsf), rounded DICAs predominantly consisting of silty clay start to appear. After vacuum drying, these aggregates are visually similar to formation silty claystone cuttings. However, when exposed to water, they easily disaggregate, and they do not show the angular shape of "real" silty claystone cuttings (Fig. F62D). It may also be noted that cuttings from Samples 338-C0002F-311-SMW, >4 mm, and 322-SMW, >4 mm (1975 and 1982.5 mbsf), which are produced only by the underreamer, do not contain DICAs and do not show a sawtooth shape.

Drilling-induced disturbance not only destroys preexisting rock textures but also creates DICAs. Careful mesoscopic and microscopic observations of cuttings are therefore necessary in order to exclude DICAs from any subsequent analysis.

Relationship between structural observations and lithology

During the investigation of deformation structures in cuttings, we also estimated the amount of sandstone versus that of silty claystone in the >4 mm and 1–4 mm size fractions (Figs. F58, F63). The derived concentrations of silty claystone are in good agreement for both size fractions. Down to ~1150 mbsf, only silty claystone cuttings are observed. From 1150 to 1650 mbsf, silty claystone concentrations fluctuate between 60% and 90%. Below 1650 mbsf, silty claystone concentrations increase to >90%. These results can be qualitatively compared to the silty claystone to sandstone ratio determined by lithologic observations of the cuttings mix, sieved at >63 µm (Fig. F63; see also "Lithology").

The overall trends derived from structural and lithologic analyses are in good agreement. Low concentrations of sandstone are observed above 1150 mbsf and below 1700 mbsf, whereas the interval between shows higher concentrations. Although the overall trends agree rather well, the absolute values as well as the locations of local maxima and minima do not always match exactly.

Over most of the interval from 1150 to 1750 mbsf, the overall concentration of sandstone inferred from lithologic observations on bulk cuttings is slightly higher than the concentration inferred from the appearance of sieved cuttings for 1–4 mm and >4 mm size fractions. One reason for this discrepancy possibly originates in the different methods applied. Lithologic observations were done on easy-sieved cuttings with a 63 µm mesh (see "Lithology"). Structural observations of cuttings were carried out after standard sieving and drying (see "Structural geology" in the "Methods" chapter [Strasser et al., 2014a]). Many of the sandstones were less consolidated and therefore could have disaggregated during processing. Therefore, some of the sandstones investigated directly after easy sieving may have been disaggregated during the standard cuttings workflow and were not preserved in the 1–4 mm and >4 mm size fractions. As structural observations of cuttings only counted intact cuttings, this may explain the observed lower sandstone percentages.

Relation of structural observations and logging data

A fundamental difference between the structural observations on cuttings and the LWD data is the vertical resolution. Cuttings were sampled every 5 m but were generally analyzed every 10 m and were mixed at least over the 43.8 m depth interval spanning from the drill bit to the underreamer (see "Structural geology" in the "Methods" chapter [Strasser et al., 2014a]); the LWD data have a sampling interval (vertical resolution) of 0.152 m. These differences in vertical resolutions make correlations between log features and structural observations difficult.

However, there are some ways to qualitatively compare the results obtained by the different methods. Figure F54 shows the downhole distribution of deformation structures in cuttings. These can be correlated to the distribution of faults and fractures documented in the logging data (Fig. F8). In the structural data, the type of deformation structures changes at ~1020 mbsf. Here, the last occurrence of vein structures coincides with the first occurrence of slickenlines and carbonate veins. This structural change likely reflects the Unit III/IV boundary (see "Logging while drilling" and "Lithology") and may be caused by different styles of deformation in the Kumano Basin sediment and the accretionary prism.

Maximum concentrations of carbonate veins (2.5%) between 1050 and 1150 mbsf may correlate to logging Subunit IVB. However, no increased concentration of slickenlined surfaces is found at this depth.

Intervals with a high abundance of slickenlined surfaces are observed at 1060.5, 1215.5–1285.5, 1345.5–1375.5, 1550.5–1675.5, and 1895.5–1985.5 mbsf. The 1345.5–1375.5 mbsf interval correlates to an interval where the LWD data show a prominent change in the dominant dip direction (Fig. F8). The 1550.5–1675.5 mbsf interval, which hosts the highest concentrations of slickenlined surfaces, correlates to the basal part of Unit IV, including the boundary to Unit V, which is situated at ~1638 mbsf based on LWD data and 1740.5 mbsf based on lithology data. For a comparison between the above discussed variations in the lithology of the cuttings and the LWD data, refer to "Lithology."

Structures in core from Holes C0002H, C0002J, C0002K, and C0002L

Cores retrieved from Holes C0002H and C0002J–C0002L during Expedition 338 show a large variety of structures (e.g., Fig. F64). Bedding, faults, and deformation bands are well represented and locally abundant, whereas shear zones, carbonate-cemented breccias, fractures without noticeable displacement, vein structures, disrupted bedding, fissility, and incipient scaly cleavage are rare.

Deformation observed in core or X-ray CT images is localized in specific core intervals. Deformation structures are rarely observed in cores from the upper part of the Kumano Basin deposits (Unit II), whereas they are numerous in cores from the lowermost part of the Kumano Basin sediment (Unit III) and from the accretionary prism sediment (Unit IV). A total of 27 bedding orientations, 49 faults, 13 striations, and 24 deformation bands measured on core from Holes C0002H and C0002J were reoriented into true geographic coordinates using paleomagnetic data measured on board the ship.

Bedding

Bedding from Holes C0002K and C0002L (lower Kumano Basin sediment; Unit II) is subhorizontal to gently dipping and dips at angles <30° (Fig. F65). In cores from Hole C0002J, which were retrieved from the interval including the Unit III (basal Kumano Basin)/IV (accretionary prism) boundary, bedding dips gently at angles <12° at the interval 900–922.77 mbsf, whereas bedding angle gradually increases with depth from 923.0 mbsf to 61° at 932.2 mbsf. In Hole C0002H (Unit IV), bedding shows a tendency to increase in dip angle with depth (7°–50° in Core 338-C0002H-1R and 17°–64° in Core 2R). However, the limited data set does not allow us to determine if this tendency is significant at the scale of Hole C0002H.

Reoriented bedding in Unit III from Hole C0002J is subhorizontal (Fig. F66A). On the other hand, reoriented bedding in Unit IV from Holes C0002H and C0002J is subhorizontal to steeply dipping toward south or north (Fig. F66B). Poles to bedding roughly lie on a girdle, suggesting the presence of an east-west–trending fold. However, the scarcity of orientation data and the lack of layer polarity indicators (see "Lithology") do not clarify this hypothesis. Bedding dipping north or south at 900–1100 mbsf is consistent with bedding orientations derived from resistivity images obtained during Expedition 314 (Expedition 314 Scientists, 2009).

Disrupted bedding

Intensely disrupted bedding is observed in Sections 338-C0002J-5R-3 through 5R-8 between 922.76 and 927.7 mbsf. An example of such disrupted bedding is depicted in Figure F64A. Where they are still recognizable, disrupted beds have variable thicknesses and a boudinaged appearance. Sets of Riedel shears and preferred orientations (P-foliations) within those intervals suggest bedding-parallel shearing to form disrupted bedding. Bedding orientation measurement cannot be done with accuracy in the disrupted interval. In particular, among the five bedding orientations measured in this interval, the two ~30° values, which depart from the low (<20°) dip values measured elsewhere in Unit III, likely result from disrupted bedding.

Faults

Most faults were observed in cores from the bottom of Kumano Basin Unit III (Hole C0002J) and from Unit IV (Hole C0002H). Of 48 observed faults, only 4 faults were observed in Kumano Basin Unit II (Holes C0002K and C0002L, Fig. **F67**). The lowermost part (Unit III) of the Kumano Basin sedimentary pile appears more intensely faulted than the shallower layers of Unit II. Fault dips range between 11° and 82°.

In Kumano Basin Unit III (Hole C0002J), fault orientations are variable and no preferred orientation is clearly expressed (Fig. **F68A**). However, contouring of poles to faults suggests a predominance of east-west–striking and north-dipping low-angle to moderate-angle faults. The scarcity of striations and sense of slip data as well as the lack of relative chronology constraints prevent any paleostress analysis for Unit III faults.

In accretionary prism Unit IV (Hole C0002H), four fault sets can be distinguished (Fig. **F68B**): north-south–striking and east-dipping high-angle faults, northwest-striking and northeast-dipping high-angle faults, east-west–striking high-angle faults, and north-south–striking and west-dipping low-angle faults. Only four faults bear striations with clear slip sense. The trend of these striations suggests extension in the east–west to northwest–southeast directions, which is consistent with normal fault data from Hole C0002B (Byrne et al., 2009; Lewis et al., 2013).

A series of faults occur in interval 338-C0002H-1R-1, 99–121 cm (Fig. **F69**). Their dip angles are between 57° and 76° for faults with normal displacement components and between 75° and 82° for faults with reverse displacement components. Faults with normal displacement components strike north–south to northwest–southeast, whereas those with reverse displacement components strike around east–west. This contrast in strike suggests that the two fault types pertain to two diachronous episodes of deformation. As observed on split core surfaces, most of these faults have apparent displacements of no more than a few centimeters (Fig. **F69A**).

In summary, faulting at Site C0002 increases in intensity with depth, but the lack of information regarding slip sense along most faults and the lack of relative chronology criteria between faults prevent any reliable paleostress analysis.

Deformation bands

Most deformation bands (26 out of 27 occurrences) were observed in Kumano Basin sediment Unit III (Fig. **F67**). On cores, deformation bands appear as dark bands with thicknesses between <1 and 5 mm (Fig. **F64B**). The boundary between a deformation band and the host sediment is sharp, at least to the naked eye. Thickness commonly changes along strike over a few centimeters. Most deformation bands are oblique to bedding. No clear offset could be observed along these structures.

Deformation bands dip variably between 0° and 90° but predominantly between 20° and 60° (Fig. **F67**). Deformation bands, reoriented based on paleomagnetic data, do not show any preferred orientation (Fig. **F70**).

Shear zones

Shear zones are found only in Section 338-C0002J-1R-3. Unlike faults, for which displacement is accommodated along discrete planar surfaces, shear zones are several millimeter thick zones consisting of an anastomosing network of undulating fault surfaces (Fig. **F64C**). The boundary between shear zones and host sediment is usually not clear and can look progressive. Displacement along shear zones is on the order of a few centimeters. The absence of crosscutting relationships in cores precludes any tentative relative chronology among deformation bands, faults, and shear zones.

Carbonate-cemented breccia

Fragments of calcite-cemented breccia were observed in indurated claystone at interval 338-C0002J-7R-1, 6–11 cm (Fig. **F64D**). This breccia, which can be described as a mosaic breccia (Mort and Woodcock, 2008), clearly experienced dilatancy in several directions, suggesting that it was formed by hydraulic fracturing (pore pressure in excess of the least principal stress; Cosgrove, 1995). The breccia was retrieved from 932.11 to 932.6 mbsf, which is <5 m below the Unit III/IV boundary. It is, however, difficult to correlate this occurrence to any specific structure (e.g., unconformity or fault zone) crossed by Hole C0002J. Moreover, the breccia fragments were found at the top of Core 338-C0002J-7R, suggesting that they may have fallen from above when drilling resumed after recovery of Core 338-C0002J-6R. The fact that the fragments are rounded and bear RCB tool scars supports this hypothesis.

Fractures without noticeable displacement

Natural fractures in cores from Site C0002 are not readily distinguished from drilling-induced fractures. In some cases, however, features borne by fracture surfaces allow rejecting a drilling-induced origin. One joint striking N89°E to N94°E and dipping 78°N to 81°N has been observed at interval 338-C0002H-1R-1, 65–83 cm (Fig. **F64E**). Its smooth surface suggests a Mode I opening, similar to the joint described in Section 316-C0006F-18R-1 (Expedition 316 Scientists, 2009). Other natural fractures have shiny surfaces that bear faint striations. Since no displacement across them can be noticed with the naked eye, these fractures are interpreted as shear or hybrid fractures (Hancock, 1985).

Vein structures

Sediment-filled vein structures (Cowan, 1982) were observed in silty claystone in cores from the lowermost part of Unit III in Hole C0002J (e.g., Fig. **F64F**). They appear as sets of vertical to steeply dipping, parallel, fine veins with either planar or sigmoidal shapes (Ohsumi and Ogawa, 2008). The distribution of vein structures with depth is consistent with core data from Hole C0002B (Expedition 315 Scientists, 2009b) and cuttings data from Hole C0002F (Fig. **F54**).

Fissility and incipient scaly cleavage

Fissility is locally observed in Holes C0002K and C0002L (e.g., Fig. **F64G**). It is generally well developed in mudstone layers and absent in coarser siltstones or sand intervals. Fissility is always horizontal and is suspected to result from drilling-induced sediment unloading. Orientation of fissility was not measured at Site C0002.

Incipient scaly cleavage is locally observed in mudstone from interval 338-C0002J-3R-5, 76–79 cm (Fig. **F64H**). Incipient scaly cleavage is an irregularly spaced cleavage along which the mudstone easily breaks apart. Cleavage surfaces are shiny and bear faint striations. Given the scarcity of incipient scaly cleavage, orientation of this structure was not measured.

Unit III/IV structural boundary

As already reported from Holes C0002A (Expedition 314 Scientists, 2009), C0002B, C0002C, C0002D (Expedition 315 Scientists, 2009b), and C0002F (**"Logging while drilling"**), Kumano Basin forearc sediment is characterized by subhorizontal to gently dipping bedding with dips <30° (Fig. **F65**). A total of 87% of the 238 bedding dip angles measured in Kumano sediment are <10°, and 11% are between 11° and 30°. In contrast, bedding in the accretionary prism (20 measurements) dips between 5° and 64° with 11 measurements steeper than 30°. This difference in bedding dip can help locate the boundary between the lowest Kumano Basin sediment (Unit III) and the underlying accretionary prism (Unit IV). The enlarged part of Figure **F65** shows that a gap in bedding angles is present at ~923–927 mbsf in Hole C0002J, suggesting that this hole likely intersected the Unit III/IV boundary there. As we mentioned in **"Disrupted bedding,"** two relatively high dip angles at 923.9–924.09 mbsf seem to be related to bedding disruption. In that case, the structural boundary can be defined between 925.91 and 926.78 mbsf, which is comparable with the boundary defined by lithologic analyses (see **"Lithology"**).

Biostratigraphy

Preliminary biostratigraphy for Hole C0002F is based on shore-based examination of calcareous nannofossils and radiolarians, whereas that for Holes C0002J–C0002L is exclusively based on calcareous nannofossils.

Calcareous nannofossils from Hole C0002F suggest that cuttings samples from 935.5 and 985.5 mbsf are early to middle Pliocene and late Miocene in age, respectively. These nannofossil ages likely reflect that the majority of cuttings at 935.5 mbsf are derived from Unit III, whereas those at 985.5 mbsf are derived from Unit IV. Radiolarian ages, which are less precise, are overall consistent with this interpretation. In this hole, a discrepancy between the logging Unit III/IV boundary (918.5 mbsf) and the lithologic Unit III/IV boundary (1025.5 mbsf) is considered to be due to mixing of cuttings over an interval of as much as ~100 m (see the **"Methods"** chapter [Strasser et al., 2014a]). Mixing of nannofossils occurs accordingly.

Calcareous nannofossils from Hole C0002J suggest that sediment above 925.5 mbsf is middle to late Pliocene in age, whereas sediment below 926.7 mbsf contains rare nannofossils. This supports the lithologic Unit III/IV boundary at 926.7 mbsf in this hole, below which sediment of Unit IV is noncalcareous and supposed to have been deposited below the carbonate compensation depth (see **"Lithology"**).

The age range of the Kumano Basin section between 200 and 500 mbsf in Holes C0002K and C0002L was constrained from biostratigraphy and magnetostratigraphy data from Expedition 315 to be older than 1.04 Ma but younger than 1.34 Ma (Expedition 315 Scientists, 2009b). Calcareous nannofossils from Hole C0002L confirmed that the base of this hole (502.74 mbsf) is older than 1.34 Ma. The nannofossil event of 1.04 Ma, however, was found at ~250 mbsf in Hole C0002K, so an interval of normal polarity paleomagnetism between 240.72 and 299.37 mbsf (see "Paleomagnetism") may rather be correlated with the Jaramillo Subchron of 0.988–1.07 Ma. However, this nannofossil event and the top of the Jaramillo Subchron were also encountered at 137.46 and 119.58 mbsf, respectively, in Hole C0002D. The duplicate occurrence of the nannofossil event and the Jaramillo Subchron is possibly due to the presence of a normal fault between Holes C0002D and C0002K, where the former hole penetrated the footwall and the latter hole penetrated the hanging wall.

Calcareous nannofossils

Calcareous nannofossils of 17 cuttings samples (338-C0002F-22-SMW [935.5 mbsf] to 284-SMW [1985.5 mbsf]) from Hole C0002F, 9 core samples (338-C0002J-1R-CC, 0–5 cm, to 7R-CC, 19.5–24.5 cm) from Hole C0002J, 8 core samples (338-C0002K-1H-CC, 36.0–41.0 cm, to 11X-CC, 20.0–25.0 cm) from Hole C0002K, and 14 core samples (338-C0002L-1X-CC, 36.0–41.0 cm, to 24X-CC, 33.5–38.5 cm) from Hole C0002L were examined. Well to poorly preserved, abundant nannofossil specimens are found in these holes.

Hole C0002F

The uppermost sample (338-C0002F-22-SMW; 935.5 mbsf) examined contains *Reticulofenestra pseudoumbilicus* and *Sphenolithus* spp. without a typical form of *Discoaster quinqueramus* (Table T19). This together with other accompanying nannofossil species indicate that this sample may be assigned a Pliocene age, corresponding to calcareous nannofossil Zones NN15–NN12 (Table T19; see also Table T11 in the "Methods" chapter [Strasser et al., 2014a]). *D. quinqueramus* and/or *Discoaster berggrenii*, which characterize the Miocene nannofossil Zone CN9 (NN11) (Table T11 in the "Methods" chapter [Strasser et al., 2014a]), consistently occur below Sample 338-C0002F-34-SMW (985.5 mbsf) (Table T19). This may indicate that the entire section to 1986 mbsf is younger than 5.59 Ma. However, the occurrence of nannofossils becomes sporadic in the lower part of the hole and species composition is incomplete. Therefore, downhole contamination by those younger species cannot be excluded.

Hole C0002J

The presence of *Discoaster tamalis* and the absence of *Sphenolithus* spp. indicate that Sample 338-C0002J-1R-CC (906.085 mbsf) is clearly correlated with nannofossil Zone NN16 and corresponds to 2.87–3.65 Ma (Table T20). Moreover, the last occurrence (LO) of *Sphenolithus* spp. is placed between Samples 338-C0002J-1R-CC and 2R-CC (907.85 mbsf). The interval between Samples 338-C0002J-4R-CC (921.78 mbsf) and 5R-7 (925.481 mbsf) may coincide with nannofossil Zone NN14–NN15 because of the consistent occurrence of middle Pliocene species. No age indication is obtained below Sample 338-C0002J-5R-8 (926.7 mbsf) because these samples are barren of nannofossils.

Hole C0002K

The uppermost sample (338-C0002K-1H-CC; 204.48 mbsf) contains dominant *Reticulofenestra asanoi* along with common occurrence of medium *Gephyrocapsa* spp. (≥4 µm) (Table T27). The first occurrence of medium *Gephyrocapsa* spp. (≥4 µm) (= *Gephyrocapsa* sp. 3) is placed between Samples 338-C0002K-7X-CC (244.58 mbsf) and 8X-CC (254.83 mbsf), which provides an age of 1.04 Ma. *R. asanoi* is continuously observed to the lowermost sample, and thus, this hole is entirely correlated with the interval above the first consistent occurrence (FCO) of this species (i.e., younger than 1.078–1.136 Ma) (note that according to Raffi [2002] this event is diachronous in the world's oceans; we therefore assigned the medium age of 1.107 Ma).

Hole C0002L

The FCO of *R. asanoi*, which occurs at 1.107 Ma, is placed between Samples 338-C0002L-4H-CC (314.49 mbsf) and 5H-CC (324.23 mbsf) (Table T28). The LO of *Gephyrocapsa* spp. (>5.5 µm), corresponding to 1.24 Ma, is found between Samples 338-C0002L-5H-CC and 6H-CC (333.98 mbsf). Samples from 338-C0002L-6H-CC to 24X-CC (502.74 mbsf) are correlated with the interval between the LO of *Gephyrocapsa* spp. (>5.5 µm) and that of *Helicosphaera sellii*, which corresponds to 1.24–1.34 Ma.

Radiolarians

Radiolarians in Hole C0002F are present in 4 samples and absent from the other 19 samples examined. In the four samples, radiolarians are rare to very rare and show signs of dissolution (moderate preservation) (Table T21). The occurrences of *Stichocorys delmontensis* from Sample 338-C0002F-22-SMW (935.5 mbsf) and of *Stichocorys peregrina* from Sample 34-SMW (985.5 mbsf) indicate that the two samples can be correlated to the *Lychnodictyum audax* Zone

(RN11) or older zones (i.e., 2.7 Ma or older [Pliocene–Miocene]). No age-diagnostic radiolarian species were found from Samples 46-SMW and 56-SMW.

Geochemistry

Inorganic geochemistry

Interstitial water geochemistry by standard squeezing method

Interstitial water (IW) was analyzed according to the standard analytical procedures for cores taken from Holes C0002J–C0002L. Analytical results are given in Table T29. Samples were taken from 200 to 500 and 900 to 940 mbsf. In addition, selected samples were used for comparing results from the ground rock interstitial normative determination (GRIND) method and the standard squeezing method. IW samples taken from Holes C0002H (Section 338-C0002H-2R-2; 1111 mbsf) and C0002J (Section 338-C0002J-7R-1; 933 mbsf) were extracted using only the GRIND method because core recovery was too low to provide enough volume from the whole-round core (WRC) sample for the standard method. The results of the GRIND method are shown in Figures F71 and F72 and are described in "Interstitial water geochemistry by GRIND method."

Concentrations of dissolved components with depth are shown in Figure F71, in which previously reported results from Expedition 315 are also included (Holes C0002B and C0002D; Expedition 315 Scientists, 2009b). Data obtained during Expedition 338 fill the gap in the previously obtained data, and continuous geochemical profiles with depth were documented to ~1000 mbsf at Site C0002.

Salinity decreases from the seafloor until it reaches a minimum value near 500 mbsf. Chlorinity and Na^+ values have profiles similar to salinity from 300 to 500 mbsf. Between 400 and 500 mbsf, IW samples show low salinity, chlorinity, and Na^+ concentrations. Because a bottom-simulating reflector (BSR) exists at ~400 mbsf at this site, this low dissolved salt concentration could be attributable to freshwater derived from dissociation of methane hydrate. Salinity, chlorinity, and Na^+ concentrations gradually increase to 800 mbsf and then decrease again. Sulfate decreases rapidly beneath the seafloor surface and concentrations remain below 10 mM. However, IW samples from Holes C0002K and C0002L (200–500 mbsf) contain slightly higher SO_4^{2-} than the shallower and deeper samples previously analyzed. Seawater and/or mud water contamination into the core is not obvious from the other elements analyzed, and the reason for this higher SO_4^{2-} concentration cannot be explained at present. The reason for the higher SO_4^{2-} in IW samples from Hole C0002J (at ~900 mbsf) can vary. The core was fragmented when it was recovered, and it was difficult to separate fresh sediment from disturbed samples. Oxidation of H_2S is also a mechanism to increase SO_4^{2-} concentrations in those sediments. Alkalinity, PO_4^{3-}, and NH_4^+ all increase from the seafloor to 150 mbsf (roughly corresponding to the Unit I/II boundary) and then decrease with depth. Those components are produced via microbial decomposition of organic matter in the shallow sediment and then decomposed via further microbially anoxic decomposition.

Bromide increases in Unit I. Although Br^- is abundant in seawater, about the same as Cl^-, it was probably added to IW because of the decomposition of organic matter. After the decomposition of Br-bearing organic matter, Br^- follows the dilution of freshwater, similar to Cl^-. Potassium decreases with depth to 500 mbsf, becomes rather stable to 820 mbsf, and then drastically decreases below that depth. Magnesium varies in a similar manner to K^+; however, its concentration does not change below 820 mbsf. Variation of Ca^{2+} with depth seems to mirror that of K^+; it increases gradually to 820 mbsf then drastically increases with depth. Variations in concentrations of major cations (Na^+, K^+, and Mg^{2+}) resemble that of chlorinity. Minor variations might be caused by the interaction between IW and detrital and authigenic minerals.

Among minor alkaline and alkaline earth elements, Rb and Sr variations with depth are similar to that of Na^+; the minimum and maximum concentrations appear at the BSR (~400 mbsf) and the Unit II/III boundary, respectively. Lithium variation is also similar to Na^+ variation. Boron and Ba variations are similar to each other: concentrations decrease in Unit I then slightly increase and decrease at 200–300 and 400–500 mbsf, respectively, and reach the maximum at ~815 mbsf. Cesium does not change with depth very much except in Unit I, where it increases with depth.

Silicon concentration generally increases with depth and the maximum concentration is found at the Unit III/IV boundary. Trace elements, although varying in large ranges, can be categorized into two groups based on the variations with depth. The first group is elements concentrated from 200 to 300 mbsf: V, Cu, and Pb. The second group is those that increase with depth: Fe, Mn, Zn, Mo, and U. In the latter group, Fe and Zn are enriched in the lower half of Unit II and the others are enriched in Unit IV. Although controlling factor(s) on the behaviors of those elements are not clear at present, lithology and the associated chemical composition would effect the vertical distribution of the elements.

Interstitial water geochemistry by GRIND method

The GRIND method was proposed as an alternative method for when core recovery was too low to provide enough volume from the WRC sample for the standard method and/or when the sample was too hard to squeeze for the standard squeezing method (Expedition 315 Scientists, 2009b). This method was applied to samples in Holes C0002H (Section 338-C0002H-2R-2; 1111 mbsf) and C0002J (Section 338-C0002J-7R-1; 933 mbsf). In addition, we selected 10 WRCs for IW obtained from Holes C0002J–C0002L to conduct a method comparison test; those samples were extracted by both standard and GRIND methods. Water content of the studied core samples was determined prior to the process (Table **T30**). Analytical results are shown in Table **T31.** Comparison between the values obtained from the standard squeezing method and the GRIND method is shown in Figure **F72.**

The GRIND method was evaluated in detail (see **"Appendix A"** in the "Methods" chapter [Strasser et al., 2014a]). Although the GRIND method is only applicable for limited components, it is useful to provide some geochemical profiles when a limited amount of sediment can be used to extract IW. As shown in Figure **F72,** concentrations of some elements determined by the GRIND method are consistent with those determined by the standard squeezing method. Section 338-C0002H-2R-2 (1111 mbsf) used for extracting IW was fine sand, which is not usually suitable for IW analyses because sand is permeable and its IW is easily contaminated with drilling mud. However, IW extracted from Section 338-C0002H-2R-2 is likely pure IW because its chemistry is different from that of the liquid in core liner (LCL), which is seawater mixed with soluble components derived from bentonite (see **"Liquid in core liner chemistry"**). Chlorinity is 461 mM (extracted with Milli-Q water), which is much lower than that of seawater and close to that of IW in core sediment taken from Hole C0002B at ~1000–1050 mbsf (Expedition 315 Scientists, 2009b). Na^+, Mg^{2+}, and Ca^{2+} concentrations are also close to those from Hole C0002B at ~1000–1050 mbsf. SO_4^{2-} concentrations are slightly higher than those in nearby sediment; however, those are almost on the trend of SO_4^{2-} concentration with depth. K^+ concentration is much higher than in nearby sediment, as expected from the evaluation test of the GRIND method (see **"Geochemistry"** and **"Appendix A"** both in the "Methods" chapter [Strasser et al., 2014a]). Strontium concentration, which is expected to be almost the same as that obtained by the standard squeezing method, also lies on the previously obtained profile of Sr with depth. Boron concentration is also expected to be similar to that obtained by the standard squeezing method; however, it was much higher than those of IW at 1000–1050 mbsf in Hole C0002B. The reason for this large difference in B concentration is unknown at present.

Reasonable concentrations of dissolved components extracted using the GRIND method suggest that this method would be applicable to IW not only in clayey sediment but also in sandy sediment if the pore pressure of core sediment is high enough to prohibit the incorporation of mud invasion. Analysis of IW from sand intervals, however, should be carefully evaluated for contamination.

Interstitial water geochemistry of cuttings

Interstitial pore water was extracted from two underreamer samples (cuttings) at 1975 and 1982.5 mbsf using both squeezing and GRIND methods (see **"Geochemistry"** in the "Methods" chapter [Strasser et al., 2014a]). We also analyzed one drilling mud water sample from the mud tank. Aliquots were analyzed for anions and cations, as well as major, minor, and trace elemental concentrations following the detailed analytical methods (see **"Geochemistry"** in the "Methods" chapter [Strasser et al., 2014a]). The results are listed in Table **T32.** It is not possible to assess any trend from two data points; however, the absolute elemental values shed some light on whether or not the samples were contaminated by the drilling mud. Concentrations of dissolved species are higher in aliquots extracted using the traditional squeezing method compared to those of dissolved species extracted by the GRIND method. In general, concentrations of anions, cations, and major, minor, and trace elements are 2–100 times higher than those of pore water data from Site C0001 (Expedition 315 Scientists, 2009a) with the exception of Na^+ and SO_4^{2-}. Na^+ concentration is closer to International Association for the Physical Sciences of the Oceans (IAPSO) standard seawater values and might originate either from contamination by seawater or from the formation. SO_4^{2-} values are closer to the values of shallower depth (i.e., 3–4 mbsf) in Hole C0001E, although they were extracted from 1975.5 and 1982.5 mbsf in Hole C0002F. Taking into account the concentrations of elements, anions, and cations, these data suggest that IW of two samples are severely contaminated. In the following, we shed further light on the contamination using the chemical composition of the drilling mud water derived from one sample.

The major water-soluble constituents of drilling mud used during operations are generally 50 g KCl, 170 g NaCl, and 5 g soda ash (Na_2CO_3) dissolved in 1 L of seawater (assumed to contain 40 g/L salts) and adjusted to a pH of 9.0 to 10.5 with KOH solution. These salts were combined with a number of commercial products that act as colloidal lubricants and viscosifiers, including 5 g TelGel (bentonite), 8 g TelPolymerL (cellulose derivative), 10 g TelPolymerDX (starch derivative), 2.5 g Xanvis (xanthan gum derivative), 50 g CleanLubeL (lubricant and gas-hydrate inhibitor), 100 g RevDust (pseudocuttings), and 1 g TelniteGXL (antiseptic agent). K^+ concentration could be used as a first-order proxy for contamination, as its concentration was ~30 times higher than that of K^+ concentration in Hole C0001E, in which a water-based drilling mud was used. Furthermore, SO_4^{2-} concentration is as high as seawater at 1975.5 or 1982.5 mbsf, which again suggests contamination by drilling mud. However, K^+ and SO_4^{2-} concentrations in drilling mud used during Expedition 338 were up to 6 and 10 times smaller, respectively, than in the cuttings. Following the analytical results shown in Table T32, the only proxy suitable for contamination of drilling mud would be Zn, Fe, and Si. Zn and Fe in particular are significantly enriched in drilling mud, whereas concentrations in cuttings samples are ~10 and ~100 times smaller, respectively. Consequently, contamination of the analyzed cuttings by drilling mud seems less likely.

Liquid in core liner chemistry

Analytical results of LCL samples are given in Table T33. LCL concentrations are almost the same as those of seawater: chlorinity varies within the range of 530 and 552 mM except for three samples from Hole C0002K. However, the differences in major element concentrations between LCL samples are larger than the analytical error (e.g., analytical error determined by repeating analyses of standard seawater was about ±0.6% for chlorinity). Thus, most LCL likely contains a small amount of IW, in which chlorinity is lower than that of seawater.

Organic geochemistry

Gas chemistry from cores

Headspace gas samples were taken from cores in Holes C0002H and C0002J–C0002L (Tables T34, T35). In addition, void gas samples were collected from gas pockets in core liners (Table T36). Methane, ethane, and propane concentrations in the headspace and void gases were measured by flame ionization detector, and carbon isotopic compositions of methane ($\delta^{13}C$-CH_4) were measured by methane carbon isotope analyzer (MCIA) (see **"Sampling and analysis of gas samples from cores"** in the "Methods" chapter [Strasser et al., 2014a]). Concentrations of methane, ethane, and propane are shown in Tables T34, T35, and T36. Concentrations are shown in parts per million by volume (ppmv) and moles per kilogram, the gas molecules dissolved in 1 kg of interstitial water as calculated by the equation in **"Sampling and analysis of gas samples from cores"** in the "Methods" chapter (Strasser et al., 2014a). $\delta^{13}C$-CH_4 and ratios of methane to ethane and propane ($C_1/[C_2 + C_3]$) are also shown in Tables T34, T35, and T36.

Methane is the predominant hydrocarbon in all core samples. Ethane and propane are detected in most samples. These features are ubiquitous in deep-sea sediment as shown world-wide by Deep Sea Drilling Project, ODP, and IODP studies. Void gas is richer in methane than headspace gas (Tables T35, T36), which might be due to the lower solubility of methane compared to ethane. Because void gas originates from dissolved gas in interstitial water and headspace gas data show chemical features of gas in sediment, void gas should concentrate more volatile gas and headspace gas taken from sediment should have less volatile gas. Nevertheless, $\delta^{13}C$-CH_4 values are not different between void and headspace gases, suggesting that degassing processes did not affect $\delta^{13}C$-CH_4 values. The $C_1/(C_2 + C_3)$ ratios of headspace gas from core at 1101.9 and 1111.0 mbsf in Hole C0002H showed good agreement with those of mud gas from Hole C0002F (Table T35).

During this expedition, in addition to the conventional headspace gas extraction, headspace gases were extracted by alkaline solution (see **"Sampling and analysis of gas samples from cores"** in the "Methods" chapter [Strasser et al., 2014a]). We compared the gas data obtained by the two methods with respect to methane concentration, ethane concentration, $C_1/(C_2 + C_3)$, and $\delta^{13}C$-CH_4 (Fig. F73). For ethane, the headspace gases obtained by the NaOH addition method showed lower concentrations than those obtained by the oven-heating conventional method. Such a difference was not observed in methane concentrations. This could be due to higher solubility of ethane compared to that of methane. Such a difference in ethane concentrations causes higher $C_1/(C_2 + C_3)$ ratios obtained by the additional headspace gas extraction than those obtained by the conventional headspace gas extraction. We did not find a significant difference in $\delta^{13}C$-CH_4 data between the two methods. The depth profiles of methane, ethane, and propane concentrations are shown in Figure **F74.** Methane peaks at 30, 270, 920, and 1050 mbsf, whereas ethane peaks at 920 and 1050 mbsf. Propane was not detected at most depths. The methane peak at 30 mbsf could be produced by microbes utilizing relatively fresh organic matter. The methane peak at 270 mbsf could be caused by the presence of gas hydrates, indicated by IW data. The methane peak at 920 mbsf corresponds to the Unit III/IV boundary. Unit III is the transition unit from the Kumano Basin sediment to the old accretionary prism, which is characterized by multiple volcanic ash layers. Methane is concentrated just below Unit III, indicating that sediment in Unit III could play a role as a seal for methane. The methane peak at ~920 mbsf was also observed in mud monitoring data from Hole C0002F (Fig. **F75**). Additionally, the methane peak was accompanied by an ethane peak (Fig. **F74**), suggesting the hydrocarbons are derived from a common process.

The $C_1/(C_2 + C_3)$ and $\delta^{13}C$-CH_4 data are shown in Figure **F76.** Data from this expedition are consistent with data from Expedition 315 (Expedition 315 Scientists, 2009b). The $C_1/(C_2 + C_3)$ ratio decreases with increasing depth to 1100 mbsf. The $\delta^{13}C$-CH_4 values gradually increase from 100 to 600 mbsf, below which they decrease slightly. The $C_1/(C_2 + C_3)$ ratios and $\delta^{13}C$-CH_4 values are generally used to consider the origin of methane (Bernard et al., 1978). Microbial origin methane has $\delta^{13}C$-CH_4 values less than –55‰ Vienna Peedee belemnite (VPDB) (Rice and Claypool, 1981), and $C_1/(C_2 + C_3)$ ratios are as high as 1000 (Bernard et al., 1978). On the other hand, thermogenic methane has $\delta^{13}C$-CH_4 values between –50‰ and –25‰ VPDB (Schoell, 1983) and $C_1/(C_2 + C_3)$ ratios lower than 100 (Bernard et al., 1978). The data from Site C0002 are plotted on the Bernard diagram (Fig. **F77**). The methane sampled during Expedition 338 primarily falls in the region of microbial origin. A few samples fall in the region of mixing with thermogenic methane or that of oxidized microbial methane.

Chemical components in IW, resistivity during LWD, and infrared camera data indicate the presence of gas hydrates between 200 and 400 mbsf. The methane taken from the methane hydrate zone corresponding to core samples from Holes C0002K and C0002L falls in the region of microbial origin. The data suggest the methane hydrates are composed of microbial methane. According to the temperature profile at Site C0002, obtained by downhole temperatures and thermal conductivity on cores measured on board the ship during Expedition 315 (Expedition 315 Scientists, 2009b), the temperature is ~43°C at ~1000 mbsf and estimated to be ~86°C at ~2000 mbsf. Because generation of thermogenic methane occurs at temperatures >80°C, any thermogenic methane should have originated from deeper than 2000 mbsf.

Gas chemistry of mud gas

Overview of mud-gas composition

Continuous drilling with mud-gas monitoring took place while drilling Hole C0002F from 875.5 to 2005.5 mbsf. In total, three autonomous data sets were generated during the operation (i.e., the SSX data set including data from the gas chromatograph [GC]-natural gas analyzer [NGA], Geoservices, and the MCIA; the process gas mass spectrometer (PGMS) data set; and the Rn data set) (see **"On-line radon analysis"** in the "Methods" chapter [Strasser et al., 2014a]). The SSX and PGMS data sets were generated by the newly installed mud-gas monitoring system on the *Chikyu* (see **"Recording of on-line gas analysis and monitoring of drilling operations, time, and depth"** in the "Methods" chapter [Strasser et al., 2014a]). Most likely due to air contamination in the onboard system (see **"Background control, quality checks, and comparison of different sampling techniques"** in the "Methods" chapter [Strasser et al., 2014a]), absolute gas concentrations determined by the MCIA, GC-NGA, and PGMS differ from those measured by Geoservices. For the PGMS, this is only of secondary importance because the concentrations of different gases were normalized to 100% (see **"Geochemistry"** in the "Methods" chapter [Strasser et al., 2014a]). At the same time, the individual data sets include data from different instruments, measurement techniques, and sampling intervals. Nonetheless, general trends in the hydrocarbon gas data and the nonhydrocarbon gas data can be correlated across the data sets (Figs. **F75, F78, F79, F80, F81, F82**).

Following the Geoservices data set (Fig. **F78**), the total gas content as well as the methane concentration ranged between 0% and 16.4%. Ethane concentrations reached 0.03%. Higher homologues (propane, *n*-butane, and *i*-butane) were below 0.01%, and consequently, did not add significantly to the total gas composition. Gas concentrations determined by the stationary onboard instruments are different than those from the Geoservices data set: up to 8.64%, 0.09%, and 0.23% for methane, ethane, and propane, respectively, whereas the remaining hydrocarbons remain below 0.01% (Figs. **F75, F79**).

For the nonhydrocarbons, the PGMS data set was dominated by nitrogen (76.6%) and oxygen (24.8%), whereas the concentrations of the remaining nonhydrocarbons ranged from 0.02% for Xe to 1.55% for H_2 (Fig. **F80**). Although absolute concentrations are not reliable (see discussion in **"Liquid in core liner chemistry"**), general trends can be observed.

Mud-gas distribution with depth

From 875.5 to 2005.5 mbsf, the total gas concentration shows an overall decline from a maximum of 16.4% near 918 mbsf to values below 0.01% near 1996 mbsf (Fig. **F78**). Gases in this interval are mainly hydrocarbons. At 918 mbsf, a sharp increase in gas remains to 1000 mbsf and is composed of two different peaks, indicating concentrations of 16.4% at 936 mbsf and 13.8% at 944 mbsf. The total gas from 918 to 1000 mbsf is mainly methane with minor amounts of propane (Figs. **F75, F78, F79**). Below 1000 mbsf, gas concentrations generally decrease with increasing depth. The total gas concentration is still dominated by methane, and, in the Geoservices data, decreases, on average, by 75 ppm/m. Methane decreases by almost the same rate with 65 ppm/m, whereas no clear trend is visible in the higher homologues. Throughout the whole section, the relative changes of Rn, not in terms of trend but in terms of increase and decrease in concentrations, show a good correlation with relative changes in methane (Fig. **F75**). The same is true for ethane, except between 918 and 1000 mbsf (Fig. **F79**). Ethane determined by the GC peaks at 0.005% at 1122 mbsf, and although absent in the Geoservices data, this peak correlates well with the methane and propane data in all data sets (Figs. **F78, F79**). From 1100 to 1240 mbsf, generally high ethane and propane values are present, which correspond to elevated Rn concentrations (Fig. **F79**). Between 1240 and 1460 mbsf, generally higher ethane values are visible, which peak with 0.035% in the Geoservices data set and in the GC data (0.04%) at 1378 mbsf. This again corresponds well to relatively small increases in methane and propane to 2.7% and 0.003%, respectively. Between 1460 and 1600 mbsf, an overall decrease in ethane and propane occurs, and beginning near 1600 mbsf, propane shows overall higher values. Below 1827 mbsf, a drop in total gas concentration exists, which corresponds to decreases in methane and ethane concentrations in all data sets, whereas propane shows no overall difference in concentration.

The variations of the nonhydrocarbon components with depth are characterized by significant shifts in concentration of the individual gases at 918, 1000, 1060, 1240, 1540, 1600, 1855, and 1933 mbsf (Fig. **F80**). Almost all changes correspond to a downtime longer than 120 min (red arrows in Fig. **F80;** Table **T3**) (see **"Operations"**). Here, downtime is defined as the interval during operations when the bit is off bottom and the mud pumps might have been turned off. The shifts can be characterized as follows:

- 918 mbsf: small increase in H_2 and CO_2 (Geoservices only) and decrease in N_2, O_2, and Ar; ~10 m deeper, Rn increases.
- 1000 mbsf: sharp positive peak in the CO_2 data, which correlates with a positive shift in air-derived gases like N_2, Ar, O_2, and Xe, as well as with a positive shift in the CO_2 data provided by Geoservices. This anomaly correlates with a downtime period.
- 1060 mbsf: decrease in H_2, Ar, and Rn and a positive peak in CO_2 (only PGMS data) and He. Here, a downtime period was reported, and calibration of the PGMS was carried out.
- 1232 mbsf: increase in H_2, Ar, CO_2 (Geoservices), and He. Subtle positive peaks were identifiable in He, Xe, and N_2, whereas CO_2 (PGMS) shows a strong positive peak. Here, a downtime period of ~25 min was reported, and calibration of the PGMS was carried out.
- 1540 mbsf: sharp decrease and peak in CO_2 derived by Geoservices and PGMS analysis, respectively, as well as a decrease in Ar, an increase in N_2, and positive peaks in H_2 and O_2. For O_2, this peak is followed by an overall decrease in concentration. These changes in concentration correspond to a downtime period of almost 13 h and calibration of the gas monitoring instruments.
- 1600 mbsf: increase in all gases except for N_2 and Rn, which decrease. The data shifts correlate with a downtime period of ~16 h.
- 1855 mbsf: sharp decrease in H_2, Ar, O_2, He, and Rn and increase in N_2 and CO_2 (Geoservices only; PGMS shows only a small peak). The shift at this depth corresponds to a downtime period of almost 7 h.
- 1933 mbsf: Change in trends of Ar and O_2 (increase) as well as N_2 and Rn (decrease). This change is close to a downtime period of 39.5 min at 1921 mbsf.

Classification of hydrocarbons

A clear classification of the hydrocarbon (HC) gases proved to be difficult. Above 918 mbsf, the Bernard parameter [methane/(ethane + propane)] combined with the $\delta^{13}C$ of methane (Bernard et al., 1978) indicates a mixed-gas regime (Fig. **F81**). A close examination of the gas signature of the major gas increases between 918 and ~1000 mbsf (Figs. **F78, F79, F80**), showed that the composition of HC gases is defined by the presence of methane and a small concentration of propane, as well as low $\delta^{13}C$ values of around –70‰ (Figs. **F75, F79, F81**). Below 1000 mbsf, a steady decline of the Bernard parameter is evident, similar to the one found in the total gas and the methane data provided by Geoservices. The $\delta^{13}C$ and the Bernard parameter point to a thermogenic source of HC gases below 1700 mbsf, which start to increase significantly at ~1830 mbsf.

Preliminary interpretation

The increase of gas at 918 mbsf correlates well with the LWD and lithology findings (see **"Logging while drilling,"** and **"Lithology"**). Based on the results of Expedition 315 Scientists (2009b) and Expedition 319 Scientists (2010), it is most likely that at 918 mbsf, an unconformity separates the Kumano Basin (Unit III) and the upper section of the accretionary prism (Unit IV). The dominance of bacterial methane between 918 and 1000 mbsf contradicts the findings on core samples from Hole C0002H and of previous investigations at Site C0002 (Expedition 315 Scientists, 2009b), where gas with a higher thermogenic signature was detected (i.e., Bernard parameter of 100–200). In contrast, the presence of microbial methane is also supported by the results of Expedition 319 Scientists (2010; see figures F48 and F49) and the relatively high amount of organic material found in cuttings from Hole C0002F (see **"Lithology"**) (Fig. **F81**). When considering the Rn data, which sharply increase 10 m below the inferred boundary, migration of the fluids from deeper sections might also be possible. Whether the source of the HC gases is the same as that for Rn remains speculative at this point. Based on the compartmentalization (i.e., high gas content below 918 mbsf compared to low gas content above) seen in the gas data, Unit III might act as a seal for upward migration of gases, allowing accumulation of gases below the unconformity. This corresponds with the sharp increase in gas concentration found in cores from Hole C0002J (Fig. **F74**). The interpretation that the sediment below the unconformity might act as reservoir is supported by an increase in porosity as determined based on LWD resistivity-derived porosity (see **"Logging while drilling"**).

With increasing depth, the presence of marine organic matter is supported by the Bernard parameter and the $\delta^{13}C$ values (see Bernard diagram Fig. **F18** in the "Methods" chapter [Strasser et al., 2014a]). During IODP Expedition 319, elevated methane concentrations of up to 12% were found at IODP Site C0009 between 1050 and 1300 mbsf (Expedition 319 Scientists, 2010). Based on the Bernard parameters and a very high percentage (up to 100%) of wood fragments found in this interval, the Expedition 319 Scientists (2010) suggested that the methane is of microbial origin. In Hole C0002F, fragments of wood and lignite were also found, relatively abundant in the upper part of the borehole <1685.5 mbsf and less common in depths >1685.5 mbsf (Figs. **F75, F79, F81**).

Based on the overall changes detected in hydrocarbons in the Geoservices and SSX data sets (see **"Overview of mud-gas composition"**) and the Rn data, six boundaries (seven gas packages) can be defined (Fig. **F82**). The first boundary, separating logging Unit III from Unit VI, is set at 918 mbsf, where the major gas increase exists (Fig. **F78**). A second boundary is proposed at ~1100 mbsf, followed by boundaries at 1240 and 1460 mbsf. The fifth boundary is set at 1600 mbsf, and the last boundary, where the overall gas concentration is declining and shifts to a more thermogenic regime, exists at 1827 mbsf (Figs. **F81, F82**). Considering other shipboard data allows correlation of some gas geochemical data to logging unit boundaries at 918 mbsf (logging Units III/IV), 1100 mbsf (logging Subunits IVB/IVC), and 1638 mbsf (logging Units IV/V). The logging unit boundaries at 1638 mbsf are 38 m deeper than the observed changes based on drilling mud–gas data (Fig. **F82**). There are many possible explanations for this observation, including upward migration pathways for gases, which cannot be adequately explained based only on the shipboard data. Postcruise research might elucidate these differences.

Defining additional boundaries and/or constraining unit boundaries by data shifts and peaks reported for the nonhydrocarbons is difficult because the sources of data shifts are not resolved. Most of the anomalies in the PGMS data and the CO_2 data from Geoservices correlate well with downtimes >120 min (Fig. **F80**), although not all shifts appear after every downtime. Changes in mud composition, and in particular the pH of the mud, can have a significant effect on the CO_2 data, but no clear correlation can be made based on the information provided by the daily mud report, even if the lag time is taken into account. Additionally, in the PGMS data after the sudden increase or decrease in concentration, the concentrations stay on this level until the next shift occurs. This might be due to instrument calibrations being carried out during longer downtimes. The downtime itself is likely not the sole reason for the anomalies because after one complete circulation (i.e., 1 lag time), the concentrations should return to previous values, which is not the case. Structural and/or lithologic features cannot be excluded and may have contributed to shifts. The changes at 1060, 1600, and 1933 mbsf are close to the boundaries observed in logging and structural data (see "Logging while drilling" and "Structural geology"), whereas the shifts at 1000, 1232, 1540, and 1855 mbsf correlate well with gas package boundaries found in the HC data (Fig. F82). Of particular interest is the change in trend at 1933 mbsf, which is different from the other signals. This boundary is well correlatable with the top of logging Subunit VB and, thus, the change in the gas data may be dominated by a change in lithology and/or structure. Because most of the anomalies are also visible in the CO_2 data provided by Geoservices, a combination of real changes and calibration of the PGMS during downtimes, which superimposes the natural shift to higher/lower concentrations, might explain the observed shifts and peaks in the PGMS data set. Because of the several uncertainties, a clear distinction between artificially created data shifts and actual data cannot be resolved at this time.

The overall low CO_2 concentrations (0.03% in the PGMS data, almost atmospheric values) were caused by the high pH of the drilling mud (9.9–10.6). Once CO_2 enters the highly alkaline mud, hydrogen carbonate is generated:

$$CO_2 + 2H_2O \leftrightarrow H_3O^+ + HCO_3^-. \quad (1)$$

Occasionally, CO_2 concentration increased to two times the atmospheric value (~0.07%), but this might be due to calibration issues associated with highly concentrated standard gases. The high He concentration (up to 0.03%) is also influenced by the standard gas used for the calibration having a He concentration of almost 1%, which is too high for defining low values such as atmospheric (~5.2×10^{-5}%). Considering the overall constant He/Ar ratios and the overall low ethane values, He is most likely derived from air. The origin of He will be constrained by postcruise analysis of the $^4He/^3He$ ratio.

Similar to He and CO_2, Xe concentration is unreasonably high (up to 500 times higher than the normal value in air, ~0.09×10^{-5}%). Here again, calibration with a highly concentrated standard gas (Xe = 0.97%) is the most likely reason. Later shore-based analysis of noble gases will constrain the shipboard results.

For N_2, although it can originate from various sources including clay-rich sedimentary rock (e.g., Krooss et al., 1995; Mingram et al., 2005), the N_2/Ar ratio of 70–87 supports an atmospheric source (Jenden et al., 1988; Krooss et al., 1995). The dominance of O_2 and N_2 as well as the low values of the other nonhydrocarbon gases in the PGMS data set also indicate air contamination.

Inorganic carbon, total carbon, and total nitrogen

Calcium carbonate ($CaCO_3$), total organic carbon (TOC), and total nitrogen (TN) concentrations were determined from total inorganic carbon, total carbon, and TN measurements of 237 cuttings samples from the >4 mm and 1–4 mm cuttings size fractions from 920.5 to 2004.5 mbsf in Hole C0002F as well as from core samples from Holes C0002K, C0002L, C0002J, and C0002H (see "Geochemistry" in the "Methods" chapter [Strasser et al., 2014a] for analytical procedures). $CaCO_3$, TOC, and TN concentrations and TOC/TN (C/N) ratios are plotted in Figures F83 and F84. These data and total sulfur (TS) and the TOC/TS ratio are provided in Tables T13 and T37.

$CaCO_3$ in core samples varies between 0.03 and 26.42 wt%, with a median of 5.33 wt%. Generally, concentrations fit well with the values found in Hole C0002B (Fig. F84). The highest values were found at 250 mbsf in Hole C0002K and 900 mbsf in Hole C0002J. The data obtained from cuttings correspond well with the results obtained from core samples with the highest $CaCO_3$ concentrations close to 900 mbsf. Overall, $CaCO_3$ in cuttings ranges from 2.63 to 15.76 wt% with a median of 4.20 wt% (Fig. F83). Between 920.5 and 1105.5 mbsf, $CaCO_3$ decreases from 15.76 to 3.5 wt% (0.089 wt%/m) with a few scattered data points. High $CaCO_3$ concentrations near 945.5 mbsf match those determined on cores from Expedition 315 (Expedition 315 Scientists, 2009b). In addition, the decreasing trends from 945.5 to 1049.5 mbsf match those of the decreasing $CaCO_3$ values in Hole C0002B. The magnitudes, however, differ with $CaCO_3$ concentrations ~7% lower based on cuttings. Between 1355.5 and 1895.5 mbsf, $CaCO_3$ shows less variation (from 2.63 to 4.49 wt%), with a median value of 3.57 wt%. From 1895.5 to 1955.5 mbsf, $CaCO_3$ concentration increases to 6.41 wt% then decreases to 3.35 wt% at 2004.5 mbsf. Two $CaCO_3$ values of 1.25 and 1.20 wt% at 880.5 and 915.5 mbsf, respectively, were determined to be influenced by cement (Table T37). $CaCO_3$ concentrations of eight mud water samples range from 2.48 to 2.84 wt% (see Table T13 in the "Methods" chapter [Strasser et al., 2014a]), and these data allow us to assess the background concentration and any potential contamination by mud water to those of the $CaCO_3$ data of cuttings. We also report $CaCO_3$ concentrations of 5.4 and 4.9 wt% at 1975.5 and 1985.5 mbsf, respectively, from the underreamer samples (Table T37). The trend of $CaCO_3$ concentration and distribution with depth generally agrees with the downcore weight percent calcite data, which are derived from XRD measurements (see "Lithology"). However, there are differences in the absolute values (Fig. F23).

TOC found in core samples remains almost constant with depth, with values ranging from 0.21 to 0.97 wt% and a median of 0.58 wt%. Surprisingly, the TOC of cuttings is significantly higher and more variable. Concentrations between 0.80 and 3.89 wt% with a median of 1.61 wt% were detected. Between 920.5 and 1240 mbsf, TOC of cuttings is higher than those of core samples (920–1049.18 mbsf) (Fig. F83, F84). Between 1345.5 and 1655.5 mbsf, TOC ranges from 1.00 to 2.02 wt% and generally decreases downhole along a linear trend but also has a wide scatter. TOC changes to an increasing trend from 1655.5 to 1875.5 mbsf with values from 1.04 to 1.77 wt%. From 1875.5 to 2004.5 mbsf, TOC is almost the same (0.8–1.77 wt%). To some extent, the TOC data correlate with those of the methane gas data (Figs. F78, F83).

TN obtained from core samples varies between 0.01 and 0.12 wt% with a median of 0.08 wt%. TN of cuttings is in the same range, with concentrations from 0.03 to 0.07 wt% and a median of 0.06 wt% (Fig. F83). In the TN of cuttings, three trends can be identified: (1) a downward increase between 920.5 and 1050 mbsf, (2) a scatter of data with no apparent trend between 1050 and 1355.5 mbsf, and (3) an increasing trend between 1355.5 and 2004.5 mbsf with a more gentle slope in comparison to TN between 920.5 and 1050 mbsf. TOC and TN data show opposite trends downhole. It is noteworthy that the TN content of cuttings is generally lower compared to those of the TN data from the other holes at Site C0002 (Fig. F84) (Expedition 315 Scientists, 2009b) but consistent with TN at Site C0009 (Expedition 319 Scientists, 2010).

TS was only determined from core samples and ranges between 0.02 and 1.22 wt% with a median of 0.12 wt%. Although highly variable, TS usually stays below 1 wt% downhole. Between 930 and 940 mbsf, a general increase to values >1 wt% can be observed, but below 1000 mbsf, the concentrations are again <1 wt% (Fig. F84).

C/N ratios in core samples range between 4.5 and 13.1 with a median of 7.2. A clear trend is not visible; the data are scattered. C/N ratios in cuttings are generally higher and highly variable with concentrations between 14.7 and 69.7 and a median of 28.0 (Fig. F83). Between 920.5 and 1265.5 mbsf, an increasing trend in C/N from 22.6 to 69.7 with a median of 28.9 is observed. Relatively higher values from 20.9 to 40.1 between 1265.5 and 1635.5 mbsf also occur. Between 1635.5 and 1855.5 mbsf, C/N is constant with a median of 20.8. Again, C/N between 1875.5 and 2004.5 mbsf is almost constant with a median of 16.4, which is lower than that of the values between 1635.5 and 1855.5 mbsf.

It is commonly accepted that the C/N of marine organic matter typically ranges from ~4 to ~10 (Meyers, 1997), compared to higher values (>10) in terrestrial organic matter. This distinction arises from the absence of cellulose in algae, its abundance in terrestrial plants, and the protein richness of algae (Meyers, 1997). Therefore, data in Hole C0002F suggest that organic matter in the upper section (920.5–1355.5 mbsf) might be dominated by a terrestrial source, consistent with the more negative $\delta^{13}C$ values of methane (Fig. F18 in the "Methods" chapter [Strasser et al., 2014a]). However, when the difference in TOC between cuttings and core is considered, the elevated TOC in cuttings is most likely spurious. To assess any contamination by drilling mud, we have determined TOC from eight drilling mud samples (see Table T13 in the "Methods" chapter [Strasser et al., 2014a]). Indeed, TOC is extraordinarily high with concentrations between 13.65 and 17.00 wt%. Consequently, whether terrestrial organic matter is more abundant in Hole C0002F than in the other holes or not can not be evaluated at this point because of the artificial increase in TOC.

The $CaCO_3$, TOC, and TN data from Hole C0002F allow identification of two significant shifts: (1) between 1635.50 and 1645.50 mbsf and (2) between 1885.50 and 1895.5 mbsf (Fig. F83). These shifts are consistent with the boundaries defined by LWD data (Fig. F8; Table T4) that show significant changes in the rock physical properties. Furthermore, the overall trend of the $CaCO_3$ data seem to match with those of the bulk mineralogical data derived from XRD (calcite, Fig. F28) and XRF (CaO, Fig. F30A) (see "Lithology"). However, the lithologic Unit III/IV boundary appears diffuse, although it is well identified in the LWD data at 918.5 mbsf as well as in earlier reports from Hole C0002B (Expedition 315 Scientists, 2009b) and bulk mineralogical data (Figs. F28, F30A).

Physical properties

At Site C0002, physical properties measurements were performed on unconsolidated to slightly consolidated sediment from Holes C0002K and C0002L, consolidated mudstone/sandstone samples from Holes C0002H and C0002J, and cuttings from Hole C0002F. These data provide essential material characterizations for lithologic unit discriminations and their corresponding consolidation states. Determination of physical properties on cores and cuttings also helps calibration as well as correlation with LWD data (see **"Logging while drilling"** and **"Cuttings-core-log-seismic integration"**).

MAD measurements were conducted on both cores and cuttings. Thermal conductivity was measured on whole-round cores of soft sediment from Holes C0002K and C0002L using a full-space needle probe, whereas it was measured on the working halves from Holes C0002H and C0002J using a half-space probe. Electrical resistivity was measured on soft-sediment cores from Holes C0002K and C0002L with a four-pin electrode array inserted directly into the working half. Where sediment was too consolidated (Holes C0002H and C0002J), discrete samples were taken from the working half for *P*-wave and electrical resistivity measurements. Vane shear and penetrometer measurements were made on soft-sediment cores from Holes C0002K and C0002L, and discrete samples were taken for unconfined compressive strength (UCS) measurements for consolidated cores from Holes C0002H and C0002J. Two LOTs were performed at 872.5 mbsf in Hole C0002F.

Whole-round multisensor core logger

Whole-round cores from Holes C0002H and C0002J–C0002L were analyzed using the whole-round multisensor core logger (MSCL-W). The results of gamma ray attenuation (GRA) density, magnetic susceptibility, natural gamma radiation (NGR), and electrical resistivity measurements (see the **"Methods"** chapter [Strasser et al., 2014a]) on whole-round cores are summarized with Expedition 315 data (Fig. **F85**) (Expedition 315 Scientists, 2009b). MSCL-W *P*-wave measurements are not presented because they exhibit an extreme amount of noise because of poor contact between liner and sediment.

MSCL-W data collected during Expeditions 315 and 338 provide a continuous record for the forearc basin sediment. GRA density increases with depth. In lithologic Unit II, magnetic susceptibility and NGR increase with depth above 450 mbsf; below 450 mbsf both decrease with depth. Electrical resistivity also shows a similar but less pronounced trend.

The diameter of the core (called "core thickness" and equal to the liner wall plus the core thickness; see the **"Methods"** chapter [Strasser et al., 2014a]) is usually measured by a linear variable differential transformer located 42 cm from the zero-distance reference where the *P*-wave transducer is also located. During the multisensor core logger (MSCL) runs on Cores 338-C0002H-1R and 2R, the core thickness was accidentally measured with an offset of 2 cm compared to the *P*-wave traveltime measurement. A 40 cm long core liner filled with water was used to estimate errors associated with the offset (Table **T38**). The errors in thickness are mostly within 1% except at the ends of the core liner. The errors at the ends were probably caused by end caps and vinyl tape wrapping the liner and caps. This offset of 2 cm in core thickness measurements thus has little effect on the measured values of *P*-wave velocity (V_P), GRA density, and magnetic susceptibility. However, the offset error has been corrected on V_P for Cores 338-C0002H-1R and 2R.

Moisture and density measurements (cores)

A total of 355 discrete samples from Holes C0002H and C0002J–C0002L were measured for MAD. All MAD data from Expedition 338 cores are summarized in Table **T39** and Figure **F86.** Between 200 and 502 mbsf in Holes C0002K and C0002L, bulk density ranges from 1.47 to 2.08 g/cm^3, grain density ranges from 2.40 to 2.96 g/cm^3, and porosity ranges from 37% to 74%. Both bulk density and porosity show less scatter with an increase in depth. This probably corresponds to a decrease in the number of sand layers with depth (see **"Lithology"**). Sandy samples yield lower porosity and higher bulk density. Between 902 and 1113 mbsf in Holes C0002H and C0002J, bulk density ranges from 1.83 to 2.15 g/cm^3, grain density ranges from 2.54 to 2.84 g/cm^3, and porosity ranges from 35% to 52%.

Thermal conductivity (cores)

Thermal conductivity was measured on whole-round cores from Holes C0002K and C0002L using a needle probe sensor and measured on working-half cores from Holes C0002H and C0002J. All data are shown with data from Expedition 315 Holes C0002B–C0002D in Figure **F87** (Expedition 315 Scientists, 2009b). Thermal conductivity ranges from 0.74 to 1.40 W/(m·K) in Holes C0002K and C0002L between 200 and 502 mbsf and from 1.11 to 2.19 W/(m·K) in Holes C0002H and C0002J. Thermal conductivity increases linearly with depth to ~550 mbsf, whereas it shifted to values of 1.50 W/(m·K) and slightly increases through lithologic Units III and IV.

Ultrasonic *P*-wave velocity and electrical resistivity (cores)

A total of 11 discrete cube samples from Holes C0002H and C0002J (2 samples from Hole C0002H and 9 samples from Hole C0002J) were analyzed for electrical resistivity and V_P along three orthogonal directions (*x*, *y*, and *z*). The results of electrical resistivity and V_P are summarized in Tables T40 and T41 and Figure F88.

Electrical resistivity ranges from 1.28 to 3.32 Ωm. All samples except three (Samples 338-C0002H-1R-1, 13 cm, 338-C0002J-1R-1, 45 cm, and 2R-1, 53 cm) record an anisotropy such that electrical resistivity in the vertical *z*-direction is higher than that in the horizontal *x*- or *y*-direction because of the bedding oriented within the *x*-*y* plane (Fig. F88). Resistivity is usually the lowest along the bedding plane in sedimentary rocks because of better pore connectivity. Vertical anisotropy is between 6.6% and 48.6% with negative values, except for the three cubes that probably have a bedding aligned within *x*-*z* or *y*-*z* planes. The measurements with bedding within the *x*-*y* plane present a transverse anisotropy (i.e., lineation) with a horizontal anisotropy from 0.2% (quasi-isotropic) up to 50.3% (strong lineation). V_P ranges from 1.923 to 2.307 km/s. The horizontal and vertical anisotropies range from 0.4% to 5.2% in Hole C0002H and from 1.9% to 9.5% in Hole C0002J. The higher vertical anisotropy of electrical resistivity and V_P suggests dominantly gravitational-driven porosity reduction at the base of the Kumano Basin.

Between 200 and 503 mbsf (Holes C0002K and C0002L), a total of 428 electrical resistivity measurements were conducted on working-half cores using the Wenner four-pin array probe for soft sediment. Each measurement was recorded in the dominant lithology types per section to evaluate the general resistivity of the mud, silty mud, and sand as well as their textures such as consolidated or soupy. The results of electrical resistivity from Holes C0002K and C0002L are summarized in Table T42 and Figure F89.

Electrical resistivity ranges from 0.037 to 7.56 Ωm with an average of 0.93 Ωm through lithologic Unit II. Resistivity increases with depth associated with porosity loss (Fig. F89). Sandy samples have higher electrical resistivity (~1.2 Ωm) than muddy sediment (~0.9 Ωm). This observation may reflect the higher porosity of the muddy sediment in combination with a strong electrical clay-bound water effect that leads to lower resistivity and may also be influenced by the high electrical surface conduction along the extended clay surfaces compared to quartz or other lithic minerals. Soupy sand and soupy mud sediments show much lower resistivity of 0.86 and 0.40 Ωm, respectively, and the rare ash layers show a resistivity of 0.95 Ωm. Although the resistivity of ash layers is similar to that of mud, ash layers systematically have a nonnegligible increase of resistivity toward their base, often marked by a much whiter colored thin layer.

The formation factor (*F*), cementation factor (*m*), and pore network tortuosity (τ) are calculated based on Archie's law using resistivity and MAD:

$$F = R_0/R_W, \qquad (2)$$

where

R_0 = resistivity of the formation water–saturated sample;
R_W = resistivity of the formation pore fluid;
m = –(log[*F*]/log[ϕ]), where ϕ is the fractional porosity of the rock; and
τ = $F\phi$ also defined as ϕ^{1-m}.

The MAD porosity is chosen at the closest to the resistivity measurement location. These parameters are essential to calibrate the LWD electrical resistivity logs for water and porosity estimates. The derived Archie's parameters are summarized in Table T42 and Figure F90.

The formation factor ranges from 1.05 to 5 with some outliers up to 28.21 (Table T42; Fig. F90). The average formation factor is 3.68 and is close to the typical values found during previous expeditions (ODP Legs 131 and 196; Shipboard Scientific Party, 1991; Bourlange et al., 2003). The cementation factor (Archie's *m* exponent) is ~1.78 with maximum values up to 5.02. The pore network tortuosity parameters of Archie's law are 7.53. The values are higher in mud-rich sediment, often defined by higher porosity, and lower in less porous sand-rich sediment.

The relationship between the cementation factor and electrical resistivity is independent of lithology at least at the first order (Fig. F91). As previously observed, lower values of *m* as well as resistivity are found in soupy units, intermediate values are found in muddy lithologies, and higher values are found in sandy units along this trend.

Similar trends are observed in the MSCL-W resistivity data (Fig. F92). MSCL-W resistivity shows a progressive increase from 200 to 320 mbsf and stays constant below 320 mbsf. Note that MSCL-W resistivity data from Holes C0002K and C0002L are higher than electrical resistivity measurements on working-half cores. The difference is ~0.65 Ωm at shallower depth and decreases with depth to 0.2 Ωm. This difference is possibly because the correct values of standard seawater resistivity were not obtained for the Wenner probe because of the use of a small container when measurements on cores from Sites C0002 and C0022 were conducted. Unexpectedly low-resistivity values obtained for cores at Sites C0002 and C0022 are probably due to overestimation of seawater impedance. This problem was resolved when resistivity was measured on cores from

Site C0021 by using a larger container of seawater (see also "Physical properties" in the "Site C0021" chapter [Strasser et al., 2014b]).

Shear strength (working halves)

Shear strength measurements using a vane shear device and a pocket penetrometer (see the "Methods" chapter [Strasser et al., 2014a]) were made on Hole C0002K and C0002L working halves from 200 to 500 mbsf. One measurement for each method was made per core. Penetrometer measurements range from 55 to 255 kPa, and vane shear measurements range from 24 to 158 kPa and are consistently lower than the penetrometer measurements (Fig. F93; Table T43). There is considerable scatter in the data, which increases with depth. One trend that may be observed is an increase in the maximum penetrometer measurements with depth, which generally correspond to the maximum values measured during Expedition 315 (Expedition 315 Scientists, 2009b) (Fig. F93).

Unconfined compressive strength (discrete cores)

Unconfined compression tests (see the "Methods" chapter [Strasser et al., 2014a]) were conducted on four samples (1 cm × 1 cm × 2 cm each) that were subsampled from cubic samples (2 cm × 2 cm × 2 cm) used for V_P and electrical resistivity measurements at 1111 mbsf in Hole C0002H and nine samples that were subsampled from 902 to 912 mbsf in Hole C0002J. A vertical load is applied along the long axis of the sample, which is parallel to the core axis. UCS (maximum force per unit area) ranges between 1.5 and 9.7 MPa with an average of 6.9 MPa (Fig. F93). Two measurements made at 907 mbsf yielded noticeably lower UCS values (1.5 and 2.9 MPa); however, both samples may have been fractured before testing. The variability in UCS data is probably due to sample heterogeneity, sample size, control of loading rate (manual versus computer control), and sensitivity of the load cell (±0.02 kN for the load cell on the *Chikyu*).

Color spectroscopy (archive halves)

The results of color reflectance measurements using the color spectroscopy logger (MSCL-C) are summarized in Figure F94. L*, a*, and b* values (see the "Methods" chapter [Strasser et al., 2014a]) show no significant difference from those obtained from Holes C0002B–C0002D cores during Expedition 315 (Expedition 315 Scientists, 2009b). L* ranges mainly from 29 to 52, a* ranges mainly from –3.4 to 2.5, and b* ranges mainly from –0.95 to 4.3 for the entire coring intervals. Higher values in both L* and b* observed in Core 338-C0002L-3X (296–299 mbsf) reflect volcanic fine ash.

Moisture and density (cuttings)

MAD measurements were made on 285 cuttings samples from 875.5 to 2004.5 mbsf to provide detailed characterization of grain density, bulk density, and porosity. The sampling interval was 5 m but was changed to 10 m below 1060.5 mbsf. Samples from the 1–4 mm size fraction were measured from 915.5 to 2004.5 mbsf (n = 125) and samples from the >4 mm size fraction (n = 133) were measured below 875.5 mbsf. Shallow samples (<940.5 mbsf) were primarily used to assess the mixing of cuttings when the bit and the hole opener (underreamer) crossed the transition of the cement at the 20 inch casing shoe (860.2 mbsf) and the formation.

Density and porosity

Measured grain density values for both the 1–4 and >4 mm size fractions maintain close agreement throughout Hole C0002F (Fig. F95A). In addition, grain density values generally show less scatter compared to previous NanTroSEIZE expeditions, which reported values of 2.02–3.5 g/cm^3 (Expedition 315 Scientists, 2009b; Expedition 316 Scientists, 2009; Expedition 322 Scientists, 2010a). The good data quality obtained during Expedition 338 may be related to the calm sea conditions necessary for riser drilling operations, providing stable conditions during pycnometer measurements. Also, the high sample volume of 20 cm^3 used for MAD measurements of cuttings reduces analytical error.

Grain density measurements above 945.5 mbsf were influenced by cement at the 20 inch casing point. Grain density values range from ~1.87 g/cm^3 for the cement to an average of 2.61 g/cm^3 for the formation (see "Mixing of cuttings across lithologic and structural boundaries"). From 945.5 to 1050.5 mbsf, grain density is characterized by considerable scatter with values as low as 2.52 g/cm^3 and as high as 2.75 g/cm^3 (Fig. F95A). Low grain density values suggest that contamination with cement cuttings occurs below 945.5 mbsf. Based on a cement grain density of 1.87 g/cm^3 and a formation grain density of 2.61 g/cm^3, a cement content of up to 12% can explain the low grain densities between 945.5 and 1050.5 mbsf. The low grain density values may also be explained by abundant wood content, discovered during Expedition 319 in lithologic Unit III (Expedition 319 Scientists, 2010), if a mixing interval of up to 90 m for cuttings is assumed. At this depth interval, relative abundant organic material/wood/lignite was also identified in the >63 µm sand-size fraction from cuttings (see "Lithology") (Fig. F20). Assuming a wood density of 0.9 g/cm³, a wood content of up to 5% can explain the low grain density values in the 945.5–1050.5 mbsf interval. This wood content is in the range of the 5%–10% content reported by Expedition 319 Scientists (2010). From 1050.5 to 1135.5 mbsf, the scatter in grain density diminishes and grain density decreases slightly to ~2.62 g/cm³. This interval correlates to lithologic Subunit IVA. Grain density values from 1135.5 to 1400.5 mbsf remain relatively constant with an average of ~2.61 g/cm³. A transition zone with increasing grain density exists between 1400.5 and 1550.5 mbsf before grain density resumes a constant value of 2.66 g/cm³ downhole. At 1920.5 mbsf, grain density shifts to a higher value of 2.68 g/cm³.

In contrast to grain density values, bulk density for the two size fractions maintains a close agreement only to ~1500 mbsf. Beneath 1500 mbsf, bulk density values for the 1–4 mm size fraction are consistently lower than for the >4 mm size fraction. Bulk density values generally increase from 1.85 g/cm³ at 945.5 mbsf to 1.91 g/cm³ at 1406 mbsf. This corresponds to a decrease in water content with constant grain density (Fig. F95B). An increase in bulk density to an average of 1.96 g/cm³ occurs from 1406 to 1426 mbsf; bulk density remains generally constant at this value to 1500 mbsf. Below 1500 mbsf, the trends for the two size fractions become more scattered and begin to diverge, while maintaining a similar pattern in changes with depth to 1740.5 mbsf. From 1500 to 1740.5 mbsf, there is a large spike at 1620.5 mbsf, where bulk density reaches 2.07 g/cm³ (1–4 mm size fraction) and 2.21 g/cm³ (>4 mm size fraction). Bulk density values for the two size fractions begin to completely diverge below the lithologic Unit IV/V boundary (1740.5 mbsf). Below 1740.5 mbsf, bulk density of the 1–4 mm size fraction decreases gradually to 1.89 g/cm³, whereas bulk density of the >4 mm size fraction follows a constant average of 2.05 g/cm³ although the data show larger scatter. The difference in bulk density between the 1–4 and >4 mm size fractions may relate to DICAs that are formed by the drilling process. DICAs are more prominent in the smaller cuttings size fraction (see "MAD cuttings data quality" and "Structural geology").

Similar to the bulk density measurements, measured porosity values for the two size fractions maintain a close agreement to 1500 mbsf and follow similar trends to 1740.5 mbsf. From 1536 to 1740.5 mbsf, the >4 mm size fraction produces porosity values that are consistently lower than the 1–4 mm size fraction, although the two trends continue to correspond in terms of where minimum and maximum values occur. Below 1740.5 mbsf, the two trends diverge. Porosity generally decreases downhole from 48% at 945 mbsf to 40% at 1456 mbsf before increasing slightly to 43% at 1500 mbsf (Fig. F95C). This general decreasing trend is in accordance with normal compaction because of increasing overburden. From 1500 to 1740.5 mbsf, porosity is scattered about 42% (1–4 mm) and 39% (>4 mm), with a large negative spike at 1625.5 mbsf to 37% (1–4 mm) and 29% (>4 mm). The separation by cuttings size beneath 1500 mbsf and the low-porosity zone at ~1625.5 mbsf may be attributed to lithology. Sedimentological observations suggest that sandstone is present in this zone (see "Lithology"). Drying of cuttings surfaces (see the "Methods" chapter [Strasser et al., 2014a]) probably leads to removal of additional water from the interior of the permeable sandstone cuttings, and thus, the porosity is underestimated in this zone. Beneath 1740.5 mbsf, porosity shows contrasting trends for the two size fractions. Porosity of the 1–4 mm size fraction gradually increases from 42% at 1740.5 mbsf to 47% at 2005 mbsf. For the >4 mm size fraction, there is a large amount of scatter in porosity values below 1740.5 mbsf with a minimum of 32% at 1886 mbsf and a maximum of 42% at 1956 mbsf. As shown in the bulk density data, separation of porosity by size fraction is probably due to a larger amount of DICAs in the smaller cuttings size fraction (see "MAD cuttings data quality").

MAD cuttings data quality

Expedition 338 is the third IODP expedition to use cuttings to characterize physical properties (Expedition 319 Scientists, 2010; Inagaki et al., 2012). Previous expeditions focused on analyzing the 1–4 mm size fraction and reported an overestimation of porosity and a relatively large variation of measured values (Expedition 319 Scientists, 2010; Inagaki et al., 2012). Compared to the MAD results on cores, cuttings show higher porosity and lower bulk density. Possible reasons for this difference include (1) incomplete removal of water from the surface of the cuttings, (2) drilling-induced microcracks, (3) swelling of clay minerals and mechanical expansion during washing and soaking (up to 18 h) in seawater, and (4) residue from drilling mud on the surface of cuttings. The procedure for MAD measurements on cuttings during Expedition 338 was therefore changed based on sensitivity tests of cuttings before cuttings from Hole C0002F were collected. MAD measurements were conducted directly after washing to reduce the effect of swelling and mechanical expansion. Care was taken to completely remove water from the surface (see the **"Methods"** chapter [Strasser et al., 2014a]).

The size fractions show good agreement between porosity and bulk density above 1500 mbsf with ratios of ~1, suggesting that surface effects do not play a role (Fig. **F96**). However, the different porosity and bulk density trends between the two cuttings sizes below 1500 mbsf suggest other causes may lead to higher water content in cuttings of the smaller size fraction. Visual observation suggests that cuttings below 1500 mbsf include two types with different induration or strength (see **"Structural geology"**). The first type consists of hard, intact formation cuttings, which are sometimes characterized by sharp edges. The other type appears stiff but is weaker than the first type; these DICAs may be formed during the drilling and recovery process. The good correlation of grain density values for both 1–4 and >4 mm size fractions suggests that both fractions originate from the same depth (Fig. **F96A**). The prominent difference between the two size fractions in bulk density and porosity values below 1500 mbsf is probably a result of greater induration of the formation in combination with less formation cuttings (or more DICAs) of 1–4 mm size fraction (see **"Structural geology"**).

Errors in MAD measurements on cuttings were estimated from a reference compaction curve that is determined based on MAD measurements of both handpicked hard formation cuttings and cores recovered during Expeditions 315 and 338 (Expedition 315 Scientists, 2009b). Hand-picked samples, which are considered as representative formation samples, and DICAs were taken from the >4 mm size fraction from 1700.5 to 2000.5 mbsf at 100 m intervals. Four additional samples, recovered from 1975 and 1982.5 mbsf during the opening of the hole in preparation of casing the borehole, were also measured. A representative porosity-depth model (Athy, 1930) can be constructed for the prism sediment by combining porosity data from the hand-picked cuttings and the cores from previous expeditions (Fig. **F97A**):

$$\phi = \phi_0 e^{-\alpha z}, \qquad (3)$$

where

z = depth below seafloor,
α = 5.15 × 10^{-4} is an empirical constant, and
ϕ_0 = 0.64 (a reference porosity).

The computed porosity can also be used to correct the bulk density by (Fig. **F97B**)

$$\rho_{cb} = \rho_g(1-\phi) + \rho_f\phi, \qquad (4)$$

where

ρ_{cb} = corrected bulk density,
ρ_g = measured grain density, and
ρ_f = density of the pore fluid (1.024 g/cm³).

The difference between the corrected and the original data set of the >4 mm size fraction is shown in Figure **F97C.** Measured porosity on cuttings is overestimated by 6% at 940.5 mbsf and 17% at 2004.5 mbsf. The errors in bulk density are 0.14 g/cm³ at 940.5 mbsf and 0.28 g/cm³ at 2004.5 mbsf. The average bulk density of DICAs is 1.93 g/cm³, which is equivalent to the bulk density of the 1–4 mm size fraction in that depth interval. The bulk density of these DICAs is higher than the MAD bulk density at shallower depths (e.g., ~1.85 g/cm³ at 1000 mbsf), which suggests an increase in induration and strength of the DICAs. Based on an average value of 1.93 g/cm³ for the interval from 1800 to 2000.5 mbsf, a DICA content of 47%–83% is necessary to explain the bulk density of the bulk cuttings with >4 mm size fraction (Fig. **F98**). Underreamer depths with a small fraction of DICAs partly correlate with periods when the bit was off bottom. This corroborates the assumption that the formation of DICAs is related to the RWD process. In summary, the differences in porosity and bulk density between cuttings and cores are caused by mixing of the formation material with DICAs. Drilling-induced microcracks, swelling of clay minerals, mechanical expansion, or residue from drilling mud on the surface of cuttings are second-order effects.

Magnetic susceptibility (cuttings)

Magnetic susceptibility (MS) was measured for comparison with MAD data, NGR measurements, and lithologic descriptions. A total of 299 vacuum-dried cuttings samples from both 1–4 and >4 mm size fractions were measured. Because sample weight varied between the two cuttings sizes as a result of cuttings packing in the sample cylinder, we calculated the mass magnetic susceptibility (MMS) from measured raw data MS (bulk susceptibility):

$$\text{MMS (m}^3\text{/kg)} = [\text{MS} \times \text{sample volume (m}^3)]/[\text{sample weight (g)} \times 10^{-3}]. \qquad (5)$$

MMS ranges from 1.03 × 10^{-7} to 4.40 × 10^{-6} m³/kg above 1050.5 mbsf, probably as a result of the cement that extended to 872.5 mbsf and was mixed into cuttings to 1050.5 mbsf (Fig. **F99**). However, scatter below the interpreted cement contamination (940.5 mbsf) may also reflect a heterogeneity of lithologic Unit III consistent with the observed scatter in MAD results because of wood content (Expedition 319 Scientists, 2010; see **"Lithology"**) (Fig. **F20**). Between 1050.5 and 1170.5 mbsf, MMS decreases slightly from ~2.02 × 10^{-7} to 1.07 × 10^{-7} m^3/kg, which correlates broadly with Subunit IVA. MMS then decreases to ~1.00 × 10^{-7} m^3/kg at 1200 mbsf and remains relatively constant at that value to 1400.5 mbsf. This zone corresponds to lithologic Subunits IVB and IVC (see **"Lithology"**). MMS values increase again to 1.17 × 10^{-7} m^3/kg at 1550.5 mbsf, probably associated with the Subunit IVD/IVE boundary. Beneath 1550.5 mbsf, MMS gradually decreases to 1.00 × 10^{-7} m^3/kg at 2004.5 mbsf. Contrary to MAD data, magnetic susceptibility is independent of cuttings size fraction. This suggests that there is no fractionation of the solid phase during the drilling and recovery process between the two cuttings sizes or between DICAs and formation cuttings.

Natural gamma radiation (cuttings)

Unwashed cuttings were collected in the core cutting area and packed in a 12 cm long core liner. The liner filled with cuttings was scanned with a MSCL-W to determine the NGR of the cuttings mix. To provide a background reference, NGR was measured from a liner, identical to those used for cuttings, filled with distilled water. The recorded value was 34.0 counts per second (cps). The NGR of drilling mud measured on a regular basis for background values has no significant effect on data bias. The MSCL-W NGR data and the downhole gamma ray (GR) logging data from LWD (see **"Logging while drilling"**) have similar values and trends (Fig. **F100**). The unit of logging data (gAPI) was converted to counts per second (cps) for comparison with MSCL-W data using the following equation (Mountain, Miller, Blum, et al., 1994):

$$\text{NGR (cps)} = [\text{GR (gAPI)} - 12]/2.12. \qquad (6)$$

There is a sharp increase in MSCL-W NGR at ~920 mbsf (877.2 mbsf underreamer depth); however, there is no significant variation in LWD-GR data at this depth. The low values of MSCL-W NGR above 920 mbsf are likely influenced by cement cuttings dominating the cuttings mixture. There is no such variation in LWD-GR because the LWD sensor started below the interface and detected signals mostly from the formation. MSCL-W NGR gradually increases with depth from 920 to 1200 mbsf. There is no noticeable variation in the interval of 1200–1750 mbsf. A remarkable increase from ~35 to ~40 cps at ~1750–1900 mbsf may reflect a change in lithology to a more claystone rich interval (see **"Lithology"**). MSCL-W NGR is slightly decreased below 1900 mbsf.

Consistent values of LWD-GR to 1500 mbsf in logging depth are followed by a clear increase at 1600–1800 mbsf, which correlates to the increase in MSCL-W NGR. Below 1800 mbsf, no significant variation is found in either MSCL-W NGR or LWD-GR. Other noticeable correlations between MSCL-W NGR and LWD-GR are found at ~1300 and 1600 mbsf and may relate to lithologic changes. Based on those correlations, the cuttings depths are deeper than the logging depths by ~30–70 m. This can be explained by the configuration of the BHA. The cuttings from the drill bit (~⅓ of the total cuttings volume) and those from the underreamer (~⅔ of the total cuttings volume) were mixed while they traveled with drilling mud to the surface (see also the **"Methods"** chapter [Strasser et al., 2014a]).

Mixing of cuttings across lithologic and structural boundaries

Mixing of cuttings occurs when a lithologic or structural boundary is penetrated with RWD. Grain density and NGR data allow us to constrain the mixing interval when the bit and the underreamer crossed the transition of the cement at the 20 inch casing shoe (860.2 mbsf) and the formation. Grain density has an average value of 1.87 g/cm^3 above 895.5 mbsf, which characterizes the cement plug. Density then increases to an average value of 2.61 g/cm^3 at 940.5 mbsf, which represents the formation (Fig. **F101**). Mixing of cuttings is also observed in the MSCL-W NGR data. The transition in MSCL-W NGR from 10 to 30 cps at ~920 mbsf correlates with the mixture of cement cuttings and formation cuttings. One potential explanation is that this transition results from the variation in the velocity of cuttings related to drilling mud velocity as well as particle shape, size, and density. This causes hydrodynamic dispersion of cement cuttings and formation cuttings. Assuming a Gaussian distribution of cuttings velocity, we used dispersion theory to characterize the transition of the cuttings mixture (Todd and Mays, 2005). The average velocity of drilling mud calculated from the average pumping rate (272.4 m^3/h) and the average annulus area (0.171 m^2) provided by Geoservices Ltd. was 1593 m/h. The average ROP given by LWD data for this interval was 24 m/h. As a model parameter, the coefficient of dispersion used for curve fitting for both data sets is 50 m^2/s. Based on this simplified model (the S-shaped curve), most cuttings are from the underreamer in this interval, and the cuttings were mixed in a range of at least ~42.8 m at this depth.

Dielectrics and electrical conductivity (cuttings)

A total of 110 seawater-washed cuttings samples from Hole C0002F were sampled at a 10 m interval.

Pastes prepared from each cuttings sample (1–4 mm size fraction) were used to measure electrical properties at high frequency (30 kHz–6 GHz). Salinity index from the extracted water and mass water content from cuttings pastes was compared with the porosity/density data set of the same cuttings using the MAD method to complement the data.

The purpose behind this pilot study experiment is to

- Assess if the dielectrics can detect any change from the formation despite the mixing interval of cuttings,
- Evaluate the cuttings as a proxy for formation evaluation,
- Extract the rough pore water salinity with depth, and
- Test the correlations among cuttings, core, and LWD data sets.

Before preparation of pastes, 1–4 mm size fraction cuttings samples, which were preserved in sealed bags and stored in the refrigerator since recovery, were photographed to evaluate color and general texture (Fig. **F102A, F102B**). The pictures were taken at the same distance, light, and field of view for comparative analysis. The color was evaluated in a representative area of the cuttings using a circle with an 11 pixel diameter on Adobe Photoshop software. The gray color value mean, minimum, and maximum are measured in 8 bit format from 0 (black) to 256 (white) along with their corresponding gray color histogram. Note that seawater washing was able to remove most of the drilling mud that was coating the cuttings and would have affected the original colors of the cuttings.

The analysis of gray color histograms revealed four main populations of samples (Fig. **F103**):

- Population P1 records the lowest gray values centered around 50 ± 10 grayscale and occurs in all of the sample collection.
- Population P2 is centered around 75 ± 10 grayscale and represents 46 samples (i.e., 42% of the sample collection). Population P2 particularly integrates Population P1 as a secondary population.
- Population P3 is centered at 95 ± 10 grayscale and represents the dominant population from the collection with 52 samples (47% of the collection).
- Population P4 exists in some specific intervals with the highest grayscale centered at 110 ± 10.

The computation of the gray mean values from each histogram as well as the difference between their minimum and mean gray value with depth seems to reveal a pattern related to some lithologic units (Fig. **F104;** Table **T44**). The general gray mean value spans from 40 to 90 with an average of ~63 ± 8. The gray mean with depth can be correlated with lithologic subunits based on silty claystone percentage (see **"Lithology"**). Data smoothing using a moving average window of five data points from the data set, which computes a difference between the minimum and mean gray values, well correlates with the suggested lithologic or logging units. The trough in mean gray value at ~1027 mbsf correlates with the lithologic Unit III/IV boundary, and the negative peaks of mean gray value and decrease in difference of gray value at ~1610 mbsf correlates with the logging Unit IV/V boundary.

Salinity and porosity from cuttings

During the sample paste preparation from cuttings for dielectrics measurement, the decanted water obtained after centrifuging was measured for salinity index (Table **T45**). Because the same amount of powder and milli-Q water was used for the whole cuttings collection, relative comparison with depth can be used to check any change in the general salinity of the formation, assuming no invasion by drilling fluid (Fig. **F105A**). Indeed, despite the dilution effect by the addition of water to the dried cuttings powder, the salinity evolution reveals some useful aspects. The general relative salinity is ~11.5 g/L through the whole formation, but at the base of lithologic Units III and IV, salinity increases up to 31 and 25 g/L, respectively (2.5–3 times the salinity background). Within lithologic Unit IV, salinity slightly decreases with depth from 16 to 10 g/L before becoming relatively constant at 10.5 ± 1 g/L through Unit V. This is consistent with pore water geochemistry analysis of cored prism sediment that documents decreasing chlorinity content (see **"Geochemistry"**). Not enough points are available in lithologic Unit III to average the salinity with reasonable confidence.

The water mass content from the prepared paste was converted into porosity using the grain density results from the MAD method and plotted against the porosity measured from the MAD method on the same cuttings (Fig. **F105B**). Two trends can be observed that are related to the lithologic types. The muddy samples are characterized with the following trend of porosity:

$$\text{MAD-derived porosity} = 1.3 \times (\text{porosity from paste}) - 9.6. \quad (7)$$

The average porosity from paste and MAD in such lithology type is 40% ± 1.6% and 43% ± 2.2%, respectively. In the sandy mud lithology, the porosity between MAD and paste is almost 1 to 1 with a slight positive linear shift of 4.4 for the MAD porosity. The average porosity is 39% ± 1.5% from the paste method and 45% ± 1.8% from the MAD method. Note that the coarse sand sample (338-C0002F-311-SMW) records much lower porosity than the muddy and sandy mud lithology units (29% of paste porosity and 24% of MAD porosity).

Dielectric properties

The dielectrics measurements were acquired from pastes as soon as possible after centrifuging. The dielectric constant (ε'_r) and the dielectric absorption (ε''_r) were measured, and the equivalent electrical conductivity was computed. Table **T45** summarizes these results at different frequencies of acquisition. Only the dielectrics data above 3 MHz are reported because the data below 3 MHz include low-frequency parasitic noise probably due to ship heave and drill string vibration.

The dielectric constant (real part) at 3 MHz is ~356 with a maximum of 504 and a minimum of 205. The standard deviation at 3 MHz remains very low (<3). The dielectric constant decreases from 56 to 33 toward the 6 GHz frequency, with a standard deviation lower than 0.3. The dielectric absorption (imaginary part of the dielectric) is very high at low frequency (3 MHz) with an average value of 3958 and maximum and minimum values of 6171 and 1885. This absorption intensity decreases rapidly to 7 at 6 GHz, where no loading electrical charge can occur. The standard deviation is also very low with values of 36 at 3 MHz and <1 at higher frequencies.

The dielectric constant at low frequency is more sensitive to lithologic variations (Fig. **F106**), as well as the dielectric absorption with depth. Some unit intervals with a specific range of values can be extracted. These sediments have a linear relationship between the dielectric constant and its absorption (Fig. **F107**): at high frequencies the sediments are purely discharging (dielectric constant very low) because of the dielectrically "lossy" behavior of the clay minerals, which do not load much electrical charge. At lower frequencies of 3–30 MHz, the water–clay interaction is fully charging and polarizable, and the dielectric constant becomes higher, with a material much more conductive through the water film at the clay surface. At higher frequencies between 100 MHz and 1 GHz, on the other hand, two groups are observed along the linear trend. The dominant group corresponds to the mudstone, and the minor group, which is often defined by lower salinity, corresponds to the sandy materials. These two groups are not clear at lower frequencies.

The electrical conductivity was derived from the dielectric results. Because the material is more conductive at low frequencies, the 3 MHz frequency is the most appropriate to evaluate the electrical resistivity (Fig. **F106**). Electrical resistivity ranges from 1 to 3.36 Ωm with an average of 1.66 Ωm (Fig. **F108**). These values match the resistivity range observed from the LWD resistivity logs. Further analysis may allow for correlation with LWD data and lithologic boundaries.

Leak-off test

A LOT was performed at 872.5 mbsf, 12.3 m below the 20 inch casing shoe (Fig. **F109**). This test helped define the maximum mud weight for drilling to 2300 mbsf and the proposed location of the 16 inch casing set point and allowed assessment of the least principal stress. To perform the LOT, the cement was drilled out and the hole was deepened to 875.5 mbsf, providing a 3 m long, 17 inch diameter open borehole for performing the LOT with drilling mud of density of 1100 kg/m^3. The LOT was conducted with the outer annulus closed by the BOP, and mud pressure was measured at the cement pumps. The pressure at the bottom of the hole was calculated by the recorded pressure plus the static pressure of the mud column.

Two LOTs were conducted in Hole C0002F. The pressure-time and flow rate–time records of the two pressurization cycles allow estimation of the leak-off pressure (LOP) and instantaneous shut in pressure (ISIP) (Fig. **F110A**). The LOP can be defined at the point where the pressure-volume curve deviates from linear behavior if we assume the borehole is elastic and impermeable (White et al., 2002; Engelder, 1993). During the first pressurization cycle, a total volume of 446 L of drilling mud was injected at a rate of 31.8 L/min. Borehole pressure peaked at 31.9 MPa. Based on the pressure-time curve, estimated values for the LOP and ISIP were 31.6 MPa and 31.8 MPa, respectively. The LOP was not clearly defined because a large volume of mud (302 L) was lost. A second cycle of pressurization was conducted by injecting 144 L at a rate of 47.7 L/min. The pressure-time curve of the second cycle suggests that leak-off took place at ~31.9 MPa because of the clear deviation of the pressure curve from the linear behavior. A proposed value of ISIP is 32.0 MPa from the maximum curvature on the pressure decay curve after pumping ceased (White et al., 2002). Plotting borehole pressure versus injected mud volume shows S-shaped curves with a linear part in the middle in both pressurization cycles (Fig. **F110B**). The rapid increase in pressure with a lower volume (e.g., ~144 L in total) of mud injected during the second cycle suggests that mud cake formed around the borehole wall, possibly due to mud flowing into the rock formation during the first cycle.

The deviation points (i.e., LOP) on the pressure-volume curves are not consistent between the two cycles (31.6 MPa for the first cycle and 31.9 MPa for the second cycle). If unsteady radial flow of injected drilling mud occurred (likely for the first cycle and possibly even during the second cycle), the deviation point on the pressure-volume curve is no longer valid for the LOP. A method to account for variable pressure gradients (dP/dV) can be used to estimate LOP as borehole pressure increases during continuous loss of mud (Fig. **F110C**). The variation in dP/dV can be approximated as linear if the permeability of the formation is constant (Todd and Mays, 2005). The linear approximation of dP/dV as a function of pressure in the entire range at the first cycle suggests flow of mud fluid into the formation with no change in permeability until the maximum stress of test. In the second cycle, the dP/dV curve deviates from linear behavior at 32.0 MPa. A sudden increase in formation permeability because of opening of fractures would explain the deviation of the dP/dV curve for the second pressurization cycle (Song et al., 2001). Based on these observations, it is interpreted that leak-off did not take place during the first cycle, but did during the second cycle at 32.0 MPa; thus, the ISIP (32.0 MPa) found in the second cycle is more reliable. The LOT revealed that the least horizontal principal stress is possibly ~32.0 MPa. A summary of the results is listed in Table **T46.**

Paleomagnetism

Holes C0002K and C0002L

Remanent magnetization of archive-half sections from Holes C0002H and C0002J–C0002L were measured at demagnetization levels of 0, 5, 10, 15, and 20 mT peak fields to identify characteristic remanent magnetization. Profiles of declination, inclination, and intensity after demagnetization at 20 mT with depth (mbsf) are shown in Figure **F111.**

Inclinations of archive sections in the interval of Holes C0002K and C0002L (200–500 mbsf), which were mostly cored using the ESCS (only the top 5.5 m and the interval from 205.5 to 239 mbsf of Hole C0002K were cored using the HPCS and EPCS, respectively), are significantly biased toward the positive side. However, because the results of Holes C0002B and C0002D during Expedition 315 (Expedition 315 Scientists, 2009a, 2009b) revealed that the interval of 160–490 mbsf at Site C0002 ranges from 1.078 to 1.24 Ma, all the interval of Holes C0002K and C0002L should correspond to the middle part of the Matuyama reversed polarity interval, and the inclinations are expected to be in the negative side. Thus, we suspected that the predominant positive magnetization of the archive sections is due to a modification of the initial paleomagnetic record.

In order to examine the magnetic nature of the interval, discrete samples were carefully collected from consolidated biscuit pieces, not from the softer sediment, which is probably a mixture of sediment and drilling slurry. Magnetic grain fabric of the interval was measured by the anisotropy of magnetic susceptibility (AMS) apparatus to detect any indication of coring disturbance. AMS results show clear magnetic foliations parallel to the horizontal plane (Fig. **F112**). It is interpreted that grain fabrics were formed by a natural vertical compaction and have no evidence for coring disturbance. The discrete samples were demagnetized with a higher level than those on the archive-half sections. Demagnetization experiments on the discrete samples reveal that magnetizations of samples are stable (Fig. **F113**), and a substantial number of discrete samples show negative inclination (Fig. **F111**). This fact indicates that the original magnetization remains in biscuit pieces and suggests that a significant amount of softer sediment was magnetized strongly with positive inclination during coring. Although this situation makes it difficult to interpret magnetic data of archive sections, magnetic polarity interpretation based on data from discrete samples is still valid. According to the results of Expedition 315, the interval of Holes C0002K and C0002L should correspond to the middle part of the Matuyama Reversed Chron. The normal polarity interval observed between 240.72 and 299.37 mbsf seems to be assigned to the "Cobb Mountain" Subchron (1.173–1.185 Ma). However, the nannofossil event of 1.04 Ma is found in the interval at ~250 mbsf in Hole C0002K (see **"Biostratigraphy"**). It is, therefore, more reasonable that this normal polarity interval is correlated to the Jaramillo Subchron, although the horizon at 119.58 mbsf in Hole C0002D is interpreted to be the top of the Jaramillo Subchron (Expedition 315 Scientists, 2009b).

Magnetic fabric of Hole C0002J

Paleomagnetic inclinations of Hole C0002J are mostly positive but widely scattered. AMS, an index of sediment grain fabric, shows that sediment in Holes C0002K and C0002L are compacted subvertically (Fig. **F112**). On the other hand, AMS of Hole C0002J appears more prolate (Fig. **F114A**), suggesting that grain fabrics in this interval did not form by vertical compaction alone. Restored AMS directions of the interval with paleomagnetic declinations reveal that magnetic foliations gently dip southeastward (Fig. **F114B**). Preliminary interpretation of those data indicates bedding planes in this interval gently dip southeastward.

Cuttings-core-log-seismic integration

Site C0002 encompasses 11 holes situated within ~150 m of each other (Fig. **F4**) and includes riser Hole C0002F, a focal point of the NanTroSEIZE project. Both LWD data and cores have been collected at this site during previous expeditions (Expedition 314 Scientists, 2009; Expedition 315 Scientists, 2009b; Expedition 332 Scientists, 2011).

Figure **F115** presents a summary of core, log, and seismic data at Site C0002 along with a summary of the units defined from each of those data sets. The seismic reflection profile shows the major regional features, such as the northwest-dipping Kumano Basin strata (seafloor to ~850 mbsf at Site C0002) that are cross-cut by a prominent BSR (~400 mbsf), a transition zone (~850–920 mbsf), and the seismically chaotic accretionary prism (deeper than ~920 mbsf).

A seismic, lithology, and logging correlation of the gas hydrate zone (~200–550 mbsf) (Expedition 314 Scientists, 2009; Expedition 315 Scientists, 2009b) is revisited here using new data from cores collected between 200 and 500 mbsf (Holes C0002K and C0002L), as this interval was not targeted by previous expeditions. The lack of coherent reflections in the seismic data below ~900 mbsf (i.e., within the highly deformed prism) prevents further seismic correlation with deeper logging data. The logging Unit III/IV boundary, placed at 935.6 mbsf in Hole C0002A (Expedition 314 Scientists, 2009) and at 931 mbsf in Hole C0002G (Expedition 332 Scientists, 2011) is revisited using new core data from Hole C0002J cores and LWD data from riser LWD in Hole C0002F. Integration of core, cuttings, and LWD data within the accretionary prism is also discussed.

The Kumano 3-D prestack depth migration (PSDM) seismic volume (Moore et al., 2009) ties to Hole C0002F at the intersection of In-line 2532 and Crossline 6228. A number of prominent reflections were identified by Gulick et al. (2010) and compared to the logging unit boundaries identified in Hole C0002A (Expedition 314 Scientists, 2009). Many of the reflections do not tie with large lithologic or physical properties contrasts. The strongest correlations were made between Zones A and B (as defined using LWD data from Expedition 314 Scientists [2009]) within logging Unit II (Fig. **F115**).

New cores in the gas hydrate zone

The base of Zone A matches the BSR in the seismic data at ~400 mbsf (Fig. **F115**). This zone was suggested to be the gas hydrate zone because of its high resistivity compared to the rest of Unit II. Additionally, the drop in *P*-wave velocity at the base of Zone A was postulated to represent the presence of trace amounts of free gas (Expedition 314 Scientists, 2009) that leads to a prominent reversed polarity seismic reflection of the BSR.

The interval from 200 and 505 mbsf was cored continuously in two holes (Hole C0002K: 200–286.5 mbsf; Hole C0002L: 277–505 mbsf). Because of a high concentration of trapped gas, the resulting recovery rate was highly variable (<13% to >100%), and one core liner (486.0–495.5 mbsf) failed explosively. Peaks of methane gas concentration in core headspace and void gas samples from 200 to 400 mbsf (see **"Geochemistry"**) correspond to high-resistivity spikes at 270, 295, 370, and 390 mbsf (Fig. **F115**). Higher concentrations of propane were also observed between 200 and 380 mbsf, within Zone A, and a small peak in ethane concentrations was observed at 390–400 mbsf (Fig. **F74**), which correlates with an interval of high resistivity (>4.5 Ωm) and the depth of the BSR observed in the seismic data. A spike to extremely low salinity/chlorinity values at ~400 mbsf in Hole C0002L (Fig. **F71**) matches the location of the BSR (Fig. **F115**). Overall, these observations appear to support the interpretations of the Expedition 314 Scientists (2009).

The upper surface of Zone B corresponds to a high-amplitude, negative polarity reflection (~480 mbsf) (Fig. **F115**). This zone has low *P*-wave velocity and highly variable resistivity and was suggested to represent a package of coarser sediment containing small amounts of free gas that is migrating updip (Expedition 314 Scientists, 2009).

Peaks of hydrocarbon gas concentration were observed at 460–470 mbsf (see **"Geochemistry"**), preceding an exploded core liner from the interval of 486.0–495.5 mbsf, suggesting that the upper boundary of Zone B, a gas-rich zone correlating with a negative polarity reflection (Fig. **F115**), had been reached. A second negative polarity reflection is observed at this depth to the southeast of Hole C0002F. There is also increased variation in resistivity within this zone, which may represent another pocket of gas trapped beneath the dipping reflection.

Logging curves below ~900 mbsf, hole enlargement (riserless) versus mud cake (riser)

It was noted that in Hole C0002A, the gamma ray curve matches the borehole shape below ~935 mbsf with low gamma ray values occurring where the borehole diameter increased (Fig. **F116**) (Expedition 314 Scientists, 2009). A correlation was made between borehole enlargement, the presence of cohesionless sediment (i.e., sandy), and low gamma ray values. A departure to low gamma ray values also occurs in Hole C0002G at ~931 mbsf (Expedition 332 Scientists, 2011). In the same depth interval in Hole C0002F, on the other hand, an increase in gamma ray values from ~70 gAPI at 920 mbsf to ~80 gAPI occurs at 940 mbsf. A similar increase was observed in both the MSCL-W NGR results from Hole C0002J core samples and Hole C0002F cuttings (see also **"Physical properties"**).

Although no direct caliper measurement was made during Expedition 338, Hole C0002F was drilled in riser mode, and as a result, the hole is generally expected to be more stable than previous riserless operations at this site. A comparison of resistivity images in the region of overlap in both Holes C0002F and C0002A confirms that the borehole wall is generally in better condition in Hole C0002F (Expedition 314 Scientists, 2009) (see **"Logging while drilling"**). The attenuation distance for gamma radiation (1 MeV energy) through water is ~10 cm (4 inches) (Hubbell and Seltzer, 1996). Therefore, the low gamma ray values obtained below ~920 mbsf in Holes C0002A and C0002G are probably due to a reduction in natural gamma ray emissions reaching the detector. For example, the 6¾ inch diameter geoVISION tool used during Expedition 314 has an operational borehole size range of 8.00–9.88 inches (e.g., Schlumberger, 2011), and as the borehole diameter increases, especially beyond the operational maximum, the gamma ray intensities recorded will be damped with respect to measurements made directly adjacent to the formation.

For this reason, the composite LWD data curves in Figure **F115** comprise Hole C0002A data from 0 to 900 mbsf and Hole C0002F data below 900 mbsf. Note that neither the location of the Unit III/IV boundary nor the increase in the abundance of sandy material below the boundary are disputed; rather the interpretation of riserless gamma ray logs is challenged, especially where borehole diameter is unknown.

Cuttings and log integration in the accretionary prism

The Unit III/IV boundary determined based on both core lithology (Holes C0002B and C0002J) and LWD (Holes C0002F and C0002G) data is located between 918.5 and 935.6 mbsf. The mismatches between the depths of this boundary interpreted in different holes reflect the irregular nature of this unconformable boundary between the Kumano Basin sediment and underlying, older accretionary prism. Detailed mapping of this surface in the 3-D seismic data shows that the boundary is highly variable in three dimensions (G. Moore, unpubl. data).

Unit and subunit boundaries identified from cuttings analyses (Hole C0002F) are consistently deeper (by ~100 m) than those identified from the logging data (Fig. **F115**). The population of cuttings sampled at each depth reflect the mixing experienced both during transport in the return mud flow up the riser pipe and on the shale shaker, and for this reason lithologic cuttings boundaries should be defined by the first downhole occurrence of marker features from the underlying unit (see **"Lithology"**).

References

Angelier, J., 1994. Fault slip analysis and palaeostress reconstruction. *In* Hancock, P.L. (Ed.), *Continental Deformation:* Tarrytown, NY (Pergamon Press), 53–100.

Athy, L.F., 1930. Density, porosity, and compaction of sedimentary rocks. *AAPG Bull.,* 14(1):1–24.

Bernard, B.B., Brooks, J.M., and Sackett, W.M., 1978. Light hydrocarbons in recent Texas continental shelf and slope sediments. *J. Geophys. Res.: Oceans,* 83(C8):4053–4061. **doi:10.1029/JC083iC08p04053**

Bourlange, S., Henry, P., Moore, J.C., Mikada, H., and Klaus, A., 2003. Fracture porosity in the décollement zone of Nankai accretionary wedge using logging-while-drilling resistivity data. *Earth Planet. Sci. Lett.,* 209(1–2):103–112. **doi:10.1016/S0012-821X(03)00082-7**

Brothers, R.J., Kemp, A.E.S., and Maltman, A.J., 1996. Mechanical development of vein structures due to the passage of earthquake waves through poorly consolidated sediments. *Tectonophysics,* 260(4):227–244. **doi:10.1016/0040-1951(96)00088-1**

Byrne, T.B., Lin, W., Tsutsumi, A., Yamamoto, Y., Lewis, J.C., Kanagawa, K., Kitamura, Y., Yamaguchi, A., and Kimura, G., 2009. Anelastic strain recovery reveals extension across SW Japan subduction zone. *Geophys. Res. Lett.,* 36(23):L23310. **doi:10.1029/2009GL040749**

Cole, K.S., and Cole, R.H., 1941. Dispersion and absorption in dielectrics, 1. Alternating current characteristics. *J. Chem. Phys.,* 9(4):341. **doi:10.1063/1.1750906**

Cosgrove, J.W., 1995. The expression of hydraulic fracturing in rocks and sediments. *In* Ameen, M.S. (Ed.), *Fractography: Fracture Topography as a Tool in Fracture Mechanics and Stress Analysis.* Geol. Soc. Spec. Publ., 92(1):187–196. doi:10.1144/GSL.SP.1995.092.01.10

Cowan, D.S., 1982. Origin of "vein structure" in slope sediments on the inner slope of the Middle America Trench off Guatemala. *In* Aubouin, J., von Huene, R., et al., *Init. Repts. DSDP,* 67: Washington, DC (U.S. Govt. Printing Office), 645–650. doi:10.2973/dsdp.proc.67.132.1982

Day-Stirrat, R.J., Schleicher, A.M., Schneider, J., Flemings, P.B., Germaine, J.T., and van der Pluijm, B.A., 2011. Preferred orientation of phyllosilicates: effects of composition and stress on resedimented mudstone microfabrics. *J. Struct. Geol.,* 33(9):1347–1358. doi:10.1016/j.jsg.2011.06.007

Ellis, D.V., and Singer, J.M., 2007. *Well Logging for Earth Scientists* (2nd ed.): New York (Elsevier).

Engelder, T.J., 1993. *Stress in the Lithosphere:* New York (Princeton).

Expedition 314 Scientists, 2009. Expedition 314 Site C0002. *In* Kinoshita, M., Tobin, H., Ashi, J., Kimura, G., Lallemant, S., Screaton, E.J., Curewitz, D., Masago, H., Moe, K.T., and the Expedition 314/315/316 Scientists, *Proc. IODP,* 314/315/316: Washington, DC (Integrated Ocean Drilling Program Management International, Inc.). doi:10.2204/iodp.proc.314315316.114.2009

Expedition 315 Scientists, 2009a. Expedition 315 Site C0001. *In* Kinoshita, M., Tobin, H., Ashi, J., Kimura, G., Lallemant, S., Screaton, E.J., Curewitz, D., Masago, H., Moe, K.T., and the Expedition 314/315/316 Scientists, *Proc. IODP,* 314/315/316: Washington, DC (Integrated Ocean Drilling Program Management International, Inc.). doi:10.2204/iodp.proc.314315316.123.2009

Expedition 315 Scientists, 2009b. Expedition 315 Site C0002. *In* Kinoshita, M., Tobin, H., Ashi, J., Kimura, G., Lallemant, S., Screaton, E.J., Curewitz, D., Masago, H., Moe, K.T., and the Expedition 314/315/316 Scientists, *Proc. IODP,* 314/315/316: Washington, DC (Integrated Ocean Drilling Program Management International, Inc.). doi:10.2204/iodp.proc.314315316.124.2009

Expedition 316 Scientists, 2009. Expedition 316 Site C0006. *In* Kinoshita, M., Tobin, H., Ashi, J., Kimura, G., Lallemant, S., Screaton, E.J., Curewitz, D., Masago, H., Moe, K.T., and the Expedition 314/315/316 Scientists, *Proc. IODP,* 314/315/316: Washington, DC (Integrated Ocean Drilling Program Management International, Inc.). doi:10.2204/iodp.proc.314315316.134.2009

Expedition 319 Scientists, 2010. Site C0009. *In* Saffer, D., McNeill, L., Byrne, T., Araki, E., Toczko, S., Eguchi, N., Takahashi, K., and the Expedition 319 Scientists, *Proc. IODP,* 319: Tokyo (Integrated Ocean Drilling Program Management International, Inc.). doi:10.2204/iodp.proc.319.103.2010

Expedition 322 Scientists, 2010a. Site C0011. *In* Saito, S., Underwood, M.B., Kubo, Y., and the Expedition 322 Scientists, *Proc. IODP,* 322: Tokyo (Integrated Ocean Drilling Program Management International, Inc.). doi:10.2204/iodp.proc.322.103.2010

Expedition 322 Scientists, 2010b. Site C0012. *In* Saito, S., Underwood, M.B., Kubo, Y., and the Expedition 322 Scientists, *Proc. IODP,* 322: Tokyo (Integrated Ocean Drilling Program Management International, Inc.). doi:10.2204/iodp.proc.322.104.2010

Expedition 326 Scientists, 2011. NanTroSEIZE Stage 3: plate boundary deep riser: top hole engineering. *IODP Prel. Rept.,* 326. doi:10.2204/iodp.pr.326.2011

Expedition 332 Scientists, 2011. Site C0002. *In* Kopf, A., Araki, E., Toczko, S., and the Expedition 332 Scientists, *Proc. IODP,* 332: Tokyo (Integrated Ocean Drilling Program Management International, Inc.). doi:10.2204/iodp.proc.332.104.2011

Gulick, S.P.S., Bangs, N.L.B., Moore, G.F., Ashi, J., Martin, K.M., Sawyer, D.S., Tobin, H.J., Kuramoto, S., and Taira, A., 2010. Rapid forearc basin uplift and megasplay fault development from 3D seismic images of Nankai margin off Kii Peninsula, Japan. *Earth Planet. Sci. Lett.,* 300(1–2):55–62. doi:10.1016/j.epsl.2010.09.034

Hancock, P.L., 1985. Brittle microtectonics: principles and practice. *J. Struct. Geol.,* 7(3–4):437–457. doi:10.1016/0191-8141(85)90048-3

Heki, K., 2007. Secular, transient, and seasonal crustal movements in Japan from a dense GPS array: implication for plate dynamics in convergent boundaries. *In* Dixon, T.H., and Moore, J.C. (Eds.), *The Seismogenic Zone of Subduction Thrust Faults:* New York (Columbia Univ. Press), 512–539.

Hubbell, J.H., and Seltzer, S.M., 1996. Tables of X-ray mass attenuation coefficients and mass energy-absorption coefficients from 1 keV to 20 MeV for elements Z = 1 to 92 and 48 additional substances of dosimetric interest (SRD 126). In *National Institute of Standards and Technology Standard Reference Database:* Gaithersburg, MD (NIST). http://www.nist.gov/pml/data/xraycoef/index.cfm

Inagaki, F., Hinrichs, K.-U., Kubo, Y., and the Expedition 337 Scientists, 2012. Deep coalbed biosphere off Shimokita: microbial processes and hydrocarbon system associated with deeply buried coalbed in the ocean. *IODP Prel. Rept.,* 337. doi:10.2204/iodp.pr.337.2012

Isozaki, Y., and Itaya, T., 1990. Chronology of Sanbagawa metamorphism. *J. Metamorph. Geol,* 8(4):401–411. doi:10.1111/j.1525-1314.1990.tb00627.x

Jenden, P.D., Newell, K.D., Kaplan, I.R., and Watney, W.L., 1988. Composition and stable-isotope geochemistry of natural gases from Kansas, midcontinent, USA. *Chem. Geol.,* 71(1–3):117–147. doi:10.1016/0009-2541(88)90110-6

Kinoshita, M., Tobin, H., Ashi, J., Kimura, G., Lallemant, S., Screaton, E.J., Curewitz, D., Masago, H., Moe, K.T., and the Expedition 314/315/316 Scientists, 2009. *Proc. IODP,* 314/315/316: Washington, DC (Integrated Ocean Drilling Program Management International, Inc.). doi:10.2204/iodp.proc.314315316.2009

Krooss, B.M., Littke, R., Müller, B., Frielingsdorf, J., Schwochau, K., and Idiz, E.F., 1995. Generation of nitrogen and methane from sedimentary organic matter: implications on the dynamics of natural gas accumulations. *Chem. Geol.,* 126(3–4):291–318. doi:10.1016/0009-2541(95)00124-7

Lewis, J.C., Byrne, T.B., and Kanagawa, K., 2013. Evidence for mechanical decoupling of the upper plate at the Nankai subduction zone: constraints from core-scale faults at NantroSEIZE Sites C0001 and C0002. *Geochem., Geophys., Geosyst.,* 14(3):620–633. doi:10.1029/2012GC004406

McBride, E.F., and Picard, M.D., 1991. Facies implications of *Trichichnus* and *Chondrites* in turbidites and hemipelagites, Marnosoarenacea Formation (Miocene), northern Apennines, Italy. *Palaios,* 6(3):281–290. doi:10.2307/3514908

Meyers, P.A., 1997. Organic geochemical proxies of paleoceanographic, paleolimnologic, and paleoclimatic processes. *Org. Geochem.,* 27(5–6):213–250. doi:10.1016/S0146-6380(97)00049-1

Milliken, K.L., and Reed, R.M., 2011. Multiple causes of diagenetic fabric anisotropy in weakly consolidated mud, Nankai accretionary prism, IODP Expedition 316. *J. Struct. Geol.,* 32(12):1887–1898. doi:10.1016/j.jsg.2010.03.008

Mingram, B., Hoth, P., Lüders, V., and Harlov, D., 2005. The significance of fixed ammonium in Palaeozoic sediments for the generation of nitrogen-rich natural gases in the North German Basin. *Int. J. Earth Sci.,* 94(5–6):1010–1022. doi:10.1007/s00531-005-0015-0

Moore, G.F., Park, J.-O., Bangs, N.L., Gulick, S.P., Tobin, H.J., Nakamura, Y., Sato, S., Tsuji, T., Yoro, T., Tanaka, H., Uraki, S., Kido, Y., Sanada, Y., Kuramoto, S., and Taira, A., 2009. Structural and seismic stratigraphic framework of the NanTroSEIZE Stage 1 transect. *In* Kinoshita, M., Tobin, H., Ashi, J., Kimura, G., Lallemant, S., Screaton, E.J., Curewitz, D., Masago, H., Moe, K.T., and the Expedition 314/315/316 Scientists, *Proc. IODP,* 314/315/316: Washington, DC (Integrated Ocean Drilling Program Management International, Inc.). doi:10.2204/iodp.proc.314315316.102.2009

Moore, G.F., Taira, A., Klaus, A., et al., 2001. *Proc. ODP, Init. Repts.,* 190: College Station, TX (Ocean Drilling Program). doi:10.2973/odp.proc.ir.190.2001

Mort, K., and Woodcock, N.H., 2008. Quantifying fault breccia geometry: Dent Fault, NW England. *J. Struct. Geol.,* 30(6):701–709. doi:10.1016/j.jsg.2008.02.005

Mountain, G.S., Miller, K.G., Blum, P., et al., 1994. *Proc. ODP, Init. Repts.,* 150: College Station, TX (Ocean Drilling Program). doi:10.2973/odp.proc.ir.150.1994

Ogawa, Y., 1980. Beard-like veinlet structure as fracture cleavage in the Neogene siltstone in the Miura and Boso peninsulas, central Japan. *Sci. Rep. Dept. Geol., Kyushu Univ.,* 13:321–327.

Ohsumi, T., and Ogawa, Y., 2008. Vein structures, like ripple marks, are formed by short-wavelength shear waves. *J. Struct. Geol.,* 30(6):719–724. doi:10.1016/j.jsg.2008.02.002

Petit, J.P., 1987. Criteria for the sense of movement on fault surfaces in brittle rocks. *J. Struct. Geol.,* 9(5–6):597–608. doi:10.1016/0191-8141(87)90145-3

Pickering, K.T., Underwood, M.B., and Taira, A., 1993. Stratigraphic synthesis of the DSDP-ODP sites in the Shikoku Basin, Nankai Trough, and accretionary prism. *In* Hill, I.A., Taira, A., Firth, J.V., et al., *Proc. ODP, Sci. Results,* 131: College Station, TX (Ocean Drilling Program), 313–330. doi:10.2973/odp.proc.sr.131.135.1993

Raffi, I., 2002. Revision of the early-middle Pleistocene calcareous nannofossil biochronology (1.75–0.85 Ma). *Mar. Micropaleontol.,* 45(1):25–55. doi:10.1016/S0377-8398(01)00044-5

Rice, D.D., and Claypool, G.E., 1981. Generation, accumulation, and resource potential of biogenic gas. *AAPG Bull.,* 65(1):5–25. doi:10.1306/2F919765-16CE-11D7-8645000102C1865D

Schlumberger, 2011. *Drilling Tools: Quick Reference Guide:* Houston (Schlumberger). http://www.slb.com/~/media/Files/drilling/specs/ht_quick_ref_guide.pdf

Schoell, M., 1983. Genetic characterization of natural gases. *AAPG Bull.,* 67(3):546. doi:10.1306/03B5B4C5-16D1-11D7-8645000102C1865D

Seno, T., Stein, S., and Gripp, A.E., 1993. A model for the motion of the Philippine Sea plate consistent with NUVEL-1 and geological data. *J. Geophys. Res.: Solid Earth,* 98(B10):17941–17948. doi:10.1029/93JB00782

Shipboard Scientific Party, 1991. Site 808. *In* Taira, A., Hill, I., Firth, J.V., et al., *Proc. ODP, Init. Repts.,* 131: College Station, TX (Ocean Drilling Program), 71–269. doi:10.2973/odp.proc.ir.131.106.1991

Shipboard Scientific Party, 2001a. Site 1175. *In* Moore, G.F., Taira, A., Klaus, A., et al., *Proc. ODP, Init. Repts.,* 190: College Station, TX (Ocean Drilling Program), 1–92. doi:10.2973/odp.proc.ir.190.106.2001

Shipboard Scientific Party, 2001b. Site 1176. *In* Moore, G.F., Taira, A., Klaus, A., et al., *Proc. ODP, Init. Repts.,* 190: College Station, TX (Ocean Drilling Program), 1–80. doi:10.2973/odp.proc.ir.190.107.2001

Song, I., Suh, M., Won, K.S., and Haimson, B., 2001. A laboratory study of hydraulic fracturing breakdown pressure in tablerock sandstone. *Geosci. J.,* 5(3):263–271. doi:10.1007/BF02910309

Strasser, M., Dugan, B., Kanagawa, K., Moore, G.F., Toczko, S., Maeda, L., Kido, Y., Moe, K.T., Sanada, Y., Esteban, L., Fabbri, O., Geersen, J., Hammerschmidt, S., Hayashi, H., Heirman, K., Hüpers, A., Jurado Rodriguez, M.J., Kameo, K., Kanamatsu, T., Kitajima, H., Masuda, H., Milliken, K., Mishra, R., Motoyama, I., Olcott, K., Oohashi, K., Pickering, K.T., Ramirez, S.G., Rashid, H., Sawyer, D., Schleicher, A., Shan, Y., Skarbek, R., Song, I., Takeshita, T., Toki, T., Tudge, J., Webb, S., Wilson, D.J., Wu, H.-Y., and Yamaguchi, A., 2014a. Methods. *In* Strasser, M., Dugan, B., Kanagawa, K., Moore, G.F., Toczko, S., Maeda, L., and the Expedition 338 Scientists, *Proc. IODP,* 338: Yokohama (Integrated Ocean Drilling Program). doi:10.2204/iodp.proc.338.102.2014

Strasser, M., Dugan, B., Kanagawa, K., Moore, G.F., Toczko, S., Maeda, L., Kido, Y., Moe, K.T., Sanada, Y., Esteban, L., Fabbri, O., Geersen, J., Hammerschmidt, S., Hayashi, H., Heirman, K., Hüpers, A., Jurado Rodriguez, M.J., Kameo, K., Kanamatsu, T., Kitajima, H., Masuda, H., Milliken, K., Mishra, R., Motoyama, I., Olcott, K., Oohashi, K., Pickering, K.T., Ramirez, S.G., Rashid, H., Sawyer, D., Schleicher, A., Shan, Y., Skarbek, R., Song, I., Takeshita, T., Toki, T., Tudge, J., Webb, S., Wilson, D.J., Wu, H.-Y., and Yamaguchi, A., 2014b. Site C0021. *In* Strasser, M., Dugan, B., Kanagawa, K., Moore, G.F., Toczko, S., Maeda, L., and the Expedition 338 Scientists, *Proc. IODP,* 338: Yokohama (Integrated Ocean Drilling Program). **doi:10.2204/iodp.proc.338.106.2014**

Taira, A., Katto, J., Tashiro, M., Okamura, M., and Kodama, K., 1988. The Shimanto Belt in Shikoku, Japan: evolution of Cretaceous to Miocene accretionary prism. *Mod. Geol.,* 12:5–46.

Tobin, H.J., and Kinoshita, M., 2006. NanTroSEIZE: the IODP Nankai Trough Seismogenic Zone Experiment. *Sci. Drill.*, 2:23–27. **doi:10.2204/iodp.sd.2.06.2006**

Todd, D.K., and Mays, L.W., 2005. *Groundwater Hydrology* (3rd ed.): Hoboken, NJ (John Wiley & Sons).

Underwood, M.B., Moore, G.F., Taira, A., Klaus, A., Wilson, M.E.J., Fergusson, C.L., Hirano, S., Steurer, J., and the Leg 190 Shipboard Scientific Party, 2003. Sedimentary and tectonic evolution of a trench-slope basin in the Nankai subduction zone of southwest Japan. *J. Sediment. Res.,* 73(4):589–602. **doi:10.1306/092002730589**

White, A.J., Traugott, M.O., and Swarbrick, R.E., 2002. The use of leak-off tests as means of predicting minimum in-situ stress. *Pet. Geosci.,* 8(2):189–193. **doi:10.1144/petgeo.8.2.189**

Publication: 13 January 2014
MS 338-103

Figure F1. Regional location map showing Site C0002 in context of the NanTroSEIZE project sites. Box = region with 3-D seismic data, red = Expedition 338 sites, blue = NanTroSEIZE Stage 1 and 2 sites, yellow arrows = estimated far-field vectors between Philippine Sea plate and Japan (Seno et al., 1993; Heki, 2007), stars = locations of 1944 and 1946 tsunamigenic earthquakes.

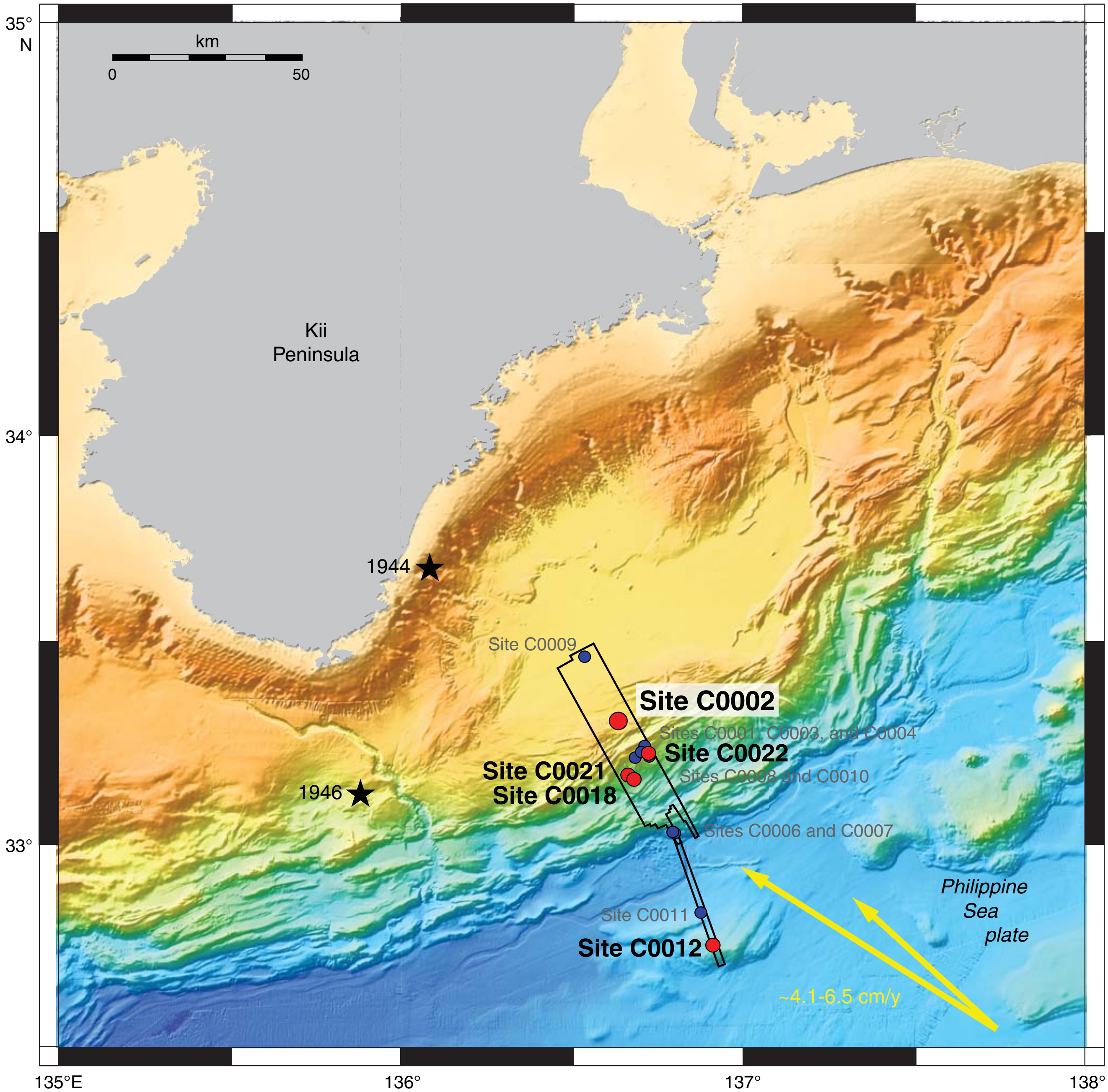

Figure F2. In-line (IL) 2529 extracted from the 3-D seismic volume, showing Site C0002 in relation to Stage 1 Sites C0001, C0003, C0004, and C0008 (black lines). Green box = extent of LWD and cuttings obtained in Hole C0002F, red boxes = sections of cores obtained from Holes C0002H, C0002J, C0002K, and C0002L, dashed extension below the green box = ultimate planned path through the megasplay fault at ~5200 mbsf. VE = vertical exaggeration.

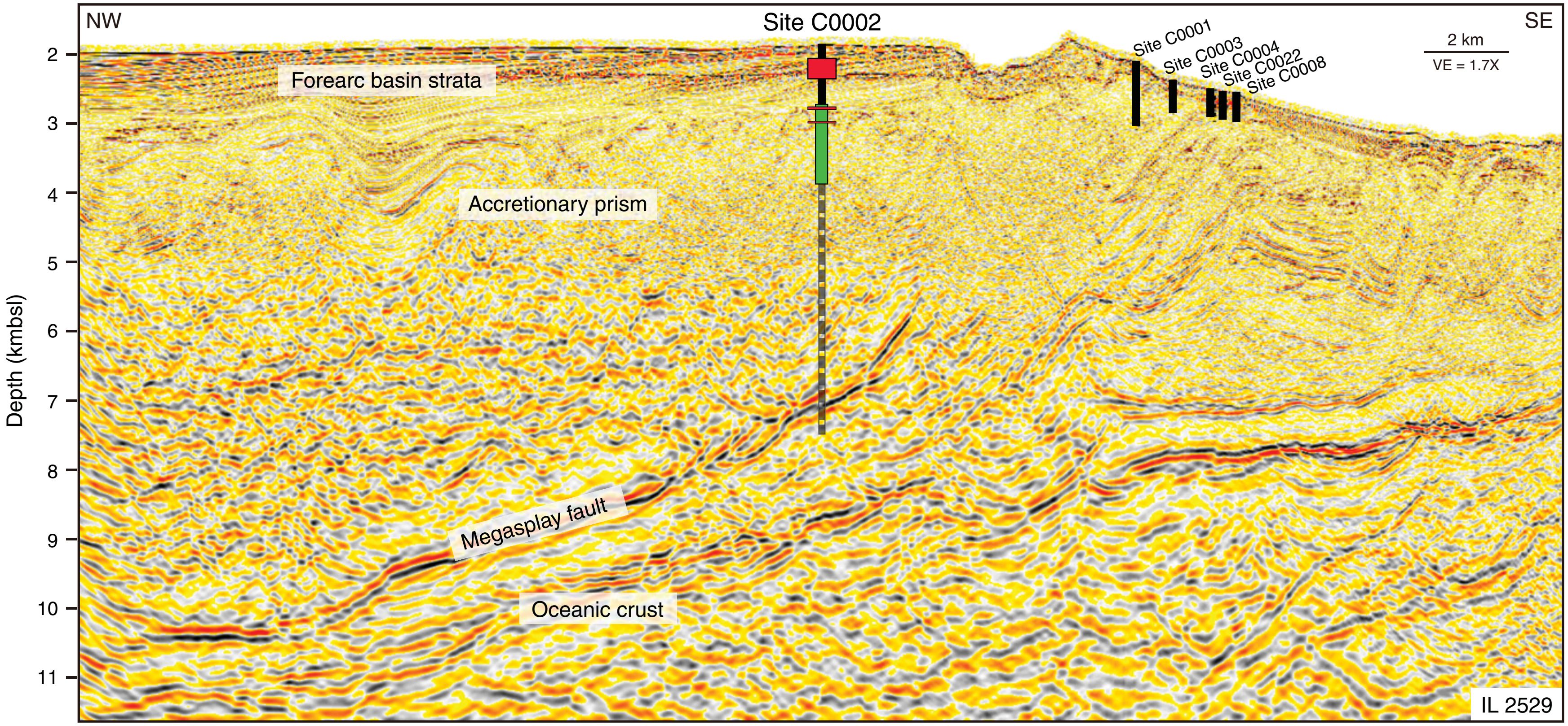

Figure F3. A. Seismic In-line 2532 showing relative locations of holes drilled at Site C0002. LWD = logging while drilling, VE = vertical exaggeration. (Continued on next page.)

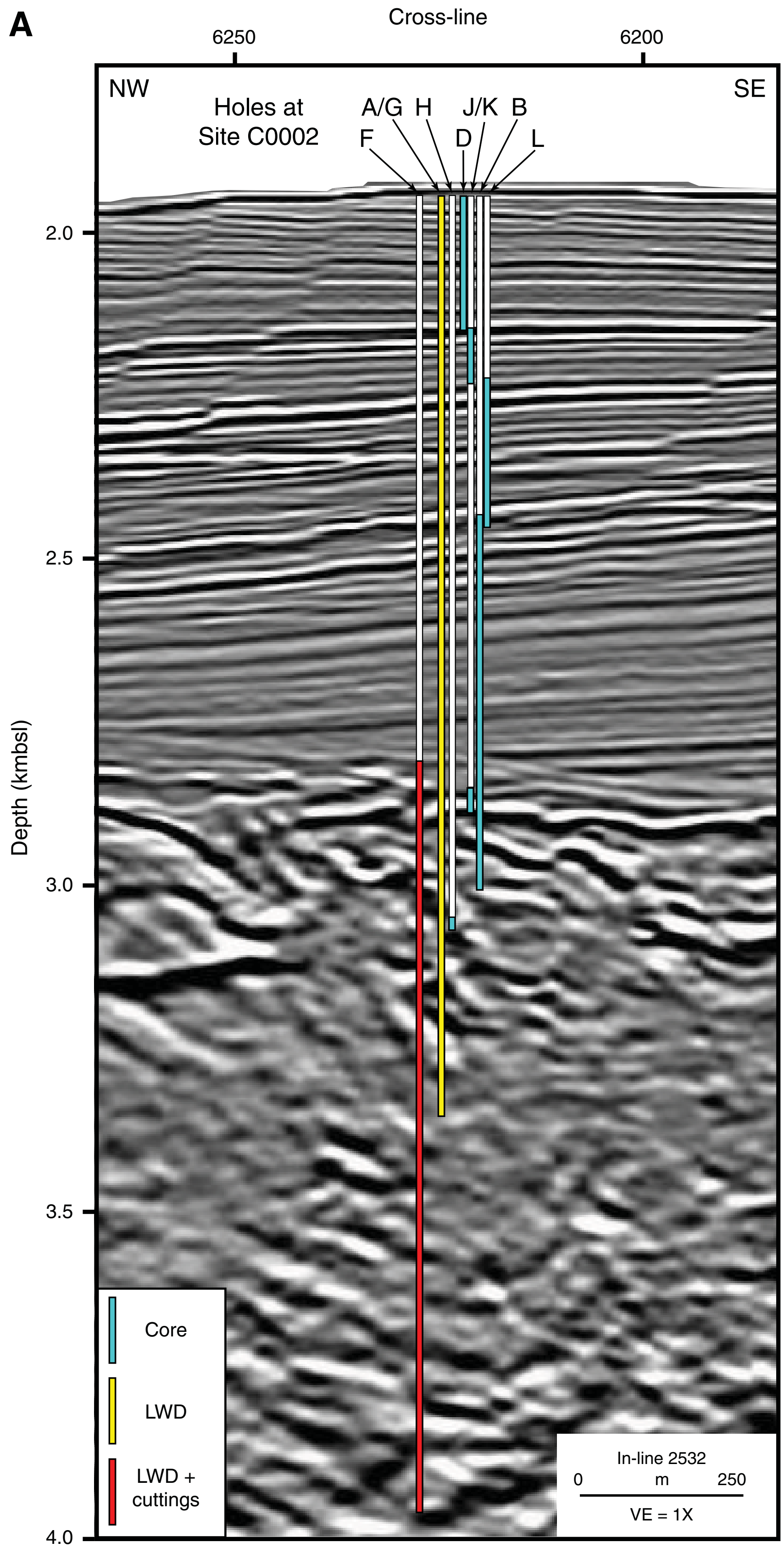

Figure F3 (continued). B. Seismic Cross-line 6223 showing relative locations of holes drilled at Site C0002.

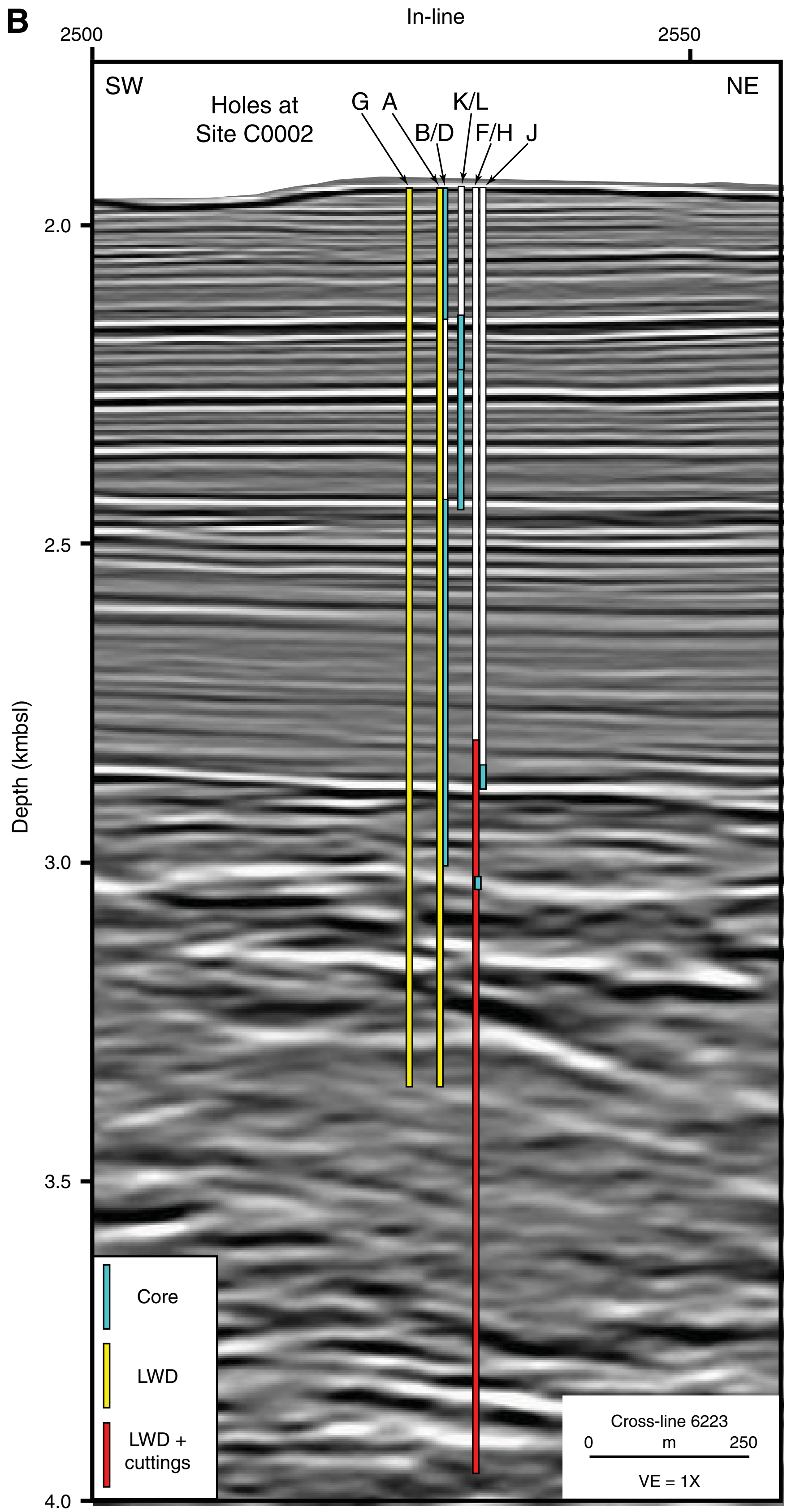

Figure F4. Map of drilled holes, Site C0002. Red = holes drilled during Expedition 338, blue = holes drilled during previous expeditions. IL = in-line, XL = cross-line.

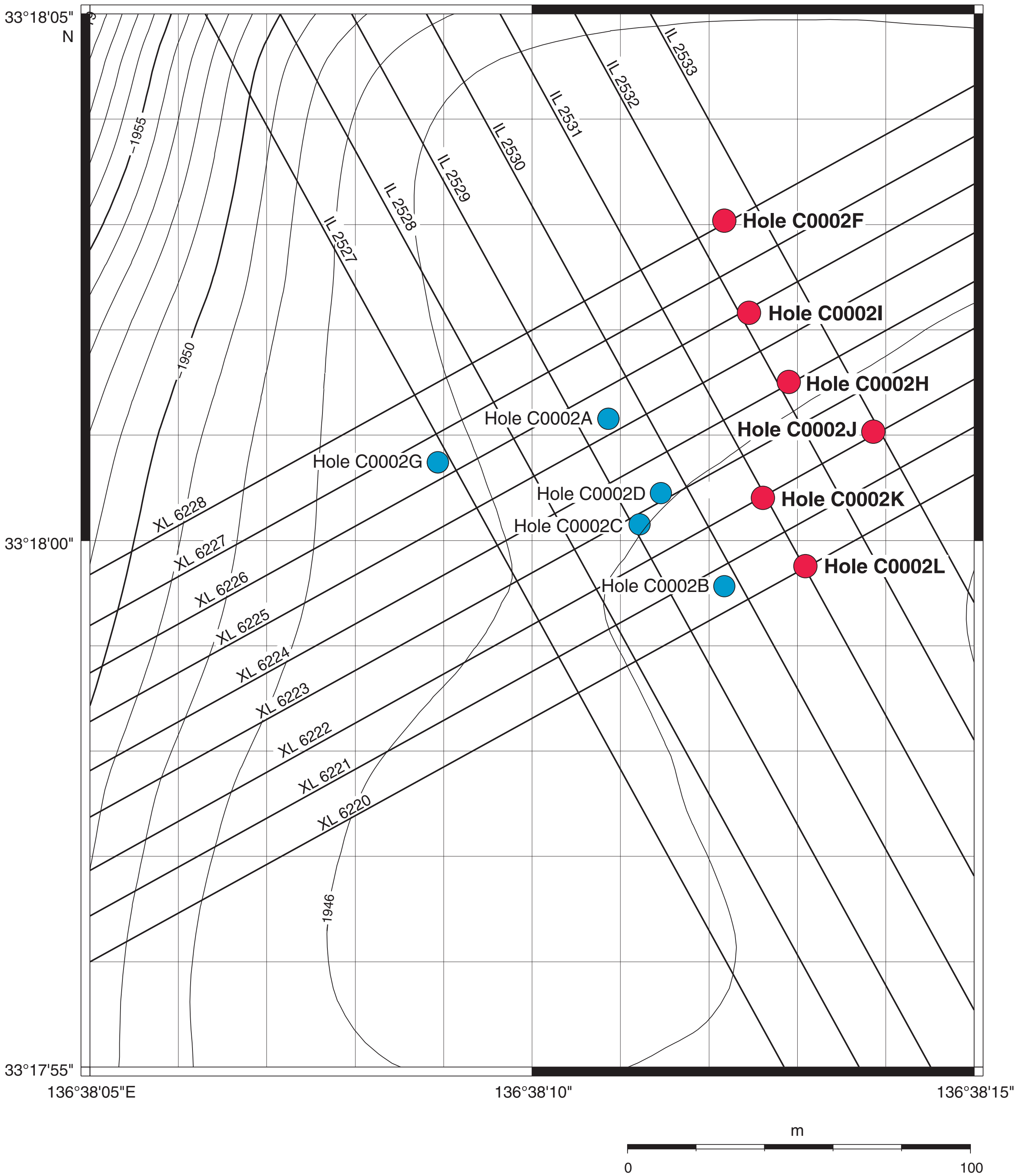

Figure F5. Wind condition changes at Site C0002 from 1700 to 1800 h on 17 November 2012.

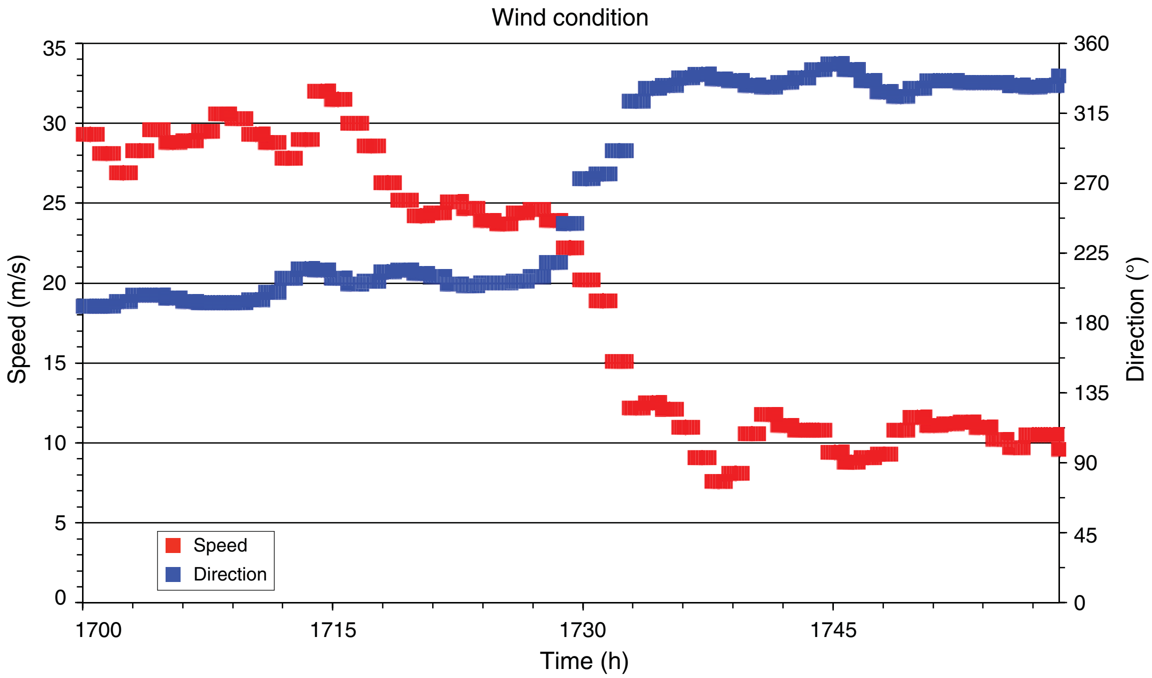

Figure F6. MWD logs, Hole C0002F. Off-bottom times were obtained from the time series data.

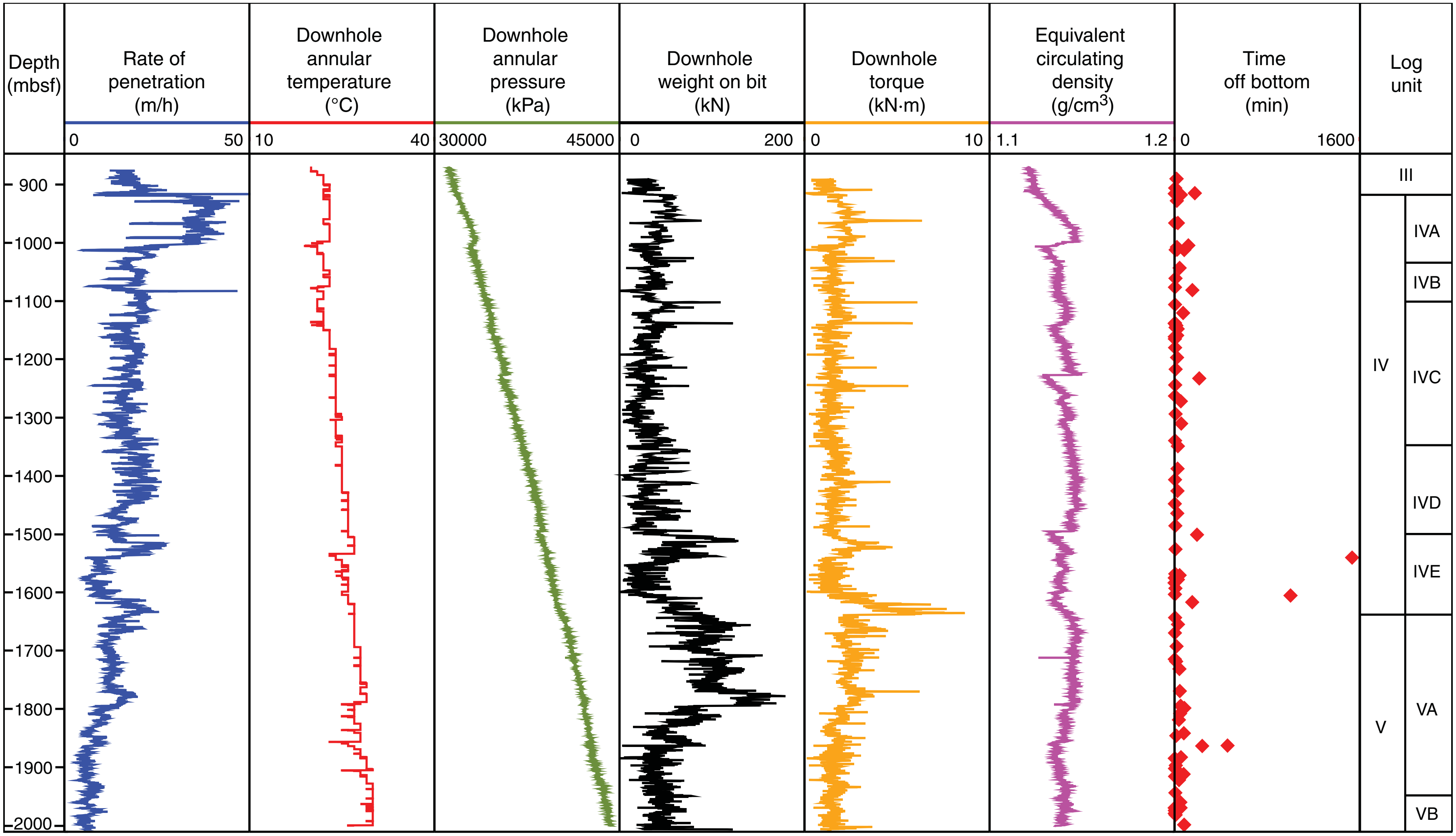

Figure F7. Comparison of the logs from Holes C0002A and C0002F, showing the correlation between logging Units III and IV. The logging Unit III/IV boundary in Hole C0002A is recognized as a sharp lithologic change interpreted from gamma ray data, whereas in Hole C0002F the boundary was defined by a more subtle change characterized by minor excursions in gamma radioactivity, resistivity, and sonic slowness values. Similar gamma ray trends interpreted to represent interbedded sand and clay are observed for logging Unit IV in Holes C0002A and C0002F. RES_BS = shallow resistivity, RES_BM = medium resistivity, RES_BD = deep resistivity. GR = gamma radiation, RAB = resistivity at the bit. DTCO = compressional wave slowness.

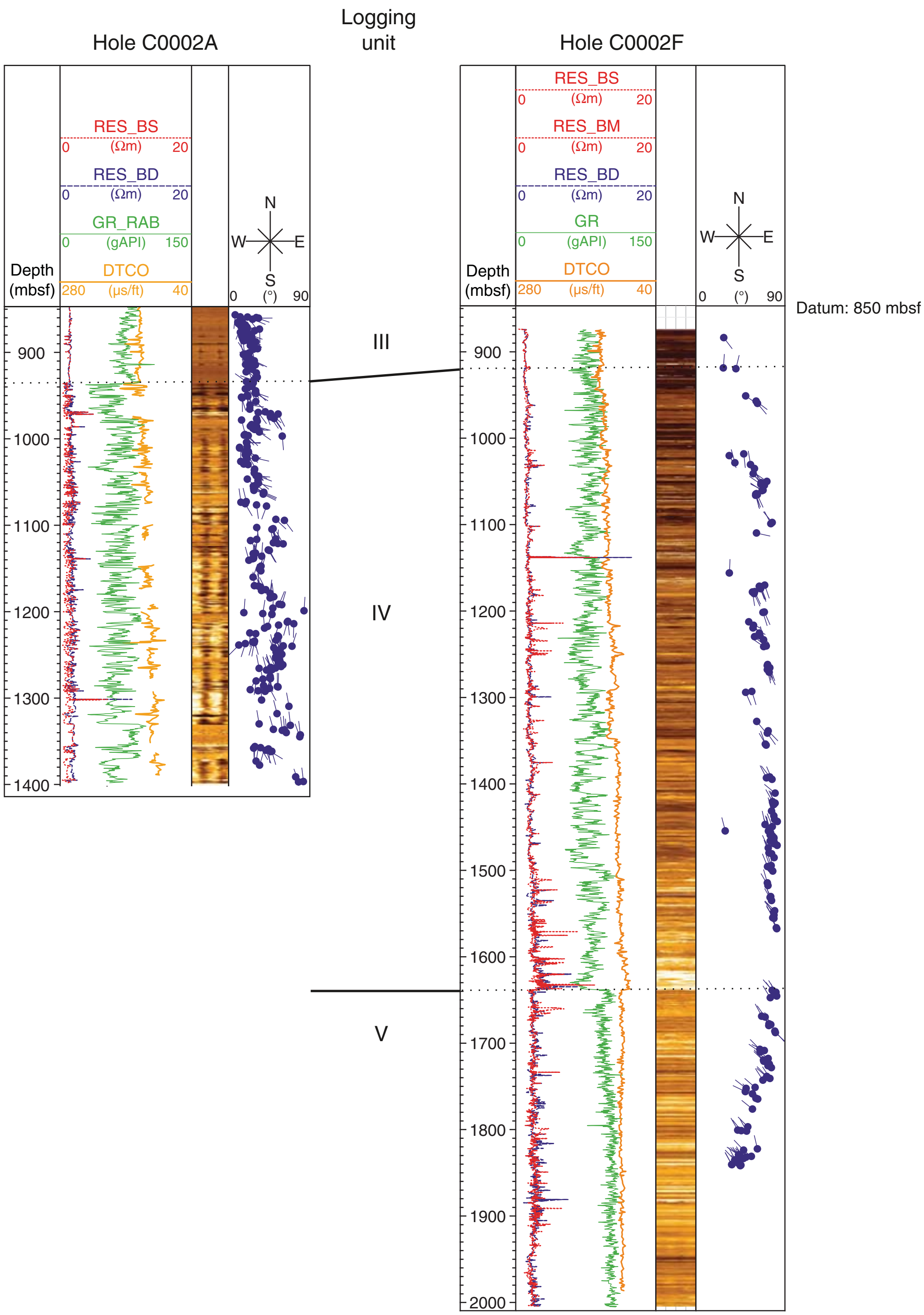

Figure F8. Composite plot of LWD data for Hole C0002F showing gamma ray, deep button resistivity image, resistivity logs, sonic slowness (velocity), fracture and bedding orientation, resistivity-derived bulk density and porosity, and logging units.

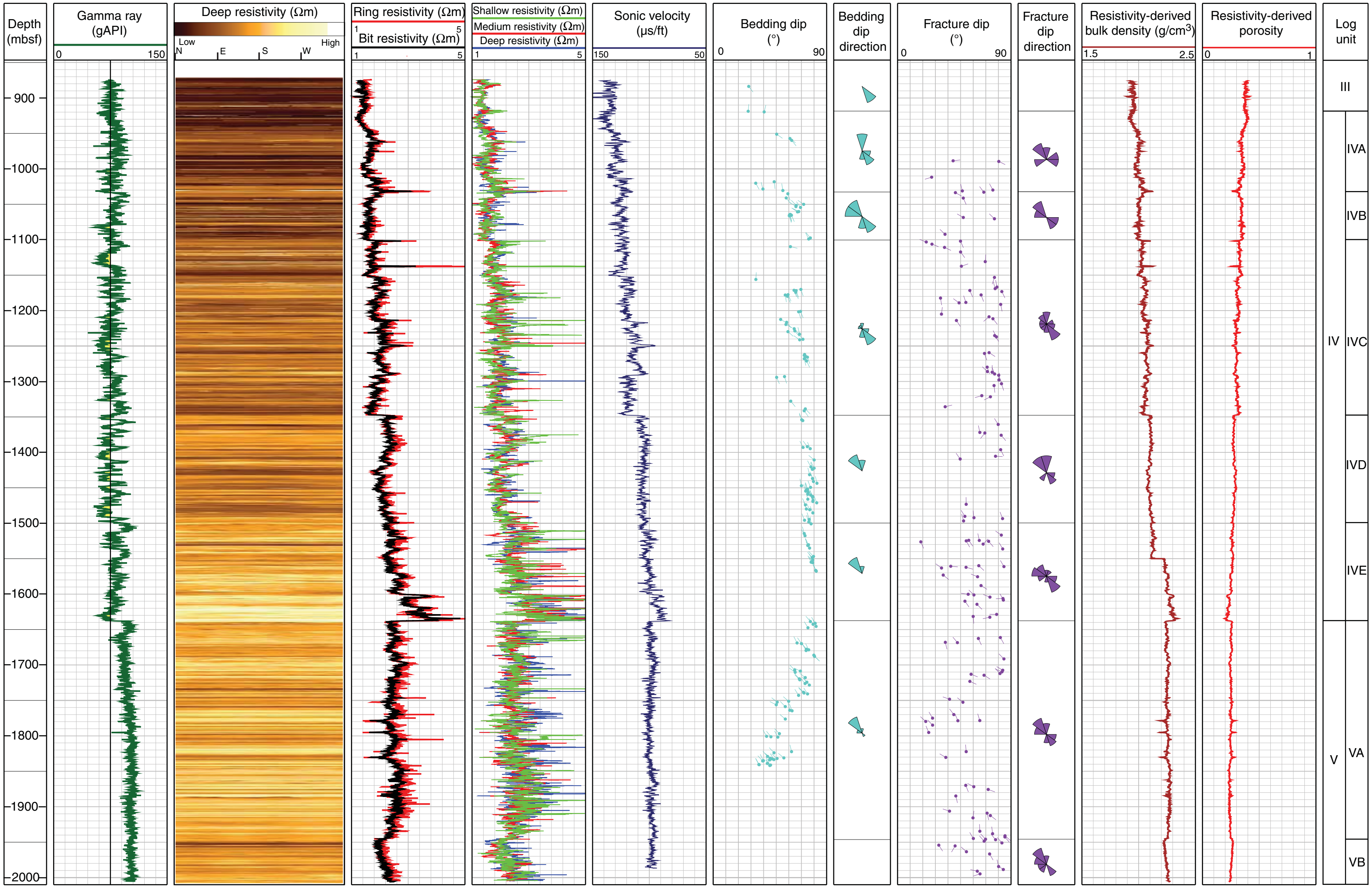

Figure F9. Representative deep resistivity-at-the-bit (RAB) images of logging Units IV and V, Hole C0002F. Bedding dips and azimuths are shown on the tadpole track (0°–90°) and apparent dips along a north–south virtual section. **A.** Logging Unit IV bedding dipping in opposite directions (fold). **B.** Logging Unit IV beds can be characterized by changing resistivity, indicating changes in composition and/or structure. **C.** Logging Unit V steeply dipping (deformed) beds characterized by conductive (clay-rich) interbeds. **D.** Logging Unit V gently dipping (<45°) beds showing a mottled texture.

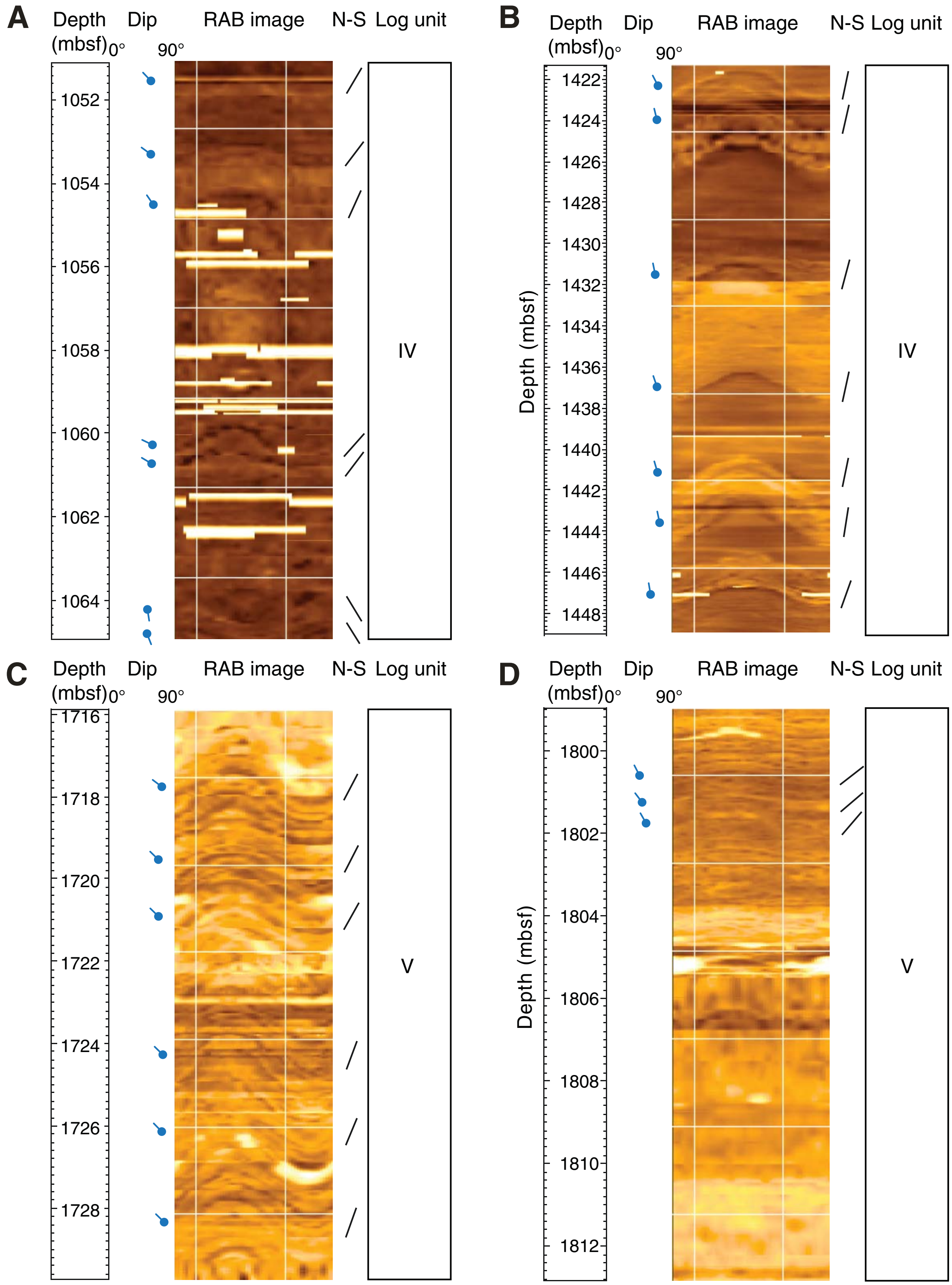

Figure F10. Shallow button resistivity image, fracture orientations, and fracture frequency, Hole C0002F. Fracture counts were normalized over 10 m intervals to show areas of higher fracture concentration. Also shown are equal area lower hemisphere stereonets for all of the poles to fracture planes, separated by logging unit.

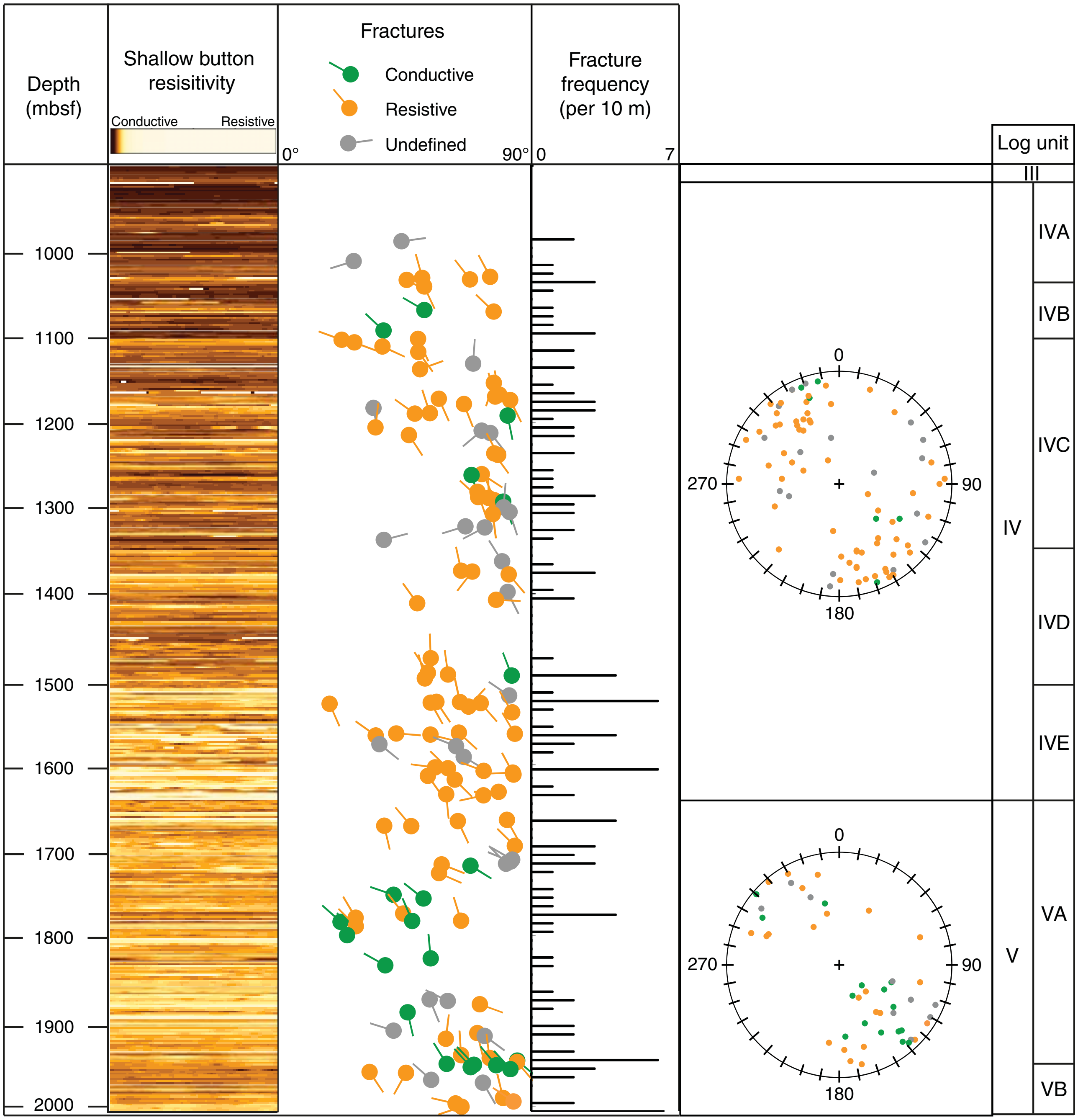

Figure F11. Azimuth of compressional borehole breakouts (BOs) and drilling-induced tensile fractures (DITFs), Hole C0002F.

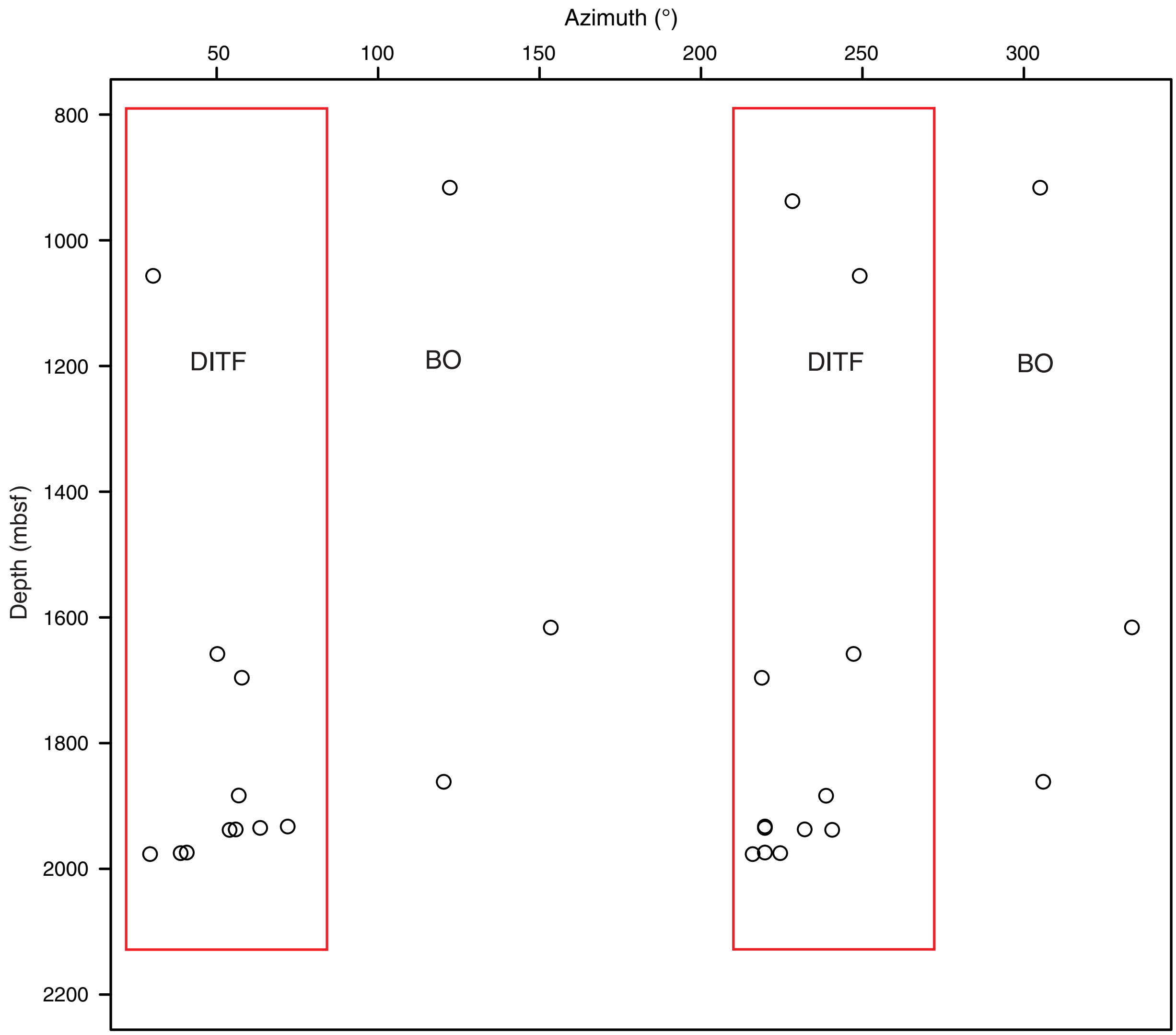

Figure F12. Width of compressional borehole breakouts with depth, Hole C0002F.

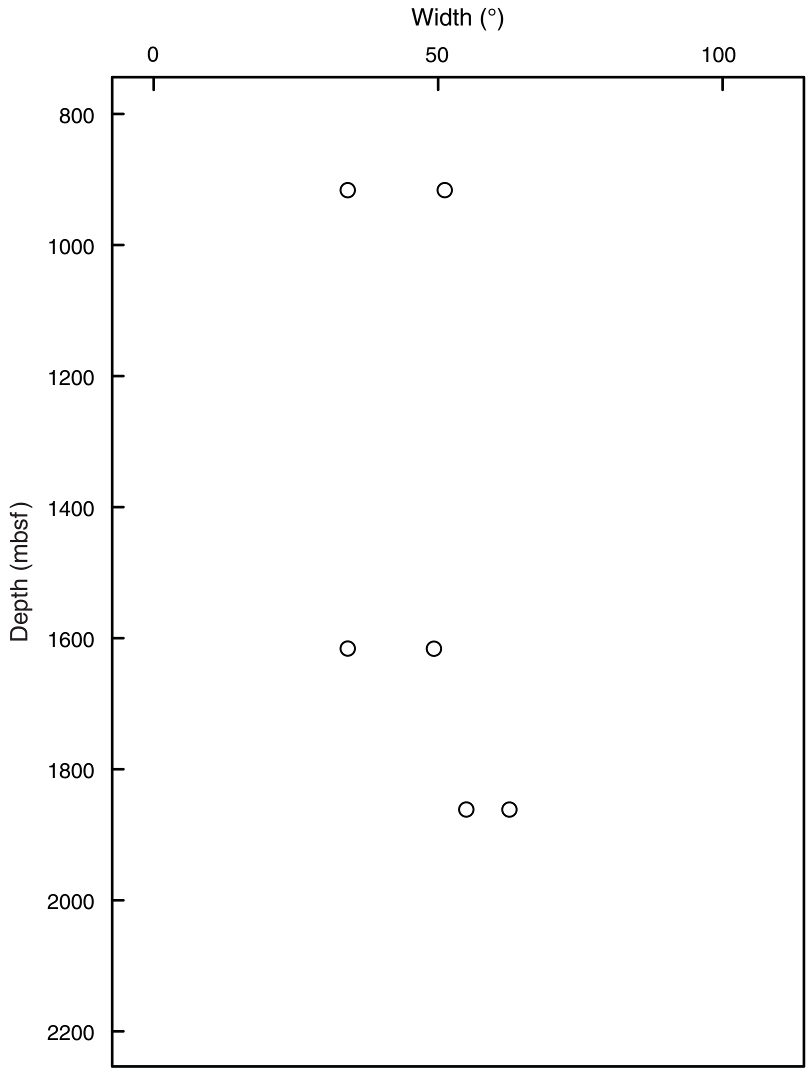

Figure F13. Example of compressional borehole breakouts (BOs) (purple boxes) observed on dynamic resistivity images, Hole C0002F.

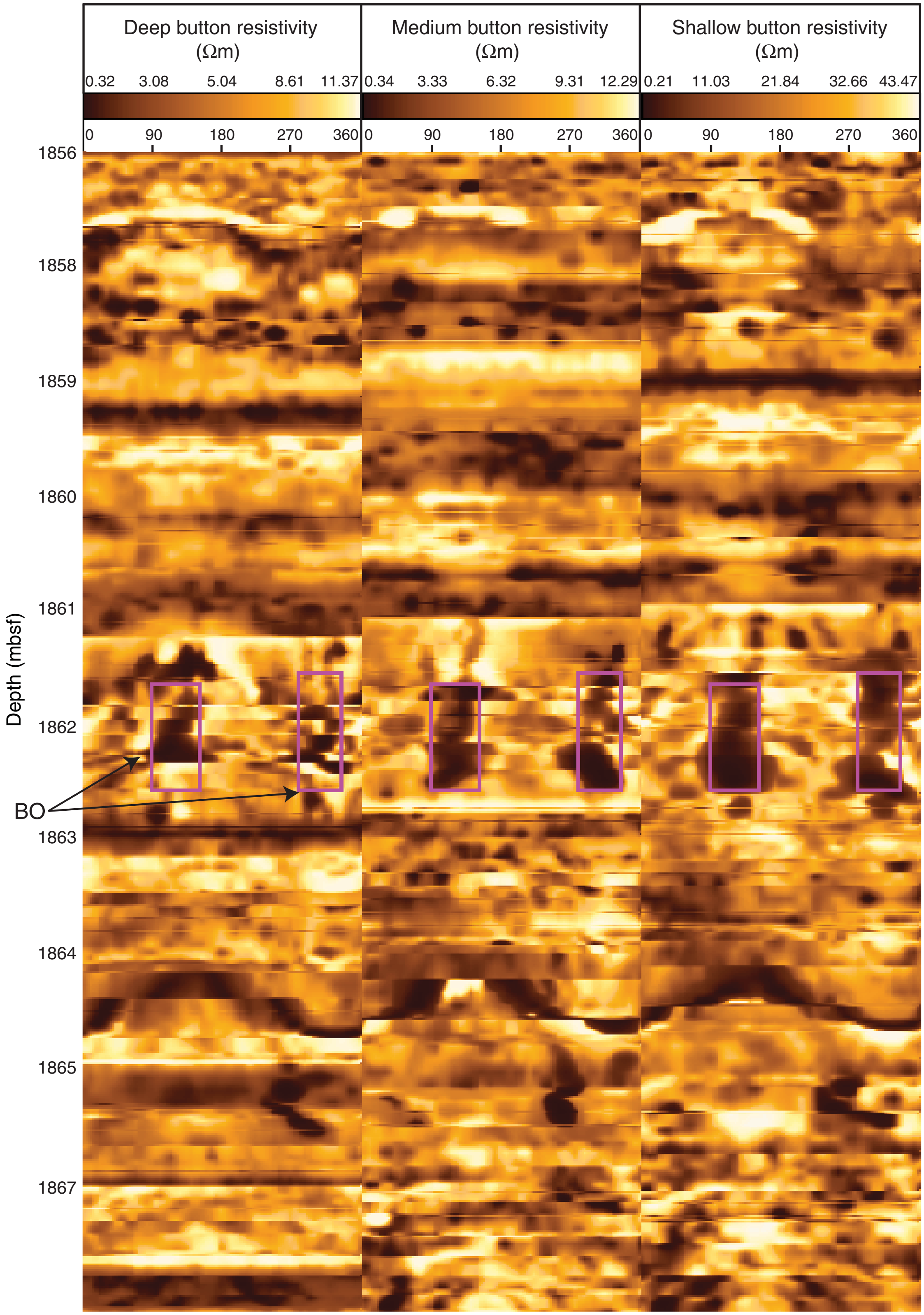

Figure F14. Example of drilling-induced tensile fractures (DITFs) (purple boxes) measured in Hole C0002F.

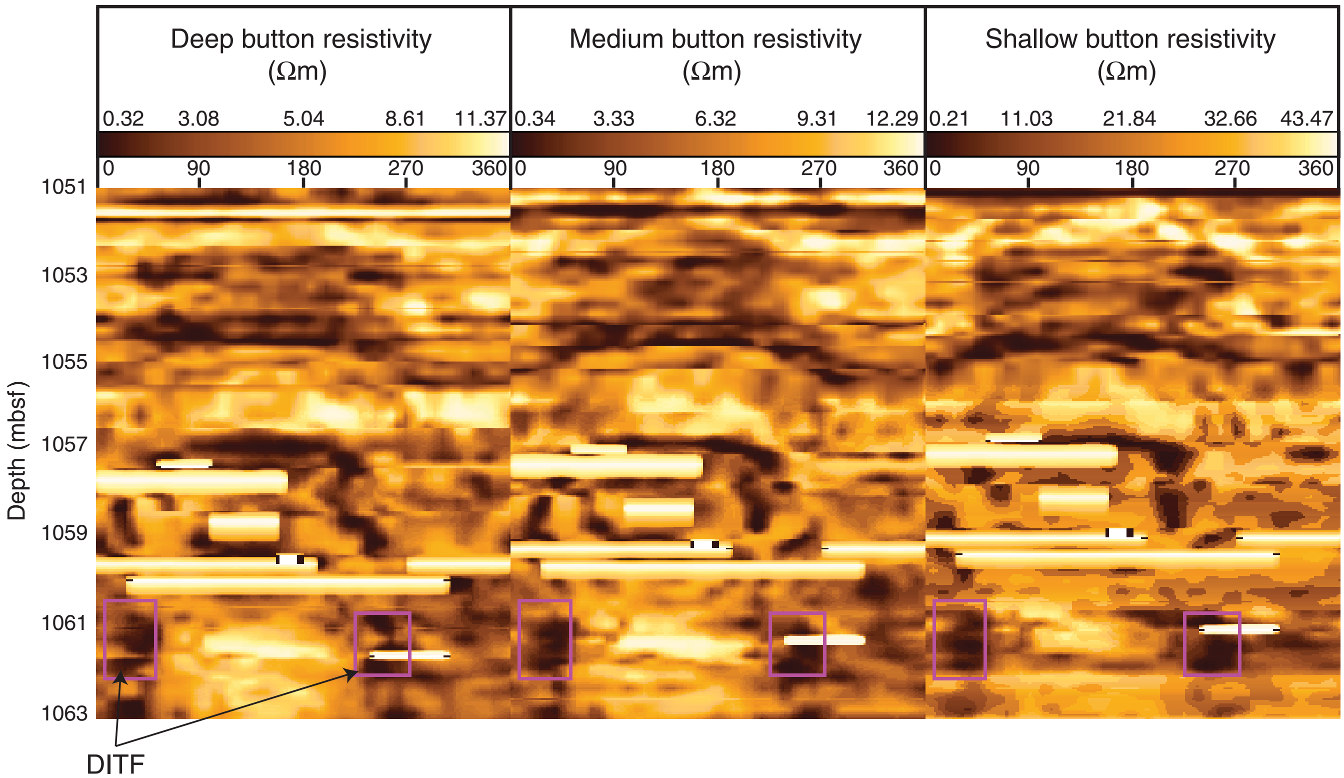

Figure F15. Section of the same depth interval from Holes C0002A and C0002F showing well-developed compressional borehole breakouts (BOs) in Hole C0002A that are not present in riser Hole C0002F.

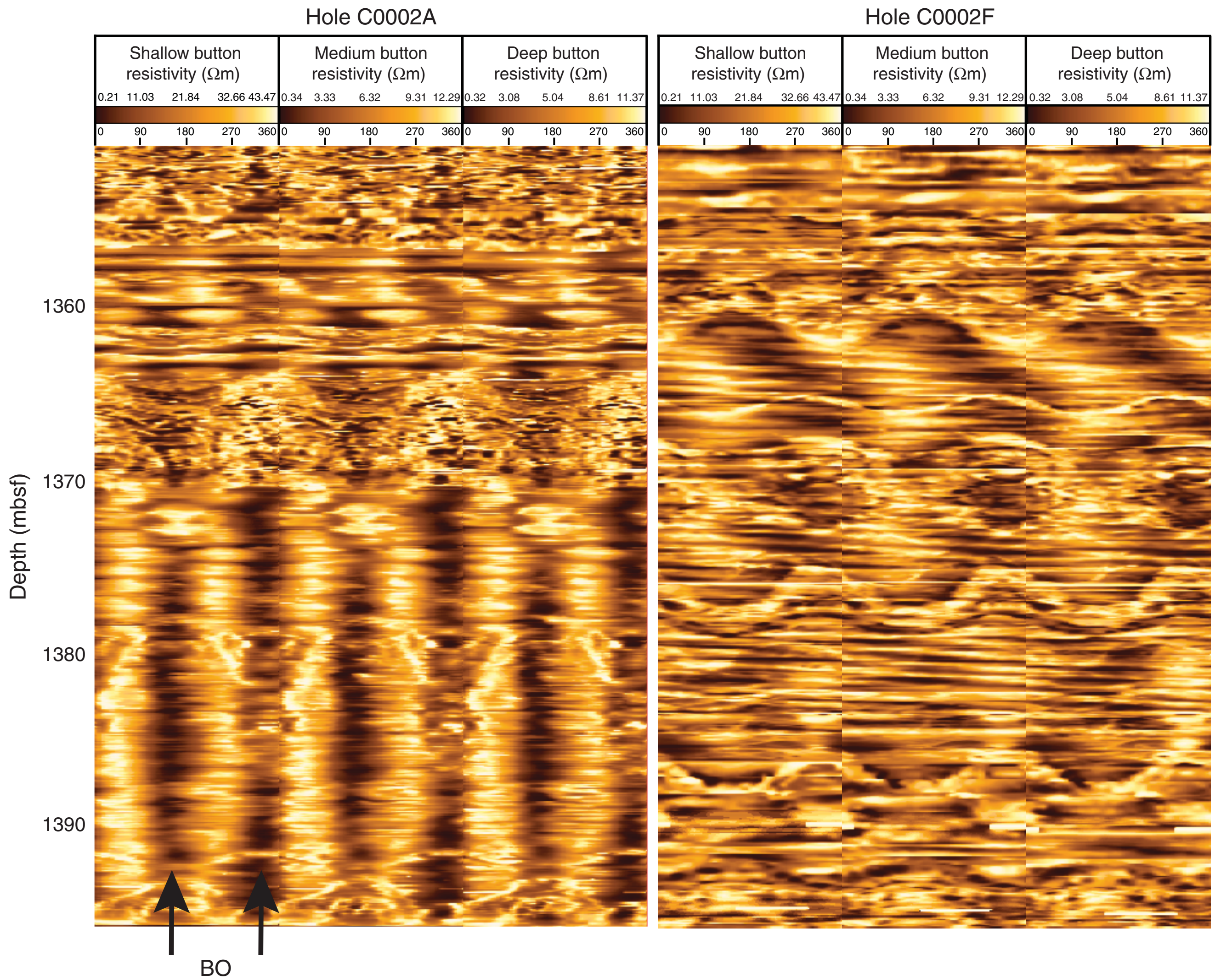

Figure F16. Resistivity logs (bit, ring, shallow, deep, and medium), gamma ray log, and resistivity-derived porosity and bulk density logs, Hole C0002F.

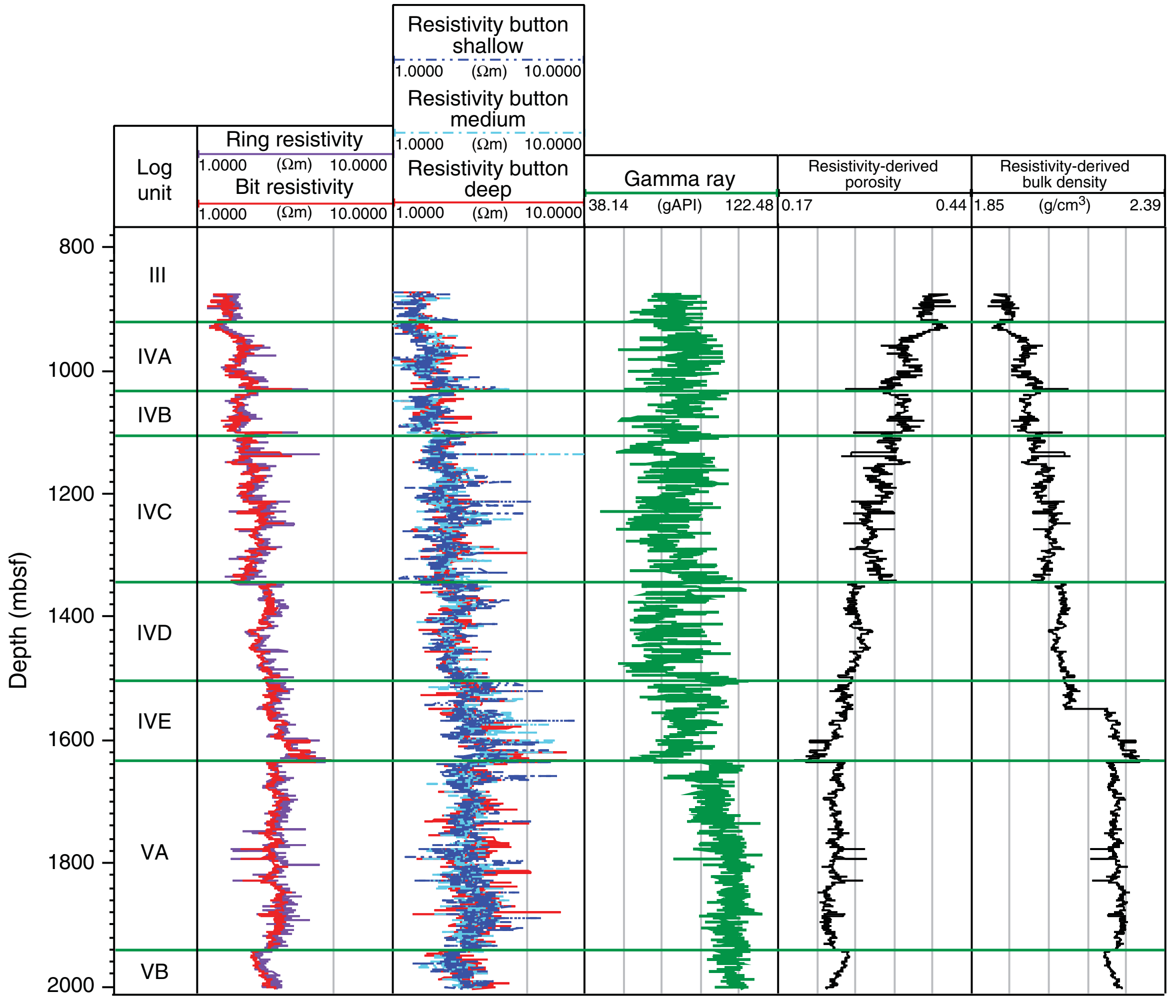

Figure F17. Comparison of resistivity images obtained from a relogged section (left) with the original data (right), Hole C0002F.

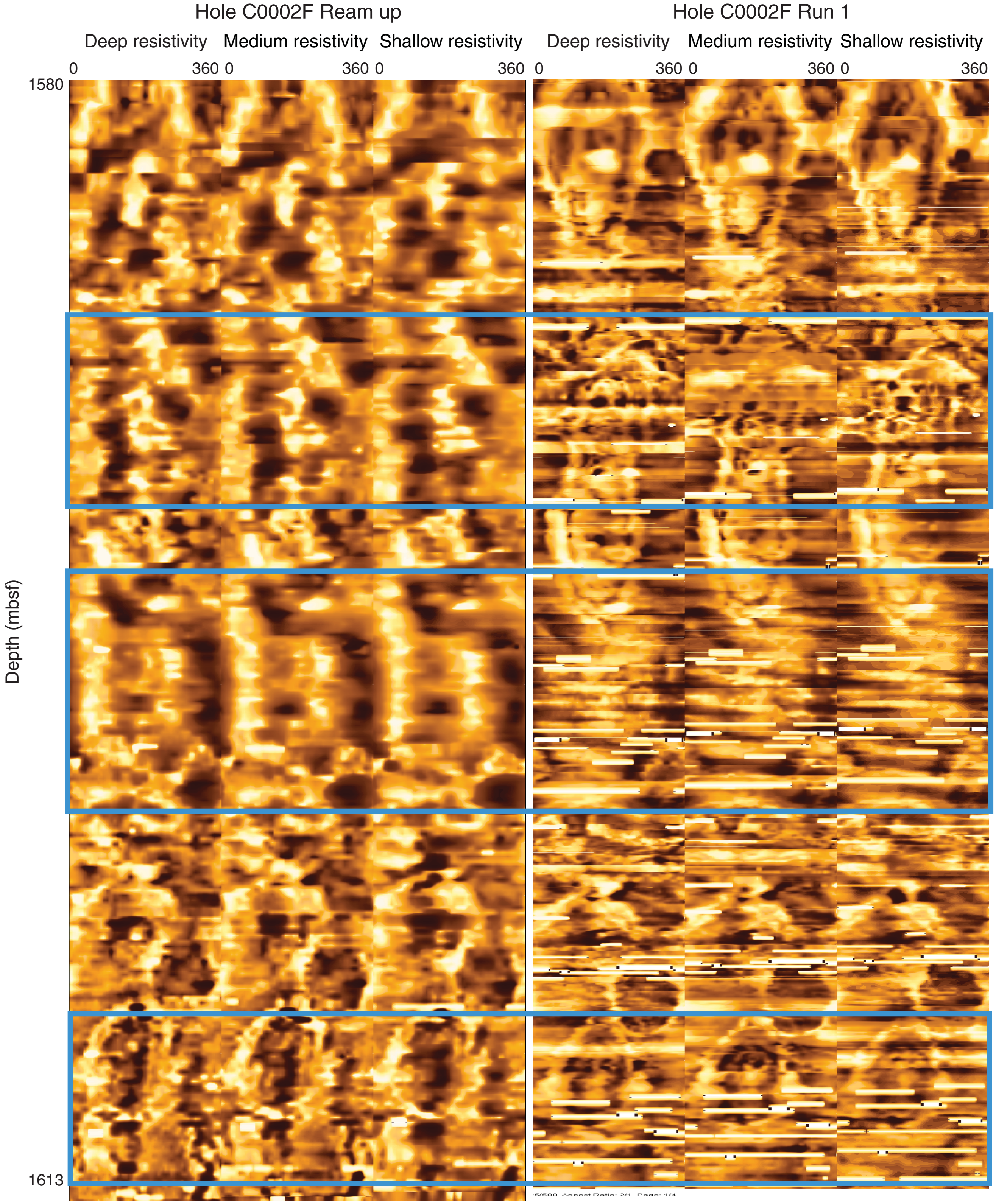

Figure F18. Graph showing percent silty claystone versus percent sand/sandstone, Hole C0002F. Dashed lines = lithologic unit boundaries, dotted lines = subunit boundaries. See Table T6 for details of units and subunits.

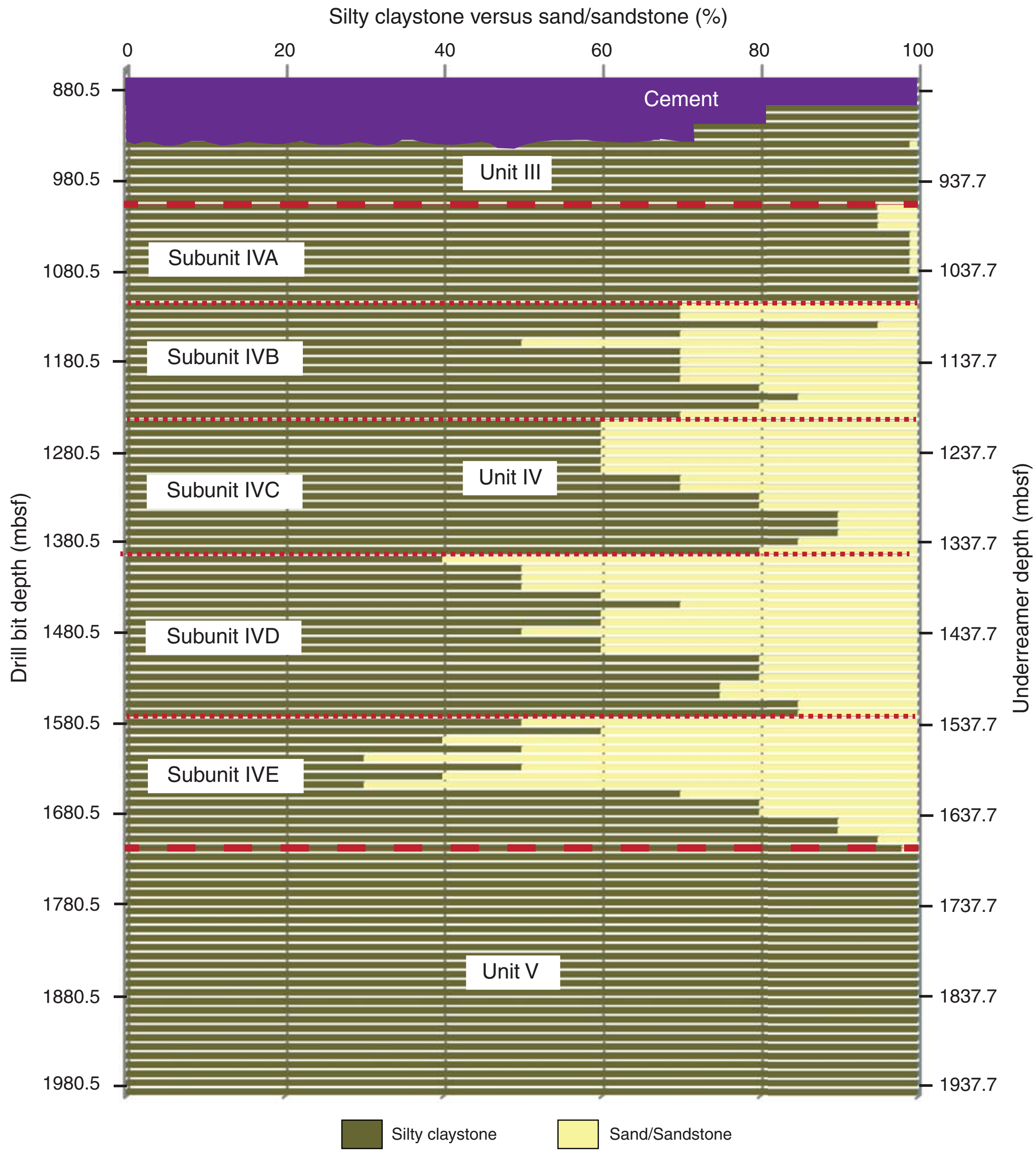

Figure F19. A–D. Examples showing dominant lithologies in lithologic units, Hole C0002F. Major lithology, sample identification, and scale shown. (Continued on next page.)

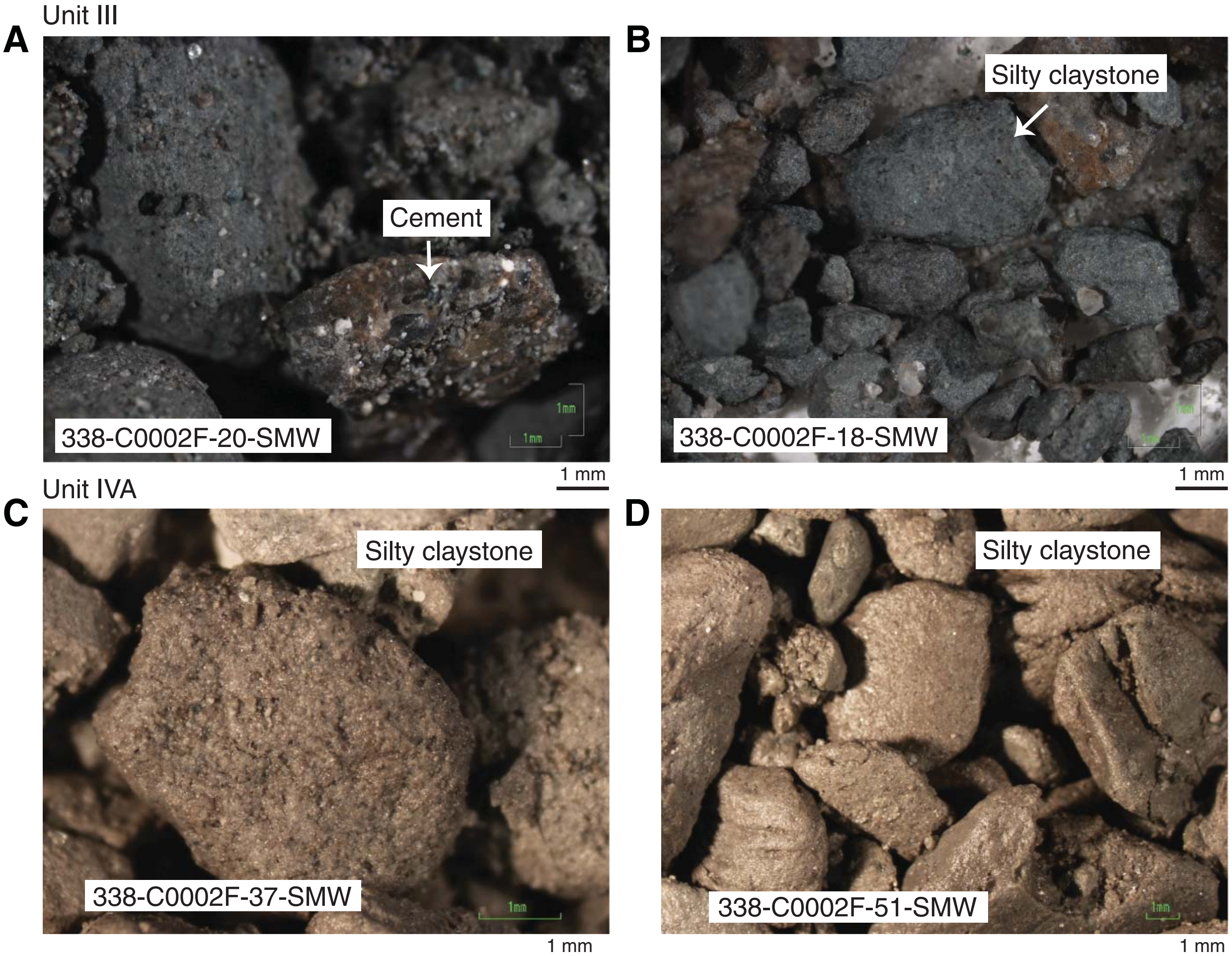

Figure F19 (continued). E–H. Dominant lithologies, Hole C0002F.

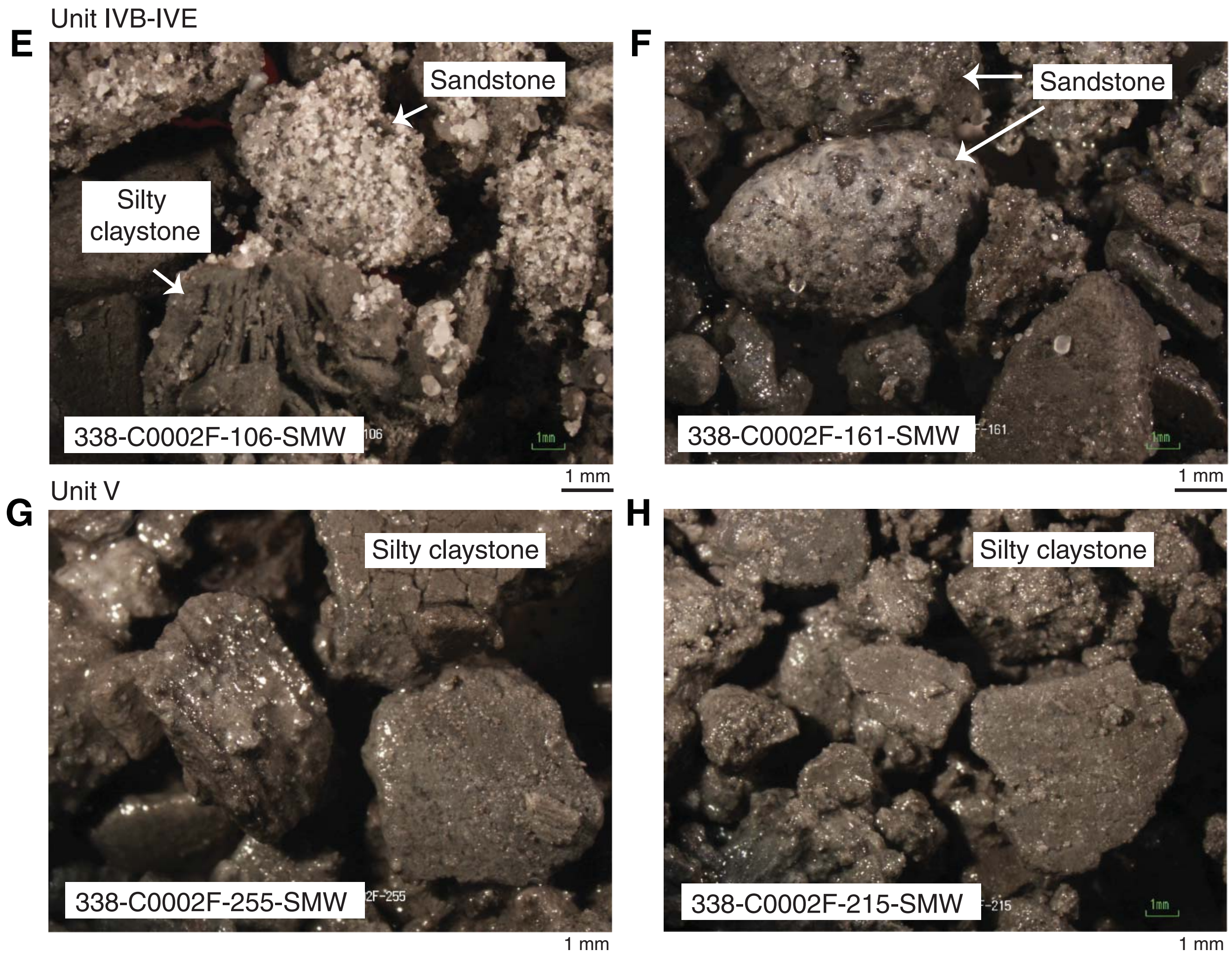

Figure F20. Microscopic cuttings characterization of lithologic components for >63 µm sieved sand fraction, Hole C0002F.

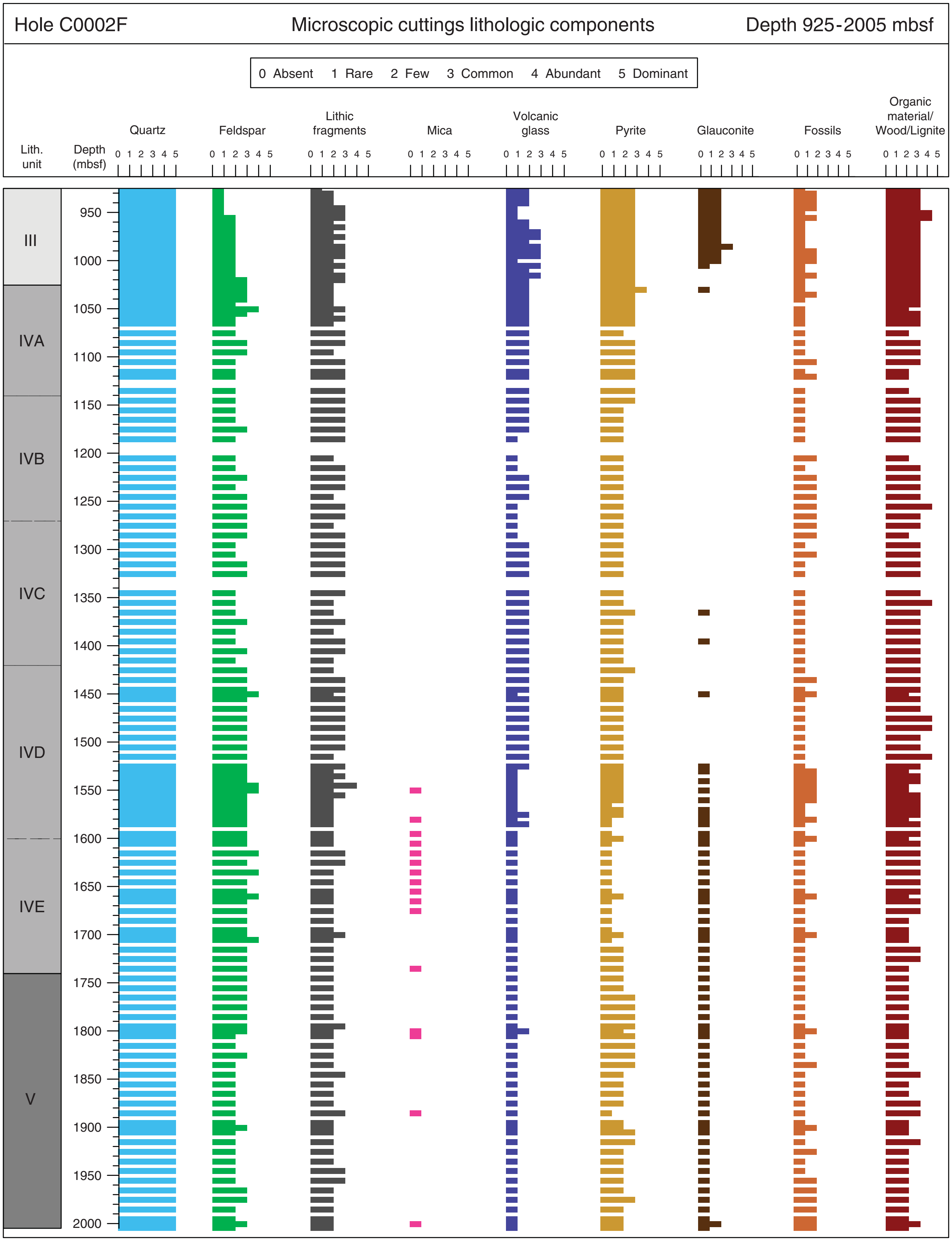

Figure F21. Example of Q-index for >63 µm sieved sand fraction (1685.5 mbsf), Hole C0002F.

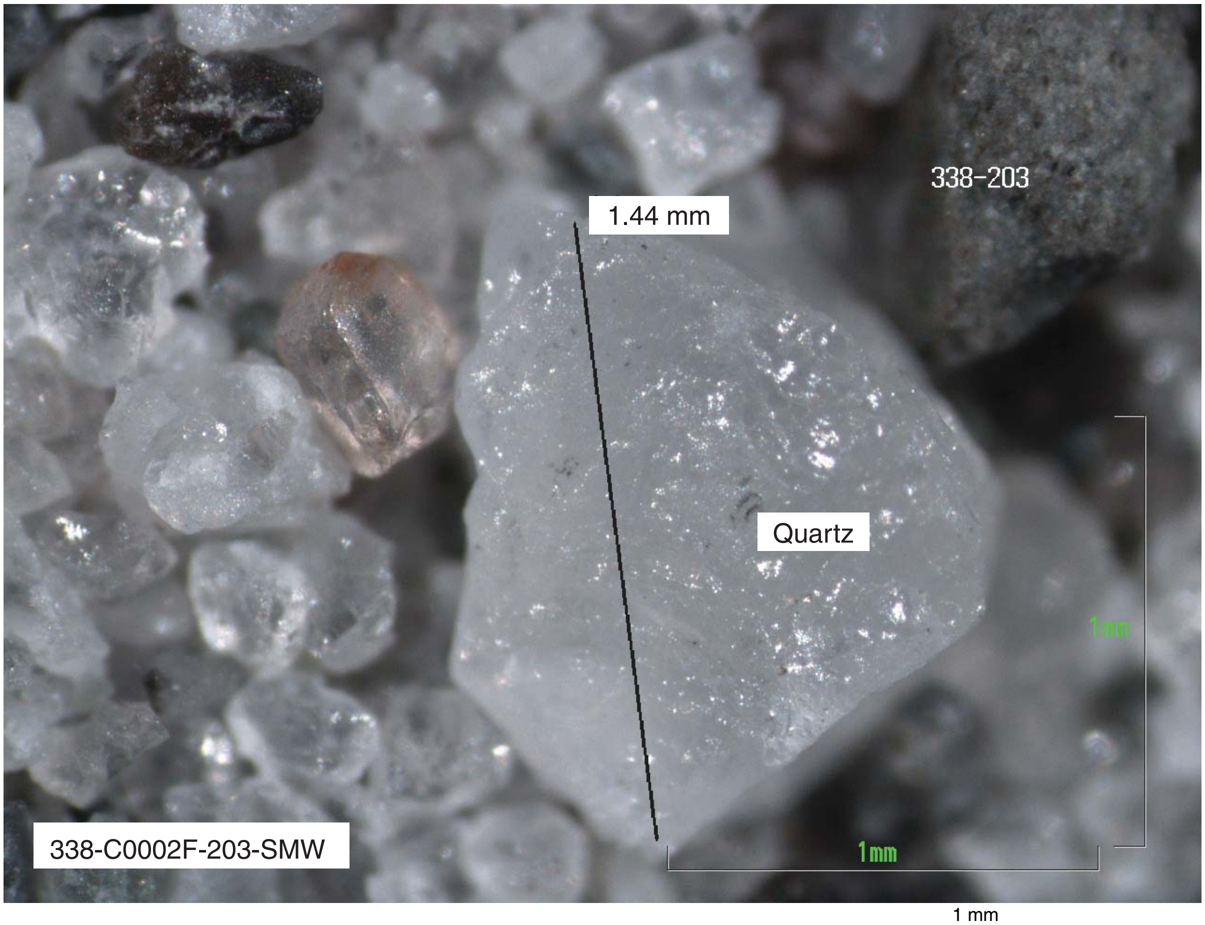

Figure F22. Q-index for >63 µm sieved sand fraction, Hole C0002F.

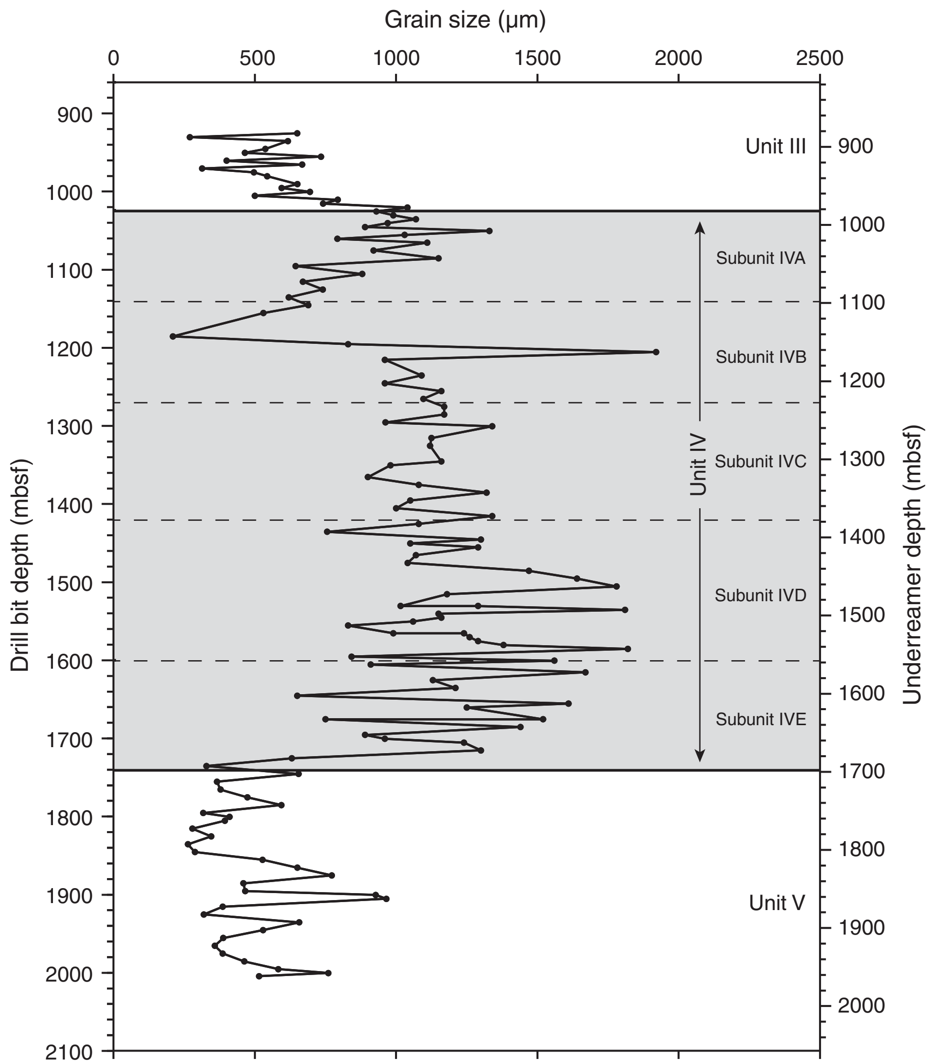

Figure F23. Smear slide and binocular microscope images of mineralogy in cuttings samples. **A.** Representative quartz and plagioclase feldspar (Sample 338-C0002F-80-SMW; 1185.5 mbsf; cross-polarized light [XPL]). **B.** Glauconite grains under binocular microscope (Sample 338-C0002F-37-SMW; 1000.5 mbsf). **C, D.** Glauconite (Sample 338-C0002F-29-SMW; 965.5 mbsf) in (C) plane-polarized light (PPL) and (D) XPL. **E, F.** Hornblende (Sample 338-C0002F-66-SMW; 1125.5 mbsf) in (E) PPL and (F) XPL.

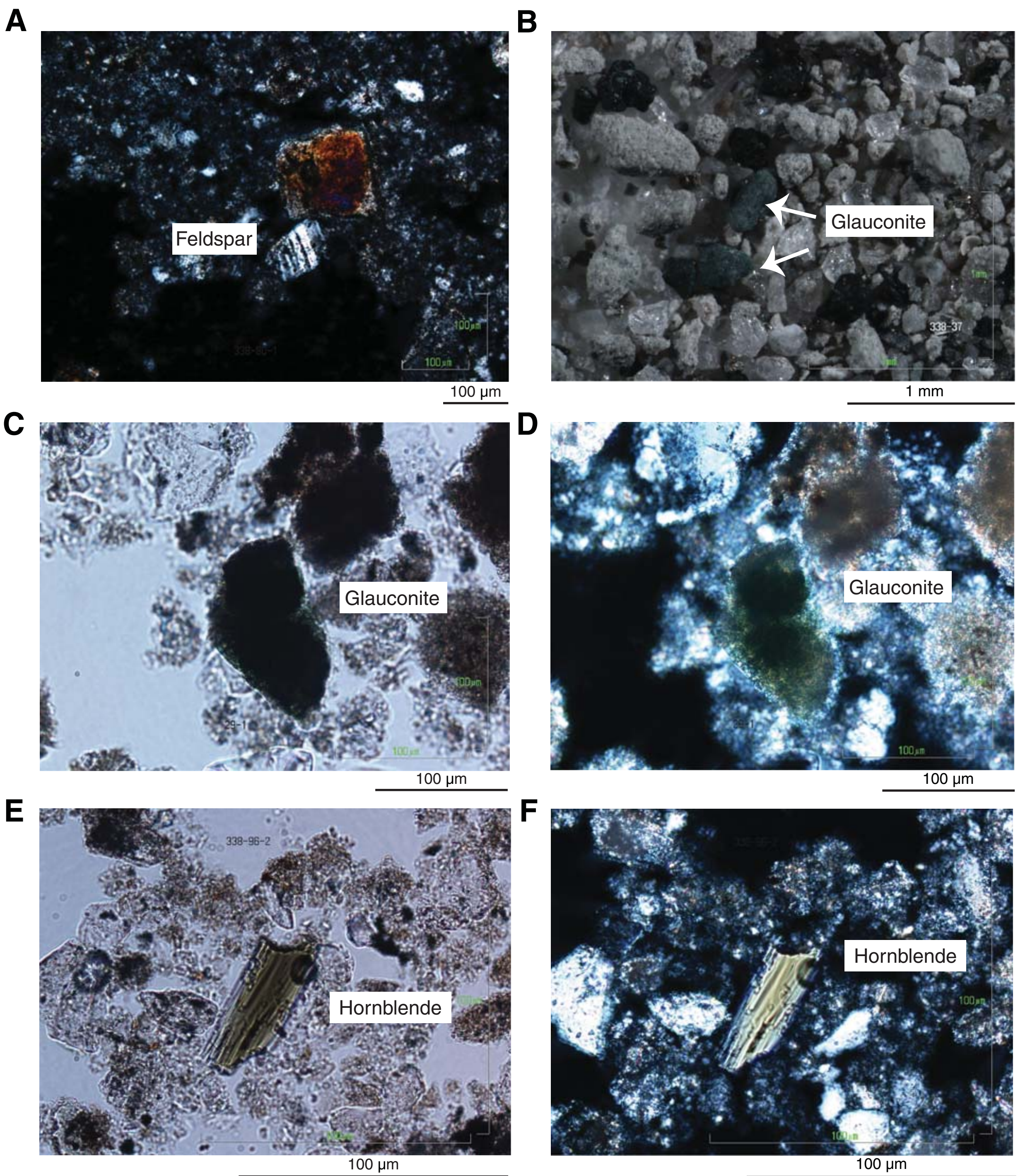

Figure F24. Smear slide and binocular microscope plates of mineralogy in cuttings samples. **A, B.** Carbonate sediment, showing fibrous calcium-carbonate (possible slickenfibers) (Sample 338-C0002F-112-SMW; 1335.5 mbsf) in (A) PPL and (B) XPL. **C.** Representative volcanic glass (Sample 338-C0002F-24-SMW; 940.5 mbsf; PPL). **D.** Zoned zircon (Sample 338-C0002F-50-SMW; 1055.5 mbsf; PPL). **E, F.** Tourmaline (Sample 338-C0002F-50-SMW; 1055.5 mbsf) in (E) PPL and (F) XPL.

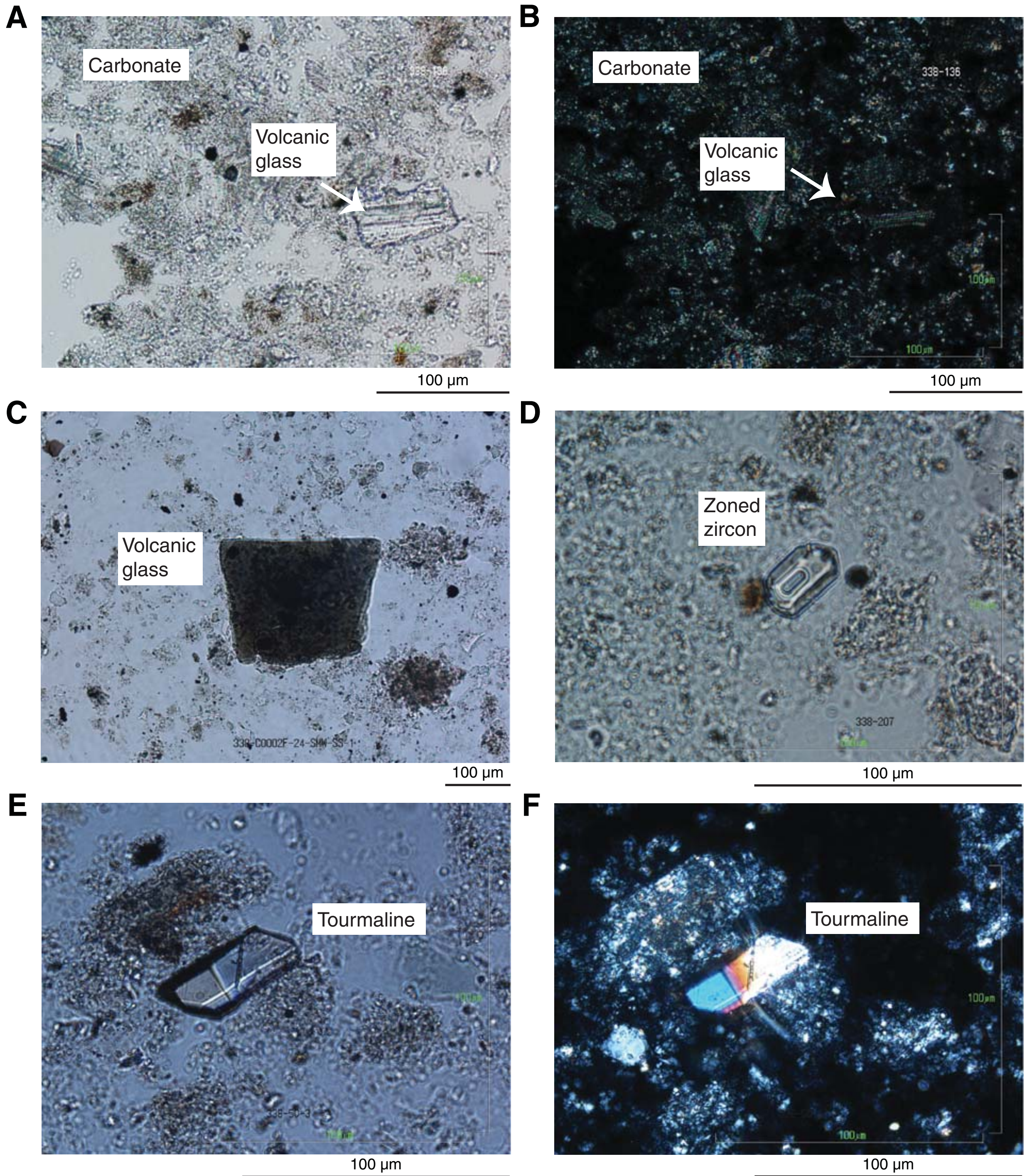

Figure F25. Smear slide and binocular microscope plates of mineralogy and fossils in cuttings samples. **A, B.** Corundum (Sample 338-C0002F-96-SMW; 1255.5 mbsf) in (A) PPL and (B) XPL. **C, D.** Hypersthene (Sample 338-C0002F-42-SMW; 1015.5 mbsf) in (C) PPL and (D) XPL. **E, F.** Binocular microscope images of (E) pyrite concretion (Sample 338-C0002F-41-SMW, 1010.5 mbsf) and (F) pyritized worm tube (Sample 338-C0002F-126-SMW; 1395.5 mbsf).

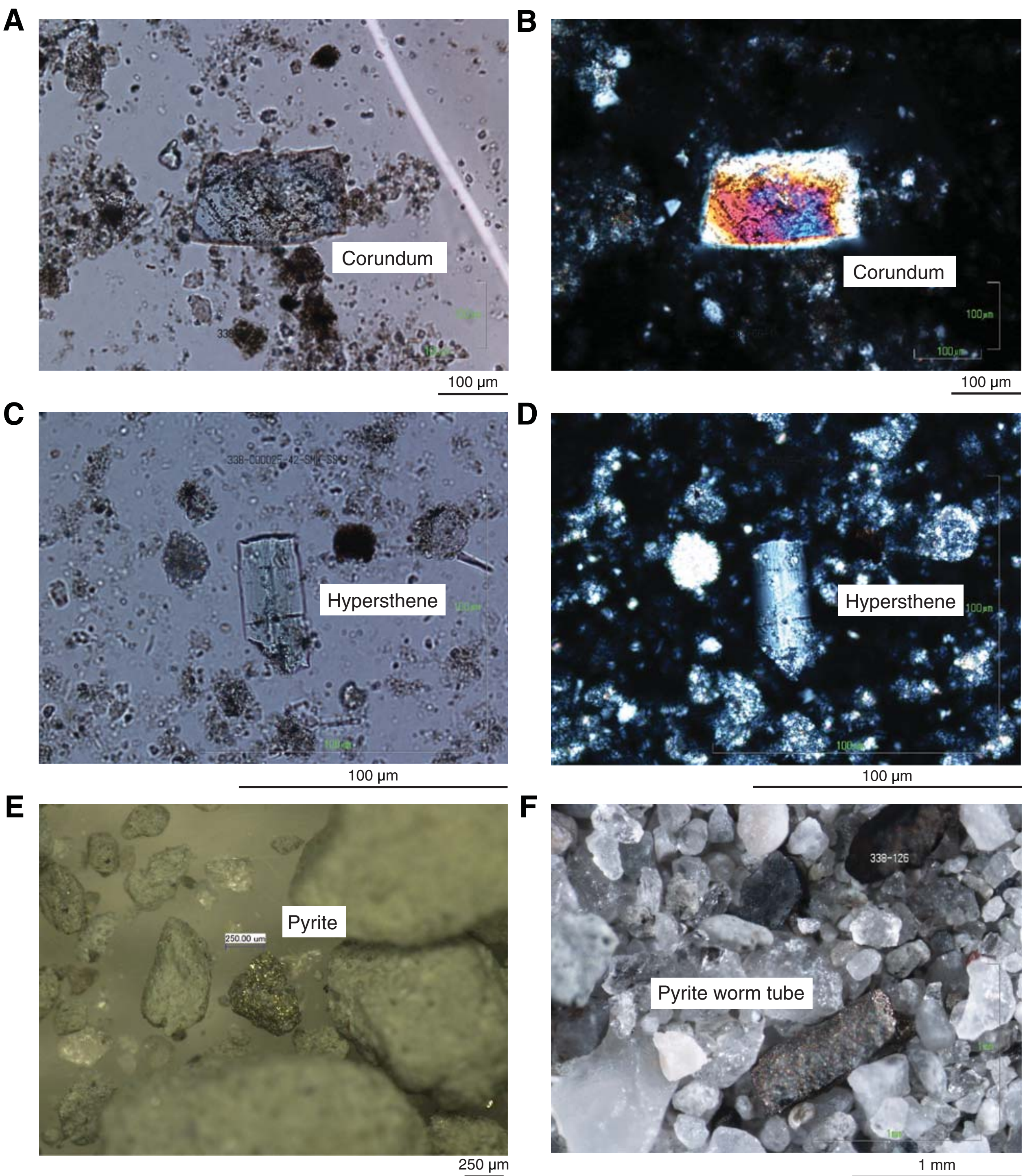

Figure F26. Smear slide and binocular microscope plates of mineralogy and fossils in cuttings samples. **A–C.** Binocular microscope images of (A) granite clast (Sample 338-C0002F-258-SMW; 1885.5 mbsf), (B) metamorphic schist clast (Sample 338-C0002F-153-SMW; 1505.5 mbsf), and (C) coal clast (Sample 338-C0002F-96-SMW; 1255.5 mbsf). **D–F.** Smear slides under PPL of (D) organic matter (Sample 338-C0002F-26-SMW; 950.5 mbsf), (E) calcareous nannofossils (Sample 338-C0002F-21-SMW; 930.5 mbsf), and (F) diatom fragments (Sample 338-C0002F-62-SMW; 1105.5 mbsf).

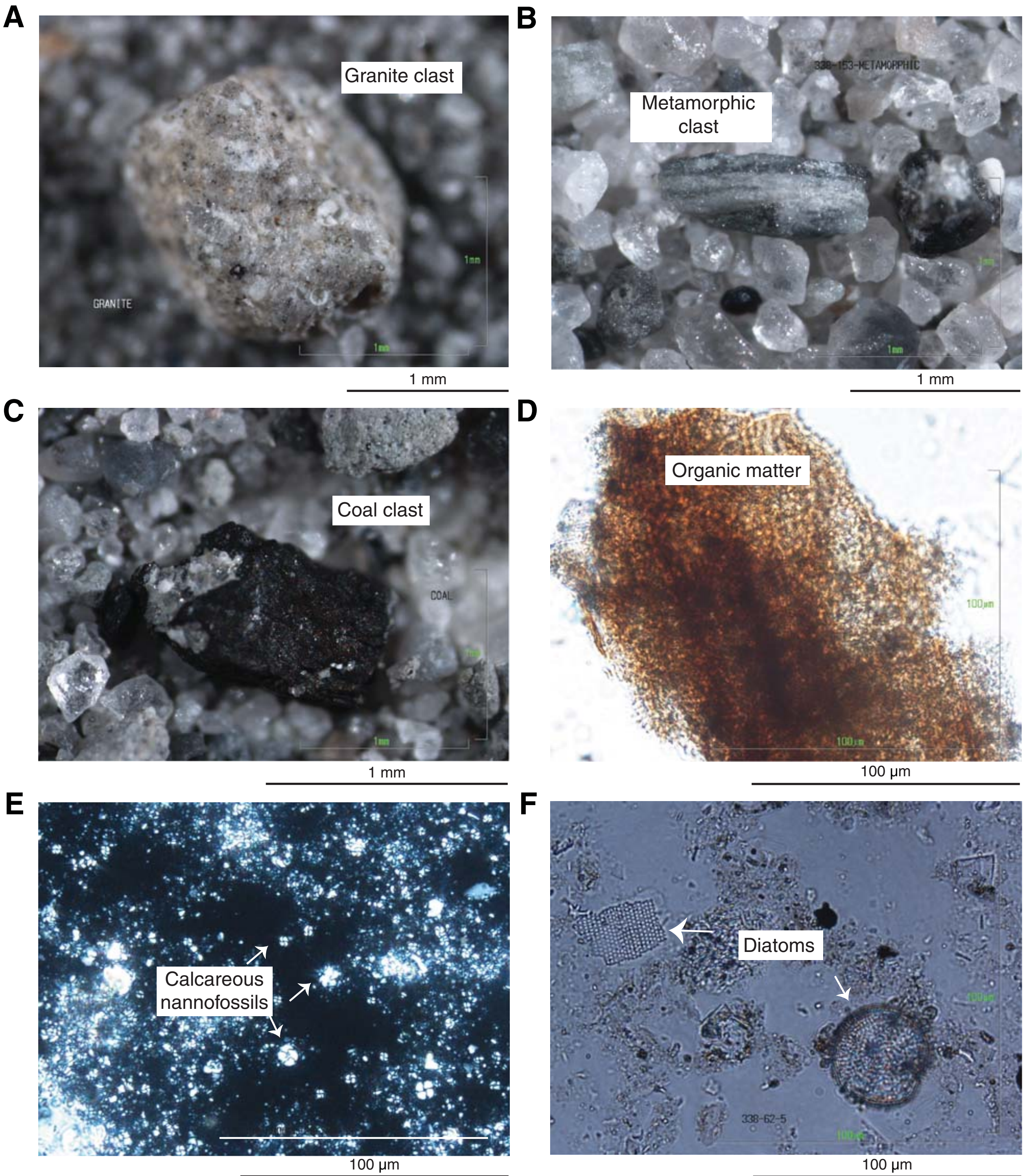

Figure F27. Ratio of calcium carbonate measured onboard (see "Geochemistry") versus X-ray diffraction (XRD) calcite on cuttings samples from Hole C0002F. Note the strong correlation (correlation coefficient = 0.97).

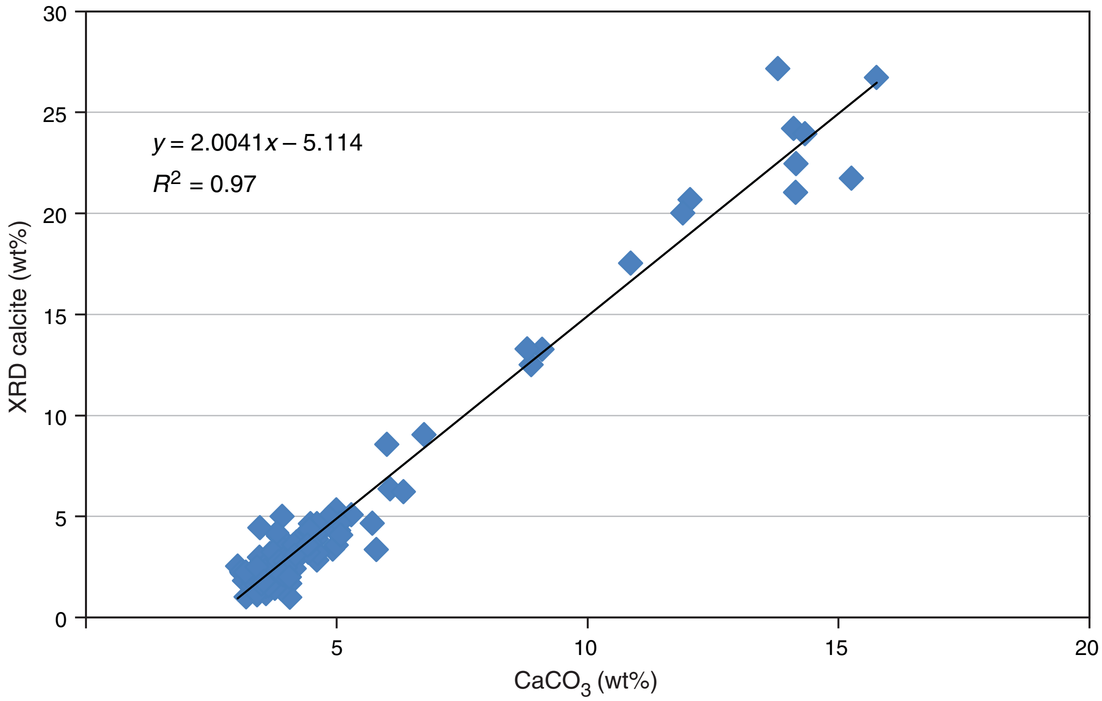

Figure F28. Summary of lithology and bulk powder XRD analyses for 1–4 mm and >4 mm cuttings size fractions of silty claystone samples from Hole C0002F, reported in relative weight percent. Dashed lines = unit boundaries, dotted lines = subunit boundaries.

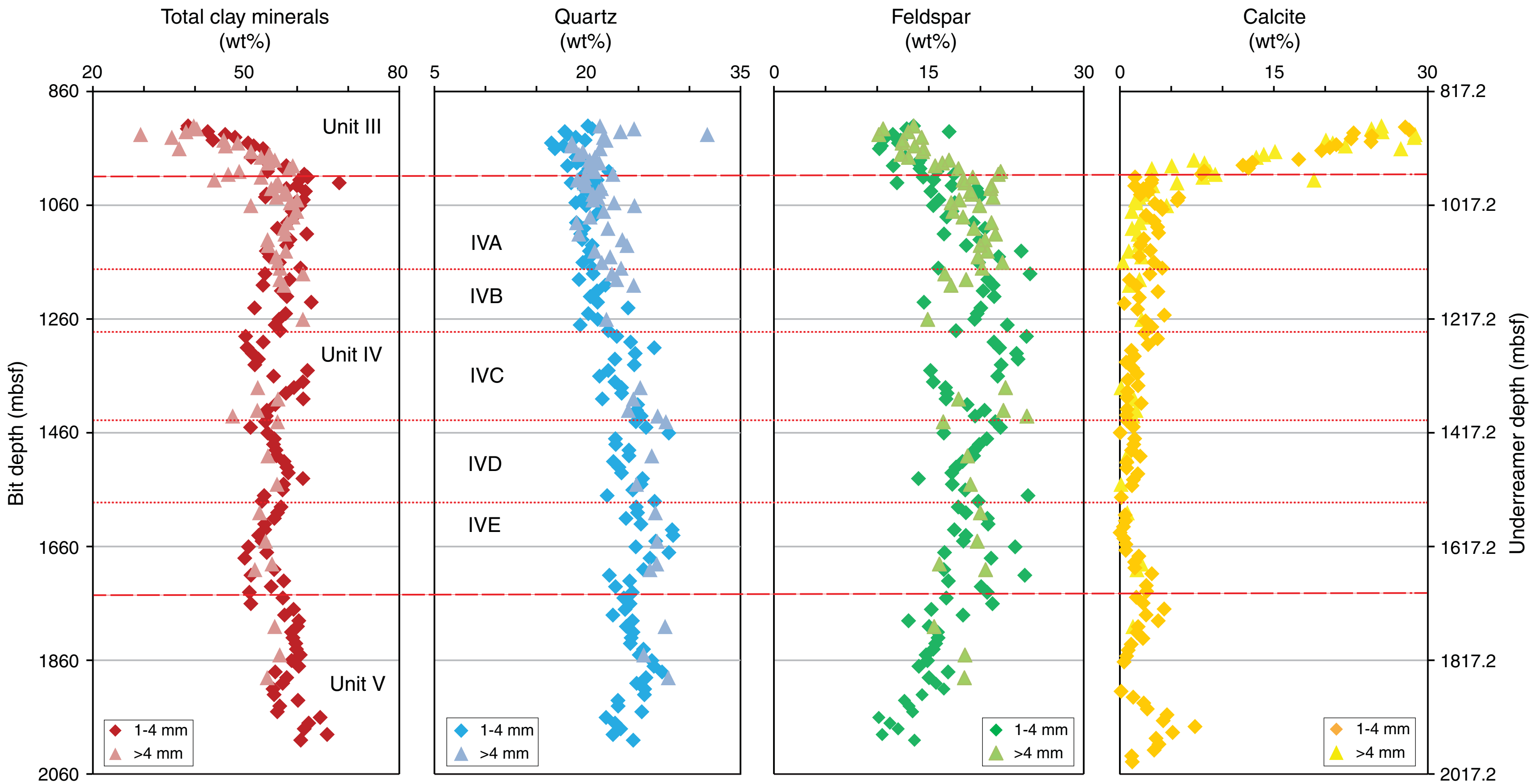

Figure F29. Summary of lithology and bulk powder XRD analyses for 1–4 mm cuttings size fraction of silty claystone samples from Hole C0002F, reported in relative weight percent. Included are data from Hole C0002B (Expedition 315 Scientists, 2009b). Dashed lines = unit boundaries, dotted lines = subunit boundaries.

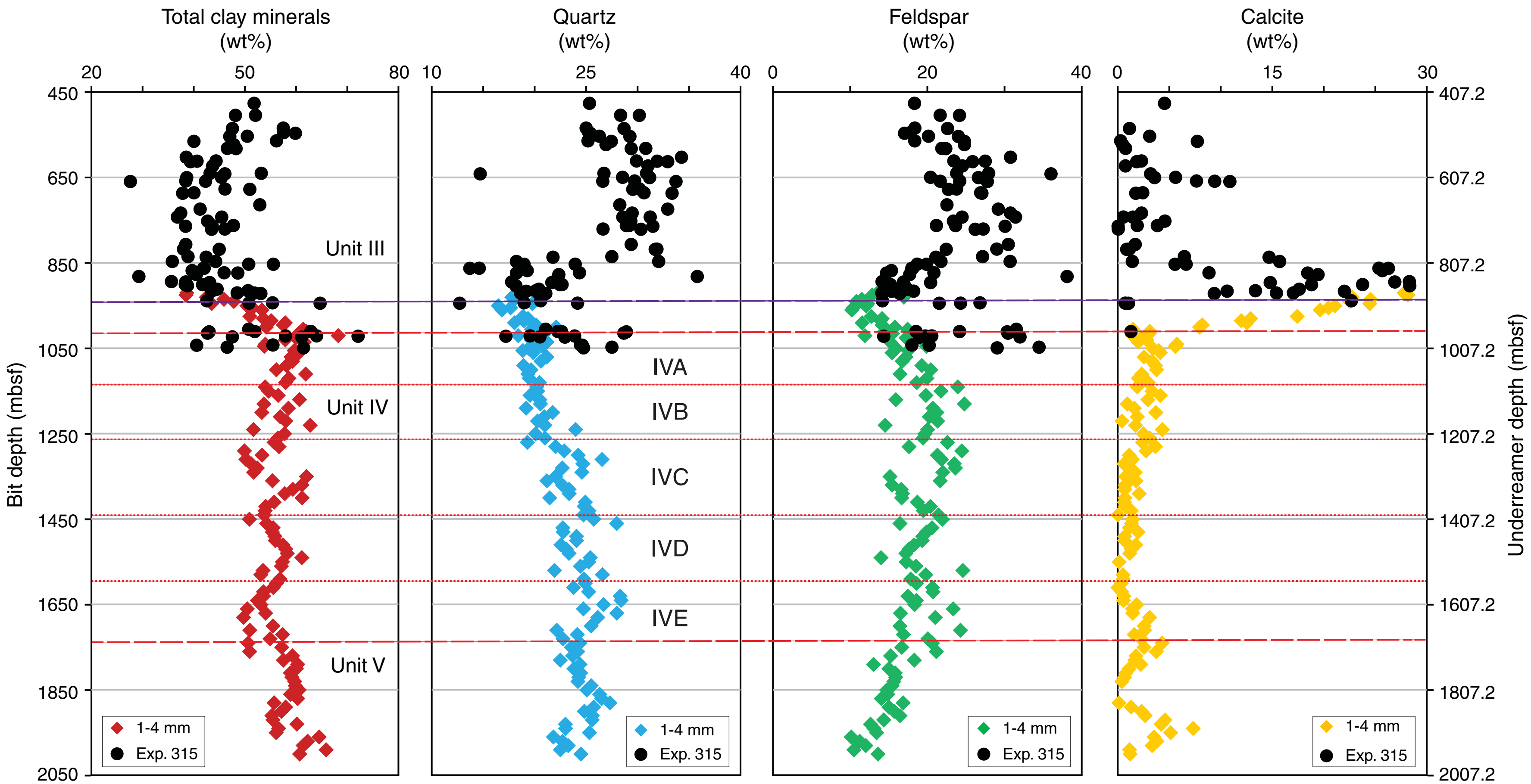

Figure F30. A, B. Downhole profiles of major element contents from XRF analysis on 1–4 mm and >4 mm cuttings size fractions, Hole C0002F. MnO is not depicted due to very low weight percent (<0.1 wt%). Dashed lines = unit boundaries, dotted lines = subunit boundaries. (Continued on next page.)

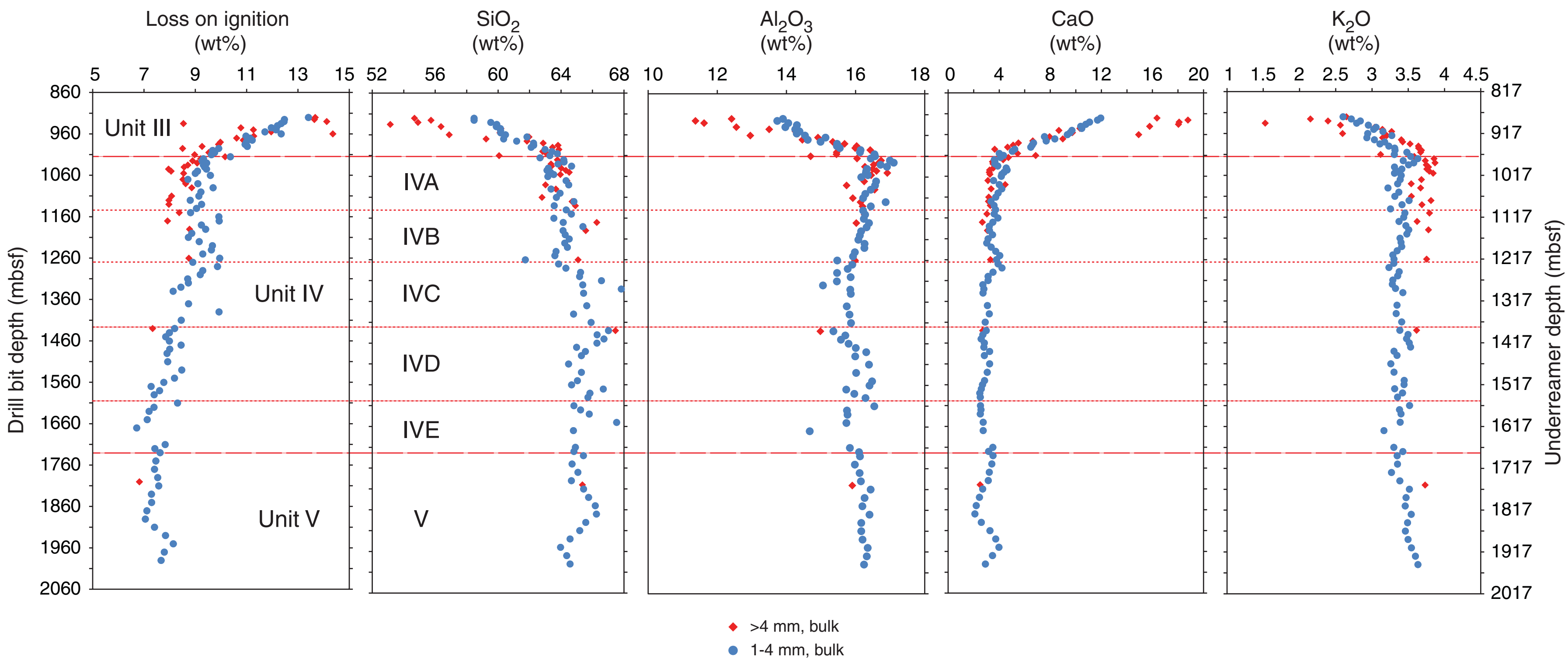

Figure F30 (continued).

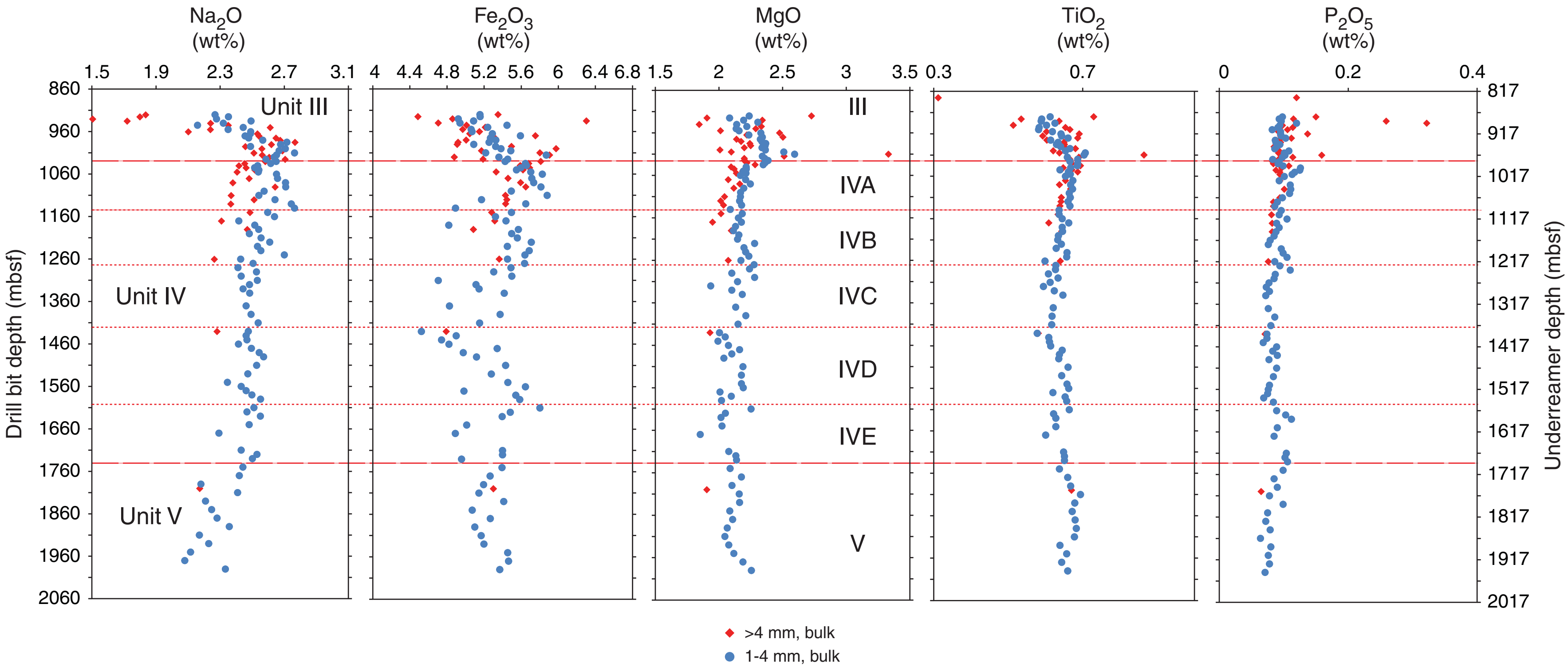

Figure F31. Cross-plots for major element contents from XRF analysis for 1–4 mm cuttings size fraction, Hole C0002F. **A.** Al_2O_3 versus SiO_2. **B.** SiO_2 versus CaO. **C.** Al_2O_3 versus CaO. **D.** Al_2O_3 versus K_2O. **E.** Loss on ignition (LOI) versus CaO. Arrows reflect overall geochemical trend in Population 1 (920.5–990.5 mbsf; Samples 338-C0002F-20-SMW through 36-SMW) and Population 2 (Samples 338-C0002F-37-SMW through 286-SMW; 995.5–1990.5 mbsf).

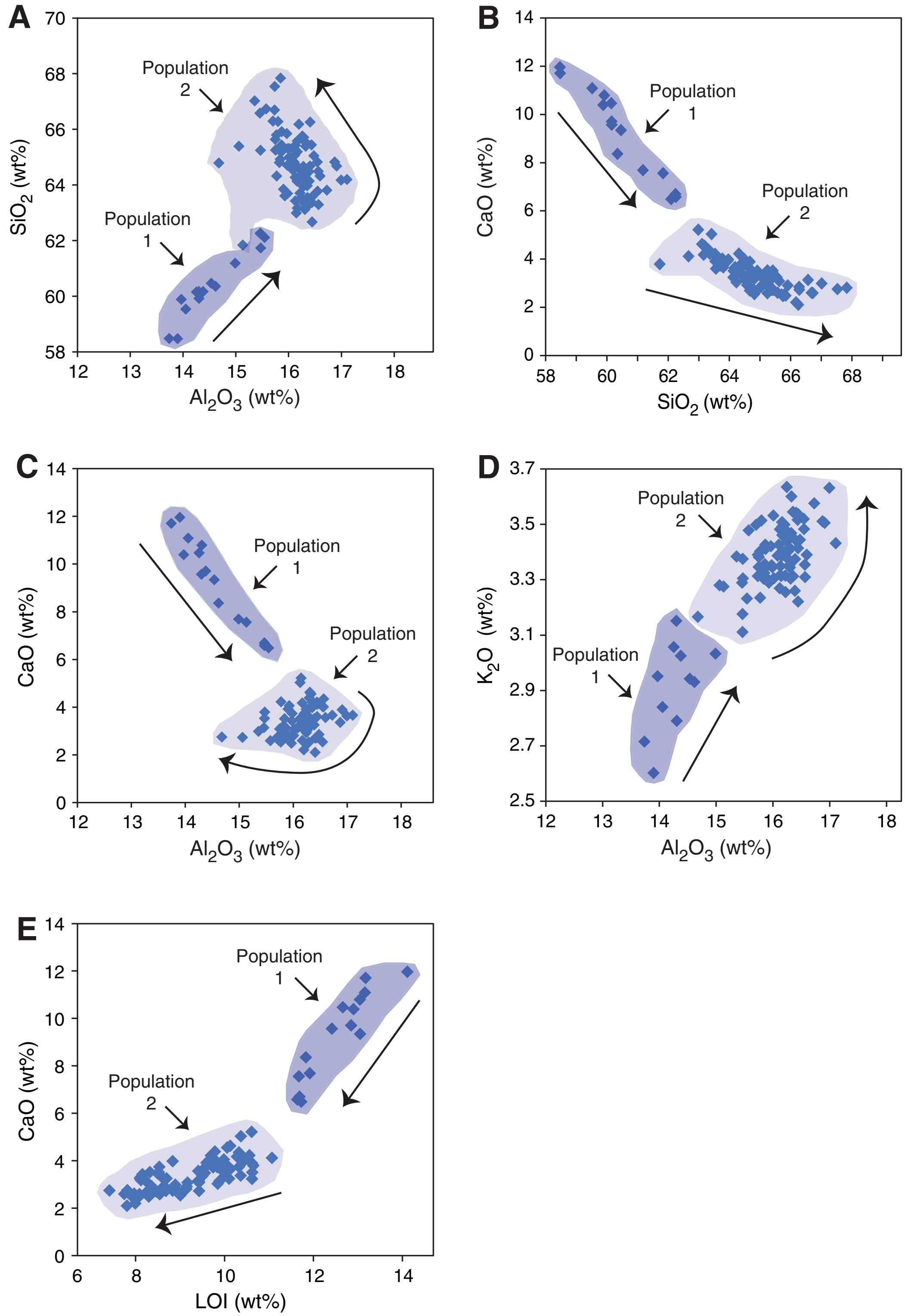

Figure F32. Lithologic column for Core 338-C0002H-1R. CT = X-ray computed tomography.

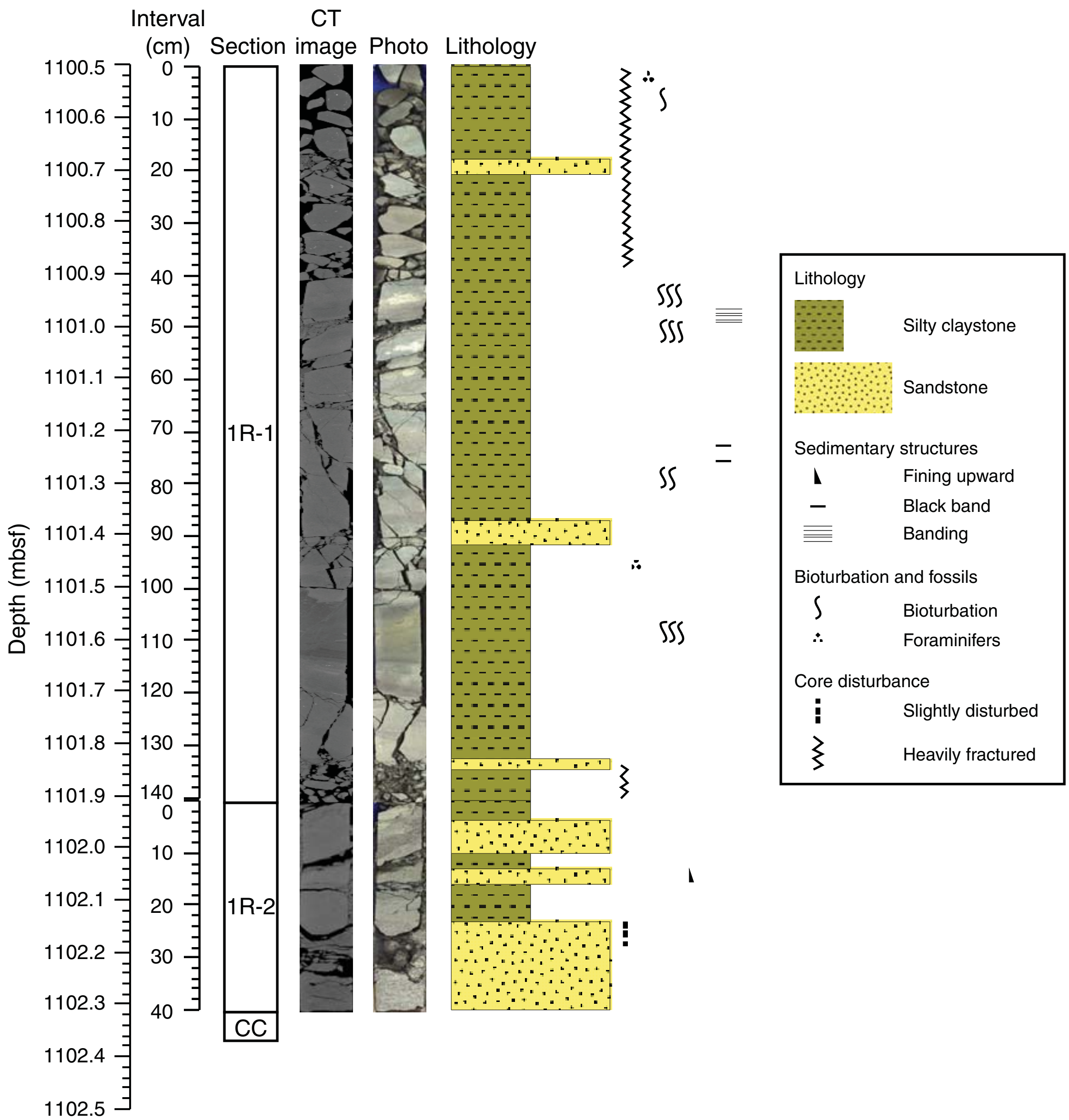

Figure F33. Lithologic column for Core 338-C0002H-2R. CT = X-ray computed tomography.

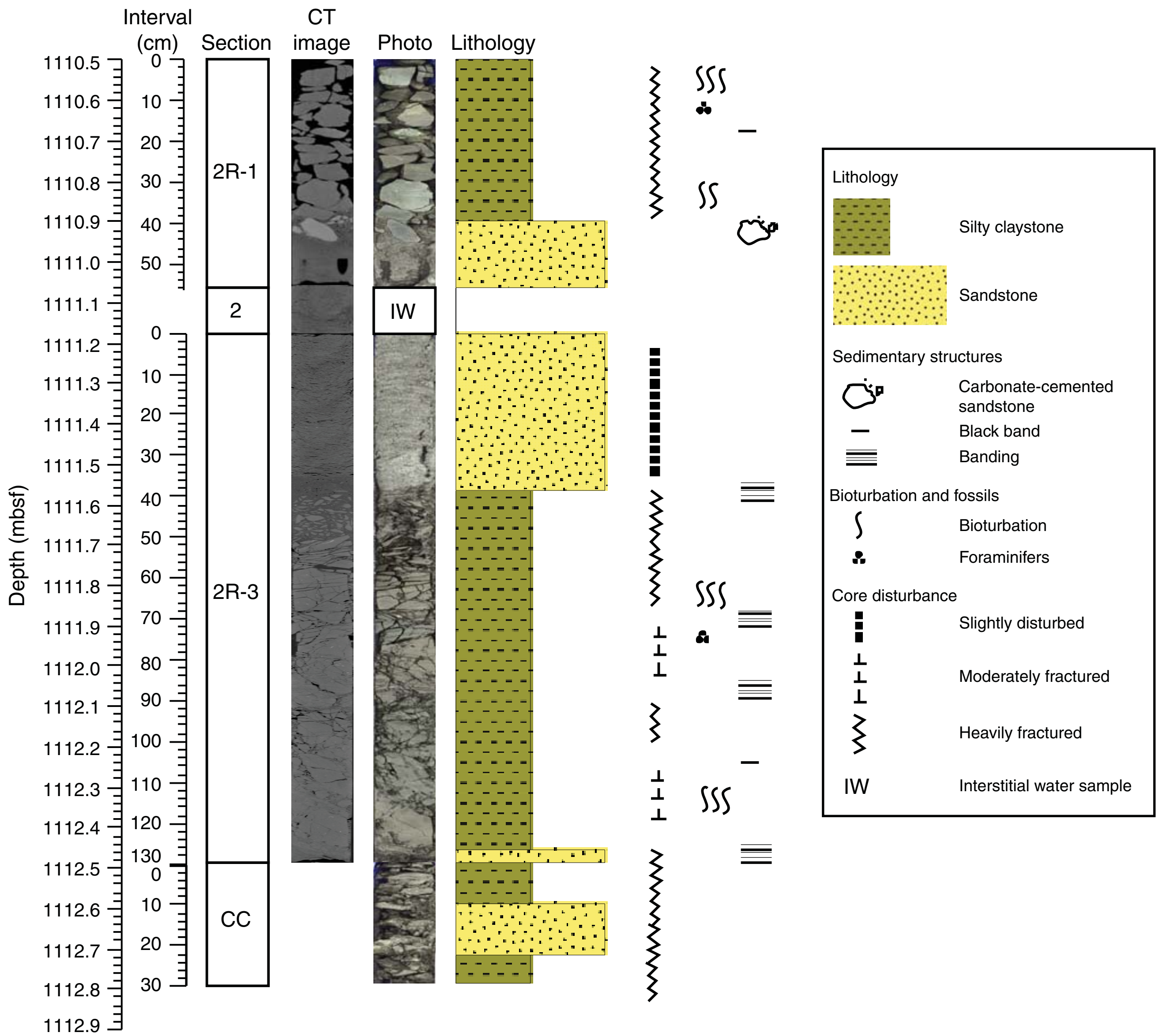

Figure F34. Examples of petrographic features. **A.** Largely undisaggregated silty claystone fragments (Sample 338-C0002H-1R-1, 129 cm; PPL). **B.** Nannofossil-bearing silty claystone (Sample 338-C0002H-1R-1, 45 cm; XPL). Red arrows = coccoliths. **C.** Red-brown organic matter (kerogen) of terrestrial origin (Sample 338-C0002H-2R-3, 70 cm; PPL). Red arrows = pyrite framboids. **D.** Possible microdolomite crystals (red arrows) in a calcareous silty claystone (Sample 338-C0002H-1R-1, 102 cm; XPL).

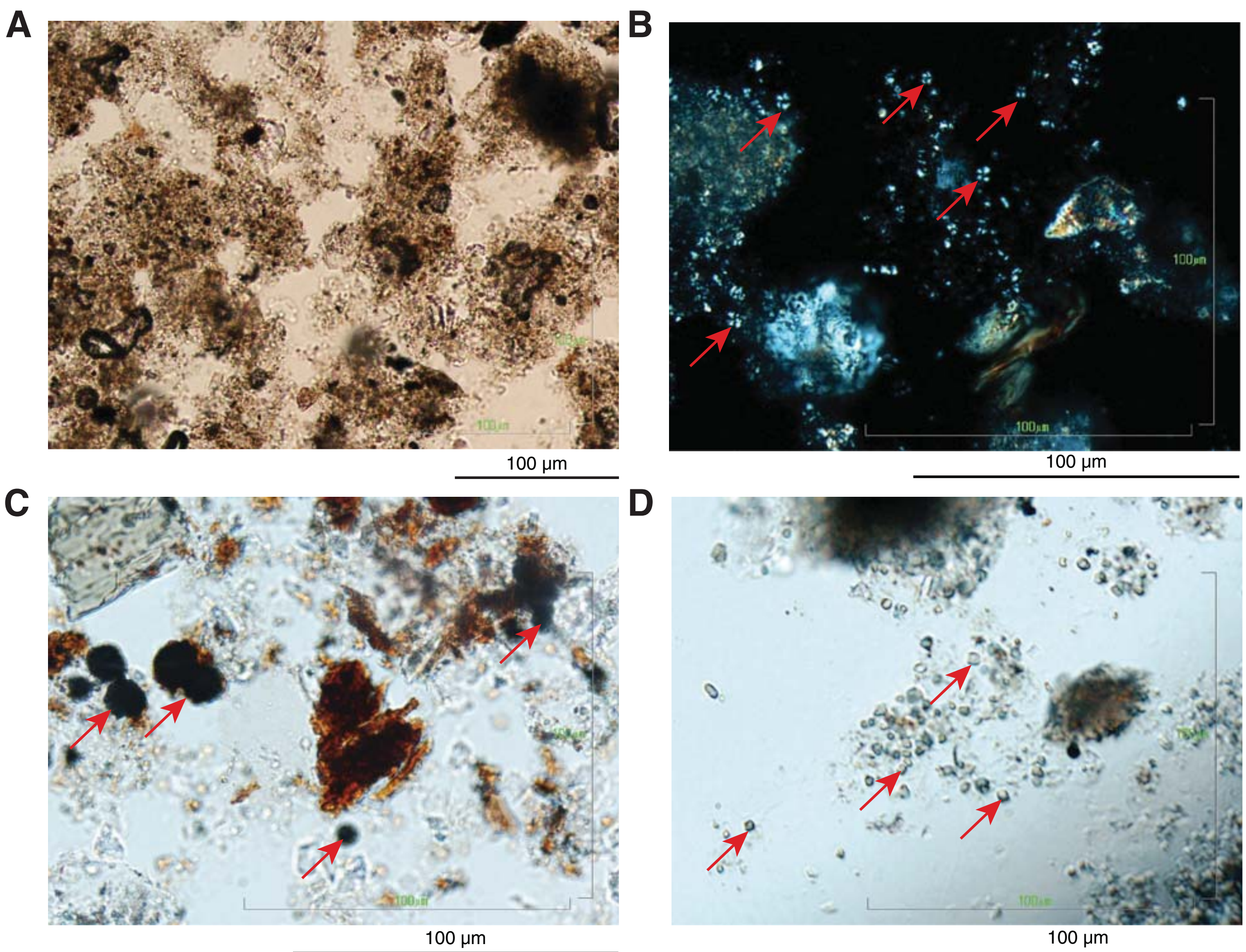

Figure F35. X-ray CT image of bioturbation, Hole C0002H. Carbonate-bearing silty claystone is mixed into layer below by burrowing. Arrows = discrete burrows filled with calcareous silty claystone from the overlying layer (brighter layer on CT image).

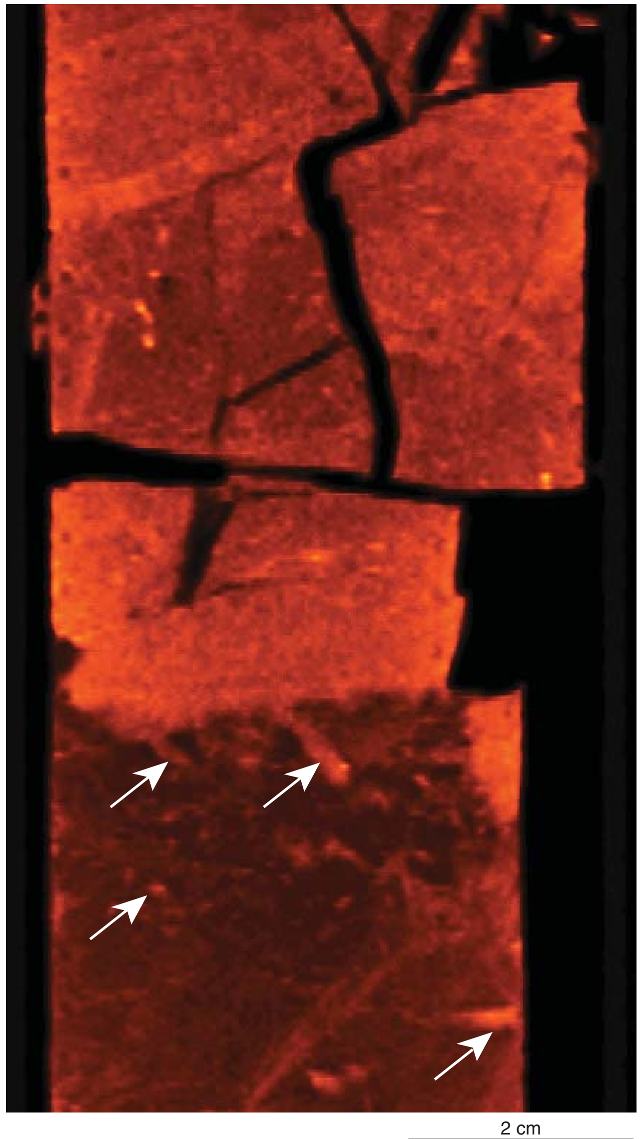

Figure F36. Mineralogical bulk compositions determined by XRD analyses of core samples, Hole C0002H. A limited depth range is plotted for cuttings samples from Hole C0002F for comparison. Note that the cuttings sampled from Hole C0002F are relatively homogeneous in composition across depth because of mixing across the drilled interval.

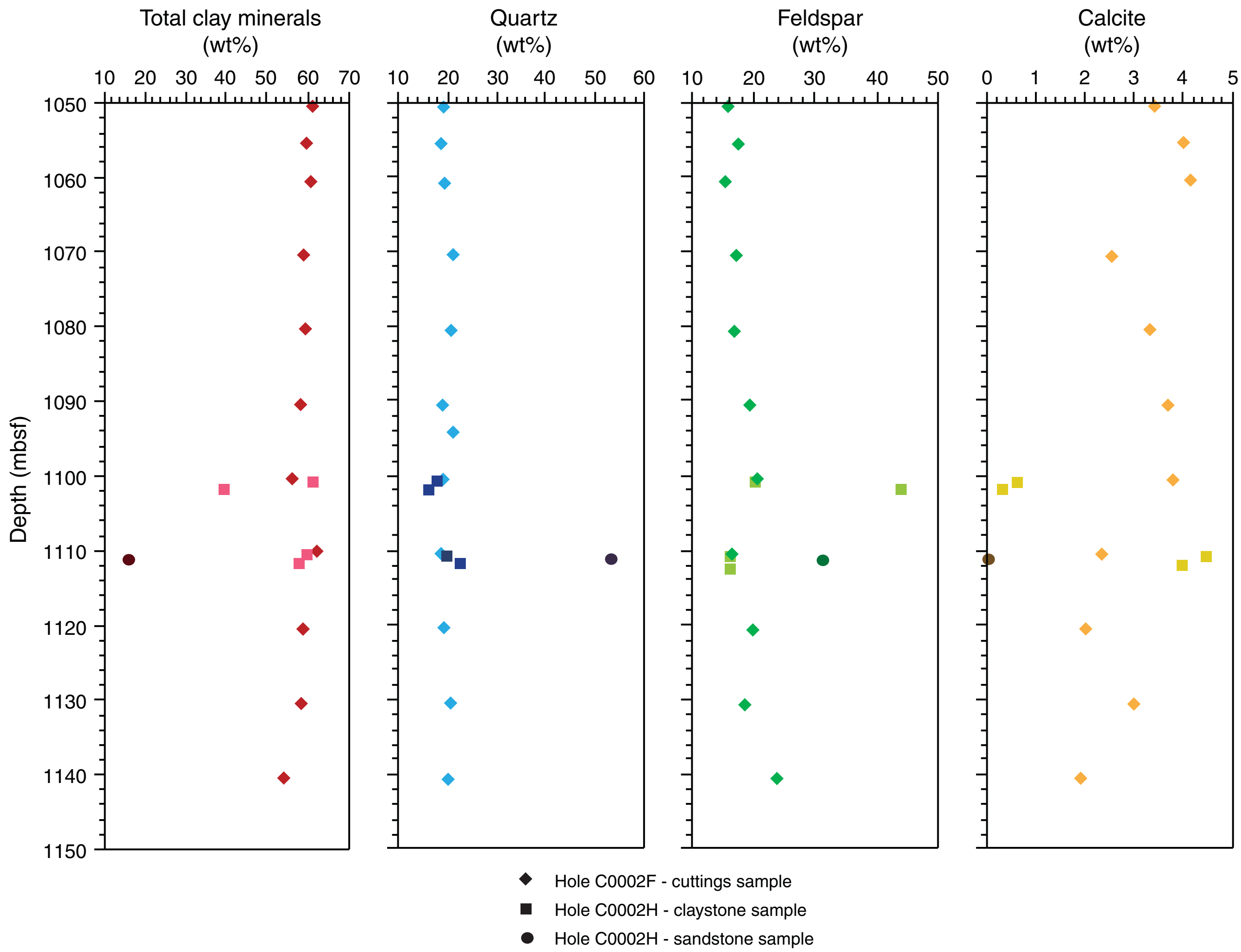

Figure F37. Bulk chemical compositions determined by XRF analyses of core samples, Hole C0002H. A limited depth range is plotted for cuttings samples from Hole C0002F for comparison. LOI = loss on ignition.

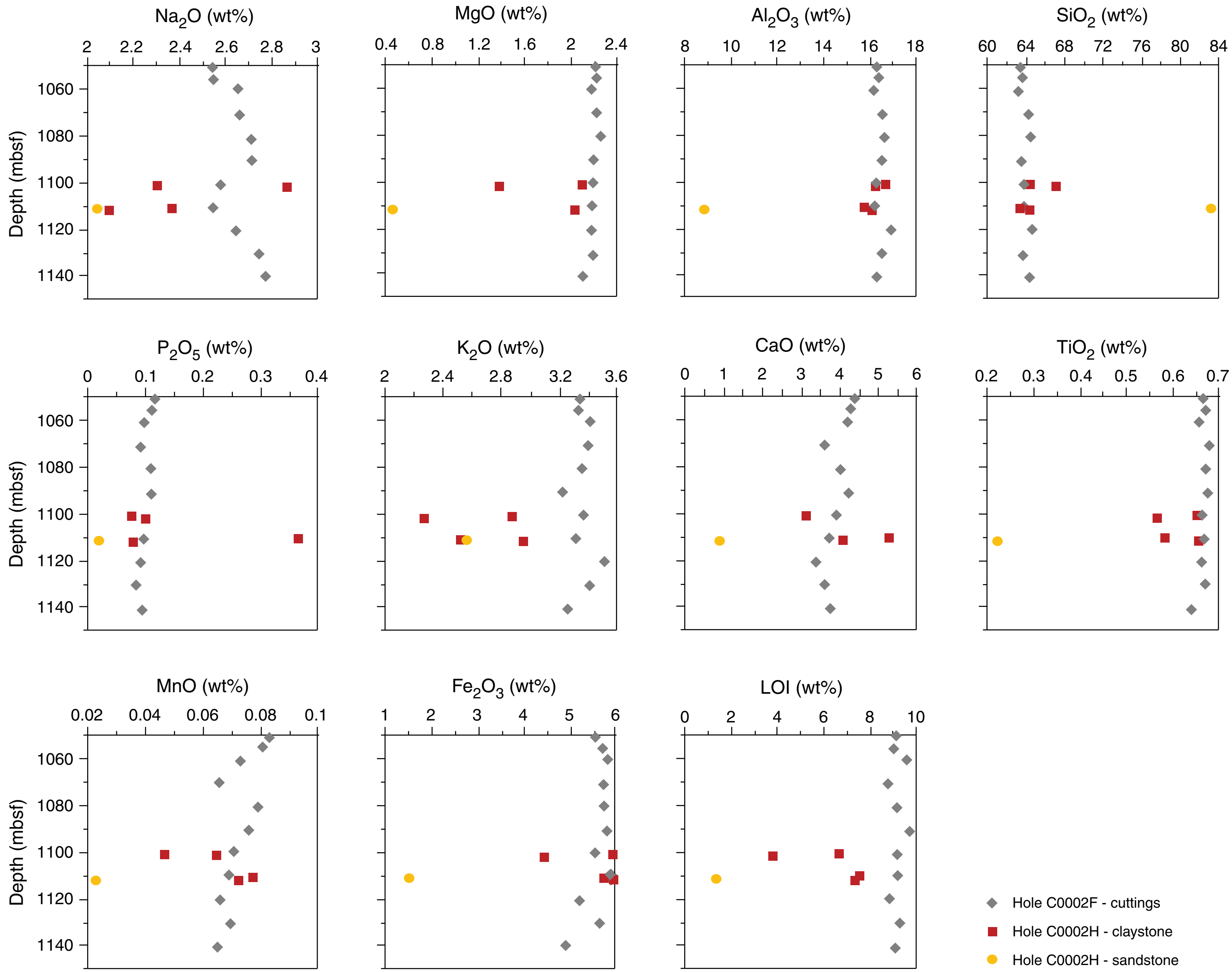

Figure F38. Generalized lithologic column for Hole C0002J.

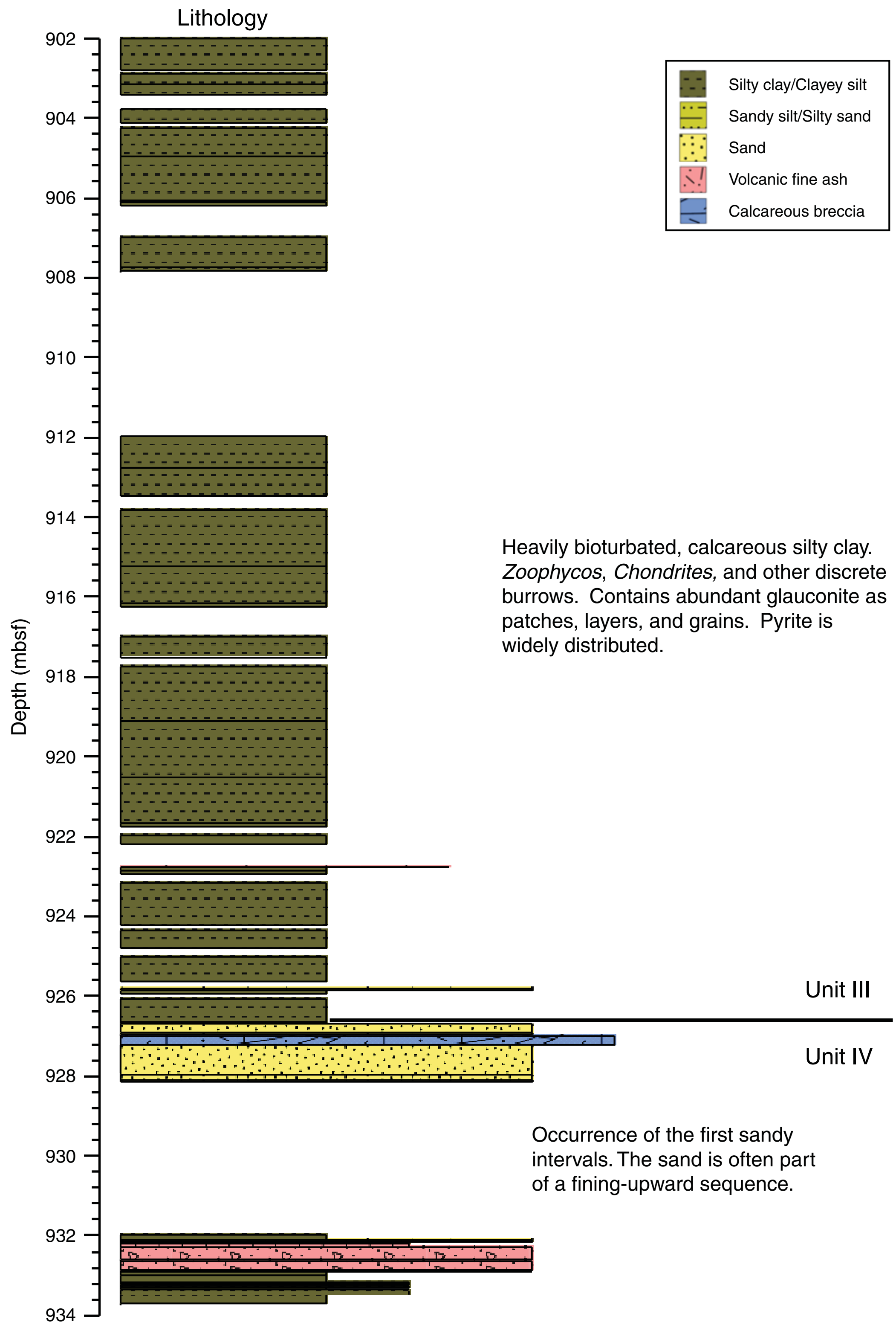

Figure F39. Mineralogical bulk compositions determined by XRD analyses of core samples, Hole C0002J. A limited depth range is plotted for core samples from Hole C0002B (Expedition 315 Scientists, 2009b) and cuttings samples from Hole C0002F for comparison. Note that the cuttings sampled from Hole C0002F retain the compositional character of Unit III deeper in the hole because of mixing across the drilled interval. Cuttings samples may also show somewhat higher carbonate content in Unit III than is observed in other holes.

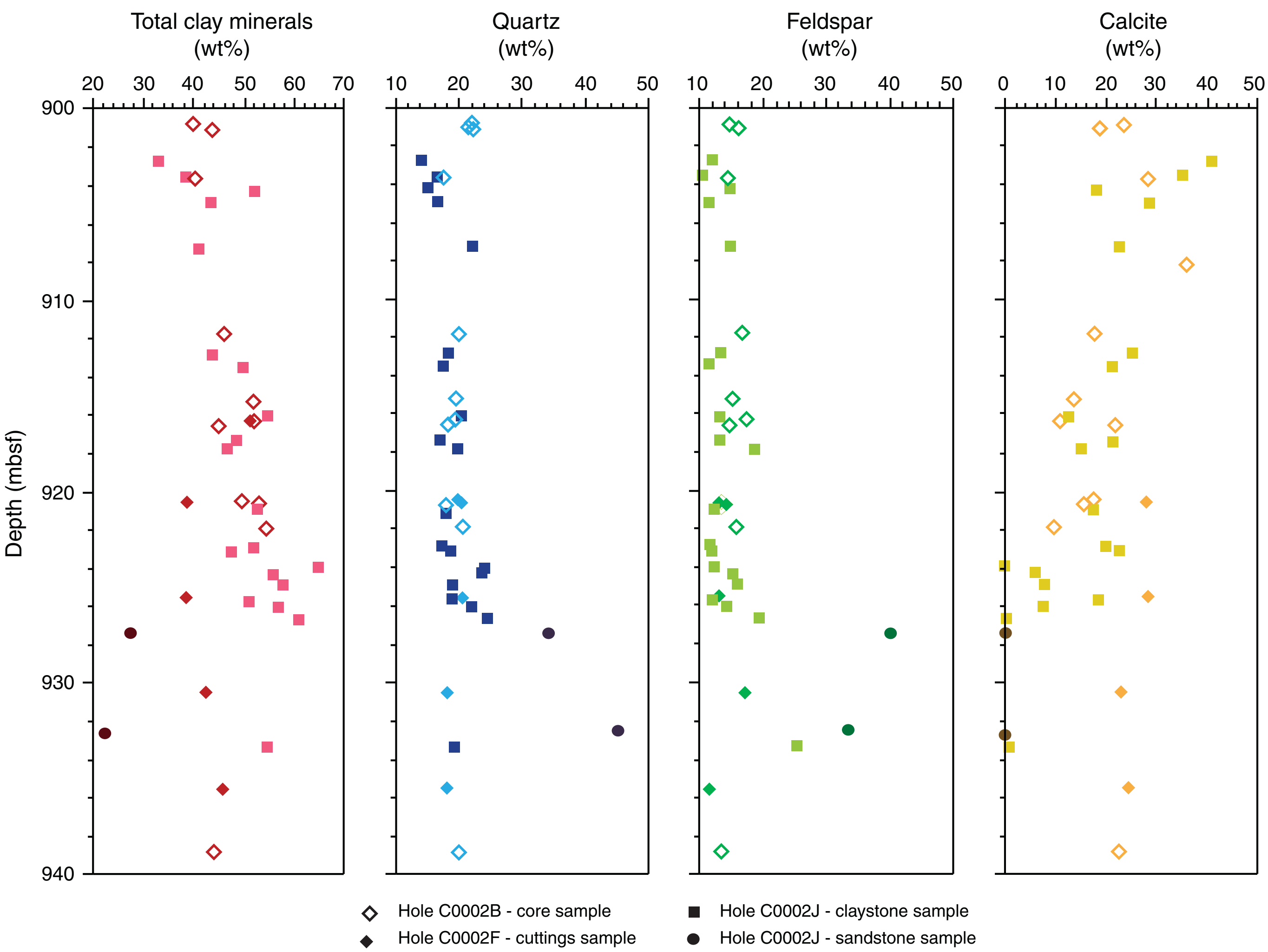

Figure F40. Bulk chemical compositions determined by XRF analyses of core samples, Hole C0002J. A limited depth range is plotted for cuttings samples from Hole C0002F for comparison. LOI = loss on ignition.

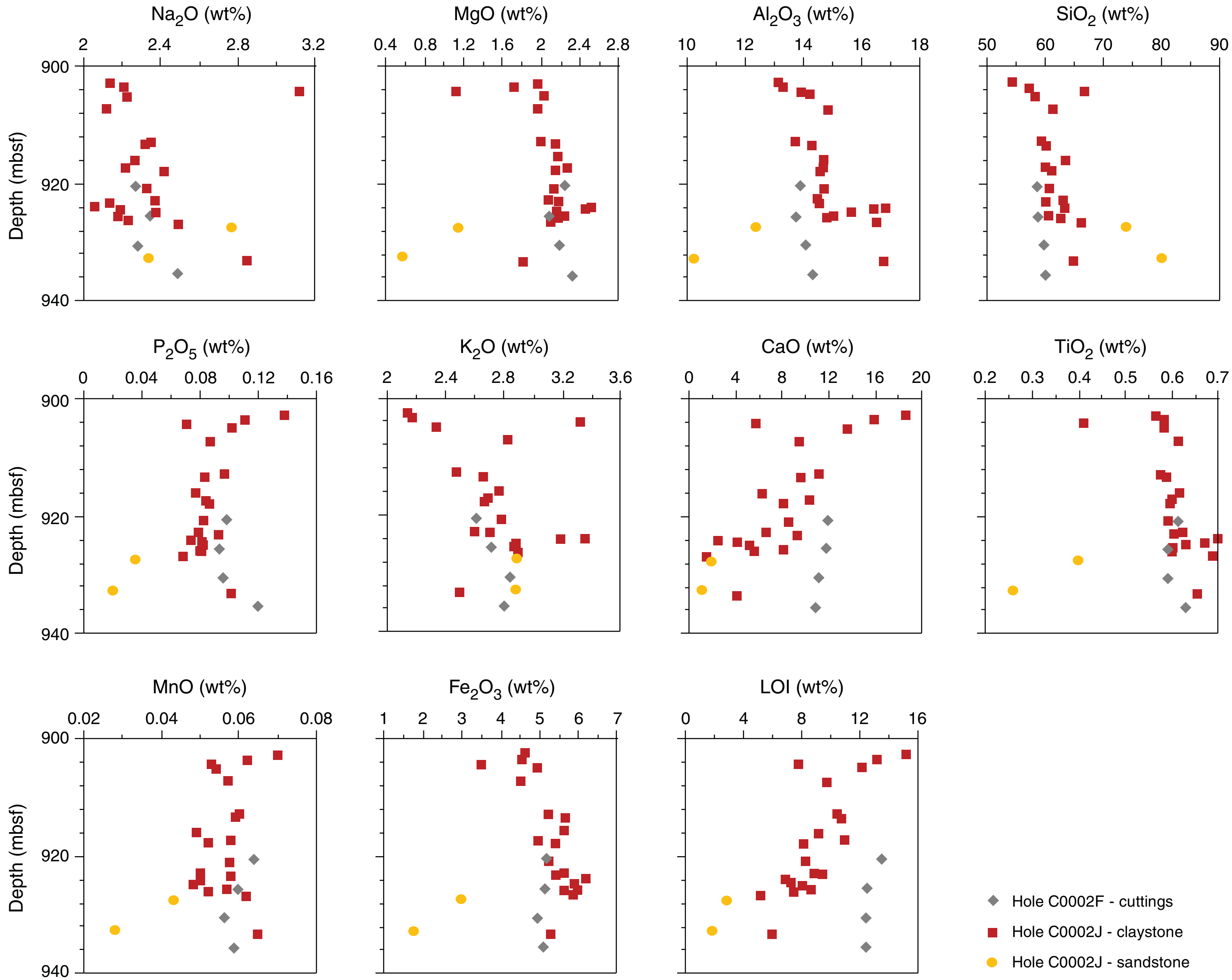

Figure F41. Nonvolcanic fragment types observed in smear slides. **A–C.** Sample 338-C0002J-5R-CC, 2 cm in XPL: (A) grain of polycrystalline quartz, (B) chert fragment, and (C) quartz-mica metamorphic lithic fragment with apparent foliation. **D.** Quartz-mica metamorphic lithic fragment lacking apparent foliation (Sample 338-C0002J-6R-1, 30 cm; XPL).

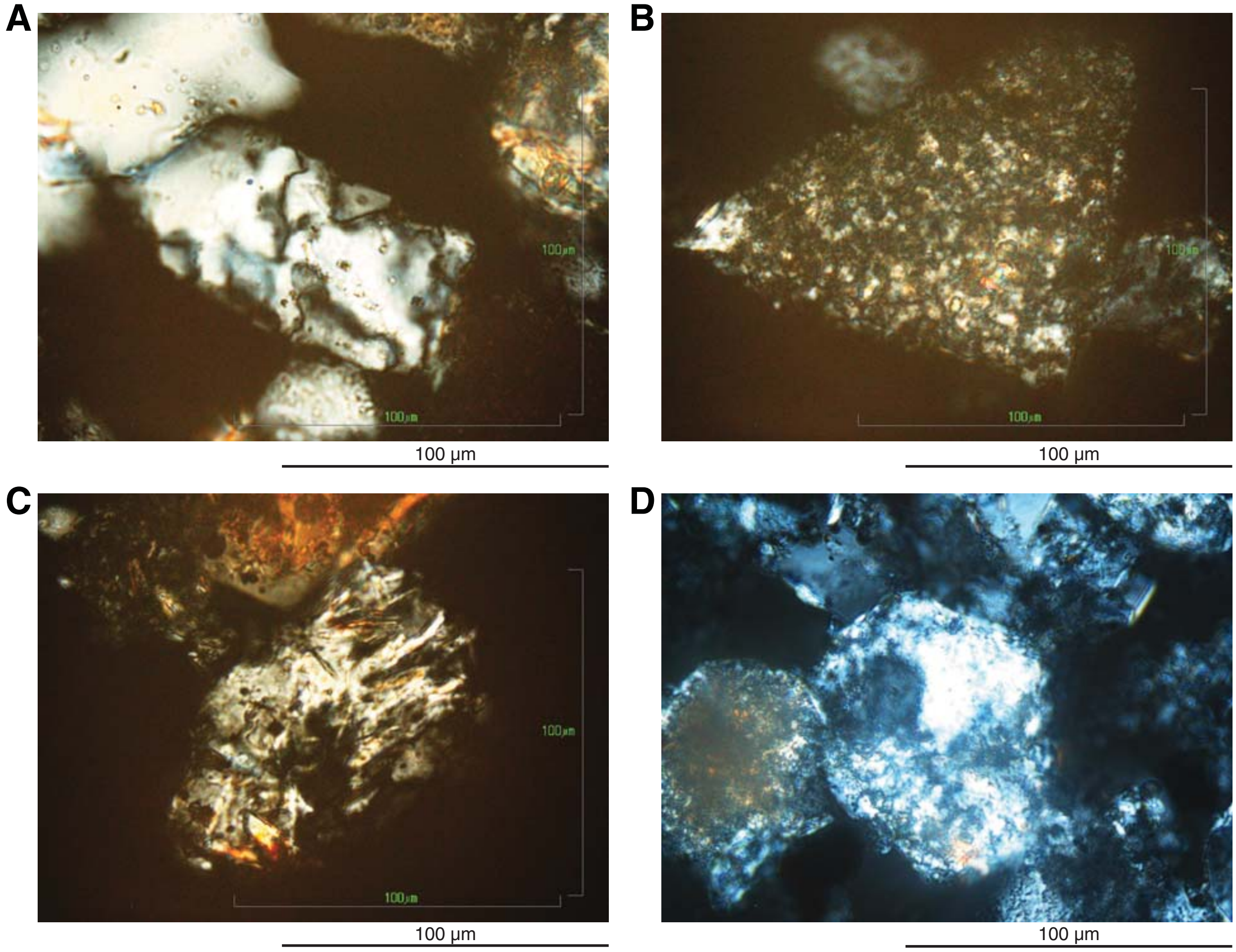

Figure F42. Common volcanogenic grains observed in smear slides. **A.** Pumice fragments (sand size) and vitric ash (silt size) (Sample 338-C0002J-1R-1, 56 cm; PPL). **B.** Brown volcanic glass (Sample 338-C0002J-2R-1, 5 cm; PPL). **C.** Microlitic clear glass with flow structure (Sample 338-C0002J-2R-1, 5 cm; PPL). **D.** Microlitic brown glass (Sample 338-C0002J-4R-5, 36 cm; PPL).

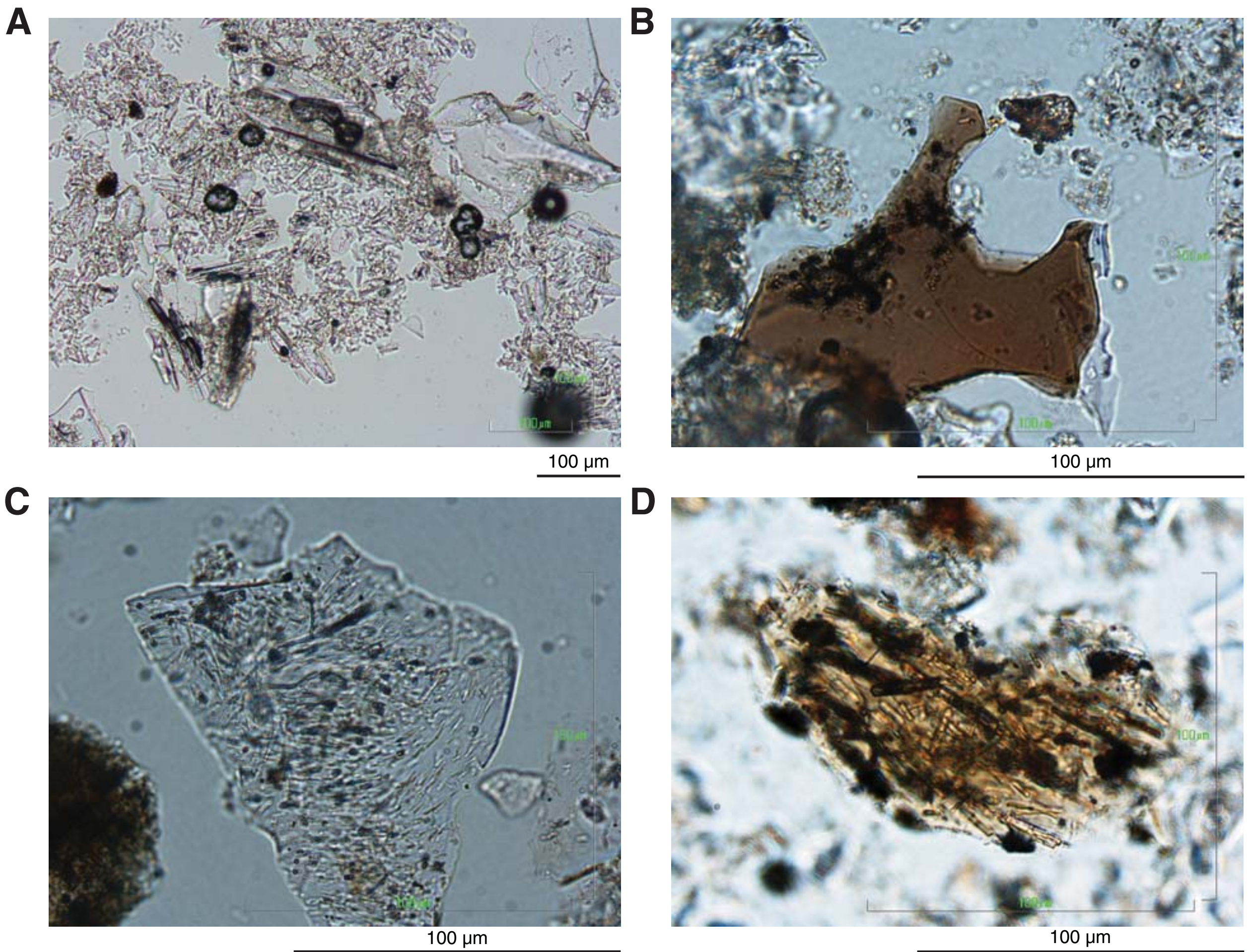

Figure F43. Images of ichnotaxa and other discrete burrows generally associated with Unit III. **A.** *Zoophycos* burrows (interval 338-C0002J-1R-1, 59–64 cm). **B.** *Chondrites* burrows (interval 338-C0002J-1R-1, 19–22 cm). **C.** Possible cross-sections of *Zoophycos* (interval 338-C0002J-1R-3, 21–23 cm). **D.** Variety of discrete burrows, including *Zoophycos;* central clay-lined burrow appears to have a localized deformation structure along the left side (arrow) (interval 338-C0002J-1R-7, 16–25 cm). **E.** Discrete layer of pyritized burrows (interval 338-C0002J-1R-8, 75–77.4 cm). **F.** Unidentified discrete burrow (interval 338-C0002J-1R-7, 2–5 cm).

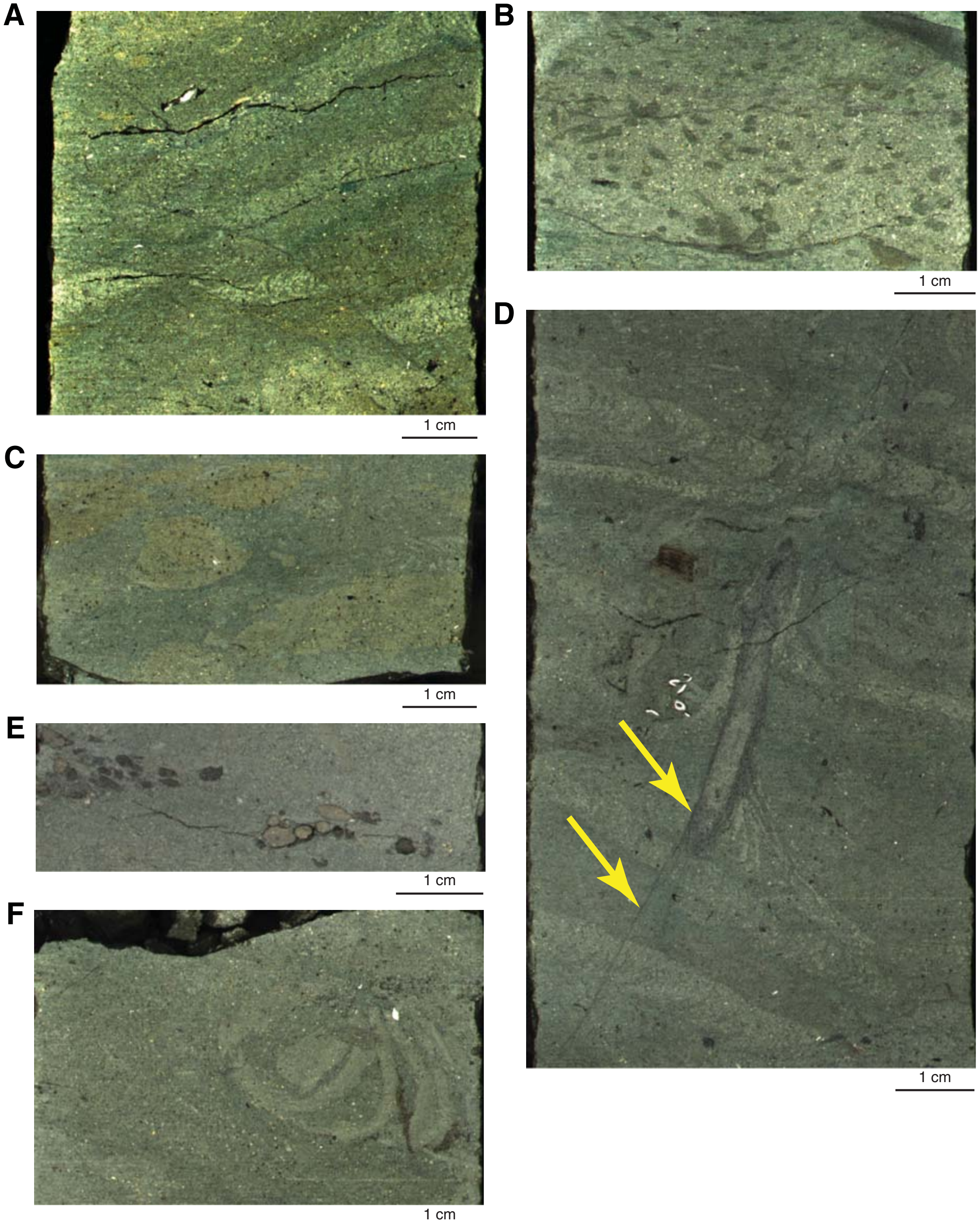

Figure F44. Evidence for syndepositional erosional processes in the lower part of Unit III. **A.** Angular clast of calcareous silty claystone (C) surrounded by glauconitic sandy claystone above a sharp contact between the two lithologies (interval 338-C0002J-5R-8, 20–25 cm). **B.** Inclined laminae (lighter dashed lines) and high-angular erosional surface (heavier dashed line) within a bed of glauconitic sandy claystone (interval 338-C0002J-5R-8, 77–92 cm). **C.** Angular clasts of brownish silty claystone within a lighter claystone (interval 338-C0002J-4R-4, 0–5 cm). **D.** Sharp boundary with millimeter-scale scour between two silty claystones (interval 338-C0002J-5R-6, 1.5–5.5 cm).

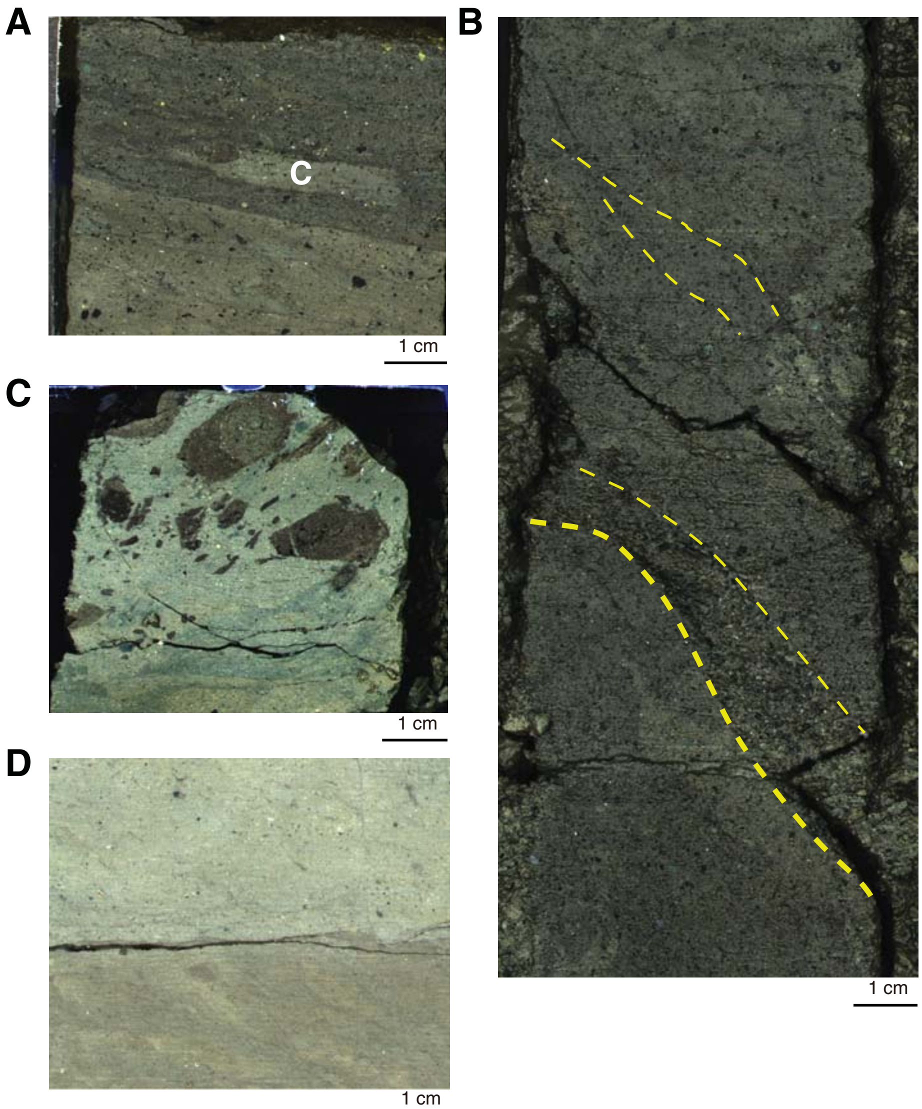

Figure F45. Occurrences of glauconite. **A.** Irregular greenish mottling (Sample 338-C0002J-3R-5, 60–64 cm). **B.** Repetitive green bands (Sample 338-C0002J-4R-4, 100–107 cm). **C.** Scattered glauconite sand and granules (Sample 338-C0002J-3R-1, 38–41 cm). **D.** Glauconite (green grains) in smear slide (Sample 338-C0002J-2R-1, 41 cm; PPL). **E.** Discrete layer of glauconite sand (Sample 338-C0002J-5R-7, 35–39 cm).

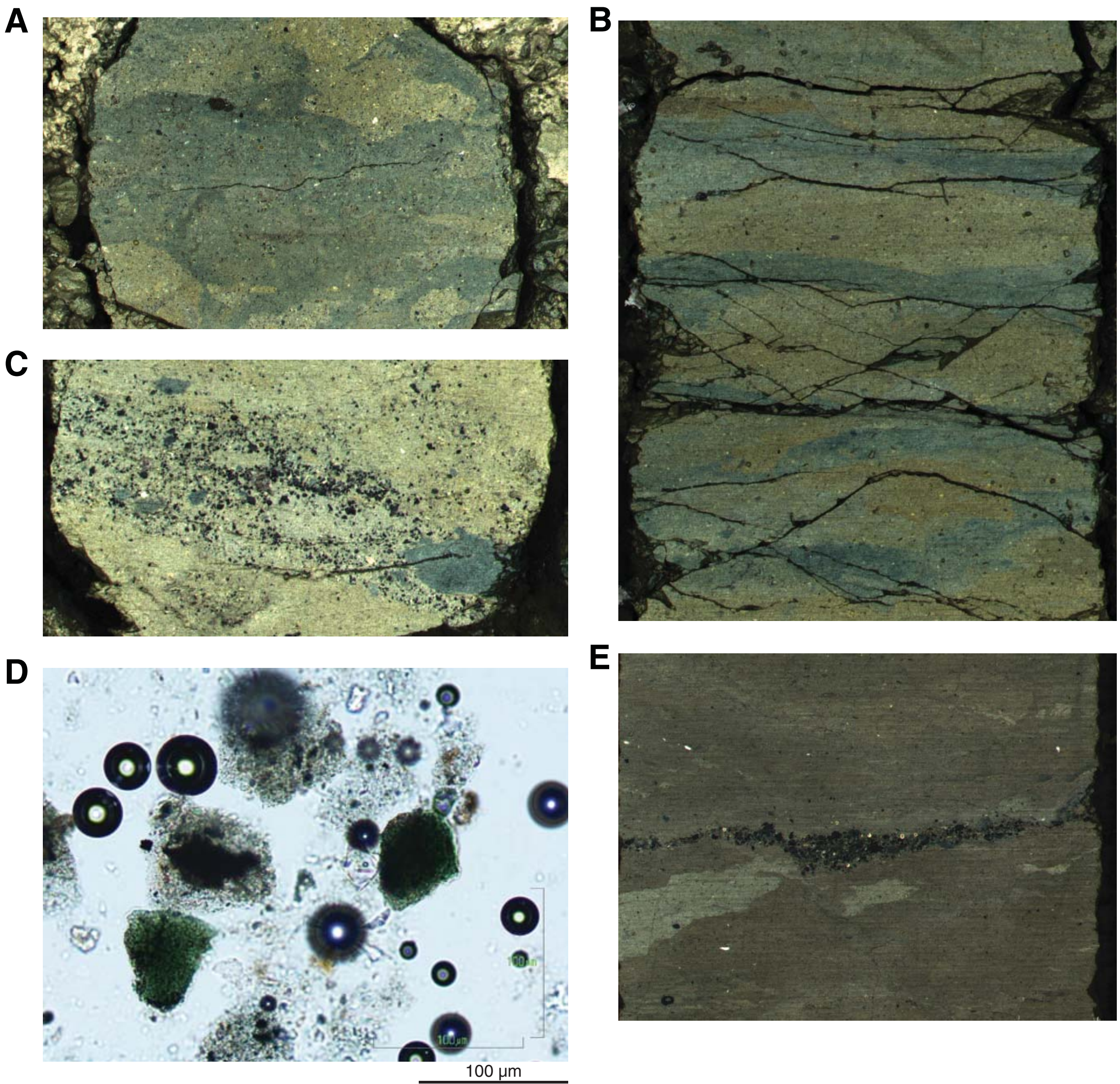

Figure F46. Odd microcrystalline carbonate lithology (Section 338-C0002J-6R-1; XPL).

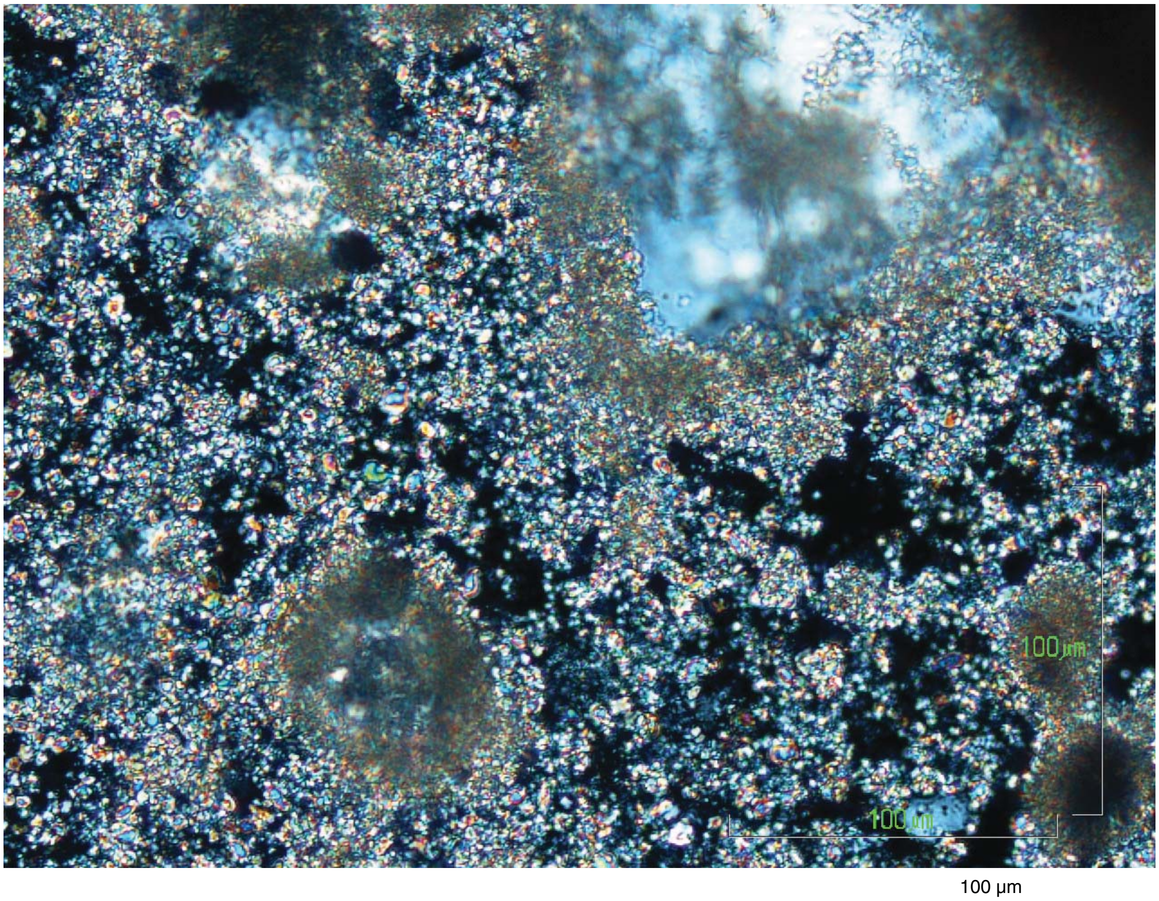

Figure F47. Detailed view of possible unit boundary zone (interval 338-C0002J-5R-8, 98–126 cm). Variations in Fe and Al content were obtained from XRF. A discrete XRD sample (marked X) shows only a trace of calcite, whereas analyses of other silty claystones in this section at 0–1 and 30–31 cm show calcite with amounts of 18.0% and 7.2%, respectively. Cored interval is between 927 and 932 mbsf.

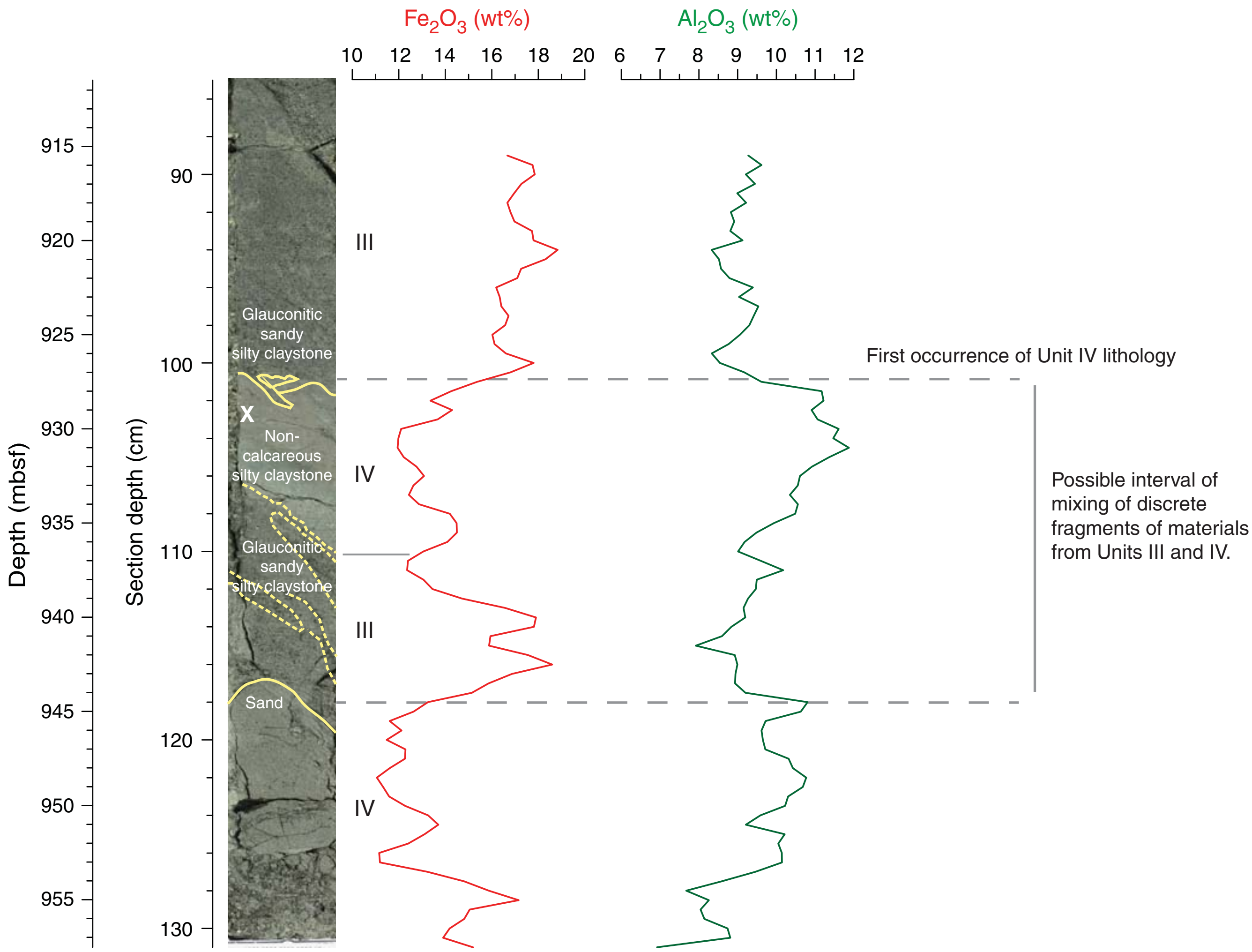

Figure F48. Generalized lithologic column for Holes C0002K and C0002L. Black = cored intervals.

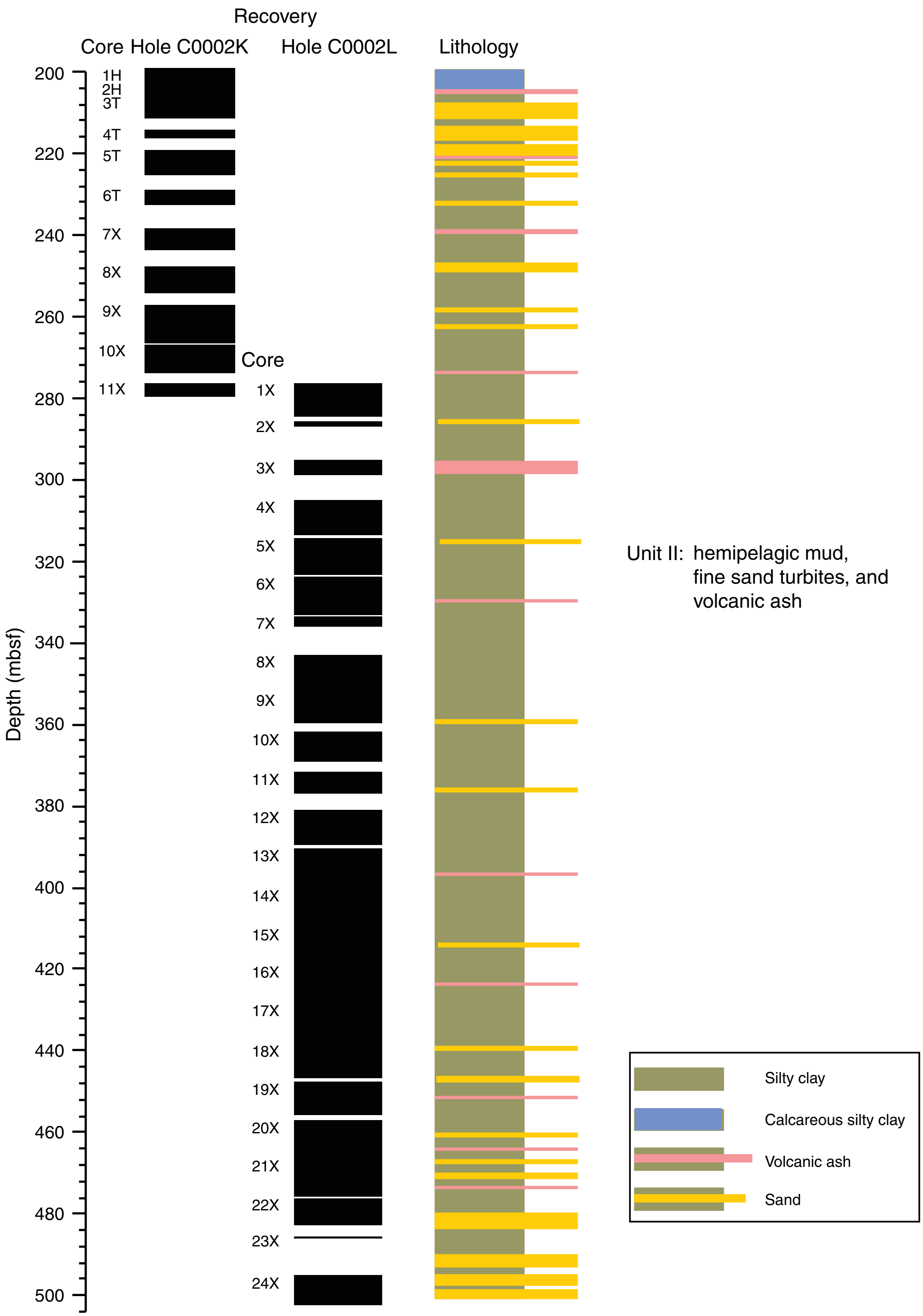

Figure F49. XRD mineralogical bulk compositions of core samples, Holes C0002K and C0002L.

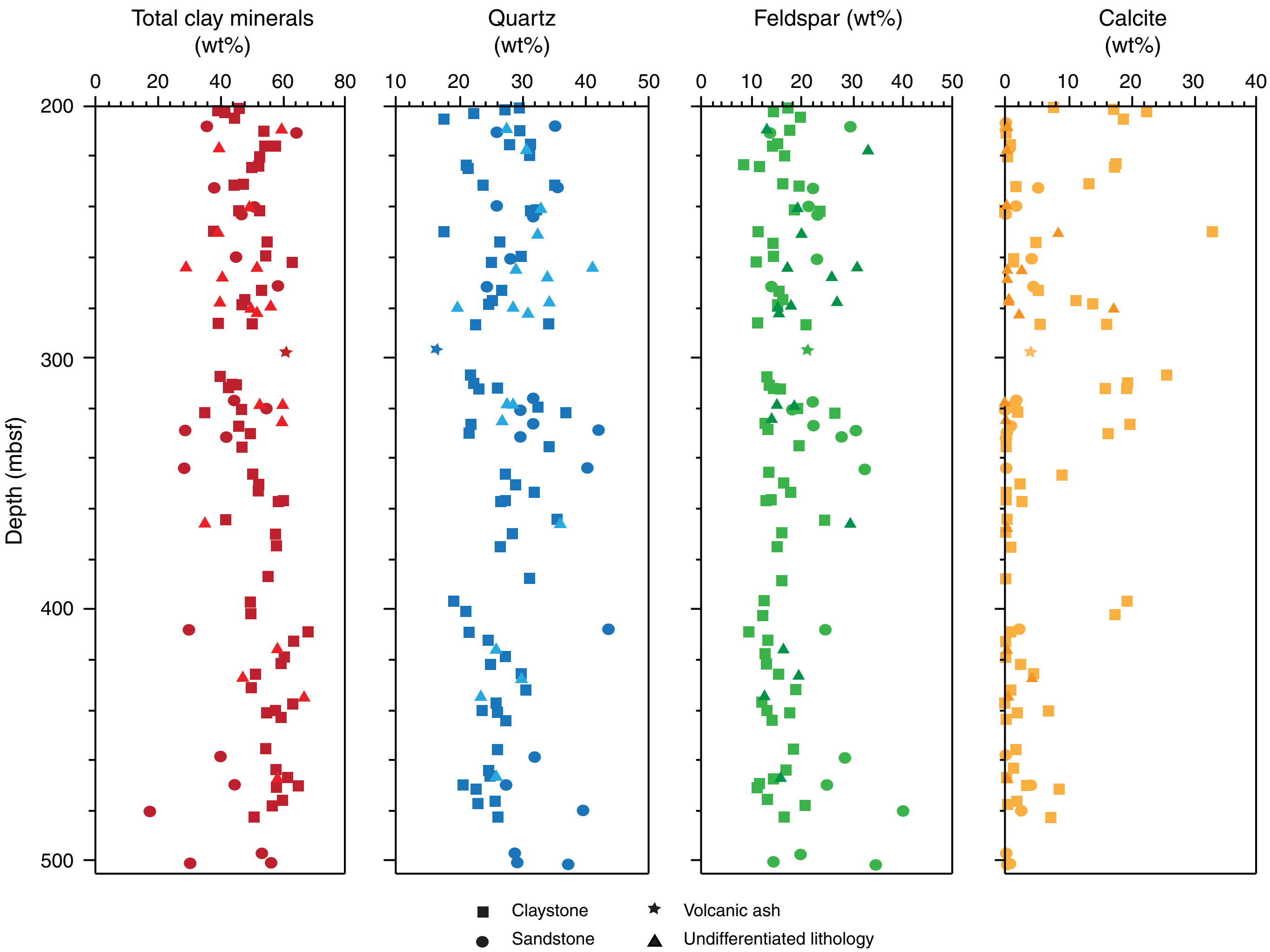

Figure F50. XRF bulk chemical compositions of core samples, Holes C0002K and C0002L. LOI = loss on ignition.

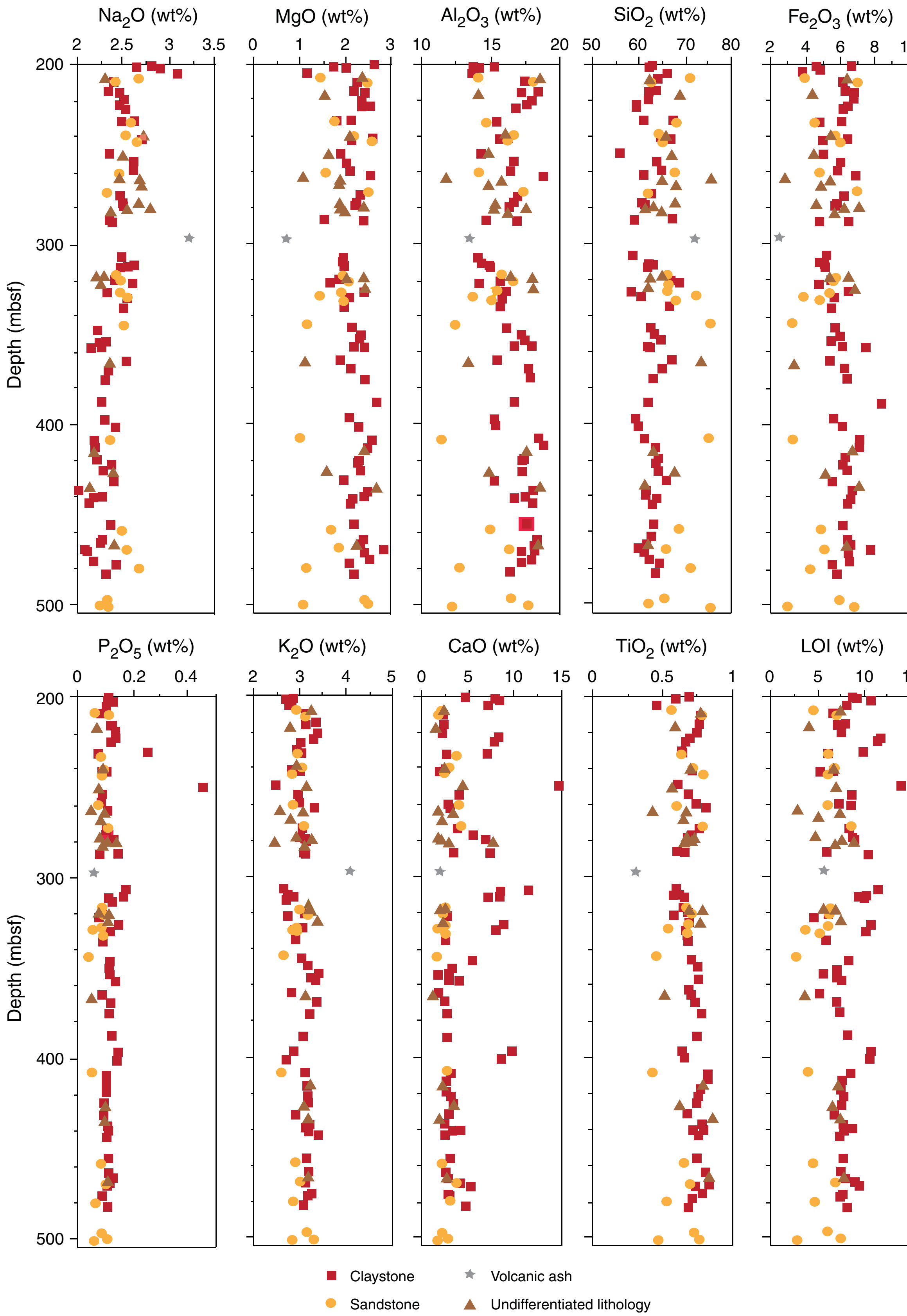

Figure F51. Common sand grain types. **A.** Biosiliceous debris (Sample 338-C0002K-1H-4, 90 cm; PPL). **B.** Vacuolized untwinned feldspar (pc) and chert (ch) (Sample 338-C0002L-10X-8, 80 cm; XPL). **C.** Quartz-chlorite metamorphic lithic fragment with foliation (chlorite schist) (Sample 338-C0002L-11X-7, 77 cm; PPL). **D.** Quartz-muscovite metamorphic lithic fragment with foliation (muscovite schist) (Sample 338-C0002L-1H-4, 90 cm; XPL).

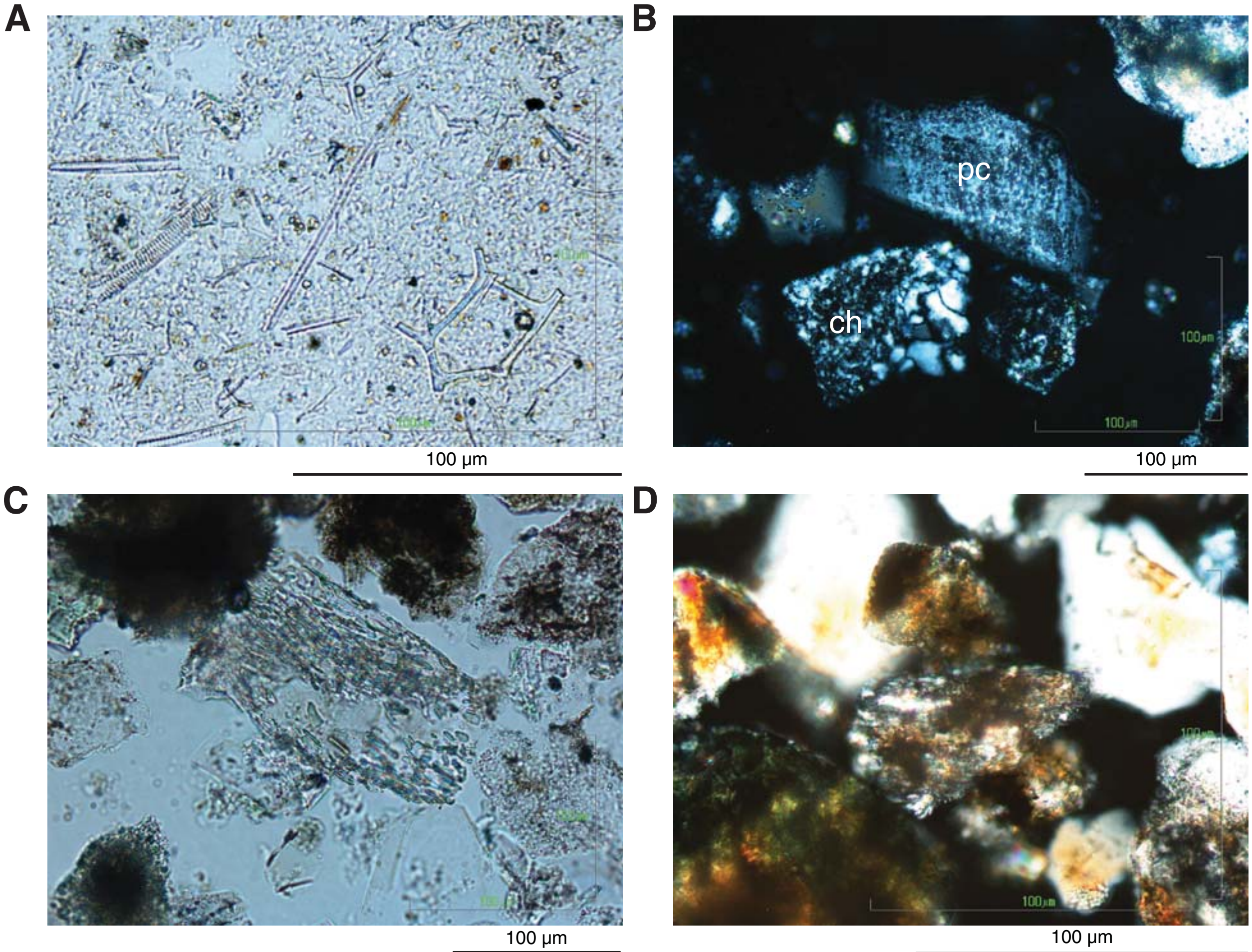

Figure F52. Variations in turbidite character in Hole C0002K and C0002L cores, ranging from (**A**) coarser cycles containing sand through (**B**) thinner ones with coarser layers composed of sandy silt or clayey silt to (**C**) the finest ones represented by slightly more silty clay scoured into the underlying finer and pelagic-rich calcareous silty clay.

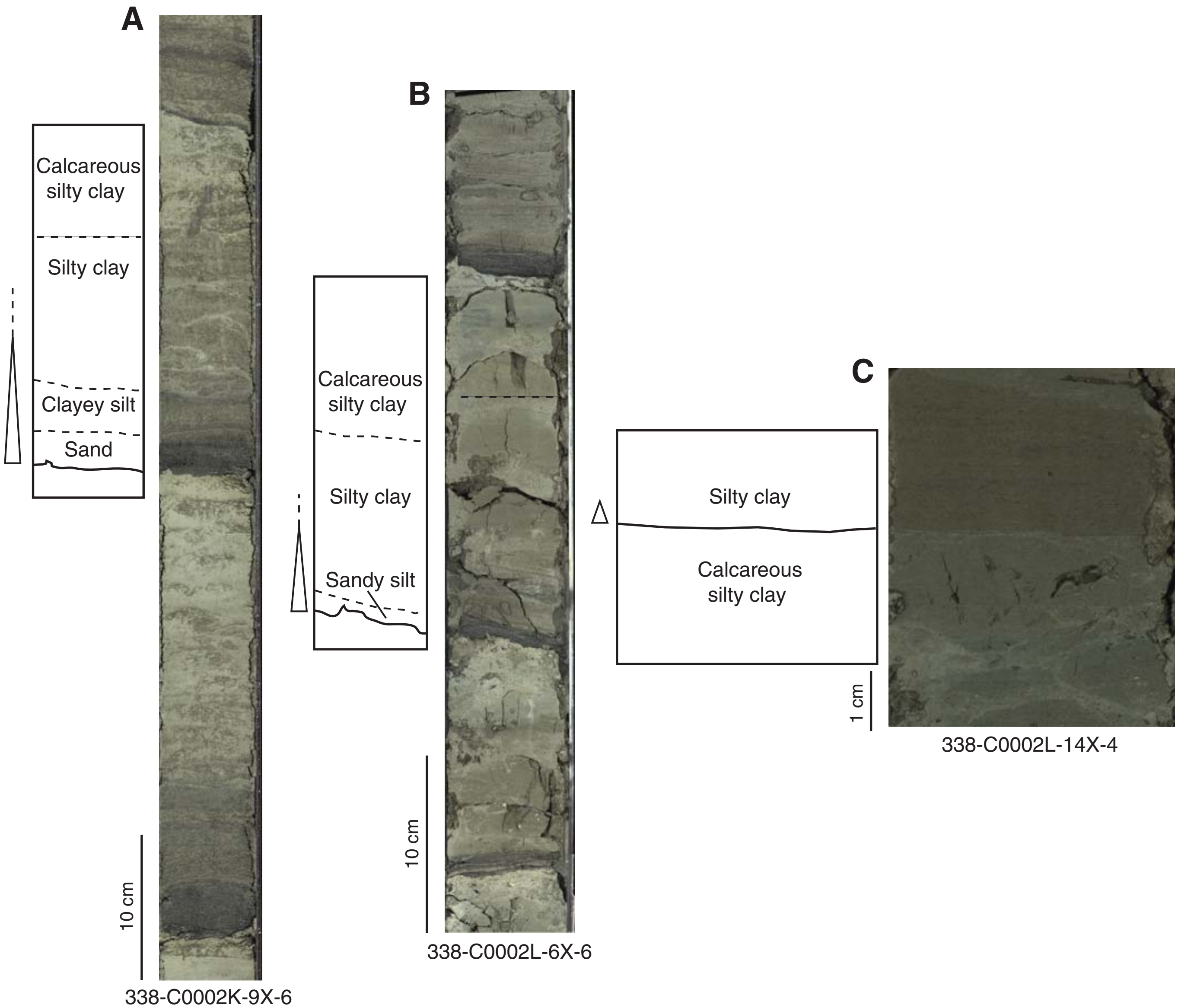

Figure F53. Sand occurrence in Holes C0002K and C0002L. Values plotted are averages calculated from data tabulated for each section (from Table T26).

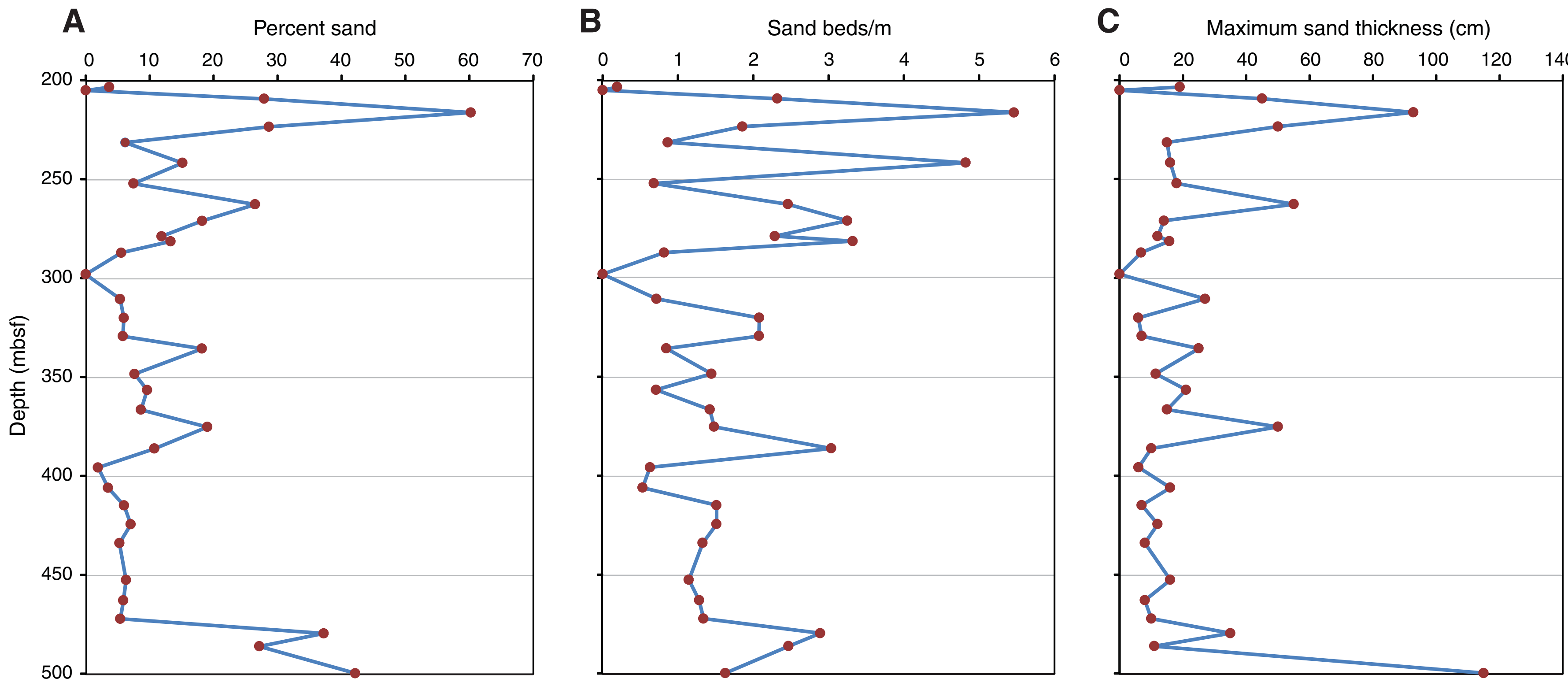

Figure F54. Depth distribution of documented deformation structures in cuttings samples, Hole C0002F. **A.** >4 mm size fraction. **B.** 1–4 mm size fraction. Abundance of grains with deformation structures at each depth is obtained by dividing the number of grains that show deformation structures by the number of investigated grains. Solid horizontal lines = lithologic unit boundaries. Note that the method of counting deformation structures in the >4 mm size fraction changed at 1415.5 mbsf (dashed line in A), and observations on 1–4 mm cuttings were routinely performed only for depths deeper than 1375.5 mbsf (interval with only spot counting; shaded area in B) (see **"Structural geology"** in the "Methods" chapter [Strasser et al., 2014a]).

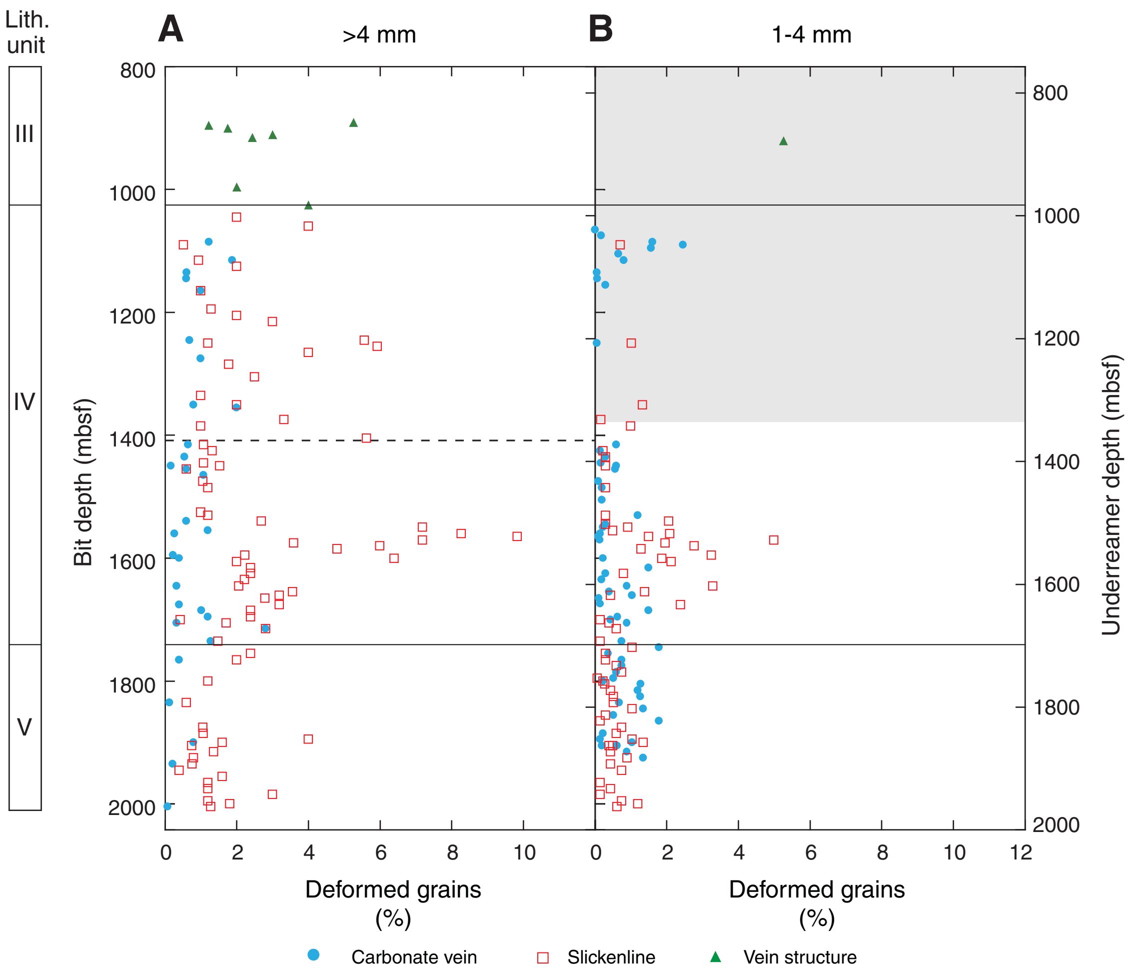

Figure F55. Characteristic examples of vein structures in cuttings from the >4 mm size fraction. **A.** Sample 338-C0002F-16-SMW (905.5 mbsf). **B.** Sample 338-C0002F-19-SMW (920.5 mbsf).

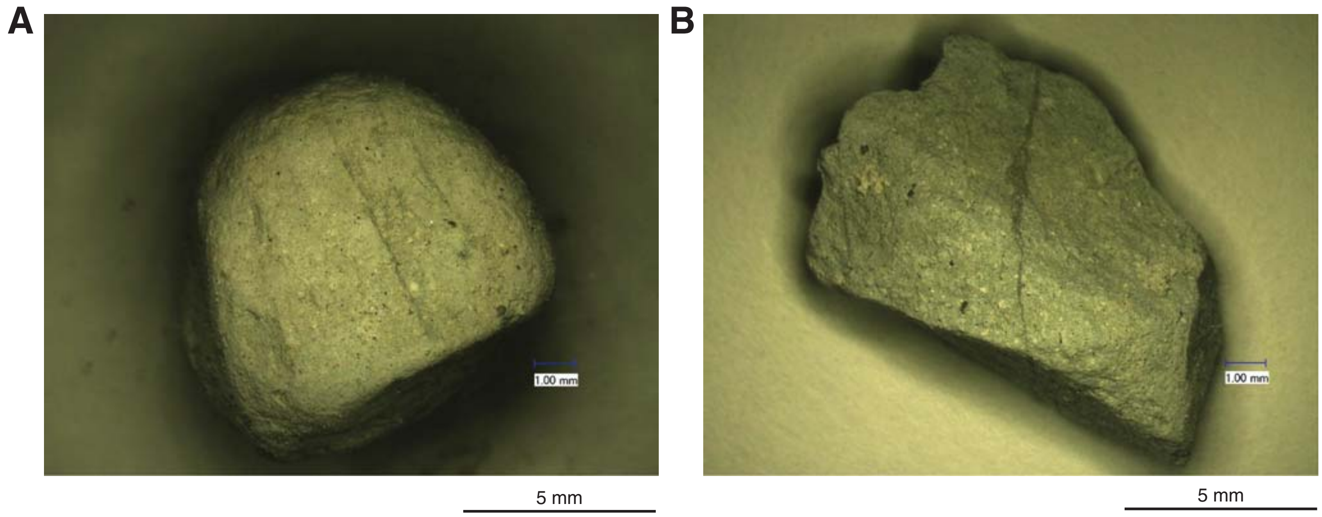

Figure F56. Characteristic examples of carbonate veins in cuttings. **A.** Veins with different orientations (Sample 338-C0002F-56-SMW, >4 mm; 1085.5 mbsf). **B.** Carbonate vein with slickenlined surface (Sample 338-C0002F-62-SMW, 1–4 mm; 1105.5 mbsf). **C.** Fiber growth (Sample 338-C0002F-258-SMW, 1–4 mm; 1885.5 mbsf). **D.** Growth of calcite grains from the wall rock (limestone) (Sample 338-C0002F-56-SMW, >4 mm; 1085.5 mbsf; PPL). **E.** Mechanical twins in calcite grains (arrows) (Sample 338-C0002F-56-SMW, >4 mm; 1085.5 mbsf; XPL). **F.** Selvages in carbonate veins (Sample 338-C0002F-56-SMW, >4 mm; 1085.5 mbsf; PPL).

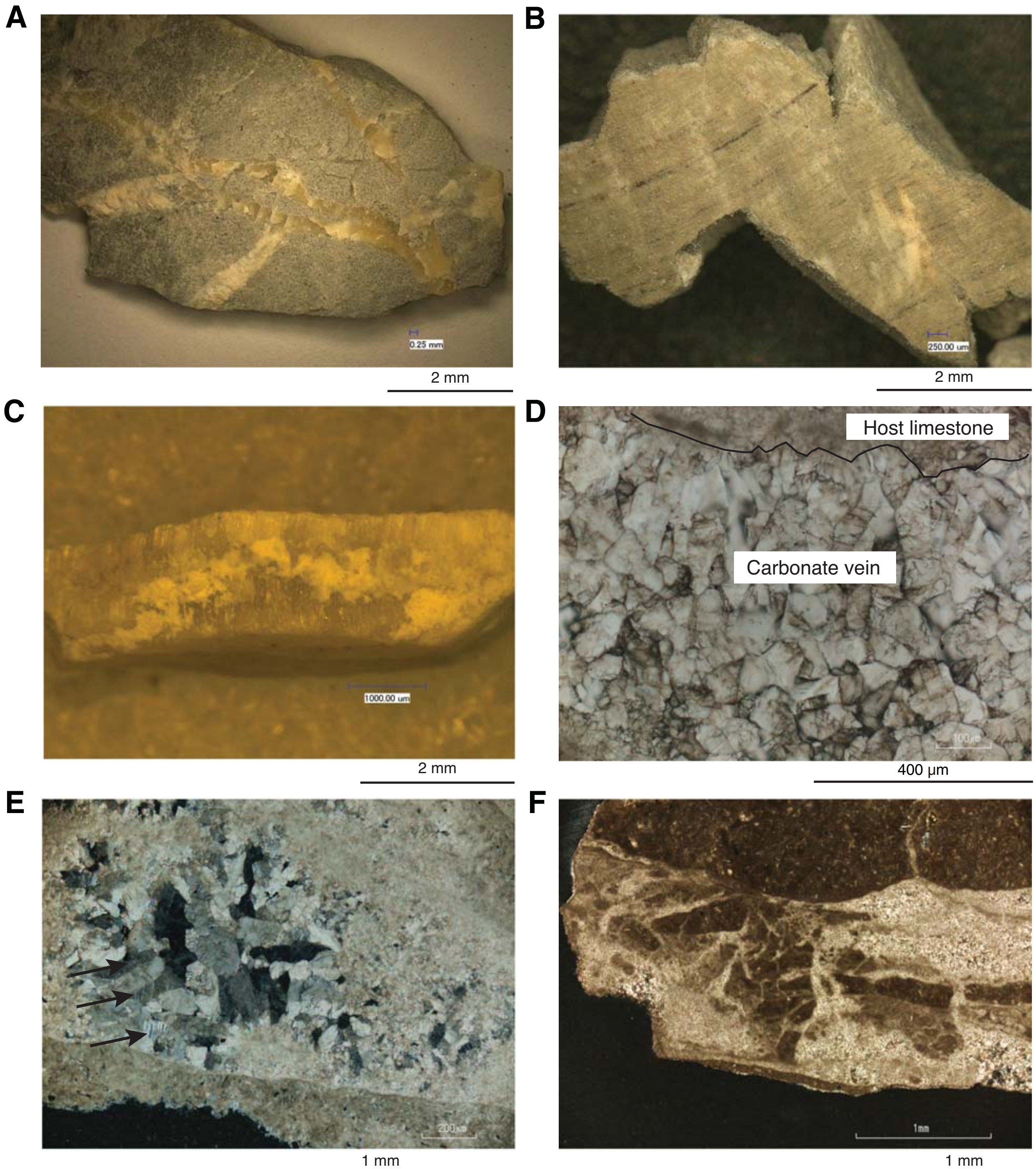

Figure F57. Characteristic examples of slickenlined surfaces in cuttings. **A.** Sample 338-C0002F-86-SMW, >4 mm (1215.5 mbsf). **B.** Enlargement of A (box). **C.** Thin section photomicrograph of incipient slickenlined surface (plane of view is perpendicular to the slickenlined surface) (Sample 338-C0002F-98-SMW, >4 mm; 1265.5 mbsf; XPL). White dashed lines and arrow = preferred alignment of clay minerals parallel to slickenlined surface, constituting a 200–400 µm wide zone. **D.** Stepped slickenlined surface (Sample 338-C0002F-169-SMW, >4 mm; 1565.5 mbsf). Arrow = movement direction of the (presently missing) upper side.

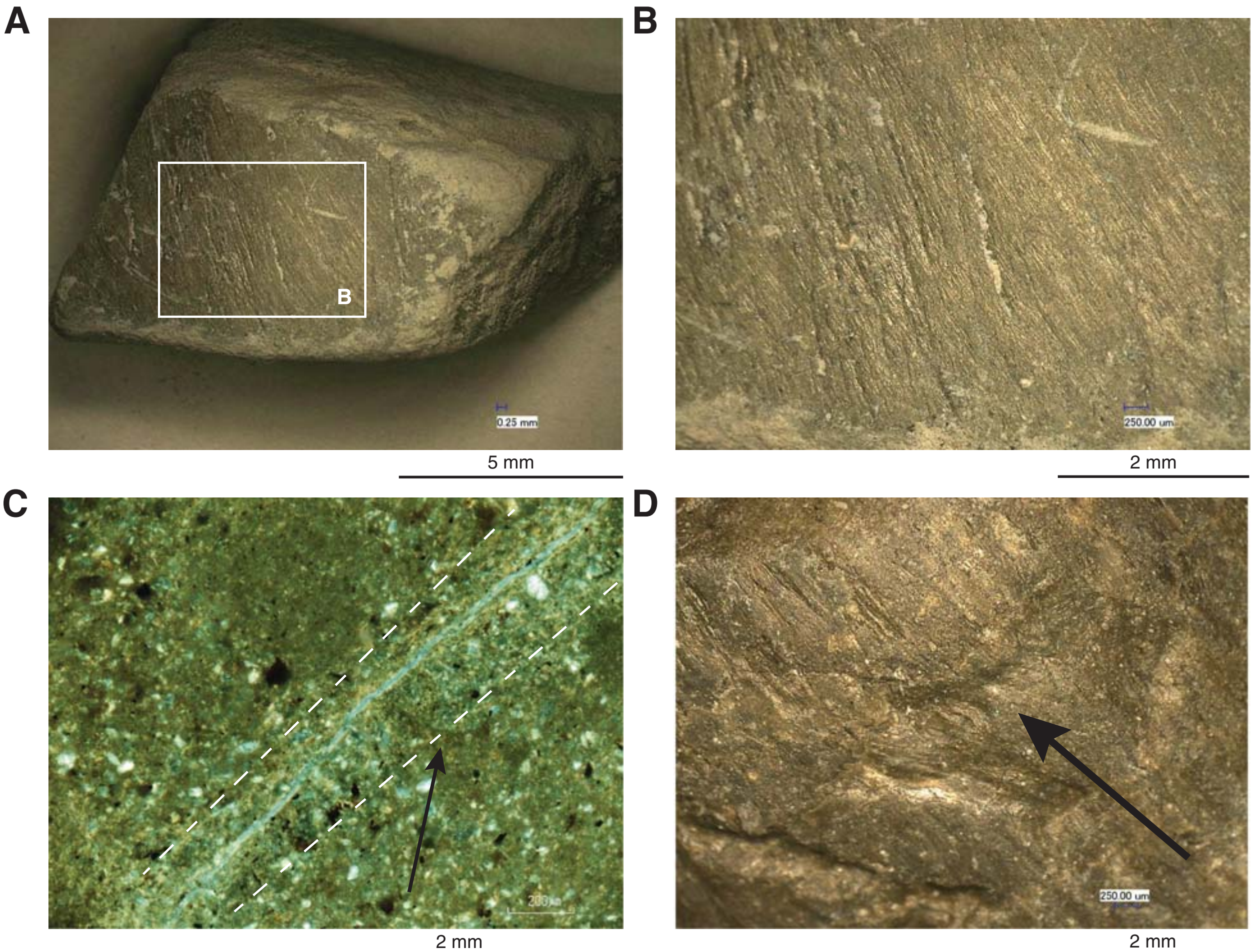

Figure F58. Depth distribution of deformation structures documented in cuttings compared to silty claystone concentration, Hole C0002F. **A.** >4 mm size fraction. **B.** 1–4 mm size fraction. Solid horizontal lines = lithologic unit boundaries. Note that the method of counting deformation structures in the >4 mm size fraction changed at 1415.5 mbsf (dashed line in A), and observations on 1–4 mm cuttings were performed routinely only for depths larger than 1375.5 mbsf (interval with only spot counting; shaded area in B) (see **"Structural geology"** in the "Methods" chapter [Strasser et al., 2014a]).

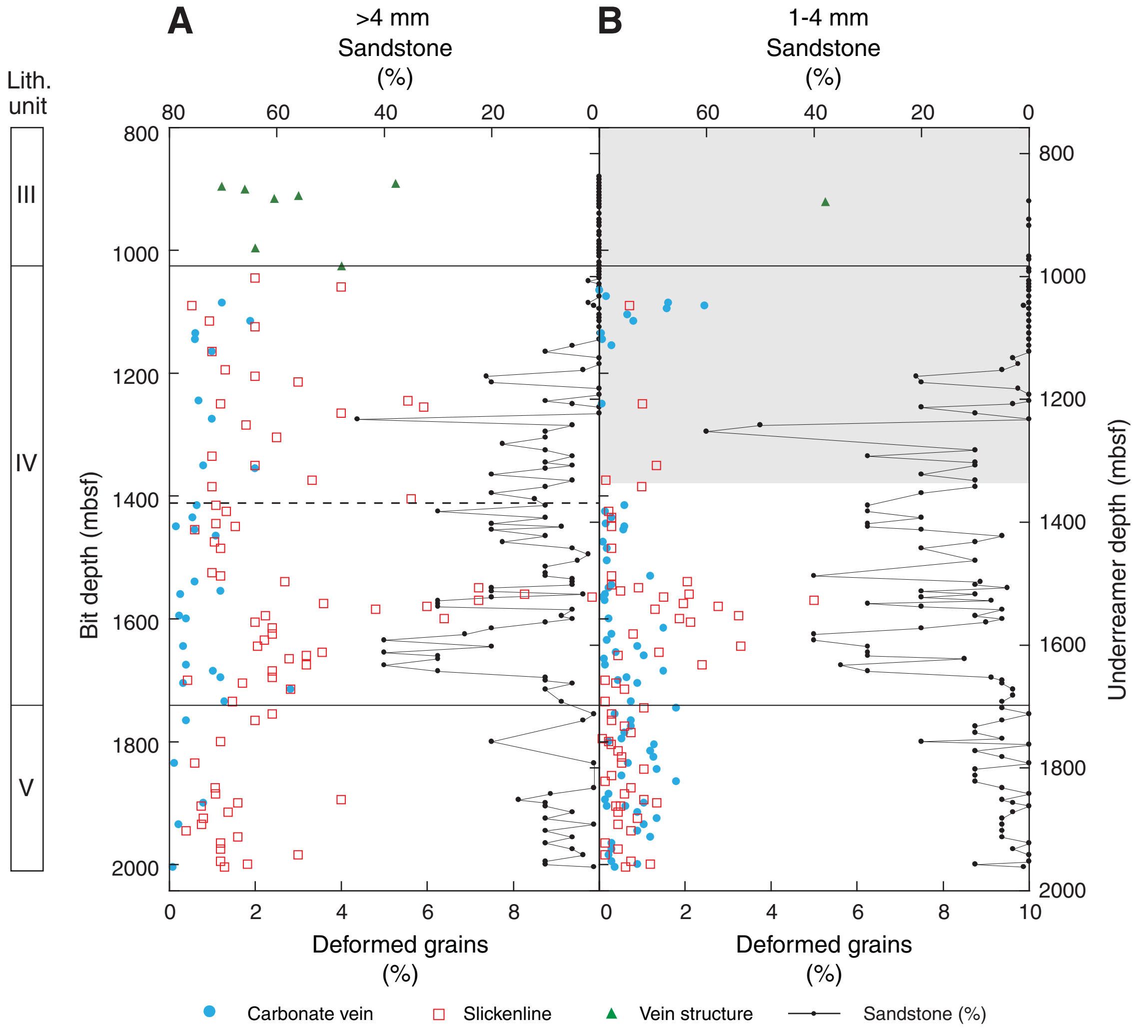

Figure F59. Characteristic examples of minor faults. **A.** Black-colored faults (Sample 338-C0002F-169-SMW, >4 mm; 1565.5 mbsf). **B.** Enlargement of A (box). **C, D.** Black-colored fault slip zone (Sample 338-C0002F-169-SMW, >4 mm; 1565.5 mbsf; XPL); (C) with stepovers (dashed circle); (D) showing that quartz grain within the slip zone and foraminifer fossil along the zone are not fractured. **E.** Fault plane with 0.6 mm displacement of laminations in sandstone (Sample 338-C0002F-238-SMW, >4 mm; 1835.5 mbsf; XPL). Dashed line and arrows = fault plane and sense of displacement. **F.** Enlargement of E (box).

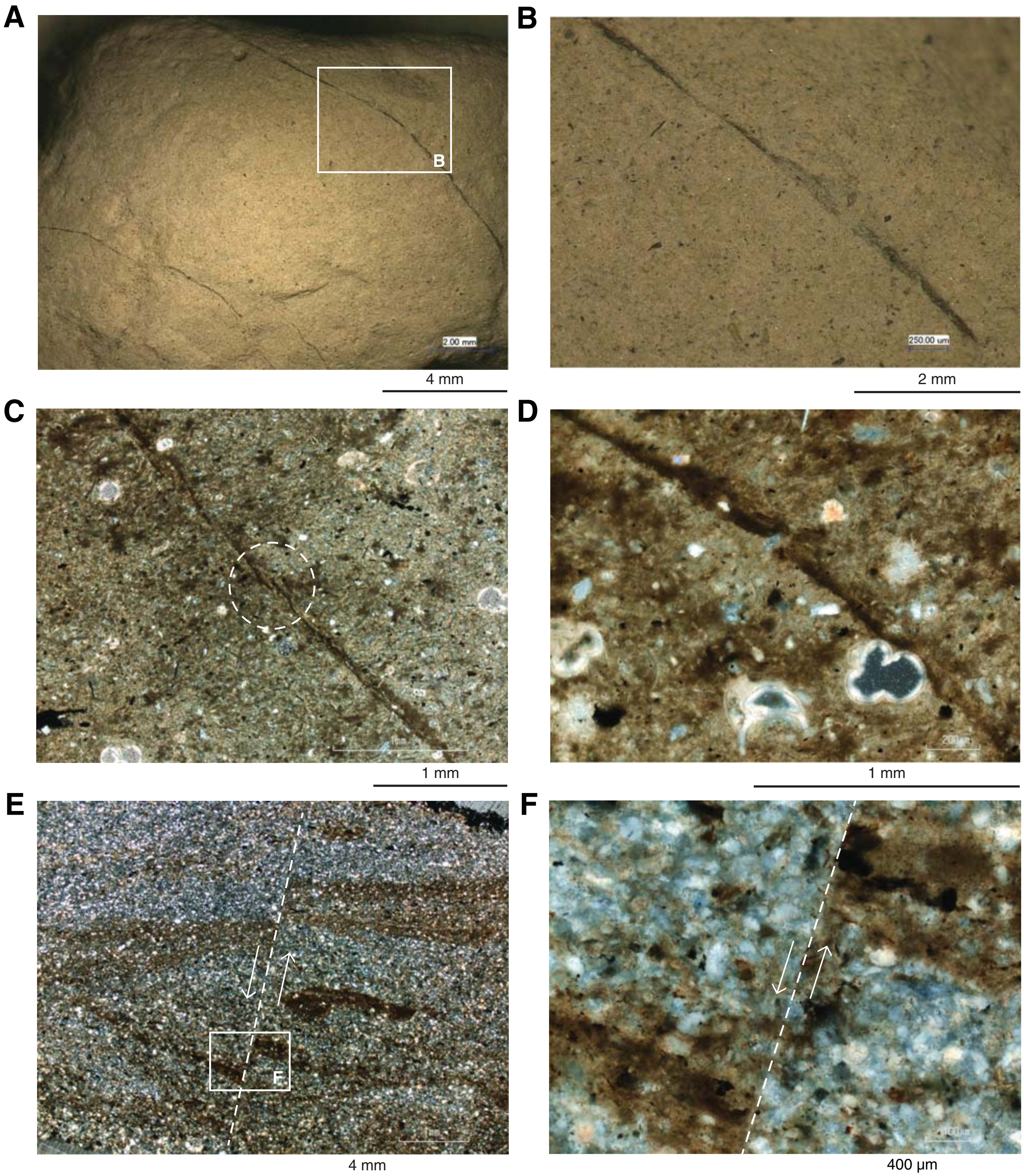

Figure F60. Microstructures of sandstone cuttings under XPL. **A.** Semiconsolidated sandstone with loosely packed sand grains surrounded by clay minerals (Sample 338-C0002F-110-SMW, >4 mm; 1325.5 mbsf). **B.** Graded bedding of sand- to silt-sized clasts and laminations (Sample 338-C0002F-193-SMW, >4 mm; 1645.5 mbsf). **C.** Closely packed consolidated sandstone (Sample 338-C0002F-217-SMW, >4 mm; 1755.5 mbsf). **D.** Enlargement of C (box). Cavities are filled with quartz cement.

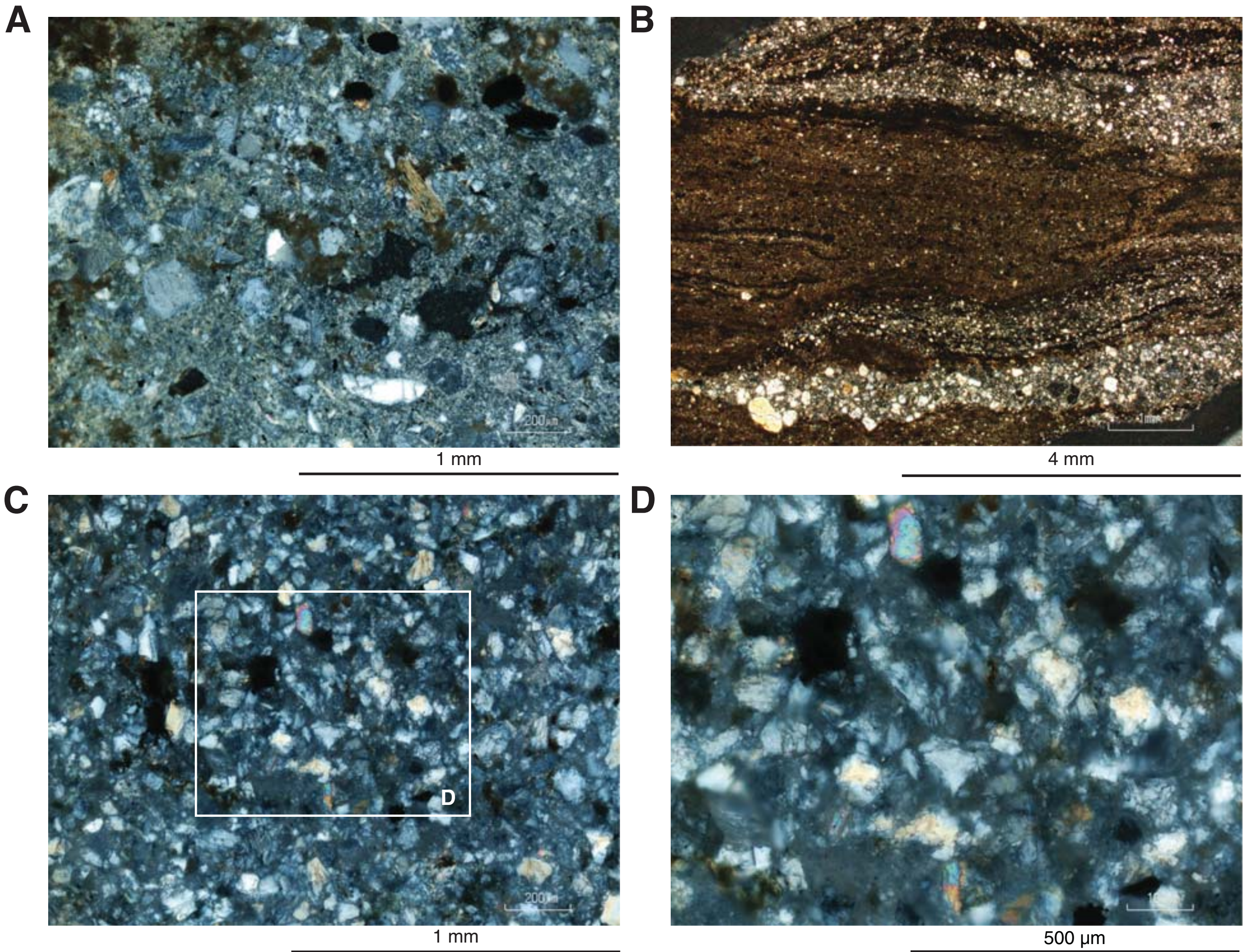

Figure F61. Microstructures of silty claystone cuttings under XPL. The degree of preferred alignment of clay minerals in silty claystone increases with increasing depth. **A.** Silty claystone with no preferred orientation of clay minerals (Sample 338-C0002F-86-SMW, >4 mm; 1215.5 mbsf). **B.** Silty claystone with weakly oriented clay minerals and sandstone (Sample 338-C0002F-144-SMW, >4 mm; 1475.5 mbsf). Dashed line = sandstone/silty claystone boundary. **C–F.** Silty claystone with preferred orientation of clay minerals (dashed line); (C) Sample 338-C0002F-169-SMW, >4 mm; 1565.5 mbsf; (D) Sample 338-C0002F-187-SMW, >4 mm; 1625.5 mbsf; (E) Sample 338-C0002F-255-SMW, >4 mm; 1875.5 mbsf; (F) Sample 338-C0002F-289-SMW, >4 mm; 2004.5 mbsf.

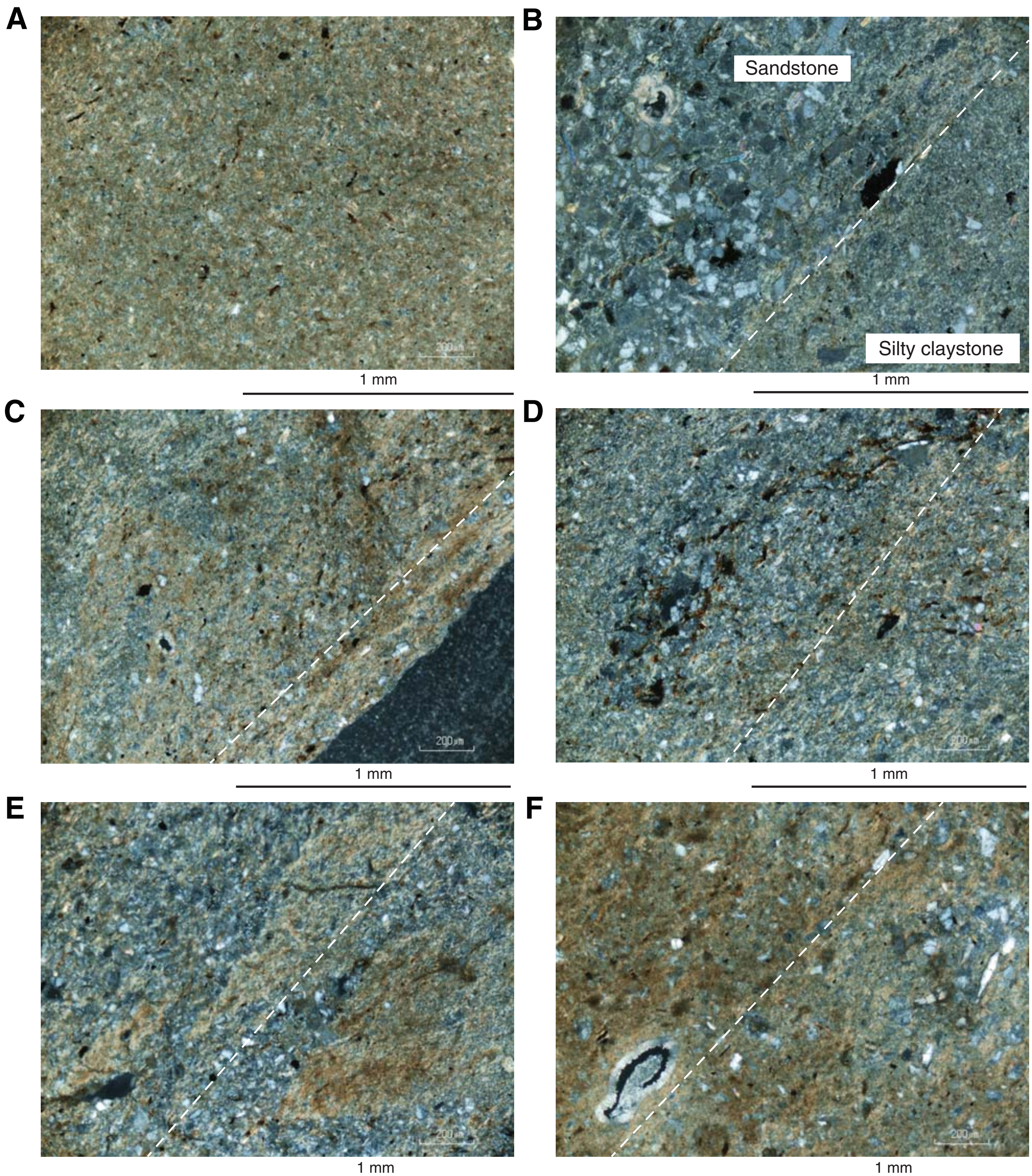

Figure F62. Structures in cuttings formed by drilling disturbance. **A.** Sawtooth shape (Sample 338-C0002F-41-SMW, >4 mm; 1010.5 mbsf). **B.** Drilling mud invasion into formation mudstone (Sample 338-C0002F-75-SMW, >4 mm; 1165.5 mbsf; XPL). **C.** DICAs composed of aggregates of dispersed sand and mud fragments (Sample 338-C0002F-110-SMW, >4 mm; 1325.5 mbsf; XPL). **D.** DICA of clay-size fraction easily disaggregated in water (Sample 338-C0002F-289-SMW, >4 mm; 2004.5 mbsf).

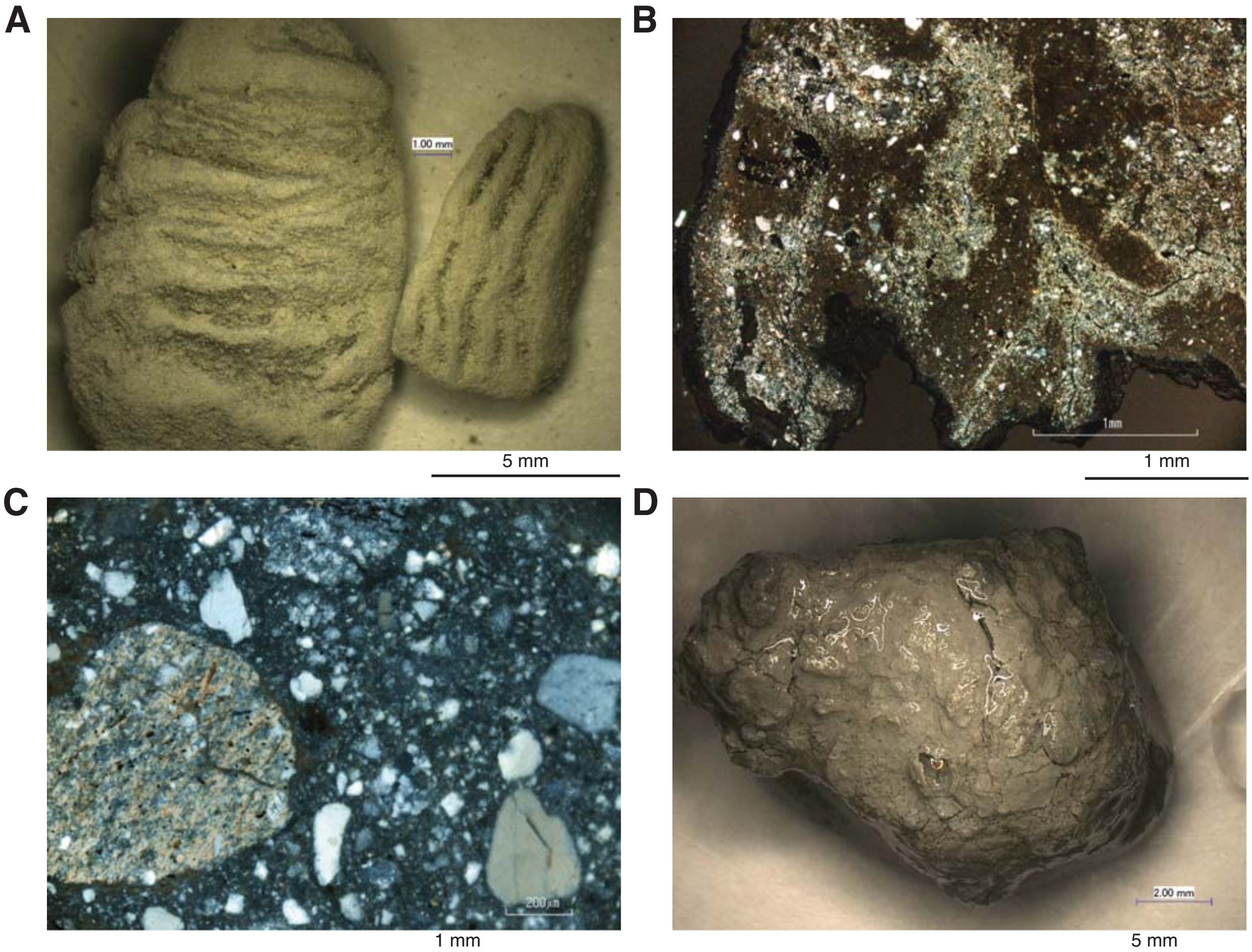

Figure F63. Comparison of concentrations of silty claystone based on observations of cuttings during structural interpretation and during lithologic description after easy sieving with 63 µm mesh (orange-shaded region), Hole C0002F. Note that the orange-shaded region is considered to include sandstones that were disaggregated during recovery and processing of cuttings.

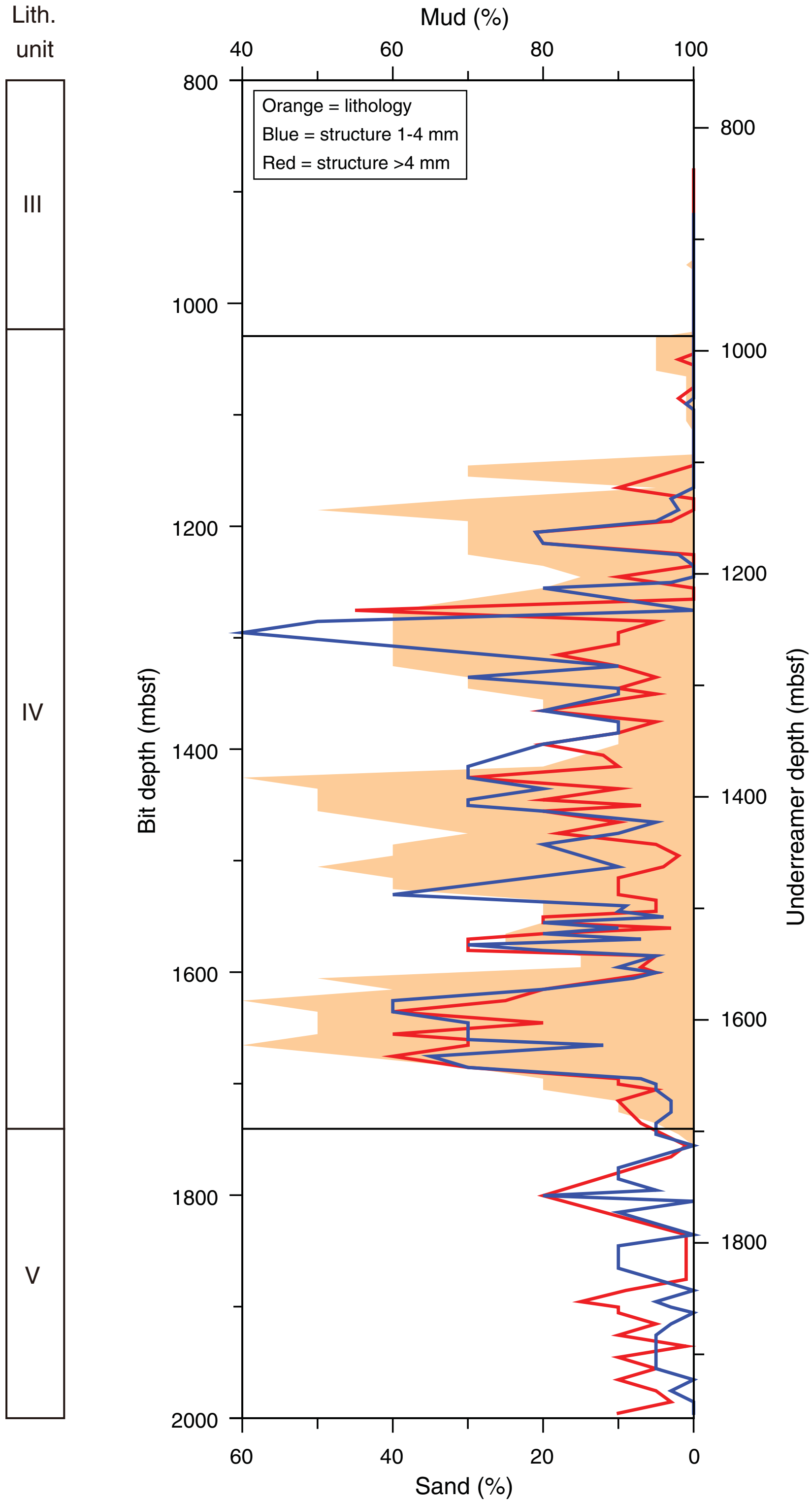

Figure F64. Examples of structures observed on working halves of split cores. **A.** Disrupted bedding close to the Unit III/IV boundary (interval 338-C0002J-5R-6, 13–25 cm). **B.** Deformation bands (arrows) (interval 338-C0002J-1R-7, 92–105 cm). **C.** Shear zone (interval 338-C0002J-1R-3, 10–20 cm). The releasing bend geometry of the upper shear zone and the Riedel shear geometry of secondary shear zones between the upper and central shear zones suggest a normal displacement component for the entire shear zone. **D.** Fragments of calcite-cemented breccia (interval 338-C0002J-7R-1, 6–12 cm). (Continued on next page.)

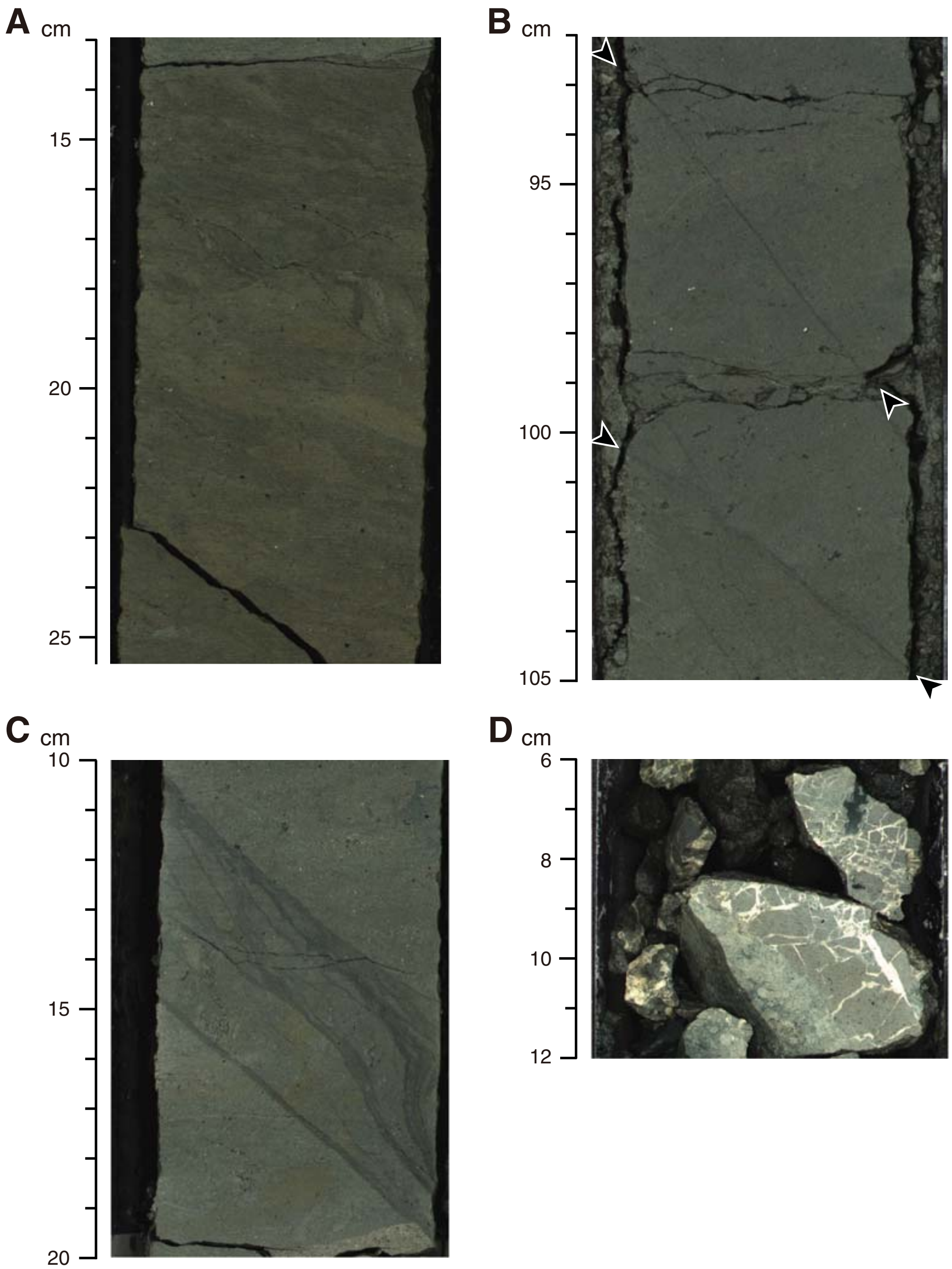

Figure F64 (continued). **E.** Joints (interval 338-C0002H-1R-1, 65–83 cm). **F.** Vein structures (interval 338-C0002J-1R-8, 30–34 cm). **G.** Fissility (interval 338-C0002K-1H-1, 91–99 cm). **H.** Incipient scaly cleavage (interval 338-C0002J-3R-5, 76–79 cm).

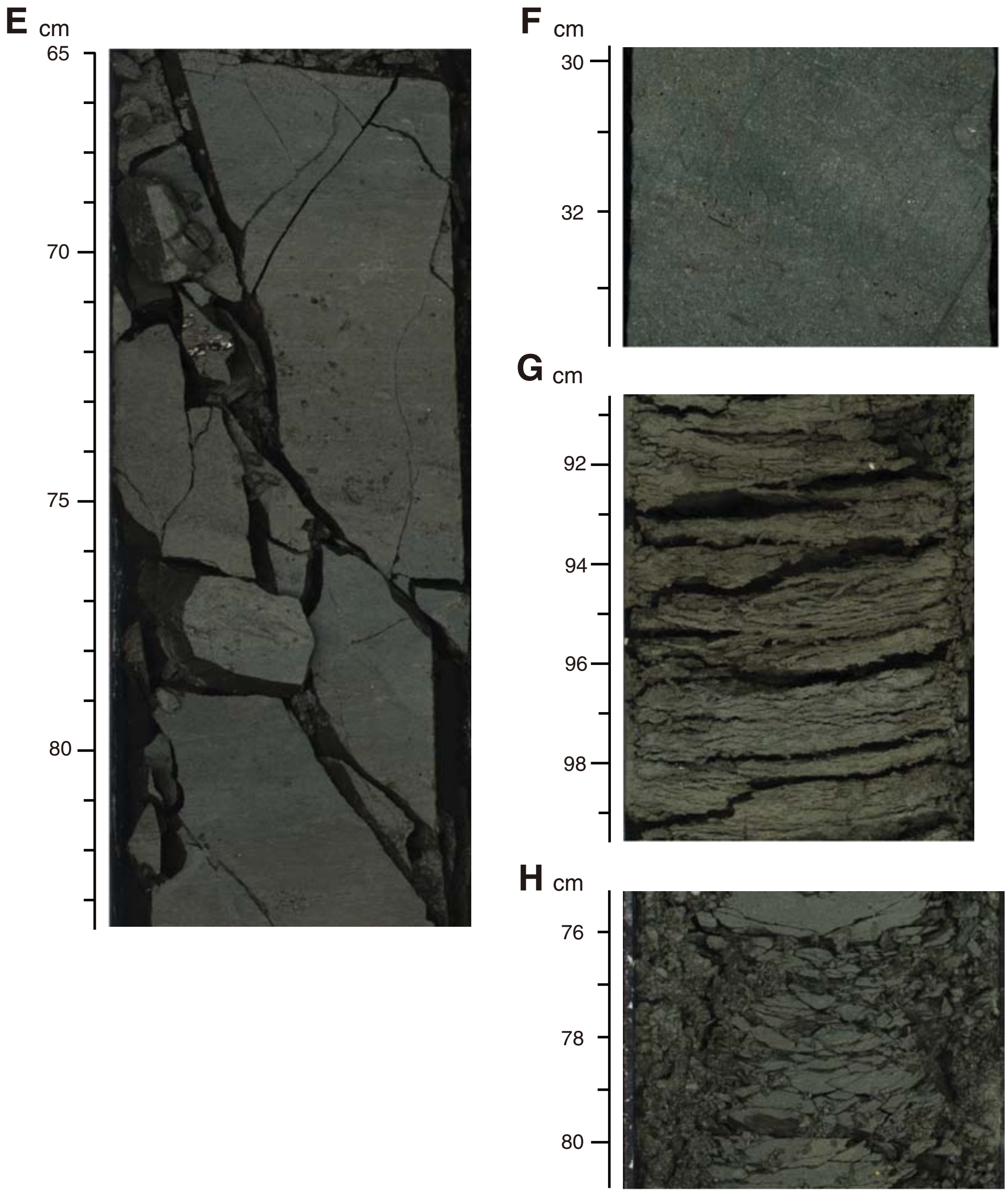

Figure F65. Dip angle variation of bedding, Holes C0002H, C0002J, C0002K, and C0002L.

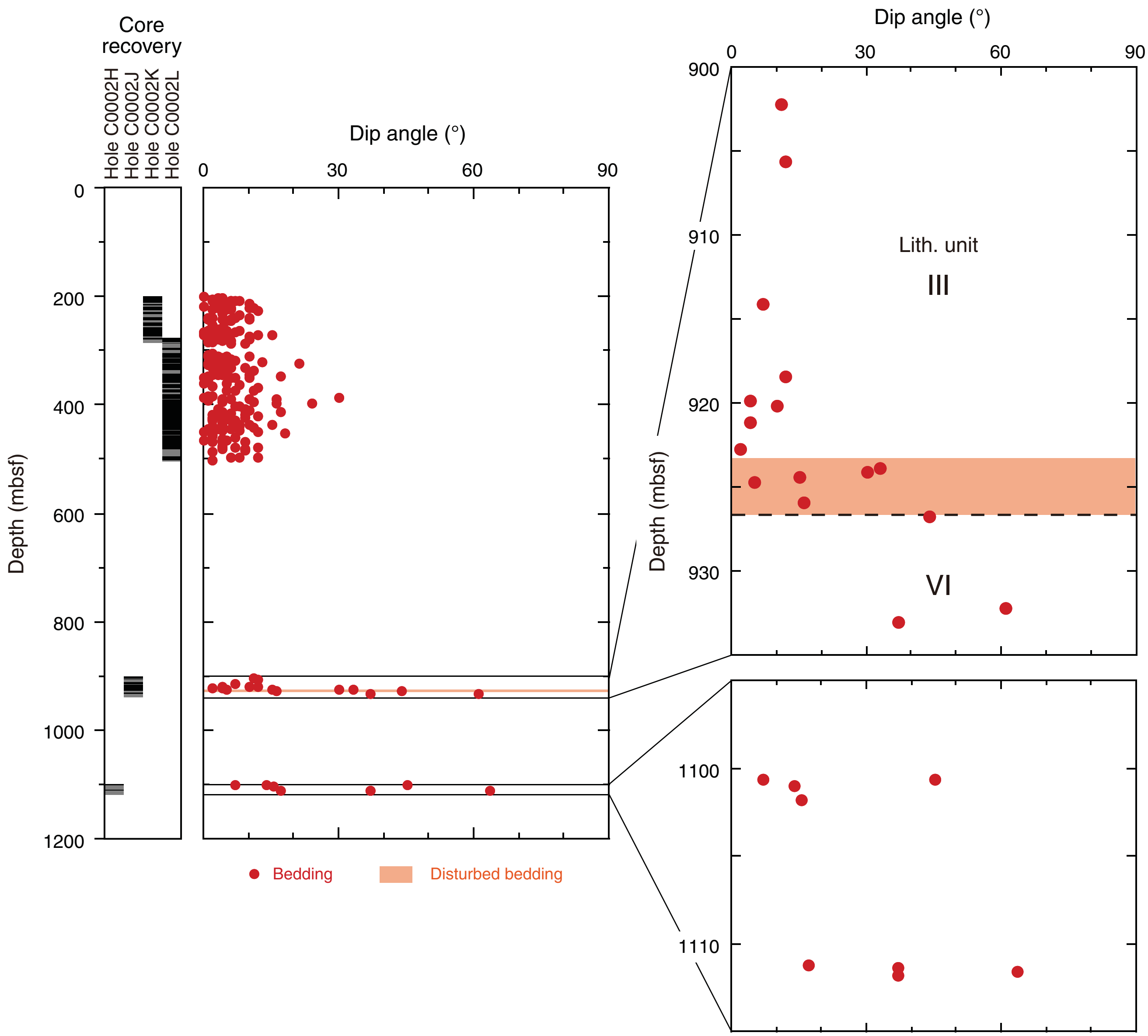

Figure F66. Lower-hemisphere equal-area projections of poles to bedding in cores. **A.** Bedding in Kumano Basin Unit III (Hole C0002J). **B.** Bedding in accretionary prism Unit IV (Holes C0002H and C0002J).

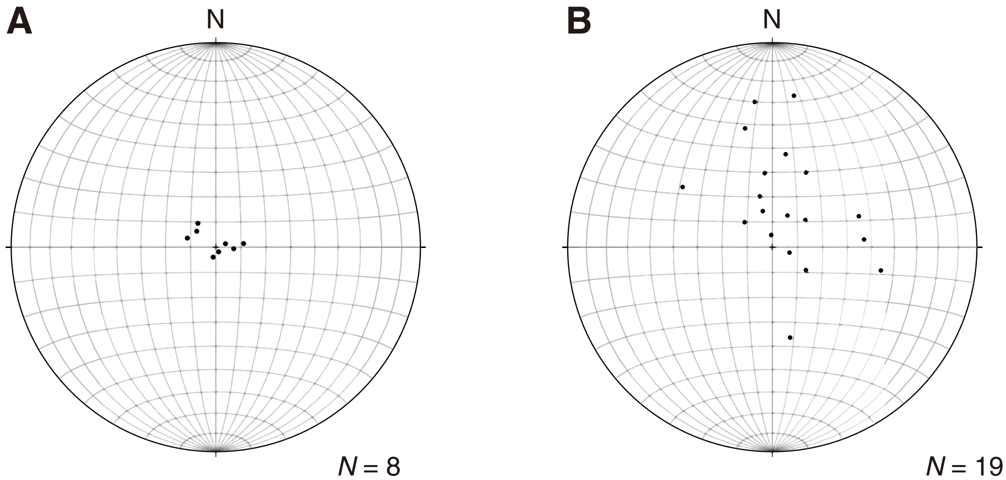

Figure F67. Dip angle variation of faults, joints, and deformation bands, Holes C0002H and C0002J–C0002L.

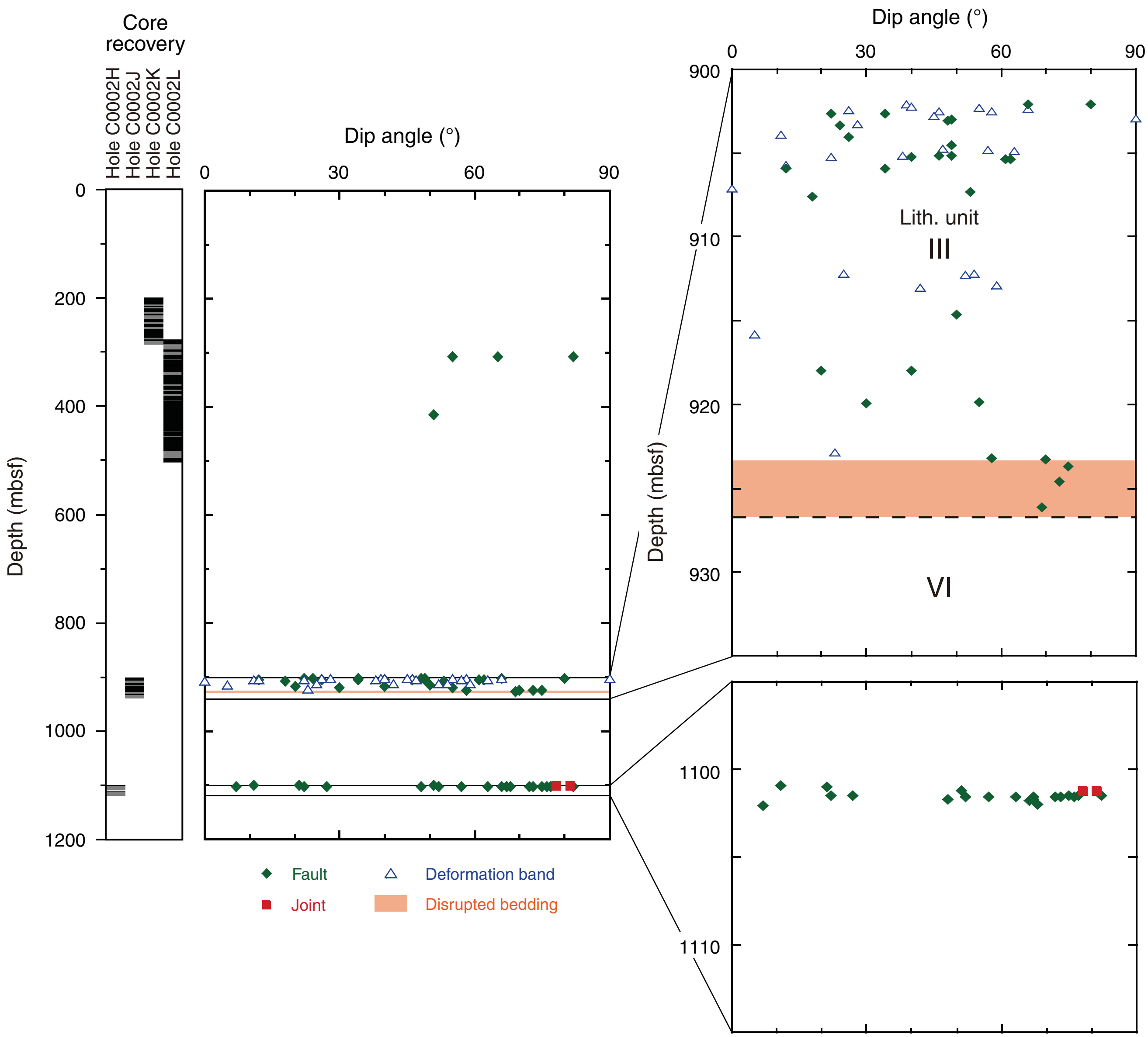

Figure F68. Lower-hemisphere equal-area projections of fault orientations in cores (reoriented into true geographic coordinates). Lines (left) and dots (right) show great circles and their poles, respectively. Dots and arrows on great circles = striations and slip vectors of hanging wall relative to footwall. **A.** Faults in Kumano Basin Unit III (Hole C0002J). **B.** Faults in accretionary prism Unit IV (Holes C0002H and C0002J).

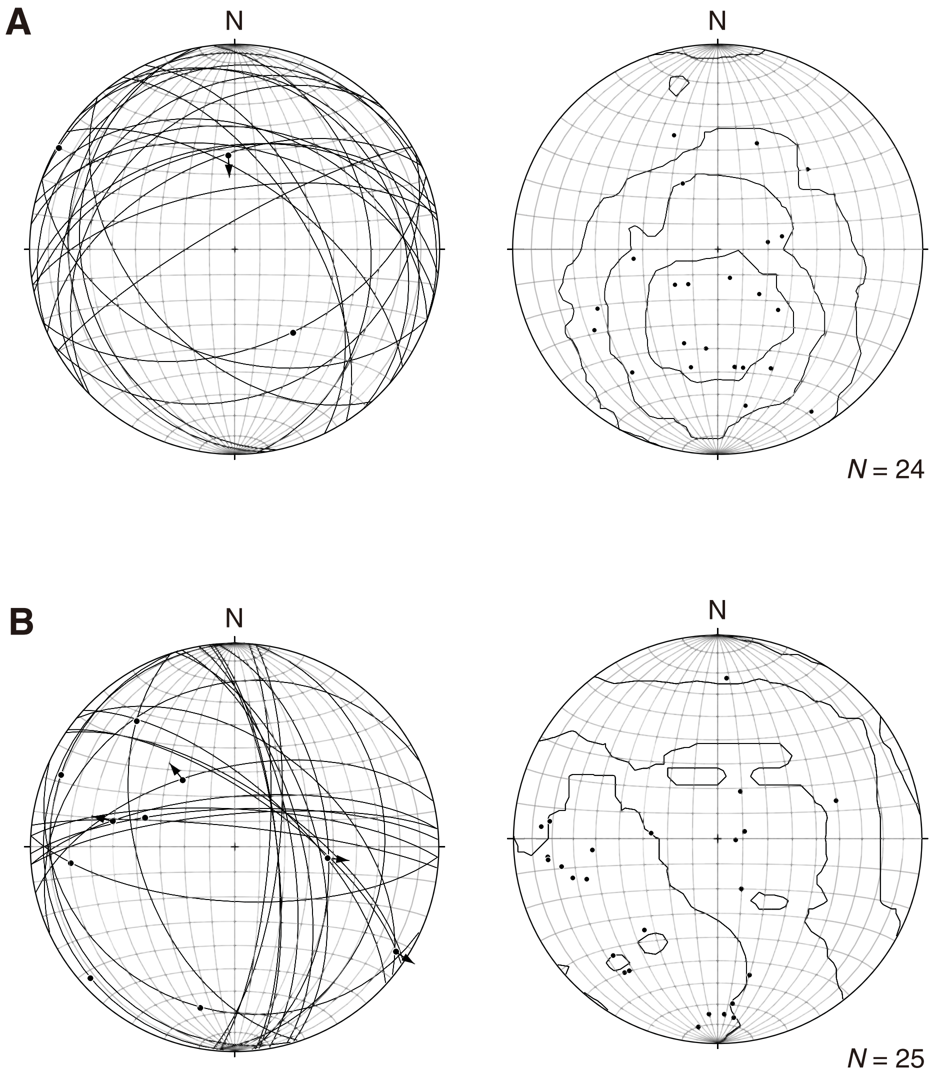

Figure F69. Normal fault zone (interval 338-C0002H-1R-1, 99–120 cm). **A.** Photograph of the working-half split surface and corresponding sketch. **B.** X-ray computed tomography (CT) image corresponding to A. **C.** Lower-hemisphere equal-area projections of bedding and fault planes obtained from CT images of the same interval (reoriented into true geographic coordinates).

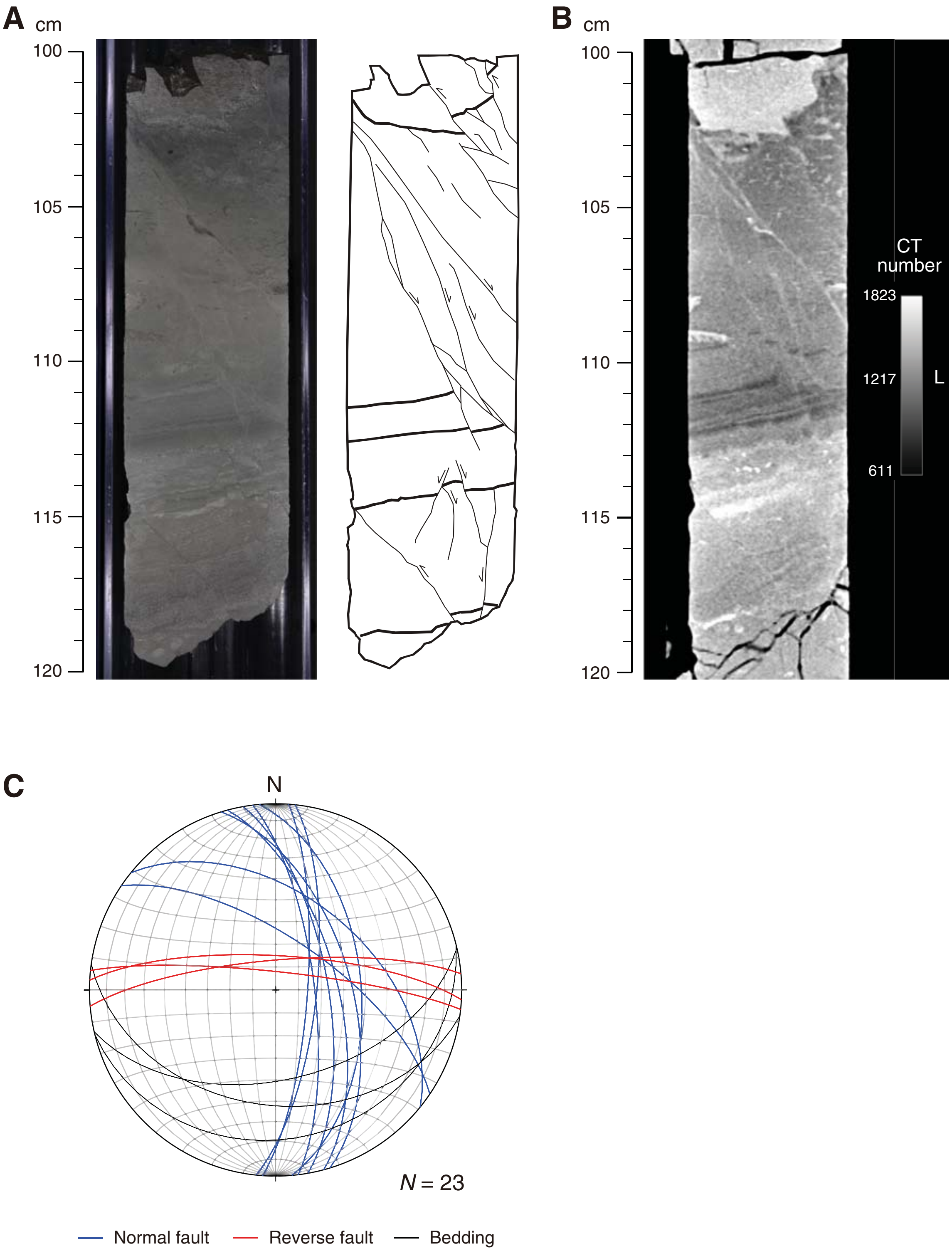

Figure F70. Lower-hemisphere equal-area projections of deformation bands (great circles and poles), Hole C0002J (reoriented into true geographic coordinates).

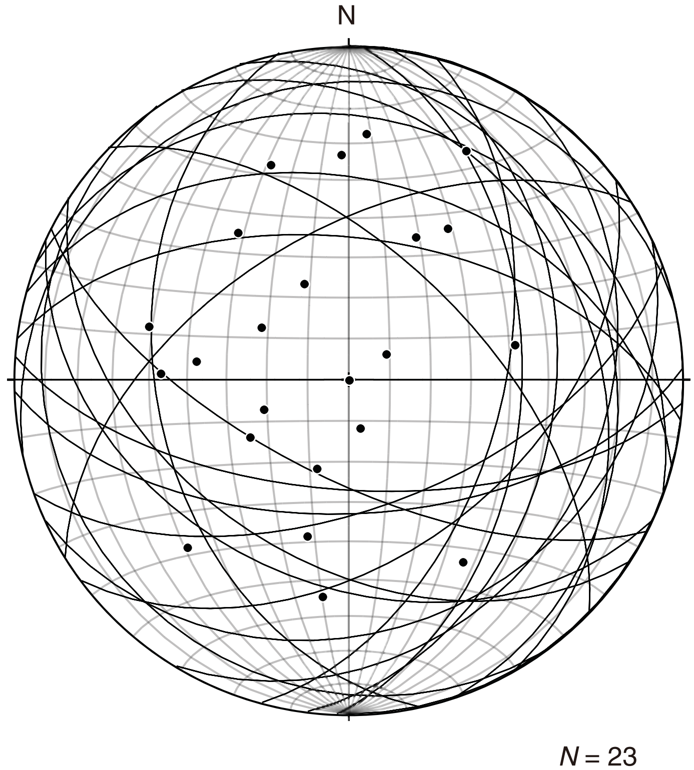

Figure F71. Variation of geochemical parameters and concentrations of dissolved salt in interstitial water samples from Holes C0002H (ground rock interstitial normative determination [GRIND] method), C0002J, C0002K, C0002L, C0002B, and C0002D. Salinity is calculated from refractive index. * = based on standard squeezing method. (Continued on next two pages.)

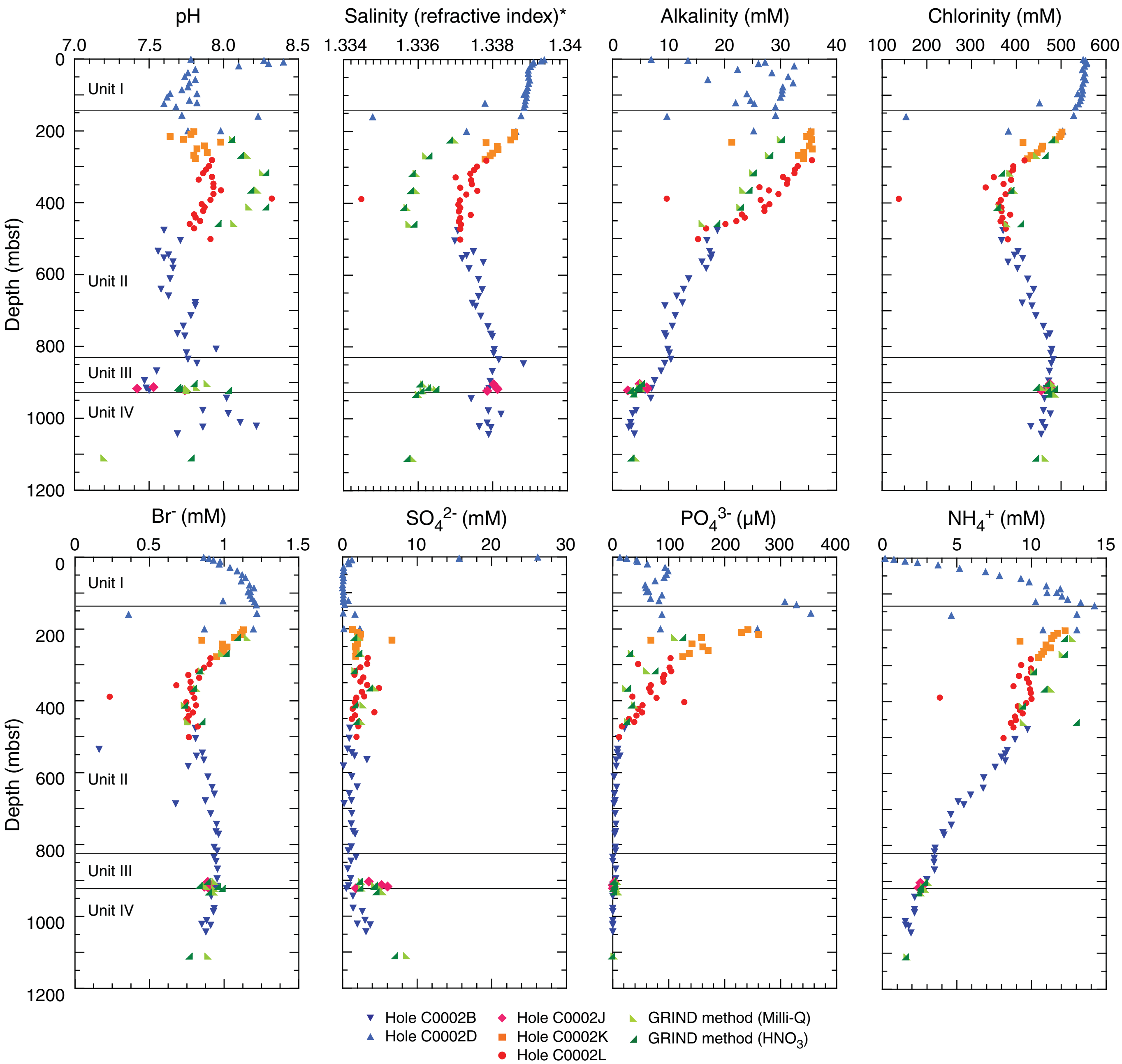

Figure F71 (continued). (Continued on next page.)

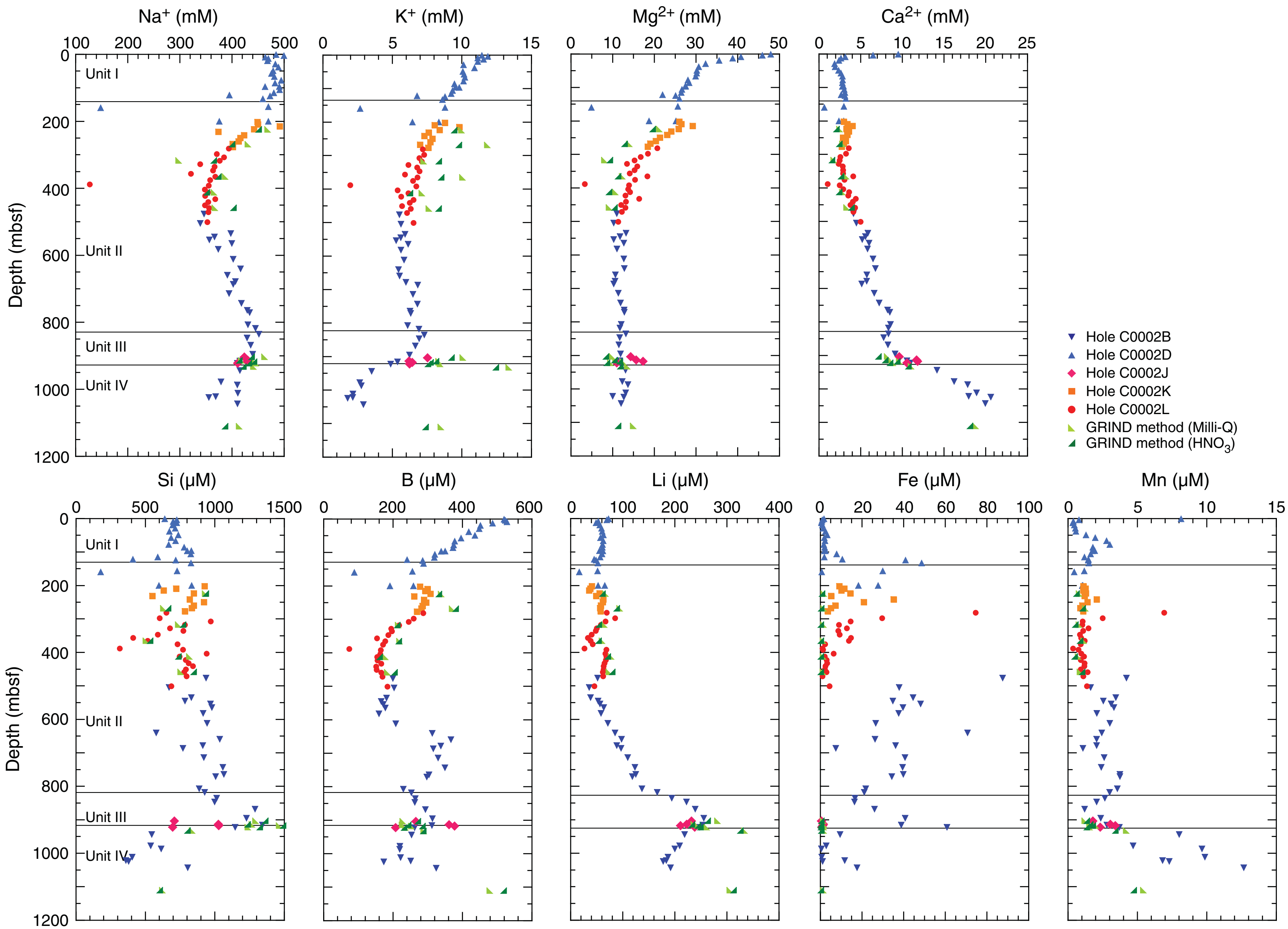

Figure F71 (continued).

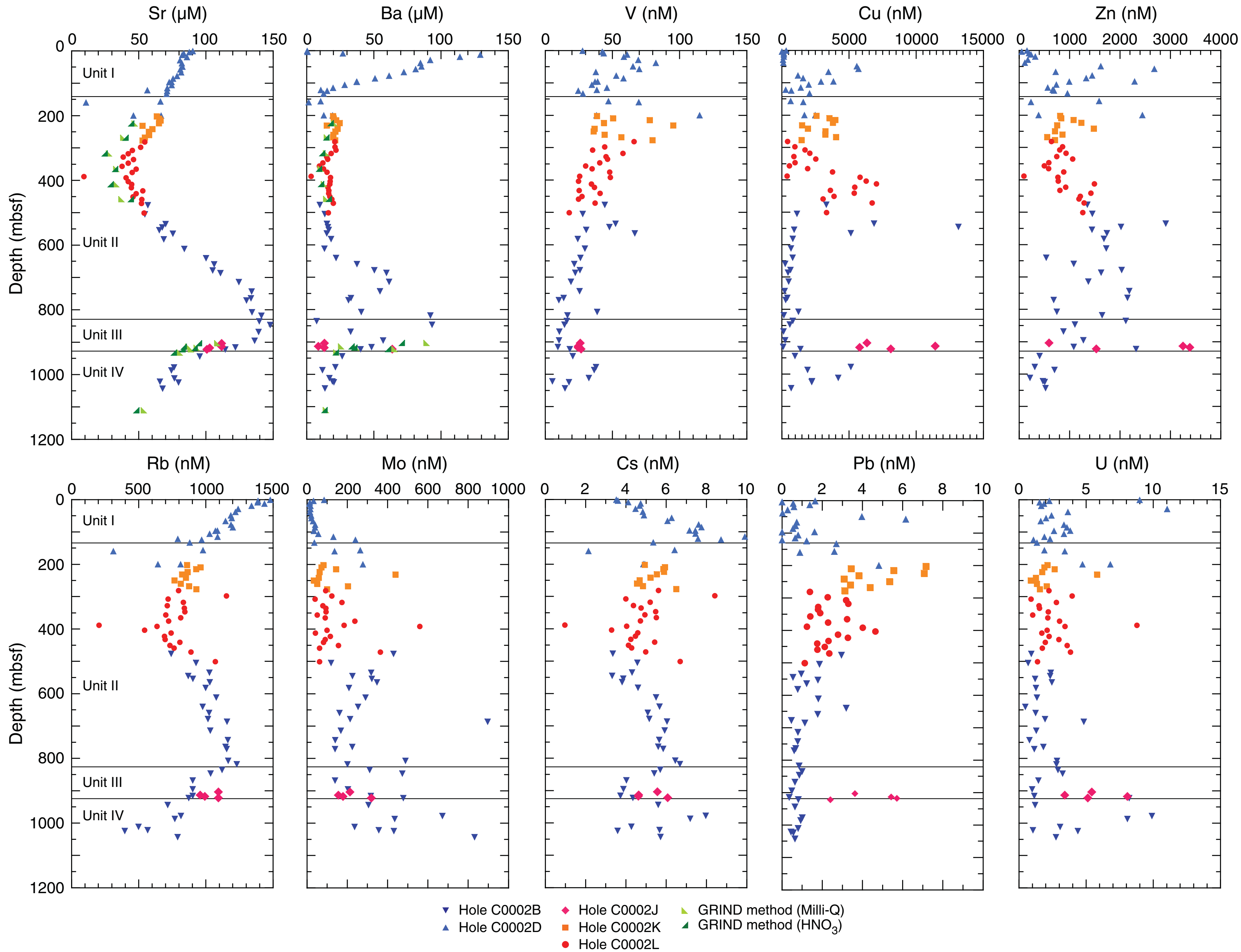

Figure F72. Concentrations obtained using the standard squeezing method plotted against those obtained using the ground rock interstitial normative determination (GRIND) method, Holes C0002H and C0002J. Milli-Q and HNO_3 numbers give the slope of least-square fitted lines and correlation coefficients (*R*) in parentheses. Light green triangles = data from Milli-Q water extracted solution, dark green triangles = data from diluted HNO_3 extracted solution, black line = 1:1 ratio of the concentrations, green lines = least-square fitted lines, corresponding to each colored data. (Continued on next four pages.)

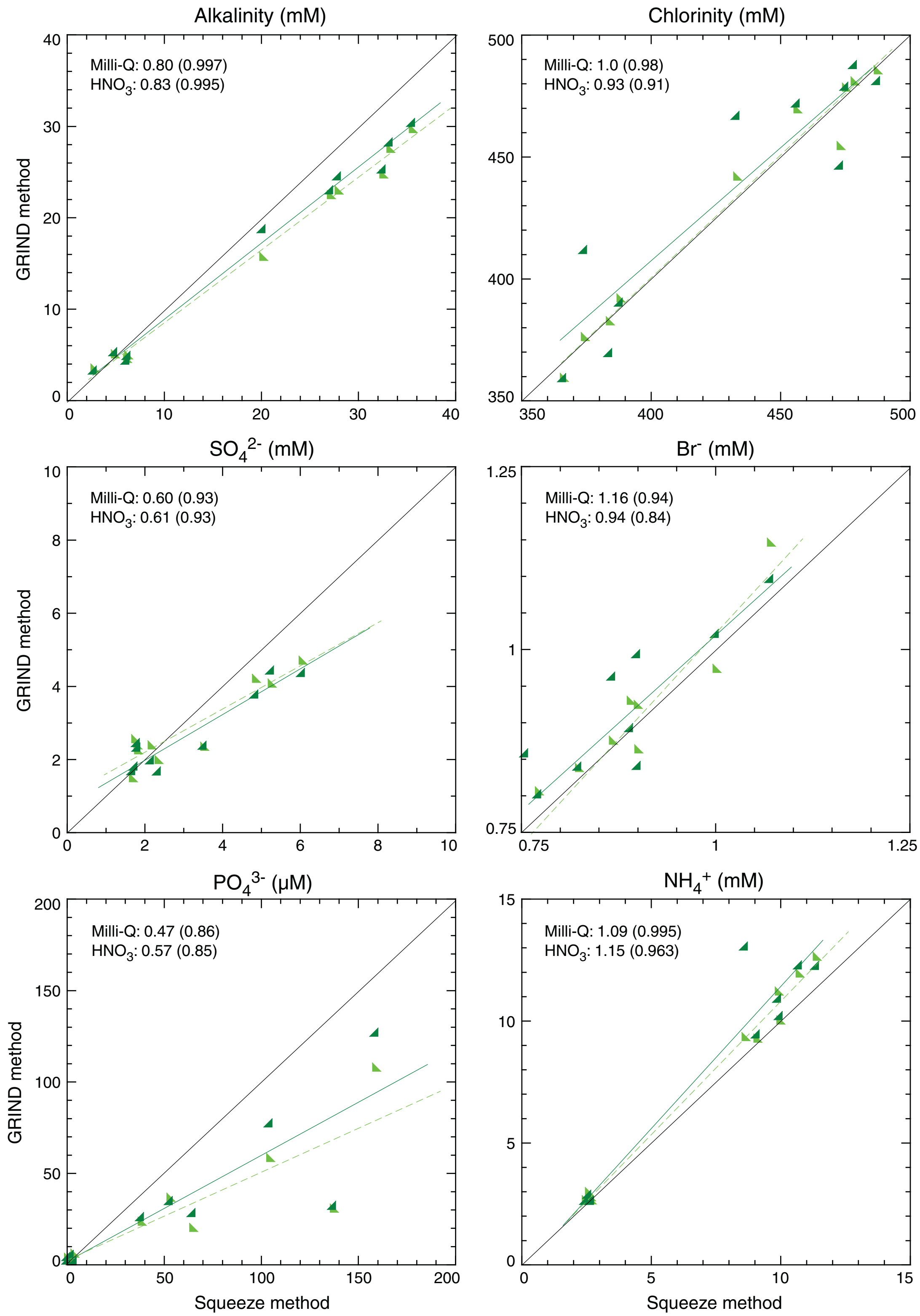

Figure F72 (continued). (Continued on next page.)

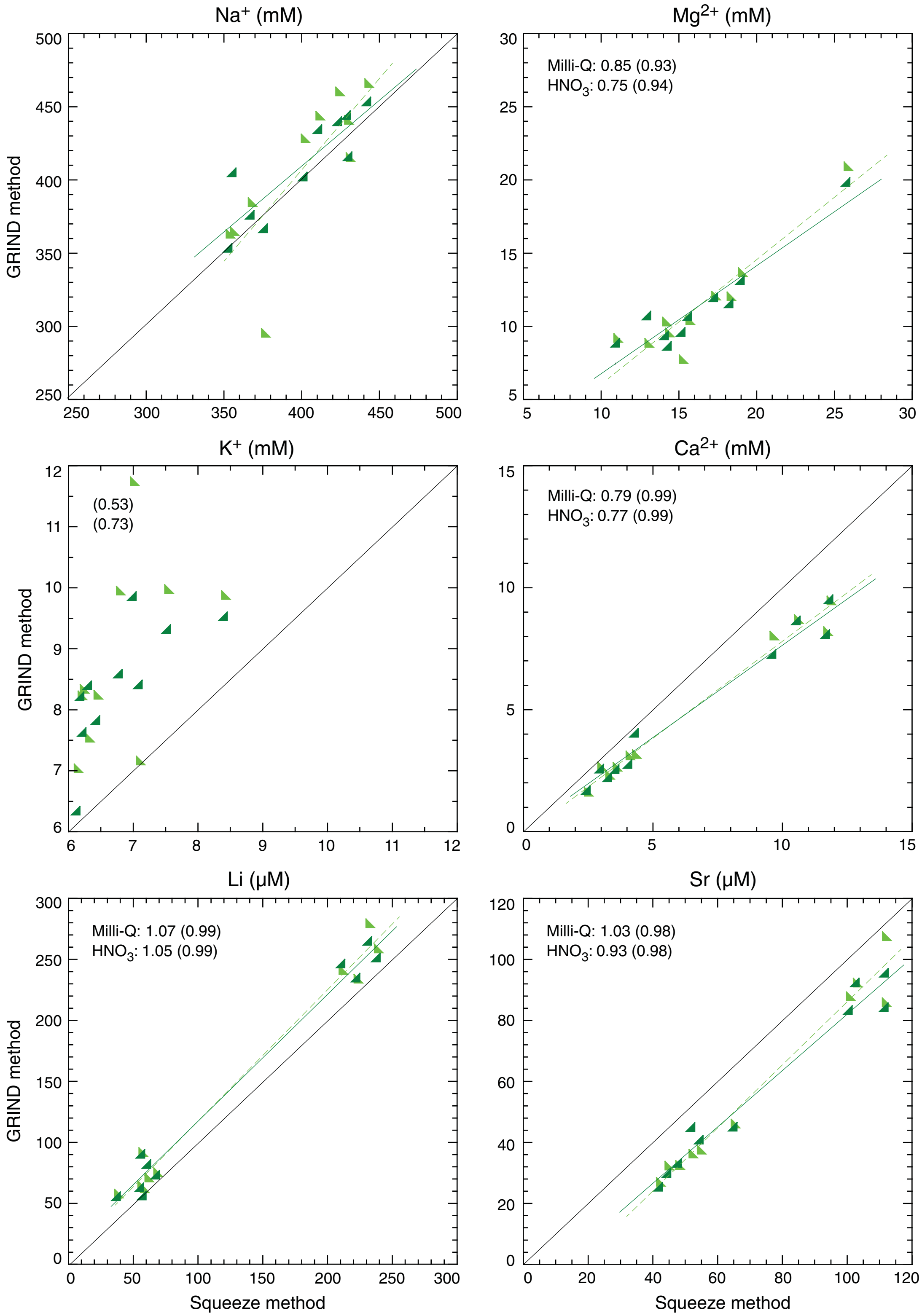

Figure F72 (continued). (Continued on next page.)

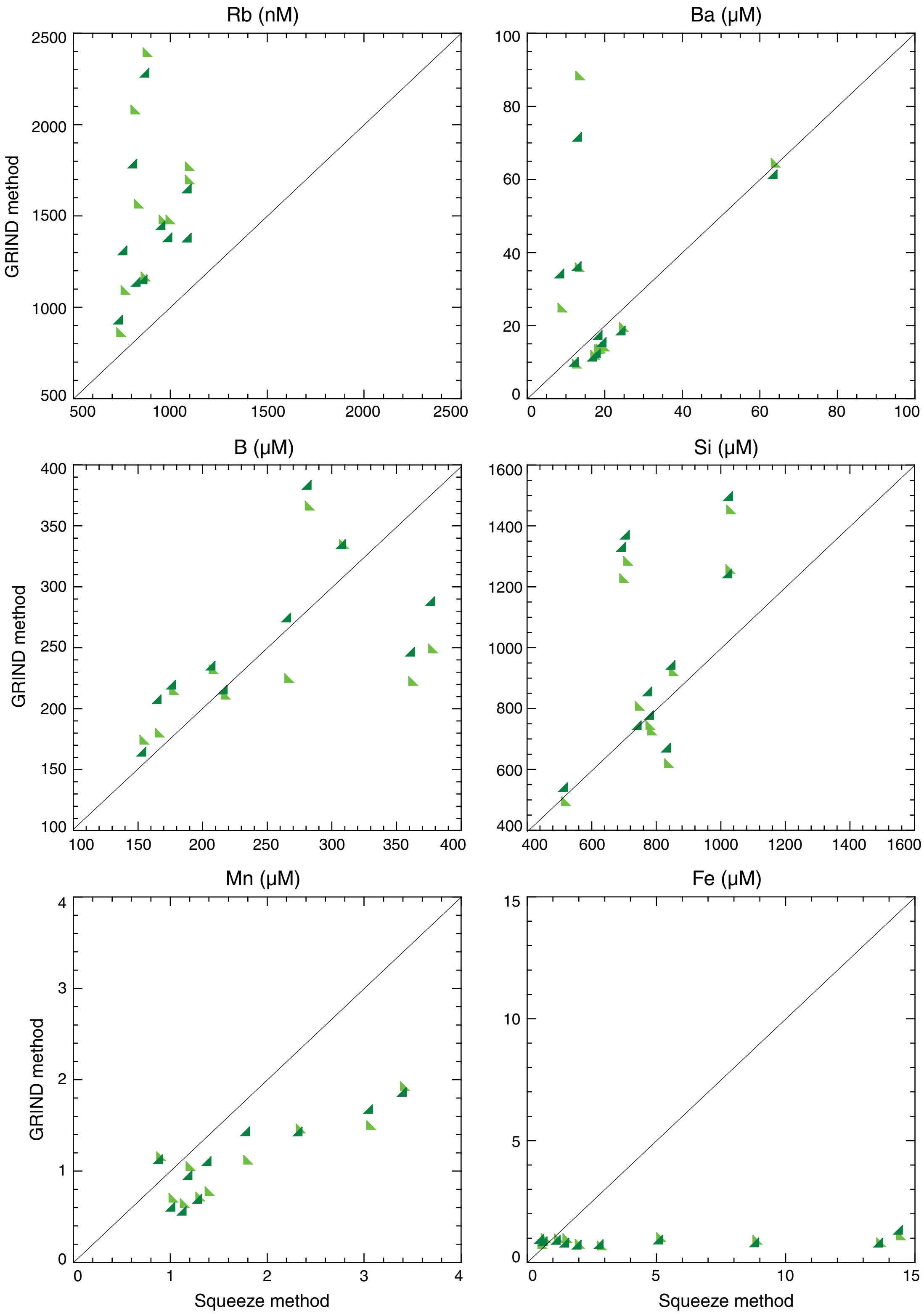

Figure F72 (continued). (Continued on next page.)

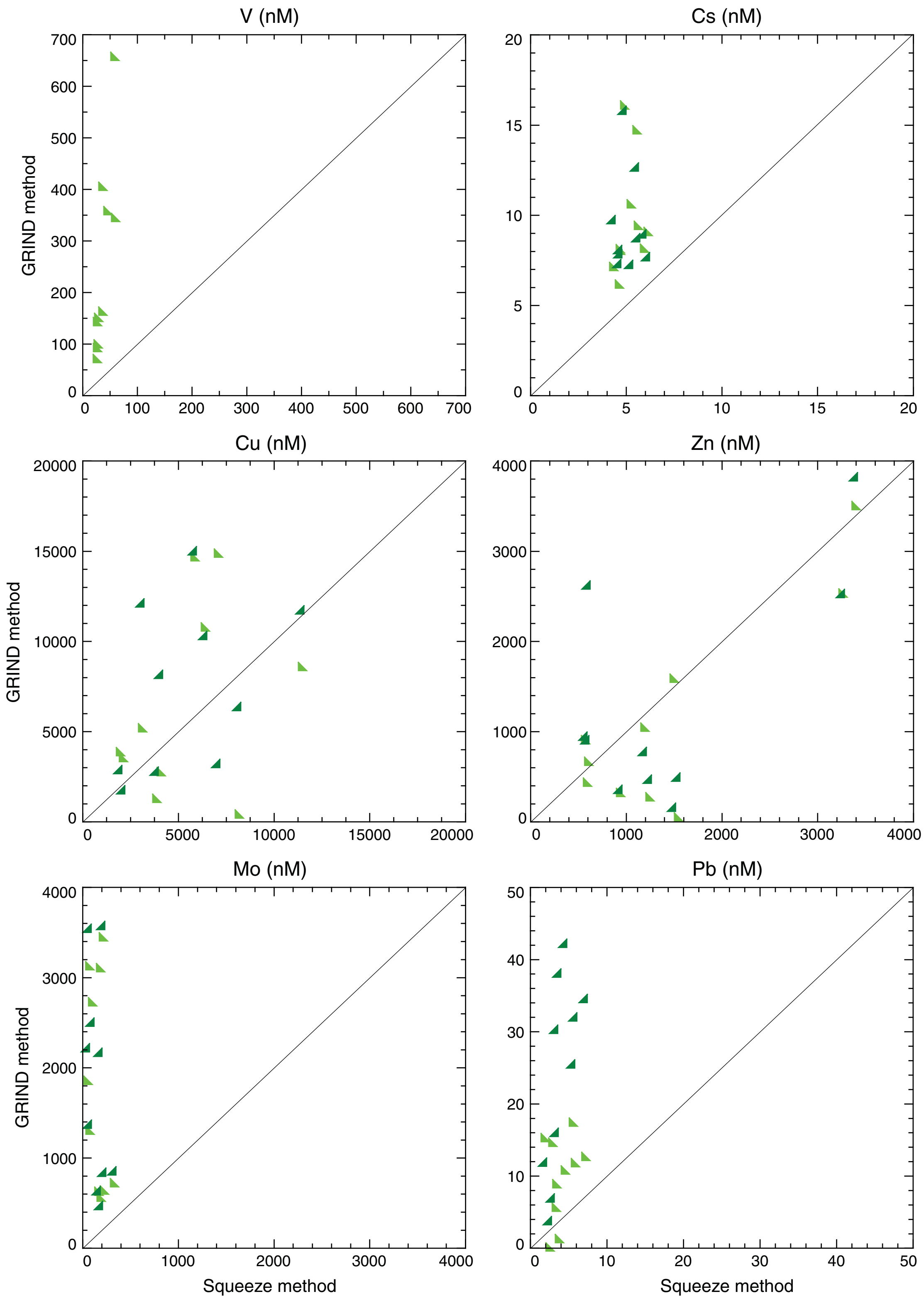

Figure F72 (continued).

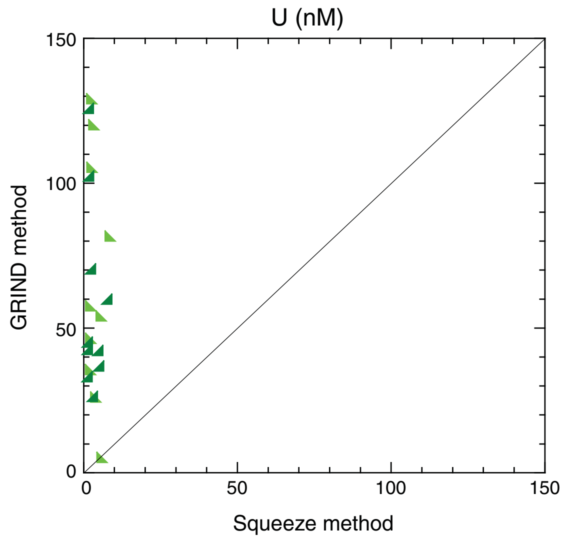

Figure F73. Comparison of data obtained by conventional and additional methods for extracting headspace gas, Holes C0002H and C0002J–C0002L. Oven = samples analyzed by the conventional method using an oven, NaOH = samples analyzed by the additional method using an alkaline solution (NaOH). Dashed diagonal 1:1 line is provided for reference.

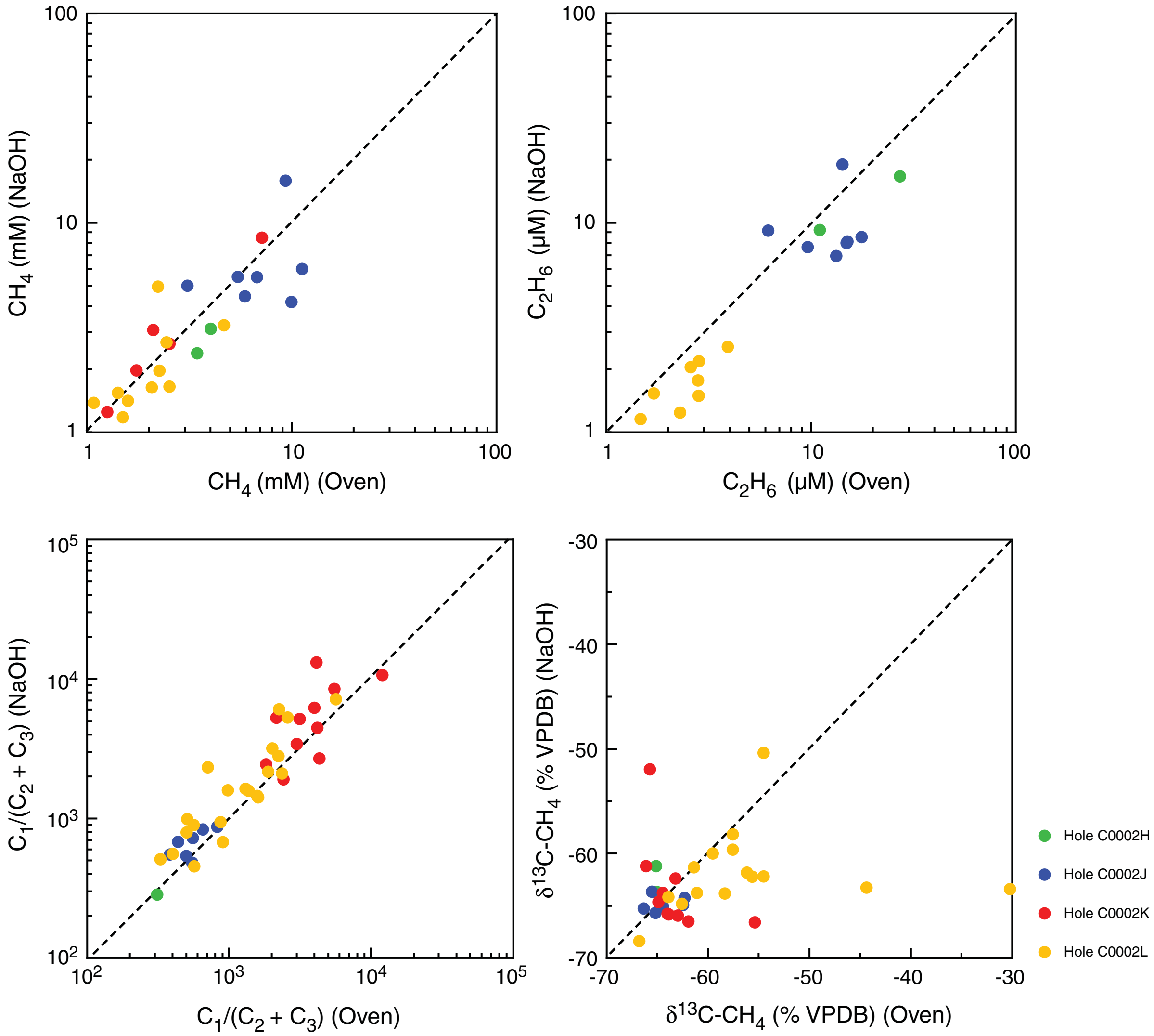

Figure F74. Vertical profiles of methane, ethane, and propane concentrations in headspace gas samples, Site C0002. Horizontal lines = Hole C0002B lithologic unit boundaries.

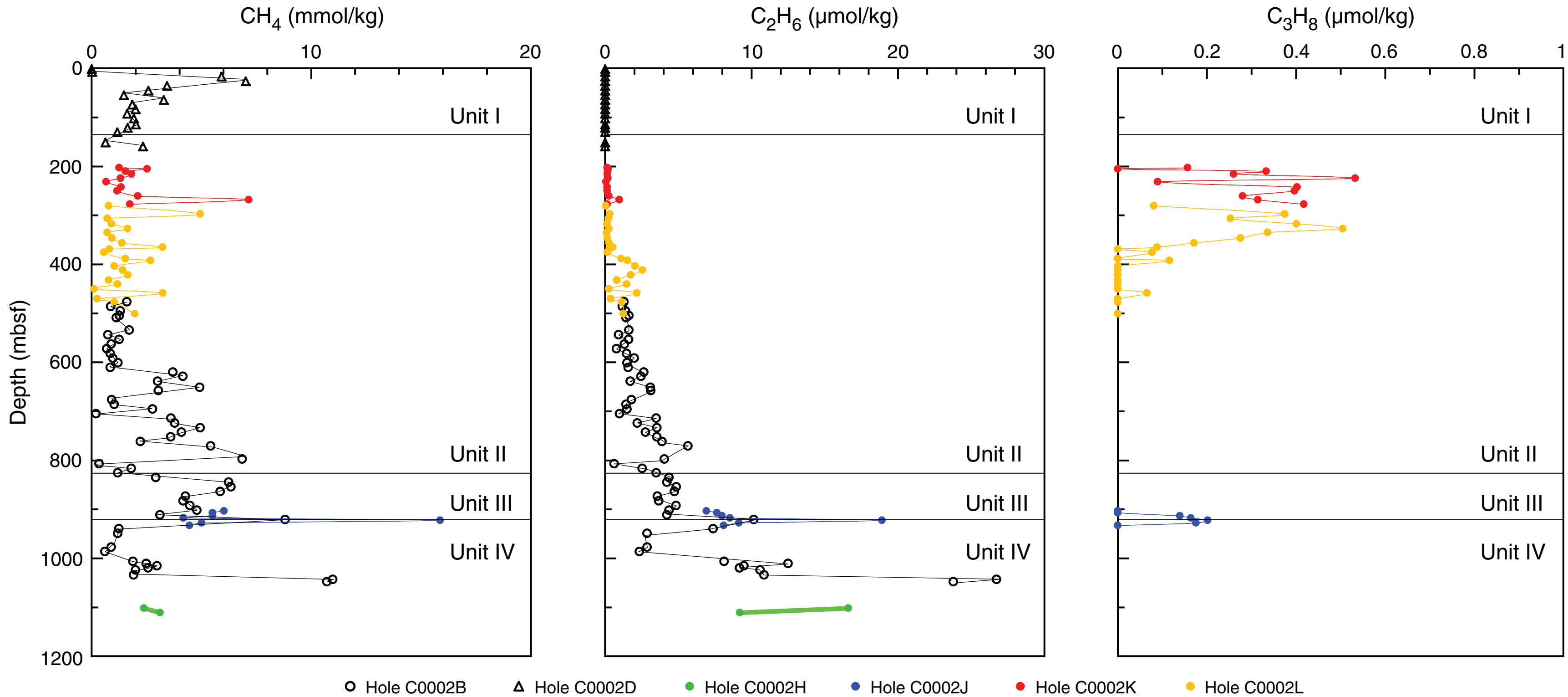

Figure F75. Methane concentrations determined by different measurement techniques, estimates of organic matter from cuttings (see **"Lithology"**), and Rn data, Hole C0002F. For methane carbon isotope analyzer (MCIA), an envelope was plotted (black); shaded region = original data. The different gas data sets show an overall good correlation in trends. Six different hydrocarbon gas boundaries were defined. GC-FID = gas chromatograph–flame ionization detector, PGMS = process gas mass spectrometer.

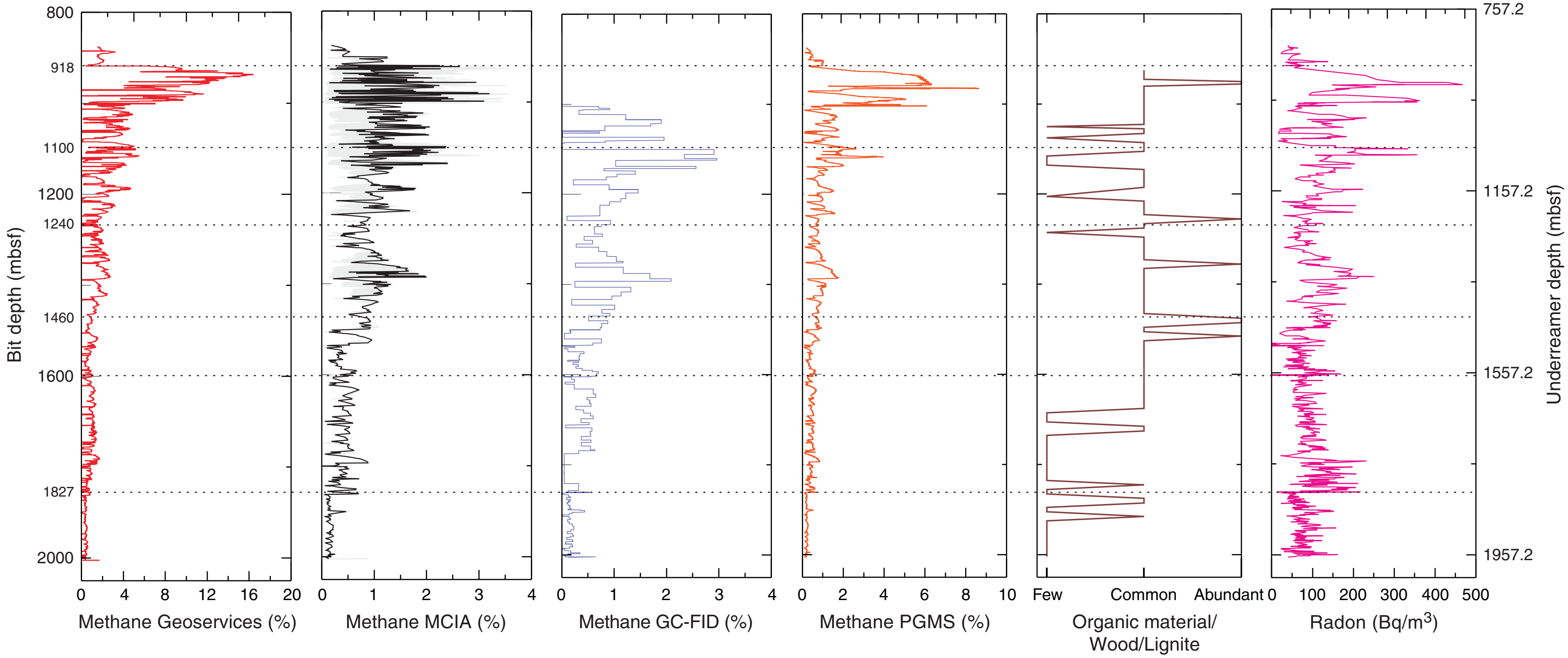

Figure F76. Vertical profiles of $C_1/(C_2 + C_3)$ ratios as well as $\delta^{13}C\text{-}CH_4$ calculated from headspace gas samples (solid symbols) (see Table T35), Site C0002. VPDB = Vienna Peedee belemnite. Horizontal lines = Hole C0002B lithologic unit boundaries.

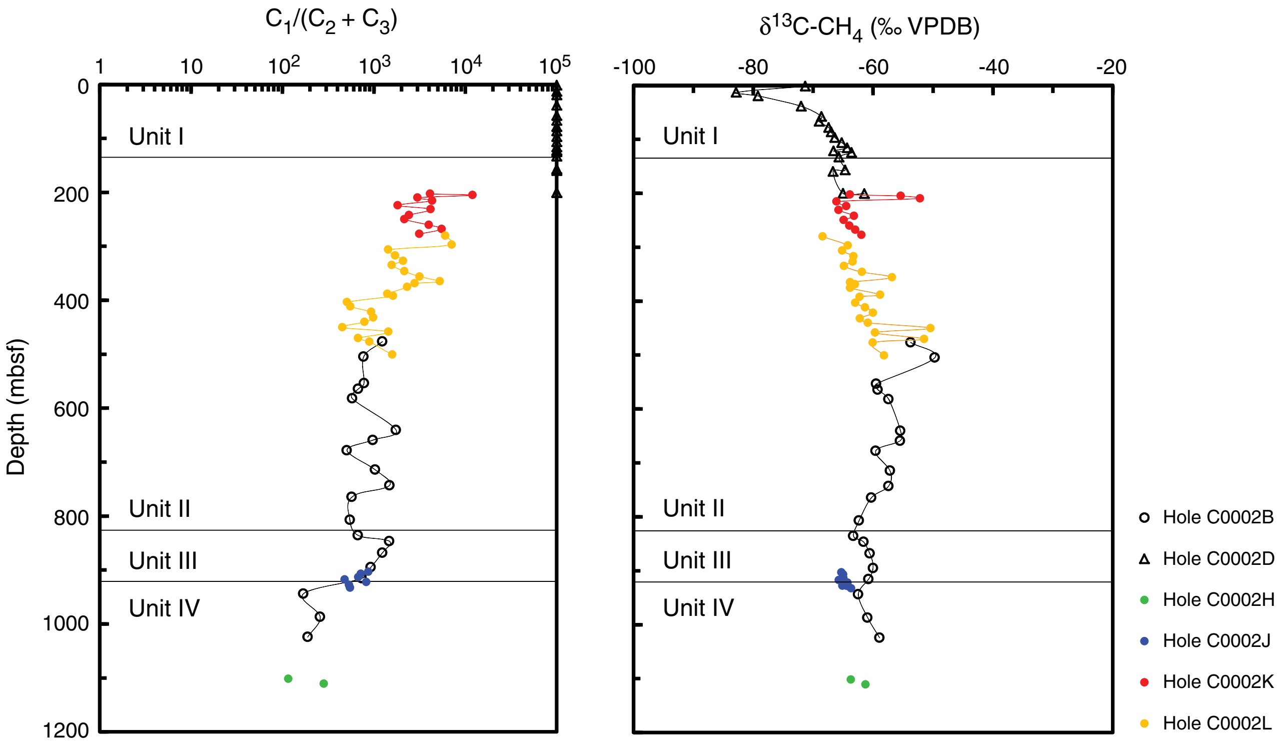

Figure F77. Relationship between the $C_1/(C_2 + C_3)$ ratios and $\delta^{13}C\text{-}CH_4$ in headspace gas, Site C0002. Open star = end-member of microbial methane, solid star = end-member of thermogenic methane, presumed so that the mixing line between the two end-members best fits the observed data. Solid curve = mixing line between the two end-members. Percent values indicate the contribution of thermogenic methane. VPDB = Vienna Peedee belemnite.

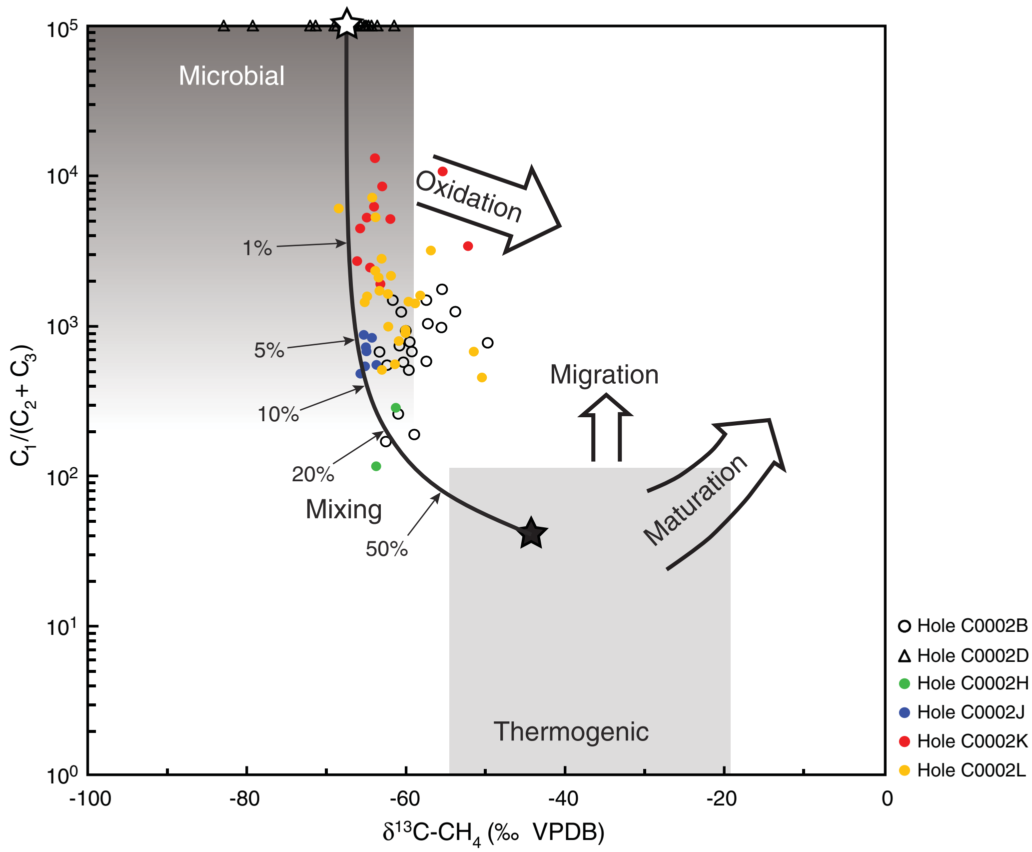

Figure F78. Overview of hydrocarbon gas and total gas concentrations determined by Geoservices, Hole C0002F. With increasing depth, total gas and methane concentrations decrease significantly.

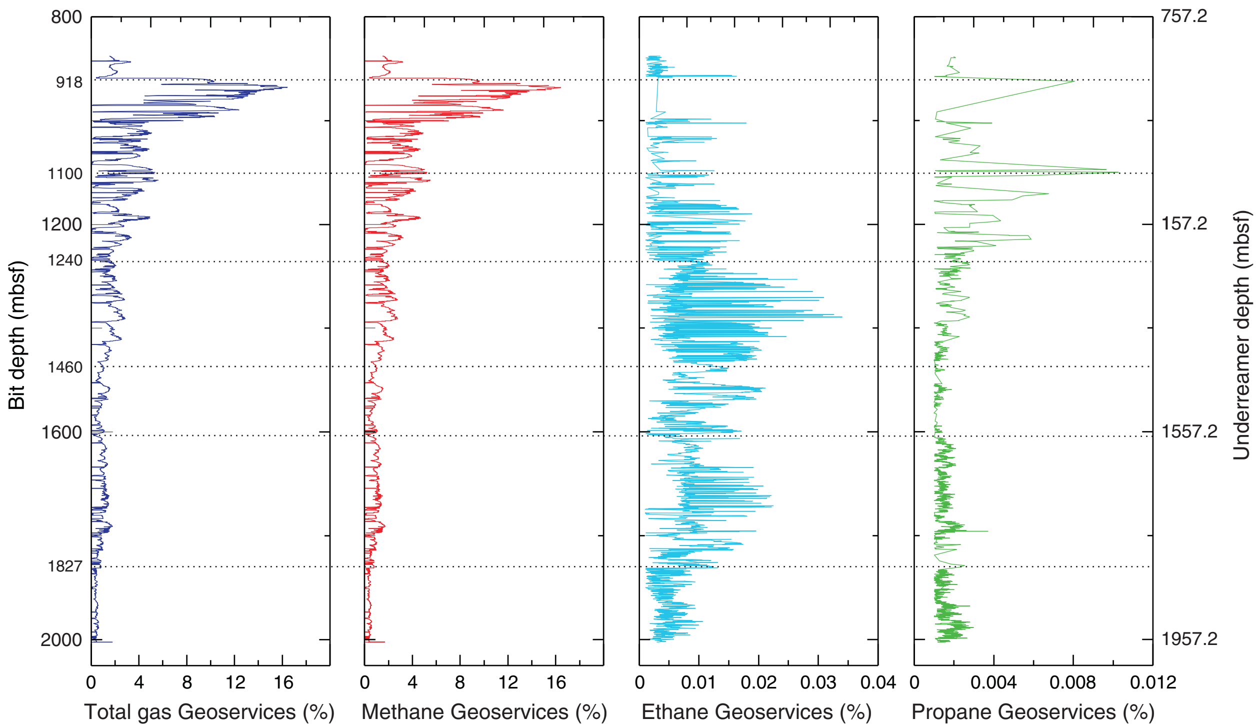

Figure F79. Ethane and propane data determined by gas chromatograph–flame ionization detector (GC-FID) and data set provided by Geoservices, estimates of organic matter from cuttings (see **"Lithology"**), and Rn data, Hole C0002F. The different gas data sets show overall good correlation in relative trends. Six different hydrocarbon gas boundaries were defined.

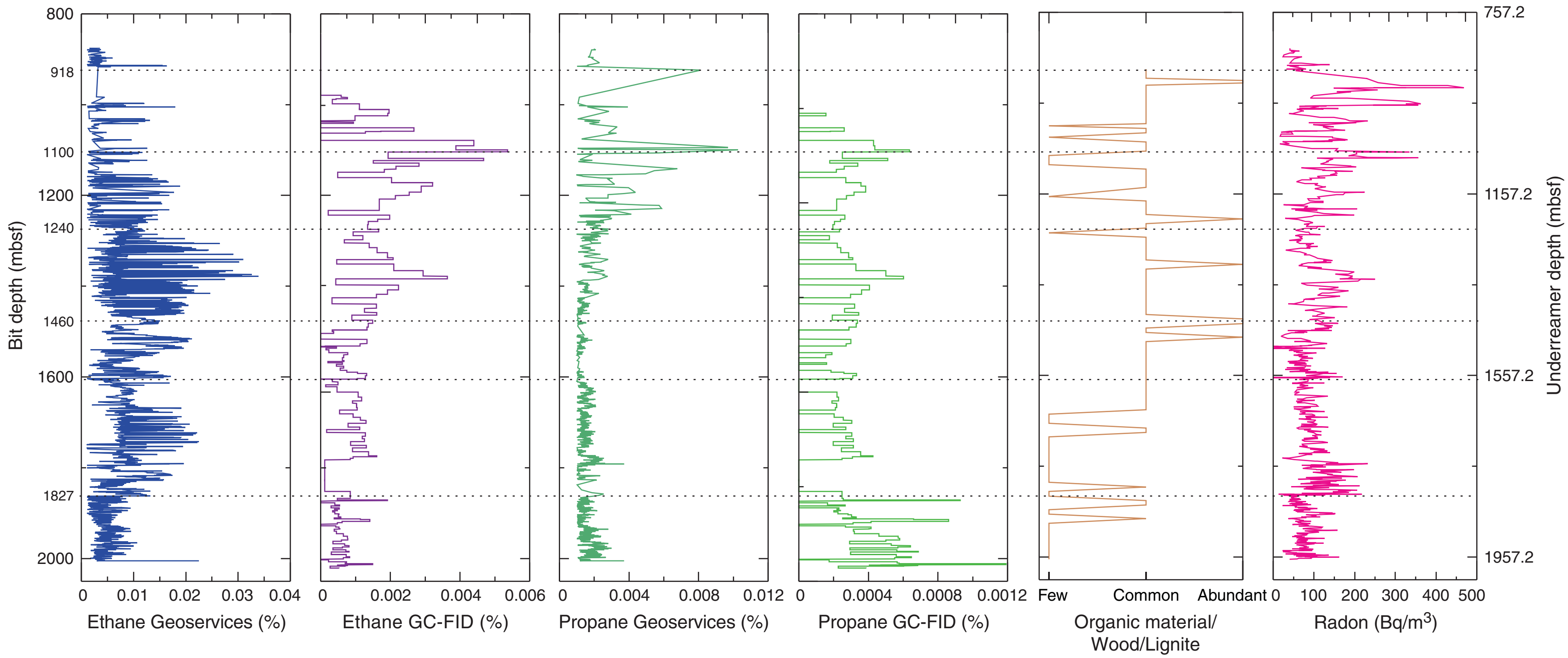

Figure F80. Plot of PGMS, Rn, and CO_2 data provided by Geoservices, Hole C0002F. The data are characterized by several different shifts and/or peaks, some of which are correlatable across all gas species. Red arrows = depths where downtimes exceeded 120 min, green arrow = downtime of 39.5 min. Nonhydrocarbon boundary depths: A = 918 mbsf, B = 1000 mbsf, C = 1060 mbsf, D = 1240 mbsf, E = 1540 mbsf, F = 1600 mbsf, G = 1855 mbsf, and H = 1933 mbsf. (Continued on next page.)

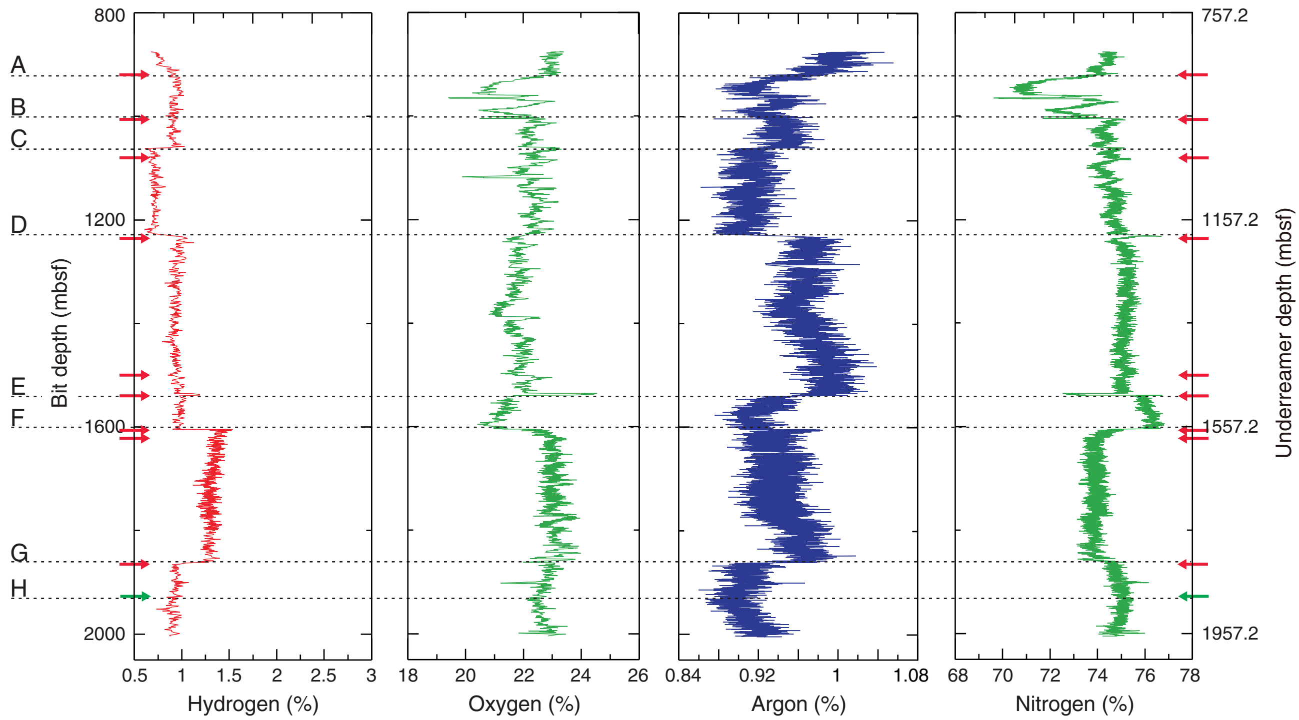

Figure F80 (continued).

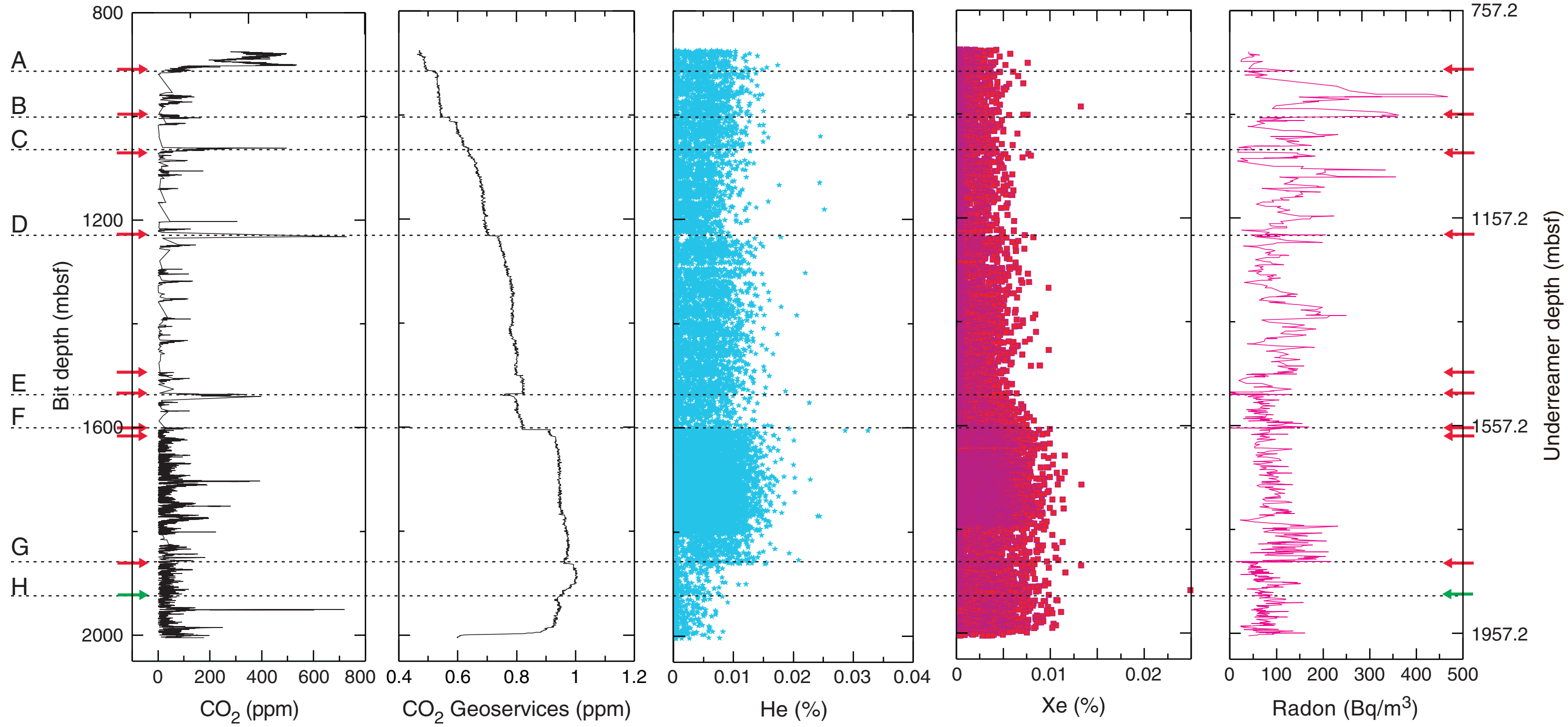

Figure F81. Total gas and Bernard parameters based on hydrocarbon gas data provided by Geoservices and determined by gas chromatograph–flame ionization detector (GC-FID), Hole C0002F. $\delta^{13}C$ values were measured by the MCIA and relative abundance of organic material is given as estimated from cuttings (see **"Lithology"**). For better visualization, only Bernard parameters based on significant amounts of ethane and/or propane (i.e., >0.0001%) were plotted. Red dotted line in $\delta^{13}C$ plot = beginning of a thermogenic signature (> –60‰). The boundary at 918 mbsf as seen in the gas data and defined by LWD (left column) and lithology is also visible in Bernard parameters and organic material. At ~1700 mbsf, a gradual shift to thermogenic signatures such that ($C_1/(C_2 + C_3)$) decreases and $\delta^{13}C$ becomes > –60‰ is visible. Between 1800 and 1827 mbsf, a step in the Bernard parameter occurs, whose lower boundary correlates well with a drop in total gas concentration.

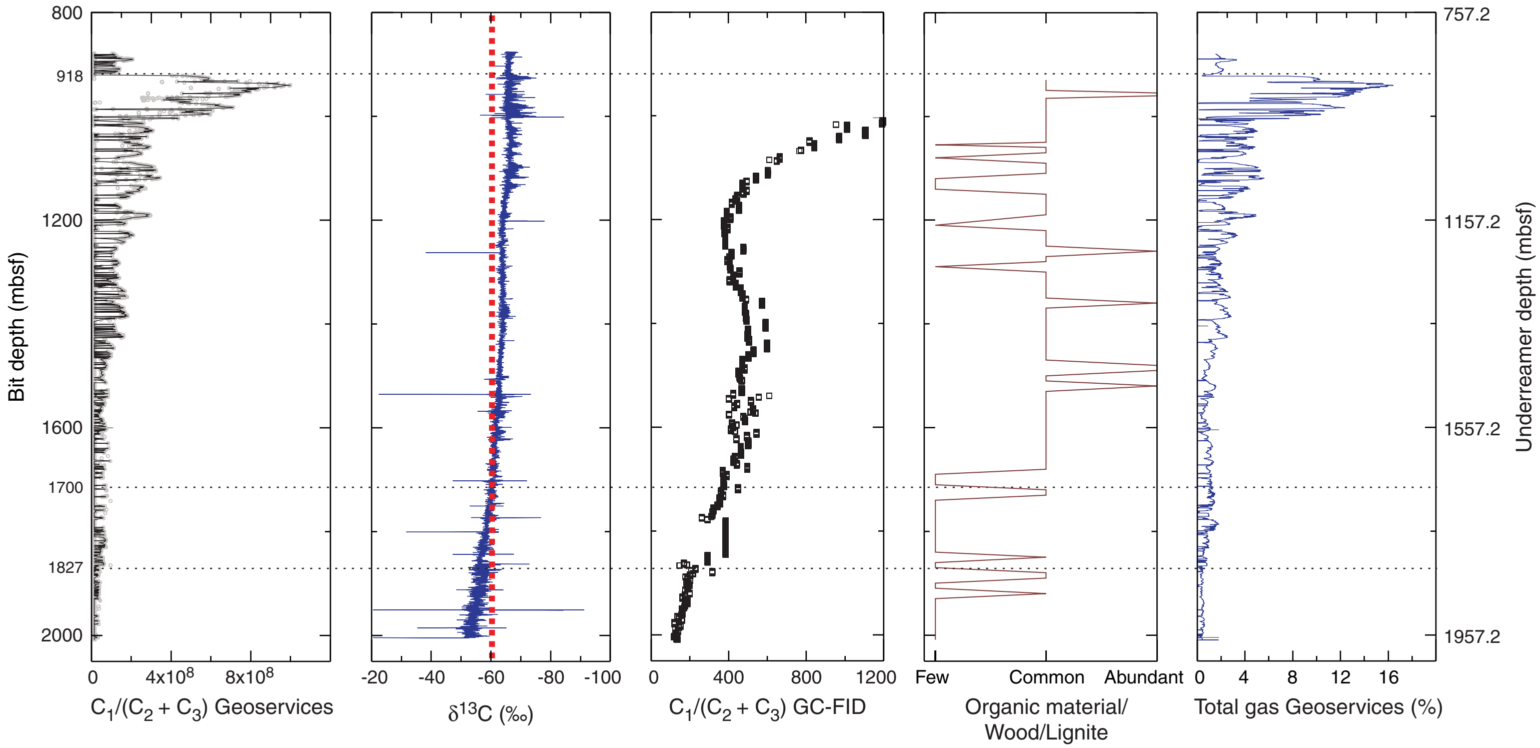

Figure F82. Logging unit boundaries, hydrocarbon (HC), and nonHC gas package boundaries, as defined in previous figures, Hole C0002F. See text for further explanation.

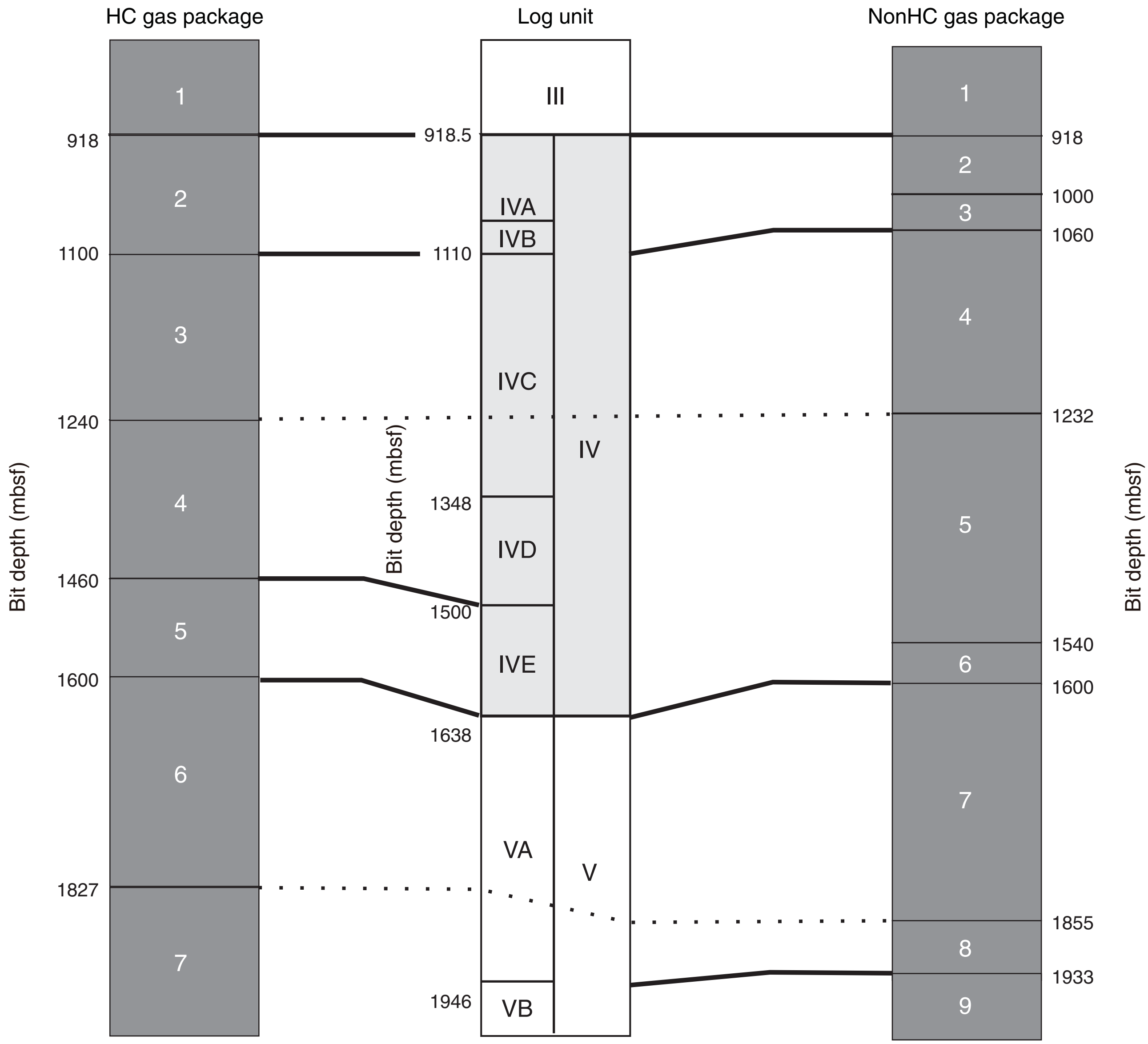

Figure F83. $CaCO_3$, total organic carbon (TOC), total nitrogen (TN), and C/N from Holes C0002F (solid symbols) and C0002B (open symbols). Dashed vertical line in the C/N plot = distinction between marine (<10) and terrestrial (>10) sources of organic matter (Meyers, 1997).

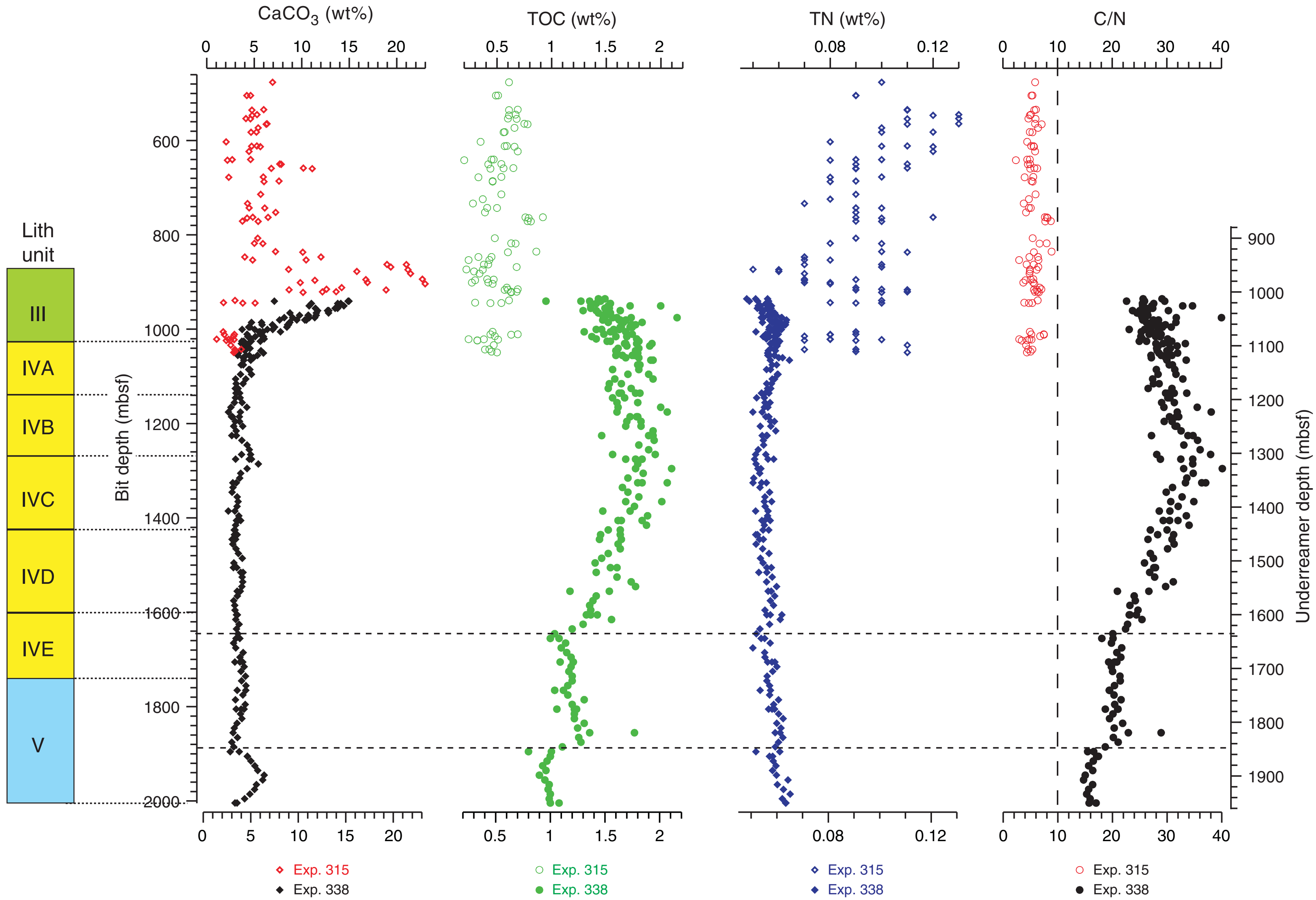

Figure F84. $CaCO_3$, total organic carbon (TOC), total nitrogen (TN), total sulfur (TS), and C/N from Holes C0002B, C0002H, C0002J, C0002K, C0002L, and C0002F.

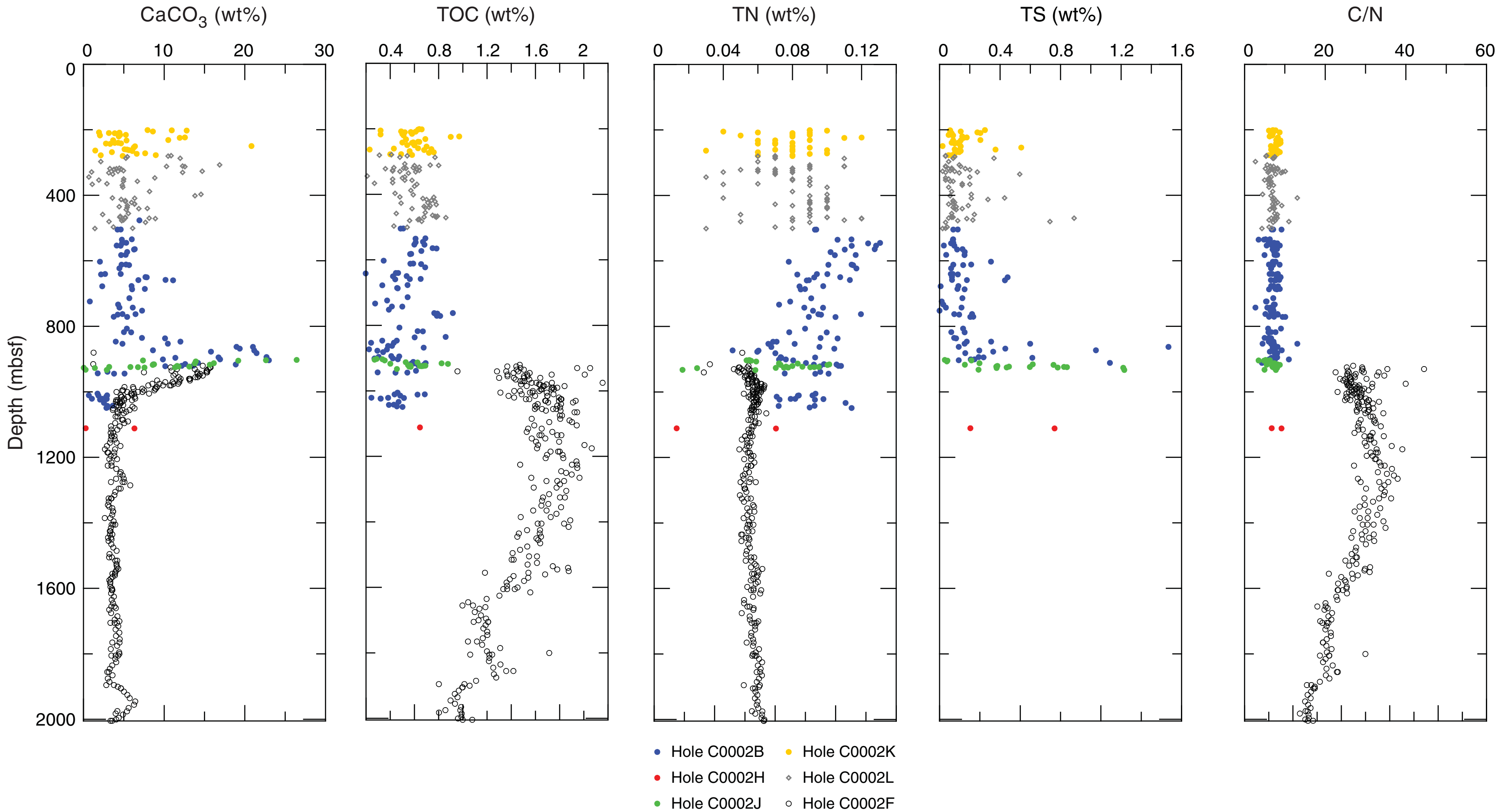

Figure F85. MSCL-W measurements, Site C0002. Red = Expedition 338 data, black = Expedition 315 data. **A.** Gamma ray attenuation (GRA) bulk density. **B.** Magnetic susceptibility. **C.** Natural gamma radiation (NGR). cps = counts per second. **D.** Noncontact electrical resistivity.

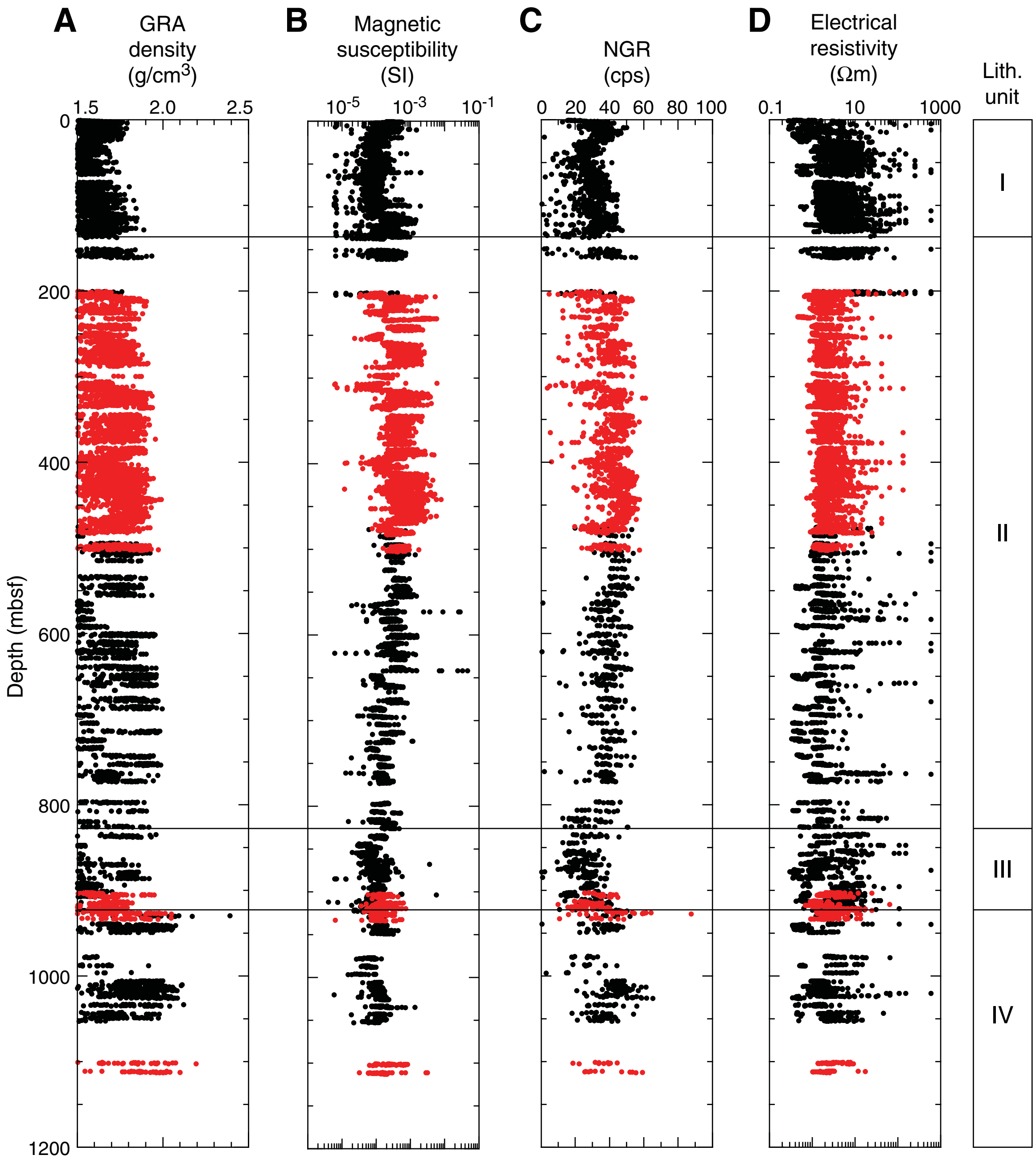

Figure F86. MAD measurements on core samples, Site C0002. Red = Expedition 338 mud samples, yellow = Expedition 338 sand samples, black = Expedition 315 data. **A.** Bulk density. **B.** Porosity. **C.** Grain density.

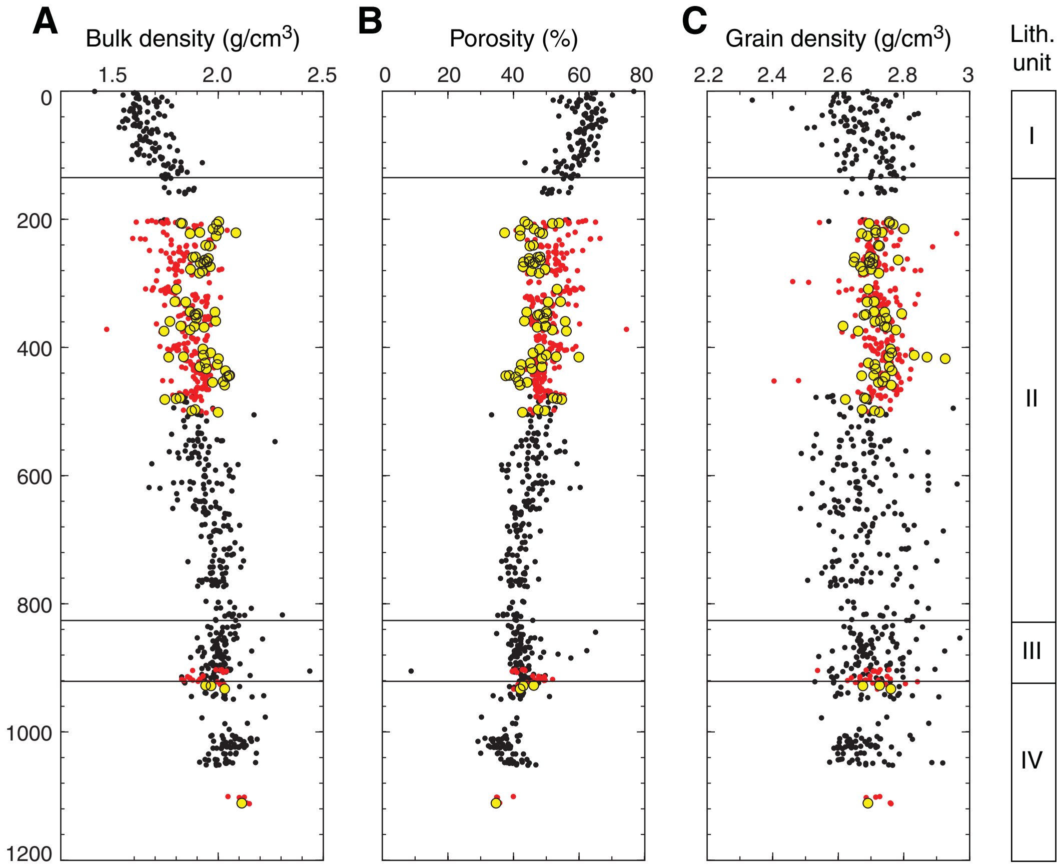

Figure F87. Thermal conductivity, Site C0002. Red = Expedition 338 data, black = Expedition 315 data.

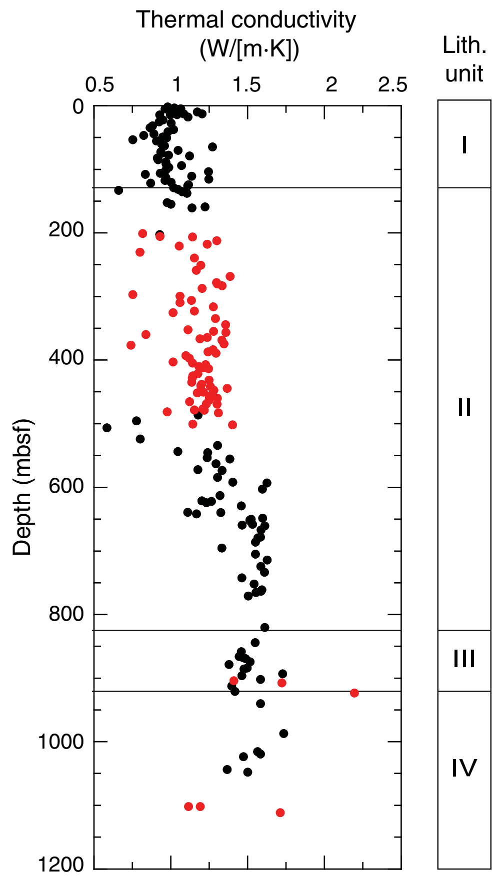

Figure F88. V_P and electrical resistivity measurements on discrete samples, Holes C0002H and C0002J. **A.** V_P along three orthogonal axes. **B.** Electrical resistivity along three orthogonal axes. **C.** Anisotropy of V_P. **D.** Anisotropy of electrical resistivity.

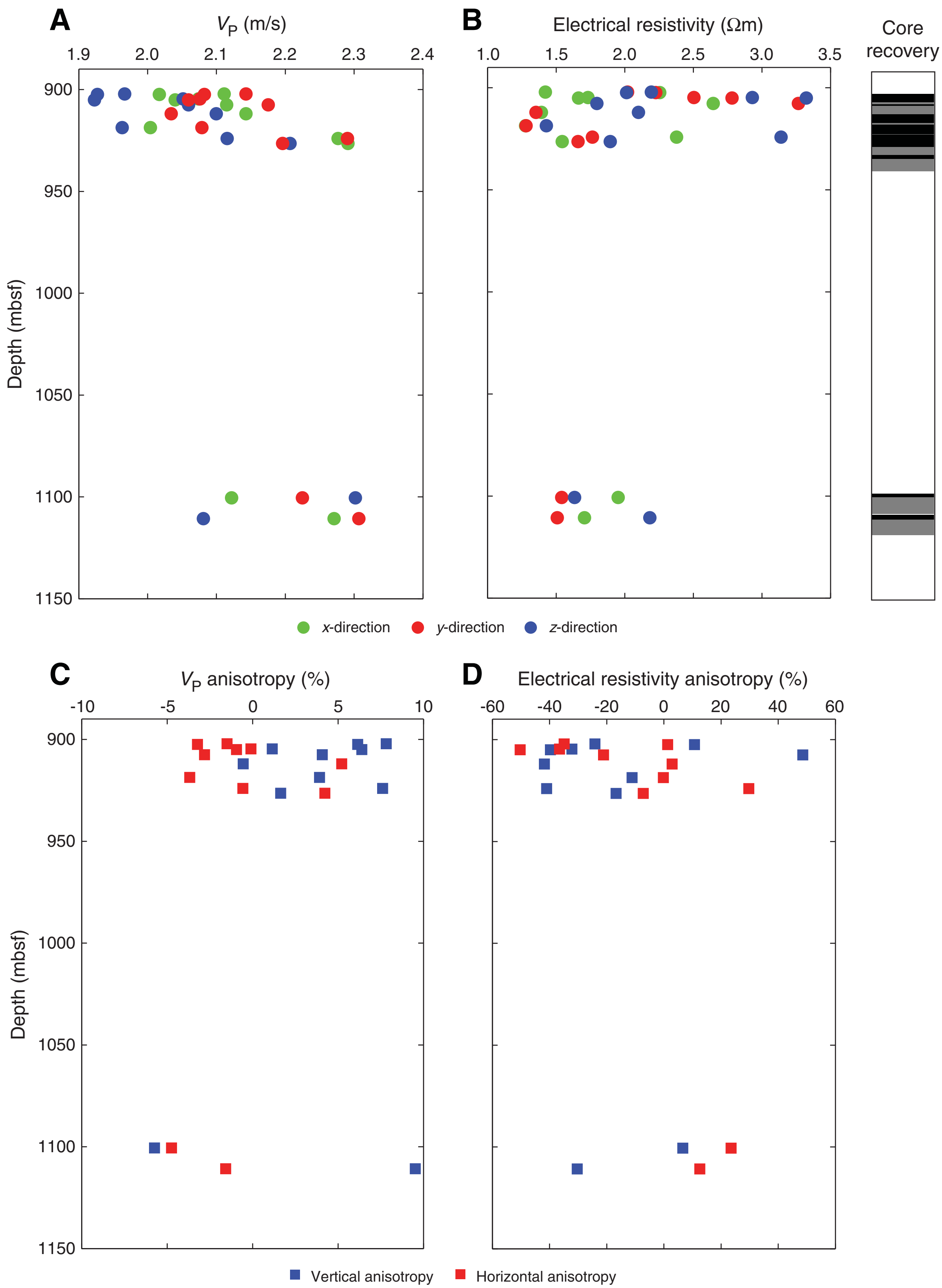

Figure F89. Electrical resistivity data from four-pin electrodes, Holes C0002K and C0002L.

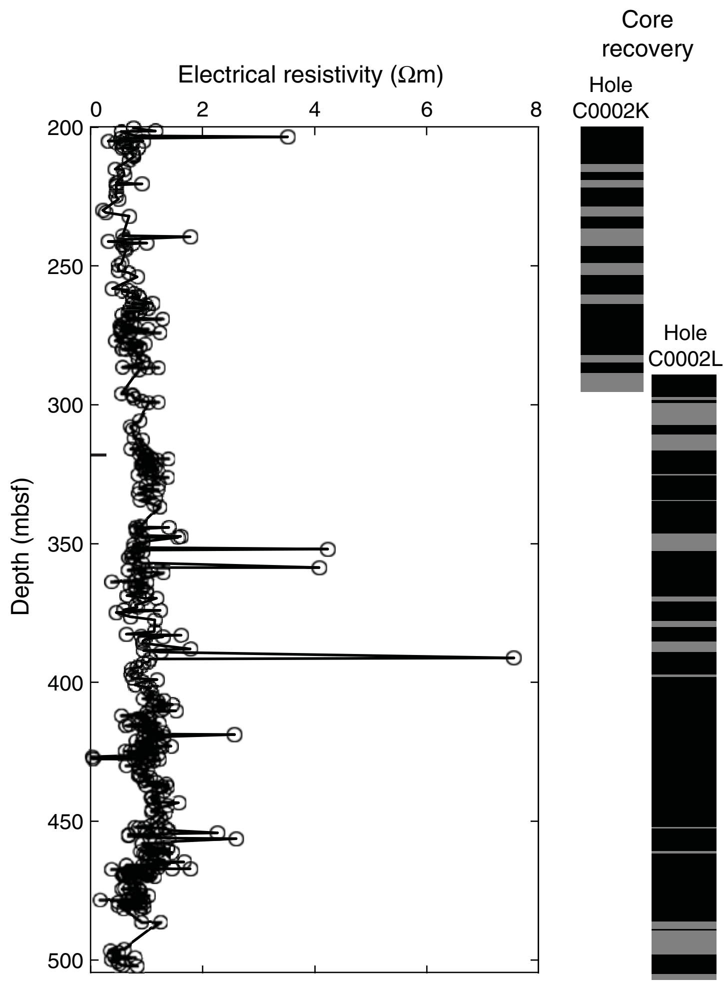

Figure F90. Electrical resistivity from four-pin electrodes with derived Archie parameters using MAD-derived porosity, Holes C0002K and C0002L.

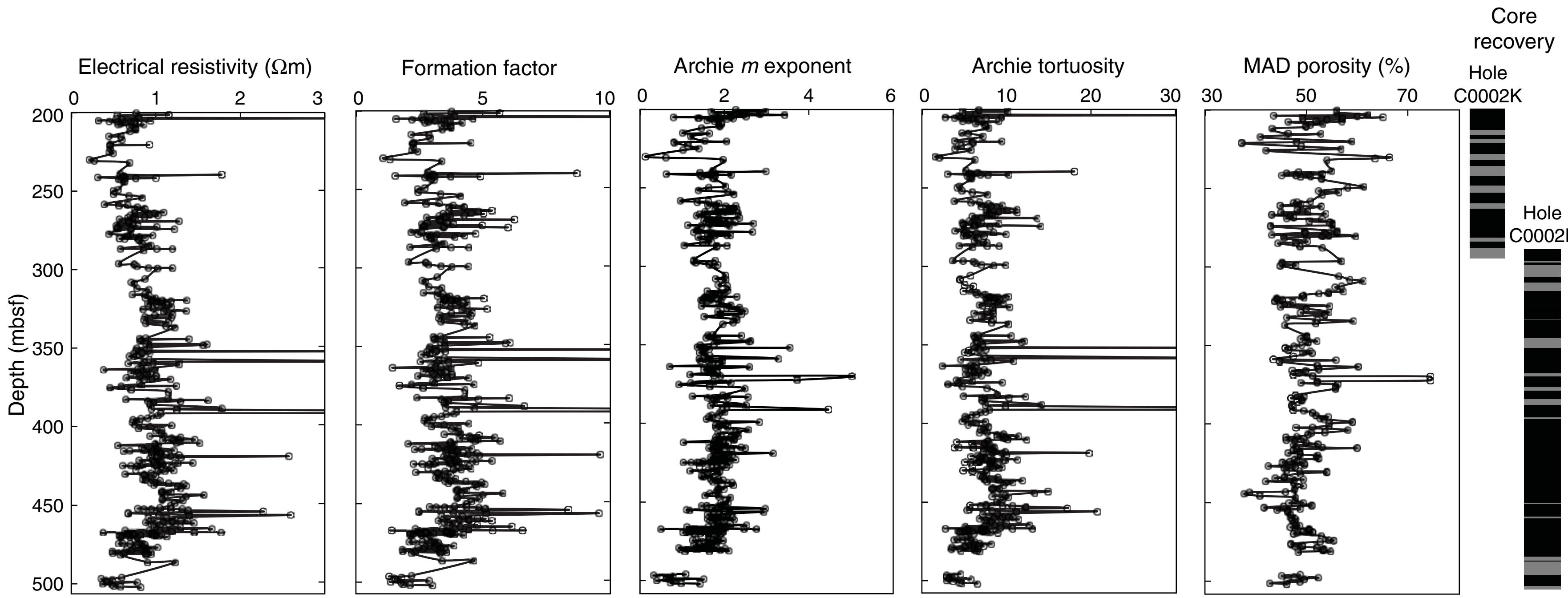

Figure F91. Evolution of Archie cementation factor (*m*) versus electrical resistivity with lithologic discrimination, Holes C0002K and C0002L. Circles = muddy sediment, triangles = sandy sediment. Colors represent the texture of these sediment: dark colors = consolidated, intermediate colors = low consolidation, light colors = soupy sediment. A similar logarithmic fitting between muddy and sandy material is extracted.

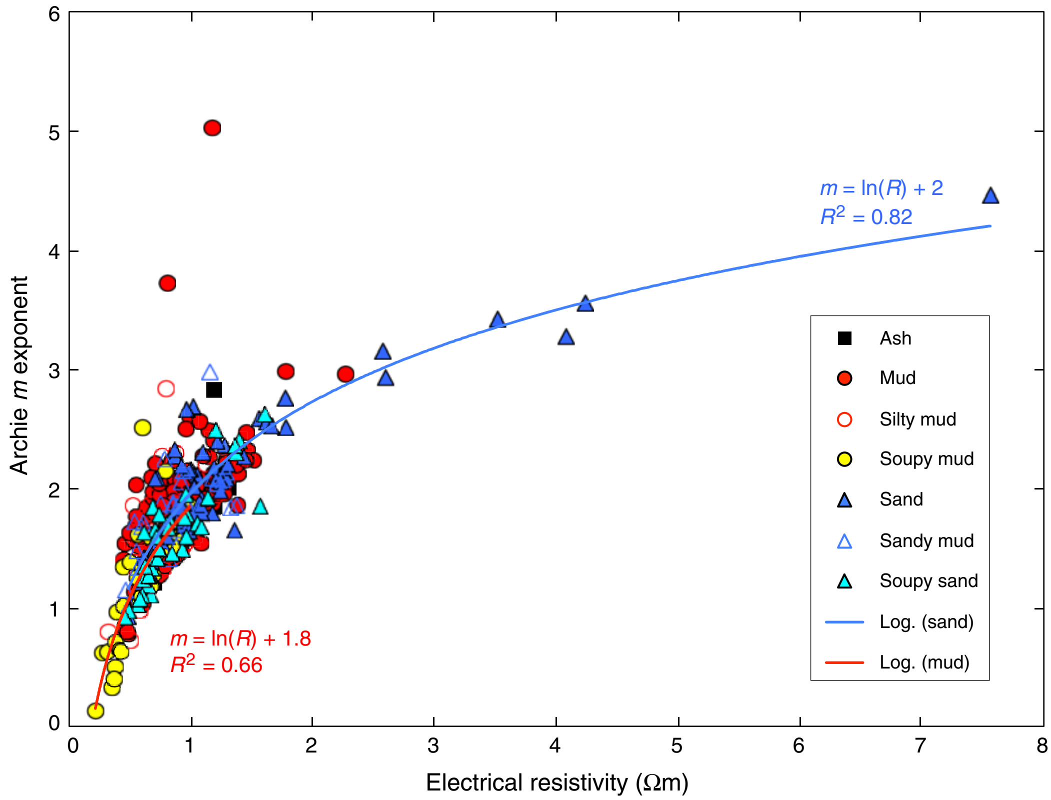

Figure F92. Comparisons of electrical resistivity measurements between discrete samples and whole-round multisensor core logger (MSCL-W) for Holes C0002H, C0002J, C0002K, and C0002L. Note the slight shift between discrete and MSCL-W measurements.

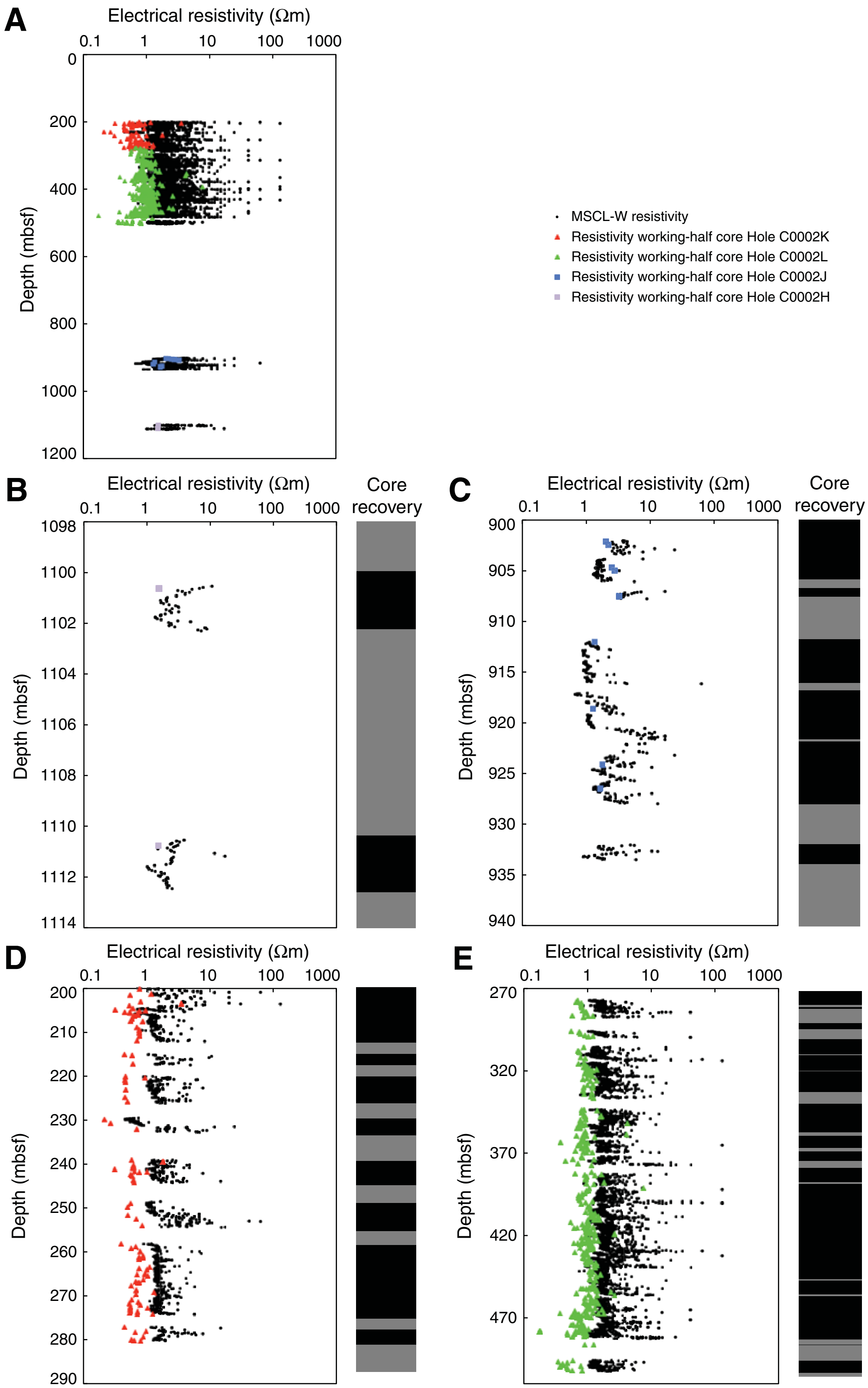

Figure F93. **A.** Undrained shear strength, Holes C0002B, C0002D, C0002K, and C0002L. **B.** Unconfined compressive strength (UCS), Holes C0002H and C0002J.

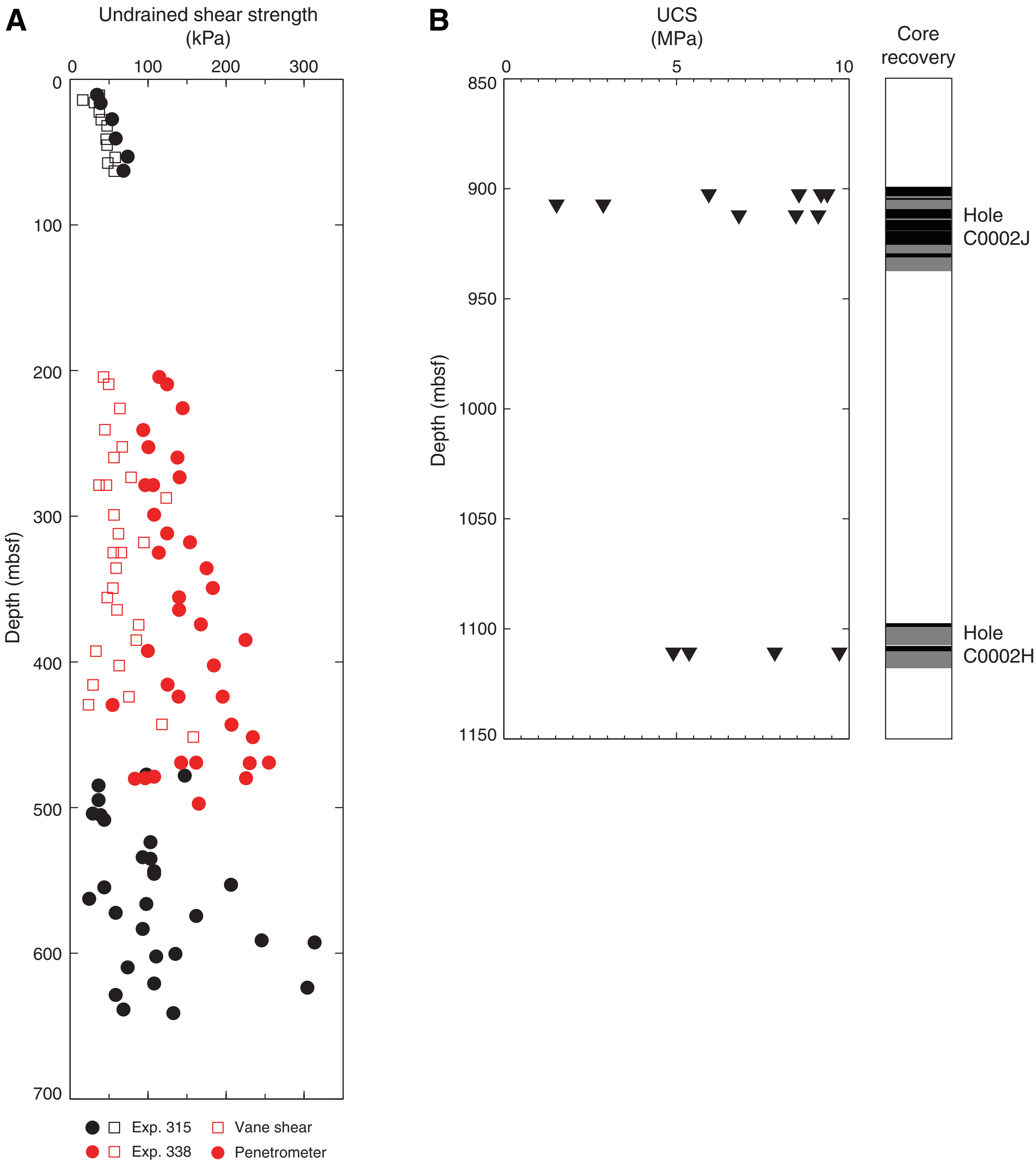

Figure F94. A–C. Color reflectance, Site C0002. Red = Expedition 338 data, black = Expedition 315 data.

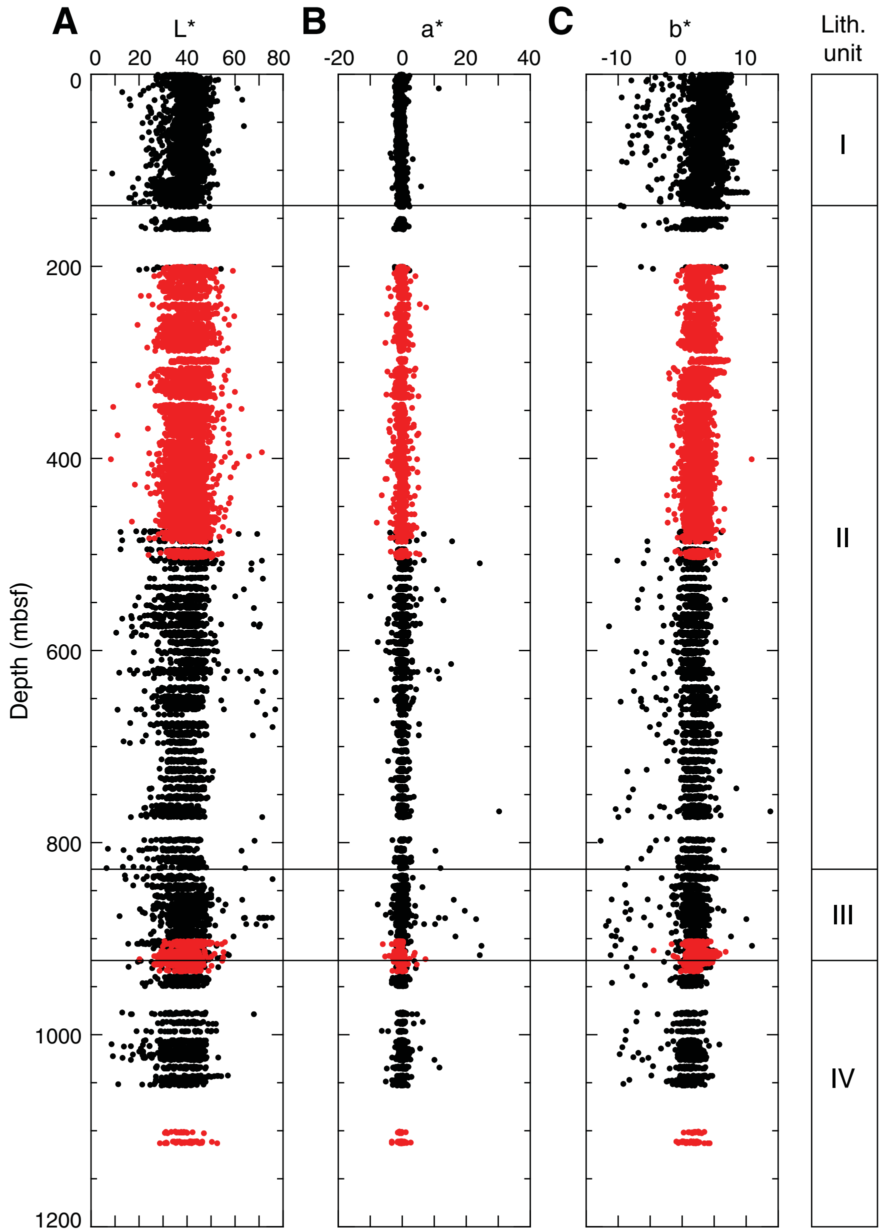

Figure F95. MAD data for 1–4 and >4 mm cuttings size fractions versus bit depth for (**A**) grain density, (**B**) bulk density, and (**C**) porosity in Hole C0002F. Note that data above a bit depth of 940.5 mbsf are not shown because of mixing with cement. Underreamer depths are shown as a reference.

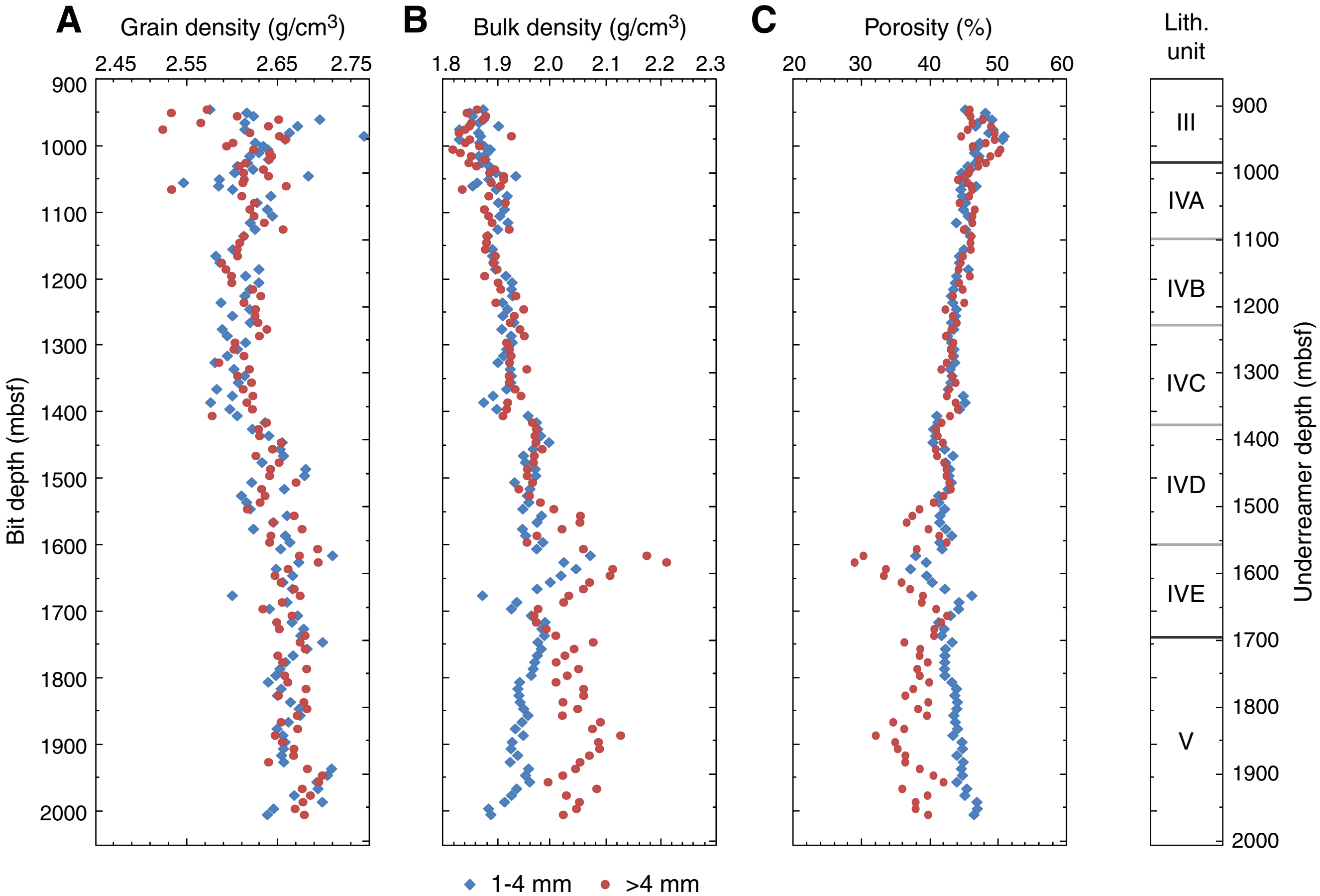

Figure F96. Ratio of 1–4 and >4 mm cuttings size fractions for (**A**) grain density, (**B**) bulk density, and (**C**) porosity, Hole C0002F. Porosity and bulk density deviate from the 1:1 ratio (red line) below 1550 mbsf. Underreamer depths are shown as a reference.

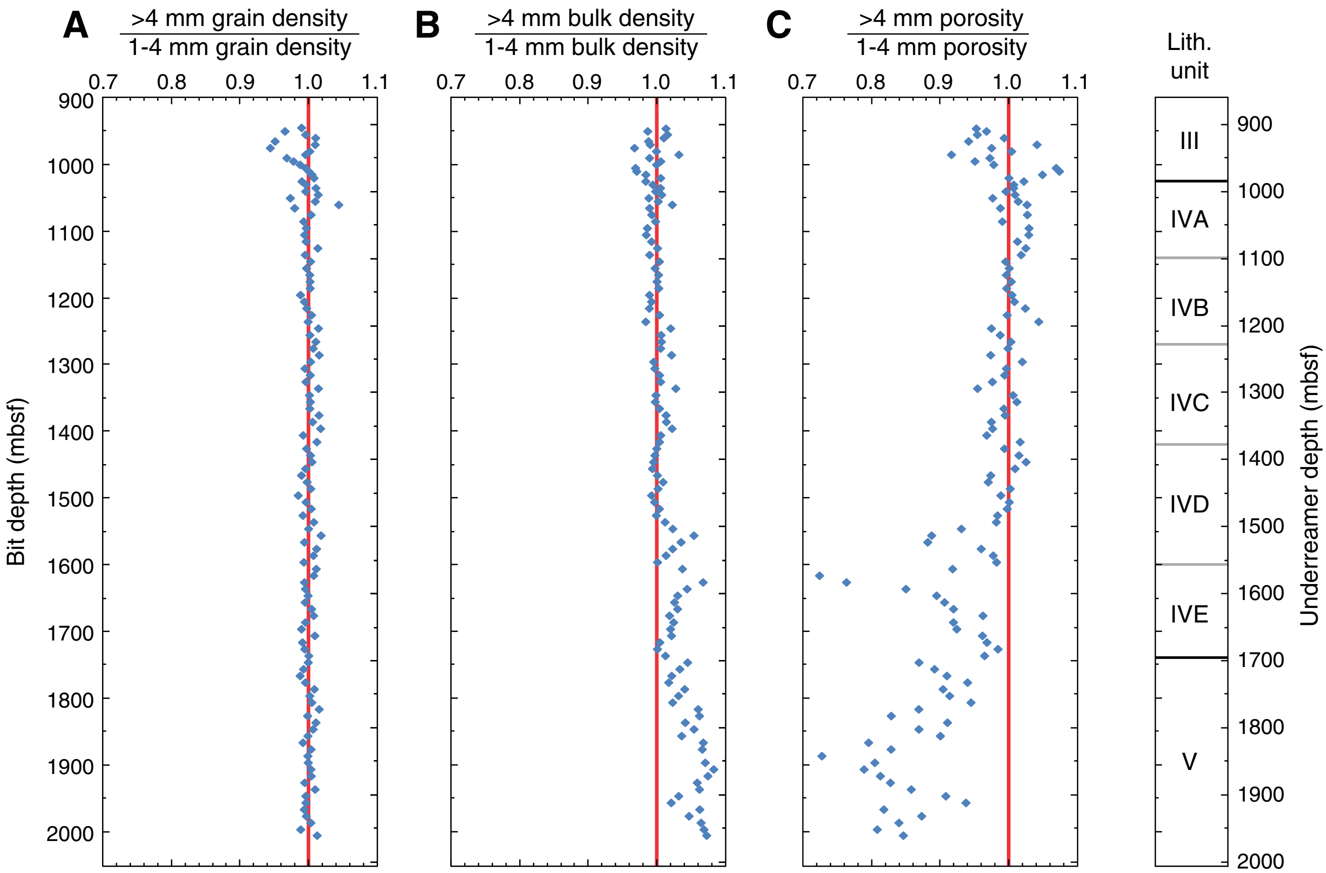

Figure F97. **A.** Compiled MAD porosity data from Hole C0002B (Expedition 315 Scientists, 2009b) and hand-picked samples of intact formation cuttings from Hole C0002F in comparison with porosity data of the >4 mm cuttings from Hole C0002F. Black line = best-fit Athy model to Expedition 315 and hand-picked data (see Equation 3). **B.** MAD bulk density data from >4 mm cuttings size fraction data in comparison with bulk density calculated from the Athy model porosity. **C.** Difference between MAD bulk data and data based on the Athy model. Underreamer depths are shown as a reference.

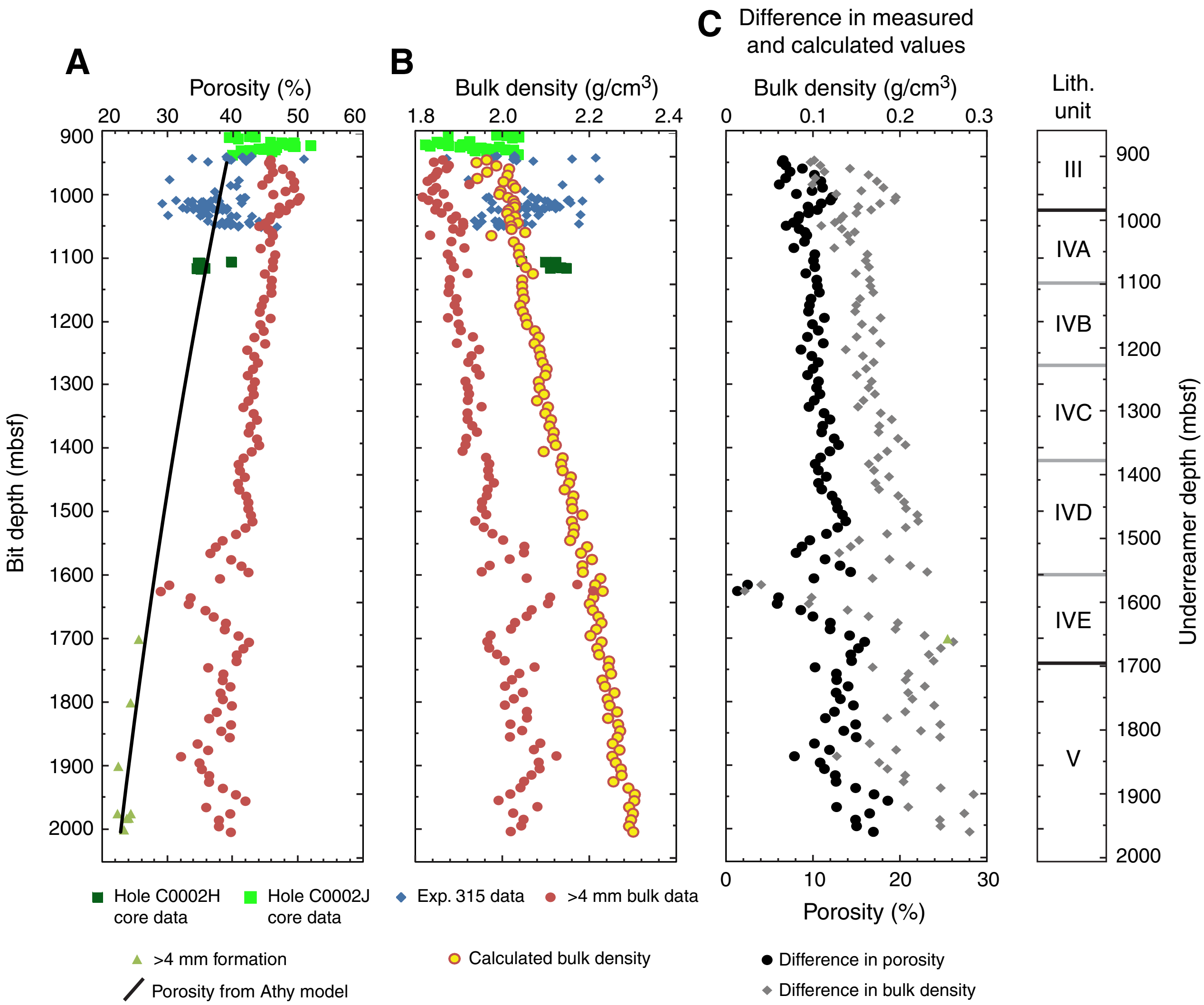

Figure F98. Fraction of drilling-induced cohesive aggregates (DICAs) in the bulk >4 mm cuttings size fraction for the interval 1800–2004.5 mbsf in comparison with times when the bit was off bottom, Hole C0002F. Underreamer depths of minima in DICAs (blue arrows) seem to correlate with depths when the bit was off bottom for long times (yellow arrows).

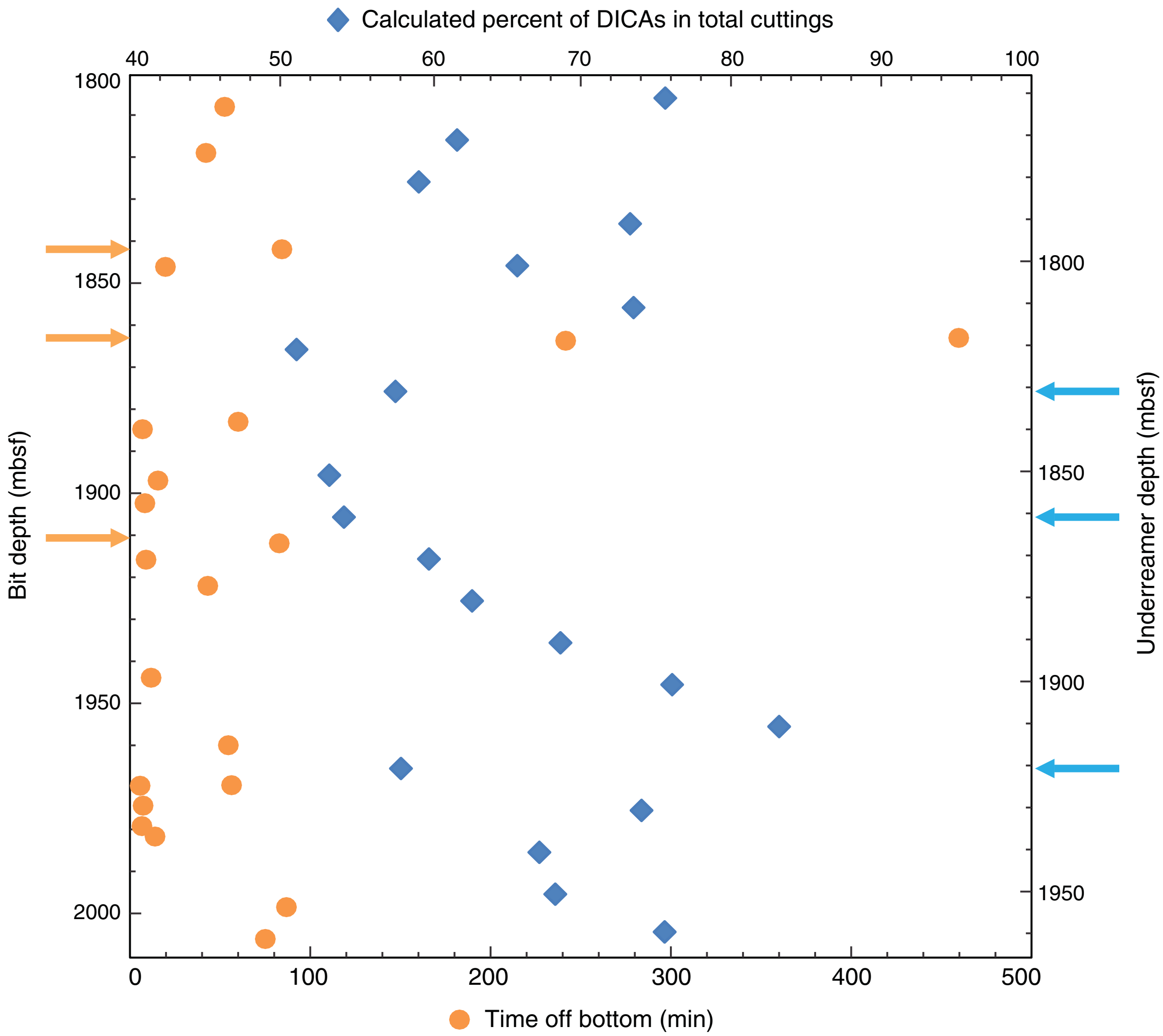

Figure F99. Mass magnetic susceptibility data measured for 1–4 and >4 mm cuttings size fractions, Hole C0002F. Underreamer depths are shown as a reference.

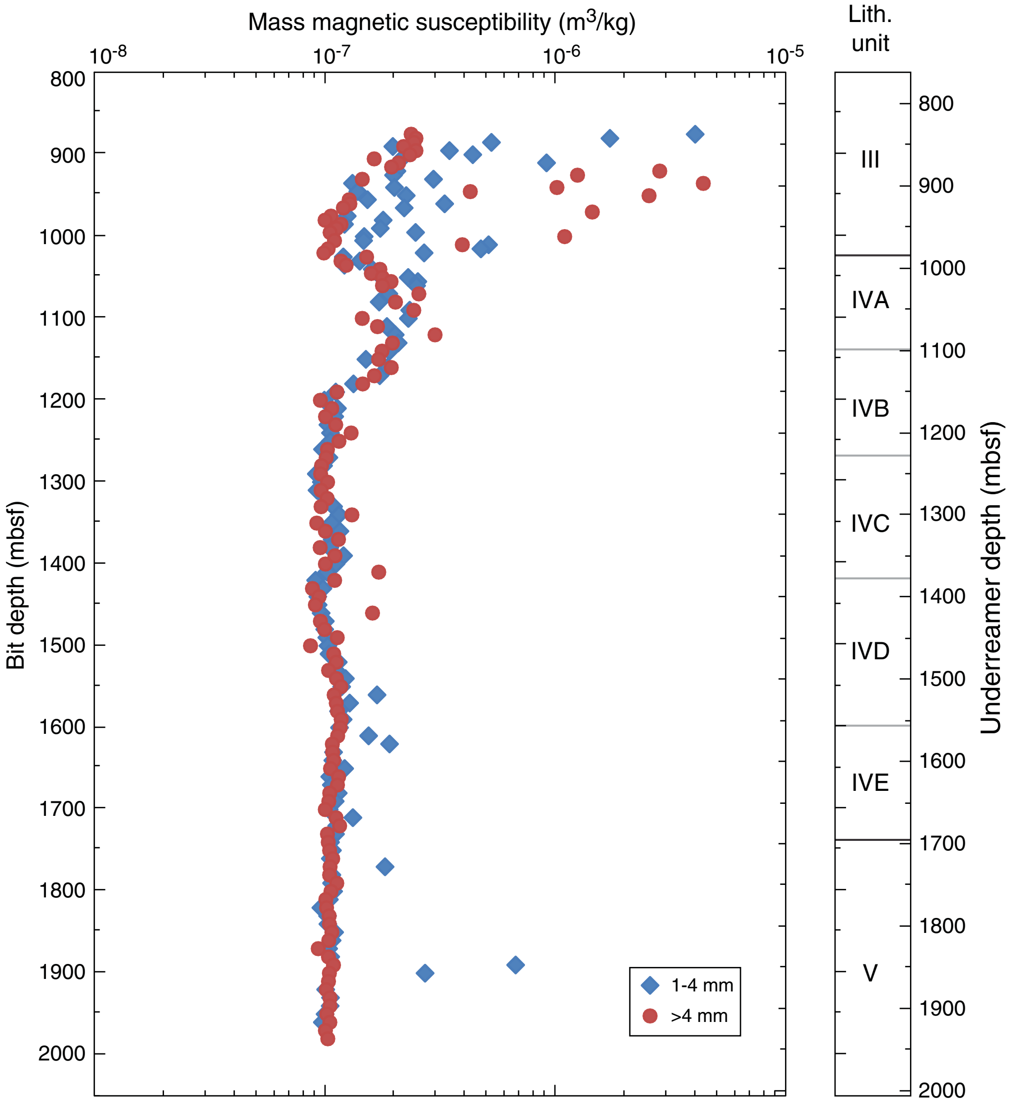

Figure F100. Natural gamma radiation (NGR) of cuttings mix measured using the whole-round multisensor core logger (MSCL-W) and downhole logging data for gamma radiation (GR) from logging while drilling (LWD), Hole C0002F. Logging data are converted to counts per second for comparison with MSCL-W data: NGR (cps) = (GR [gAPI] – 12)/2.12 (Mountain, Miller, Blum, et al., 1994). Notable correlations between MSCL-W NGR and LWD-GR (blue and red circles) suggest a depth shift between cuttings and logging. Underreamer depths are shown as a reference.

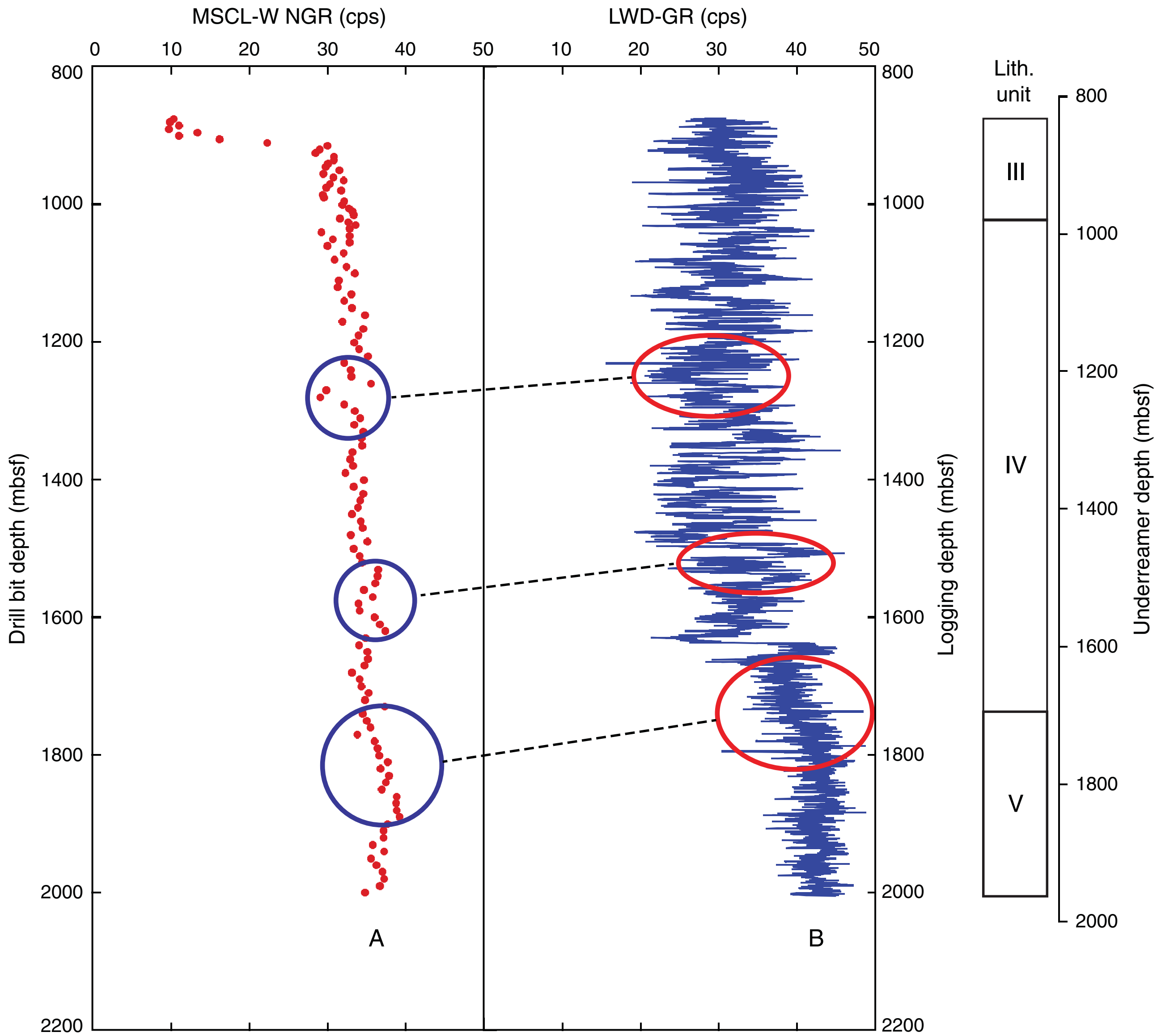

Figure F101. Normalized whole-round multisensor core logger (MSCL-W) natural gamma radiation (NGR) and grain density of cuttings from 875 to 980 mbsf showing that cement and formation cuttings generated around their interface at 875.5 mbsf were mixed, Hole C0002F. The mixture of cuttings with different depths is well fitted by the advection-dispersion model for data of cuttings produced by the underreamer. Normalized NGR and grain density were calculated by $(NGR - NGR_c)/(NGR_f - NGR_c)$, where NGR_c (6.64 cps) and NGR_f (26.86 cps) are the averages of cement and formation cuttings NGR data, respectively. Normalized grain density (GD) were obtained by $(GD - GD_c)/(GD_f - GD_c)$, where GD_c (1.87 g/cm^3) and GD_f (2.61 g/cm^3) are the averages of cement and formation cuttings grain density, respectively.

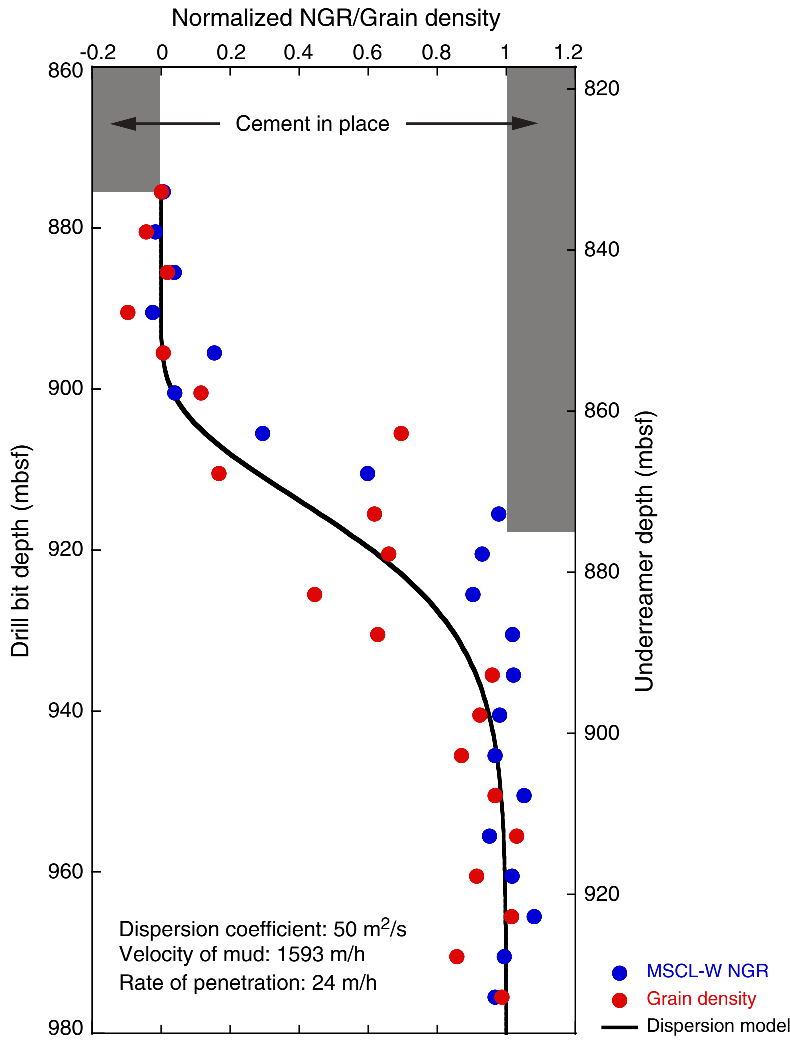

Figure F102. Photographs of cuttings bags in order of depth from top to bottom. **A.** Samples 338-C0002F-22-SMW (930.5 mbsf) through 148-SMW (1480.5 mbsf). (Continued on next page.)

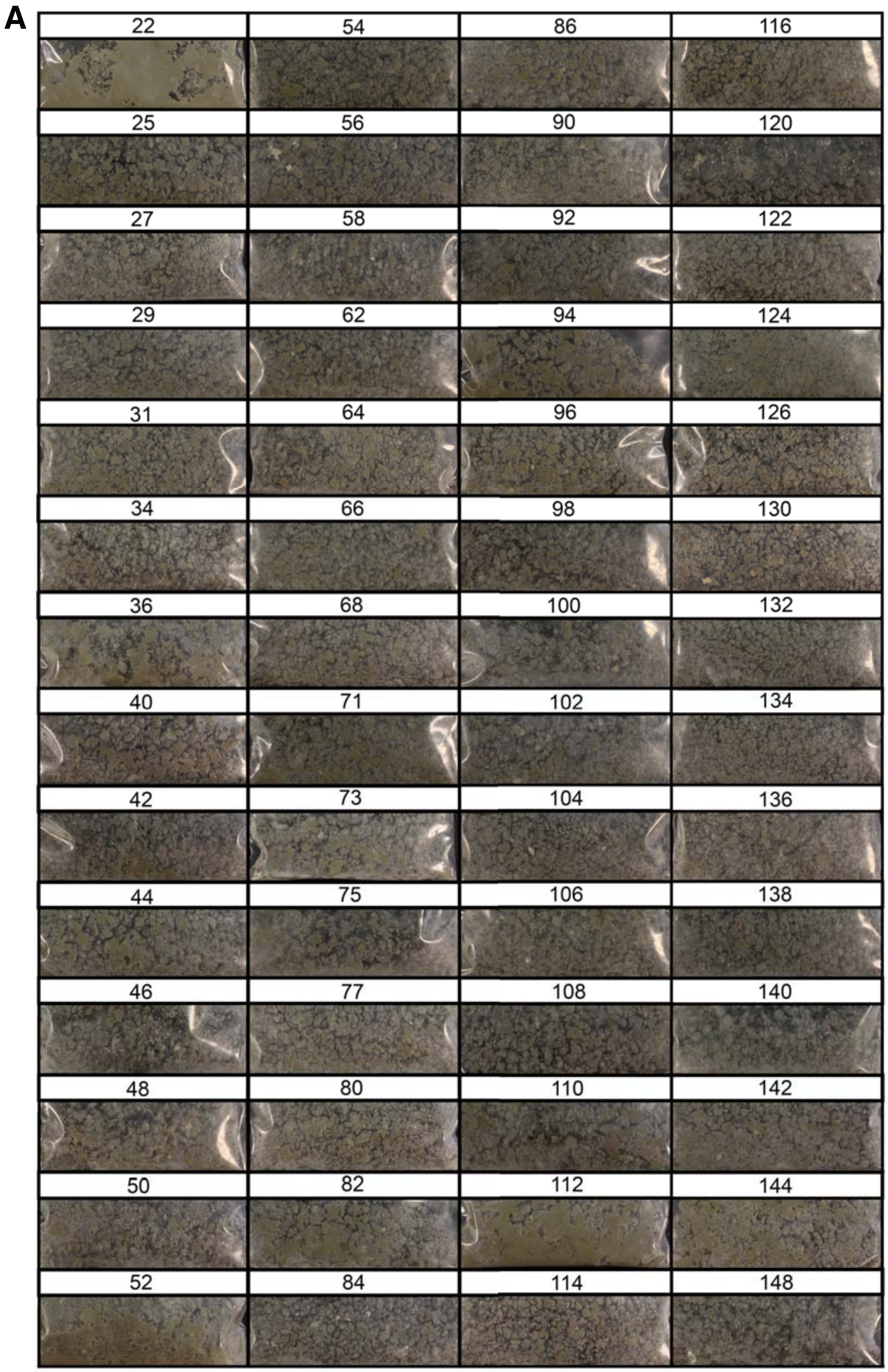

Figure F102 (continued). B. Samples 338-C0002F-150-SMW (1490.4 mbsf) through 289-SMW (2005.5 mbsf) and Sample 311-SMW (sample at 1970 mbsf produced only by the underreamer).

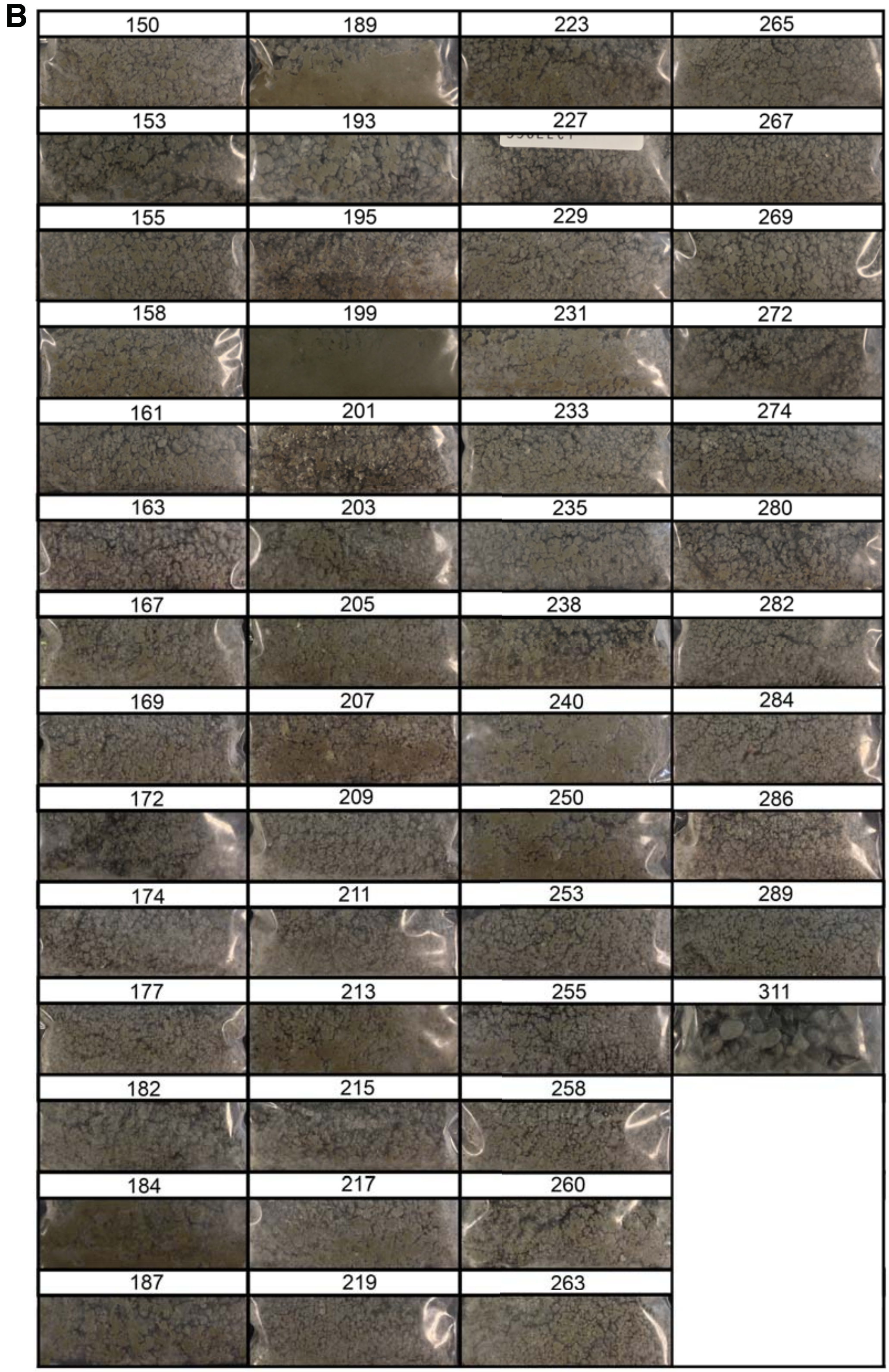

Figure F103. Histograms of gray color distribution in 8 bits from (**A**) all cuttings photographs using a circular window 11 pixels in diameter, Hole C0002F. **B.** Four populations from the collection are discriminated based on their maximum peak gray intensity. The cuttings collection was classified based on these four populations: (**C**) Population P1 centered at 50 grayscale and occurring among all the collections, Population P2 centered at 75 grayscale, (**D**) Population P3 centered at 95 grayscale, and (**E**) Population P4 centered at 110 grayscale.

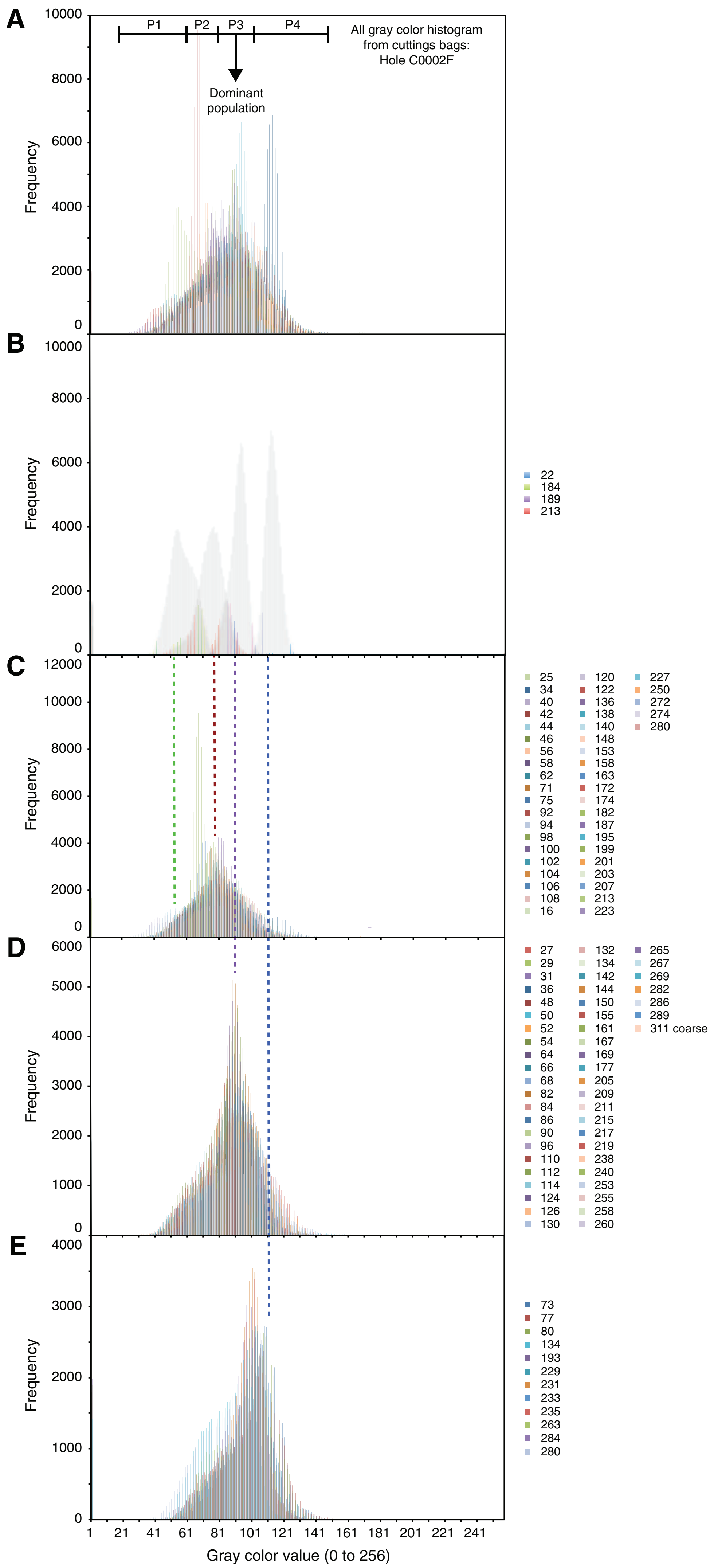

Figure F104. Distribution of the mean gray values with depth and the grayscale difference between the minimum accounted from the gray color histogram and the mean gray value on each cuttings sample, Hole C0002F.

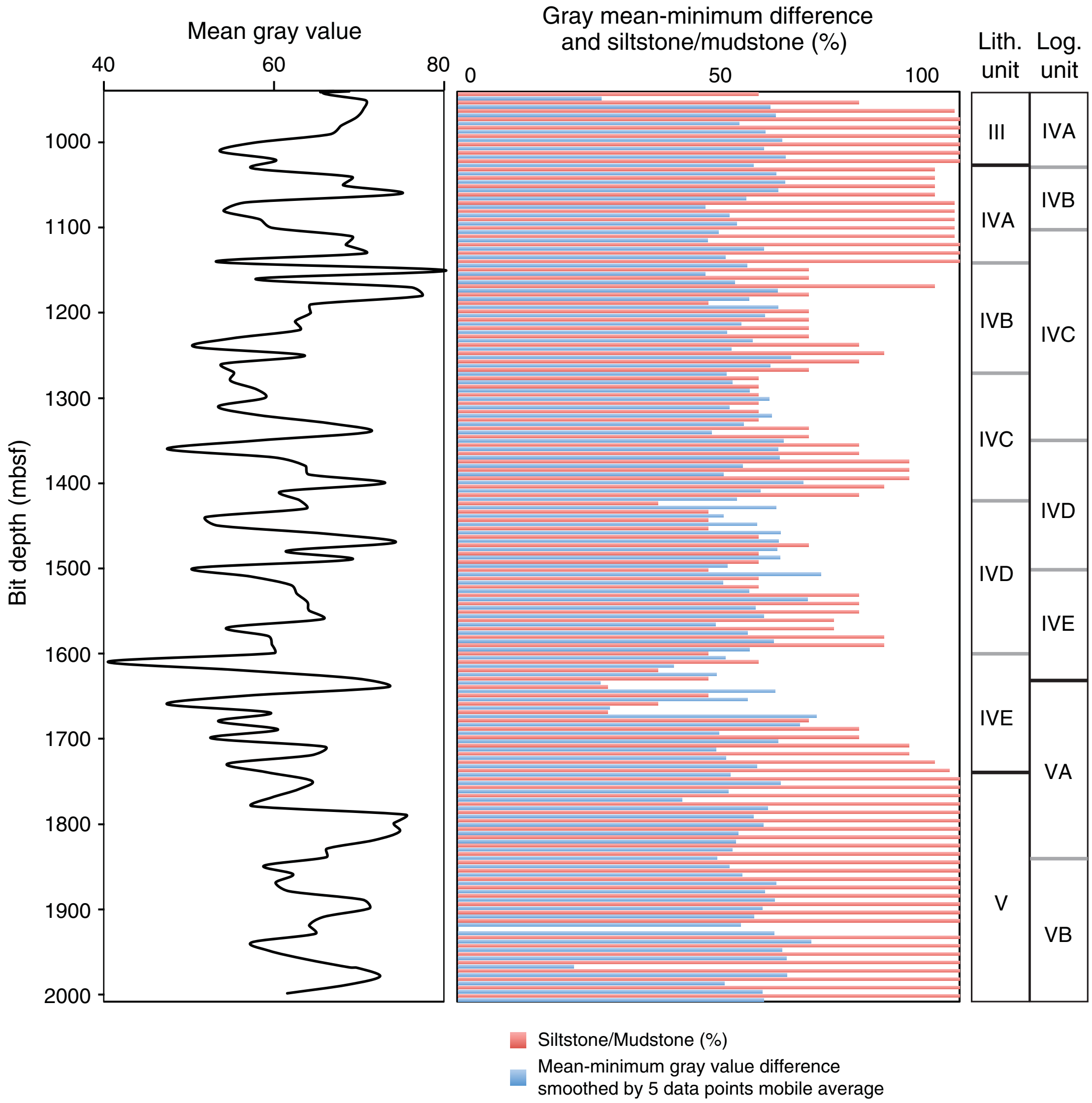

Figure F105. **A.** Distribution of the salinity index with depth extracted from decanted water after centrifuging of the cuttings pastes, Hole C0002F. **B.** Comparison of MAD-derived porosity and porosity derived from pastes used for dielectric measurements.

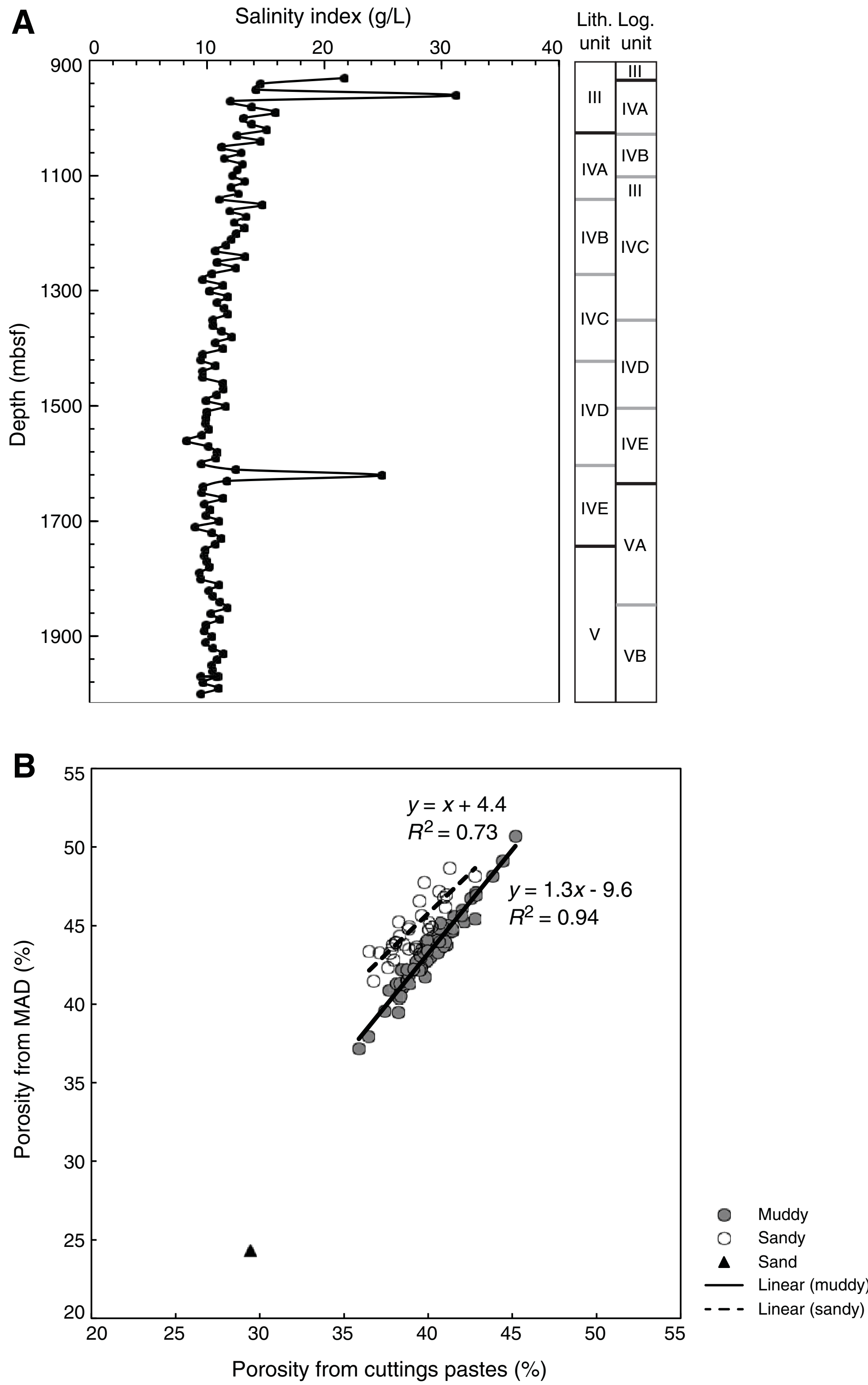

Figure F106. Depth distribution of the (**A**) dielectric constant, (**B**) dielectric dispersion, and (**C**) equivalent electrical conductivity of cuttings pastes measured at different frequencies, Hole C0002F.

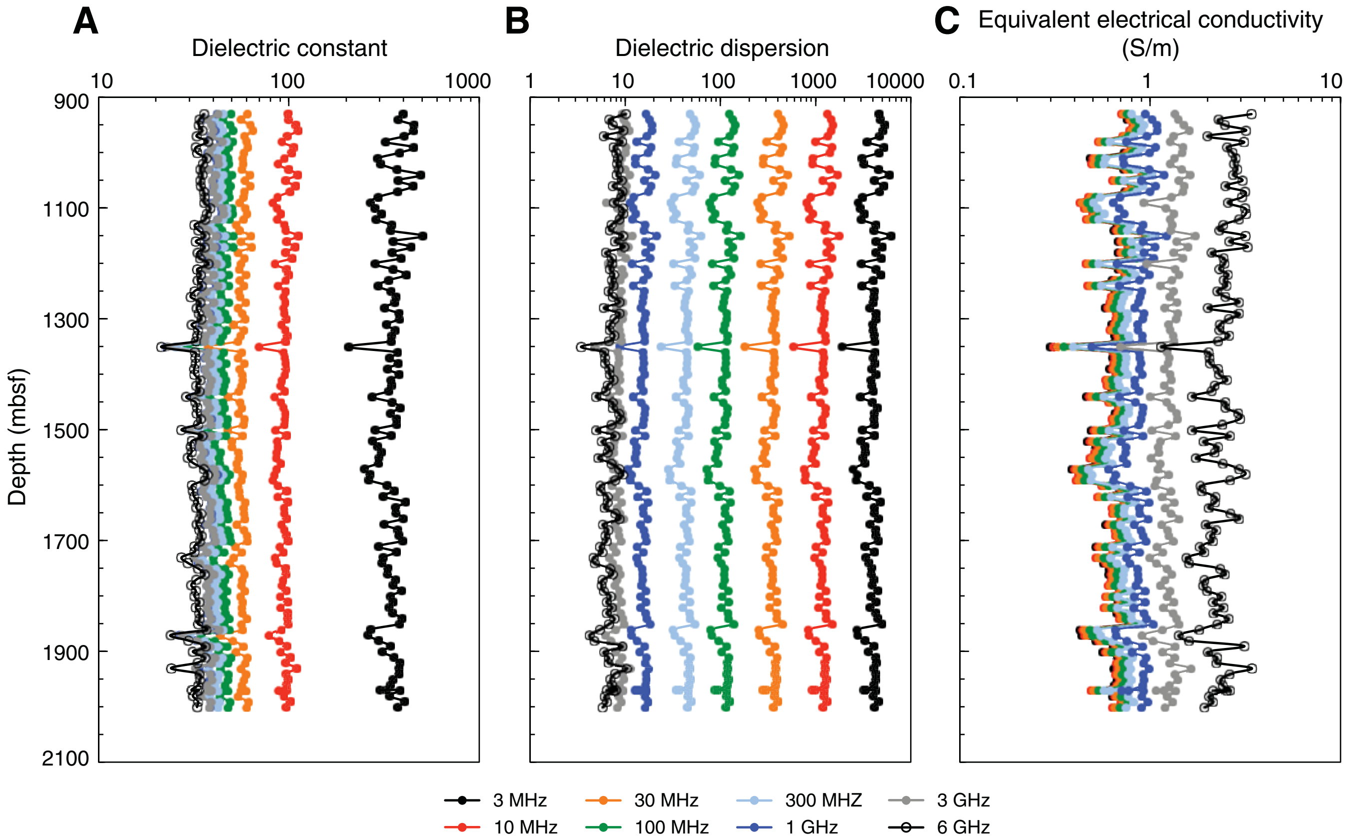

Figure F107. Comparison of the dielectric dispersion with the dielectric constant at three measurement frequencies on all the cuttings pastes, Hole C0002F. Note the sandy materials cloud out of the general trend at 100 MHz and 1 GHz.

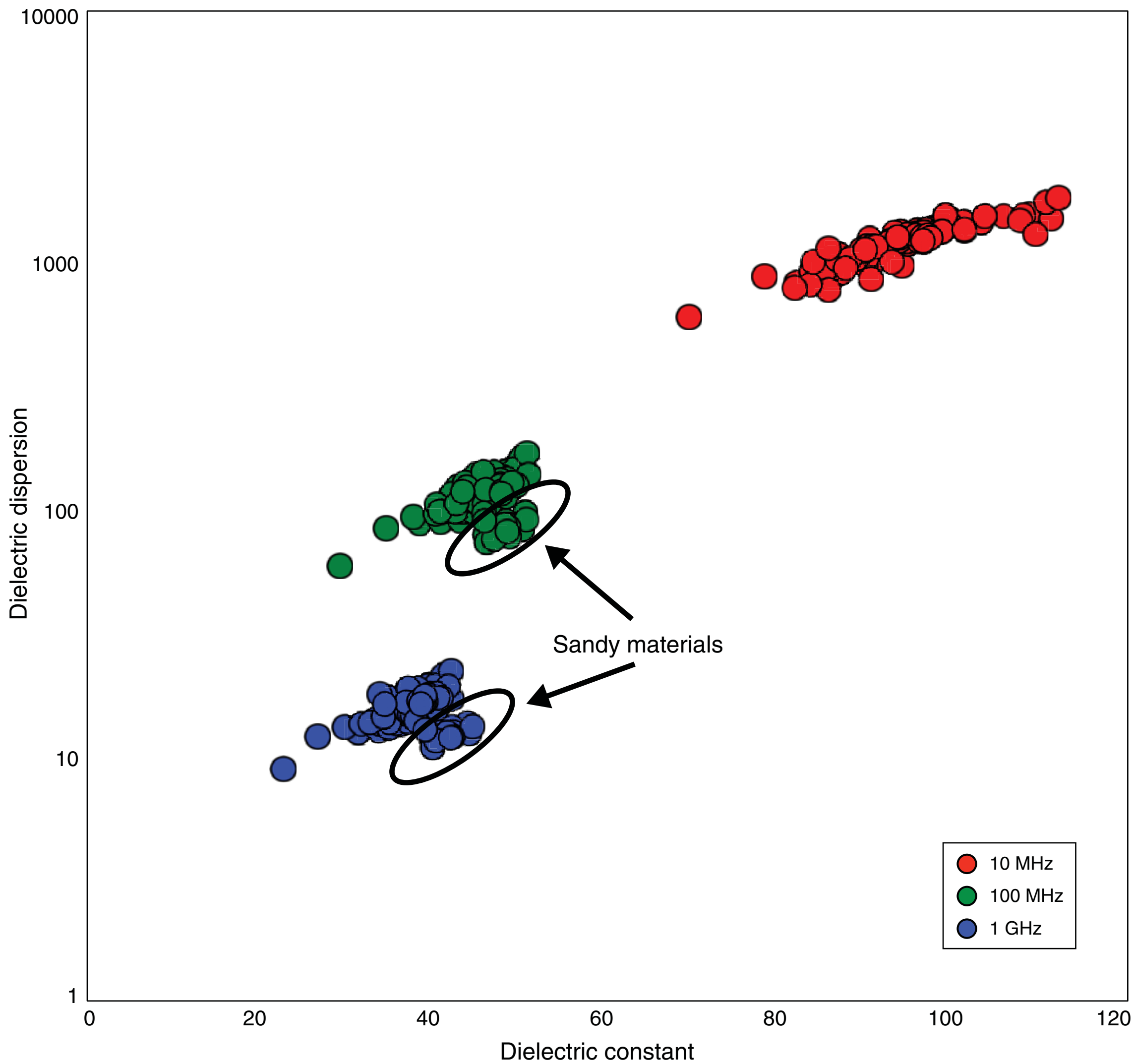

Figure F108. Distribution of the electrical resistivity computed from the electrical conductivity using the dielectric data at 3 MHz on cuttings from Hole C0002F with the corresponding logging-while-drilling (LWD) logs of resistivity, gamma ray, and sonic velocity at the same depth.

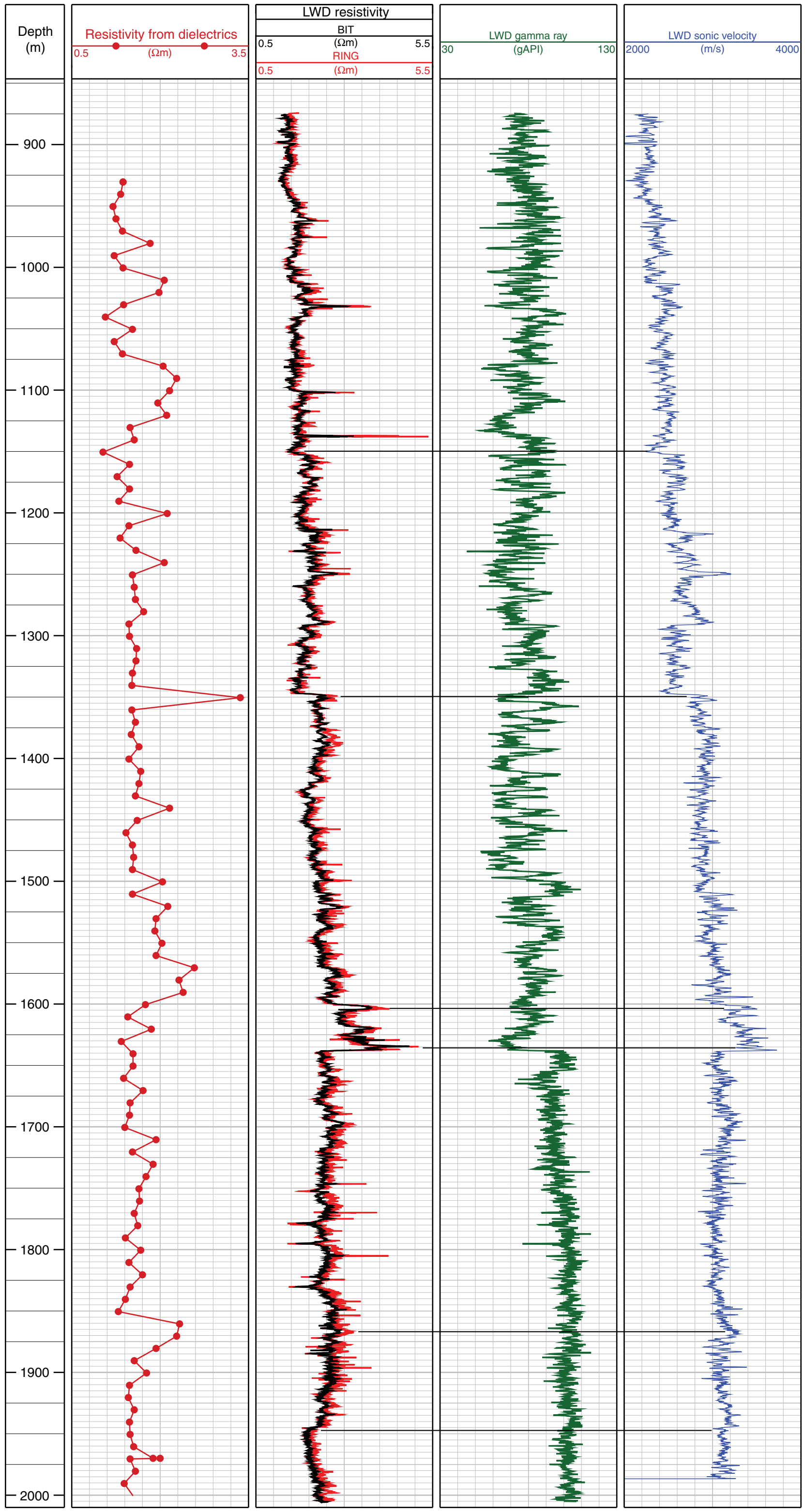

Figure F109. Borehole configuration for the leak-off test at the 20 inch casing shoe, Hole C0002F.

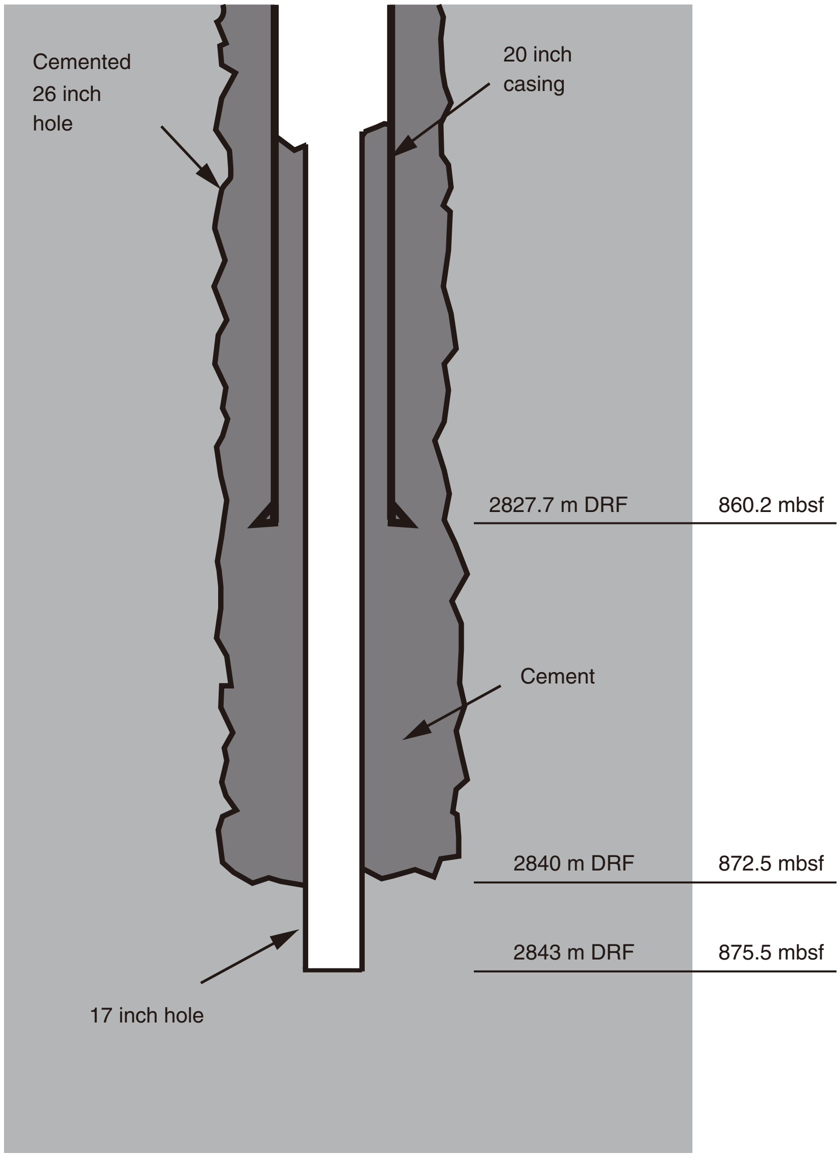

Figure F110. **A.** Pressure (red) and mud flow rate (blue) for leak-off test, Hole C0002F. **B.** Plot for borehole pressure versus mud volume injected. **C.** Plot of dP/dV with respect to mud volume versus borehole pressure revealing Leak-off pressure (LOP) = 32.0 MPa. ISIP = instantaneous shut in pressure.

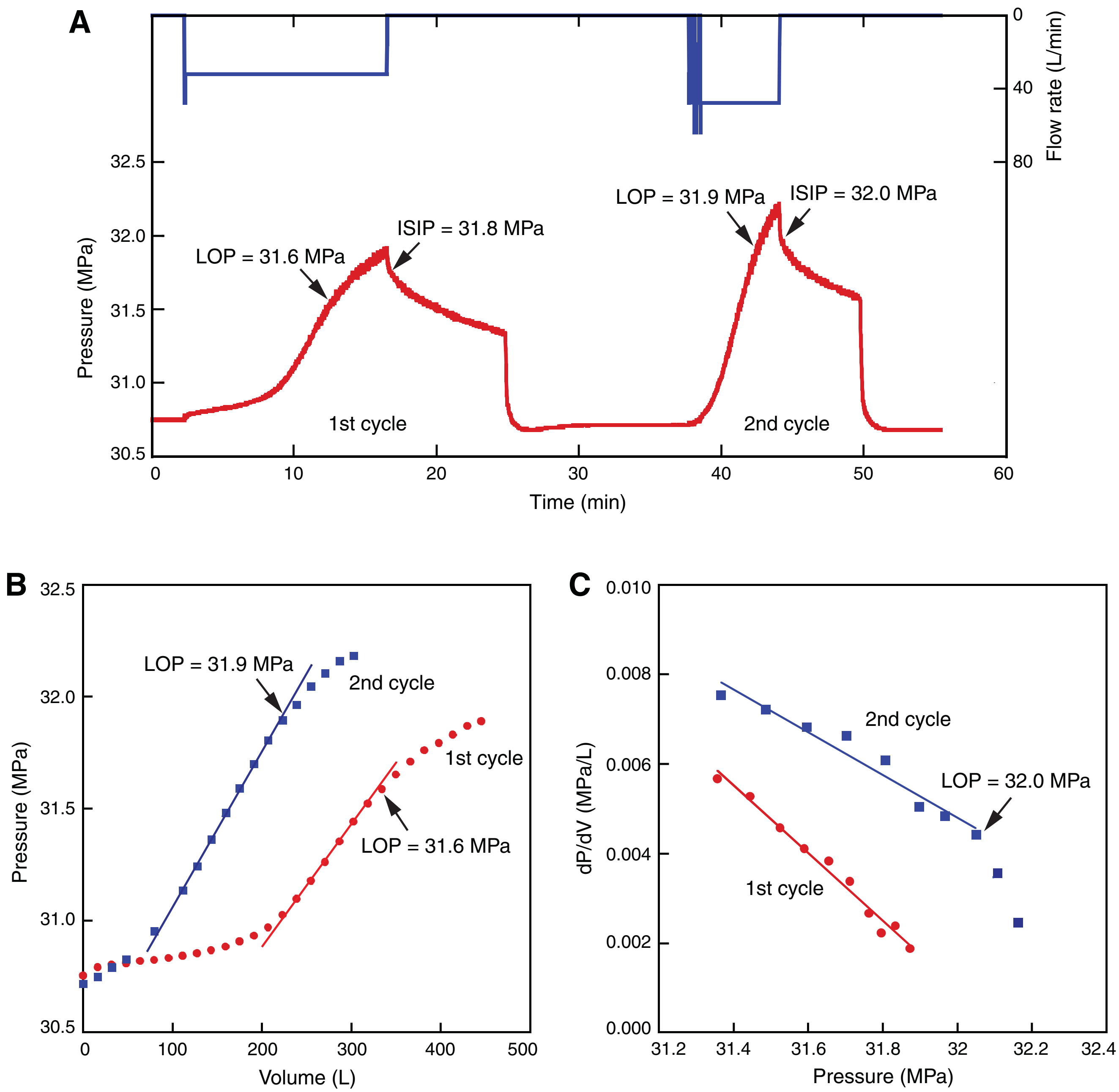

Figure F111. Declinations and inclinations of cores from Expedition 338 Holes C0002H, C0002J, C0002K, and C0002L and Expedition 315 Holes C0002B and C0002D after 20 mT alternating field demagnetization, with polarity interpretation. Black = normal polarity, white = reversed polarity, gray = unknown.

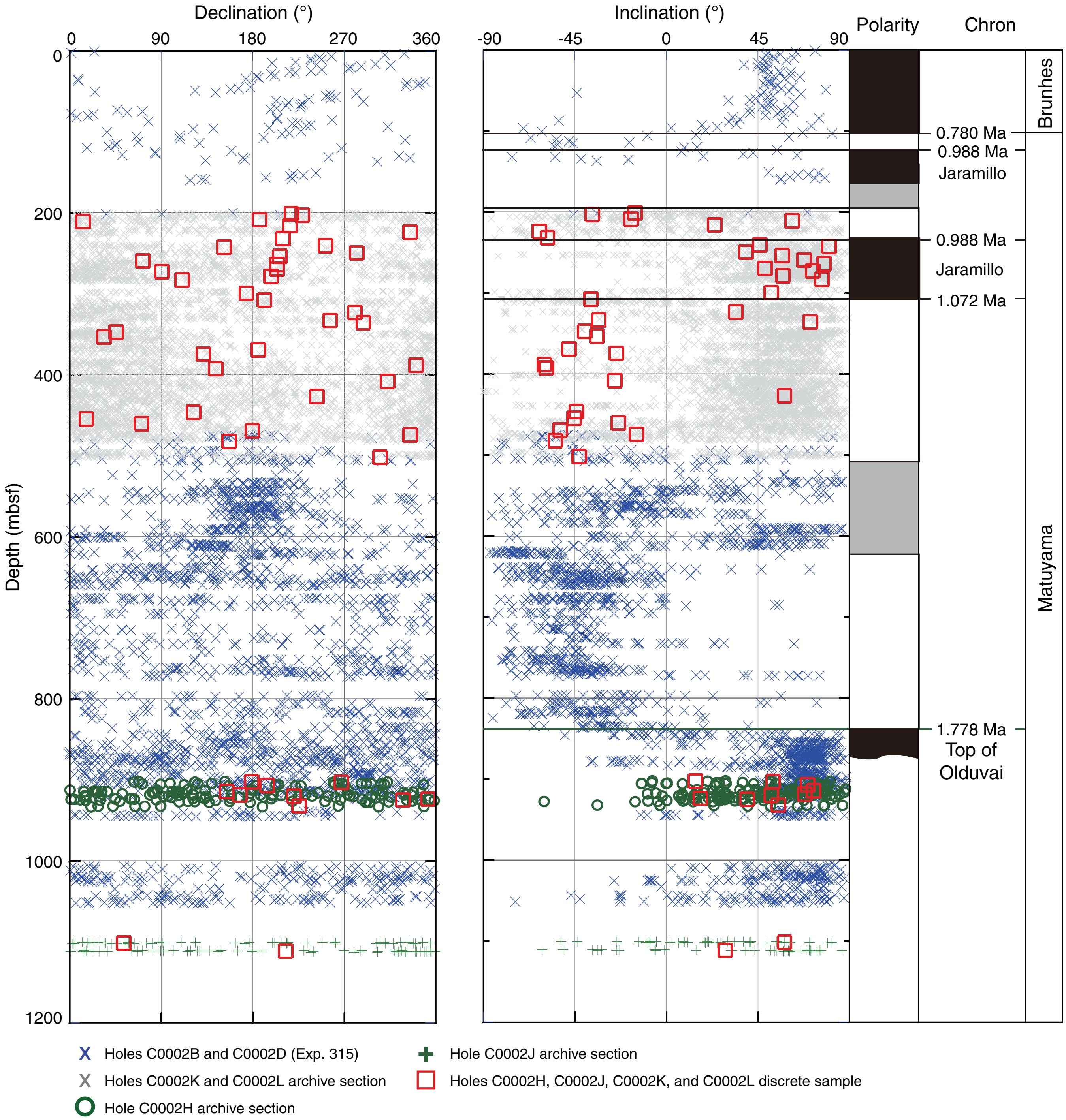

Figure F112. A. Flinn-type diagram of magnetic fabric obtained from Hole C0002K and C0002L discrete samples. L = lineation, F = foliation. **B.** AMS directions of Hole C0002K and C0002L discrete samples. Lower hemisphere equal-area projections of K1 (blue squares), K2 (red triangles), and K3 (green circles) principal magnetic susceptibility directions.

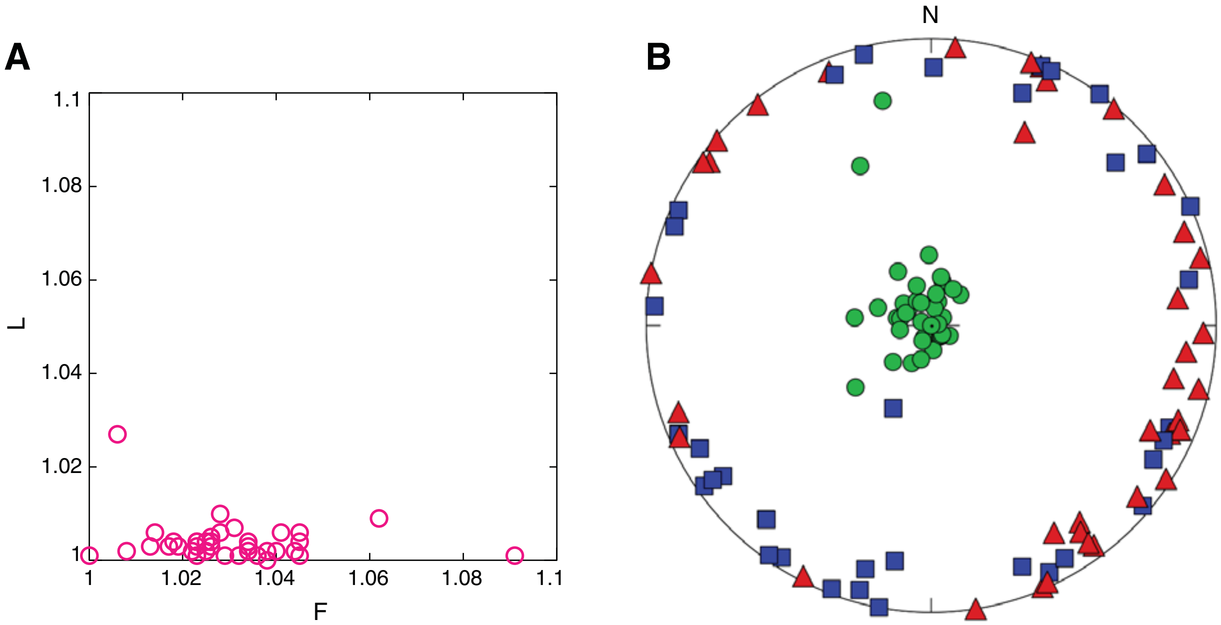

Figure F113. Vector component diagrams of progressive alternating field demagnetization of Samples 338-C0002K-10X-6, 104–106 cm, and 338-C0002L-18X-8, 21–23 cm. Steps are in mT for AF demagnetization. Solid squares = projections onto the horizontal plane, open squares = projections onto the vertical plane.

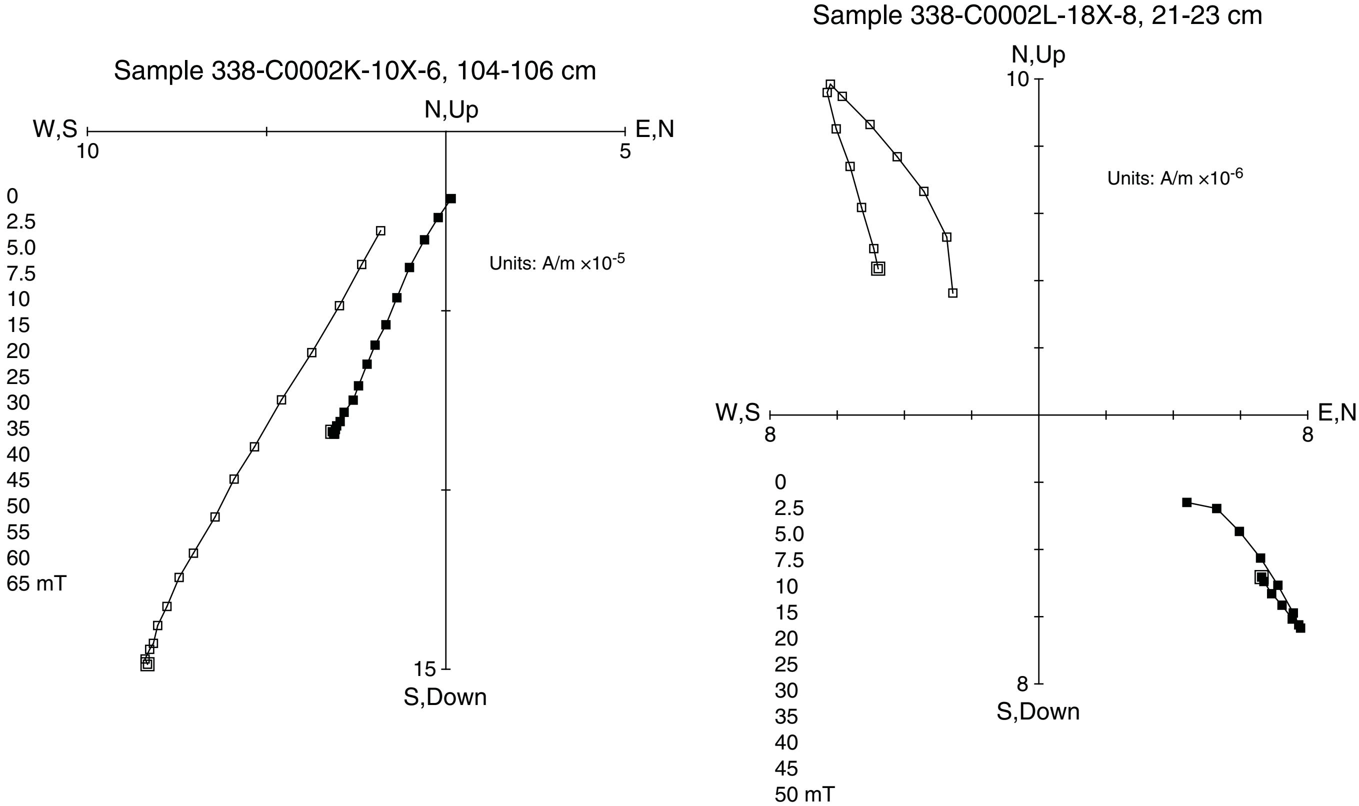

Figure F114. **A.** Depth profiles of AMS parameter T, Holes C0002H, C0002J, C0002K, and C0002L. **B.** AMS directions of Hole C0002H and C0002J discrete samples. Lower hemisphere equal-area projections of K1 (blue squares), K2 (red triangles), and K3 (green circles) principal magnetic susceptibility directions.

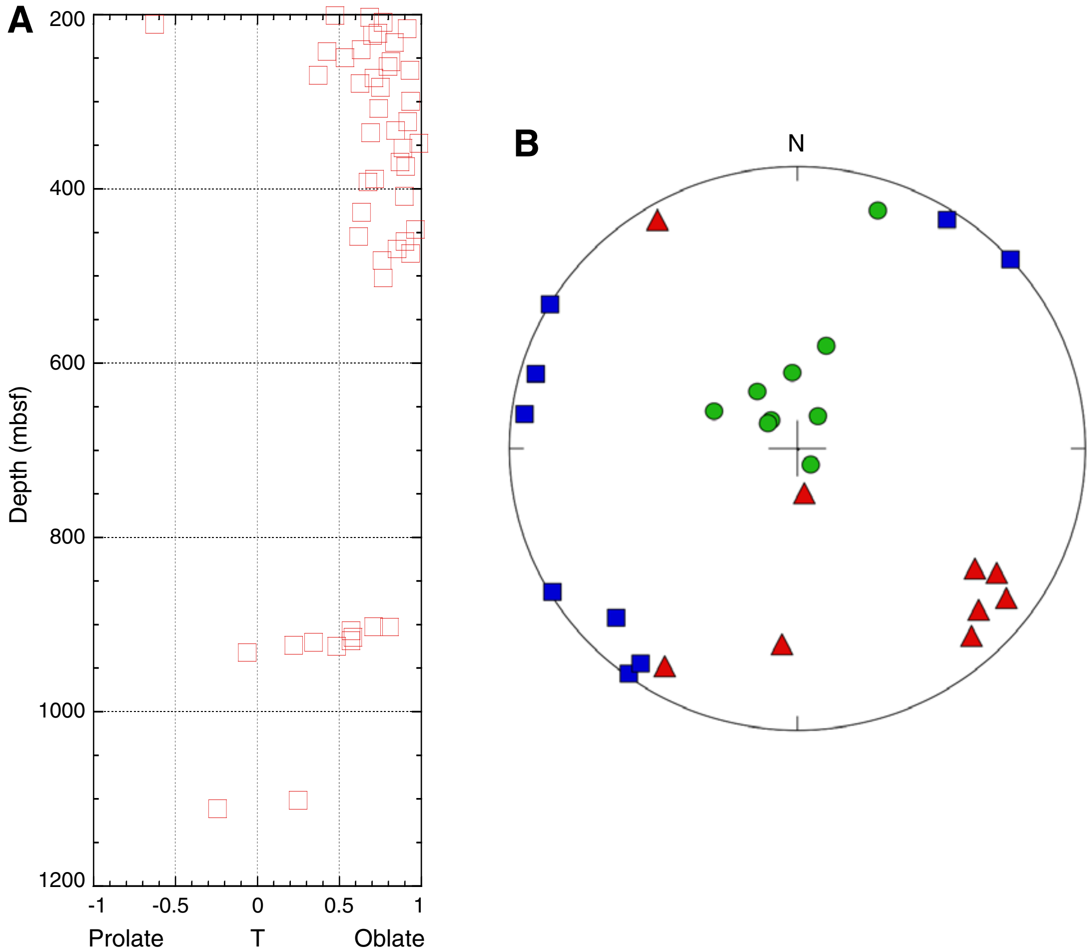

Figure F115. Cuttings-core-log-seismic integration, Site C0002. Composite medium button static resistivity image, seismic data from In-line 2532 of the Kumano 3-D PSDM volume (Moore et al., 2009) with all Site C0002 holes projected onto the seismic line, composite core lithology plot, cuttings-derived unit boundaries, logging-while-drilling (LWD) unit boundaries, and composite LWD data. The composite LWD data comprise Hole C0002A data from 0 to 900 mbsf and Hole C0002F data below 900 mbsf. VE = vertical exaggeration.

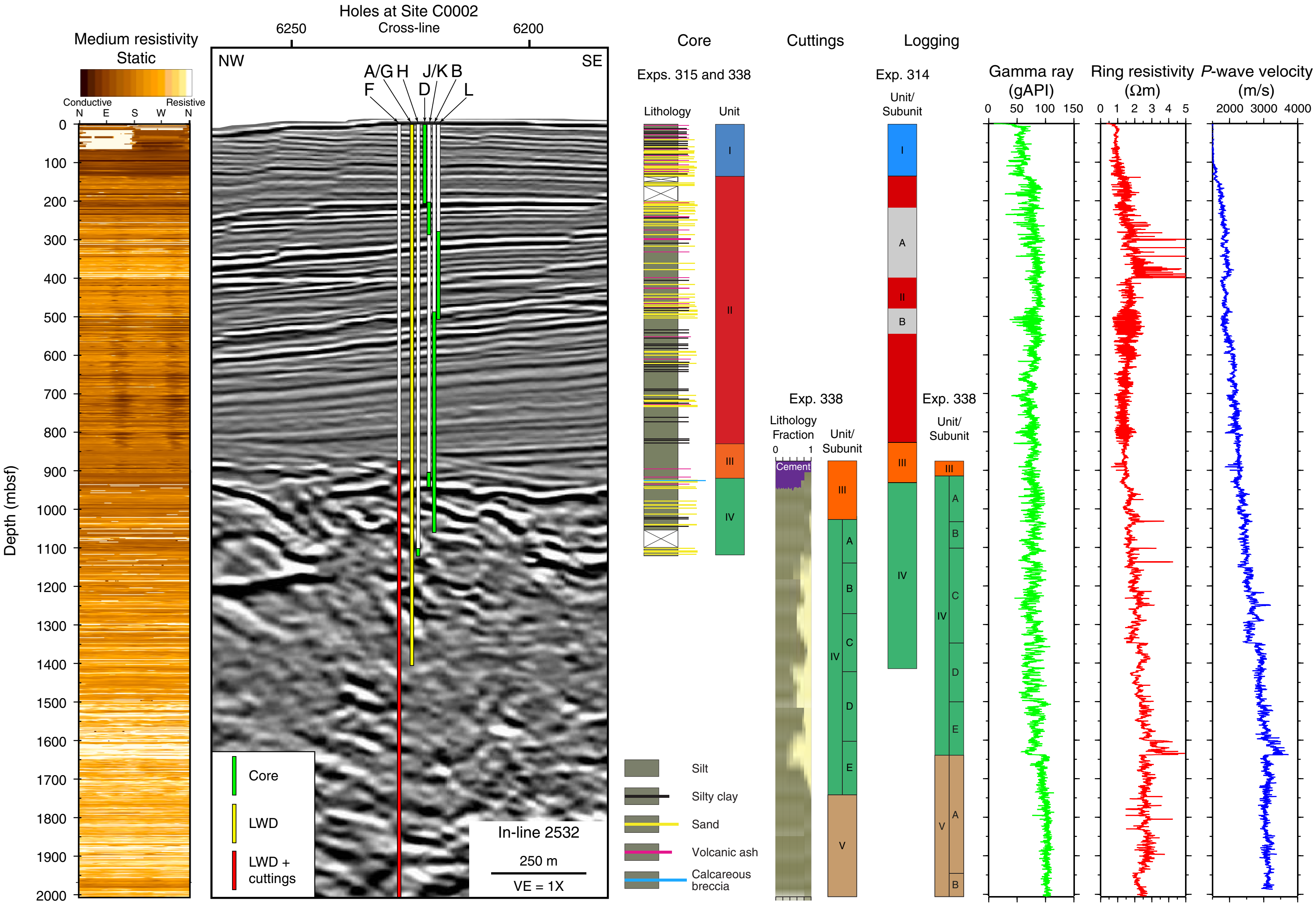

Figure F116. Comparison of natural gamma ray values at the Unit III/IV boundary, Site C0002. A reference baseline of 75 gAPI is included on all LWD gamma ray curves. From left to right: caliper measurement in Hole C0002A (blue line = bit diameter, red line = maximum operational borehole diameter for the LWD tool); LWD gamma ray curves for Holes C0002A, C0002G, and Hole C0002F; whole-round multisensor core logger (MSCL-W) natural gamma ray measurements from Hole C0002B (black dots) and C0002J (red dots) cores; and natural gamma ray measurements from Hole C0002F cuttings.

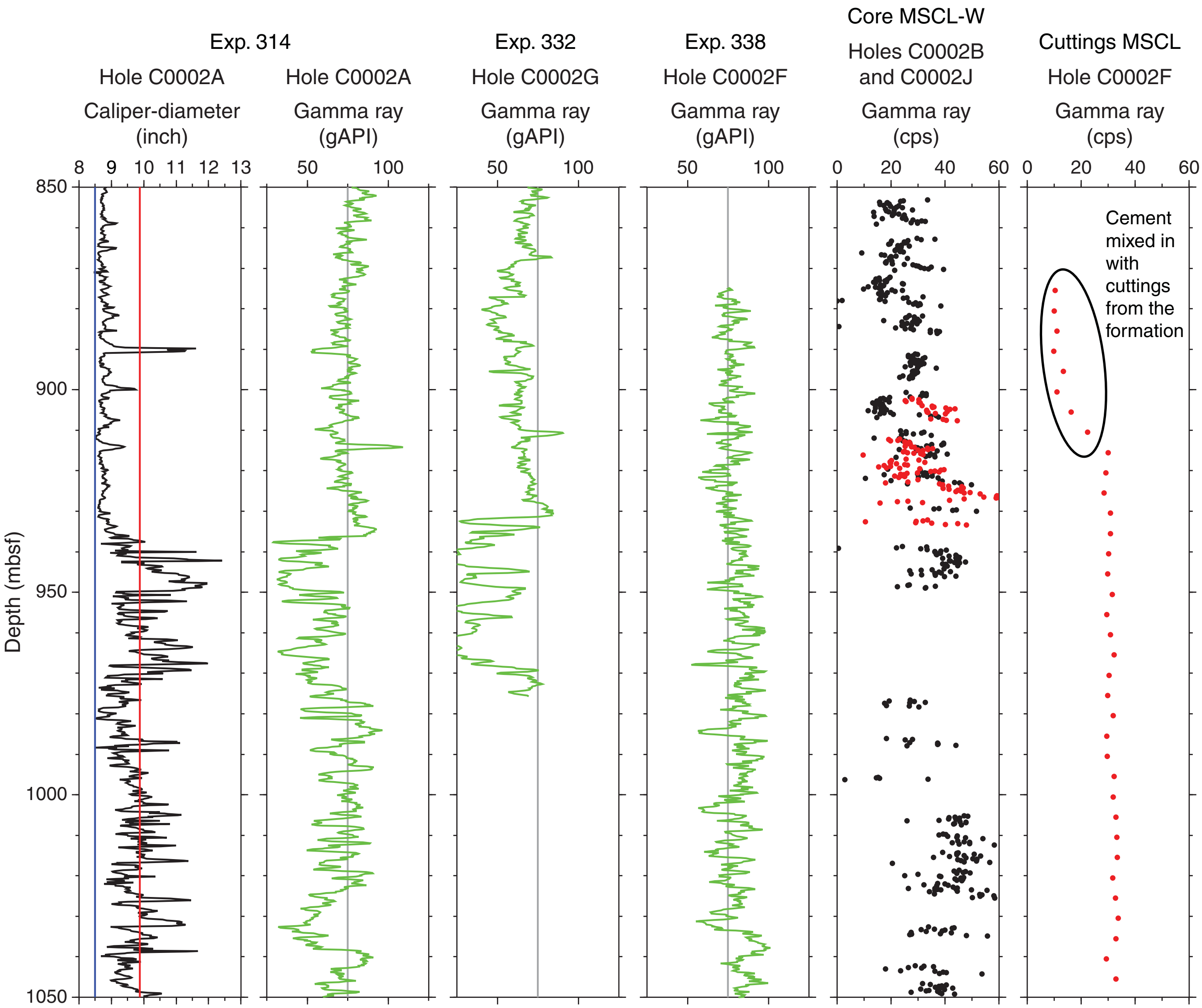

Table T1. LWD/MWD bottom-hole assembly (BHA) components for 12¼ inch bit and 20 inch underreamer.

BHA component	Length of tool (m)	Total length of the top of tool from the bit (m)
12-1/4 inch PDC bit	0.290	0.290
GVR-8 w/2 × 12-1/8 inch stabilizer	3.882	4.172
ARC-8	5.644	9.816
TeleScope 825	8.435	18.251
12-1/8 inch ILS (stabilizer)	0.830	19.081
sonicVISION 825	7.299	26.380
12-1/8 inch stabilizer	2.375	28.755
8-1/2 inch drill collar	9.223	37.978
CST 10-5/8 inch × 16-1/2 inch	1.310	39.288
Cutter part of CST	0.340	38.318
Anderreamer 16-3/8 inch × 20 inch	7.500	46.788
Cutter part of Anderreamer	4.500	43.788
Float sub	1.085	47.873
9-1/2 inch drill collar	9.308	57.181
9-1/2 inch drill collar	9.246	66.427
17 inch stabilizer	1.706	68.133
9-1/2 inch drill collar	9.310	77.443
Crossover	1.000	78.443
8-1/2 inch drill collar	9.310	87.753
8-1/2 inch drill collar	8.930	96.683
8-1/2 inch drill collar	9.310	105.993
7-3/4 inch drilling jar	10.635	116.628
8-1/2 inch drill collar	9.220	125.848
8-1/2 inch drill collar	9.310	135.158
8-1/2 inch drill collar	9.305	144.463
Crossover	0.508	144.971
5.68 inch heavy weight drill pipe	9.050	154.021
5.68 inch heavy weight drill pipe	9.042	163.063
5.68 inch heavy weight drill pipe	9.042	172.105
5.68 inch heavy weight drill pipe	9.043	181.148
5.68 inch heavy weight drill pipe	9.043	190.191
5.68 inch heavy weight drill pipe	9.050	199.241
5.68 inch heavy weight drill pipe	9.050	208.291
5.68 inch heavy weight drill pipe	9.050	217.341
5.68 inch heavy weight drill pipe	9.042	226.383
5.68 inch heavy weight drill pipe	9.050	235.433
5.68 inch heavy weight drill pipe	8.963	244.396
5.68 inch heavy weight drill pipe	9.050	253.446
Crossover	1.002	254.448

PDC = polycrystalline diamond compact. GVR = geoVISION resistivity tool. ILS = instrument landing system. CST = concentric string tool.

Table T2. Summary of LWD data acquired in Hole C0002F during Expedition 338.

Data	Raw	Processed	Processing by	Depth reference	Logs included	Data included	Available formats
Real time	x	x	LSS	Raw: DRF, mbsf Processed: mbsf	Main Ream Up 1 (1432.40–494.63 mbsf), Ream Down 2 (1480.86–1538.48 mbsf), Ream Down 3 (1557.82–1615.47 mbsf)	Gamma ray, shallow, medium, and deep button resistivity; unprocessed compressional slowness; rate of penetration; downhole annular pressure; downhole annular temperature; downhole weight on bit; downhole torque; surface weight on bit; surface torque; equivalent circulating density	DLIS/LAS
Memory data	x	x	LSS	Raw: DRF, mbsf Processed: mbsf	Main Ream Up 1 (1432.40–494.63 mbsf), Ream Down 2 (1480.86–1538.48 mbsf), Ream Down 3 (1557.82–1615.47 mbsf)	Gamma ray; bit resistivity; ring resistivity; shallow, medium, and deep button resistivity; rate of penetration; rotational speed; collar rotational speed; downhole annular pressure; downhole annular temperature; downhole weight on bit; downhole torque; surface weight on bit; surface torque; equivalent circulating density; equivalent static density; minimum and maximum static density; standpipe pressure; stick ratio; total flow rate of all active pumps	
Time	x	x	LSS	Time	Main (includes relogged sections in same file)	Borehole and bit depth; gamma ray; rate of penetration; rotational speed; collar rotational speed; downhole annular pressure; downhole annular temperature; downhole weight on bit; downhole torque; surface weight on bit; surface torque; equivalent circulating density; equivalent static density; minimum and maximum static density; standpipe pressure; stick ratio; axial, tool, and radial show level; Pump 1, 2, and 3 stroke rates; total stroke rate for all pumps; total flow rate of all active pumps; average hook load; status of the slips (in or out); status of the drill bit (on bottom); composite on bottom status	
Image logs		x	LSS	mbsf	Main Ream Up 1 (1432.40–494.63 mbsf), Ream Down 2 (1480.86–1538.48 mbsf), Ream Down 3 (1557.82–1615.47 mbsf)	Shallow, medium, and deep image logs with static normalization	DLIS/PDF
Sonic		x	SLB onshore	mbsf	Main	Compressional slowness, compressional velocity	DLIS/LAS

LSS = logging staff scientist, SLB = Schlumberger. DLIS = digital log information standard, LAS = log ASCII standard.

Table T3. Depth where the drill bit was off bottom longer than 30 min and the time the bit was off bottom, Hole C0002F.

Depth (mbsf)	Time spent off bottom (min)
914.807	176.17
916.557	33.50
917.557	55.33
1012.225	84.50
1043.03	44.67
1081.034	154.67
1120.321	74.50
1232.500	214.00
1271.688	55.50
1309.975	58.50
1500.610	195.17
1539.815	1534.83
1570.116	45.00
1604.836	1003.33
1616.272	153.50
1654.314	30.67
1730.807	43.00
1768.739	46.83
1793.992	53.50
1797.755	85.17
1807.054	49.00
1818.042	38.50
1841.011	81.00
1862.168	459.50
1862.823	239.67
1882.176	56.50
1911.141	79.50
1921.315	39.50
1959.318	51.00
1968.848	52.83
1997.940	83.50
2005.541	71.67

Table T4. Logging units described in text and typical log values for each interval, Hole C0002F.

Depth (mbsf)	Log unit	Depth (mbsf)	Subunit	Gamma ray (gAPI)			Bit resistivity values (Ωm)			Sonic velocity (m/s)		
				Low	High	Average	Low	High	Average	Low	High	Average
875.5–918.5	III			60	91	76	1.1	1.6	1.4	1940	2420	2270
918.5–1638	IV	918.5–1033	IVA	52	100	80	1.2	3	1.6	2028	2660	2340
		1033–1100	IVB	53	101	80	1.3	2.1	1.6	2240	2630	2440
		1100–1348	IVC	45	102	77	1.4	3	1.6	2240	3200	2590
		1348–1500	IVD	52	108	74	1.8	2.7	2.2	2670	3090	2890
		1500–1638	IVE	57	110	83	2.1	4.8	2.7	2760	3730	3100
1638–2005.5	V	1638–1946	VA	72	115	100	1.6	3	2.5	2830	3460	3090
		1946–2005.5	VB	91	111	102	1.9	2.5	2.1	2980	3300	3120

Table T5. Main structural features characterized from log images, including the number of conductive, resistive, and undefined fractures for each logging unit, Hole C0002F.

Depth (mbsf)	Log unit	Fracture type			Depth (mbsf)		
		Undefined	Resistive	Conductive	Interpreted faults	Fractured zones	Folds
875.5–918.5	III	0	0	0			
918.5–1638	IV	17	59	6	1013.4	1234–1238	1063
					1182	1370–1374	1099
					1189	1394–1397	1281
					1207	1506–1550	1506
					1360	1601–1603	1544
1638–2005.5	V	9	23	15	1639	1778–1781	1648
					1642	1795–1796	1682
					1869.3		
					1874		
					1955		

Table T6. Summary of lithologic units, depths, and sample intervals, Hole C0002F.

Unit	Depth (mbsf)	Interval	Lithology		Environmental interpretation
			Major	Minor	
		338-C0002F-			
III	875.5–1025.5	7-SMW to 45-SMW	Silty claystone	Silty claystone	Lower part of the Kumano forearc basin
IV	1025.5–1740.5				
Subunit IVA	1025.5–1140.5	45-SMW to 71-SMW	Silty claystone	Sandstone	Upper accretionary prism slope basin
Subunit IVB	1140.5–1270.5	71-SMW to 100-SMW	Silty claystone	Sandstone	Trench, accretionary prism slope basin, or Shikoku Basin submarine fan and related deposits
Subunit IVC	1270.5–1420.5	100-SMW to 134-SMW	Silty claystone	Sandstone	
Subunit IVD	1420.5–1600.5	134-SMW to 182-SMW	Silty claystone	Sandstone	
Subunit IVE	1600.5–1740.5	182-SMW to 215-SMW	Silty claystone	Sandstone	
V	1740.5–2004.5	215-SMW to 289-SMW	Silty claystone	Sandstone	Hemipelagic deposits—trench or Shikoku Basin?

Table T7. Visual lithologic estimations (binocular microscope) of percent silty clay(stone), percent sand(stone), induration, grain shape, and fossil content, Hole C0002F. (Continued on next page.)

Cuttings sample	Depth (mbsf)			Silty claystone			Sandstone			Fossils
	Top	Bottom	Underreamer	(%)	Induration	Shape	(%)	Induration	Shape	
338-C0002F-										
7-SMW	875.5	880.5	832.7	0			0			Not observed
8-SMW	880.5	885.5	837.7	0			0			Not observed
9-SMW	885.5	890.5	842.7	1	Semi	Angular	0			Not observed
14-SMW	890.5	895.5	847.7	5	Semi	Angular	0			Not observed
15-SMW	895.5	900.5	852.7	20	Semi	Angular	0			Not observed
16-SMW	900.5	905.5	857.7	5	Semi	Angular	0			Not observed
17-SMW	905.5	910.5	862.7	5	Semi	Angular	0			Rare
18-SMW	910.5	915.5	867.7	15	Semi	Angular	0			Not observed
19-SMW	915.5	920.5	872.7	5	Semi	Angular	0			Not observed
20-SMW	920.5	925.5	877.7	30	Semi	Angular	0			Rare
21-SMW	925.5	930.5	882.7	30	Semi	Angular	0			Not observed
22-SMW	930.5	935.5	887.7	65	Semi	Angular	0			Not observed
24-SMW	935.5	940.5	892.7	60	Semi	Angular	0			Not observed
25-SMW	940.5	945.5	897.7	85	Semi	Angular	0			Not observed
26-SMW	945.5	950.5	902.7	80	Semi	Angular	0			Not observed
27-SMW	950.5	955.5	907.7	80	Semi	Angular	0			Not observed
28-SMW	955.5	960.5	912.7	99	Semi	Angular	0			Not observed
29-SMW	960.5	965.5	917.7	99	Semi	Angular	1	Soft		Not observed
30-SMW	965.5	970.5	922.7	100	Semi	Angular	0			Rare
31-SMW	970.5	975.5	927.7	100	Semi	Angular	0			Rare
32-SMW	975.5	980.5	932.7	100	Semi	Angular	0			Rare
34-SMW	980.5	985.5	937.7	100	Semi	Angular	0			Rare
35-SMW	985.5	990.5	942.7	100	Semi	Angular	0			Rare
36-SMW	990.5	995.5	947.7	100	Semi	Angular	0			Rare
37-SMW	995.5	1000.5	952.7	100	Semi	Angular	0			Rare
40-SMW	1000.5	1005.5	957.7	100	Semi	Angular	0			Rare
41-SMW	1005.5	1010.5	962.7	100	Semi	Angular	0			Rare
42-SMW	1010.5	1015.5	967.7	100	Semi	Angular	0			Rare
43-SMW	1015.5	1020.5	972.7	100	Semi	Angular	0			Rare
44-SMW	1020.5	1025.5	977.7	100	Semi	Angular	0			Rare
45-SMW	1025.5	1030.5	982.7	95	Semi	Angular	5	Soft	Round	Rare
46-SMW	1030.5	1035.5	987.7	95	Semi	Angular	5	Soft	Round	Rare
47-SMW	1035.5	1040.5	992.7	95	Semi	Angular	5	Soft	Round	Rare
48-SMW	1040.5	1045.5	997.7	95	Semi	Angular	5	Soft	Round	Rare
49-SMW	1045.5	1050.5	1002.7	95	Semi	Angular	5	Soft	Round	Rare
50-SMW	1050.5	1055.5	1007.7	95	Semi	Angular	5	Soft	Round	Rare
51-SMW	1055.5	1060.5	1012.7	95	Semi	Angular	5	Soft	Round	Rare
52-SMW	1060.5	1065.5	1017.7	99	Semi	Angular	1	Soft	Round	Not observed
54-SMW	1070.5	1075.5	1027.7	99	Semi	Angular	1	Soft	Round	Not observed
56-SMW	1080.5	1085.5	1037.7	99	Semi	Angular	1	Soft	Round	Not observed
58-SMW	1090.5	1095.5	1047.7	99	Semi	Angular	1	Soft	Round	Not observed
62-SMW	1100.5	1105.5	1057.7	99	Semi	Angular	1	Soft	Round	Rare
64-SMW	1110.5	1115.5	1067.7	100	Semi	Angular	0			Rare
66-SMW	1120.5	1125.5	1077.7	100	Semi	Angular	0			Rare
68-SMW	1130.5	1135.5	1087.7	100	Semi	Angular	0			Not observed
71-SMW	1140.5	1145.5	1097.7	70	Semi	Angular	30	Soft	Round	Not observed
73-SMW	1150.5	1155.5	1107.7	70	Semi	Angular	30	Soft	Round	Not observed
75-SMW	1160.5	1165.5	1117.7	95	Semi	Angular	5	Soft	Round	Not observed
77-SMW	1170.5	1175.5	1127.7	70	Semi	Angular	30	Soft	Round	Not observed
80-SMW	1180.5	1185.5	1137.7	50	Semi	Angular	50	Soft	Round	Not observed
82-SMW	1190.5	1195.5	1147.7	70	Semi	Angular	30	Soft	Round	Rare
84-SMW	1200.5	1205.5	1157.7	70	Semi	Angular	30	Soft	Round	Not observed
86-SMW	1210.5	1215.5	1167.7	70	Semi	Angular	30	Soft	Round	Rare
90-SMW	1220.5	1225.5	1177.7	70	Semi	Angular	30	Soft	Round	Rare
92-SMW	1230.5	1235.5	1187.7	80	Semi	Angular	20	Soft	Round	Rare
94-SMW	1240.5	1245.5	1197.7	85	Semi	Angular	15	Soft	Round	Rare
96-SMW	1250.5	1255.5	1207.7	80	Semi	Angular	20	Soft	Round	Rare
98-SMW	1260.5	1265.5	1217.7	70	Semi	Angular	30	Soft	Round	Not observed
100-SMW	1270.5	1275.5	1227.7	60	Semi	Angular	40	Soft	Round	Not observed
102-SMW	1280.5	1285.5	1237.7	60	Semi	Angular	40	Soft	Round	Not observed
104-SMW	1290.5	1295.5	1247.7	60	Semi	Angular	40	Soft	Round	Not observed
106-SMW	1300.5	1305.5	1257.7	60	Semi	Angular	40	Soft	Round	Not observed
108-SMW	1310.5	1315.5	1267.7	60	Semi	Angular	40	Soft	Round	Not observed
110-SMW	1320.5	1325.5	1277.7	60	Semi	Angular	40	Soft	Round	Not observed
112-SMW	1330.5	1335.5	1287.7	70	Semi	Angular	30	Soft	Round	Rare

Table T7 (continued).

Cuttings sample	Depth (mbsf)			Silty claystone			Sandstone			Fossils
	Top	Bottom	Underreamer	(%)	Induration	Shape	(%)	Induration	Shape	
114-SMW	1340.5	1345.5	1297.7	70	Semi	Angular	30	Soft	Round	Rare
116-SMW	1350.5	1355.5	1307.7	80	Semi	Angular	20	Soft	Round	Rare
120-SMW	1360.5	1365.5	1317.7	80	Semi	Angular	20	Soft	Round	Rare
122-SMW	1370.5	1375.5	1327.7	90	Semi	Angular	10	Soft	Round	Rare
124-SMW	1380.5	1385.5	1337.7	90	Semi	Angular	10	Soft	Round	Rare
126-SMW	1390.5	1395.5	1347.7	90	Semi	Angular	10	Soft	Round	Rare
130-SMW	1400.5	1405.5	1357.7	85	Semi	Angular	15	Soft	Round	Rare
132-SMW	1410.5	1415.5	1367.7	80	Semi	Angular	20	Soft	Round	Rare
134-SMW	1420.5	1425.5	1377.7	40	Semi	Angular	60	Soft	Round	Not observed
136-SMW	1430.5	1435.5	1387.7	50	Semi	Angular	50	Soft	Round	Not observed
138-SMW	1440.5	1445.5	1397.7	50	Semi	Angular	50	Soft	Round	Not observed
140-SMW	1450.5	1455.5	1407.7	50	Semi	Angular	50	Soft	Round	Not observed
142-SMW	1460.5	1465.5	1417.7	60	Semi	Angular	40	Soft	Round	Not observed
144-SMW	1470.5	1475.5	1427.7	70	Semi	Angular	30	Soft	Round	Rare
148-SMW	1480.5	1485.5	1437.7	60	Semi	Angular	40	Soft	Round	Not observed
150-SMW	1490.5	1495.5	1447.7	60	Semi	Angular	40	Soft	Round	Not observed
153-SMW	1500.5	1505.5	1457.7	50	Semi	Angular	50	Soft	Round	Not observed
155-SMW	1510.5	1515.5	1467.7	60	Semi	Angular	40	Soft	Round	Not observed
158-SMW	1520.5	1525.5	1477.7	60	Semi	Angular	40	Soft	Round	Not observed
161-SMW	1530.5	1535.5	1487.7	80	Semi	Angular	20	Soft	Round	Rare
163-SMW	1540.5	1545.5	1497.7	80	Semi	Angular	20	Soft	Round	Rare
167-SMW	1550.5	1555.5	1507.7	80	Semi	Angular	20	Soft	Round	Rare
169-SMW	1560.5	1565.5	1517.7	75	Semi	Angular	25	Soft	Round	Rare
172-SMW	1570.5	1575.5	1527.7	75	Semi	Angular	25	Soft	Round	Rare
174-SMW	1580.5	1585.5	1537.7	85	Semi	Angular	15	Soft	Round	Rare
177-SMW	1590.5	1595.5	1547.7	85	Semi	Angular	15	Soft	Round	Rare
182-SMW	1600.5	1605.5	1557.7	50	Semi	Angular	50	Soft	Round	Rare
184-SMW	1610.5	1615.5	1567.7	60	Semi	Angular	40	Semi	Round	Rare
187-SMW	1620.5	1625.5	1577.7	40	Semi	Angular	60	Semi	Round	Rare
189-SMW	1630.5	1635.5	1587.7	50	Semi	Angular	50	Semi	Round	Rare
193-SMW	1640.5	1645.5	1597.7	30	Semi	Angular	70	Soft	Round	Rare
195-SMW	1650.5	1655.5	1607.7	50	Semi	Angular	50	Soft	Round	Rare
199-SMW	1660.5	1665.5	1617.7	40	Semi	Angular	60	Soft	Round	Rare
201-SMW	1670.5	1675.5	1627.7	30	Semi	Angular	70	Soft	Round	Rare
203-SMW	1680.5	1685.5	1637.7	70	Semi	Angular	30	Soft	Round	Rare
205-SMW	1690.5	1695.5	1647.7	80	Semi	Angular	20	Soft	Round	Rare
207-SMW	1700.5	1705.5	1657.7	80	Semi	Angular	20	Soft	Round	Rare
209-SMW	1710.5	1715.5	1667.7	90	Semi	Angular	10	Soft	Round	Rare
211-SMW	1720.5	1725.5	1677.7	90	Semi	Angular	10	Soft	Round	Rare
213-SMW	1730.5	1735.5	1687.7	95	Soft	Round	5	Soft	Round	Not observed
215-SMW	1740.5	1745.5	1697.7	98	Soft	Round	2	Soft	Round	Not observed
217-SMW	1750.5	1755.5	1707.7	100	Soft	Round	0			Not observed
219-SMW	1760.5	1765.5	1717.7	100	Soft	Round	0			Not observed
223-SMW	1770.5	1775.5	1727.7	100	Soft	Round	0			Not observed
227-SMW	1780.5	1785.5	1737.7	100	Soft	Round	0			Not observed
229-SMW	1790.5	1795.5	1747.7	100	Soft	Round	0			Not observed
231-SMW	1800.5	1805.5	1757.7	100	Soft	Round	0			Not observed
233-SMW	1810.5	1815.5	1767.7	100	Soft	Round	0			Not observed
235-SMW	1820.5	1825.5	1777.7	100	Soft	Round	0			Not observed
238-SMW	1830.5	1835.5	1787.7	100	Soft	Round	0			Not observed
240-SMW	1840.5	1845.5	1797.7	100	Soft	Round	0			Not observed
250-SMW	1850.5	1855.5	1807.7	100	Soft	Round	0			Not observed
253-SMW	1860.5	1865.5	1817.7	100	Soft	Round	0			Not observed
255-SMW	1870.5	1875.5	1827.7	100	Soft	Round	0			Not observed
258-SMW	1880.5	1885.5	1837.7	100	Soft	Round	0			Not observed
260-SMW	1890.5	1895.5	1847.7	100	Soft	Round	0			Not observed
263-SMW	1900.5	1905.5	1857.7	100	Soft	Round	0			Not observed
265-SMW	1910.5	1915.5	1867.7	100	Soft	Round	0			Not observed
267-SMW	1920.5	1925.5	1877.7	100	Soft	Round	0			Not observed
269-SMW	1930.5	1935.5	1887.7	100	Soft	Round	0			Not observed
272-SMW	1940.5	1945.5	1897.7	100	Soft	Round	0			Not observed
274-SMW	1950.5	1955.5	1907.7	100	Soft	Round	0			Not observed
280-SMW	1960.5	1965.5	1917.7	100	Soft	Round	0			Not observed
282-SMW	1970.5	1975.5	1927.7	100	Soft	Round	0			Not observed
284-SMW	1980.5	1985.5	1937.7	100	Soft	Round	0			Not observed
286-SMW	1990.5	1995.5	1947.7	100	Soft	Round	0			Not observed
288-SMW	2000.5	2005.5	1957.7	100	Soft	Round	0			Not observed
289-SMW	2005.5	2005.5	1962.7	100	Soft	Round	0			Not observed

Table T8. Q-index database of samples from Hole C0002F, with maximum quartz grain *a*-axis dimension in principal grain-size population. (Continued on next page.)

Cuttings sample	Depth (mbsf)		Q-index (µm)
	Drill bit	Underreamer	
338-C0002F-			
20-SMW	925.5	882.7	650
21-SMW	930.5	887.7	270
22-SMW	935.5	892.7	617
25-SMW	945.5	902.7	537
26-SMW	950.5	907.7	465
27-SMW	955.5	912.7	734
28-SMW	960.5	917.7	400
29-SMW	965.5	922.7	667
30-SMW	970.5	927.7	313
31-SMW	975.5	932.7	497
32-SMW	980.5	937.7	544
35-SMW	990.5	947.7	651
36-SMW	995.5	952.7	595
37-SMW	1000.5	957.7	695
40-SMW	1005.5	962.7	500
41-SMW	1010.5	967.7	793
42-SMW	1015.5	972.7	741
43-SMW	1020.5	977.7	1040
44-SMW	1025.5	982.7	930
45-SMW	1030.5	987.7	990
46-SMW	1035.5	992.7	1070
47-SMW	1040.5	997.7	970
48-SMW	1045.5	1002.7	890
49-SMW	1050.5	1007.7	1330
50-SMW	1055.5	1012.7	1030
51-SMW	1060.5	1017.7	792
52-SMW	1065.5	1022.7	1110
54-SMW	1075.5	1032.7	920
56-SMW	1085.5	1042.7	1150
58-SMW	1095.5	1052.7	644
62-SMW	1105.5	1062.7	880
64-SMW	1115.5	1072.7	670
66-SMW	1125.5	1082.7	740
68-SMW	1135.5	1092.7	620
71-SMW	1145.5	1102.7	689
73-SMW	1155.5	1112.7	530
80-SMW	1185.5	1142.7	210
82-SMW	1195.5	1152.7	830
84-SMW	1205.5	1162.7	1920
86-SMW	1215.5	1172.7	960
92-SMW	1235.5	1192.7	1090
94-SMW	1245.5	1202.7	960
96-SMW	1255.5	1212.7	1160
90-SMW	1265.5	1222.7	1096
100-SMW	1275.5	1232.7	1170
102-SMW	1285.5	1242.7	1170
104-SMW	1295.5	1252.7	962
106-SMW	1300.5	1257.7	1340
108-SMW	1315.5	1272.7	1125
110-SMW	1325.5	1282.7	1120
114-SMW	1345.5	1302.7	1160
116-SMW	1350.5	1307.7	980
120-SMW	1365.5	1322.7	900
122-SMW	1375.5	1332.7	1080
124-SMW	1385.5	1342.7	1320
126-SMW	1395.5	1352.7	1050
130-SMW	1405.5	1362.7	1000
132-SMW	1415.5	1372.7	1340
134-SMW	1425.5	1382.7	1080
136-SMW	1435.5	1392.7	756
138-SMW	1445.5	1402.7	1300
140-SMW	1455.5	1412.7	1290
142-SMW	1465.5	1422.7	1070
144-SMW	1475.5	1432.7	1041
148-SMW	1485.5	1442.7	1470
150-SMW	1495.5	1452.7	1640

Table T8 (continued).

Cuttings sample	Depth (mbsf) Drill bit	Depth (mbsf) Underreamer	Q-index (µm)
153-SMW	1505.5	1462.7	1780
155-SMW	1515.5	1472.7	1180
158-SMW	1530.5	1487.7	1016
161-SMW	1535.5	1492.7	1810
163-SMW	1545.5	1502.7	1160
167-SMW	1555.5	1512.7	830
169-SMW	1565.5	1522.7	1240
172-SMW	1575.5	1532.7	1290
174-SMW	1585.5	1542.7	1820
177-SMW	1595.5	1552.7	842
182-SMW	1605.5	1562.7	910
184-SMW	1615.5	1572.7	1670
187-SMW	1625.5	1582.7	1130
189-SMW	1635.5	1592.7	1210
193-SMW	1645.5	1602.7	650
195-SMW	1655.5	1612.7	1610
199-SMW	1675.5	1632.7	1520
200-SMW	1675.5	1632.7	750
203-SMW	1685.5	1642.7	1440
205-SMW	1695.5	1652.7	890
207-SMW	1705.5	1662.7	1240
209-SMW	1715.5	1672.7	1300
211-SMW	1725.5	1682.7	631
213-SMW	1735.5	1692.7	329
215-SMW	1745.5	1702.7	655
217-SMW	1755.5	1712.7	366
219-SMW	1765.5	1722.7	379
223-SMW	1775.5	1732.7	474
227-SMW	1785.5	1742.7	594
229-SMW	1795.5	1752.7	317
231-SMW	1805.5	1762.7	394
233-SMW	1815.5	1772.7	279
235-SMW	1825.5	1782.7	346
238-SMW	1835.5	1792.7	263
240-SMW	1845.5	1802.7	288
250-SMW	1855.5	1812.7	527
253-SMW	1865.5	1822.7	650
255-SMW	1875.5	1832.7	772
258-SMW	1885.5	1842.7	459
260-SMW	1895.5	1852.7	466
263-SMW	1905.5	1862.7	965
265-SMW	1915.5	1872.7	386
267-SMW	1925.5	1882.7	319
269-SMW	1935.5	1892.7	657
272-SMW	1945.5	1902.7	529
274-SMW	1955.5	1912.7	388
280-SMW	1965.5	1922.7	358
282-SMW	1975.5	1932.7	386
284-SMW	1985.5	1942.7	463
287-SMW	1995.5	1952.7	583
289-SMW	2004.5	1961.7	515

Table T9. Results of X-ray diffraction analysis, performed on random bulk powder of cuttings samples, Hole C0002F. (Continued on next three pages.)

Cuttings sample	Depth (mbsf)	Size fraction (mm)	Integrated peak area (total counts)				Absolute mineral abundance calculated from SVD normalization factors (wt%)					Relative abundance (wt%)			
			Total clay minerals	Quartz	Feldspar	Calcite	Total clay minerals	Quartz	Feldspar	Calcite	Sum	Total clay minerals	Quartz	Feldspar	Calcite
338-C0002F-															
20-SMW	920.5	1–4	2,259	29,484	10,946	18,777	30.9	16.0	10.8	22.2	80.0	38.6	20.0	13.5	27.8
21-SMW	925.5	1–4	2,147	28,403	9,929	17,977	29.1	15.5	9.7	21.3	75.7	38.5	20.5	12.9	28.2
22-SMW	930.5	1–4	2,683	29,409	14,704	17,657	37.4	15.6	14.9	20.0	87.9	42.5	17.8	17.0	22.8
24-SMW	935.5	1–4	2,931	27,551	9,877	17,808	37.7	14.8	9.5	20.2	82.2	45.9	18.0	11.5	24.5
25-SMW	940.5	1–4	3,293	30,430	9,999	17,796	41.7	16.4	9.4	19.7	87.3	47.8	18.8	10.8	22.5
26-SMW	945.5	1–4	2,736	30,021	10,457	17,686	35.8	16.3	10.1	20.2	82.4	43.5	19.8	12.3	24.5
27-SMW	950.5	1–4	3,420	26,805	10,833	16,829	43.5	14.2	10.4	18.2	86.4	50.4	16.5	12.1	21.1
28-SMW	955.5	1–4	3,554	28,379	9,608	16,511	44.4	15.2	9.0	17.6	86.2	51.5	17.7	10.4	20.5
29-SMW	960.5	1–4	3,517	25,803	8,993	15,303	43.6	13.8	8.4	16.1	81.8	53.3	16.8	10.2	19.7
32-SMW	975.5	1–4	3,139	27,620	10,381	13,316	40.0	14.8	10.0	13.7	78.5	51.0	18.9	12.7	17.4
34-SMW	980.5	1–4	3,498	30,184	12,114	11,615	44.7	16.1	11.8	10.8	83.4	53.6	19.4	14.1	12.9
35-SMW	985.5	1–4	3,523	28,857	11,671	10,860	44.7	15.4	11.3	9.7	81.2	55.1	19.0	13.9	12.0
36-SMW	990.5	1–4	3,774	27,319	9,928	11,264	46.7	14.6	9.3	10.1	80.6	57.9	18.0	11.6	12.5
37-SMW	995.5	1–4	3,744	30,913	12,033	8,944	47.2	16.5	11.6	6.7	82.1	57.5	20.1	14.1	8.2
40-SMW	1000.5	1–4	3,229	31,546	12,376	8,065	41.6	17.0	12.1	6.1	76.9	54.2	22.1	15.8	7.9
41-SMW	1005.5	1–4	4,181	32,480	15,341	5,509	53.4	17.1	15.2	1.3	87.0	61.4	19.7	17.4	1.5
42-SMW	1010.5	1–4	3,673	28,274	11,108	5,608	45.8	15.1	10.7	2.3	73.9	62.0	20.4	14.5	3.1
43-SMW	1015.5	1–4	3,749	30,697	12,453	5,823	47.3	16.4	12.1	2.4	78.2	60.5	21.0	15.5	3.1
44-SMW	1020.5	1–4	4,833	29,882	11,042	5,863	58.5	15.8	10.2	1.2	85.8	68.2	18.4	11.9	1.4
45-SMW	1025.5	1–4	3,721	30,723	13,869	5,427	47.7	16.3	13.7	1.8	79.5	60.0	20.5	17.2	2.3
46-SMW	1030.5	1–4	3,685	31,290	16,285	5,867	48.5	16.5	16.4	2.4	83.7	57.9	19.7	19.6	2.8
47-SMW	1035.5	1–4	4,065	32,836	13,005	5,611	51.0	17.5	12.6	1.7	82.8	61.6	21.2	15.2	2.0
48-SMW	1040.5	1–4	3,318	31,646	16,189	7,257	44.5	16.8	16.4	4.7	82.3	54.0	20.4	19.9	5.7
49-SMW	1045.5	1–4	3,259	31,744	15,939	7,075	43.7	16.8	16.1	4.5	81.2	53.8	20.7	19.9	5.6
50-SMW	1050.5	1–4	4,232	32,096	14,279	6,737	53.5	17.0	14.0	3.0	87.5	61.2	19.4	16.0	3.4
51-SMW	1055.5	1–4	4,070	31,468	15,472	6,999	52.4	16.6	15.4	3.5	87.8	59.6	18.9	17.5	4.0
52-SMW	1060.5	1–4	4,052	31,588	13,383	6,916	51.1	16.8	13.0	3.5	84.4	60.6	19.9	15.4	4.1
54-SMW	1070.5	1–4	3,951	34,174	15,006	5,988	50.7	18.2	14.8	2.2	86.0	59.0	21.2	17.2	2.6
56-SMW	1080.5	1–4	3,966	33,129	14,524	6,438	50.7	17.6	14.3	2.8	85.5	59.3	20.6	16.7	3.3
58-SMW	1090.5	1–4	3,825	31,145	16,538	6,575	50.2	16.3	16.7	3.2	86.3	58.1	18.9	19.3	3.7
62-SMW	1100.5	1–4	3,506	31,118	16,786	6,287	46.8	16.4	17.0	3.1	83.3	56.1	19.6	20.4	3.8
64-SMW	1110.5	1–4	4,233	31,765	14,540	6,042	53.6	16.8	14.3	2.0	86.7	61.9	19.3	16.5	2.3
66-SMW	1120.5	1–4	3,847	32,035	17,065	5,588	50.6	16.8	17.2	1.7	86.4	58.6	19.5	19.9	2.0
68-SMW	1130.5	1–4	3,677	31,963	15,410	5,914	47.9	16.9	15.4	2.5	82.8	57.9	20.5	18.6	3.0
71-SMW	1140.5	1–4	3,493	34,667	20,869	5,425	48.4	23.3	22.2	0.6	94.4	51.2	24.7	23.5	0.6
73-SMW	1150.5	1–4	3,461	33,141	18,326	6,126	48.5	18.2	21.5	1.7	90.0	54.0	20.2	23.9	1.9
75-SMW	1160.5	1–4	3,586	31,229	16,484	6,588	47.0	17.5	18.7	2.9	86.0	54.6	20.3	21.8	3.3
77-SMW	1170.5	1–4	4,098	32,938	13,936	6,277	47.5	16.4	16.7	3.5	84.1	56.5	19.5	19.8	4.1
80-SMW	1180.5	1–4	3,723	38,126	23,290	5,176	51.9	17.5	13.6	2.5	85.5	60.7	20.5	15.9	2.9
82-SMW	1190.5	1–4	4,073	33,788	18,836	5,691	52.2	20.0	24.1	0.9	97.2	53.7	20.6	24.8	0.9
84-SMW	1200.5	1–4	3,140	32,741	16,686	5,873	54.0	17.7	19.1	1.5	92.2	58.5	19.2	20.7	1.6
86-SMW	1210.5	1–4	3,865	35,627	18059	5,678	42.7	17.4	17.0	3.0	80.0	53.3	21.8	21.2	3.7
90-SMW	1220.5	1–4	3,948	34,983	19,044	4,812	51.3	18.9	18.2	1.7	90.1	56.9	20.9	20.3	1.9
92-SMW	1230.5	1–4	4,669	36,403	14,023	6,179	52.6	18.4	19.4	0.4	90.8	58.0	20.3	21.3	0.4

Table T9 (continued). (Continued on next page.)

Cuttings sample	Depth (mbsf)	Size fraction (mm)	Integrated peak area (total counts)				Absolute mineral abundance calculated from SVD normalization factors (wt%)					Relative abundance (wt%)			
			Total clay minerals	Quartz	Feldspar	Calcite	Total clay minerals	Quartz	Feldspar	Calcite	Sum	Total clay minerals	Quartz	Feldspar	Calcite
94-SMW	1240.5	1–4	2,615	30,477	13,576	5,290	58.1	19.4	13.5	1.6	92.6	62.8	21.0	14.5	1.7
96-SMW	1250.5	1–4	4,051	35,171	18,039	6,259	35.3	16.4	13.7	3.0	68.4	51.7	24.0	20.0	4.3
98-SMW	1260.5	1–4	3,686	34,098	16,647	6,157	53.3	18.6	18.2	2.3	92.4	57.7	20.1	19.7	2.5
100-SMW	1270.5	1–4	3,863	34,875	20,803	6,156	48.6	18.1	16.8	2.7	86.2	56.4	21.0	19.4	3.1
102-SMW	1280.5	1–4	3,817	35,992	15,532	6,647	52.6	18.2	21.4	2.3	94.5	55.7	19.3	22.6	2.4
104-SMW	1290.5	1–4	3,151	38,751	21,313	5,774	49.5	19.3	15.4	3.2	87.4	56.7	22.0	17.6	3.7
106-SMW	1300.5	1–4	3,346	38,373	17,859	4,728	45.0	20.6	22.0	2.5	90.1	49.9	22.9	24.5	2.8
108-SMW	1310.5	1–4	3,151	42,527	18,647	4,848	45.4	20.6	18.1	1.0	85.0	53.3	24.2	21.3	1.1
110-SMW	1320.5	1–4	3,457	43,463	21,621	4,748	43.5	23.0	19.0	1.2	86.7	50.2	26.5	21.8	1.4
112-SMW	1330.5	1–4	3,392	38,526	20,737	4,986	47.3	20.5	21.3	1.1	90.2	52.4	22.7	23.6	1.3
114-SMW	1340.5	1–4	3,322	40,426	19,083	5,176	45.7	21.7	19.4	1.5	88.4	51.7	24.6	22.0	1.7
116-SMW	1350.5	1–4	4,128	34,270	13,101	4,968	51.7	18.4	12.6	0.6	83.3	62.0	22.0	15.2	0.8
120-SMW	1360.5	1–4	3,721	36,343	19,296	5,531	50.3	19.2	19.7	1.6	90.8	55.4	21.2	21.7	1.8
122-SMW	1370.5	1–4	4,284	37,202	14,060	5,178	53.8	20.0	13.6	0.6	88.1	61.1	22.7	15.4	0.7
124-SMW	1380.5	1–4	3,971	36,967	14,474	4,871	50.6	19.9	14.2	0.6	85.2	59.4	23.3	16.6	0.7
126-SMW	1390.5	1–4	3,791	36,462	14,366	5,547	48.6	19.6	14.1	1.7	84.1	57.8	23.3	16.8	2.1
130-SMW	1400.5	1–4	4,449	37,143	15,694	5,361	56.5	19.8	15.4	0.6	92.3	61.2	21.5	16.7	0.7
132-SMW	1410.5	1–4	3,626	39,350	16,032	4,645	47.5	21.3	16.0	0.6	85.3	55.7	24.9	18.7	0.7
134-SMW	1420.5	1–4	3,674	41,918	18,421	4,872	49.2	22.6	18.6	0.7	91.0	54.1	24.8	20.4	0.7
136-SMW	1430.5	1–4	3,876	44,619	18,566	5,520	51.5	24.1	18.6	1.2	95.4	53.9	25.3	19.5	1.3
138-SMW	1440.5	1–4	3,664	42,445	19,500	4,451	49.6	22.8	19.8	0.0	92.2	53.8	24.7	21.4	0.0
140-SMW	1450.5	1–4	3,253	42,052	19,018	4,973	44.9	22.7	19.4	1.3	88.2	50.9	25.7	21.9	1.4
142-SMW	1460.5	1–4	3,456	41,989	13,883	4,880	44.6	23.0	13.5	1.1	82.2	54.2	28.0	16.5	1.4
144-SMW	1470.5	1–4	3,819	39,143	18,736	5,236	51.0	20.9	18.9	1.0	91.9	55.5	22.7	20.6	1.1
148-SMW	1480.5	1–4	3,713	37,935	17,590	5,611	49.3	20.3	17.7	1.8	89.1	55.4	22.8	19.9	2.0
150-SMW	1490.5	1–4	3,657	38,634	16,729	4,700	48.2	20.8	16.7	0.6	86.3	55.9	24.1	19.4	0.7
153-SMW	1500.5	1–4	3,903	41,136	17,760	5,000	51.4	22.1	17.8	0.6	91.9	55.9	24.1	19.3	0.7
155-SMW	1510.5	1–4	3,818	36,401	15,872	5,442	49.6	19.5	15.8	1.5	86.4	57.4	22.5	18.3	1.7
158-SMW	1520.5	1–4	3,917	37,484	15,551	5,271	50.5	20.1	15.4	1.1	87.2	58.0	23.1	17.6	1.3
161-SMW	1530.5	1–4	4,065	38,896	15,683	5,361	52.2	20.9	15.4	1.1	89.6	58.3	23.3	17.2	1.2
163-SMW	1540.5	1–4	4,290	40,673	12,887	4,415	53.2	22.1	12.2	–0.5	87.1	61.1	25.4	14.0	T
167-SMW	1550.5	1–4	3,773	39,493	14,894	4,422	48.6	21.4	14.6	0.1	84.7	57.3	25.3	17.3	0.1
169-SMW	1560.5	1–4	4,157	42,974	17,675	4,740	54.1	23.2	17.6	–0.1	94.7	57.1	24.4	18.5	T
172-SMW	1570.5	1–4	4,119	44,691	25,649	4,987	57.6	23.6	26.5	–0.1	107.6	53.5	21.9	24.6	T
174-SMW	1580.5	1–4	3,480	42,879	17,295	4,538	46.5	23.3	17.3	0.4	87.5	53.1	26.6	19.8	0.5
177-SMW	1590.5	1–4	3,811	39,850	15,694	4,733	49.4	21.5	15.5	0.5	86.9	56.8	24.8	17.8	0.5
182-SMW	1600.5	1–4	3,801	40,802	16,543	4,653	49.7	22.0	16.4	0.3	88.5	56.2	24.9	18.6	0.3
184-SMW	1610.5	1–4	3,597	38,365	17,709	4,266	48.0	20.6	17.9	0.0	86.5	55.5	23.8	20.7	0.0
187-SMW	1620.5	1–4	3,568	41,896	18,394	4,556	48.0	22.6	18.6	0.3	89.5	53.6	25.2	20.7	0.4
189-SMW	1630.5	1–4	3,522	44,267	15,224	4,575	45.9	24.2	15.0	0.5	85.6	53.6	28.3	17.5	0.6
193-SMW	1640.5	1–4	3,851	50,437	18,199	5,085	50.9	27.6	18.0	0.6	97.1	52.5	28.4	18.6	0.6
195-SMW	1650.5	1–4	3,685	44,849	16,906	5,630	48.6	24.4	16.8	1.7	91.4	53.1	26.7	18.3	1.8
199-SMW	1660.5	1–4	3,330	42,682	21,082	5,155	46.7	22.9	21.6	1.3	92.6	50.5	24.7	23.4	1.4
201-SMW	1670.5	1–4	3,926	47,929	15,895	5,628	50.7	26.2	15.5	1.4	93.8	54.0	28.0	16.5	1.5
203-SMW	1680.5	1–4	3,040	40,542	17,443	5,688	41.8	22.0	17.7	2.6	84.1	49.7	26.1	21.0	3.1
207-SMW	1700.5	1–4	3,866	42,042	15,083	6,127	49.7	22.8	14.7	2.3	89.6	55.5	25.5	16.4	2.6
209-SMW	1710.5	1–4	3,596	41,764	23,495	6,361	50.9	22.1	24.3	2.6	100.0	51.0	22.1	24.3	2.6
211-SMW	1720.5	1–4	3,836	38,380	14,781	5,361	49.3	20.7	14.5	1.4	85.9	57.4	24.1	16.9	1.6
213-SMW	1730.5	1–4	3,881	40,086	18,747	6,091	51.7	21.4	18.9	2.1	94.2	54.9	22.8	20.1	2.3

Table T9 (continued). (Continued on next page.)

Cuttings sample	Depth (mbsf)	Size fraction (mm)	Integrated peak area (total counts)				Absolute mineral abundance calculated from SVD normalization factors (wt%)					Relative abundance (wt%)			
			Total clay minerals	Quartz	Feldspar	Calcite	Total clay minerals	Quartz	Feldspar	Calcite	Sum	Total clay minerals	Quartz	Feldspar	Calcite
217-SMW	1750.5	1–4	3,903	38,279	14,901	6,041	43.9	21.2	17.9	3.7	86.7	50.6	24.4	20.7	4.3
219-SMW	1760.5	1–4	3,360	40,656	18,835	6,555	50.1	20.6	14.6	2.2	87.6	57.2	23.6	16.7	2.6
223-SMW	1770.5	1–4	4,249	39,610	14,262	5,886	46.1	21.9	19.1	3.4	90.4	50.9	24.2	21.2	3.7
229-SMW	1790.5	1–4	4,268	39,272	12,154	6,091	53.6	21.4	13.8	1.6	90.3	59.3	23.7	15.2	1.8
231-SMW	1800.5	1–4	4,140	38,146	13,521	5,274	54.2	21.2	17.2	1.6	94.2	57.5	22.5	18.3	1.7
233-SMW	1810.5	1–4	4,404	42,835	15,475	5,504	52.8	21.3	11.4	2.0	87.5	60.3	24.4	13.0	2.2
235-SMW	1820.5	1–4	4,187	40,261	14,684	5,122	52.0	20.6	13.0	1.0	86.6	60.1	23.8	15.0	1.1
238-SMW	1830.5	1–4	4,166	39,428	14,253	4,911	55.8	23.2	15.0	0.8	94.8	58.9	24.5	15.8	0.8
250-SMW	1850.5	1–4	4,539	43,253	14,436	4,764	53.0	21.8	14.2	0.6	89.6	59.2	24.3	15.9	0.7
255-SMW	1870.5	1–4	4,283	42,878	13,108	4,232	52.6	21.3	13.8	0.4	88.1	59.7	24.2	15.7	0.4
260-SMW	1890.5	1–4	3,956	40,692	13,461	5,277	52.4	22.3	13.5	–0.7	87.5	59.9	25.5	15.4	T
265-SMW	1910.5	1–4	3,886	42,622	15,239	6,237	56.7	23.5	13.8	–0.4	93.6	60.6	25.1	14.7	T
269-SMW	1930.5	1–4	4,502	39,215	12,465	7,694	51.1	22.8	12.9	–0.1	86.8	58.9	26.3	14.9	T
274-SMW	1950.5	1–4	3,943	40,829	12,486	7,694	53.2	23.4	12.4	–0.8	88.3	60.3	26.5	14.0	T
286-SMW	1990.5	1–4	5,194	39,432	11,097	6,224	49.8	24.4	15.1	0.1	89.4	55.7	27.3	16.9	0.1
288-SMW	2000.5	1–4	4,214	38,825	12,406	5,377	49.9	22.2	12.9	1.1	86.1	58.0	25.7	15.0	1.3
20-SMW	920.5	>4	1,645	21,835	7,728	12,308	22.3	11.9	7.6	14.3	56.1	39.7	21.2	13.5	25.5
21-SMW	925.5	>4	1,881	26,851	6,838	12,956	24.4	14.9	6.4	14.8	60.5	40.3	24.6	10.6	24.5
22-SMW	930.5	>4	1,801	26,997	8,525	14,016	24.4	14.9	8.3	16.3	63.9	38.2	23.2	13.0	25.5
24-SMW	935.5	>4	1,078	28,487	5,548	12,075	14.9	16.1	5.1	14.6	50.7	29.3	31.7	10.2	28.8
25-SMW	940.5	>4	1,526	24,013	8,746	14,551	21.6	13.1	8.7	17.5	60.9	35.5	21.6	14.3	28.7
26-SMW	945.5	>4	2,674	30,400	9,871	14,082	34.7	16.6	9.5	15.2	76.0	45.6	21.8	12.5	20.1
27-SMW	950.5	>4	2,908	26,570	9,944	14,773	37.4	14.3	9.6	16.0	77.2	48.4	18.5	12.4	20.7
28-SMW	955.5	>4	2,789	27,422	11,080	15,801	36.7	14.7	10.9	17.5	79.8	46.0	18.4	13.6	22.0
29-SMW	960.5	>4	1,490	22,039	8,236	13,052	20.9	12.0	8.2	15.5	56.6	36.9	21.2	14.5	27.4
32-SMW	975.5	>4	3,379	31,074	10,992	11,484	42.8	16.8	10.5	10.7	80.9	53.0	20.7	13.0	13.3
34-SMW	980.5	>4	3,310	29,326	13,195	7,731	43.0	15.6	13.1	5.6	77.2	55.6	20.2	17.0	7.2
35-SMW	985.5	>4	3,307	31,205	13,054	8,433	42.9	16.7	12.9	6.5	79.0	54.3	21.2	16.3	8.2
36-SMW	990.5	>4	3,818	31,075	13,095	7,164	48.4	16.5	12.8	4.1	81.9	59.1	20.2	15.6	5.1
37-SMW	995.5	>4	3,919	33,639	15,589	6,331	50.7	17.9	15.5	2.7	86.8	58.4	20.6	17.9	3.1
40-SMW	1000.5	>4	2,944	33,147	18,167	8,987	41.4	17.6	18.7	7.4	85.1	48.6	20.6	22.0	8.8
41-SMW	1005.5	>4	2,398	30,756	15,488	7,932	34.0	16.5	15.9	6.8	73.2	46.5	22.5	21.7	9.3
42-SMW	1010.5	>4	3,099	29,229	14,924	8,161	41.5	15.5	15.1	6.3	78.4	52.9	19.7	19.3	8.1
43-SMW	1015.5	>4	2,600	29,656	14,952	14,494	36.4	15.8	15.2	15.7	83.1	43.8	19.0	18.3	18.9
44-SMW	1020.5	>4	3,375	29,339	14,512	6,971	44.3	15.5	14.6	4.4	78.7	56.2	19.7	18.5	5.6
45-SMW	1025.5	>4	3,580	32,689	17,845	6,140	48.1	17.2	18.2	2.8	86.2	55.8	20.0	21.1	3.2
46-SMW	1030.5	>4	3,404	33,595	17,240	5,619	45.8	17.8	17.5	2.3	83.4	54.9	21.4	21.0	2.7
47-SMW	1035.5	>4	3,746	33,748	16,116	5,614	49.0	17.9	16.1	1.9	85.0	57.7	21.1	19.0	2.2
48-SMW	1040.5	>4	3,858	33,741	16,612	5,759	50.5	17.9	16.7	1.9	87.0	58.1	20.5	19.2	2.2
49-SMW	1045.5	>4	3,407	32,491	17,069	5,065	45.7	17.2	17.4	1.5	81.8	55.9	21.0	21.2	1.9
50-SMW	1050.5	>4	3,861	32,105	14,970	5,206	49.7	17.0	14.9	1.3	82.9	60.0	20.5	17.9	1.5
51-SMW	1055.5	>4	3,735	34,452	14,235	5,127	47.9	18.5	14.0	1.3	81.7	58.7	22.6	17.2	1.6
52-SMW	1060.5	>4	3,016	36,553	15,833	6,298	40.8	19.7	16.0	3.6	80.2	50.9	24.6	19.9	4.5
54-SMW	1070.5	>4	3,967	34,315	14,891	5,130	50.8	18.3	14.7	1.0	84.8	59.9	21.6	17.3	1.2
56-SMW	1080.5	>4	3,816	31,971	15,334	5,614	49.4	16.9	15.3	1.9	83.5	59.2	20.3	18.3	2.2
58-SMW	1090.5	>4	3,867	32,111	18,353	5,626	51.5	16.8	18.7	1.7	88.6	58.1	18.9	21.1	1.9
62-SMW	1100.5	>4	3,477	32,827	15,358	4,665	45.6	17.5	15.4	0.9	79.5	57.4	22.0	19.4	1.2
64-SMW	1110.5	>4	3,828	32,570	18,710	5,522	51.2	17.0	19.1	1.6	88.9	57.6	19.2	21.5	1.8

Table T9 (continued).

Cuttings sample	Depth (mbsf)	Size fraction (mm)	Integrated peak area (total counts)				Absolute mineral abundance calculated from SVD normalization factors (wt%)					Relative abundance (wt%)			
			Total clay minerals	Quartz	Feldspar	Calcite	Total clay minerals	Quartz	Feldspar	Calcite	Sum	Total clay minerals	Quartz	Feldspar	Calcite
66-SMW	1120.5	>4	3,393	36,676	16,986	5,200	45.5	19.7	17.2	1.6	83.9	54.2	23.4	20.4	1.9
68-SMW	1130.5	>4	3,383	36,923	16,488	5,115	45.1	19.8	16.6	1.5	83.1	54.3	23.9	20.0	1.8
71-SMW	1140.5	>4	3,886	35,005	18,221	5,016	51.5	18.5	18.4	0.8	89.2	57.8	20.7	20.7	0.9
73-SMW	1150.5	>4	3,528	34,829	16,418	5,373	46.7	18.6	16.5	1.8	83.6	55.9	22.2	19.8	2.1
75-SMW	1160.5	>4	3,587	34,919	18,716	4,397	48.5	18.5	19.1	0.3	86.3	56.2	21.4	22.1	0.3
77-SMW	1170.5	>4	3,777	38,409	17,684	4,326	50.0	20.5	17.8	–0.1	88.2	56.7	23.3	20.2	T
80-SMW	1180.5	>4	4,383	37,999	15,377	4,800	55.6	20.3	15.0	–0.1	90.9	61.1	22.4	16.5	T
82-SMW	1190.5	>4	3,706	36,515	15,969	5,440	48.5	19.6	15.9	1.6	85.6	56.6	22.9	18.6	1.9
84-SMW	1200.5	>4	4,004	40,735	15,658	5,181	51.5	22.0	15.4	0.8	89.7	57.4	24.5	17.1	0.9
98-SMW	1260.5	>4	4,239	35,419	13,430	5,957	53.1	19.0	12.9	1.8	86.9	61.1	21.9	14.9	2.1
124-SMW	1380.5	>4	3,488	42,957	20,193	4,389	48.0	23.1	20.6	0.1	91.8	52.3	25.2	22.4	0.1
130-SMW	1400.5	>4	3,658	38,341	15,268	5,068	47.5	20.7	15.1	1.2	84.5	56.2	24.5	17.9	1.4
134-SMW	1420.5	>4	3,554	41,962	20,397	5,413	48.9	22.5	20.8	1.5	93.6	52.2	24.0	22.2	1.6
136-SMW	1430.5	>4	3,340	50,712	24,236	5,351	48.3	27.4	25.0	1.3	101.9	47.4	26.9	24.5	1.2
138-SMW	1440.5	>4	4,128	47,682	15,888	4,653	52.9	26.1	15.4	–0.2	94.1	56.1	27.7	16.4	T
153-SMW	1500.5	>4	3,541	41,631	16,199	4,631	46.6	22.6	16.1	0.6	85.9	54.3	26.3	18.8	0.7
167-SMW	1550.5	>4	3,673	39,546	16,413	4,366	48.2	21.3	16.4	0.1	86.0	56.1	24.8	19.0	0.1
182-SMW	1600.5	>4	3,390	42,414	17,202	4,577	45.4	23.0	17.3	0.6	86.4	52.6	26.7	20.0	0.7
195-SMW	1650.5	>4	3,643	44,490	17,726	4,187	48.4	24.2	17.7	–0.3	90.0	53.8	26.8	19.7	T
203-SMW	1690.5	>4	3,684	42,088	14,146	5,588	47.2	23.0	13.7	1.8	85.8	55.1	26.8	16.0	2.1
207-SMW	1700.5	>4	3,303	41,705	17,576	5,089	44.7	22.6	17.7	1.4	86.5	51.7	26.1	20.5	1.7
231-SMW	1800.5	>4	3,540	40,886	13,042	4,850	45.1	22.4	12.6	1.0	81.1	55.6	27.6	15.5	1.3
250-SMW	1850.5	>4	4,033	43,795	17,326	4,309	52.6	23.7	17.2	–0.6	92.9	56.6	25.5	18.5	T
260-SMW	1890.5	>4	3,983	49,409	17,995	4,428	52.3	27.0	17.8	–0.5	96.5	54.1	27.9	18.4	T

SVD = singular value decomposition. T = trace.

Table T10. Results of XRF analysis of cuttings samples, Hole C0002F. (Continued on next two pages.)

Cuttings sample	Top depth (mbsf)	Underreamer depth (mbsf)	Bulk fraction size (mm)	Na_2O (wt%)	MgO (wt%)	Al_2O_3 (wt%)	SiO_2 (wt%)	P_2O_5 (wt%)	K_2O (wt%)	CaO (wt%)	TiO_2 (wt%)	MnO (wt%)	Fe_2O_3 (wt%)	Loss on ignition (wt%)
338-C0002F-														
7-SMW	875.5	832.7	>4	1.23	1.13	7.92	44.4	0.12	0.88	36.5	0.31	0.05	3.88	25.4
20-SMW	920.5	877.7	>4	1.84	2.73	12.4	54.7	0.15	2.65	16.4	0.73	0.07	5.35	13.7
21-SMW	925.5	882.7	>4	1.80	1.91	11.4	55.7	0.12	2.15	18.8	0.54	0.06	4.49	13.7
22-SMW	930.5	887.7	>4	1.51	2.34	11.6	54.9	0.26	2.40	18.1	0.64	0.06	4.86	14.1
24-SMW	935.5	892.7	>4	1.72	4.88	9.52	53.2	0.32	1.53	18.1	1.38	0.09	6.30	8.5
25-SMW	940.5	897.7	>4	2.24	1.85	12.6	56.4	0.10	2.57	15.8	0.51	0.05	4.71	13.6
26-SMW	945.5	902.7	>4	2.35	2.33	13.5	60.2	0.11	3.04	10.3	0.65	0.06	5.01	10.8
27-SMW	950.5	907.7	>4	2.61	2.29	14.3	60.2	0.11	3.15	8.68	0.67	0.06	5.21	11.3
28-SMW	955.5	912.7	>4	2.24	2.01	14.3	60.1	0.09	3.27	9.74	0.60	0.06	4.97	12.0
29-SMW	960.5	917.7	>4	2.10	2.48	13.0	56.9	0.14	2.59	14.9	0.69	0.06	5.15	14.4
30-SMW	965.5	922.7	>4	2.53	2.22	14.9	62.0	0.10	3.20	7.95	0.59	0.06	5.05	11.3
31-SMW	970.5	927.7	>4	2.54	2.50	14.5	59.2	0.11	3.15	8.99	0.69	0.07	5.75	10.6
32-SMW	975.5	932.7	>4	2.65	2.14	15.4	61.8	0.09	3.41	6.64	0.60	0.06	5.32	10.9
34-SMW	980.5	937.7	>4	2.68	2.17	15.7	62.9	0.10	3.42	5.51	0.65	0.06	5.01	10.0
35-SMW	985.5	942.7	>4	2.77	2.24	16.0	63.8	0.09	3.53	5.10	0.65	0.06	4.92	9.91
36-SMW	990.5	947.7	>4	2.62	2.25	16.0	63.5	0.09	3.64	4.65	0.65	0.06	4.91	9.27
37-SMW	995.5	952.7	>4	2.46	2.20	16.4	63.9	0.09	3.64	3.66	0.68	0.06	5.50	8.51
40-SMW	1000.5	957.7	>4	2.56	2.01	15.5	62.8	0.09	3.68	5.17	0.62	0.06	5.98	9.72
41-SMW	1005.5	962.7	>4	2.69	2.10	15.5	63.1	0.09	3.67	5.45	0.64	0.07	5.17	9.53
42-SMW	1010.5	967.7	>4	2.51	3.33	14.7	60.1	0.16	3.12	6.87	0.87	0.07	5.80	8.98
43-SMW	1015.5	972.7	>4	2.56	2.51	16.0	62.7	0.11	3.58	4.73	0.69	0.08	5.91	10.2
44-SMW	1020.5	977.7	>4	2.61	2.20	16.7	63.8	0.09	3.86	4.32	0.67	0.06	4.88	9.21
45-SMW	1025.5	982.7	>4	2.71	2.20	16.7	64.1	0.08	3.74	3.49	0.67	0.06	5.20	8.90
46-SMW	1030.5	987.7	>4	2.58	2.22	16.5	63.4	0.08	3.87	3.53	0.67	0.06	5.81	9.08
47-SMW	1035.5	992.7	>4	2.45	2.28	16.3	63.4	0.11	3.75	3.88	0.69	0.06	5.68	8.71
48-SMW	1040.5	997.7	>4	2.42	2.10	16.5	64.0	0.10	3.78	3.55	0.65	0.07	5.59	8.57
49-SMW	1045.5	1002.7	>4	2.46	2.12	16.6	64.3	0.09	3.76	3.26	0.67	0.06	5.69	7.96
50-SMW	1050.5	1007.7	>4	2.52	2.19	16.9	64.5	0.09	3.79	3.23	0.69	0.06	5.62	8.06
51-SMW	1055.5	1012.7	>4	2.41	2.14	16.5	64.0	0.09	3.85	3.28	0.60	0.07	5.33	8.55
54-SMW	1070.5	1027.7	>4	2.48	2.07	16.3	64.4	0.09	3.68	3.12	0.65	0.07	5.46	8.52
56-SMW	1080.5	1037.7	>4	2.38	2.16	15.7	63.0	0.57	3.54	4.48	0.64	0.07	5.60	8.63
58-SMW	1090.5	1047.7	>4	2.64	2.12	16.6	63.7	0.10	3.67	3.38	0.67	0.07	5.65	8.87
64-SMW	1110.5	1067.7	>4	2.37	2.05	15.9	62.8	0.09	3.55	3.19	0.64	0.06	5.43	8.08
66-SMW	1120.5	1077.7	>4	2.51	2.01	16.2	64.7	0.08	3.82	3.17	0.64	0.06	5.45	7.97
68-SMW	1130.5	1087.7	>4	2.37	2.04	16.2	64.9	0.08	3.70	3.31	0.64	0.06	5.43	7.97
73-SMW	1150.5	1107.7	>4	2.49	2.02	16.3	64.6	0.08	3.80	3.05	0.63	0.06	5.28	8.38
77-SMW	1170.5	1127.7	>4	2.31	1.95	16.0	66.3	0.08	3.62	2.69	0.61	0.06	5.32	7.92
82-SMW	1190.5	1147.7	>4	2.47	2.10	16.2	65.6	0.08	3.78	3.08	0.64	0.06	5.09	8.78
98-SMW	1260.5	1217.7	>4	2.26	2.07	16.0	65.1	0.08	3.76	3.32	0.64	0.06	5.36	8.76
136-SMW	1430.5	1387.7	>4	2.28	1.93	15.0	67.5	0.07	3.62	2.71	0.58	0.06	4.79	7.34
231-SMW	1800.5	1757.7	>4	2.17	1.91	15.9	65.4	0.07	3.73	2.51	0.67	0.05	5.30	6.82
20-SMW	920.5	877.7	1–4	2.27	2.24	13.9	58.5	0.10	2.60	12.0	0.61	0.06	5.16	13.4
21-SMW	925.5	882.7	1–4	2.35	2.08	13.7	58.5	0.09	2.72	12.0	0.59	0.06	5.16	12.5
22-SMW	930.5	887.7	1–4	2.28	2.19	14.1	59.5	0.10	2.84	11.1	0.59	0.06	4.92	12.5
24-SMW	935.5	892.7	1–4	2.49	2.31	14.3	59.9	0.12	2.79	10.8	0.63	0.06	5.09	12.4
25-SMW	940.5	897.7	1–4	2.32	2.14	14.0	59.9	0.09	2.95	10.4	0.60	0.05	4.94	12.2

Table T10 (continued). (Continued on next page.)

Cuttings sample	Top depth (mbsf)	Underreamer depth (mbsf)	Bulk fraction size (mm)	Na_2O (wt%)	MgO (wt%)	Al_2O_3 (wt%)	SiO_2 (wt%)	P_2O_5 (wt%)	K_2O (wt%)	CaO (wt%)	TiO_2 (wt%)	MnO (wt%)	Fe_2O_3 (wt%)	Loss on ignition (wt%)
26-SMW	945.5	902.7	1–4	2.16	2.22	14.3	60.2	0.09	3.06	10.5	0.58	0.06	5.45	12.0
27-SMW	950.5	907.7	1–4	2.44	2.14	14.4	60.2	0.08	3.03	9.71	0.58	0.06	5.24	12.2
28-SMW	955.5	912.7	1–4	2.35	2.16	14.3	60.2	0.10	3.15	9.57	0.62	0.06	5.06	11.7
29-SMW	960.5	917.7	1–4	2.49	2.33	14.5	60.5	0.10	2.94	9.34	0.64	0.06	5.07	12.4
30-SMW	965.5	922.7	1–4	2.49	2.24	15.1	61.8	0.10	3.28	7.56	0.64	0.06	5.29	11.0
31-SMW	970.5	927.7	1–4	2.46	2.34	14.6	60.4	0.10	2.93	8.36	0.66	0.06	5.59	11.1
32-SMW	975.5	932.7	1–4	2.48	2.33	15.0	61.2	0.09	3.03	7.69	0.61	0.06	5.27	11.2
34-SMW	980.5	937.7	1–4	2.57	2.34	15.5	62.3	0.09	3.18	6.70	0.63	0.06	5.33	11.0
35-SMW	985.5	942.7	1–4	2.72	2.37	15.5	62.3	0.09	3.11	6.58	0.63	0.06	5.26	11.0
36-SMW	990.5	947.7	1–4	2.68	2.36	15.6	62.1	0.09	3.23	6.48	0.64	0.06	5.10	11.0
37-SMW	995.5	952.7	1–4	2.49	2.34	16.2	63.0	0.09	3.31	5.22	0.67	0.06	5.33	9.92
40-SMW	1000.5	957.7	1–4	2.71	2.37	16.1	63.4	0.11	3.32	5.03	0.65	0.07	5.38	9.68
41-SMW	1005.5	962.7	1–4	2.67	2.51	16.6	63.8	0.10	3.48	4.02	0.71	0.07	5.49	9.76
42-SMW	1010.5	967.7	1–4	2.76	2.60	16.7	63.3	0.10	3.31	4.35	0.70	0.07	5.22	9.63
43-SMW	1015.5	972.7	1–4	2.65	2.34	16.5	62.7	0.10	3.54	4.12	0.66	0.07	5.87	10.4
44-SMW	1020.5	977.7	1–4	2.64	2.36	17.0	64.2	0.08	3.63	3.63	0.69	0.07	5.36	9.32
45-SMW	1025.5	982.7	1–4	2.59	2.39	17.1	64.2	0.09	3.43	3.66	0.67	0.06	5.46	9.27
46-SMW	1030.5	987.7	1–4	2.65	2.36	16.7	63.8	0.09	3.58	3.66	0.69	0.07	5.43	9.45
47-SMW	1035.5	992.7	1–4	2.62	2.35	16.9	64.7	0.10	3.51	3.89	0.69	0.07	5.65	9.32
48-SMW	1040.5	997.7	1–4	2.54	2.21	16.3	63.2	0.13	3.31	4.55	0.67	0.08	5.66	9.37
49-SMW	1045.5	1002.7	1–4	2.52	2.22	16.3	63.1	0.13	3.41	4.62	0.64	0.09	5.60	9.44
50-SMW	1050.5	1007.7	1–4	2.54	2.19	16.3	63.3	0.12	3.34	4.39	0.66	0.08	5.55	9.09
51-SMW	1055.5	1012.7	1–4	2.54	2.21	16.4	63.5	0.11	3.31	4.22	0.67	0.08	5.70	9.00
52-SMW	1060.5	1017.7	1–4	2.65	2.17	16.2	63.2	0.10	3.40	4.17	0.65	0.07	5.83	9.59
54-SMW	1070.5	1027.7	1–4	2.66	2.21	16.6	64.3	0.09	3.39	3.56	0.67	0.07	5.71	8.72
56-SMW	1080.5	1037.7	1–4	2.71	2.25	16.6	64.5	0.11	3.35	4.01	0.67	0.08	5.74	9.11
58-SMW	1090.5	1047.7	1–4	2.71	1.13	16.4	63.4	0.11	3.22	4.21	0.67	0.08	5.81	9.69
62-SMW	1100.5	1057.7	1–4	2.58	2.73	16.3	64.0	0.11	3.37	3.91	0.66	0.07	5.49	9.22
64-SMW	1110.5	1067.7	1–4	2.54	1.91	16.2	63.7	0.10	3.32	3.73	0.67	0.07	5.88	9.14
66-SMW	1120.5	1077.7	1–4	2.64	2.34	16.9	64.8	0.09	3.51	3.36	0.66	0.07	5.17	8.81
68-SMW	1130.5	1087.7	1–4	2.74	4.88	16.5	63.6	0.09	3.41	3.60	0.67	0.07	5.65	9.25
71-SMW	1140.5	1097.7	1–4	2.76	1.85	16.2	64.3	0.10	3.26	3.72	0.64	0.07	4.89	9.05
73-SMW	1150.5	1107.7	1–4	2.60	2.33	16.3	64.7	0.09	3.46	3.62	0.64	0.07	5.50	8.82
75-SMW	1160.5	1117.7	1–4	2.64	2.29	16.2	63.6	0.11	3.44	3.91	0.65	0.08	5.32	9.92
77-SMW	1170.5	1127.7	1–4	2.42	2.01	16.4	64.1	0.09	3.37	3.51	0.66	0.07	5.44	9.93
80-SMW	1180.5	1137.7	1–4	2.52	2.48	16.3	65.4	0.09	3.47	3.23	0.65	0.08	4.82	9.24
82-SMW	1190.5	1147.7	1–4	2.54	2.22	16.2	64.1	0.09	3.51	3.24	0.65	0.07	5.57	9.41
84-SMW	1200.5	1157.7	1–4	2.48	2.50	16.1	64.3	0.09	3.48	3.48	0.64	0.07	5.50	8.87
86-SMW	1210.5	1167.7	1–4	2.56	2.14	16.1	64.5	0.08	3.39	3.13	0.63	0.07	5.60	8.73
90-SMW	1220.5	1177.7	1–4	2.61	2.17	16.3	64.2	0.08	3.40	3.03	0.64	0.06	5.71	9.15
92-SMW	1230.5	1187.7	1–4	2.53	2.24	16.3	64.4	0.10	3.41	3.37	0.63	0.07	5.45	9.67
94-SMW	1240.5	1197.7	1–4	2.56	2.25	16.0	63.7	0.10	3.35	3.74	0.66	0.07	5.69	9.63
96-SMW	1250.5	1207.7	1–4	2.70	2.20	16.0	63.6	0.11	3.29	4.06	0.66	0.07	5.64	9.29
98-SMW	1260.5	1217.7	1–4	2.43	2.01	15.5	61.7	0.09	3.31	3.79	0.60	0.07	5.45	9.96
100-SMW	1270.5	1227.7	1–4	2.51	2.10	15.9	63.9	0.09	3.30	3.92	0.63	0.07	5.64	8.90
102-SMW	1280.5	1237.7	1–4	2.41	3.33	15.8	64.3	0.11	3.24	4.23	0.63	0.08	5.49	9.87
104-SMW	1290.5	1247.7	1–4	2.53	2.51	15.5	65.3	0.09	3.38	3.53	0.61	0.07	5.30	9.30
106-SMW	1300.5	1257.7	1–4	2.43	2.20	15.9	65.2	0.09	3.36	3.14	0.63	0.06	5.50	9.19
108-SMW	1310.5	1267.7	1–4	2.53	2.20	15.5	66.6	0.09	3.29	3.14	0.61	0.06	4.71	8.71

Table T10 (continued).

Cuttings sample	Top depth (mbsf)	Underreamer depth (mbsf)	Bulk fraction size (mm)	Na_2O (wt%)	MgO (wt%)	Al_2O_3 (wt%)	SiO_2 (wt%)	P_2O_5 (wt%)	K_2O (wt%)	CaO (wt%)	TiO_2 (wt%)	MnO (wt%)	Fe_2O_3 (wt%)	Loss on ignition (wt%)
110-SMW	1320.5	1277.7	1–4	2.48	2.22	15.1	65.4	0.07	3.28	2.73	0.60	0.06	5.11	8.74
112-SMW	1330.5	1287.7	1–4	2.44	2.28	15.9	67.8	0.08	3.32	2.81	0.62	0.06	5.15	8.44
114-SMW	1340.5	1297.7	1–4	2.49	2.10	15.9	65.4	0.07	3.43	2.74	0.65	0.06	5.42	8.14
122-SMW	1370.5	1327.7	1–4	2.46	2.12	15.8	65.6	0.08	3.35	3.09	0.62	0.06	4.83	8.74
126-SMW	1390.5	1347.7	1–4	2.49	2.19	15.8	64.8	0.09	3.33	3.23	0.62	0.06	5.37	9.93
132-SMW	1410.5	1367.7	1–4	2.54	2.14	15.9	65.9	0.08	3.41	2.91	0.62	0.06	5.15	8.45
136-SMW	1430.5	1387.7	1–4	2.48	2.07	15.6	67.0	0.07	3.38	2.98	0.58	0.06	4.53	8.20
138-SMW	1440.5	1397.7	1–4	2.46	2.16	15.7	66.3	0.07	3.50	2.73	0.61	0.07	4.90	7.99
140-SMW	1450.5	1407.7	1–4	2.47	2.12	15.6	66.7	0.07	3.48	2.59	0.61	0.06	4.74	7.85
142-SMW	1460.5	1417.7	1–4	2.42	2.05	15.8	66.3	0.09	3.51	2.85	0.61	0.06	4.82	8.00
144-SMW	1470.5	1427.7	1–4	2.50	2.01	16.0	65.0	0.08	3.53	2.81	0.65	0.07	5.34	8.45
148-SMW	1480.5	1437.7	1–4	2.54	2.04	16.3	65.6	0.09	3.30	3.25	0.64	0.07	4.98	8.01
150-SMW	1490.5	1447.7	1–4	2.57	2.02	16.0	65.3	0.08	3.35	2.85	0.64	0.06	5.12	7.90
155-SMW	1510.5	1467.7	1–4	2.53	1.95	16.4	64.5	0.09	3.26	3.25	0.66	0.06	5.43	7.93
161-SMW	1530.5	1487.7	1–4	2.47	2.10	16.0	65.3	0.08	3.31	3.07	0.64	0.07	5.28	8.48
167-SMW	1550.5	1507.7	1–4	2.35	2.07	16.5	65.1	0.08	3.44	2.85	0.66	0.07	5.46	8.19
169-SMW	1560.5	1517.7	1–4	2.43	1.93	16.4	64.7	0.08	3.44	2.70	0.66	0.06	5.65	7.77
172-SMW	1570.5	1527.7	1–4	2.46	1.91	15.7	66.7	0.08	3.31	2.60	0.62	0.07	4.98	7.28
174-SMW	1580.5	1537.7	1–4	2.50	2.10	16.0	65.8	0.07	3.42	2.49	0.65	0.06	5.54	7.61
177-SMW	1590.5	1547.7	1–4	2.55	2.24	16.3	65.7	0.08	3.35	2.53	0.66	0.06	5.59	7.40
184-SMW	1610.5	1567.7	1–4	2.51	2.08	16.6	64.8	0.09	3.52	2.54	0.66	0.07	5.80	8.31
187-SMW	1620.5	1577.7	1–4	2.47	2.19	15.8	65.3	0.10	3.38	2.58	0.62	0.07	5.48	7.40
189-SMW	1630.5	1587.7	1–4	2.55	2.31	15.8	65.8	0.11	3.40	2.53	0.63	0.07	5.40	7.20
195-SMW	1650.5	1607.7	1–4	2.48	2.14	15.7	67.5	0.09	3.39	2.75	0.63	0.06	5.01	7.13
201-SMW	1670.5	1627.7	1–4	2.29	2.22	14.7	64.8	0.09	3.17	2.75	0.60	0.06	4.89	6.72
209-SMW	1710.5	1667.7	1–4	2.43	2.14	15.8	64.9	0.10	3.30	3.51	0.65	0.07	5.40	7.83
211-SMW	1720.5	1677.7	1–4	2.53	2.16	16.1	64.8	0.10	3.43	3.18	0.65	0.06	5.40	7.43
213-SMW	1730.5	1687.7	1–4	2.50	2.33	16.1	65.4	0.11	3.35	3.52	0.65	0.06	5.00	7.63
217-SMW	1750.5	1707.7	1–4	2.44	2.24	16.0	64.7	0.10	3.35	3.42	0.64	0.06	5.40	7.47
223-SMW	1770.5	1727.7	1–4	2.42	2.34	16.1	65.1	0.09	3.27	3.24	0.66	0.06	5.27	7.41
229-SMW	1790.5	1747.7	1–4	2.18	2.33	16.2	64.7	0.09	3.39	3.15	0.67	0.06	5.20	7.54
233-SMW	1810.5	1767.7	1–4	2.41	2.34	16.4	65.4	0.08	3.52	2.72	0.69	0.06	5.15	7.58
238-SMW	1830.5	1787.7	1–4	2.21	2.37	16.3	65.8	0.10	3.47	2.46	0.68	0.06	5.41	7.30
250-SMW	1850.5	1807.7	1–4	2.25	2.36	16.2	66.2	0.08	3.46	2.20	0.67	0.05	5.07	7.30
255-SMW	1870.5	1827.7	1–4	2.28	2.34	16.4	66.3	0.07	3.54	2.10	0.68	0.06	5.27	7.11
260-SMW	1890.5	1847.7	1–4	2.36	2.37	16.2	65.6	0.08	3.49	2.60	0.68	0.05	5.10	7.05
265-SMW	1910.5	1867.7	1–4	2.17	2.51	16.2	65.2	0.06	3.46	3.28	0.68	0.06	5.17	7.41
269-SMW	1930.5	1887.7	1–4	2.23	2.60	16.2	64.6	0.08	3.50	3.74	0.64	0.06	5.20	7.84
274-SMW	1950.5	1907.7	1–4	2.12	2.34	16.4	64.0	0.08	3.55	3.98	0.66	0.06	5.46	8.14
282-SMW	1970.5	1927.7	1–4	2.08	2.36	16.3	64.4	0.08	3.60	3.48	0.64	0.07	5.46	7.80
286-SMW	1990.5	1947.7	1–4	2.33	2.39	16.3	64.6	0.07	3.64	2.93	0.66	0.06	5.37	7.67

Table T11. Core depth intervals and recovery, Hole C0002H.

Core, section	Depth (mbsf) Top	Depth (mbsf) Bottom	Curated length (m)
338-C0002H-			
1R-1	1100.50	1101.91	1.41
1R-2	1101.91	1102.32	0.41
1R-CC	1102.32	1102.37	0.05
2R-1	1110.50	1111.07	0.57
2R-2	1111.07	1111.18	0.11
2R-3	1111.18	1112.49	1.31
2R-CC	1112.49	1112.84	0.36

Table T12. Results of X-ray diffraction analysis performed on random bulk powder, Hole C0002H.

Core, section, interval (cm)	Sample	Central depth (mbsf)	Integrated peak area (total counts)				Absolute mineral abundance calculated from SVD normalization factors (wt%)					Relative abundance (wt%)			
			Total clay minerals	Quartz	Feldspar	Calcite	Total clay minerals	Quartz	Feldspar	Calcite	Sum	Total clay minerals	Quartz	Feldspar	Calcite
338-C0002H-															
1R-1, 29–31	CKY-1273510	1100.80	4,753	35,928	21,838	5,969	62.9	18.6	22.2	0.9	104.6	60.1	17.8	21.2	0.90
1R-1, 129–131	CKY-1273910	1101.80	2,542	36,262	45,212	4,041	50.0	17.6	49.1	–0.1	116.6	42.9	15.1	42.2	T
2R-1, 15–17	CKY-1273110	1110.66	4,409	34,431	15,351	8,434	56.1	18.2	15.1	5.0	94.4	59.4	19.3	16.0	5.30
2R-3, 2–5	CKY-1274910	1111.21	131	110,985	36,676	2,793	18.1	62.6	38.4	–0.4	118.8	15.3	52.7	32.3	T
2R-3, 62–65	CKY-1275210	1111.81	4,514	37,783	15,532	8,011	57.3	20.2	15.2	4.2	96.8	59.1	20.8	15.7	4.40

SVD = singular value decomposition. T = trace.

Table T13. Carbonate, carbon, nitrogen, and sulfur in sediment, Holes C0002H, C0002J, C0002K, and C0002L. (Continued on next page.)

Core, section, interval (cm)	Depth (mbsf)	IC (wt%)	$CaCO_3$ (wt%)	TN (wt%)	TC (wt%)	TS (wt%)	TOC (wt%)	C/N	C/S
338-C0002H-									
1R-1, 29–31	1100.8	0.47	3.9	0.07	1.0	0.72	0.55	8.1	0.8
1R-1, 129–131	1101.8	0.23	1.9	0.03	0.5	0.77	0.26	7.4	0.3
2R-1, 15–17	1110.7	0.93	7.8	0.05	1.3	0.33	0.34	7.1	1.1
2R-3, 2–5	1111.2	0.03	0.3	0.01	0.1	0.20	0.09	6.7	0.4
2R-3, 62–65	1111.8	0.76	6.3	0.07	1.4	0.76	0.65	9.2	0.8
338-C0002J-									
1R-1, 70–72	902.7	3.17	26.4	0.06	3.5	0.03	0.29	5.2	8.3
1R-6, 0–2	903.6	2.71	22.6	0.05	3.0	ND	0.34	6.3	?
1R-7, 45–47	904.3	0.88	7.4	0.05	1.1	0.21	0.19	3.5	0.9
1R-7, 110–112	904.9	2.30	19.2	0.06	2.6	0.05	0.27	4.8	5.2
2R-1, 21–22	907.2	1.67	13.9	0.06	2.0	0.05	0.35	6.0	7.3
3R-1, 73–78	912.7	1.94	16.2	0.07	2.5	0.26	0.53	7.3	2.0
3R-2, 63–69	913.4	1.66	13.8	0.08	2.3	ND	0.63	7.5	?
3R-6, 82–86	916.1	1.05	8.7	0.10	1.9	0.62	0.82	8.1	1.3
4R-1, 32–36	917.3	1.88	15.7	0.07	2.3	0.17	0.40	5.5	2.4
4R-3, 0–6	917.8	1.03	8.6	0.10	1.9	0.75	0.88	8.7	1.2
4R-5, 36–43	920.9	1.39	11.6	0.08	1.9	0.38	0.55	6.8	1.4
5R-3, 7–11	922.8	1.41	11.8	0.08	2.0	0.38	0.57	7.4	1.5
5R-5, 13.5–19.5	923.1	1.57	13.1	0.09	2.3	0.46	0.69	8.1	1.5
5R-6, 79–81	924.0	0.38	3.2	0.10	1.1	0.82	0.67	7.1	0.8
5R-6, 110–111	924.3	0.70	5.8	0.09	1.3	0.60	0.64	7.0	1.1
5R-7, 45–46	924.8	0.81	6.8	0.09	1.5	0.84	0.66	7.3	0.8
5R-8, 0–1	925.7	1.36	11.3	0.08	1.9	0.44	0.57	7.3	1.3
5R-8, 30–31	926.0	0.91	7.6	0.08	1.5	0.78	0.56	7.4	0.7
5R-8, 102–103.5	926.7	0.00	0.0	0.07	0.6	1.21	0.57	8.1	0.5
6R-1, 39–41	927.4	0.17	1.4	0.02	0.4	0.38	0.18	7.4	0.5
7R-1, 58–60	932.6	0.03	0.3	0.02	0.1	0.26	0.08	5.0	0.3
7R-2, 31–33	933.3	0.35	2.9	0.06	0.8	1.22	0.45	7.8	0.4
338-C0002K-									
1H-1, 113–116	201.1	0.95	7.9	0.09	1.6	0.30	0.64	7.0	2.1
1H-2, 74–77	202.1	1.31	10.9	0.09	2.0	0.07	0.66	7.7	9.2
1H-4, 4–7	202.9	1.53	12.8	0.10	2.2	0.07	0.63	6.1	8.7
2H-1, 58–61	205.1	1.03	8.6	0.04	1.4	0.14	0.32	7.1	2.2
3T-3, 59–60	207.9	0.23	1.9	0.06	0.7	0.25	0.49	8.7	2.0
3T-4, 25–27	208.7	0.53	4.5	0.09	1.1	0.07	0.61	6.8	8.4
3T-4, 134–136	209.8	0.38	3.2	0.08	1.0	0.27	0.57	7.1	2.1
3T-6, 13–15	210.4	0.47	3.9	0.08	1.0	0.08	0.52	6.5	6.6
4T-1, 36–39	215.4	0.63	5.3	0.09	1.2	0.08	0.58	6.6	7.2
4T-3, 0–3	215.7	0.55	4.5	0.08	1.1	0.06	0.50	6.6	8.0
4T-4, 101–104	217.1	0.25	2.0	0.05	0.6	0.09	0.32	6.9	3.6
5T-1, 14–17	220.1	0.52	4.4	0.08	1.0	0.15	0.51	6.2	3.5
5T-4, 73–76	223.3	1.51	12.6	0.12	2.5	0.18	0.97	8.3	5.3
5T-7, 0–3	224.5	1.43	11.9	0.11	2.3	0.16	0.90	8.2	5.6
6T-2, 70–77	231.2	1.26	10.5	0.09	2.0	0.27	0.69	7.9	2.6
6T-4, 17–20	231.8	0.44	3.7	0.07	1.0	0.09	0.53	7.9	5.6
6T-4, 95–98	232.6	0.64	5.3	0.06	1.2	0.14	0.53	8.9	3.8
7X-1, 46–48	239.5	0.52	4.3	0.08	1.1	0.08	0.63	8.0	7.5
7X-2, 38–40	240.0	0.46	3.9	0.07	1.1	0.12	0.64	8.9	5.2
7X-4, 63–65	241.4	0.56	4.7	0.07	1.2	0.13	0.59	8.4	4.6
7X-4, 106–109	241.9	0.33	2.8	0.06	0.8	0.10	0.50	7.8	4.9
7X-6, 77–79	243.0	0.40	3.3	0.07	1.0	0.13	0.58	8.6	4.5
8X-1, 110–113	249.6	2.50	20.8	0.08	3.0	0.02	0.54	6.5	23.0
8X-3, 0–3	250.4	0.77	6.4	0.08	1.4	0.14	0.60	7.8	4.4
8X-5, 116–119	254.2	0.75	6.2	0.09	1.4	0.54	0.70	7.7	1.3
9X-2, 43.5–45.5	259.4	0.61	5.1	0.08	1.2	0.10	0.63	7.4	6.3
9X-4, 0–8	260.4	0.65	5.4	0.07	1.1	0.37	0.43	6.6	1.2
9X-5, 20–22	262.0	0.68	5.6	0.10	1.4	0.13	0.74	7.2	5.6
9X-6, 19–21	263.4	0.18	1.5	0.03	0.4	0.13	0.23	6.9	1.8
9X-7, 7–9	264.7	0.73	6.1	0.08	1.4	0.14	0.68	8.3	4.8
10X-3, 0–3	268.2	0.42	3.5	0.06	1.0	0.13	0.56	8.8	4.2
10X-5, 135–138	271.7	0.92	7.6	0.10	1.7	0.10	0.76	7.7	8.0
10X-7, 16–19	273.3	0.79	6.6	0.09	1.5	0.10	0.72	8.0	7.1
11X-1, 26–32	277.3	1.08	9.0	0.08	1.6	0.06	0.49	6.1	7.7
11X-3, 2–4	277.8	0.26	2.1	0.06	0.7	0.08	0.40	7.1	5.1

Table T13 (continued).

Core, section, interval (cm)	Depth (mbsf)	IC (wt%)	$CaCO_3$ (wt%)	TN (wt%)	TC (wt%)	TS (wt%)	TOC (wt%)	C/N	C/S
11X-4, 63–65	279.9	0.58	4.9	0.08	1.2	0.09	0.58	7.1	6.6
338-C0002L-									
1X-2, 81–84	279.0	1.30	10.9	0.07	1.7	0.04	0.41	5.5	9.2
1X-3, 127–130	280.5	1.26	10.5	0.06	1.6	0.04	0.31	5.3	7.4
1X-6, 16–19	282.4	0.65	5.4	0.07	1.2	0.10	0.54	7.5	5.2
2X-1, 27–30	286.8	0.63	5.3	0.07	1.1	0.36	0.48	7.3	1.3
2X-2, 0–6	287.0	1.44	12.0	0.11	2.2	0.09	0.77	7.0	8.9
3X-1, 103–105	297.0	0.26	2.2	0.06	0.4	0.06	0.17	2.7	3.0
4X-3, 0–3	307.1	2.03	16.9	0.09	2.6	0.13	0.52	5.6	3.9
4X-5, 120–122	310.7	1.47	12.3	0.11	2.2	0.04	0.73	6.4	16.3
4X-6, 73–75	311.6	1.23	10.3	0.11	2.0	0.14	0.80	7.2	5.9
4X-7, 18–23	312.5	1.51	12.6	0.09	2.1	0.04	0.60	6.4	15.3
5X-2, 60–63	317.0	0.53	4.4	0.08	1.2	0.08	0.64	8.2	7.5
5X-4, 76–79	318.5	0.39	3.3	0.08	0.8	0.17	0.43	5.2	2.4
5X-5, 13–16	318.9	0.49	4.1	0.09	1.1	0.06	0.59	6.6	10.3
5X-6, 15–18	320.1	0.56	4.7	0.07	1.1	0.08	0.51	7.0	6.2
5X-6, 75–78	320.7	0.46	3.8	0.06	1.0	0.08	0.53	8.3	6.9
5X-8, 10–13	321.9	0.45	3.7	0.05	0.8	0.20	0.36	7.0	1.8
6X-1, 33–36	324.8	0.59	5.0	0.08	1.2	0.07	0.62	7.3	8.3
6X-2, 121–124	326.5	1.77	14.7	0.07	2.2	0.02	0.42	6.1	18.7
6X-3, 20–29.5	326.9	0.51	4.3	0.06	1.2	0.10	0.64	10.1	6.2
6X-6, 27–30	328.9	0.12	1.0	0.04	0.5	0.25	0.42	9.5	1.7
6X-7, 17–19	330.1	1.47	12.3	0.08	2.0	0.04	0.48	5.8	10.9
6X-8, 12–14	331.4	0.38	3.1	0.07	1.0	0.13	0.61	9.0	4.5
7X-3, 0–3	335.4	0.44	3.6	0.07	1.0	0.53	0.55	7.7	1.0
8X-2, 28–31	344.1	0.08	0.7	0.03	0.3	0.20	0.21	6.6	1.0
8X-5, 0–3	346.7	1.06	8.8	0.09	1.6	0.04	0.52	6.1	14.0
8X-7, 73–76	350.2	0.60	5.0	0.08	1.1	0.06	0.50	5.9	8.4
9X-1, 40–43	353.4	0.23	1.9	0.08	0.7	0.04	0.42	5.0	10.7
9X-6, 0–3	356.7	0.59	5.0	0.09	1.1	0.07	0.52	6.0	7.9
9X-6, 34.5–37.5	357.1	0.80	6.7	0.09	1.4	0.09	0.58	6.6	6.6
10X-2, 100–101	364.6	0.35	2.9	0.06	0.8	0.15	0.42	6.6	2.9
10X-5, 87–88	366.3	0.13	1.1	0.04	0.4	0.20	0.27	6.0	1.3
10X-8, 56–57	369.2	0.58	4.8	0.09	1.2	0.15	0.62	7.2	4.1
11X-3, 62–66	375.3	0.59	4.9	0.10	1.2	0.06	0.60	6.1	10.3
12X-7, 32–34	388.3	0.98	8.2	0.08	1.6	0.08	0.57	7.0	6.8
13X-6, 27–29	397.0	1.75	14.6	0.10	2.2	0.21	0.44	4.5	2.1
14X-1, 102–102.5	401.5	1.66	13.8	0.09	2.2	0.07	0.59	6.6	8.4
14X-7, 87–87.5	408.5	0.43	3.6	0.04	0.9	0.43	0.48	13.1	1.1
14X-8, 30–30.5	409.4	0.76	6.3	0.10	1.5	0.21	0.76	7.3	3.6
15X-5, 2–5	412.6	0.56	4.7	0.10	1.2	0.32	0.67	7.0	2.1
15X-7, 120–123	416.0	0.62	5.2	0.09	1.3	0.09	0.70	7.7	7.8
15X-10, 47–50	418.9	0.62	5.2	0.10	1.4	0.09	0.74	7.3	8.0
16X-2, 135–139	421.8	0.71	6.0	0.09	1.5	0.10	0.77	8.2	7.5
16X-6, 110–113	426.1	0.76	6.3	0.09	1.5	0.09	0.71	7.7	8.0
16X-7, 95–98	427.4	0.76	6.3	0.07	1.3	0.06	0.49	7.0	8.1
17X-3, 76–77	431.7	0.65	5.5	0.08	1.4	0.19	0.78	9.2	4.1
17X-7, 46–47	435.4	0.53	4.4	0.10	1.3	0.11	0.73	7.1	6.9
17X-9, 60–61	437.6	0.65	5.4	0.10	1.3	0.09	0.68	7.0	7.4
18X-2, 63–66	440.0	0.95	7.9	0.10	1.7	0.10	0.72	7.4	7.3
18X-4, 0–3	440.7	0.82	6.9	0.09	1.5	0.15	0.69	7.3	4.5
18X-6, 20–22	443.7	0.64	5.3	0.09	1.2	0.11	0.58	6.3	5.5
19X-7, 80–82	455.6	0.67	5.6	0.09	1.4	0.08	0.69	7.5	9.1
20X-1, 100–104	458.5	0.28	2.4	0.05	0.7	0.23	0.45	8.1	2.0
20X-6, 113–115	464.4	0.55	4.6	0.09	1.3	0.08	0.75	7.9	8.9
20X-CC, 50–53	467.2	0.54	4.5	0.10	1.3	0.09	0.79	7.7	8.5
21X-1, 5.5–6	467.1	0.62	5.2	0.10	1.4	0.08	0.77	7.7	10.1
21X-2, 109–112	469.5	0.62	5.2	0.08	1.3	0.06	0.68	8.1	11.2
21X-3, 10–13	469.7	0.98	8.1	0.12	1.8	0.89	0.78	6.6	0.9
21X-5, 1–2	471.1	1.07	8.9	0.12	1.9	0.18	0.86	7.4	4.7
21X-8, 61–64	475.7	0.59	5.0	0.11	1.2	0.22	0.64	6.1	3.0
22X-2, 31–34	477.5	0.57	4.7	0.08	1.2	0.12	0.63	7.6	5.5
22X-5, 98–101	480.2	0.38	3.2	0.05	0.9	0.73	0.56	11.0	0.8
22X-8, 136–139	482.6	0.92	7.7	0.09	1.6	0.04	0.66	7.1	16.1
24X-1, 129–132	496.8	0.44	3.7	0.07	0.9	0.05	0.43	6.1	8.2
24X-4, 77–80	500.4	0.73	6.1	0.08	1.3	0.04	0.54	6.8	12.5
24X-6, 33–36	501.3	0.17	1.4	0.03	0.3	0.02	0.11	4.3	4.4

IC = inorganic carbon, TN = total nitrogen, TC = total carbon, TS = total sulfur, TOC = total organic carbon.

Table T14. Results of XRF analysis, Hole C0002H.

Core, section, interval (cm)	Sample	Central depth (mbsf)	Na_2O (wt%)	MgO (wt%)	Al_2O_3 (wt%)	SiO_2 (wt%)	P_2O_5 (wt%)	K_2O (wt%)	CaO (wt%)	TiO_2 (wt%)	MnO (wt%)	Fe_2O_3 (wt%)	Loss on ignition (wt%)
338-C0002H-													
1R-1, 29–31	CKY-1273510	1100.80	2.30	2.09	16.6	64.5	0.08	2.86	3.11	0.65	0.07	5.91	6.66
1R-1, 129–131	CKY-1273910	1101.80	2.87	1.38	16.3	67.1	0.10	2.27	3.55	0.57	0.05	4.43	3.84
2R-1, 15–17	CKY-1273110	1110.66	2.37	2.13	15.8	63.2	0.36	2.52	5.28	0.58	0.08	5.74	7.45
2R-3, 2–5	CKY-1274910	1111.21	2.04	0.46	8.84	83.2	0.02	2.57	0.91	0.22	0.02	1.51	1.36
2R-3, 62–65	CKY-1275210	1111.81	2.10	2.03	16.1	64.2	0.08	2.95	4.05	0.65	0.07	5.94	7.38

Table T15. Core depth intervals and curated length, Hole C0002J.

Core, section	Depth (mbsf) Top	Depth (mbsf) Bottom	Curated length (m)
338-C0002J-			
1R-1	902.00	902.80	0.80
1R-2	902.80	902.91	0.11
1R-3	902.91	903.15	0.25
1R-4	903.15	903.42	0.27
1R-5	903.42	903.57	0.15
1R-6	903.57	903.81	0.24
1R-7	903.81	904.99	1.19
1R-8	904.99	906.06	1.07
1R-CC	906.06	906.22	0.16
2R-1	907.00	907.77	0.77
2R-CC	907.77	907.88	0.11
3R-1	912.00	912.78	0.78
3R-2	912.78	913.53	0.75
3R-3	913.53	913.74	0.21
3R-4	913.74	913.84	0.11
3R-5	913.84	915.25	1.41
3R-6	915.25	916.15	0.91
3R-CC	916.15	916.31	0.16
4R-1	917.00	917.55	0.55
4R-2	917.55	917.76	0.21
4R-3	917.76	919.14	1.38
4R-4	919.14	920.53	1.39
4R-5	920.53	921.68	1.16
4R-CC	921.68	921.81	0.13
5R-1	922.00	922.32	0.32
5R-2	922.32	922.77	0.45
5R-3	922.76	922.88	0.11
5R-4	922.87	922.99	0.11
5R-5	922.97	923.18	0.20
5R-6	923.17	924.38	1.20
5R-7	924.35	925.68	1.31
5R-8	925.64	926.99	1.31
5R-CC	926.93	927.06	0.07
6R-1	927.00	927.97	0.97
6R-CC	927.97	928.15	0.18
7R-1	932.00	933.00	1.00
7R-2	933.00	933.51	0.51
7R-CC	933.51	933.76	0.25

Table T16. Results of X-ray diffraction analysis performed on random bulk powder, Hole C0002J.

Core, section, interval (cm)	Sample	Central depth (mbsf)	Integrated peak area (total counts)				Absolute mineral abundance calculated from SVD normalization factors (wt%)					Relative abundance (wt%)			
			Total clay minerals	Quartz	Feldspar	Calcite	Total clay minerals	Quartz	Feldspar	Calcite	Sum	Total clay minerals	Quartz	Feldspar	Calcite
338-C0002J-															
1R-1, 70–72	CKY-1292810	902.71	2,086	23,545	10,551	28,616	29.4	12.6	10.5	36.2	88.8	33.2	14.2	11.9	40.8
1R-6, 0–2	CKY-1284210	903.58	2,602	26,861	9,409	25,121	34.3	14.5	9.02	30.8	88.6	38.7	16.4	10.2	34.7
1R-7, 45–47	CKY-1285810	904.27	2,664	19,287	9,742	11,398	34.5	10.1	9.63	11.8	66.0	52.3	15.3	14.6	17.9
1R-7, 110–112	CKY-1306210	904.92	2,951	27,541	10,572	21,604	38.5	14.8	10.2	25.4	88.9	43.3	16.6	11.5	28.6
2R-1, 21–22	CKY-1308910	907.22	2,625	34,964	12,880	17,152	35.7	19.1	12.8	19.3	86.8	41.1	21.9	14.7	22.3
3R-1, 73–78	CKY-1311510	912.76	2,842	29,196	11,555	18,863	37.6	15.7	11.3	21.6	86.3	43.6	18.2	13.1	25.1
3R-2, 63–69	CKY-1313510	913.44	3,308	27,406	10,301	16,493	42.0	14.7	9.84	17.9	84.4	49.8	17.4	11.7	21.2
3R-6, 82–86	CKY-1311810	916.09	3,457	29,902	10,833	10,781	43.6	16.1	10.4	9.71	79.7	54.7	20.2	13.0	12.2
4R-1, 32–36	CKY-1315110	917.34	3,471	29,665	12,352	17,992	44.9	15.8	12.0	19.6	92.4	48.6	17.1	13.0	21.3
4R-3, 0–6	CKY-1312810	917.79	2,679	29,054	14,387	11,645	36.8	15.5	14.6	11.7	78.6	46.9	19.7	18.6	14.9
4R-5, 36–43	CKY-1315410	920.92	3,585	28,860	11,003	14,710	45.3	15.4	10.5	15.0	86.3	52.5	17.9	12.2	17.4
5R-3, 7–11	CKY-1319210	922.86	3,526	27,691	10,507	15,703	44.5	14.8	10.0	16.5	85.8	51.9	17.2	11.7	19.3
5R-5, 13.5–19.5	CKY-1289410	923.15	3,031	27,991	10,268	16,760	39.0	15.1	9.87	18.6	82.5	47.3	18.3	12.0	22.5
5R-6, 79–81	CKY-1323510	923.96	4,017	33,058	9,978	3,788	48.9	17.9	9.20	–0.70	75.3	64.9	23.8	12.2	T
5R-6, 110–111	CKY-1304910	924.29	3,648	36,280	12,986	7,635	46.5	19.7	12.6	4.88	83.6	55.6	23.5	15.1	5.84
5R-7, 45–46	CKY-1307510	924.83	3,816	30,457	13,596	8,685	48.8	16.1	13.4	6.25	84.5	57.7	19.1	15.8	7.39
5R-8, 0–1	CKY-1310110	925.69	3,360	29,164	10,383	14,457	42.5	15.7	9.89	15.0	83.0	51.2	18.9	11.9	18.0
5R-8, 30–31	CKY-1309310	925.94	4,032	36,424	13,435	9,150	51.0	19.6	13.0	6.50	90.1	56.6	21.8	14.4	7.22
5R-8, 102–103.5	CKY-1323110	926.66	3,964	38,077	16,451	1,815	51.3	20.4	16.4	–3.76	84.3	60.8	24.2	19.4	T
6R-1, 39–41	CKY-1320310	927.40	941	68,285	40,420	1,338	29.4	37.1	43.4	–2.53	107.4	27.4	34.5	40.5	T
7R-1, 58–60	CKY-1320910	932.59	783	86,460	33,986	2,284	24.3	48.3	35.8	–1.19	107.2	22.7	45.0	33.4	T
7R-2, 31–33	CKY-1321310	933.32	3,019	28,788	18,907	4,143	42.4	15.0	19.6	0.71	77.7	54.6	19.3	25.3	0.91

SVD = singular value decomposition. T = trace.

Table T17. Results of XRF analysis, Hole C0002J.

Core, section, interval (cm)	Sample	Central depth (mbsf)	Na_2O (wt%)	MgO (wt%)	Al_2O_3 (wt%)	SiO_2 (wt%)	P_2O_5 (wt%)	K_2O (wt%)	CaO (wt%)	TiO_2 (wt%)	MnO (wt%)	Fe_2O_3 (wt%)	Loss on ignition (wt%)
338-C0002J-													
1R-1, 70–72	CKY-1292810	902.71	2.13	1.96	13.1	54.3	0.14	2.14	18.6	0.57	0.07	4.61	15.1
1R-6, 0–2	CKY-1284210	903.58	2.20	1.73	13.3	57.2	0.11	2.17	15.9	0.58	0.06	4.54	13.1
1R-7, 45–47	CKY-1285810	904.27	3.11	1.12	13.9	66.6	0.07	3.32	5.74	0.41	0.05	3.52	7.75
1R-7, 110–112	CKY-1306210	904.92	2.22	2.03	14.2	58.1	0.10	2.33	13.6	0.58	0.05	4.93	12.1
2R-1, 21–22	CKY-1308910	907.22	2.13	1.95	14.8	61.2	0.09	2.82	9.38	0.61	0.06	4.55	9.73
3R-1, 73–78	CKY-1311510	912.76	2.35	1.99	13.7	59.3	0.10	2.47	11.1	0.57	0.06	5.22	10.3
3R-2, 63–69	CKY-1313510	913.44	2.32	2.15	14.3	60.1	0.08	2.65	9.56	0.59	0.06	5.67	10.6
3R-6, 82–86	CKY-1311810	916.09	2.27	2.15	14.7	63.5	0.08	2.75	6.31	0.62	0.05	5.64	9.09
4R-1, 32–36	CKY-1315110	917.34	2.21	2.29	14.6	59.8	0.08	2.69	10.4	0.60	0.06	4.93	10.8
4R-3, 0–6	CKY-1312810	917.79	2.42	2.12	14.5	61.2	0.09	2.65	8.03	0.60	0.05	5.43	8.12
4R-5, 36–43	CKY-1315410	920.92	2.33	2.12	14.7	60.8	0.08	2.77	8.46	0.59	0.06	5.23	8.22
5R-3, 7–11	CKY-1319210	922.86	2.37	2.05	14.4	63.2	0.08	2.59	6.60	0.62	0.05	5.61	8.80
5R-5, 13.5–19.5	CKY-1289410	923.15	2.14	2.17	14.5	60.1	0.09	2.70	9.20	0.60	0.06	5.43	9.56
5R-6, 79–81	CKY-1323510	923.96	2.06	2.51	16.9	63.5	0.07	3.36	2.55	0.70	0.05	6.18	6.79
5R-6, 110–111	CKY-1304910	924.29	2.19	2.45	16.4	62.8	0.08	3.19	4.09	0.67	0.05	5.79	7.28
5R-7, 45–46	CKY-1307510	924.83	2.38	2.16	15.6	63.4	0.08	2.89	5.13	0.63	0.05	5.78	8.31
5R-8, 0–1	CKY-1310110	925.69	2.17	2.25	15.0	60.1	0.08	2.85	8.04	0.60	0.06	5.58	8.69
5R-8, 30–31	CKY-1309310	925.94	2.23	2.18	14.8	62.9	0.08	2.89	5.55	0.60	0.05	6.00	7.42
5R-8, 102–103.5	CKY-1323110	926.66	2.49	2.09	16.4	66.0	0.07	2.88	1.42	0.68	0.06	5.90	5.15
6R-1, 39–41	CKY-1320310	927.40	2.77	1.12	12.3	73.9	0.04	2.89	1.78	0.40	0.04	2.96	2.82
7R-1, 58–60	CKY-1320910	932.59	2.34	0.56	10.2	80.0	0.02	2.87	1.07	0.26	0.03	1.76	1.76
7R-2, 31–33	CKY-1321310	933.32	2.85	1.80	16.8	64.7	0.10	2.49	3.92	0.65	0.07	5.26	5.90

Table T18. Scanning XRF data from Section 338-C0002J-5R-8. (Continued on next page.)

Core, section, interval (cm)	Central depth (mbsf)	Na_2O (wt%)	MgO (wt%)	Al_2O_3 (wt%)	SiO_2 (wt%)	P_2O_5 (wt%)	K_2O (wt%)	CaO (wt%)	TiO_2 (wt%)	MnO (wt%)	Fe_2O_3 (wt%)
338-C0002J-											
5R-8, 89	926.53	1.02	1.19	9.27	62.0	0.77	4.95	2.70	1.35	0.14	16.7
5R-8, 89.5	926.54	0.37	1.14	9.62	61.4	1.20	4.33	2.88	1.18	0.17	17.8
5R-8, 90	926.54	1.38	1.31	9.21	59.8	1.13	4.26	3.75	1.21	0.15	17.9
5R-8, 90.5	926.55	2.31	1.59	9.45	58.4	1.10	4.31	4.18	1.24	0.14	17.3
5R-8, 91	926.55	1.80	1.28	8.99	60.0	1.08	3.99	4.46	1.25	0.15	17.0
5R-8, 91.5	926.56	1.48	1.60	9.22	59.9	1.20	4.12	4.43	1.25	0.16	16.7
5R-8, 92	926.56	2.02	1.48	8.83	59.3	1.17	4.26	4.73	1.21	0.16	16.8
5R-8, 92.5	926.57	2.18	1.48	8.91	58.8	1.15	4.15	4.94	1.25	0.16	17.0
5R-8, 93	926.57	1.38	1.21	8.81	58.8	1.22	4.31	5.13	1.30	0.16	17.7
5R-8, 93.5	926.58	1.07	1.26	9.13	58.4	1.14	4.41	5.24	1.40	0.16	17.8
5R-8, 94	926.58	2.37	1.35	8.33	57.3	1.14	4.31	4.96	1.26	0.15	18.8
5R-8, 94.5	926.59	1.76	1.64	8.52	58.3	1.25	4.27	4.56	1.27	0.15	18.3
5R-8, 95	926.59	1.65	1.49	8.57	59.8	1.08	4.23	4.52	1.25	0.14	17.3
5R-8, 95.5	926.60	1.33	1.50	8.79	59.8	1.01	4.31	4.73	1.26	0.14	17.1
5R-8, 96	926.60	2.71	1.51	9.40	59.5	1.15	4.09	4.05	1.19	0.16	16.2
5R-8, 96.5	926.61	1.83	1.05	9.03	61.4	1.33	4.08	3.62	1.19	0.17	16.3
5R-8, 97	926.61	1.48	1.54	9.54	61.1	1.26	3.97	3.33	1.22	0.15	16.4
5R-8, 97.5	926.62	2.98	1.59	9.42	59.0	1.10	3.79	4.03	1.24	0.16	16.7
5R-8, 98	926.62	1.68	1.31	9.30	59.9	1.18	3.90	4.69	1.25	0.17	16.6
5R-8, 98.5	926.63	0.65	1.75	9.06	61.6	1.09	3.96	4.54	1.19	0.18	16.0
5R-8, 99	926.63	1.35	1.40	8.77	61.5	1.04	4.05	4.44	1.15	0.15	16.1
5R-8, 99.5	926.64	2.77	1.41	8.33	60.6	1.05	4.06	3.84	1.15	0.16	16.6
5R-8, 100	926.64	1.32	1.41	8.54	60.5	1.07	4.09	3.94	1.16	0.14	17.8
5R-8, 100.5	926.65	0.66	1.24	9.17	61.2	1.02	4.24	4.24	1.23	0.17	16.8
5R-8, 101	926.65	1.21	1.12	9.61	61.5	1.10	4.24	4.45	1.27	0.17	15.4
5R-8, 101.5	926.66	0.57	1.41	11.2	61.4	1.02	4.38	4.17	1.48	0.16	14.3
5R-8, 102	926.66	2.10	0.93	11.2	61.2	1.07	4.24	4.26	1.42	0.17	13.4
5R-8, 102.5	926.67	0.79	1.01	10.9	61.4	0.97	4.25	4.78	1.48	0.18	14.3
5R-8, 103	926.67	0.46	1.00	11.1	62.4	0.99	4.37	4.45	1.50	0.16	13.7
5R-8, 103.5	926.68	1.94	0.88	11.6	63.0	0.82	4.35	3.67	1.49	0.16	12.1
5R-8, 104	926.68	1.51	0.86	11.5	63.5	0.88	4.35	3.85	1.50	0.16	12.0
5R-8, 104.5	926.69	0.87	0.84	11.9	63.8	0.78	4.28	4.07	1.42	0.16	12.0
5R-8, 105	926.69	0.78	0.63	11.4	64.1	0.82	4.32	4.31	1.33	0.17	12.2
5R-8, 105.5	926.70	1.47	1.18	10.9	62.3	0.69	4.21	5.07	1.24	0.16	12.7
5R-8, 106	926.70	1.19	1.31	10.6	62.4	0.61	4.13	5.24	1.24	0.16	13.1
5R-8, 106.5	926.71	0.95	1.33	10.6	62.6	0.76	4.38	5.24	1.42	0.16	12.6
5R-8, 107	926.71	1.32	1.16	10.4	62.6	0.67	4.73	5.05	1.52	0.16	12.4
5R-8, 107.5	926.72	2.36	0.95	10.6	62.4	0.76	4.80	3.69	1.49	0.14	12.9
5R-8, 108	926.72		1.01	10.5	62.5	0.80	5.08	4.09	1.67	0.16	14.2
5R-8, 108.5	926.73	0.05	1.09	9.94	61.5	0.89	4.75	5.43	1.65	0.20	14.5
5R-8, 109	926.73	1.55	0.99	9.49	60.7	0.89	4.64	5.66	1.47	0.16	14.5
5R-8, 109.5	926.74	0.29	1.08	9.18	62.9	0.72	4.81	5.46	1.35	0.16	14.1
5R-8, 110	926.74	3.13	1.47	9.01	61.9	0.73	4.40	4.87	1.27	0.14	13.1
5R-8, 110.5	926.75	2.59	1.10	9.60	63.0	0.87	4.37	4.64	1.30	0.18	12.4
5R-8, 111	926.75	0.97	0.75	10.2	64.1	0.96	4.70	4.40	1.41	0.16	12.4
5R-8, 111.5	926.76	2.11	1.03	9.49	62.6	1.21	4.82	4.08	1.44	0.15	13.1
5R-8, 112	926.76	0.56	1.14	9.47	63.9	1.17	4.87	3.86	1.47	0.15	13.5
5R-8, 112.5	926.77	1.60	1.20	9.27	62.7	1.24	4.71	2.96	1.42	0.16	14.7
5R-8, 113	926.77	1.07	1.30	9.15	61.4	1.28	4.74	2.98	1.38	0.17	16.6
5R-8, 113.5	926.78	0.78	1.39	9.20	59.9	1.24	4.65	3.42	1.35	0.19	17.9
5R-8, 114	926.78	1.92	1.21	8.84	59.0	1.01	4.60	4.06	1.42	0.16	17.8
5R-8, 114.5	926.79	0.32	0.84	8.60	61.7	1.29	5.08	4.64	1.48	0.17	15.9
5R-8, 115	926.79	1.48	1.06	7.92	61.8	1.37	4.74	4.27	1.37	0.14	15.9
5R-8, 115.5	926.80	1.13	1.38	8.93	60.0	1.25	4.55	3.71	1.37	0.18	17.6
5R-8, 116	926.80	0.80	1.06	8.99	59.8	1.21	4.52	3.49	1.39	0.19	18.6
5R-8, 116.5	926.81	1.22	1.50	8.94	60.9	0.94	4.68	3.56	1.26	0.17	16.9
5R-8, 117	926.81	1.30	1.02	8.93	62.5	1.02	4.74	3.31	1.19	0.17	15.9
5R-8, 117.5	926.82	1.69	0.97	9.20	63.1	1.16	4.57	2.84	1.15	0.17	15.1
5R-8, 118	926.82	1.62	1.20	10.8	63.4	1.04	4.57	2.69	1.26	0.16	13.3
5R-8, 118.5	926.83	2.12	1.02	10.6	64.0	0.80	4.55	2.80	1.31	0.17	12.6
5R-8, 119	926.83	2.71	1.37	9.72	64.9	0.82	4.67	2.82	1.19	0.15	11.6
5R-8, 119.5	926.84	1.34	1.17	9.62	65.6	0.90	4.94	2.87	1.29	0.15	12.1
5R-8, 120	926.84	2.70	1.56	9.65	64.6	0.83	4.78	2.93	1.28	0.17	11.5
5R-8, 120.5	926.85	0.89	1.43	9.72	65.5	0.84	4.85	3.04	1.27	0.17	12.3
5R-8, 121	926.85	1.71	1.59	10.3	64.4	0.88	4.64	2.76	1.34	0.16	12.3
5R-8, 121.5	926.86	2.58	1.32	10.4	64.4	0.90	4.61	2.77	1.30	0.14	11.6

Table T18 (continued).

Core, section, interval (cm)	Central depth (mbsf)	Na_2O (wt%)	MgO (wt%)	Al_2O_3 (wt%)	SiO_2 (wt%)	P_2O_5 (wt%)	K_2O (wt%)	CaO (wt%)	TiO_2 (wt%)	MnO (wt%)	Fe_2O_3 (wt%)
5R-8, 122	926.86	2.69	1.56	10.8	64.5	0.86	4.45	2.69	1.24	0.14	11.1
5R-8, 122.5	926.87	1.78	1.55	10.7	65.1	1.06	4.49	2.60	1.29	0.15	11.3
5R-8, 123	926.87	3.53	1.34	10.3	63.6	1.08	4.45	2.72	1.30	0.14	11.6
5R-8, 123.5	926.88	2.20	1.28	10.2	64.0	1.04	4.66	2.81	1.37	0.16	12.3
5R-8, 124	926.88	1.37	1.29	9.59	64.1	0.94	4.93	2.91	1.47	0.17	13.3
5R-8, 124.5	926.89	1.75	1.10	9.21	63.5	1.22	5.03	2.86	1.48	0.17	13.7
5R-8, 125	926.89	0.98	0.92	10.2	64.5	0.96	4.95	2.77	1.41	0.17	13.1
5R-8, 125.5	926.90	1.07	1.21	10.1	65.2	0.85	4.90	2.78	1.37	0.15	12.4
5R-8, 126	926.90	1.49	1.15	10.2	66.5	0.90	4.71	2.63	1.23	0.12	11.2
5R-8, 126.5	926.91	1.36	1.32	10.1	66.8	0.85	4.68	2.35	1.19	0.13	11.2
5R-8, 127	926.91	0.10	0.62	9.46	66.5	1.04	5.10	2.41	1.37	0.17	13.2
5R-8, 127.5	926.92	1.12	0.82	8.59	63.9	1.04	5.20	2.86	1.45	0.17	14.8
5R-8, 128	926.92	0.62	1.13	7.67	63.4	1.11	5.48	2.98	1.59	0.18	15.9
5R-8, 128.5	926.93	1.86	1.71	8.26	59.7	1.43	5.50	2.68	1.49	0.18	17.2
5R-8, 129	926.93	1.25	1.52	8.04	63.0	1.16	5.44	2.84	1.48	0.19	15.1
5R-8, 129.5	926.94	1.04	1.47	8.14	63.2	1.07	5.59	2.96	1.52	0.21	14.8
5R-8, 130	926.94	2.81	1.07	8.74	62.3	1.28	5.20	2.80	1.48	0.16	14.2
5R-8, 130.5	926.95	0.71	1.34	8.81	64.0	1.19	5.32	3.02	1.52	0.19	13.9
5R-8, 131	926.95	0.61	1.82	6.92	62.4	2.16	5.67	3.25	1.85	0.15	15.2

Table T19. Calcareous nannofossils in cuttings samples, Hole C0002F.

Age (Ma)	Cuttings sample	Depth (mbsf)	Abundance	Preservation	*Calcidiscus leptoporus*	*Calcidiscus macintyrei*	*Ceratolithus cristatus*	*Coccolithus pelagicus*	*Cyclicargolithus floridanus*	*Discoaster berggrenii*	*Discoaster brouweri*	*Discoaster pentaradiatus*	*Discoaster quinqueramus*	*Discoaster surculus*	*Discoaster tamalis*	*Discoaster variabilis*	*Florisphaera profunda*	*Gephyrocapsa* spp. (<4 µm)	*Helicosphaera carteri*	*Helicosphaera sellii*	*Pontosphaera japonica*	*Pontosphaera* spp.	*Pseudoemiliania lacunosa*	*Reticulofenestra pseudoumbilicus*	*Reticulofenestra* spp.	*Rhabdosphaera clavigera*	*Sphenolithus abies*	*Syracosphaera pulchra*	*Triquetrorhabdulus rugosus*	*Umbilicosphaera rotula*	*Umbilicosphaera sibogae*
	338-C0002F-																														
3.79–5.59	22-SMW	935.5	V	M	+	+		+			+	+	cf	+	+		+	+	+	+		+	+	+	+	+	+	+		+	
>5.59	34-SMW	985.5	V	M	+	+	+	+			+	+	+	+	+		+	+	+	+			+	+	+		+		+	+	+
	46-SMW	1035.5	C	M	+				re	+			+	+		+	+							+	+		+				
	56-SMW	1085.5	C	P	+	+		+		+	+	+	+				+							+	+		+				
	68-SMW	1135.5	C	M	+			+		+			+			+	+		+					+	+		+				
	80-SMW	1185.5	A	M	+	+		+		+	+	+	+	+		+	+	+	+	+	+	+		+	+		+			+	
	92-SMW	1235.5	C	M	+			+		+		+	+			+	+							+	+		+				
	102-SMW	1285.5	C	M				+				+	+			+	+		+					+	+						
	112-SMW	1335.5	C	M	+			+		+	+		+			+	+		+					+	+		+				
	124-SMW	1385.5	C	M	+	+	+	+					+	+		+			+					+	+		+				
	136-SMW	1435.5	A	M	+			+		+			+	+										+	+		+				
	148-SMW	1485.5	C	P						+		+				+			+					+	+		+				
	174-SMW	1585.5	C	P															+					+	+		+				
	203-SMW	1685.5	R	P																					+						
	227-SMW	1785.5	A	M				+					+	+										+	+		+				
	258-SMW	1885.5	C	P																				+	+		+				
	284-SMW	1985.5	R	P				+		+															+						

Abundance: V = very abundant, A = abundant, C = common, R = rare. Preservation: M = moderate, P = poor. + = present, cf = compare, re = reworked.

Table T20. Calcareous nannofossils in core samples, Hole C0002J.

Age (Ma)	Core, section, interval (cm)	Average depth (mbsf)	Abundance	Preservation	*Amaurolithus* spp.	*Calcidiscus leptoporus*	*Calcidiscus macintyrei*	*Ceratolithus cristatus*	*Coccolithus pelagicus*	*Discoaster asymmetricus*	*Discoaster brouweri*	*Discoaster pentaradiatus*	*Discoaster surculus*	*Discoaster tamalis*	*Discoaster triradiatus*	*Discoaster variabilis*	*Florisphaera profunda*	*Gephyrocapsa* spp. small (<4 µm)	*Helicosphaera carteri*	*Helicosphaera sellii*	*Helicosphaera wallichii*	*Pontosphaera japonica*	*Pontosphaera* spp.	*Pseudoemiliania lacunosa*	*Reticulofenestra pseudoumbilicus*	*Reticulofenestra* spp.	*Rhadosphaera clavigera*	*Sphenolithus abies*	*Syracosphaera pulchra*	*Umbilicosphaera rotula*
	338-C0002J-																													
2.87–3.65	1R-CC, 0.0–5.0	906.085	V	M		+	+		+	+	+	+	+	+			+	+	+					+		+				
3.65–3.79	2R-CC, 5.5–10.5	907.85	V	M	re	+	+		+	+	+	+	+	+			+		+	+	+	+	+	+		+	+		+	+
	3R-CC, 10.5–15.5	916.28	V	M		+	+	+		+	+	+	+		+		+	+	+	+				+		+		+		
>3.79	4R-CC, 7.5–12.5	921.78	V	G		+	+	+			+	+	+			+	+	+	+		+		+	+	+	+		+		+
	5R-7, 111.0–116.0	925.481	A	M		+	+		+		+	+	+			+		+	+		+				+	+		+		+
	5R-8, 103.5–108.5	926.7045	B																											
	5R-CC, 2.0–6.0	927.003	B																											
	6R-CC, 12.5–17.5	928.12	B																											
	7R-CC, 19.5–24.5	933.73	R	P																					+					

Abundance: V = very abundant, A = abundant, R = rare, B = barren. Preservation: G = good, M = moderate, P = poor, + = present, re = reworked.

Table T21. Radiolarians in cuttings samples, Hole C0002F.

Age	Zone	Cuttings sample	Depth (mbsf)	Abundance	Preservation	*Actinomma medianum*	*Actinommidae* spp.	*Amphirhopalum ypsilon*	*Anomalacantha dentata*	*Botryostrobus aquilonaris*	*Carpocanistrum* spp.	*Cenosphaera* spp.	*Collosphaera* sp.	*Cornutella profunda*	*Cycladophora* aff. *davisiana*	*Cycladophora* spp.	*Dictyocoryne* spp.	*Druppatractus irregularis*	*Eucyrtidium lene*	*Eucyrtidium* spp.	*Heliodiscus* sp.	*Hexacontium minerva*	*Larcopyle weddelium*	*Larcopyle buetschlii*	*Litheliidae* spp.	*Lithelius minor*	*Porodiscidae* spp.	*Pyloniidae* spp.	*Spongodiscidae* spp.	*Stichocorys delmontensis*	*Stichocorys peregrina*	*Stylatractus neptunus*	*Stylatractus santaeannae*	*Stylodictya aculiata*	*Stylodictya camerina*	*Stylodictya multispina*	*Stylodictya* spp.	*Theoperidae* spp.	Total radiolarians counted
		338-C0002F-																																					
Plio–Miocene	RN11 or older	22-SMW	935.5	C	M	1	57	1	1	2	4	3	1	2	1	1	3	12		1	1	5	3	1	30	2	17	3	26	1		2	3			8	6	2	200
Plio–Miocene	RN11 or older	34-SMW	985.5	C	M		71	1			2					2	2	2	2			6		1	38	4	13	4	16		1	2	1	3	3	12			186
Unknown	Unzoned	46-SMW	1035.5	VR	M		3					2													1														6
Unknown	Unzoned	56-SMW	1085.5	VR	M		3																																3

Abundance: C = common, VR = very rare. Preservation: M = moderate.

Table T22. Currently available NanTroSEIZE data on the boundary between Pliocene sediments of the Kumano Basin and underlying Miocene rocks of the prism, Site C0002.

Expedition	Hole	Data type	Basin units	Prism units	Depth of boundary	Lithologies above/below boundary	Basin lithology	Prism lithology	Biostratigraphic unconformity
314	A	LWD	x	x	935.6	Mud/Sand	Mud	Sandstone and mud	
315	B	Core	x	x	922.7	Mud/Mud	Glauconitic, abundant trace fossils, calcareous, vein structures, microfault; minor ash	Noncalcareous silty claystone, highly deformed with scaly fabric, sand with quartzo-feldspathic compositions	3.79–5.59
338	F	LWD	x	x	918.5	Subtle; clay-rich/silty sandy	Claystone	Sandstone and claystone	
338	F	Cuttings	?	x	1025*	Mud/Sand	Calcareous claystone, glauconitic claystone	Noncalcareous silty claystone, highly deformed with scaly fabric, sand with quartzo-feldspathic compositions	
332	G	LWD	x	x	931	Sharp boundary	Heterogeneous materials	Heterogeneous materials	
338	H	Core		x		Not observed		Noncalcareous silty claystone, highly deformed with scaly fabric, sand with quartzo-feldspathic compositions	
338	J	Core	x	x	926.7	Mud/Sand	Glauconitic, abundant trace fossils, calcareous silty claystone, vein structures, microfaults	Noncalcareous silty claystone, sand with quartzo-feldspathic compositions	

* = anomalous data, ? = unclear, x = unit identified. LWD = logging while drilling.

Table T23. Depth intervals and recovery, Holes C0002K and C0002L. (Continued on next three pages.)

Core, section	Depth (mbsf)		Curated length (m)
	Top	Bottom	
338-C0002K-			
1H-1	200.00	201.06	1.34
1H-2	201.06	201.88	1.05
1H-3	201.88	202.28	0.51
1H-4	202.28	203.39	1.41
1H-5	203.39	203.69	0.38
1H-6	203.69	204.18	0.62
1H-CC	204.18	204.50	0.41
2H-1	204.50	205.28	0.78
2H-CC	205.28	205.49	0.21
3T-1	205.50	206.40	0.90
3T-2	206.40	207.27	0.87
3T-3	207.27	208.48	1.21
3T-4	208.48	209.88	1.40
3T-5	209.88	210.30	0.42
3T-6	210.30	211.69	1.39
3T-7	211.69	212.05	0.37
3T-CC	212.05	212.40	0.35
4T-1	215.00	215.41	0.41
4T-2	215.41	215.72	0.31
4T-3	215.72	216.12	0.40
4T-4	216.12	217.36	1.24
4T-CC	217.36	217.51	0.15
5T-1	220.00	220.74	0.74
5T-2	220.74	221.72	0.98
5T-3	221.72	222.61	0.90
5T-4	222.61	223.70	1.09
5T-5	223.70	224.12	0.42
5T-6	224.12	224.52	0.40
5T-7	224.52	225.51	0.99
5T-8	225.51	226.13	0.62
5T-CC	226.13	226.33	0.21
6T-1	229.50	230.50	1.00
6T-2	230.50	231.28	0.78
6T-3	231.28	231.65	0.37
6T-4	231.65	232.78	1.13
6T-CC	232.78	232.98	0.20
7X-1	239.00	239.60	0.60
7X-2	239.60	240.21	0.61
7X-3	240.21	240.80	0.59
7X-4	240.80	241.89	1.09
7X-5	241.89	242.21	0.32
7X-6	242.21	243.50	1.30
7X-7	243.50	244.25	0.75
7X-CC	244.25	244.60	0.36
8X-1	248.50	249.92	1.42
8X-2	249.92	250.40	0.48
8X-3	250.40	251.65	1.26
8X-4	251.65	253.06	1.41
8X-5	253.06	254.46	1.41
8X-CC	254.46	254.85	0.39
9X-1	258.00	259.00	1.01
9X-2	259.00	259.96	0.97
9X-3	259.96	260.38	0.42
9X-4	260.38	261.77	1.41
9X-5	261.77	263.17	1.40
9X-6	263.17	264.57	1.41
9X-7	264.57	265.97	1.40
9X-8	265.97	267.15	1.19
9X-CC	267.15	267.50	0.35
10X-1	267.50	267.88	0.38
10X-2	267.88	268.19	0.31
10X-3	268.19	269.08	0.89
10X-4	269.08	270.32	1.25
10X-5	270.32	271.74	1.42
10X-6	271.74	273.15	1.41

Table T23 (continued). (Continued on next page.)

Core, section	Depth (mbsf) Top	Depth (mbsf) Bottom	Curated length (m)
10X-7	273.15	274.22	1.07
10X-CC	274.22	274.58	0.36
11X-1	277.00	277.32	0.32
11X-2	277.32	277.73	0.41
11X-3	277.73	279.22	1.49
11X-4	279.22	280.22	1.00
11X-CC	280.22	280.47	0.25
338-C0002L-			
1X-1	277.00	278.19	1.19
1X-2	278.19	279.23	1.04
1X-3	279.23	280.53	1.30
1X-4	280.53	280.83	0.31
1X-5	280.83	282.25	1.42
1X-6	282.25	283.60	1.35
1X-7	283.60	285.03	1.43
1X-CC	285.03	285.44	0.41
2X-1	286.50	286.98	0.48
2X-2	286.98	287.47	0.49
2X-CC	287.47	287.73	0.26
3X-1	296.00	297.08	1.08
3X-2	297.08	297.39	0.31
3X-3	297.39	298.69	1.30
3X-4	298.69	299.44	0.75
3X-CC	299.44	299.55	0.11
4X-1	305.50	306.43	0.93
4X-2	306.43	307.05	0.62
4X-3	307.05	308.30	1.25
4X-4	308.30	309.51	1.21
4X-5	309.51	310.91	1.40
4X-6	310.91	312.28	1.38
4X-7	312.28	313.15	0.87
4X-8	313.15	313.96	0.81
4X-CC	313.96	314.51	0.56
5X-1	315.00	316.40	1.40
5X-2	316.40	317.10	0.70
5X-3	317.10	317.70	0.60
5X-4	317.70	318.75	1.06
5X-5	318.75	319.99	1.24
5X-6	319.99	321.10	1.11
5X-7	321.10	321.85	0.75
5X-8	321.85	322.83	0.98
5X-9	322.83	323.67	0.84
5X-CC	323.67	324.26	0.59
6X-1	324.50	325.31	0.82
6X-2	325.31	326.71	1.42
6X-3	326.71	327.01	0.30
6X-4	327.01	327.42	0.42
6X-5	327.42	328.64	1.23
6X-6	328.64	329.86	1.23
6X-7	329.86	331.25	1.40
6X-8	331.25	332.36	1.12
6X-9	332.36	333.44	1.09
6X-CC	333.44	334.00	0.57
7X-1	334.00	334.96	0.96
7X-2	334.96	335.36	0.41
7X-3	335.36	336.47	1.11
7X-CC	336.47	336.77	0.30
8X-1	343.50	343.81	0.31
8X-2	343.81	344.98	1.18
8X-3	344.98	346.20	1.22
8X-4	346.20	346.70	0.51
8X-5	346.70	348.11	1.41
8X-6	348.11	349.52	1.41
8X-7	349.52	350.92	1.41
8X-8	350.92	351.62	0.70
8X-9	351.62	352.60	0.98
8X-CC	352.60	353.00	0.40
9X-1	353.00	353.62	0.62
9X-2	353.62	354.28	0.66
9X-3	354.28	355.21	0.93

Table T23 (continued). (Continued on next page.)

Core, section	Depth (mbsf) Top	Depth (mbsf) Bottom	Curated length (m)
9X-4	355.21	356.18	0.98
9X-5	356.18	356.73	0.55
9X-6	356.73	357.72	1.00
9X-7	357.72	358.71	0.99
9X-8	358.71	359.93	1.22
9X-CC	359.93	360.59	0.66
10X-1	362.50	363.64	1.14
10X-2	363.64	364.66	1.02
10X-3	364.66	365.04	0.39
10X-4	365.04	365.40	0.36
10X-5	365.40	366.62	1.22
10X-6	366.62	367.44	0.82
10X-7	367.44	368.69	1.25
10X-8	368.69	369.56	0.87
10X-CC	369.56	369.92	0.36
11X-1	372.00	373.20	1.20
11X-2	373.20	374.63	1.44
11X-3	374.63	375.30	0.67
11X-4	375.30	375.58	0.28
11X-5	375.58	376.22	0.64
11X-6	376.22	377.28	1.07
11X-CC	377.28	377.69	0.41
12X-1	381.50	382.73	1.23
12X-2	382.73	383.74	1.01
12X-3	383.74	384.84	1.10
12X-4	384.84	386.25	1.41
12X-5	386.25	387.10	0.85
12X-6	387.10	387.95	0.85
12X-7	387.95	388.37	0.42
12X-8	388.37	389.35	0.98
12X-CC	389.35	390.07	0.72
13X-1	391.00	392.12	1.12
13X-2	392.12	393.53	1.42
13X-3	393.53	394.79	1.27
13X-4	394.79	396.12	1.33
13X-5	396.12	396.71	0.60
13X-6	396.71	398.13	1.42
13X-7	398.13	399.11	0.98
13X-CC	399.11	400.50	1.40
14X-1	400.50	401.84	1.40
14X-2	401.84	402.82	1.04
14X-3	402.82	403.32	0.52
14X-4	403.32	404.65	1.40
14X-5	404.65	406.00	1.41
14X-6	406.00	407.33	1.40
14X-7	407.33	408.68	1.42
14X-8	408.68	409.62	0.98
14X-CC	409.62	410.00	0.40
15X-1	410.00	410.84	0.86
15X-2	410.84	411.75	0.93
15X-3	411.75	412.12	0.38
15X-4	412.12	412.53	0.42
15X-5	412.53	413.30	0.79
15X-6	413.30	414.68	1.40
15X-7	414.68	416.05	1.40
15X-8	416.05	417.35	1.32
15X-9	417.35	418.32	0.99
15X-10	418.32	419.10	0.79
15X-CC	419.10	419.50	0.41
16X-1	419.50	420.43	0.98
16X-2	420.43	421.77	1.40
16X-3	421.77	422.26	0.51
16X-4	422.26	423.60	1.40
16X-5	423.60	424.76	1.21
16X-6	424.76	426.12	1.42
16X-7	426.12	427.24	1.17
16X-8	427.24	428.14	0.94
16X-CC	428.14	429.00	0.90
17X-1	429.00	430.06	1.15

Table T23 (continued).

Core, section	Depth (mbsf) Top	Depth (mbsf) Bottom	Curated length (m)
17X-2	430.06	430.78	0.78
17X-3	430.78	431.53	0.82
17X-4	431.53	432.00	0.51
17X-5	432.00	433.18	1.27
17X-6	433.18	434.45	1.38
17X-7	434.45	435.29	0.91
17X-8	435.29	436.39	1.19
17X-9	436.39	437.21	0.89
17X-CC	437.21	438.50	1.40
18X-1	438.50	439.40	0.90
18X-2	439.40	440.29	0.89
18X-3	440.29	440.70	0.41
18X-4	440.70	442.10	1.40
18X-5	442.10	443.51	1.41
18X-6	443.51	444.92	1.41
18X-7	444.92	446.33	1.41
18X-8	446.33	447.17	0.84
18X-CC	447.17	447.53	0.36
19X-1	448.00	449.22	1.22
19X-2	449.22	450.30	1.08
19X-3	450.30	450.90	0.61
19X-4	450.90	452.17	1.27
19X-5	452.17	453.42	1.26
19X-6	453.42	454.75	1.33
19X-7	454.75	456.10	1.35
19X-CC	456.10	456.47	0.37
20X-1	457.50	458.50	1.04
20X-2	458.50	458.99	0.51
20X-3	458.99	460.35	1.41
20X-4	460.35	461.70	1.41
20X-5	461.70	463.06	1.41
20X-6	463.06	464.27	1.25
20X-7	464.27	465.54	1.33
20X-8	465.54	466.37	0.86
20X-CC	466.37	467.00	0.66
21X-1	467.00	468.41	1.42
21X-2	468.41	469.60	1.20
21X-3	469.60	470.44	0.85
21X-4	470.44	471.04	0.61
21X-5	471.04	472.43	1.41
21X-6	472.43	473.74	1.32
21X-7	473.74	475.07	1.34
21X-8	475.07	476.10	1.04
21X-CC	476.10	476.50	0.41
22X-1	476.50	477.16	0.66
22X-2	477.16	477.59	0.43
22X-3	477.59	477.99	0.41
22X-4	477.99	479.22	1.23
22X-5	479.22	480.51	1.29
22X-6	480.51	480.81	0.30
22X-7	480.81	481.23	0.43
22X-8	481.23	482.64	1.41
22X-CC	482.64	483.08	0.44
23X-CC	486.00	486.41	0.41
24X-1	495.50	496.90	1.40
24X-2	496.90	498.26	1.37
24X-3	498.26	499.66	1.40
24X-4	499.66	500.46	0.80
24X-5	500.46	500.98	0.52
24X-6	500.98	501.68	0.70
24X-7	501.68	502.38	0.71
24X-CC	502.38	502.77	0.39

Table T24. Results of X-ray diffraction analysis, performed on random bulk powder, Holes C0002K and C0002L. (Continued on next two pages.)

Core, section, interval (cm)	Sample	Central depth (mbsf)	Integrated peak area (total counts)				Absolute mineral abundance calculated from SVD normalization factors (wt%)					Relative abundance (wt%)			
			Total clay minerals	Quartz	Feldspar	Calcite	Total clay minerals	Quartz	Feldspar	Calcite	Sum	Total clay minerals	Quartz	Feldspar	Calcite
338-C0002K-															
1H-1, 113–116	CKY-1330410	200.91	2,357	36,605	11,887	6,812	31.7	20.2	11.7	5.3	68.9	46.0	29.3	17.0	7.70
1H-2, 74–77	CKY-1331210	201.65	2,257	39,026	12,662	12,742	31.3	21.6	12.5	13.6	78.9	39.6	27.3	15.9	17.2
1H-4, 4–7	CKY-1331510	202.33	2,116	27,777	10,010	13,602	28.6	15.1	9.87	15.3	68.9	41.5	22.0	14.3	22.2
2H-1, 58–61	CKY-1335410	205.10	2,047	21,394	12,094	11,083	28.8	11.3	12.4	12.0	64.4	44.7	17.48	19.3	18.6
3T-3, 59–60	CKY-1333610	207.87	1,869	59,964	26,389	3,255	32.9	33.0	27.6	–0.20	93.3	35.3	35.4	29.6	T
3T-4, 25–27	CKY-1339510	208.74	3,447	35,763	9,951	3,919	42.6	19.6	9.27	0.10	71.5	59.5	27.4	13.0	0.14
3T-4, 134–136	CKY-1340010	209.83	3,037	39,437	13,169	3,244	39.5	21.6	12.9	–0.57	73.5	53.8	29.4	17.6	T
3T-6, 13–15	CKY-1334510	210.44	4,059	36,968	11,303	2,274	49.9	20.1	10.6	–3.00	77.6	64.3	25.9	13.7	T
4T-1, 36–39	CKY-1341710	215.38	3,405	37,177	10,877	4,086	42.5	20.4	10.3	0.31	73.5	57.9	27.7	14.0	0.42
4T-3, 0–3	CKY-1336210	215.73	3,471	44,427	12,523	4,166	44.0	24.5	11.9	0.10	80.5	54.6	30.5	14.8	0.13
4T-4, 101–104	CKY-1342410	217.14	2,356	58,268	32,241	1,320	41.1	31.5	34.1	–3.66	103.0	39.9	30.6	33.1	T
5T-1, 14–17	CKY-1357210	220.16	2,679	37,257	11,094	3,331	34.6	20.6	10.7	0.11	66.0	52.4	31.2	16.3	0.17
5T-4, 73–76	CKY-1357510	223.36	3,093	27,974	7,154	12,467	37.9	15.3	6.38	12.7	72.2	52.5	21.2	8.83	17.6
5T-7, 0–3	CKY-1357810	224.53	3,047	30,794	9,404	13,028	38.5	16.8	8.84	13.4	77.4	49.7	21.7	11.4	17.2
6T-2, 70–77	CKY-1364010	231.24	2,889	35,120	13,007	11,313	38.4	19.1	12.8	10.9	81.2	47.2	23.5	15.8	13.4
6T-4, 17–20	CKY-1347710	231.83	2,564	50,768	15,713	4,507	35.5	28.2	15.6	1.37	80.7	44.0	35.0	19.4	1.70
6T-4, 95–98	CKY-1348510	232.61	1,982	51,499	17,390	6,009	30.0	28.6	17.7	4.06	80.3	37.3	35.6	22.0	5.05
7X-1, 46–48	CKY-1359110	239.47	3,204	41,122	17,853	5,010	43.8	22.3	18.1	1.45	85.5	51.2	26.0	21.1	1.69
7X-2, 38–40	CKY-1362410	239.99	2,607	42,566	13,924	2,721	35.1	23.5	13.8	–0.89	71.5	49.1	32.9	19.3	T
7X-4, 63–65	CKY-1360210	241.44	2,988	42,644	13,935	2,469	39.3	23.5	13.7	–1.70	74.8	52.5	31.4	18.3	T
7X-4, 106–109	CKY-1367310	241.88	2,620	48,574	19,010	2,907	37.7	26.7	19.4	–1.00	82.7	45.6	32.2	23.4	T
7X-6, 77–79	CKY-1363210	242.99	2,579	45,488	17,645	2,836	36.6	25.0	17.9	–0.92	78.6	46.6	31.8	22.8	T
8X-1, 110–113	CKY-1346410	249.62	2,311	25,752	9,215	21,616	30.8	13.9	8.93	26.3	80.0	38.6	17.4	11.2	32.9
8X-3, 0–3	CKY-1373310	250.41	2,295	48,936	16,573	8,120	33.2	27.1	16.7	6.71	83.7	39.7	32.4	19.9	8.02
8X-5, 116–119	CKY-1374010	254.23	3,204	35,453	10,842	6,286	40.5	19.4	10.3	3.64	73.8	54.8	26.3	14.0	4.93
9X-2, 43.5–45.5	CKY-1386210	259.44	3,430	42,625	12,154	4,847	43.4	23.5	11.6	1.15	79.6	54.5	29.5	14.5	1.45
9X-4, 0–8	CKY-1383610	260.42	3,054	50,905	22,142	7,017	44.2	27.7	22.7	4.00	98.6	44.8	28.1	23.0	4.06
9X-5, 20–22	CKY-1368710	261.98	3,654	32,467	8,513	4,598	44.2	17.7	7.67	0.93	70.6	62.7	25.1	10.9	1.32
9X-6, 19–21	CKY-1386510	263.37	1,546	82,338	33,070	2,740	32.3	45.8	34.7	–1.33	111.4	29.0	41.1	31.1	T
9X-7, 7–9	CKY-1386810	264.65	3,207	43,251	14,282	5,364	42.0	23.8	14.0	2.03	81.8	51.4	29.0	17.1	2.48
10X-3, 0–3	CKY-1389510	268.20	2,144	50,271	20,278	3,260	33.1	27.7	20.9	–0.04	81.6	40.5	33.9	25.6	T
10X-5, 135–138	CKY-1390210	271.69	3,391	32,804	10,776	6,015	42.5	17.8	10.3	3.11	73.7	57.7	24.2	13.9	4.22
10X-7, 16–19	CKY-1390510	273.33	3,087	36,374	11,778	6,319	39.6	19.9	11.4	3.77	74.7	53.1	26.7	15.3	5.04
11X-1, 26–32	CKY-1369510	277.29	2,873	37,032	13,317	9,908	38.2	20.2	13.2	8.92	80.5	47.5	25.1	16.3	11.1
11X-3, 2–4	CKY-1390910	277.76	2,153	53,003	22,269	2,483	34.1	29.1	23.1	–1.27	85.0	40.1	34.3	27.1	T
11X-4, 63–65	CKY-1370310	279.86	3,150	37,289	12,945	2,672	40.7	20.4	12.7	–1.44	72.3	56.3	28.2	17.6	T
338-C0002L-															
1X-2, 81–84	CKY-1403210	279.02	2,672	34,761	11,768	10,941	35.3	19.0	11.5	10.7	76.6	46.1	24.8	15.1	14.0
1X-3, 127–130	CKY-1407610	280.51	2,325	22,783	9,578	10,363	30.6	12.2	9.46	10.7	62.9	48.6	19.4	15.0	17.0
1X-6, 16–19	CKY-1408310	282.42	3,110	42,974	12,293	5,047	40.0	23.8	11.8	1.80	77.3	51.7	30.7	15.3	2.32
2X-1, 27–30	CKY-1405010	286.79	2,218	50,252	17,094	6,401	32.5	27.9	17.3	4.37	82.0	39.6	34.0	21.1	5.32
2X-2, 0–6	CKY-1404210	287.01	2,946	30,002	8,854	11,797	37.0	16.4	8.28	11.8	73.5	50.4	22.3	11.3	16.1
3X-1, 103–105	CKY-1414110	297.04	1,725	12,008	7,453	2,633	22.6	6.17	7.6	1.02	37.4	60.6	16.5	20.2	2.72
4X-3, 0–3	CKY-1426910	307.07	2,378	31,596	10,573	17,628	31.9	17.3	10.3	20.5	80.0	39.9	21.6	12.9	25.6
4X-5, 120–122	CKY-1409610	310.72	2,641	30,590	10,723	13,778	34.7	16.6	10.4	14.8	76.6	45.3	21.7	13.6	19.4
4X-6, 73–75	CKY-1410610	311.65	2,482	35,643	11,059	11,665	32.9	19.6	10.8	12.0	75.3	43.8	26.1	14.3	15.9

Table T24 (continued). (Continued on next page.)

Core, section, interval (cm)	Sample	Central depth (mbsf)	Integrated peak area (total counts)				Absolute mineral abundance calculated from SVD normalization factors (wt%)					Relative abundance (wt%)			
			Total clay minerals	Quartz	Feldspar	Calcite	Total clay minerals	Quartz	Feldspar	Calcite	Sum	Total clay minerals	Quartz	Feldspar	Calcite
4X-7, 18–23	CKY-1413110	312.49	2,654	36,082	13,223	15,208	36.1	19.7	13.1	16.6	85.4	42.2	23.0	15.4	19.4
5X-2, 60–63	CKY-1438410	317.02	2,377	44,260	16,652	4,222	34.0	24.4	16.9	1.31	76.5	44.4	31.8	22.1	1.71
5X-4, 76–79	CKY-1416310	318.47	3,277	42,807	15,259	4,609	43.2	23.4	15.1	0.87	82.6	52.3	28.3	18.3	1.06
5X-5, 13–16	CKY-1417310	318.90	3,514	37,288	11,791	2,882	44.1	20.4	11.3	–1.53	74.2	59.4	27.4	15.2	T
5X-6, 15–18	CKY-1419110	320.15	2,806	47,556	15,705	4,434	38.2	26.3	15.6	1.06	81.2	47.1	32.4	19.3	1.30
5X-6, 75–78	CKY-1418310	320.75	3,451	44,901	15,077	3,288	45.0	24.6	14.8	–1.21	83.2	54.1	29.6	17.8	T
5X-8, 10–13	CKY-1420710	321.96	1,833	58,370	22,539	4,380	30.7	32.3	23.3	1.60	88.0	34.9	36.8	26.5	1.82
6X-1, 33–36	CKY-1448310	324.84	3,468	35,398	10,563	3,404	43.1	19.4	9.96	–0.66	71.7	60.1	27.0	13.9	T
6X-2, 121–124	CKY-1422810	326.52	2,758	31,143	10,273	14,341	35.8	17.0	9.89	15.5	78.1	45.8	21.7	12.7	19.8
6X-3, 20–29.5	CKY-1425310	326.96	2,563	46,873	18,009	3,853	36.6	25.8	18.3	0.46	81.2	45.2	31.7	22.6	0.57
6X-6, 27–30	CKY-1448710	328.92	1,224	68,159	26,310	2,219	25.6	38.0	27.5	–1.06	90.0	28.5	42.2	30.6	T
6X-7, 17–19	CKY-1427710	330.04	3,025	31,179	10,660	12,710	38.8	16.9	10.3	12.9	78.9	49.2	21.5	13.0	16.3
6X-8, 12–14	CKY-1427910	331.38	2,290	47,072	22,973	3,688	36.1	25.6	24.0	0.35	86.0	42.0	29.8	27.9	0.40
7X-3, 0–3	CKY-1444110	335.38	2,668	47,775	15,005	3,278	36.3	26.5	14.9	–0.36	77.3	46.9	34.3	19.3	T
8X-2, 28–31	CKY-1452310	344.10	1,402	77,719	33,118	2,260	30.8	43.1	34.9	–1.72	107.0	28.8	40.3	32.6	T
8X-5, 0–3	CKY-1451310	346.72	3,151	39,507	11,406	8,800	40.2	21.8	10.9	7.07	79.9	50.3	27.2	13.6	8.85
8X-7, 73–76	CKY-1452010	350.26	3,055	39,528	12,891	4,896	39.7	21.7	12.6	1.71	75.7	52.5	28.7	16.6	2.26
9X-1, 40–43	CKY-1435110	353.42	2,531	36,285	11,422	2,121	33.1	20.0	11.2	–1.38	62.9	52.6	31.8	17.8	T
9X-6, 0–3	CKY-1457910	356.74	3,786	38,591	11,563	3,187	47.0	21.1	10.9	–1.45	77.6	60.6	27.2	14.1	T
9X-6, 34.5–37.5	CKY-1446910	357.09	3,373	34,582	10,005	5,039	41.9	18.9	9.37	1.76	71.9	58.2	26.3	13.0	2.45
10X-2, 100–101	CKY-1477310	364.64	2,315	53,540	20,009	2,281	34.7	29.6	20.5	–1.66	83.1	41.8	35.6	24.6	T
10X-5, 87–88	CKY-1478010	366.28	2,141	70,663	30,569	3,034	37.8	38.9	32.0	–1.25	107.5	35.2	36.2	29.7	T
10X-8, 56–57	CKY-1478410	369.25	3,633	41,510	13,071	3,347	46.0	22.7	12.6	–1.18	80.2	57.4	28.4	15.7	T
11X-3, 62–66	CKY-1433510	375.27	3,426	35,846	11,647	4,357	43.2	19.6	11.2	0.66	74.6	57.9	26.2	15.0	0.88
12X-7, 32–34	CKY-1486810	388.28	2,781	36,386	10,596	2,567	35.5	20.1	10.2	–1.03	64.7	54.8	31.0	15.7	T
13X-6, 27–29	CKY-1489810	396.99	3,118	28,420	10,107	14,627	39.72	15.3	9.67	15.5	80.2	49.5	19.1	12.1	19.3
14X-1, 102–102.5	CKY-1497910	401.48	3,011	30,139	10,128	13,057	38.4	16.3	9.69	13.4	77.9	49.4	21.0	12.4	17.2
14X-7, 87–87.5	CKY-1498710	408.17	1,698	77,141	24,027	5,049	29.7	43.3	24.6	2.19	99.8	29.8	43.4	24.6	2.20
14X-8, 30–30.5	CKY-1499110	408.97	4,584	32,120	8,707	5,276	54.6	17.3	7.62	0.77	80.3	68.0	21.6	9.49	0.96
15X-5, 2–5	CKY-1499410	412.56	3,996	35,075	10,815	3,741	49.0	19.0	10.1	–0.82	77.3	63.4	24.6	13.1	T
15X-7, 120–123	CKY-1500110	415.87	3,534	36,762	12,965	3,394	45.0	20.0	12.6	–0.88	76.7	58.7	26.1	16.4	T
15X-10, 47–50	CKY-1460710	418.80	3,753	38,002	10,414	4,161	46.1	20.8	9.64	–0.00	76.6	60.2	27.2	12.6	T
16X-2, 135–139	CKY-1503510	421.75	3,842	36,588	10,970	5,651	47.5	19.9	10.3	1.97	79.7	59.6	25.0	12.9	2.47
16X-6, 110–113	CKY-1504210	425.82	2,807	38,558	11,175	5,658	36.2	21.3	10.8	3.15	71.4	50.7	29.8	15.1	4.42
16X-7, 95–98	CKY-1504510	427.04	2,823	43,711	14,945	5,796	38.2	24.1	14.9	3.05	80.1	47.6	30.0	18.5	3.81
17X-3, 76–77	CKY-1508210	431.48	3,099	46,730	16,034	4,467	41.6	25.7	15.9	0.76	84.0	49.5	30.6	19.0	0.91
17X-7, 46–47	CKY-1508910	434.88	4,372	34,471	10,781	2,932	53.1	18.6	9.96	–2.37	79.3	67.0	23.5	12.6	T
17X-9, 60–61	CKY-1509210	436.95	3,980	36,544	10,056	4,067	48.5	20.0	9.21	–0.35	77.3	62.7	25.8	11.9	T
18X-2, 63–66	CKY-1512310	440.05	3,215	30,416	9,513	6,870	40.0	16.5	8.96	4.61	70.1	57.1	23.6	12.8	6.57
18X-4, 0–3	CKY-1512610	440.72	3,551	40,437	15,085	5,255	46.2	22.0	14.9	1.51	84.6	54.7	26.0	17.6	1.78
18X-6, 20–22	CKY-1513310	443.72	3,772	39,721	11,658	4,161	46.9	21.8	11.0	–0.12	79.6	59.0	27.3	13.8	T
19X-7, 80–82	CKY-1534910	455.56	3,389	38,944	15,018	5,027	44.4	21.1	14.9	1.42	81.9	54.3	25.8	18.2	1.73
20X-1, 100–104	CKY-1540410	458.48	2,409	56,556	26,514	3,354	39.0	30.9	27.7	–0.63	96.9	40.2	31.9	28.6	T
20X-6, 113–115	CKY-1542610	464.16	3,247	32,798	12,282	4,453	41.6	17.7	12.0	1.05	72.4	57.4	24.5	16.6	1.45
20X-CC, 50–53	CKY-1542910	466.87	3,821	35,311	11,403	4,210	47.4	19.2	10.8	0.01	77.4	61.3	24.8	14.0	0.01
21X-1, 5.5–6	CKY-1544010	467.06	3,393	34,450	12,113	3,778	43.0	18.7	11.7	–0.09	73.4	58.7	25.5	16.0	T
21X-2, 109–112	CKY-1543210	469.50	2,534	42,561	20,307	5,854	37.6	23.1	21.0	3.28	85.0	44.3	27.1	24.7	3.86
21X-3, 10–13	CKY-1485010	469.71	4,019	28,470	9,318	5,847	48.8	15.3	8.56	2.29	74.9	65.1	20.4	11.4	3.06
21X-5, 1–2	CKY-1544410	471.05	3,762	32,992	9,411	8,787	46.1	17.9	8.61	6.57	79.2	58.2	22.7	10.9	8.29
21X-8, 61–64	CKY-1543510	475.69	3,606	35,018	10,325	4,924	44.6	19.1	9.65	1.31	74.6	59.7	25.6	12.9	1.75

Table T24 (continued).

Core, section, interval (cm)	Sample	Central depth (mbsf)	Integrated peak area (total counts)				Absolute mineral abundance calculated from SVD normalization factors (wt%)					Relative abundance (wt%)			
			Total clay minerals	Quartz	Feldspar	Calcite	Total clay minerals	Quartz	Feldspar	Calcite	Sum	Total clay minerals	Quartz	Feldspar	Calcite
22X-2, 31–34	CKY-1547610	477.49	3,732	37,826	17,848	4,639	49.6	20.2	18.0	0.38	88.2	56.2	22.9	20.4	0.43
22X-5, 98–101	CKY-1547910	480.22	—	62,625	32,386	3,667	15.3	34.5	34.8	2.28	86.9	17.6	39.7	40.1	2.63
22X-8, 136–139	CKY-1548210	482.61	3,128	38,708	13,497	8,064	41.0	21.1	13.3	6.01	81.4	50.4	26.0	16.3	7.39
24X-1, 129–132	CKY-1552010	496.81	3,378	44,326	16,675	3,410	45.0	24.2	16.6	–1.01	84.8	53.0	28.5	19.6	T
24X-4, 77–80	CKY-1552310	500.45	2,944	35,192	10,058	3,721	37.1	19.4	9.6	0.43	66.4	55.8	29.2	14.4	0.65
24X-6, 33–36	CKY-1553010	501.32	1,446	72,110	34,957	2,120	32.3	39.6	37.1	–1.91	107.0	30.1	37.0	34.6	T

SVD = singular value decomposition. T = trace. — = trace quantities with negative SVD normalization factors lead to negative values of absolute wt% (see **"Lithology"** in the "Methods" chapter [Strasser et al., 2014a]).

Table T25. Results of XRF analysis, Holes C0002K and C0002L. (Continued on next two pages.)

Core, section, interval (cm)	Sample	Central depth (mbsf)	Na_2O (wt%)	MgO (wt%)	Al_2O_3 (wt%)	SiO_2 (wt%)	P_2O_5 (wt%)	K_2O (wt%)	CaO (wt%)	TiO_2 (wt%)	MnO (wt%)	Fe_2O_3 (wt%)	Loss on ignition (wt%)
338-C0002K-													
1H-1, 113–116	CKY-1330410	200.91	2.80	2.59	15.3	63.2	0.12	2.81	4.80	0.70	0.10	6.65	8.69
1H-2, 74–77	CKY-1331210	201.65	2.64	1.73	13.7	63.7	0.11	2.70	7.76	0.59	0.08	4.63	9.13
1H-4, 4–7	CKY-1331510	202.33	2.89	1.99	14.10	62.1	0.13	2.81	8.41	0.58	0.08	4.83	10.6
2H-1, 58–61	CKY-1335410	205.10	3.08	1.15	13.6	66.1	0.11	2.76	7.04	0.46	0.07	3.78	8.07
3T-3, 59–60	CKY-1333610	207.87	2.67	1.44	14.1	70.8	0.07	2.89	1.79	0.57	0.05	4.04	4.42
3T-4, 25–27	CKY-1339510	208.74	2.31	2.35	18.3	62.2	0.10	3.27	2.38	0.78	0.09	6.41	7.45
3T-4, 134–136	CKY-1340010	209.83	2.40	2.20	17.4	63.9	0.09	3.07	2.16	0.77	0.08	6.09	6.68
3T-6, 13–15	CKY-1334510	210.44	2.40	2.46	18.0	62.5	0.11	3.12	1.59	0.80	0.09	7.04	7.01
4T-1, 36–39	CKY-1341710	215.38	2.34	2.45	18.3	62.0	0.12	3.37	2.40	0.77	0.09	6.83	8.05
4T-3, 0–3	CKY-1336210	215.73	2.44	2.16	17.1	63.8	0.12	3.13	2.15	0.76	0.08	6.15	7.08
4T-4, 101–104	CKY-1342410	217.14	2.48	1.54	14.2	69.0	0.08	2.81	1.43	0.59	0.06	4.47	4.17
5T-1, 14–17	CKY-1357210	220.16	2.51	2.41	18.1	62.0	0.13	3.40	2.08	0.76	0.09	6.79	7.51
5T-4, 73–76	CKY-1357510	223.36	2.45	2.51	17.6	59.7	0.14	3.30	8.28	0.69	0.08	6.41	11.9
5T-7, 0–3	CKY-1357810	224.53	2.53	2.32	16.8	59.3	0.12	3.01	7.60	0.66	0.07	6.07	11.2
6T-2, 70–77	CKY-1364010	231.24	2.62	2.12	15.4	60.9	0.25	2.99	6.83	0.63	0.08	6.07	9.80
6T-4, 17–20	CKY-1347710	231.83	2.48	1.77	15.4	67.5	0.08	3.09	2.39	0.66	0.06	4.72	6.02
6T-4, 95–98	CKY-1348510	232.61	2.57	1.74	14.6	68.2	0.09	2.94	3.59	0.63	0.06	4.55	6.20
7X-1, 46–48	CKY-1359110	239.47	2.53	2.19	16.7	64.2	0.09	3.05	2.86	0.72	0.09	5.73	7.03
7X-2, 38–40	CKY-1362410	239.99	2.72	2.09	16.0	65.9	0.09	2.87	2.44	0.70	0.10	5.53	6.76
7X-4, 63–65	CKY-1360210	241.44	2.71	2.55	16.2	64.6	0.11	2.82	2.37	0.77	0.11	6.47	6.65
7X-4, 106–109	CKY-1367310	241.88	2.70	2.10	15.5	66.8	0.09	2.98	2.00	0.71	0.08	5.02	5.28
7X-6, 77–79	CKY-1363210	242.99	2.64	2.52	16.2	64.9	0.09	2.80	2.38	0.80	0.10	5.98	6.14
8X-1, 110–113	CKY-1346410	249.62	2.33	1.87	14.3	55.9	0.46	2.45	15.0	0.60	0.09	5.06	14.1
8X-3, 0–3	CKY-1373310	250.41	2.50	1.60	14.9	67.1	0.08	3.15	4.00	0.58	0.06	4.50	6.91
8X-5, 116–119	CKY-1374010	254.23	2.61	2.00	16.7	63.8	0.09	2.95	3.99	0.68	0.08	5.98	8.63
9X-2, 43.5–45.5	CKY-1386210	259.44	2.60	2.09	16.4	65.0	0.09	2.97	2.70	0.75	0.08	5.85	7.07
9X-4, 0–8	CKY-1383610	260.42	2.48	1.54	14.1	67.4	0.08	2.84	3.88	0.60	0.06	4.85	6.06
9X-5, 20–22	CKY-1368710	261.98	2.27	2.53	18.7	60.9	0.11	3.33	2.78	0.82	0.09	6.93	8.58
9X-6, 19–21	CKY-1386510	263.37	2.46	1.08	11.8	75.8	0.05	2.58	1.60	0.43	0.04	2.89	2.95

Table T25 (continued). (Continued on next page.)

Core, section, interval (cm)	Sample	Central depth (mbsf)	Na_2O (wt%)	MgO (wt%)	Al_2O_3 (wt%)	SiO_2 (wt%)	P_2O_5 (wt%)	K_2O (wt%)	CaO (wt%)	TiO_2 (wt%)	MnO (wt%)	Fe_2O_3 (wt%)	Loss on ignition (wt%)
9X-7, 7–9	CKY-1386810	264.65	2.66	1.86	15.8	65.5	0.10	3.04	3.23	0.66	0.07	5.53	7.56
10X-3, 0–3	CKY-1389510	268.20	2.69	1.82	14.9	68.4	0.09	2.78	2.30	0.66	0.07	4.96	5.67
10X-5, 135–138	CKY-1390210	271.69	2.33	2.48	17.3	61.5	0.12	3.10	4.00	0.80	0.10	6.91	8.80
10X-7, 16–19	CKY-1390510	273.33	2.47	2.29	16.9	62.9	0.11	3.06	3.71	0.76	0.10	6.28	8.33
11X-1, 26–32	CKY-1369510	277.29	2.50	2.25	16.6	61.6	0.11	3.14	5.51	0.71	0.11	5.80	8.71
11X-3, 2–4	CKY-1390910	277.76	2.66	1.86	15.3	67.9	0.09	3.01	1.69	0.68	0.07	4.78	4.71
11X-4, 63–65	CKY-1370310	279.86	2.55	2.40	17.5	62.8	0.11	3.26	1.95	0.73	0.11	7.17	7.29
338-C0002L-													
1X-2, 81–84	CKY-1403210	279.02	2.49	2.18	16.3	60.9	0.13	3.07	6.66	0.67	0.10	5.78	9.16
1X-3, 127–130	CKY-1407610	280.51	2.79	1.84	15.1	61.4	0.13	2.43	7.51	0.71	0.13	6.27	8.99
1X-6, 16–19	CKY-1408310	282.42	2.35	1.98	16.2	64.9	0.09	3.13	2.84	0.69	0.08	5.68	6.80
2X-1, 27–30	CKY-1405010	286.79	2.34	1.51	14.6	67.5	0.08	3.10	3.39	0.60	0.05	4.75	5.98
2X-2, 0–6	CKY-1404210	287.01	2.39	2.38	16.8	59.2	0.15	3.05	7.17	0.67	0.07	6.47	10.4
3X-1, 103–105	CKY-1414110	297.04	3.22	0.70	13.4	72.3	0.06	4.07	1.93	0.31	0.06	2.45	5.58
4X-3, 0–3	CKY-1426910	307.07	2.48	1.91	14.0	58.9	0.17	2.63	11.3	0.59	0.09	5.12	11.4
4X-5, 120–122	CKY-1409610	310.72	2.61	1.92	14.2	62.5	0.18	2.75	8.44	0.57	0.07	4.78	10.1
4X-6, 73–75	CKY-1410610	311.65	2.55	1.96	14.9	62.9	0.11	2.86	6.82	0.61	0.07	5.03	9.44
4X-7, 18–23	CKY-1413110	312.49	2.46	1.96	15.0	61.9	0.13	2.70	8.36	0.65	0.07	5.13	10.2
5X-2, 60–63	CKY-1438410	317.02	2.43	1.92	15.8	66.4	0.09	2.98	2.45	0.68	0.08	5.49	6.37
5X-4, 76–79	CKY-1416310	318.47	2.30	1.99	16.4	65.5	0.08	3.16	2.44	0.69	0.06	5.53	5.66
5X-5, 13–16	CKY-1417310	318.90	2.20	2.37	18.0	62.8	0.09	3.18	1.92	0.78	0.10	6.54	6.71
5X-6, 15–18	CKY-1419110	320.15	2.41	1.85	15.6	66.8	0.09	3.06	2.30	0.64	0.07	5.44	5.94
5X-6, 75–78	CKY-1418310	320.75	2.45	2.04	16.6	66.1	0.10	3.16	2.10	0.72	0.09	5.64	6.03
5X-8, 10–13	CKY-1420710	321.96	2.59	1.64	14.2	68.9	0.08	2.73	2.67	0.58	0.07	4.78	4.71
6X-1, 33–36	CKY-1448310	324.84	2.30	2.40	18.0	62.2	0.12	3.39	2.18	0.77	0.10	6.83	7.39
6X-2, 121–124	CKY-1422810	326.52	2.31	2.37	16.1	58.3	0.15	2.86	8.76	0.69	0.11	6.41	10.8
6X-3, 20–29.5	CKY-1425310	326.96	2.47	1.90	15.5	66.5	0.09	2.91	2.49	0.69	0.08	5.39	6.09
6X-6, 27–30	CKY-1448710	328.92	2.54	1.41	13.6	72.2	0.06	2.81	1.45	0.54	0.05	3.80	3.61
6X-7, 17–19	CKY-1427710	330.04	2.53	2.08	15.8	60.7	0.12	2.87	7.76	0.67	0.10	5.59	10.0
6X-8, 12–14	CKY-1427910	331.38	2.54	1.94	15.1	68.0	0.09	2.92	2.39	0.67	0.08	4.87	5.26
7X-3, 0–3	CKY-1444110	335.38	2.49	1.95	15.6	66.7	0.09	2.90	2.45	0.68	0.07	5.48	5.95
8X-2, 28–31	CKY-1452310	344.10	2.50	1.14	12.3	75.3	0.04	2.64	1.29	0.45	0.05	3.20	2.58
8X-5, 0–3	CKY-1451310	346.72	2.23	2.10	16.1	62.7	0.12	3.02	5.39	0.71	0.06	5.72	8.30
8X-7, 73–76	CKY-1452010	350.26	2.23	2.33	17.0	63.4	0.11	3.12	3.04	0.75	0.07	5.99	7.04
9X-1, 40–43	CKY-1435110	353.42	2.32	2.30	17.4	64.9	0.11	3.40	1.57	0.74	0.06	5.37	5.55
9X-6, 0–3	CKY-1457910	356.74	2.28	2.15	16.7	62.1	1.50	3.21	3.93	0.69	0.07	6.11	6.90
9X-6, 34.5–37.5	CKY-1446910	357.09	2.16	2.43	17.8	61.8	0.14	3.33	2.71	0.76	0.09	7.45	7.86
10X-2, 100–101	CKY-1477310	364.64	2.53	1.86	15.4	67.4	0.09	2.80	1.68	0.69	0.07	5.43	5.15
10X-5, 87–88	CKY-1478010	366.28	2.36	1.07	13.5	73.4	0.06	3.10	1.16	0.51	0.04	3.40	3.41
10X-8, 56–57	CKY-1478410	369.25	2.34	2.12	17.6	65.0	0.12	3.34	2.27	0.74	0.08	6.29	7.01
11X-3, 62–66	CKY-1433510	375.27	2.31	2.40	17.8	62.8	0.12	3.20	2.63	0.77	0.08	6.35	7.40
12X-7, 32–34	CKY-1486810	388.28	2.27	2.64	16.6	62.1	0.13	3.07	2.56	0.74	0.12	8.37	8.06
13X-6, 27–29	CKY-1489810	396.99	2.30	2.08	15.2	59.6	0.14	2.86	9.69	0.63	0.10	5.60	10.7
14X-1, 102–102.5	CKY-1497910	401.48	2.40	2.27	15.3	59.9	0.15	2.68	8.36	0.66	0.09	6.11	10.6
14X-7, 87–87.5	CKY-1498710	408.17	2.36	1.00	11.4	75.1	0.05	2.57	2.51	0.42	0.04	3.19	3.92
14X-8, 30–30.5	CKY-1499110	408.97	2.18	2.52	18.4	61.3	0.10	3.09	3.05	0.84	0.10	7.09	8.47
15X-5, 2–5	CKY-1499410	412.56	2.20	2.44	18.7	63.5	0.10	3.13	2.33	0.83	0.10	7.11	7.44
15X-7, 120–123	CKY-1500110	415.87	2.21	2.40	17.6	63.0	0.10	3.18	2.25	0.80	0.09	6.72	7.10
15X-10, 47–50	CKY-1460710	418.80	2.24	2.28	17.4	63.8	0.10	3.14	2.60	0.77	0.08	6.22	7.39
16X-2, 135–139	CKY-1503510	421.75	2.38	2.27	17.2	63.5	0.10	3.09	3.01	0.76	0.09	6.29	7.68

Table T25 (continued).

Core, section, interval (cm)	Sample	Central depth (mbsf)	Na_2O (wt%)	MgO (wt%)	Al_2O_3 (wt%)	SiO_2 (wt%)	P_2O_5 (wt%)	K_2O (wt%)	CaO (wt%)	TiO_2 (wt%)	MnO (wt%)	Fe_2O_3 (wt%)	Loss on ignition (wt%)
16X-6, 110–113	CKY-1504210	425.82	2.26	2.31	17.2	63.8	0.11	3.15	3.25	0.75	0.08	6.36	7.61
16X-7, 95–98	CKY-1504510	427.04	2.41	1.59	14.9	68.4	0.10	3.12	3.29	0.62	0.07	5.20	6.70
17X-3, 76–77	CKY-1508210	431.48	2.39	1.94	15.4	66.0	0.10	2.90	2.85	0.67	0.07	5.62	6.72
17X-7, 46–47	CKY-1508910	434.88	2.15	2.65	18.6	61.4	0.10	3.20	1.80	0.86	0.10	7.14	7.38
17X-9, 60–61	CKY-1509210	436.95	2.03	2.46	18.0	61.8	0.11	3.20	2.48	0.79	0.09	6.71	7.65
18X-2, 63–66	CKY-1512310	440.05	2.19	2.42	17.6	61.6	0.11	3.09	4.08	0.79	0.09	6.62	8.65
18X-4, 0–3	CKY-1512610	440.72	2.28	2.14	16.6	63.5	0.11	3.14	3.39	0.72	0.08	6.47	7.81
18X-6, 20–22	CKY-1513310	443.72	2.11	2.11	17.9	62.8	0.10	3.39	2.32	0.77	0.08	6.37	7.20
19X-7, 80–82	CKY-1534910	455.56	2.36	2.17	17.5	63.4	0.12	3.16	3.05	0.74	0.07	6.15	7.51
20X-1, 100–104	CKY-1540410	458.48	2.49	1.66	14.9	68.6	0.09	2.86	2.12	0.65	0.06	4.78	4.40
20X-6, 113–115	CKY-1542610	464.16	2.28	2.36	18.2	62.3	0.12	3.19	2.54	0.81	0.08	6.39	7.61
20X-CC, 50–53	CKY-1542910	466.87	2.25	2.29	18.2	62.0	0.12	3.20	2.70	0.81	0.08	6.63	7.93
21X-1, 5.5–6	CKY-1544010	467.06	2.41	2.34	18.3	62.2	0.11	3.18	2.63	0.84	0.08	6.34	7.84
21X-2, 109–112	CKY-1543210	469.50	2.55	1.81	16.2	65.9	0.10	2.97	3.64	0.69	0.07	5.08	6.83
21X-3, 10–13	CKY-1485010	469.71	2.09	2.82	18.1	59.9	0.12	3.10	3.97	0.84	0.10	7.65	9.07
21X-5, 1–2	CKY-1544410	471.05	2.11	2.36	17.1	61.3	0.11	3.11	5.08	0.73	0.08	6.40	9.56
21X-8, 61–64	CKY-1543510	475.69	2.18	2.50	18.0	62.3	0.09	3.25	2.56	0.78	0.10	6.58	7.53
22X-2, 31–34	CKY-1547610	477.49	2.42	2.05	17.1	64.1	0.09	3.13	3.03	0.71	0.07	5.57	7.30
22X-5, 98–101	CKY-1547910	480.22	2.65	1.15	12.8	71.0	0.07	2.81	2.83	0.51	0.05	4.35	4.77
22X-8, 136–139	CKY-1548210	482.61	2.32	2.16	16.3	63.7	0.11	3.09	4.53	0.68	0.06	5.81	8.11
24X-1, 129–132	CKY-1552010	496.81	2.33	2.39	16.4	65.0	0.09	3.14	2.05	0.73	0.09	6.00	6.05
24X-4, 77–80	CKY-1552310	500.45	2.24	2.48	17.6	62.1	0.11	3.26	2.76	0.76	0.09	6.85	7.53
24X-6, 33–36	CKY-1553010	501.32	2.34	1.05	12.2	75.0	0.05	2.80	1.61	0.46	0.05	2.95	2.79

Table T26. Sand occurrences in Holes C0002K and C0002L. (Continued on next four pages.)

Core, section	Curated length (m)	Top depth (mbsf)	Bottom depth (mbsf)	Mid-depth (mbsf)	Sand >2 cm (number within section)	Cumulative sand thickness (cm)	Thickness of coarsest sand (cm)
338-C0002K-							
1H-1	1.335	200	201.335	200.668	0	0.0	0.0
1H-2	1.045	201.335	202.38	201.858	0	0.0	0.0
1H-4	1.405	202.885	204.29	203.588	1	19.0	19.0
1H-5	0.375	204.29	204.665	204.478	0	0.0	0.0
1H-6	0.615	204.665	205.28	204.973	0	0.0	0.0
1H-CC	0.41	205.28	205.69	205.485	0	0.0	0.0
Totals:	5.185			203.508	1	19.0	19.0
2H-1	0.78	204.5	205.28	204.890	0	0.0	0.0
2H-CC	0.205	205.28	205.485	205.383	0	0.0	0.0
Totals:	0.985			205.136	0	0	0.0
3T-1	0.9	205.5	206.4	205.950	2	13.5	8.5
3T-2	0.87	206.4	207.27	206.835	1	2.5	2.5
3T-3	1.205	207.27	208.475	207.873	3	36.0	27.0
3T-4	1.4	208.475	209.875	209.175	2	45.7	43.0
3T-5	0.42	209.875	210.295	210.085	1	4.0	4.0
3T-6	1.39	210.295	211.685	210.990	3	53.0	45.0
3T-7	0.365	211.685	212.05	211.868	2	20.9	18.4
3T-CC	0.35	212.05	212.4	212.225	2	17.0	15.0
Totals:	6.9			209.375	16	192.6	45.0
4T-1	0.41	215	215.41	215.205	4	14.5	5.0
4T-3	0.4	215.715	216.115	215.915	5	11.0	4.0
4T-4	1.24	216.115	217.355	216.735	2	102.8	92.8
4T-CC	0.15	217.355	217.505	217.430	1	4.2	4.2
Totals:	2.2			216.321	12	132.5	92.8
5T-1	0.735	220	220.735	220.368	1	50.0	50.0
5T-2	0.98	220.735	221.715	221.225	3	19.5	10.0
5T-3	0.895	221.715	222.61	222.163	2	4.0	2.0
5T-4	1.085	222.61	223.695	223.153	3	41.0	36.0
5T-5	0.42	223.695	224.115	223.905	0	0.0	0.0
5T-7	0.99	224.515	225.505	225.010	0	0.0	0.0
5T-8	0.62	225.505	226.125	225.815	1	40.0	40.0
5T-CC	0.205	226.125	226.33	226.228	1	15.5	15.5
Totals:	5.93			223.483	11	170	50.0
6T-1	1	229.5	230.5	230.000	0	0.0	0.0
6T-2	0.78	230.5	231.28	230.890	0	0.0	0.0
6T-3	0.365	231.28	231.645	231.463	2	6.5	4.0
6T-4	1.13	231.645	232.775	232.210	0	0.0	0.0
6T-CC	0.2	232.775	232.975	232.875	1	15.0	15.0
Totals:	3.475			231.488	3	21.5	15.0
7X-1	0.6	239	239.6	239.300	4	7.5	2.5
7X-2	0.61	239.6	240.21	239.905	3	6.5	4.0
7X-3	0.59	240.21	240.8	240.505	1	16.0	16.0
7X-4	1.09	240.8	241.89	241.345	4	20.6	11.0
7X-5	0.315	241.89	242.205	242.048	2	4.0	2.0
7X-6	1.295	242.205	243.5	242.853	8	16.3	3.0
7X-7	0.745	243.5	244.245	243.873	4	11.5	6.0
7X-CC	0.355	244.245	244.6	244.423	1	2.3	2.3
Totals:	5.6			241.781	27	84.7	16.0
8X-1	1.42	248.5	249.92	249.210	1	18.0	18.0
8X-3	1.255	250.395	251.65	251.023	1	3.4	3.4
8X-4	1.405	251.65	253.055	252.353	0	0.0	0.0
8X-5	1.405	253.055	254.46	253.758	2	8.5	4.5
8X-CC	0.39	254.46	254.85	254.655	0	14.0	14.0
Totals:	5.875			252.200	4	43.9	18.0
9X-1	1.005	258	259.005	258.503	1	55.0	55.0
9X-2	0.965	259.005	259.97	259.488	3	37.5	32.0
9X-4	1.405	260.385	261.79	261.088	2	16.0	11.0
9X-5	1.4	261.79	263.19	262.490	1	13.0	13.0
9X-6	1.41	263.19	264.6	263.895	6	59.5	31.5
9X-8	1.19	266	267.19	266.595	5	18.7	8.0
9X-CC	0.35	267.19	267.54	267.365	1	5.0	5.0
Totals:	7.725			262.775	19	204.7	55.0

Table T26 (continued). (Continued on next page.)

Core, section	Curated length (m)	Top depth (mbsf)	Bottom depth (mbsf)	Mid-depth (mbsf)	Sand >2 cm (number within section)	Cumulative sand thickness (cm)	Thickness of coarsest sand (cm)
10X-1	0.375	267.5	267.875	267.688	1	11.0	11.0
10X-3	0.89	268.185	269.075	268.630	2	5.9	3.5
10X-4	1.245	269.075	270.32	269.698	4	30.8	13.0
10X-5	1.42	270.32	271.74	271.030	6	15.9	4.0
10X-6	1.41	271.74	273.15	272.445	3	26.0	14.0
10X-7	1.07	273.15	274.22	273.685	4	25.3	9.0
10X-CC	0.36	274.22	274.58	274.400	2	8.3	6.0
Totals:	6.77			271.082	22	123.2	14.0
11X-1	0.32	277	277.32	277.160	1	2.8	2.8
11X-3	1.49	277.73	279.22	278.475	2	17.0	12.0
11X-4	1	279.22	280.22	279.720	4	16.5	8.0
11X-CC	0.25	280.22	280.47	280.345	0	0.0	0.0
Totals:	3.06			278.925	7	36.3	12.0
338-C0002L-							
1X-1	1.19	277	278.19	277.595	4	7.8	2.4
1X-2	1.035	278.19	279.225	278.708	4	16.0	5.5
1X-3	1.3	279.225	280.525	279.875	4	13.2	5.7
1X-5	1.415	280.83	282.245	281.538	6	14.3	2.8
1X-6	1.35	282.245	283.595	282.920	5	29.0	4.6
1X-7	1.43	283.595	285.025	284.310	2	18.6	15.7
1X-CC	0.41	285.025	285.435	285.230	2	9.1	8.1
Totals:	8.13			281.454	27	108	15.7
2X-1	0.48	286.5	286.98	286.740	1	6.8	6.8
2X-2	0.49	286.98	287.47	287.225	0	0.0	0.0
2X-CC	0.255	287.47	287.725	287.598	0	0.0	0.0
Totals:	1.225			287.188	1	6.8	6.8
3X-1	1.08	296	297.08	296.540	0	0.0	0.0
3X-2	0.31	297.08	297.39	297.235	0	0.0	0.0
3X-3	1.3	297.39	298.69	298.040	0	0.0	0.0
3X-4	0.75	298.69	299.44	299.065	0	0.0	0.0
3X-CC	0.11	299.44	299.55	299.495	0	0.0	0.0
Totals:	3.55			298.075	0	0	0.0
4X-1	0.93	305.5	306.43	305.965	1	4.9	4.9
4X-3	1.25	307.05	308.3	307.675	0	0.0	0.0
4X-4	1.21	308.3	309.51	308.905	1	4.3	4.3
4X-5	1.395	309.51	310.905	310.208	0	0.0	0.0
4X-6	1.375	310.905	312.28	311.593	1	5.4	5.4
4X-7	0.865	312.28	313.145	312.713	1	1.5	1.5
4X-8	0.81	313.145	313.955	313.550	0	0.0	0.0
4X-CC	0.555	313.955	314.51	314.233	2	29.0	27.0
Totals:	8.39			310.605	6	45.1	27.0
5X-1	1.4	315	316.4	315.700	3	6.8	3.0
5X-2	0.695	316.4	317.095	316.748	1	5.9	5.9
5X-4	1.055	317.695	318.75	318.223	3	7.3	4.4
5X-5	1.235	318.75	319.985	319.368	3	5.9	2.3
5X-6	1.11	319.985	321.095	320.540	2	8.0	4.0
5X-7	0.75	321.095	321.845	321.470	3	7.6	4.8
5X-8	0.98	321.845	322.825	322.335	2	6.1	4.0
5X-9	0.84	322.825	323.665	323.245	0	0.0	0.0
5X-CC	0.59	323.665	324.255	323.960	1	4.0	4.0
Totals:	8.655			320.176	18	51.6	5.9
6X-1	0.815	324.5	325.315	324.908	0	0.0	0.0
6X-2	1.415	325.315	326.73	326.023	4	11.5	5.5
6X-3	0.295	326.73	327.025	326.878	1	1.3	1.3
6X-5	1.225	327.445	328.67	328.058	3	11.1	7.0
6X-6	1.23	328.67	329.9	329.285	5	10.7	3.3
6X-7	1.4	329.9	331.3	330.600	3	10.6	4.4
6X-8	1.12	331.3	332.42	331.860	3	8.0	4.2
6X-9	1.09	332.42	333.51	332.965	0	0.0	0.0
6X-CC	0.565	333.51	334.075	333.793	0	0.0	0.0
Totals:	9.155			329.374	19	53.2	7.0
7X-1	0.955	334	334.955	334.478	0	0.0	0.0
7X-3	1.11	335.36	336.47	335.915	1	18.0	18.0
7X-CC	0.3	336.47	336.77	336.620	1	25.0	25.0
Totals:	2.365			335.671	2	43	25.0

Table T26 (continued). (Continued on next page.)

Core, section	Curated length (m)	Top depth (mbsf)	Bottom depth (mbsf)	Mid-depth (mbsf)	Sand >2 cm (number within section)	Cumulative sand thickness (cm)	Thickness of coarsest sand (cm)
8X-1	0.305	343.5	343.805	343.653	0	0.0	0.0
8X-2	1.175	343.805	344.98	344.393	3	13.0	6.0
8X-3	1.215	344.98	346.195	345.588	1	2.7	2.7
8X-5	1.405	346.7	348.105	347.403	2	8.2	4.2
8X-6	1.41	348.105	349.515	348.810	2	16.2	10.9
8X-7	1.405	349.515	350.92	350.218	3	14.3	5.8
8X-8	0.7	350.92	351.62	351.270	0	0.0	0.0
8X-9	0.98	351.62	352.6	352.110	2	14.4	11.4
8X-CC	0.4	352.6	353	352.800	0	0.0	0.0
Totals:	8.995			348.471	13	68.8	11.4
9X-1	0.62	353	353.62	353.310	1	17.6	17.6
9X-2	0.66	353.62	354.28	353.950	0	0.0	0.0
9X-3	0.925	354.28	355.205	354.743	1	21.0	21.0
9X-4	0.975	355.205	356.18	355.693	0	0.0	5.6
9X-6	0.995	356.725	357.72	357.223	1	5.6	5.6
9X-7	0.985	357.72	358.705	358.213	1	19.0	19.0
9X-8	1.22	358.705	359.925	359.315	0	0.0	0.0
9X-CC	0.66	359.925	360.585	360.255	1	4.4	4.4
Totals:	7.04			356.588	5	67.6	21.0
10X-1	1.135	362.5	363.635	363.068	1	2.0	2.0
10X-2	1.02	363.635	364.655	364.145	0	0.0	0.0
10X-4	0.36	365.04	365.4	365.220	2	5.0	3.5
10X-5	1.22	365.4	366.62	366.010	2	8.4	6.4
10X-6	0.82	366.62	367.44	367.030	1	8.4	8.4
10X-7	1.245	367.44	368.685	368.063	1	10.0	10.0
10X-8	0.87	368.685	369.555	369.120	2	25.0	15.0
10X-CC	0.36	369.555	369.915	369.735	1	2.0	2.0
Totals:	7.03			366.549	10	60.8	15.0
11X-1	1.195	372	373.195	372.598	2	15.0	11.0
11X-2	1.435	373.195	374.63	373.913	3	9.8	4.0
11X-3	0.665	374.63	375.295	374.963	1	21.0	21.0
11X-5	0.64	375.575	376.215	375.895	1	7.0	7.0
11X-6	1.065	376.215	377.28	376.748	1	50.0	50.0
11X-CC	0.405	377.28	377.685	377.483	0	0.0	0.0
Totals:	5.405			375.266	8	102.8	50.0
12X-1	1.23	381.5	382.73	382.115	1	10.0	10.0
12X-2	1.01	382.73	383.74	383.235	3	15.2	7.0
12X-3	1.1	383.74	384.84	384.290	3	7.4	3.0
12X-4	1.41	384.84	386.25	385.545	4	11.0	3.0
12X-5	0.85	386.25	387.1	386.675	3	7.0	5.0
12X-6	0.85	387.1	387.95	387.525	4	17.5	5.7
12X-7	0.415	387.95	388.365	388.158	1	3.0	3.0
12X-8	0.98	388.365	389.345	388.855	4	12.0	4.0
12X-CC	0.72	389.345	390.065	389.705	3	9.0	4.0
Totals:	8.565			386.234	26	92.1	10.0
13X-1	1.12	391	392.12	391.560	2	6.8	4.8
13X-2	1.415	392.12	393.535	392.828	2	4.0	2.0
13X-3	1.27	393.535	394.805	394.170	1	1.6	1.6
13X-4	1.33	394.805	396.135	395.470	0	0.0	0.0
13X-5	0.6	396.135	396.735	396.435	1	6.0	6.0
13X-6	1.42	396.735	398.155	397.445	0	0.0	0.0
13X-7	0.98	398.155	399.135	398.645	0	0.0	0.0
13X-CC	1.4	399.135	400.535	399.835	0	0.0	0.0
Totals:	9.535			395.798	6	18.4	6.0
14X-1	1.4	400.5	401.9	401.200	1	2.0	2.0
14X-2	1.035	401.9	402.935	402.418	1	10.0	10.0
14X-4	1.4	403.455	404.855	404.155	0	0.0	0.0
14X-5	1.41	404.855	406.265	405.560	1	3.0	3.0
14X-6	1.4	406.265	407.665	406.965	0	0.0	0.0
14X-7	1.415	407.665	409.08	408.373	1	16.0	16.0
14X-8	0.98	409.08	410.06	409.570	1	2.0	2.0
14X-CC	0.4	410.06	410.46	410.260	0	0.0	0.0
Totals:	9.44			406.063	5	33	16.0
15X-1	0.855	410	410.855	410.428	0	0.0	0.0
15X-2	0.93	410.855	411.785	411.320	1	4.0	4.0

Table T26 (continued). (Continued on next page.)

Core, section	Curated length (m)	Top depth (mbsf)	Bottom depth (mbsf)	Mid-depth (mbsf)	Sand >2 cm (number within section)	Cumulative sand thickness (cm)	Thickness of coarsest sand (cm)
15X-3	0.375	411.785	412.16	411.973	1	4.0	4.0
15X-5	0.79	412.575	413.365	412.970	0	0.0	0.0
15X-6	1.4	413.365	414.765	414.065	3	11.0	7.0
15X-7	1.4	414.765	416.165	415.465	4	21.0	7.0
15X-8	1.32	416.165	417.485	416.825	2	6.0	4.0
15X-9	0.99	417.485	418.475	417.980	2	4.5	2.5
15X-10	0.79	418.475	419.265	418.870	1	5.0	5.0
15X-CC	0.41	419.265	419.675	419.470	0	0.0	0.0
Totals:	9.26			414.937	14	55.5	7.0
16X-1	0.975	419.5	420.475	419.988	0	0.0	0.0
16X-2	1.395	420.475	421.87	421.173	1	2.6	2.6
16X-3	0.51	421.87	422.38	422.125	1	4.0	4.0
16X-4	1.4	422.38	423.78	423.080	3	8.2	3.0
16X-5	1.205	423.78	424.985	424.383	3	13.5	5.0
16X-6	1.42	424.985	426.405	425.695	2	7.5	4.0
16X-7	1.17	426.405	427.575	426.990	2	22.0	12.0
16X-8	0.94	427.575	428.515	428.045	2	6.0	3.0
16X-CC	0.9	428.515	429.415	428.965	1	6.0	6.0
Totals:	9.915			424.494	15	69.8	12.0
17X-1	1.15	429	430.15	429.575	2	9.0	6.0
17X-2	0.775	430.15	430.925	430.538	2	5.0	3.0
17X-3	0.82	430.925	431.745	431.335	0	0.0	0.0
17X-5	1.27	432.255	433.525	432.890	1	3.8	3.8
17X-6	1.38	433.525	434.905	434.215	2	7.8	4.6
17X-7	0.91	434.905	435.815	435.360	2	8.0	4.0
17X-8	1.19	435.815	437.005	436.410	2	13.0	8.0
17X-9	0.89	437.005	437.895	437.450	2	5.0	2.8
17X-CC	1.4	437.895	439.295	438.595	0	0.0	0.0
Totals:	9.785			434.041	13	51.6	8.0
18X-1	0.9	438.5	439.4	438.950	2	3.7	2.0
18X-2	0.89	439.4	440.29	439.845	0	0.0	0.0
18X-4	1.4	440.7	442.1	441.400	1	3.0	3.0
18X-5	1.405	442.1	443.505	442.803	2	8.0	5.0
18X-6	1.41	443.505	444.915	444.210	1	9.0	9.0
18X-7	1.41	444.915	446.325	445.620	2	7.0	4.0
18X-8	0.84	446.325	447.165	446.745	1	2.0	2.0
18X-CC	0.36	447.165	447.525	447.345	0	0.0	0.0
Totals:	8.615			443.365	9	32.7	9.0
19X-1	1.215	448	449.215	448.608	2	4.0	2.0
19X-2	1.08	449.215	450.295	449.755	1	3.5	3.5
19X-4	1.265	450.9	452.165	451.533	1	13.0	16.0
19X-5	1.255	452.165	453.42	452.793	1	3.0	3.0
19X-6	1.33	453.42	454.75	454.085	1	9.0	9.0
19X-7	1.35	454.75	456.1	455.425	2	11.1	7.0
19X-CC	0.365	456.1	456.465	456.283	1	6.0	6.0
Totals:	7.86			452.640	9	49.6	16.0
20X-1	1.04	457.5	458.54	458.020	2	11.0	7.0
20X-3	1.41	459.045	460.455	459.750	2	6.6	3.6
20X-4	1.41	460.455	461.865	461.160	0	0.0	0.0
20X-5	1.41	461.865	463.275	462.570	1	5.5	5.5
20X-6	1.25	463.275	464.525	463.900	2	12.0	8.0
20X-7	1.325	464.525	465.85	465.188	2	8.0	4.0
20X-8	0.86	465.85	466.71	466.280	2	9.0	5.0
20X-CC	0.655	466.71	467.365	467.038	1	3.0	3.0
Totals:	9.36			462.988	12	55.1	8.0
21X-1	1.415	467	468.415	467.708	2	7.0	4.0
21X-2	1.2	468.415	469.615	469.015	7	20.5	4.0
21X-3	0.845	469.615	470.46	470.038	0	0.0	0.0
21X-5	1.405	471.065	472.47	471.768	2	16.0	10.0
21X-6	1.315	472.47	473.785	473.128	0	0.0	0.0
21X-7	1.34	473.785	475.125	474.455	0	0.0	0.0
21X-8	1.04	475.125	476.165	475.645	1	5.0	5.0
21X-CC	0.405	476.165	476.57	476.368	0	0.0	0.0
Totals:	8.965			472.265	12	48.5	10.0
22X-1	0.66	476.5	477.16	476.830	3	29.0	14.0

Table T26 (continued).

Core, section	Curated length (m)	Top depth (mbsf)	Bottom depth (mbsf)	Mid-depth (mbsf)	Sand >2 cm (number within section)	Cumulative sand thickness (cm)	Thickness of coarsest sand (cm)
22X-2	0.425	477.16	477.585	477.373	2	15.0	8.0
22X-3	0.405	477.585	477.99	477.788	2	36.7	24.7
22X-4	1.23	477.99	479.22	478.605	3	42.0	23.0
22X-5	1.29	479.22	480.51	479.865	3	53.0	28.0
22X-6	0.295	480.51	480.805	480.658	1	7.0	7.0
22X-7	0.425	480.805	481.23	481.018	1	35.0	35.0
22X-8	1.41	481.23	482.64	481.935	2	13.0	7.0
22X-CC	0.435	482.64	483.075	482.858	2	14.0	11.0
Totals:	6.575			479.659	19	244.7	35.0
23X-CC	0.405	486	486.405	486.203	1	11.0	11.0
Totals:	0.405			486.203	1	11	11.0
24X-1	1.395	495.5	496.895	496.198	1	115.0	115.0
24X-2	1.365	496.895	498.26	497.578	4	36.0	16.0
24X-3	1.4	498.26	499.66	498.960	3	34.0	20.0
24X-4	0.8	499.66	500.46	500.060	1	55.6	55.6
24X-6	0.7	500.975	501.675	501.325	1	40.0	40.0
24X-7	0.705	501.675	502.38	502.028	1	4.0	4.0
24X-CC	0.385	502.38	502.765	502.573	0	0.0	0.0
Totals:	6.75			499.817	11	284.6	115.0

Table T27. Calcareous nannofossils, Hole C0002K.

Age (Ma)	Core, section, interval (cm)	Average depth (mbsf)	Abundance	Preservation	*Braarudosphaera bigelowi*	*Calcidiscus leptoporus*	*Calciosolenia murrayi*	*Ceratolithus cristatus*	*Coccolithus pelagicus*	*Discoaster* spp.	*Florisphaera profunda*	*Gephyrocapsa* spp. large (>5.5 µm)	*Gephyrocapsa* spp. medium (4–5.5 µm)	*Gephyrocapsa* spp. small (<4 µm)	*Helicosphaera carteri*	*Helicosphaera hyalina*	*Helicosphaera sellii*	*Oolithotus antilarum*	*Pontosphaera japonica*	*Pontosphaera* spp.	*Pseudoemiliania lacunosa*	*Reticulofenestra asanoi*	*Reticulofenestra* spp.	*Rhabdosphaera clavigera*	*Sphenolithus abies*	*Syracosphaera pulchra*	*Umbilicosphaera sibogae*
	338-C0002K-																										
0.905–1.04	1H-CC, 36.0–41.0	204.48	V	G	+	+	+				+		+	+	+			+	+	+	+	+	+	+		+	+
	2H-CC, 15.5–20.5	205.46	V	G		+	+				+		+	+	+			+	+		+	+	+	+			+
	4T-CC, 10.0–15.0	217.48	V	G		+			+		+		+	+	+				+	+	+	+	+			+	
	6T-CC, 15.0–20.0	232.95	V	G		+			+	re	+		+	+	+					+	+	+	+	+	re	+	+
	7X-CC, 30.5–35.5	244.58	V	G		+		+	+	re	+		+	+	+				+	+	+	+	+	+		+	
1.04–1.107	8X-CC, 34.0–39.0	254.83	V	G		+	+		+		+	re	re	+	+		re		+	+	+	+	+	+		+	+
	9X-CC, 30.0–35.0	267.48	V	G		+			+		+			+	+	+			+	+	+	+	+	+		+	+
	11X-CC, 20.0–25.0	280.45	V	G		+	+		+	re	+			+	+				+		+	+	+	+	re	+	+

Abundance: V = very abundant. Preservation: G = good. + = present, re = reworked. Median numerical ages for last consistent occurrence and first consistent occurrence of *Reticulofenestra asanoi* and FO of large *Gephyrocapsa* are shown.

Table T28. Calcareous nannofossils, Hole C0002L.

Age (Ma)	Core, section, interval (cm)	Average depth (m)	Abundance	Preservation	*Calcidiscus leptoporus*	*Calcidiscus macintyrei*	*Calciosolenia murrayi*	*Ceratolithus cristatus*	*Coccolithus pelagicus*	*Discoaster brouweri*	*Discoaster* spp.	*Florisphaera profunda*	*Gephyrocapsa* spp. large (>5.5 µm)	*Gephyrocapsa* spp. medium (4–5.5 µm)	*Gephyrocapsa* spp. small (<4 µm)	*Helicosphaera carteri*	*Helicosphaera hyalina*	*Helicosphaera sellii*	*Oolithotus antillarum*	*Pontosphaera japonica*	*Pontosphaera* spp.	*Pseudoemiliania lacunosa*	*Reticulofenestra asanoi*	*Reticulofenestra pseudoumbilicus*	*Reticulofenestra* spp.	*Rhabdosphaera clavigera*	*Sphenolithus abies*	*Syracosphaera pulchra*	*Umbilicosphaera sibogae*
	338-C0002L-																												
?	1X-CC, 36.0–41.0	285.41	V	G	+	re	+	+	+			+	+	+	+	+				+	+	+	+			+		+	+
	2X-CC, 20.5–25.5	287.70	V	G	+		+		+			+	+	+	+	+				+		+	+		+	+		+	+
1.04–1.107	4X-CC, 50.5–55.5	314.49	V	G	+				+			+			+	+				+	+	+	+		+	+		+	+
1.107–1.24	5X-CC, 54.0–59.0	324.23	A	M	+		+		+			+			+	+					+	+			+	+			
	6X-CC, 51.5–56.5	333.98	A	M	+	re			+		re	+	+	+	+	+				+	+	+			+	+			+
1.24–1.34	8X-CC, 35.0–40.0	352.98	V	G	+	re			+			+	+	+	+	+				+	+	+		re	+	+		+	+
	10X-CC, 31.0–36.0	369.89	A	G	+				+			+	+		+	+						+		re	+				+
	12X-CC, 67.0–72.0	390.04	A	G	+			+	+			+	+	+	+	+				+		+			+				+
?	14X-CC, 35.0–40.0	409.98	V	VG	+		+	+				+		+	+	+	+			+	+	+			+	+		+	+
	16X-CC, 85.0–90.0	428.98	V	G	+		+		+			+	+	+	+	+				+	+	+			+	+			+
	18X-CC, 31.0–36.0	447.50	A	G	+							+	+		+	+				+	+	+			+				+
1.24–1.34	20X-CC, 60.5–65.5	466.98	A	M	+			+	+	re		+	+	+	+	+				+		+			+				+
	22X-CC, 38.5–43.5	483.05	V	G	+				+		re	+	+		+	+			+	+		+			+	+		+	+
	24X-CC, 33.5–38.5	502.74	V	G	+	re			+		re	+	+		+	+		re?		+		+		re	+	+	re		+

Abundance: V = very abundant, A = abundant. Preservation: VG = very good, G = good, M = moderate. + = present, re = reworked. Median numerical ages for last consistent occurrence and first consistent occurrence of *Reticulofenestra asanoi* and FO of large *Gephyrocapsa* are shown.

Table T29. Geochemistry of interstitial water sampled, Holes C0002J, C0002K, and C0002L. (Continued on next page.)

Core, section, interval (cm)	Depth (mbsf)	pH	Salinity (refractive index)*	Alkalinity (mM)	Chlorinity (mM)	Br^- (mM)	SO_4^{2-} (mM)	PO_4^{3-} (µM)	NH_4^+ (mM)	Na^+ (mM)	K^+ (mM)	Mg^{2+} (mM)	Ca^{2+} (mM)	Li (µM)	B (µM)	Mn (µM)
338-C0002J-																
1R-6, 6.8–24	903.6	—	1.33802	4.83	474.8	0.89	3.50	3	2.56	424	7.53	14.3	9.63	232	266	1.79
3R-3, 0–17.5	913.5	7.53	1.33810	6.08	472.8	0.90	5.24	ND	2.66	430	6.20	15.6	11.71	223	362	3.06
4R-2, 2–21	917.6	7.42	1.33813	6.19	478.2	0.87	6.04	2	2.44	429	6.44	17.3	11.83	211	377	3.40
5R-2, 5–44.5	922.4	7.74	1.33785	2.71	456.1	0.90	1.79	ND	2.64	411	6.23	11.0	10.57	238	207	2.33
338-C0002K-																
1H-3, 10–50.5	202.5	7.80	1.33858	35.46	501.6	1.13	1.33	242	12.26	449	8.79	26.0	2.98	41	278	1.12
3T-5, 0–25	209.9	7.78	1.33858	35.33	499.7	1.12	1.99	231	11.76	450	8.05	26.5	3.42	38	300	1.28
4T-2, 0–30	215.4	7.64	1.33858	34.67	497.0	1.11	2.41	261	11.49	492	9.82	29.2	4.05	36	293	1.10
5T-6, 0–25	224.1	7.73	1.33848	35.50	487.1	1.07	2.33	159	11.35	443	8.41	25.8	3.29	56	308	1.29
6T-3, 0–21	231.3	7.98	1.33782	21.31	414.7	0.85	6.62	68	9.24	374	7.62	24.1	3.58	49	261	1.20
7X-5, 0–16	241.9	7.87	1.33812	35.10	458.0	0.99	1.97	142	10.96	423	7.31	23.1	3.40	63	289	2.08
8X-2, 0–38	249.9	7.82	1.33814	35.69	455.7	1.02	1.74	161	11.25	416	7.88	21.4	2.89	62	295	1.42
9X-3, 0–31	260.0	7.89	1.33800	34.16	446.5	0.99	1.84	170	10.83	413	7.74	20.3	3.22	58	285	1.05
10X-2, 0–31	267.9	7.80	1.33793	33.18	432.8	1.00	1.80	137	10.69	402	7.00	19.0	2.98	57	282	0.89
11X-2, 0–31	277.3	7.81	1.33779	34.08	425.5	0.95	1.76	125	10.46	402	7.60	18.4	2.74	58	269	1.11
338-C0002L-																
1X-4, 0–30.5	280.5	7.92	1.33782	35.55	417.5	0.91	3.33	51	9.93	393	7.17	20.6	3.54	69	287	6.92
3X-2, 0–31	290.1	7.90	1.33757	33.05	392.7	0.90	3.27	45	9.30	371	7.27	18.4	3.22	85	259	2.49
4X-2, 0–44	306.4	7.88	1.33749	32.50	392.1	0.86	2.36	101	9.94	384	6.93	16.7	2.54	67	245	1.04
5X-3, 5–50	317.1	7.86	1.33739	32.46	383.7	0.82	1.67	104	9.95	376	7.09	15.2	2.46	58	217	1.02
6X-4, 0–42	327.0	7.92	1.33700	30.39	349.0	0.76	1.54	92	9.15	339	6.14	13.4	2.34	50	194	1.46
7X-2, 0–40.5	335.0	7.83	1.33741	31.19	387.5	0.83	2.76	89	9.68	366	6.77	15.8	2.81	48	196	1.07
8X-4, 0–40	346.7	7.93	1.33743	31.10	370.7	0.77	2.34	90	9.81	363	6.94	15.2	2.86	40	186	0.85
9X-5, 0–40	356.2	7.93	1.33712	26.21	331.1	0.68	3.25	68	8.78	321	5.89	14.1	2.86	33	153	0.93
10X-3, 0–33.5	364.7	7.98	1.33758	27.87	387.8	0.77	4.84	65	9.89	368	6.79	18.3	4.07	38	177	1.19
11X-4, 0–28	375.3	7.93	1.33728	29.58	375.3	0.79	2.55	67	9.94	358	6.46	15.3	3.03	42	171	0.91
12X-7, 0–27	388.0	8.32	1.33447	9.61	136.5	0.23	2.87	35	3.84	127	1.95	3.2	1.02	26	73	0.34
13X-1, 54–112	391.5	7.91	1.33711	26.40	364.4	0.80	1.82	39	9.99	355	6.70	13.8	2.44	68	164	0.75
14X-3, 11–52	403.0	7.85	1.33707	27.98	359.5	0.74	1.60	64	9.63	347	5.36	13.7	2.89	66	162	0.94
15X-4, 0–36.5	412.2	7.87	1.33712	27.06	365.9	0.81	1.73	53	9.06	353	6.13	14.1	3.57	68	154	1.13
16X-3, 0–40	421.9	7.86	1.33708	27.08	366.0	0.75	1.31	45	9.19	348	5.61	13.0	3.47	67	154	0.91
17X-4, 10–51	431.8	7.80	1.33740	23.05	385.4	0.79	4.22	52	9.39	368	6.51	16.3	4.39	64	165	1.18
18X-3, 0–41	440.3	7.81	1.33712	23.59	368.2	0.76	1.64	42	8.88	354	6.23	13.2	4.05	63	151	1.16
19X-3, 0–50	450.3	7.84	1.33708	22.04	364.3	0.75	1.23	28	8.94	348	5.68	12.0	3.75	63	152	0.90
20X-2, 5–50.5	458.6	7.77	1.33714	20.11	374.0	0.75	2.15	28	8.61	356	6.31	13.0	4.32	61	166	1.39
21X-4, 0–50	470.5	7.80	1.33712	16.66	375.4	0.82	2.07	16	8.77	354	6.03	12.2	4.09	62	169	1.09
24X-5, 0–41	500.5	7.91	1.33712	15.21	380.1	0.76	1.84	11	8.11	352	6.50	11.3	4.95	45	183	1.35

* = based on the standard squeezing method. ND = not detected.

Table T29 (continued).

Core, section, interval (cm)	Depth (mbsf)	Fe (µM)	Si (µM)	Sr (µM)	Ba (µM)	V (nM)	Cu (nM)	Zn (nM)	Rb (nM)	Mo (nM)	Cs (nM)	Pb (nM)	U (nM)
338-C0002J-													
1R-6, 6.8–4	903.6	0.5	708	112	13.3	26.1	6,339	594	1,093	213	5.57	3.63	5.42
3R-3, 0–17.5	913.5	1.5	1,025	112	8.7	24.5	11,417	3,250	957	156	4.63	5.43	3.41
4R-2, 2–21	917.6	1.2	1,027	103	13.1	24.5	5,793	3,386	993	179	4.62	5.71	8.07
5R-2, 5–44.5	922.4	0.7	696	101	63.7	26.7	8,113	1,532	1,093	319	6.08	2.40	5.12
338-C0002K-													
1H-3, 10–50.5	202.5	9.2	928	63	19.7	38.6	2,587	813	860	82	4.94	7.16	2.12
3T-5, 0–25	209.9	11.5	721	65	20.2	50.5	3,544	835	960	72	5.94	3.44	1.89
4T-2, 0–30	215.4	10.1	632	66	22.0	77.8	3,980	1,081	928	144	5.86	5.55	2.65
5T-6, 0–25	224.1	14.4	849	65	24.5	43.7	3,808	1,233	865	63	5.89	7.07	1.73
6T-3, 0–21	231.3	5.2	550	53	15.0	95.4	1,512	755	823	439	5.54	3.82	5.81
7X-5, 0–16	241.9	35.2	819	60	23.0	36.8	1,941	1,482	852	59	5.22	3.08	1.26
8X-2, 0–38	249.9	20.9	922	58	21.4	36.0	3,240	712	767	34	4.68	5.35	0.88
9X-3, 0–31	260.0	7.3	849	58	19.8	44.2	3,235	859	813	51	4.56	3.40	1.33
10X-2, 0–31	267.9	5.1	835	55	19.6	56.7	4,028	560	875	203	4.85	4.38	2.06
11X-2, 0–31	277.3	3.6	786	53	21.3	79.9	1,470	711	930	99	6.50	3.11	1.55
338-C0002L-													
1X-4, 0–30.5	280.5	67.3	649	54	20.8	65.9	412	637	795	92	5.60	1.37	2.21
3X-2, 0–31	290.1	29.5	602	51	21.0	44.1	957	859	1,152	122	8.40	2.26	3.93
4X-2, 0–44	306.4	14.4	970	45	21.6	35.0	1,708	801	717	38	3.98	3.17	0.89
5X-3, 5–50	317.1	8.8	782	42	18.1	57.6	2,057	927	830	172	5.19	3.28	2.77
6X-4, 0–42	327.0	12.6	675	38	14.7	45.1	871	741	711	77	4.37	1.79	1.48
7X-2, 0–40.5	335.0	8.5	772	46	15.5	46.2	2,506	1,056	839	92	4.74	1.78	1.51
8X-4, 0–40	346.7	9.1	588	42	11.9	40.3	961	584	842	94	5.46	1.88	2.17
9X-5, 0–40	356.2	14.6	411	37	9.3	29.9	546	493	699	50	4.93	1.40	1.01
10X-3, 0–33.5	364.7	13.6	515	48	12.4	34.7	1,906	581	812	89	5.50	3.22	2.13
11X-4, 0–28	375.3	2.2	730	45	15.0	47.8	3,750	880	721	236	4.70	2.28	3.00
12X-7, 0–27	388.0	0.9	314	9	3.1	25.4	368	89	203	183	0.96	1.23	8.76
13X-1, 54–112	391.5	1.2	769	40	17.5	48.3	5,804	765	635	559	4.02	4.00	3.41
14X-3, 11–52	403.0	6.3	939	42	17.2	24.5	6,260	771	542	99	3.28	4.63	2.08
15X-4, 0–36.5	412.2	2.0	744	45	17.1	34.3	7,026	1,488	738	41	4.58	2.77	1.68
16X-3, 0–40	421.9	2.9	789	44	15.7	36.4	5,405	921	690	115	4.46	3.26	2.22
17X-4, 10–51	431.8	3.1	810	53	16.3	25.0	3,596	802	694	89	4.23	2.30	2.96
18X-3, 0–41	440.3	2.3	841	48	16.2	40.7	5,373	1,419	804	81	5.42	1.73	1.94
19X-3, 0–50	450.3	2.1	790	45	17.0	27.1	3,873	1,206	731	155	4.11	2.11	3.57
20X-2, 5–50.5	458.6	2.8	777	52	18.6	24.6	3,058	1,181	761	61	4.27	1.75	1.72
21X-4, 0–50	470.5	0.9	795	52	19.7	36.9	6,702	1,283	888	363	4.97	2.34	3.82
24X-5, 0–41	500.5	4.4	685	54	16.1	17.6	3,304	1,257	1,069	61	6.68	1.11	1.36

Table T30. Water content, Holes C0002H, C0002J, C0002K, and C0002L.

Core, section, interval (cm)	Depth (mbsf)	Water content (wt%)
338-C0002H-		
2R-2, 0–11	1111.1	15.2
338-C0002J-		
1R-6, 2–6.8	903.6	20.0
3R-3, 17.5–20.5*	913.7	27.3
4R-2, 0–2	917.6	25.6
5R-2, 0–5	922.3	20.8
7R-1, 60–65	932.6	16.8
338-C0002K-		
5T-6, 25–30	224.4	33.6
10X-2, 26–31	268.2	22.7
338-C0002L-		
5X-3, 0–5	317.1	27.2
10X-3, 33.5–38.5	365.0	22.3
15X-4, 36.5–41.5	412.5	23.0
20X-2, 0–5	458.5	24.0

* = average values of the sediment samples taken from Section 338-C0002J-3R-2.

Table T31. Geochemistry of interstitial water in sampled sediment, Holes C0002H, C0002J, C0002K, and C0002L, based on the GRIND method. (Continued on next page.)

Core, section, interval (cm)	Depth (mbsf)	Extraction method	pH	Salinity (refractive index)*	Alkalinity (mM)	Chlorinity (mM)	Br^- (mM)	SO4^{2-} (mM)	PO_4^{3-} (µM)	NH_4^+ (mM)	Na^+ (mM)	K^+ (mM)	Mg^{2+} (mM)	Ca^{2+} (mM)	Li (µM)	B (µM)
338-C0002H-																
2R-2, 0–11	1111.1	GRIND-1	7.19	1.33583	4.0	461.4	0.88	8.42	ND	1.6	412	8.4	14.6	18.6	303	475
2R-2, 0–11	1111.1	GRIND-2	7.79	1.33573	3.5	446.0	0.77	7.13	ND	1.6	389	7.5	11.6	18.2	315	522
338-C0002J-																
1R-6, 2–6.8	903.6	GRIND-1	7.88	1.33611	5.1	478.7	0.93	2.36	6.4	3.0	464	9.39	9.68	8.93	280	225
1R-6, 2–6.8	903.6	GRIND-2	7.81	1.33607	5.4	507.1	0.89	2.39	2.2	2.9	444	8.72	8.74	8.12	265	275
3R-3, 17.5–20.5	913.5	GRIND-1	7.81	1.33632	4.6	468.3	0.86	4.09	3.5	2.7	419	7.70	10.6	9.09	234	223
3R-3, 17.5–20.5	913.5	GRIND-2	7.70	1.33628	4.4	429.9	0.84	4.45	4.5	2.6	420	7.68	10.8	8.95	235	247
4R-2, 0–2	917.6	GRIND-1	7.75	1.33645	5.0	412.4	0.88	4.72	4.0	2.7	445	7.69	12.3	10.4	241	249
4R-2, 0–2	917.6	GRIND-2	7.71	1.33651	4.9	430.2	0.96	4.38	5.7	2.6	448	7.28	12.2	10.5	247	288
5R-2, 0–2	922.4	GRIND-1	7.74	1.33610	3.6	488.2	0.93	2.40	4.1	2.8	448	7.76	9.30	9.65	259	232
5R-2, 0–2	922.4	GRIND-2	8.04	1.33611	3.4	525.0	0.99	2.46	2.7	2.6	438	7.04	8.96	9.58	251	235
7R-1, 60–65	932.6	GRIND-1	—	1.33597	3.7	518.9	0.93	5.25	8.0	2.5	442	12.7	13.4	12.0	332	285
7R-1, 60–65	932.6	GRIND-2	—	1.33596	3.9	475.1	0.90	4.66	3.6	2.5	427	11.9	12.2	12.0	328	290
338-C0002K-																
5T-6, 25–30	224.1	GRIND-1	8.05	1.33695	29.8	485.8	1.15	2.00	108	12.7	470	9.9	20.9	2.3	65	335
5T-6, 25–30	224.1	GRIND-2	8.06	1.33688	30.4	481.3	1.10	1.68	127	12.3	457	9.5	19.9	2.2	63	335
10X–2, 26–31	267.9	GRIND-1	8.15	1.33617	27.6	442.2	0.97	2.27	31	12.0	432	11.7	13.7	2.7	92	367
10X–2, 26–31	267.9	GRIND-2	8.12	1.33632	28.3	467.1	1.02	2.34	33	12.3	405	9.9	13.1	2.6	90	384
338-C0002L-																
5X-3, 0–5	317.1	GRIND-1	8.25	1.33591	24.8	382.8	0.84	1.69	59	10.6	295	7.2	7.8	1.6	62	211
5X-3, 0–5	317.1	GRIND-2	8.29	1.33587	25.3	369.8	0.84	1.50	78	10.3	367	8.4	9.6	1.7	56	216
10X-3, 33.5–38.5	364.7	GRIND-1	8.22	1.33592	23.0	392.2	0.81	4.22	21	10.7	385	10.0	12.0	3.1	58	215
10X-3, 33.5–38.5	364.7	GRIND-2	8.19	1.33582	24.6	390.5	0.80	3.79	29	10.9	376	8.6	11.6	2.8	56	220
15X-4, 36.5–41.5	412.2	GRIND-1	8.16	1.33567	22.5	359.7	0.72	2.57	37	9.3	363	7.0	10.3	2.7	75	175
15X-4, 36.5–41.5	412.2	GRIND-2	8.29	1.33564	23.1	359.5	0.74	1.82	35	9.5	354	6.3	9.4	2.6	73	165
20X-2, 0–5	458.6	GRIND-1	8.06	1.33572	15.8	376.4	0.75	2.40	24	9.4	365	7.5	8.9	3.2	71	180
20X-2, 0–5	458.6	GRIND-2	7.97	1.33592	18.8	412.1	0.86	1.99	26	9.6	405	8.4	10.7	4.0	82	208

* = data not corrected. GRIND Runs 1 and 2 use Milli-Q water and diluted HNO_3 solution with pH adjusted to 3. Analytical data are corrected to be the primary concentrations of interstitial water using dilution rate (see text) except the pH and salinity. ND = not detected.

Table T31 (continued).

Core, section, interval (cm)	Depth (mbsf)	Mn (µM)	Fe (µM)	Si (µM)	Sr (µM)	Ba (µM)	V (nM)	Cu (nM)	Zn (nM)	Rb (nM)	Mo (nM)	Cs (nM)	Pb (nM)	U (nM)
338-C0002H-														
2R-2, 0–11	1111.1	5.35	0.86	614	53	13.5	99.7	10,740	1,898	3,379	1589	19.9	5.6	60.4
2R-2, 0–11	1111.1	4.82	0.75	610	49	14.1	115.4	10,567	1,667	3,395	1291	19.0	33.0	89.2
338-C0002J-														
1R-6, 2–6.8	903.6	1.12	0.75	1,285	108	88.4	100.3	10,800	673	1,772	645	9.4	3.7	36.9
1R-6, 2–6.8	903.6	1.43	0.97	1,371	96	71.6	97.3	10,327	2,626	1,651	843	8.8	38.1	36.9
3R-3, 17.5–20.5	913.5	1.50	1.00	1,259	86	24.9	72.2	8,611	2,537	1,480	633	8.1	17.5	26.2
3R-3, 17.5–20.5	913.5	1.68	0.81	1,244	84	34.3	74.5	11,745	2,531	1,448	638	7.9	25.5	26.4
4R-2, 0–2	917.6	1.93	0.99	1,455	92	36.0	93.2	14,696	3,506	1,481	566	8.2	11.8	81.8
4R-2, 0–2	917.6	1.87	0.93	1,498	92	36.3	90.8	15,022	3,826	1,382	474	8.1	32.1	60.0
5R-2, 0–2	922.4	1.47	1.00	1,228	88	64.6	151.7	436	54	1,699	726	9.1	ND	54.2
5R-2, 0–2	922.4	1.43	0.87	1,331	83	61.4	137.6	6,394	498	1,381	859	7.7	3.8	42.3
7R-1, 60–65	932.6	4.11	1.00	828	80	21.2	91.1	16,041	2,429	4,146	745	23.1	17.4	47.6
7R-1, 60–65	932.6	3.49	1.03	811	77	22.5	120.7	25,013	1,200	4,289	640	23.5	7.3	49.9
338-C0002K-														
5T-6, 25–30	224.1	0.72	1.10	922	46	19.6	358.8	1,302	279	1,169	1309	8.2	12.7	57.6
5T-6, 25–30	224.1	0.70	1.33	943	45	18.6	337.6	2,809	474	1,153	1375	9.0	34.6	42.6
10X–, 26–31	267.9	1.16	1.04	620	38	14.3	658.4	2,782	912	2,396	3454	16.1	10.8	129.2
10X–, 26–31	267.9	1.13	0.93	671	41	15.5	574.3	8,182	952	2,283	3578	15.8	42.3	125.9
338-C0002L-														
5X-3, 0–5	317.1	0.71	0.93	728	27	13.6	345.7	3,571	328	1,566	3110	10.6	8.9	120.2
5X-3, 0–5	317.1	0.61	ND	779	25	12.4	246.0	1,778	362	1,139	2172	7.3	16.1	70.3
10X-3, 33.5–38.5	364.7	1.06	ND	495	33	9.6	406.3	3,891	440	2,082	2732	14.7	5.7	105.5
10X-3, 33.5–38.5	364.7	0.95	ND	542	33	10.1	324.4	2,899	908	1,787	2507	12.7	30.3	102.4
15X-4, 36.5–41.5	412.2	0.65	0.76	808	32	12.0	164.1	14,893	1,592	864	1862	6.2	14.7	35.6
15X-4, 36.5–41.5	412.2	0.56	ND	745	30	11.5	212.9	3,236	162	932	2222	7.3	7.0	33.2
20X-2, 0–5	458.6	0.78	ND	746	36	13.7	143.5	5,210	1,051	1,093	3131	7.2	15.3	46.4
20X-2, 0–5	458.6	1.11	ND	856	45	17.4	136.9	12,135	780	1,311	3548	9.8	11.9	45.2

Table T32. Interstitial water geochemistry, Hole C0002F.

Sampling method	Depth (mbsf) Top	Depth (mbsf) Bottom	Alkalinity (mM)	Chlorinity (mM)	Br^- (mM)	SO_4^{2-} (mM)	Na^+ (mM)	K^+ (mM)	Mg^{2+} (mM)	Ca^{2+} (mM)	Li (µM)	B (µM)	Mn (µM)	Fe (µM)	Si (µM)	Sr (µM)
GRIND Run 1	1970.0	1975.5	15.9	726.0	0.628	20.4	480	275	ND	17.5	17.4	197	0.55	0.5	351	54.7
GRIND Run 2	1970.0	1975.5	NA	481.8	0.415	22.0	321	205	ND	9.8	17.6	219	0.38	0.5	376	42.8
Standard squeezing	1970.0	1975.5	10.0	947.8	0.885	35.9	627	372	ND	20.3	22.0	279	0.49	0.7	228	85.2
GRIND Run 1	1977.5	1982.5	7.5	682.6	0.685	30.5	474	266	ND	15.9	16.7	276	0.43	0.7	356	66.2
GRIND Run 2	1977.5	1982.5	NA	490.5	0.499	23.5	335	186	ND	15.1	15.8	214	0.40	0.6	485	45.0
Standard squeezing	1977.5	1982.5	8.8	863.9	0.892	37.1	590	327	ND	19.4	20.1	284	0.50	0.8	211	83.1
CMW	LMT	LMT	4.4	142.9	0.117	3.7	83	60	0.6	1.4	13.2	23	0.69	77.4	753	7.1

GRIND = ground rock interstitial normative determination, CMW = centrifuged mud water, LMT = mud water collected at mud tank. ND = not detected.

Sampling method	Depth (mbsf) Top	Depth (mbsf) Bottom	Ba (µM)	V (nM)	Cu (nM)	Zn (nM)	Rb (nM)	Mo (nM)	Cs (nM)	Pb (nM)	U (nM)
GRIND Run 1	1970.0	1975.5	4.41	1,360	5,700	841	12,952	26,283	20.8	179	1.38
GRIND Run 2	1970.0	1975.5	4.02	1,749	6,786	223	10,205	10,724	21.3	42	1.69
Standard squeezing	1970.0	1975.5	3.36	1,809	8,910	321	20,087	15,389	41.7	61	0.72
GRIND Run 1	1977.5	1982.5	3.77	1,910	4,284	227	12,338	15,125	20.9	52	1.39
GRIND Run 2	1977.5	1982.5	3.41	1,717	6,717	533	9,724	18,981	20.7	61	1.51
Standard squeezing	1977.5	1982.5	3.23	1,620	6,965	285	17,151	14,214	35.1	51	1.38
CMW	LMT	LMT	3.93	324	255	2,282	3,098	737	9.7	11	1.24

Table T33. Core liner liquid geochemistry, Holes C0002H, C0002J, C0002K, and C0002L.

Core, section	Depth (mbsf)	pH	Salinity (refractive index)*	Alkalinity (mM)	Chlorinity (mM)	Br^- (mM)	SO_4^{2-} (mM)	PO_4^{3-} (µM)	NH_4^+ (mM)	Na^+ (mM)	K^+ (mM)	Mg^{2+} (mM)	Ca^{2+} (mM)	Li (µM)	B (µM)	Mn (µM)	Fe (µM)
338-C0002H-																	
1R-1	1100.5	7.84	1.33927	2.1	545.5	0.84	25.7	ND	0.5	464	7.3	48.3	14.2	62.1	395	6.45	0.5
2R-1	1110.5	7.89	1.33937	2.5	551.8	0.83	26.7	ND	0.1	474	9.4	52.1	12.0	49.4	400	2.83	0.5
338-C0002J-																	
1R-1	902	7.66	1.33927	2.8	534.5	0.84	25.2	3	0.5	467	8.4	49.5	10.8	58.2	404	1.93	0.7
3R-1	912	7.56	1.33912	2.7	535.4	0.83	22.4	3	1.3	466	8.5	42.6	11.9	88.6	367	2.09	0.8
4R-1	917	7.58	1.33925	2.7	544.4	0.86	24.7	3	0.9	475	8.7	48.4	12.0	66.3	393	2.98	0.8
5R-1	922	7.47	1.33920	2.9	540.3	0.85	24.4	ND	1.0	472	8.0	47.1	12.4	72.7	386	3.18	0.7
7R-1	932	7.91	1.33936	2.3	551.0	0.91	26.8	2	0.1	472	9.7	52.4	11.0	46.1	420	0.95	0.6
338-C0002K-																	
1H-6	203.7	7.83	1.33855	38.8	493.4	1.15	1.0	294	11.8	454	8.2	27.4	3.3	38.3	286	8.71	1.3
2H-1	206.5	7.69	1.33887	26.3	516.0	1.03	9.6	104	8.0	467	9.2	37.1	6.1	44.7	347	6.89	1.0
4T-1	215.6	7.56	1.33935	2.3	548.8	0.88	26.4	3	0.3	481	10.3	53.7	11.0	40.9	415	1.33	0.7
5T-3	222.6	7.76	1.33908	12.9	531.4	0.88	19.7	6	8.3	467	8.1	44.6	8.1	48.1	345	5.27	0.9
6T-1	229.5	7.58	1.33903	5.6	544.0	0.86	23.7	ND	4.1	469	10.1	47.8	9.2	45.6	440	6.24	3.0
11X-1	277	7.45	1.33895	7.9	515.0	0.80	21.6	18	5.9	455	9.5	43.7	8.5	54.1	371	4.30	58.6
338-C0002L-																	
7X-1	334	7.68	1.33927	3.9	543.9	0.89	25.4	8	2.1	477	9.6	51.0	10.2	44.2	379	1.24	0.8
18X-1	438.5	7.55	1.33921	3.9	533.9	0.83	25.3	3	3.6	468	9.9	48.1	10.2	50.5	344	4.55	0.7
19X-1	448	7.65	1.33925	3.1	539.6	0.83	26.1	4	1.9	468	10.0	50.6	10.5	44.0	366	3.78	0.6

Core, section	Depth (mbsf)	Si (µM)	Sr (µM)	Ba (µM)	V (nM)	Cu (nM)	Zn (nM)	Rb (nM)	Mo (nM)	Cs (nM)	Pb (nM)	U (nM)
338-C0002H-												
1R-1	1100.5	81	81.1	4.9	26	93.4	107	1090	212	6.92	ND	12.2
2R-1	1110.5	44	82.5	2.1	30	18.1	92	1202	223	5.51	ND	13.4
338-C0002J-												
1R-1	902	202	92.4	4.6	26	17.0	110	1177	183	3.35	0.72	15.8
3R-1	912	444	98.2	4.8	30	6.7	142	1212	237	4.82	ND	13.0
4R-1	917	309	93.1	6.8	26	13.4	1298	1109	161	3.43	ND	13.7
5R-1	922	308	97.1	7.0	24	43.0	164	1021	141	3.48	ND	17.3
7R-1	932	48	87.6	1.4	28	71.7	150	1206	145	3.00	ND	13.9
338-C0002K-												
1H-6	203.7	752	68.7	19.5	49	14.3	60	720	58	3.36	1.82	1.4
2H-1	206.5	498	76.1	13.1	119	13.5	1913	920	472	3.55	2.30	8.7
4T-1	215.6	22	86.0	1.6	31	34.2	1172	1216	259	2.05	2.73	14.4
5T-3	222.6	407	79.0	3.3	55	7.6	117	901	389	6.58	0.50	8.3
6T-1	229.5	284	78.4	5.3	48	19.3	321	1192	4745	3.51	ND	10.3
11X-1	277	480	76.5	5.5	30	8.3	241	1267	418	6.54	0.59	3.9
338-C0002L-												
7X-1	334	148	83.0	6.9	77	20.8	85	1130	331	2.38	1.29	15.1
18X-1	638.5	394	76.5	4.0	28	15.2	76	1342	1020	5.12	ND	10.0
19X-1	448	154	83.1	3.8	31	11.2	133	1191	982	3.18	0.54	16.0

* = data not corrected. ND = not detected.

Table T34. Hydrocarbon gas composition in conventionally extracted headspace gas, Holes C0002H, C0002J, C0002K, and C0002L.

Core, section, interval (cm)	Depth (mbsf)	Headspace gas (ppmv)			$C_1/(C_2 + C_3)$	Headspace gas (µM)			$\delta^{13}C$-CH_4 (‰ VPDB)
		Methane	Ethane	Propane		Methane	Ethane	Propane	
338-C0002H-									
1R-1, 137–141	1101.9	6,731	53.0	18.3	94	3,452	27.2	9.39	–65.0
2R-1, 52.5–56.5	1111.0	9,478	26.0	4.3	312	4,018	11.0	1.84	–65.1
338-C0002J-									
1R-4, 0–4	903.2	12,262	14.5	0.3	828	11,226	13.3	0.28	–66.3
2R-1, 0–4	907.0	9,104	16.1	0.3	556	5,457	9.6	0.17	–64.5
3R-2, 71–74	913.5	12,533	27.7	0.9	438	6,750	14.9	0.49	–62.4
4R-1, 51–55	917.5	37,579	66.6	1.5	551	9,964	17.7	0.41	–65.2
5R-1, 28–32	922.3	26,987	41.2	0.1	654	9,336	14.3	0.03	–62.3
6R-1, 93–97	928.0	4,534	9.1	ND	500	3,089	6.2	ND	–64.4
7R-1, 96–100	933.0	8,234	21.0	0.4	384	5,899	15.1	0.31	–65.5
338-C0002K-									
1H-4, 0–4	202.9	3,723	0.4	0.5	4,137	1,257	0.1	0.16	–63.9
2H-1, 74–78	205.3	11,861	1.0	ND	12,042	2,530	0.2	ND	–55.4
3T-4, 136–140	209.9	4,971	0.6	1.1	3,008	1,539	0.2	0.33	–52.2
4T-1, 37–41	215.4	4,396	0.4	0.6	4,341	1,823	0.2	0.26	–66.1
5T-5, 38–42	224.1	4,035	0.6	1.6	1,830	1,322	0.2	0.53	–64.4
6T-2, 74–78	231.3	2,265	0.2	0.3	4,194	660	0.1	0.09	–65.7
7X-6, 0–4	242.2	3,861	0.4	1.2	2,423	1,339	0.2	0.40	–63.2
8X-1, 138–142	249.9	3,432	0.4	1.2	2,161	1,156	0.1	0.40	–64.9
9X-4, 0–4	260.4	5,866	0.7	0.8	3,993	2,106	0.2	0.28	–64.0
10X-1, 33.5–37.5	267.9	9,999	1.4	0.4	5,548	7,152	1.0	0.31	–63.0
11X-1, 28–32	277.3	4,745	0.4	1.1	3,147	1,743	0.1	0.42	–61.9
338-C0002L-									
1X-3, 126–130	280.5	2,926	0.3	1.0	2,251	855	0.1	0.29	–66.8
3X-1, 103–108	297.1	4,773	0.4	0.5	5,672	2,217	0.2	0.22	–63.9
4X-1, 89–93	306.4	174	ND	ND	—	56	ND	ND	—
5X-2, 64.5–69.5	317.1	54	ND	ND	—	12	ND	ND	–44.4
6X-3, 24.5–29.5	327.0	11,183	1.6	3.2	2,365	2,073	0.3	0.59	–30.2
7X-1, 91.5–95.5	334.9	4,493	0.7	2.6	1,381	1,455	0.2	0.83	–62.5
8X-3, 117.5–121.5	346.2	6,336	0.2	3.1	1,888	1,950	0.1	0.96	–56.2
9X-4, 93.5–97.5	356.2	2,879	0.6	0.8	2,026	1,079	0.2	0.31	—
10X-4, 0–4	365.1	4,735	1.2	0.6	2,590	875	0.2	0.11	–61.1
10X-8, 24–27	368.9	317	0.1	ND	2,238	104	0.0	ND	—
11X-5, 0–4	375.6	2,588	1.8	1.9	712	558	0.4	0.40	–58.3
12X-8, 0–4	388.4	3,075	1.9	ND	1,607	1,416	0.9	ND	—
13X-2, 0–4	392.1	4,812	3.4	0.3	1,311	2,445	1.7	0.16	–55.6
14X-4, 0–4	403.5	3,553	10.3	0.5	329	889	2.6	0.12	—
15X-2, 89–93	411.8	4,650	11.6	ND	402	1,582	3.9	ND	–61.4
16X-2, 135.5–139.5	421.9	11,157	12.4	0.4	873	2,530	2.8	0.09	–59.5
17X-5, 0–4	432.3	2,966	5.5	0.3	509	942	1.7	0.10	–54.5
18X-2, 85–89	440.3	5,278	10.0	0.5	505	1,495	2.8	0.14	—
19X-2, 104–108	450.3	5,175	8.7	0.4	569	692	1.2	0.05	–54.1
20X-1, 100–104	458.5	12,550	7.6	0.3	1,587	4,657	2.8	0.10	–57.5
21X-3, 80.5–84.5	470.4	7,577	8.0	0.3	908	2,603	2.8	0.11	—
22X-1, 62–66	477.1	4,146	7.3	ND	565	831	1.5	ND	—
24X-6, 0–4	501.0	4,720	4.8	ND	983	2,256	2.3	ND	–42.6

ND = not detected. — = not enough methane to measure $\delta^{13}C$-CH_4. VPDB = Vienna Peedee belemnite.

Table T35. Hydrocarbon gas composition in additionally extracted headspace gas, Holes C0002H, C0002J, C0002K, and C0002L.

Core, section, interval (cm)	Depth (mbsf)	Headspace gas (ppmv)			$C_1/(C_2+C_3)$	Headspace gas (µM)			$\delta^{13}C$-CH_4 (‰ VPDB)
		Methane	Ethane	Propane		Methane	Ethane	Propane	
338-C0002H-									
1R-1, 137–141	1101.9	8,863	61.9	14.6	116	2,329	16.3	3.8	–63.7
2R-1, 52.5–56.5	1111.0	8,795	26.0	4.9	284	3,034	9.0	1.7	–61.2
338-C0002J-									
1R-4, 0–4	903.2	12,116	13.9	ND	870	3,632	4.2	ND	–65.3
2R-1, 0–4	907.0	13,680	19.0	ND	721	3,683	5.1	ND	–65.0
3R-2, 71–74	913.5	25,808	37.5	0.7	677	4,215	6.1	0.1	–65.7
4R-1, 51–55	917.5	16,078	32.8	0.6	481	2,972	6.1	0.1	–64.9
5R-1, 28–32	922.3	57,710	68.8	0.7	830	11,465	13.7	0.1	–64.3
6R-1, 93–97	928.0	9,019	16.5	0.3	538	2,819	5.1	0.1	–65.1
7R-1, 96–100	933.0	8,321	15.2	ND	549	2,628	4.8	ND	–63.7
338-C0002K-									
1H-4, 0–4	202.9	5,481	0.4	ND	13,074	789	0.1	ND	–65.8
2H-1, 74–78	205.3	17,023	1.3	0.3	10,657	1,828	0.1	0.0	–66.6
3T-4, 136–140	209.9	1,330	0.4	ND	3,399	211	0.1	ND	—
4T-1, 37–41	215.4	2,922	0.4	0.7	2,690	651	0.1	0.2	–61.2
5T-5, 38–42	224.1	2,663	0.4	0.7	2,436	401	0.1	0.1	–63.8
6T-2, 74–78	231.3	4,691	0.5	0.5	4,442	386	0.0	0.0	–52.0
7X-6, 0–4	242.2	1,894	0.6	0.4	1,900	424	0.1	0.1	–62.4
8X-1, 138–142	249.9	3,506	0.3	0.4	5,251	522	0.0	0.1	–64.7
9X-4, 0–4	260.4	11,900	1.1	0.8	6,209	2,003	0.2	0.1	–65.8
10X-1, 33.5–37.5	267.9	17,332	2.0	ND	8,478	4,787	0.6	ND	–66.0
11X-1, 28–32	277.3	7,693	0.5	1.0	5,140	1,290	0.1	0.2	–66.5
338-C0002L-									
1X-3, 126–130	280.5	4,738	0.3	0.5	6,049	560	0.0	0.1	–68.4
3X-1, 103–108	297.1	17,024	1.1	1.3	7,140	3,369	0.2	0.3	–64.2
4X-1, 89–93	306.4	1,968	0.7	0.7	1,436	400	0.1	0.1	–65.1
5X-2, 64.5–69.5	317.1	9,056	1.3	4.0	1,710	827	0.1	0.4	–63.3
6X-3, 24.5–29.5	327.0	5,959	1.0	1.8	2,094	1,175	0.2	0.4	–63.4
7X-1, 91.5–95.5	334.9	3,595	0.6	1.7	1,573	710	0.1	0.3	–64.8
8X-3, 117.5–121.5	346.2	5,182	0.9	1.5	2,156	927	0.2	0.3	–61.8
9X-4, 93.5–97.5	356.2	5,339	1.0	0.7	3,173	1,381	0.3	0.2	–56.8
10X-4, 0–4	365.1	18,685	3.0	0.5	5,269	3,228	0.5	0.1	–63.8
10X-8, 24–27	368.9	6,127	2.2	ND	2,797	812	0.3	ND	–63.0
11X-5, 0–4	375.6	3,240	0.9	0.5	2,318	551	0.2	0.1	–63.8
12X-8, 0–4	388.4	5,518	3.9	ND	1,410	1,540	1.1	ND	–58.8
13X-2, 0–4	392.1	7,464	4.3	0.3	1,629	2,680	1.5	0.1	–62.2
14X-4, 0–4	403.5	6,687	13.1	ND	509	1,036	2.0	ND	–63.0
15X-2, 89–93	411.8	6,049	10.9	ND	554	1,413	2.5	ND	–61.3
16X-2, 135.5–139.5	421.9	9,475	10.1	ND	938	1,652	1.8	ND	–60.0
17X-5, 0–4	432.3	5,403	5.5	ND	988	780	0.8	ND	–62.2
18X-2, 85–89	440.3	5,686	7.2	ND	792	1,178	1.5	ND	–60.8
19X-2, 104–108	450.3	688	1.5	ND	453	114	0.3	ND	–50.4
20X-1, 100–104	458.5	15,647	10.5	0.3	1,447	3,243	2.2	0.1	–59.6
21X-3, 80.5–84.5	470.4	2,174	3.2	ND	674	254	0.4	ND	–51.4
22X-1, 62–66	477.1	3,349	3.7	ND	895	1,029	1.1	ND	–60.0
24X-6, 0–4	501.0	7,164	4.5	ND	1,590	1,966	1.2	ND	–58.2

ND = not detected. — = not enough methane to measure $\delta_{13}C$-CH_4. VPDB = Vienna Peedee belemnite.

Table T36. Hydrocarbon gas composition in void gas, Holes C0002K and C0002L.

Core, section, interval (cm)	Depth (mbsf)	Headspace gas (ppmv)			$C_1/(C_2 + C_3)$	$\delta^{13}C\text{-}CH_4$ (‰ VPDB)
		Methane	Ethane	Propane		
338-C0002K-						
1H-4, 31	203.2	190,689	14.8	0.1	12,791	–71.8
3T-4, 74	209.2	158,596	5.8	2.1	19,937	–66.5
4T-4, 38.5	216.5	3	ND	ND	—	—
5T-4, 48.5	223.1	221,853	12.4	3.5	13,933	–65.9
6T-2, 78	231.3	154,372	4.2	2.5	22,871	–65.9
7X-4, 43.5	241.2	238,183	13.7	3.6	13,811	–66.8
8X-2, 47.5	250.4	221,699	15.7	1.9	12,537	–64.1
9X-3, 0	260.0	213,377	17.8	0.8	11,490	–66.2
10X-3, 4	268.2	217,825	17.1	1.9	11,440	–66.2
11X-3, 0	277.7	138,703	5.9	4.4	13,384	–63.7
338-C0002L-						
1X-2, 103.5	279.2	240,886	12.0	6.1	13,296	–65.6
1X-5, 92	281.8	215,812	7.4	6.6	15,412	–65.6
3X-3, 130	298.7	243,900	8.4	7.9	14,964	–66.6
4X-1, 93	306.4	174,490	9.8	5.3	11,565	–63.5
5X-6, 56.5	320.6	186,728	12.6	3.7	11,435	–63.3
6X-6, 16	328.8	216,266	17.3	2.8	10,770	–64.3
7X-3, 0	335.4	274,400	12.5	6.0	14,782	–63.6
8X-8, 24	351.2	52,734*	2.6*	0.9*	15,183	–58.3
9X-6, 55	357.3	216,637	13.2	3.4	13,001	–62.7
10X-2, 87	364.5	205,789	13.1	3.9	12,134	–62.5
11X-2, 36	373.6	216,444	22.1	2.1	8,971	–62.0
12X-8, 51	388.9	220,027	78.6	0.6	2,780	–62.0
13X-3, 105	394.6	241,100	68.9	1.0	3,451	–61.2
14X-4, 0	403.5	171,595	74.4	ND	2,308	–63.3
15X-5, 0	412.6	255,824	98.7	ND	2,592	–58.9
16X-6, 27.5	425.3	224,389	70.2	0.9	3,159	–62.1
17X-6, 119	434.7	296,252	78.1	0.9	3,748	–61.5
18X-2, 29	439.7	1,790	1.1	ND	1,696	–56.4
19X-5, 102.5	453.2	130,036	40.8	0.4	3,158	–58.3
20X-7, 20.5	464.7	121,826	29.7	ND	4,098	–58.9
21X-5, 96	472.0	72,599	15.0	ND	4,846	–59.8
22X-5, 41	479.6	232,135	68.5	0.7	3,351	–59.0
24X-2, 21	497.1	210,184	48.5	0.5	4,290	–61.4

* = the data of measurement was not saved, and the data were acquired by remeasurement. Based on the experiment for confirmation, the concentrations decreased to 70%–80% of original concentration, but the hydrocarbon ratio was preserved in the original ratio. ND = not detected. — = not enough methane to measure $\delta^{13}C\text{-}CH_4$. VPDB = Vienna Peedee belemnite.

Table T37. Organic and inorganic carbon and nitrogen data of cuttings samples, Hole C0002F. (Continued on next three pages.)

Cuttings sample	Depth (mbsf)	IC (wt%)	$CaCO_3$ (wt%)	TN (wt%)	TC (wt%)	TS (wt%)	TOC (wt%)	C/N	C/S	Remarks
338-C0002F-										
7-SMW	875.5	0.15	1.3	0.05	8.9	NA	8.70	170.8	NA	>4 mm bulk
18-SMW	910.5	0.14	1.2	0.03	7.2	NA	7.08	219.5	NA	>4 mm cement
19-SMW	915.5	1.77	14.8	0.05	3.2	NA	1.47	26.9	NA	>4 mm mudstone
20-SMW	920.5	1.89	15.8	0.05	3.3	NA	1.37	25.3	NA	1–4 mm bulk
20-SMW	920.5	1.30	10.8	0.05	3.6	NA	2.30	46.9	NA	>4 mm bulk
20-SMW	920.5	1.88	15.7	0.05	3.3	NA	1.44	29.2	NA	1–4 mm mudstone
21-SMW	925.5	1.39	11.6	0.05	3.4	NA	2.05	44.5	NA	>4 mm bulk
21-SMW	925.5	1.86	15.5	0.05	3.3	NA	1.48	29.3	NA	1–4 mm mudstone
21-SMW	925.5	1.66	13.8	0.05	3.6	NA	1.94	35.4	NA	1–4 mm bulk
22-SMW	930.5	1.31	10.9	0.05	3.5	NA	2.24	46.4	NA	>4 mm bulk
22-SMW	930.5	1.84	15.3	0.05	3.3	NA	1.50	29.1	NA	1–4 mm mudstone
22-SMW	930.5	1.83	15.3	0.06	3.3	NA	1.44	25.6	NA	1–4 mm bulk
24-SMW	935.5	0.90	7.5	0.03	1.9	NA	0.96	33.2	NA	>4 mm bulk
24-SMW	935.5	1.83	15.2	0.05	3.3	NA	1.46	29.6	NA	>4 mm mudstone
24-SMW	935.5	1.84	15.3	0.05	3.2	NA	1.36	25.9	NA	1–4 mm mudstone
24-SMW	935.5	1.69	14.1	0.06	3.0	NA	1.28	22.6	NA	1–4 mm bulk
25-SMW	940.5	1.74	14.5	0.06	3.3	NA	1.55	27.6	NA	1–4 mm mudstone
25-SMW	940.5	1.70	14.2	0.06	3.1	NA	1.42	25.5	NA	1–4 mm bulk
25-SMW	940.5	1.37	11.4	0.06	5.3	NA	3.89	69.7	NA	>4 mm bulk
26-SMW	945.5	1.34	11.2	0.05	2.7	NA	1.37	25.5	NA	>4 mm bulk
26-SMW	945.5	1.77	14.8	0.06	3.3	NA	1.53	27.2	NA	1–4 mm mudstone
26-SMW	945.5	1.72	14.3	0.06	3.7	NA	2.01	34.7	NA	1–4 mm bulk
26-SMW	945.5	1.72	14.3	0.05	3.4	NA	1.73	32.8	NA	>4 mm mudstone
27-SMW	950.5	1.42	11.8	0.06	3.0	NA	1.54	27.4	NA	>4 mm bulk
27-SMW	950.5	1.70	14.1	0.06	3.2	NA	1.50	26.0	NA	1–4 mm bulk
27-SMW	950.5	1.67	13.9	0.05	3.0	NA	1.37	26.1	NA	1–4 mm mudstone
28-SMW	955.5	1.45	12.0	0.05	2.7	NA	1.30	23.7	NA	1–4 mm bulk
28-SMW	955.5	1.57	13.1	0.05	3.2	NA	1.64	30.2	NA	>4 mm mudstone
28-SMW	955.5	1.58	13.1	0.06	3.1	NA	1.51	26.5	NA	1–4 mm mudstone
28-SMW	955.5	1.59	13.2	0.06	3.0	NA	1.42	25.0	NA	>4 mm bulk
29-SMW	960.5	1.43	11.9	0.06	2.9	NA	1.44	24.5	NA	1–4 mm bulk
29-SMW	960.5	1.58	13.2	0.06	3.1	NA	1.55	26.2	NA	1–4 mm mudstone
29-SMW	960.5	1.10	9.1	0.05	4.3	NA	3.20	59.0	NA	>4 mm bulk
30-SMW	965.5	1.43	11.9	0.06	2.9	NA	1.51	26.5	NA	>4 mm mudstone
30-SMW	965.5	1.33	11.1	0.06	2.8	NA	1.49	26.4	NA	>4 mm bulk
30-SMW	965.5	1.32	11.0	0.06	2.8	NA	1.48	25.3	NA	1–4 mm mudstone
30-SMW	965.5	1.22	10.1	0.06	2.7	NA	1.51	25.3	NA	1–4 mm bulk
31-SMW	970.5	1.34	11.2	0.06	2.9	NA	1.57	25.4	NA	1–4 mm bulk
31-SMW	970.5	1.02	8.5	0.05	3.2	NA	2.16	40.0	NA	>4 mm bulk
31-SMW	970.5	1.41	11.7	0.06	3.0	NA	1.61	25.9	NA	1–4 mm mudstone
31-SMW	970.5	1.13	9.4	0.05	2.9	NA	1.74	31.7	NA	>4 mm mudstone
32-SMW	975.5	0.96	8.0	0.06	2.4	NA	1.48	25.9	NA	>4 mm bulk
32-SMW	975.5	1.18	9.9	0.06	2.9	NA	1.69	28.4	NA	>4 mm mudstone
32-SMW	975.5	1.28	10.7	0.06	2.9	NA	1.64	27.5	NA	1–4 mm mudstone
32-SMW	975.5	1.30	10.9	0.06	2.9	NA	1.63	25.6	NA	1–4 mm bulk
34-SMW	980.5	1.09	9.1	0.06	2.8	NA	1.66	26.2	NA	1–4 mm bulk
34-SMW	980.5	0.61	5.1	0.05	2.1	NA	1.53	28.1	NA	>4 mm bulk
34-SMW	980.5	0.74	6.1	0.06	2.6	NA	1.84	31.6	NA	>4 mm mudstone
34-SMW	980.5	1.09	9.1	0.06	2.8	NA	1.67	27.2	NA	1–4 mm mudstone
35-SMW	985.5	1.07	8.9	0.06	2.8	NA	1.75	27.6	NA	1–4 mm bulk
35-SMW	985.5	0.88	7.3	0.06	2.7	NA	1.78	29.7	NA	>4 mm mudstone
35-SMW	985.5	1.08	9.0	0.06	2.8	NA	1.74	28.6	NA	1–4 mm mudstone
35-SMW	985.5	0.74	6.2	0.06	2.5	NA	1.74	27.9	NA	>4 mm bulk
36-SMW	990.5	0.59	4.9	0.06	2.2	NA	1.64	26.5	NA	>4 mm bulk
36-SMW	990.5	0.58	4.8	0.06	2.3	NA	1.73	29.2	NA	>4 mm mudstone
36-SMW	990.5	0.90	7.5	0.06	2.6	NA	1.65	27.1	NA	1–4 mm mudstone
36-SMW	990.5	1.06	8.8	0.06	2.8	NA	1.75	30.8	NA	1–4 mm bulk
37-SMW	995.5	0.49	4.1	0.06	2.0	NA	1.47	25.9	NA	>4 mm bulk
37-SMW	995.5	0.88	7.3	0.06	2.3	NA	1.42	23.1	NA	1–4 mm mudstone
37-SMW	995.5	0.65	5.4	0.06	2.2	NA	1.58	26.7	NA	>4 mm mudstone
37-SMW	995.5	0.81	6.7	0.06	2.4	NA	1.63	28.4	NA	1–4 mm bulk
40-SMW	1000.5	0.75	6.3	0.05	2.1	NA	1.31	25.3	NA	>4 mm bulk
40-SMW	1000.5	0.71	5.9	0.06	2.4	NA	1.69	29.0	NA	1–4 mm mudstone
40-SMW	1000.5	0.98	8.1	0.06	2.6	NA	1.58	27.5	NA	>4 mm mudstone
40-SMW	1000.5	0.72	6.0	0.06	2.3	NA	1.55	27.1	NA	1–4 mm bulk

Table T37 (continued). (Continued on next page.)

Cuttings sample	Depth (mbsf)	IC (wt%)	$CaCO_3$ (wt%)	TN (wt%)	TC (wt%)	TS (wt%)	TOC (wt%)	C/N	C/S	Remarks
41-SMW	1005.5	0.72	6.0	0.06	2.2	NA	1.49	26.7	NA	>4 mm bulk
41-SMW	1005.5	0.55	4.6	0.06	2.3	NA	1.75	28.9	NA	1–4 mm bulk
42-SMW	1010.5	0.76	6.3	0.05	2.1	NA	1.38	25.2	NA	>4 mm bulk
42-SMW	1010.5	0.57	4.8	0.06	2.3	NA	1.70	28.8	NA	1–4 mm bulk
42-SMW	1010.5	0.66	5.5	0.06	2.3	NA	1.60	27.9	NA	>4 mm mudstone
42-SMW	1010.5	0.56	4.7	0.06	2.3	NA	1.70	28.6	NA	1–4 mm mudstone
43-SMW	1015.5	0.60	5.0	0.06	2.4	NA	1.79	30.1	NA	1–4 mm bulk
43-SMW	1015.5	0.77	6.4	0.06	2.2	NA	1.42	25.4	NA	>4 mm bulk
44-SMW	1020.5	0.51	4.3	0.06	2.3	NA	1.81	30.7	NA	1–4 mm mudstone
44-SMW	1020.5	0.60	5.0	0.06	2.1	NA	1.52	24.9	NA	>4 mm bulk
44-SMW	1020.5	0.72	6.0	0.06	2.3	NA	1.55	26.2	NA	>4 mm mudstone
44-SMW	1020.5	0.49	4.1	0.06	2.3	NA	1.81	30.8	NA	1–4 mm bulk
45-SMW	1025.5	0.48	4.0	0.06	2.2	NA	1.68	29.2	NA	>4 mm bulk
45-SMW	1025.5	0.57	4.8	0.06	2.4	NA	1.79	30.3	NA	1–4 mm mudstone
45-SMW	1025.5	0.54	4.5	0.06	2.5	NA	1.93	33.3	NA	1–4 mm bulk
45-SMW	1025.5	0.50	4.2	0.06	2.2	NA	1.69	28.0	NA	>4 mm mudstone
46-SMW	1030.5	0.54	4.5	0.06	2.2	NA	1.70	28.4	NA	>4 mm bulk
46-SMW	1030.5	0.55	4.6	0.06	2.5	NA	1.91	31.8	NA	1–4 mm bulk
47-SMW	1035.5	0.49	4.1	0.06	2.1	NA	1.62	28.1	NA	>4 mm bulk
47-SMW	1035.5	0.59	4.9	0.06	2.4	NA	1.81	30.6	NA	1–4 mm bulk
48-SMW	1040.5	0.53	4.4	0.06	2.1	NA	1.60	28.2	NA	>4 mm bulk
48-SMW	1040.5	0.73	6.1	0.06	2.5	NA	1.78	30.8	NA	1–4 mm bulk
49-SMW	1045.5	0.44	3.7	0.06	2.1	NA	1.61	28.5	NA	>4 mm bulk
49-SMW	1045.5	0.76	6.3	0.06	2.6	NA	1.80	31.9	NA	1–4 mm bulk
50-SMW	1050.5	0.54	4.5	0.06	2.2	NA	1.65	29.7	NA	>4 mm mudstone
50-SMW	1050.5	0.58	4.8	0.06	2.4	NA	1.77	30.8	NA	1–4 mm mudstone
50-SMW	1050.5	0.69	5.7	0.06	2.4	NA	1.75	30.9	NA	1–4 mm bulk
50-SMW	1050.5	0.44	3.6	0.06	2.0	NA	1.60	27.8	NA	>4 mm bulk
51-SMW	1055.5	0.64	5.3	0.06	2.4	NA	1.81	30.6	NA	1–4 mm bulk
51-SMW	1055.5	0.50	4.2	0.06	2.2	NA	1.69	27.9	NA	>4 mm bulk
52-SMW	1060.5	0.51	4.3	0.06	2.5	NA	1.94	30.0	NA	>4 mm bulk
52-SMW	1060.5	0.60	5.0	0.06	2.5	NA	1.92	34.4	NA	1–4 mm bulk
54-SMW	1070.5	0.51	4.2	0.06	2.3	NA	1.82	31.2	NA	1–4 mm bulk
54-SMW	1070.5	0.48	4.0	0.06	2.3	NA	1.80	31.8	NA	>4 mm bulk
56-SMW	1080.5	0.57	4.8	0.05	2.1	NA	1.57	28.8	NA	>4 mm bulk
56-SMW	1080.5	0.59	4.9	0.06	2.4	NA	1.80	32.3	NA	1–4 mm bulk
57-SMW	1085.5	0.66	5.5	0.06	2.5	NA	1.88	32.1	NA	1–4 mm bulk
58-SMW	1090.5	0.61	5.1	0.06	2.5	NA	1.90	32.5	NA	1–4 mm bulk
58-SMW	1090.5	0.47	3.9	0.06	2.2	NA	1.71	28.3	NA	>4 mm bulk
62-SMW	1100.5	0.41	3.4	0.06	2.0	NA	1.59	28.1	NA	>4 mm bulk
62-SMW	1100.5	0.54	4.5	0.06	2.5	NA	1.94	33.8	NA	1–4 mm bulk
64-SMW	1110.5	0.41	3.5	0.05	2.0	NA	1.54	28.3	NA	>4 mm bulk
64-SMW	1110.5	0.50	4.2	0.06	2.2	NA	1.65	29.3	NA	1–4 mm bulk
66-SMW	1120.5	0.44	3.7	0.05	2.2	NA	1.74	31.7	NA	1–4 mm bulk
66-SMW	1120.5	0.40	3.4	0.06	1.9	NA	1.53	27.3	NA	>4 mm bulk
68-SMW	1130.5	0.42	3.5	0.06	2.2	NA	1.78	31.3	NA	1–4 mm mudstone
68-SMW	1130.5	0.41	3.4	0.05	2.0	NA	1.63	31.0	NA	>4 mm bulk
68-SMW	1130.5	0.46	3.8	0.05	2.3	NA	1.81	34.5	NA	1–4 mm bulk
68-SMW	1130.5	0.42	3.5	0.06	2.1	NA	1.65	29.7	NA	>4 mm mudstone
71-SMW	1140.5	0.47	3.9	0.05	2.1	NA	1.68	31.3	NA	1–4 mm bulk
71-SMW	1140.5	0.41	3.4	0.05	2.0	NA	1.57	31.0	NA	>4 mm bulk
73-SMW	1150.5	0.39	3.3	0.05	2.0	NA	1.60	29.8	NA	>4 mm bulk
73-SMW	1150.5	0.49	4.1	0.06	2.3	NA	1.80	32.2	NA	1–4 mm bulk
75-SMW	1160.5	0.55	4.6	0.05	2.6	NA	2.01	36.5	NA	1–4 mm bulk
75-SMW	1160.5	0.35	2.9	0.05	2.0	NA	1.62	30.2	NA	>4 mm bulk
77-SMW	1170.5	0.47	3.9	0.05	2.5	NA	2.07	39.1	NA	1–4 mm bulk
77-SMW	1170.5	0.32	2.7	0.05	1.9	NA	1.61	32.7	NA	>4 mm bulk
80-SMW	1180.5	0.37	3.1	0.05	2.2	NA	1.79	33.0	NA	1–4 mm mudstone
80-SMW	1180.5	0.36	3.0	0.06	2.1	NA	1.72	31.3	NA	>4 mm bulk
80-SMW	1180.5	0.46	3.8	0.06	2.3	NA	1.80	32.6	NA	1–4 mm bulk
82-SMW	1190.5	0.46	3.8	0.06	2.3	NA	1.82	31.8	NA	1–4 mm bulk
82-SMW	1190.5	0.40	3.4	0.06	2.1	NA	1.70	30.3	NA	>4 mm bulk
84-SMW	1200.5	0.50	4.2	0.06	2.3	NA	1.83	32.6	NA	1–4 mm bulk
84-SMW	1200.5	0.38	3.2	0.05	2.1	NA	1.68	32.3	NA	>4 mm bulk
86-SMW	1210.5	0.42	3.5	0.06	2.4	NA	1.94	33.5	NA	1–4 mm bulk
90-SMW	1220.5	0.42	3.5	0.06	2.3	NA	1.90	33.8	NA	1–4 mm mudstone
90-SMW	1220.5	0.42	3.5	0.06	2.4	NA	1.94	34.7	NA	1–4 mm bulk
90-SMW	1220.5	0.36	3.0	0.05	1.8	NA	1.47	27.1	NA	>4 mm mudstone
92-SMW	1230.5	0.49	4.1	0.05	2.4	NA	1.95	36.6	NA	1–4 mm bulk
94-SMW	1240.5	0.55	4.6	0.05	2.4	NA	1.81	33.1	NA	1–4 mm bulk

Table T37 (continued). (Continued on next page.)

Cuttings sample	Depth (mbsf)	IC (wt%)	$CaCO_3$ (wt%)	TN (wt%)	TC (wt%)	TS (wt%)	TOC (wt%)	C/N	C/S	Remarks
95-SMW	1245.5	0.54	4.5	0.05	2.4	NA	1.85	35.3	NA	1–4 mm bulk
96-SMW	1250.5	0.58	4.8	0.05	2.5	NA	1.90	37.0	NA	1–4 mm bulk
98-SMW	1260.5	0.60	5.0	0.05	2.6	NA	1.96	38.0	NA	1–4 mm bulk
98-SMW	1260.5	0.49	4.0	0.06	2.1	NA	1.57	28.1	NA	>4 mm bulk
100-SMW	1270.5	0.58	4.8	0.05	2.4	NA	1.84	33.4	NA	1–4 mm mudstone
100-SMW	1270.5	0.41	3.4	0.06	2.1	NA	1.69	28.8	NA	>4 mm mudstone
100-SMW	1270.5	0.61	5.1	0.05	2.4	NA	1.78	35.6	NA	1–4 mm bulk
102-SMW	1280.5	0.70	5.8	0.05	2.5	NA	1.80	34.7	NA	1–4 mm bulk
104-SMW	1290.5	0.52	4.4	0.05	2.1	NA	1.59	30.1	NA	>4 mm mudstone
104-SMW	1290.5	0.55	4.6	0.05	2.3	NA	1.77	33.9	NA	1–4 mm bulk
106-SMW	1300.5	0.47	3.9	0.05	2.3	NA	1.85	34.8	NA	1–4 mm bulk
108-SMW	1310.5	0.46	3.8	0.05	2.2	NA	1.71	34.5	NA	1–4 mm bulk
110-SMW	1320.5	0.37	3.1	0.05	2.2	NA	1.84	36.3	NA	1–4 mm bulk
110-SMW	1320.5	0.42	3.5	0.05	2.2	NA	1.80	33.4	NA	1–4 mm mudstone
110-SMW	1320.5	0.41	3.4	0.06	2.1	NA	1.66	29.7	NA	>4 mm mudstone
112-SMW	1330.5	0.38	3.1	0.05	2.0	NA	1.65	31.8	NA	1–4 mm bulk
114-SMW	1340.5	0.36	3.0	0.06	2.1	NA	1.71	29.8	NA	1–4 mm bulk
115-SMW	1345.5	0.38	3.2	0.06	2.0	NA	1.65	28.5	NA	1–4 mm bulk
116-SMW	1350.5	0.43	3.6	0.05	2.2	NA	1.81	33.6	NA	1–4 mm bulk
120-SMW	1360.5	0.44	3.7	0.06	2.0	NA	1.58	27.3	NA	>4 mm mudstone
120-SMW	1360.5	0.44	3.7	0.06	2.1	NA	1.69	30.7	NA	1–4 mm bulk
122-SMW	1370.5	0.43	3.6	0.05	2.2	NA	1.77	32.9	NA	1–4 mm bulk
124-SMW	1380.5	0.40	3.3	0.06	2.1	NA	1.73	30.5	NA	1–4 mm bulk
124-SMW	1380.5	0.32	2.6	0.05	1.8	NA	1.48	28.6	NA	>4 mm bulk
126-SMW	1390.5	0.45	3.7	0.05	2.3	NA	1.89	34.4	NA	1–4 mm bulk
130-SMW	1400.5	0.42	3.5	0.06	2.0	NA	1.62	29.3	NA	>4 mm bulk
130-SMW	1400.5	0.44	3.7	0.06	2.3	NA	1.84	32.0	NA	1–4 mm bulk
130-SMW	1400.5	0.47	3.9	0.05	2.1	NA	1.65	30.5	NA	1–4 mm mudstone
132-SMW	1410.5	0.41	3.4	0.05	2.3	NA	1.87	35.0	NA	1–4 mm bulk
134-SMW	1420.5	0.40	3.4	0.05	2.0	NA	1.64	30.0	NA	1–4 mm bulk
134-SMW	1420.5	0.39	3.3	0.06	1.9	NA	1.53	26.9	NA	>4 mm bulk
136-SMW	1430.5	0.39	3.3	0.05	1.9	NA	1.46	29.0	NA	>4 mm bulk
136-SMW	1430.5	0.43	3.6	0.05	2.1	NA	1.64	32.0	NA	1–4 mm bulk
138-SMW	1440.5	0.41	3.4	0.05	2.1	NA	1.65	30.9	NA	1–4 mm bulk
138-SMW	1440.5	0.37	3.0	0.05	1.8	NA	1.45	26.5	NA	>4 mm bulk
139-SMW	1445.5	0.42	3.5	0.06	2.0	NA	1.61	29.2	NA	1–4 mm bulk
140-SMW	1450.5	0.37	3.1	0.05	2.0	NA	1.62	32.1	NA	1–4 mm bulk
142-SMW	1460.5	0.41	3.4	0.05	2.1	NA	1.64	30.1	NA	1–4 mm bulk
144-SMW	1470.5	0.44	3.7	0.06	2.0	NA	1.53	27.7	NA	1–4 mm bulk
148-SMW	1480.5	0.49	4.1	0.05	2.0	NA	1.47	27.5	NA	1–4 mm bulk
150-SMW	1490.5	0.39	3.2	0.05	1.8	NA	1.41	26.6	NA	1–4 mm bulk
153-SMW	1500.5	0.42	3.5	0.06	2.0	NA	1.55	27.6	NA	1–4 mm bulk
153-SMW	1500.5	0.38	3.2	0.06	2.0	NA	1.61	27.9	NA	>4 mm bulk
155-SMW	1510.5	0.50	4.2	0.05	1.9	NA	1.42	26.8	NA	1–4 mm bulk
155-SMW	1510.5	0.47	3.9	0.06	1.9	NA	1.40	25.0	NA	1–4 mm mudstone
158-SMW	1520.5	0.49	4.1	0.06	2.1	NA	1.61	27.7	NA	1–4 mm bulk
159-SMW	1525.5	0.49	4.1	0.06	2.0	NA	1.53	26.0	NA	1–4 mm bulk
161-SMW	1530.5	0.50	4.2	0.06	2.2	NA	1.74	31.1	NA	1–4 mm bulk
162-SMW	1535.5	0.52	4.3	0.06	2.4	NA	1.87	29.9	NA	1–4 mm bulk
163-SMW	1540.5	0.49	4.1	0.06	2.3	NA	1.78	29.7	NA	1–4 mm bulk
164-SMW	1545.5	0.47	4.0	0.06	2.3	NA	1.88	31.0	NA	1–4 mm bulk
167-SMW	1550.5	0.47	3.9	0.06	2.0	NA	1.54	26.7	NA	1–4 mm bulk
167-SMW	1550.5	0.43	3.6	0.06	1.6	NA	1.18	20.9	NA	>4 mm bulk
168-SMW	1555.5	0.47	3.9	0.06	2.1	NA	1.68	28.1	NA	1–4 mm bulk
169-SMW	1560.5	0.43	3.6	0.06	1.9	NA	1.42	24.0	NA	1–4 mm bulk
170-SMW	1565.5	0.41	3.4	0.06	1.9	NA	1.54	26.8	NA	1–4 mm bulk
172-SMW	1570.5	0.38	3.2	0.06	1.8	NA	1.39	24.8	NA	1–4 mm bulk
173-SMW	1575.5	0.40	3.3	0.06	1.9	NA	1.51	25.1	NA	1–4 mm bulk
174-SMW	1580.5	0.40	3.3	0.06	1.8	NA	1.36	23.2	NA	1–4 mm bulk
177-SMW	1590.5	0.40	3.3	0.05	1.8	NA	1.37	25.3	NA	1–4 mm bulk
178-SMW	1595.5	0.42	3.5	0.06	1.9	NA	1.45	25.3	NA	1–4 mm bulk
182-SMW	1600.5	0.43	3.6	0.06	1.9	NA	1.43	23.1	NA	>4 mm bulk
182-SMW	1600.5	0.42	3.5	0.06	1.8	NA	1.33	23.2	NA	1–4 mm mudstone
182-SMW	1600.5	0.43	3.6	0.06	1.8	NA	1.37	24.4	NA	1–4 mm bulk
184-SMW	1610.5	0.41	3.4	0.06	2.0	NA	1.56	25.4	NA	1–4 mm bulk
187-SMW	1620.5	0.45	3.8	0.06	1.8	NA	1.30	22.8	NA	1–4 mm bulk
189-SMW	1630.5	0.42	3.5	0.05	1.6	NA	1.20	23.0	NA	1–4 mm bulk
193-SMW	1640.5	0.44	3.7	0.05	1.5	NA	1.04	20.1	NA	1–4 mm bulk
195-SMW	1650.5	0.46	3.8	0.05	1.5	NA	1.08	20.1	NA	1–4 mm bulk

Table T37 (continued).

Cuttings sample	Depth (mbsf)	IC (wt%)	$CaCO_3$ (wt%)	TN (wt%)	TC (wt%)	TS (wt%)	TOC (wt%)	C/N	C/S	Remarks
195-SMW	1650.5	0.41	3.5	0.06	1.4	NA	1.00	18.0	NA	>4 mm bulk
196-SMW	1655.5	0.48	4.0	0.06	1.7	NA	1.19	20.6	NA	1–4 mm bulk
199-SMW	1660.5	0.38	3.2	0.06	1.5	NA	1.14	19.8	NA	1–4 mm bulk
201-SMW	1670.5	0.41	3.4	0.05	1.5	NA	1.10	21.7	NA	1–4 mm bulk
203-SMW	1680.5	0.50	4.2	0.06	1.7	NA	1.15	20.8	NA	1–4 mm bulk
205-SMW	1690.5	0.46	3.9	0.06	1.7	NA	1.19	21.5	NA	1–4 mm bulk
206-SMW	1695.5	0.53	4.4	0.06	1.7	NA	1.13	18.8	NA	1–4 mm bulk
207-SMW	1700.5	0.40	3.3	0.06	1.5	NA	1.09	19.3	NA	>4 mm bulk
207-SMW	1700.5	0.50	4.1	0.06	1.7	NA	1.21	20.8	NA	1–4 mm bulk
207-SMW	1700.5	0.46	3.9	0.06	1.7	NA	1.21	20.4	NA	1–4 mm mudstone
209-SMW	1710.5	0.52	4.3	0.06	1.7	NA	1.19	20.3	NA	1–4 mm bulk
211-SMW	1720.5	0.48	4.0	0.06	1.6	NA	1.17	20.0	NA	1–4 mm bulk
213-SMW	1730.5	0.53	4.4	0.06	1.7	NA	1.20	21.4	NA	1–4 mm bulk
215-SMW	1740.5	0.48	4.0	0.06	1.7	NA	1.20	21.4	NA	1–4 mm bulk
217-SMW	1750.5	0.54	4.5	0.06	1.7	NA	1.16	20.4	NA	1–4 mm bulk
219-SMW	1760.5	0.43	3.6	0.05	1.5	NA	1.04	19.5	NA	>4 mm bulk
219-SMW	1760.5	0.54	4.5	0.06	1.7	NA	1.12	19.4	NA	1–4 mm bulk
223-SMW	1770.5	0.50	4.2	0.06	1.7	NA	1.16	20.3	NA	1–4 mm bulk
227-SMW	1780.5	0.41	3.4	0.06	1.7	NA	1.31	21.6	NA	1–4 mm bulk
229-SMW	1790.5	0.53	4.4	0.06	1.7	NA	1.20	20.4	NA	1–4 mm bulk
230-SMW	1795.5	0.53	4.4	0.06	2.2	NA	1.71	30.0	NA	1–4 mm bulk
231-SMW	1800.5	0.52	4.3	0.06	1.8	NA	1.24	21.0	NA	1–4 mm bulk
231-SMW	1800.5	0.48	4.0	0.06	1.7	NA	1.22	21.0	NA	1–4 mm mudstone
231-SMW	1800.5	0.42	3.5	0.06	1.5	NA	1.06	18.7	NA	>4 mm bulk
233-SMW	1810.5	0.47	3.9	0.06	1.7	NA	1.22	20.1	NA	1–4 mm bulk
235-SMW	1820.5	0.49	4.1	0.06	1.7	NA	1.22	19.5	NA	1–4 mm bulk
238-SMW	1830.5	0.43	3.6	0.06	1.7	NA	1.31	21.9	NA	1–4 mm bulk
240-SMW	1840.5	0.39	3.3	0.06	1.6	NA	1.25	20.3	NA	1–4 mm bulk
250-SMW	1850.5	0.38	3.1	0.06	1.7	NA	1.36	22.9	NA	1–4 mm bulk
250-SMW	1850.5	0.35	2.9	0.06	1.8	NA	1.42	23.1	NA	>4 mm bulk
253-SMW	1860.5	0.43	3.6	0.06	1.7	NA	1.26	20.2	NA	1–4 mm bulk
255-SMW	1870.5	0.36	3.0	0.06	1.6	NA	1.28	21.0	NA	1–4 mm bulk
258-SMW	1880.5	0.39	3.2	0.06	1.5	NA	1.11	18.7	NA	1–4 mm bulk
260-SMW	1890.5	0.45	3.8	0.06	1.5	NA	1.01	16.6	NA	1–4 mm bulk
260-SMW	1890.5	0.34	2.8	0.05	1.1	NA	0.80	15.5	NA	>4 mm bulk
261-SMW	1895.5	0.51	4.2	0.06	1.6	NA	1.06	17.4	NA	1–4 mm bulk
263-SMW	1900.5	0.56	4.6	0.06	1.6	NA	1.00	17.4	NA	1–4 mm mudstone
263-SMW	1900.5	0.56	4.6	0.06	1.6	NA	1.00	17.1	NA	1–4 mm bulk
265-SMW	1910.5	0.60	5.0	0.06	1.6	NA	0.97	16.5	NA	1–4 mm bulk
267-SMW	1920.5	0.65	5.4	0.06	1.6	NA	0.93	15.6	NA	1–4 mm bulk
269-SMW	1930.5	0.69	5.7	0.06	1.6	NA	0.96	16.4	NA	1–4 mm bulk
272-SMW	1940.5	0.77	6.4	0.06	1.7	NA	0.90	15.0	NA	1–4 mm bulk
274-SMW	1950.5	0.75	6.3	0.06	1.7	NA	0.94	15.8	NA	1–4 mm bulk
280-SMW	1960.5	0.67	5.6	0.06	1.7	NA	0.99	16.4	NA	1–4 mm bulk
311-SMW	1970	0.50	4.2	0.06	1.4	NA	0.86	15.1	NA	1–4 mm bulk
282-SMW	1970.5	0.65	5.4	0.06	1.6	NA	0.98	15.6	NA	1–4 mm bulk
312-SMW	1977.5	0.48	4.0	0.06	1.3	NA	0.80	13.7	NA	1–4 mm bulk
284-SMW	1980.5	0.59	4.9	0.06	1.6	NA	0.99	15.9	NA	1–4 mm bulk
286-SMW	1990.5	0.52	4.4	0.06	1.5	NA	0.99	15.9	NA	1–4 mm bulk
288-SMW	1995.5	0.49	4.1	0.06	1.4	NA	0.96	15.1	NA	1–4 mm bulk
289-SMW	2000.5	0.43	3.6	0.06	1.5	NA	1.08	17.0	NA	1–4 mm bulk
289-SMW	2000.5	0.40	3.3	0.06	1.4	NA	1.00	15.7	NA	1–4 mm mudstone

IC = inorganic carbon, TN = total nitrogen, TC = total carbon, TS = total sulfur, TOC = total organic carbon. NA = not analyzed.

Table T38. Errors in core liner thickness, *P*-wave velocity, and gamma density of a core liner filled with water caused by 2 cm offset of measurement point, Site C0002.

Interval (cm)	Core thickness (cm) Correct position	Wrong position	Difference	Error (%)	*P*-wave (m/s) Correct position	Wrong position	Difference	Error (%)	Gamma density (g/cm³) Correct position	Wrong position	Difference	Error (%)
*4	6.862	6.895	–0.033	0.48								
8	6.641	6.731	–0.09	1.36	1486.347	1488.172	–1.825	0.12	1.0177	1.007	0.0107	1.05
12	6.612	6.651	–0.039	0.59	1488.184	1477.015	11.169	0.75	1.0257	1.0176	0.0081	0.79
16	6.601	6.64	–0.039	0.59	1490.741	1477.854	12.887	0.86	1.0046	1.0159	–0.0113	1.12
20	6.595	6.633	–0.038	0.58	1491.069	1479.59	11.479	0.77	1.0115	1.0147	–0.0032	0.32
24	6.587	6.623	–0.036	0.55	1485.901	1487.312	–1.411	0.09	1.027	1.0285	–0.0015	0.15
28	6.586	6.609	–0.023	0.35	1489.035	1489.184	–0.149	0.01	1.0286	1.0211	0.0075	0.73
32	6.598	6.613	–0.015	0.23	1491.748	1486.736	5.012	0.34	1.0126	1.0319	–0.0193	1.91
*36	6.872	6.682	0.19	2.76	1483.272	1437.608	45.664	3.08	0.9886	1.0313	–0.0427	4.32
*40	6.908	6.896	0.012	0.17	1508.956	1509.632	–0.676	0.04	0.9538	0.9277	0.0261	2.74

* = 0–2.5 and 37.5–40 cm are end cap; 0–4.5 and 35–40 cm are wrapping vinyl tape. Core thickness resolution = 0.02 mm, *P*-wave accuracy = 0.2%, gamma density resolution is better than 1%. (information from GEOTEK, www.geotek.co.uk/products/mscl-s/)

Table T39. Moisture and density measurements from core measurements, Site C0002. (Continued on next five pages.)

Core, section, interval (cm)	Depth (mbsf)	Density (g/cm³) Bulk	Grain	Porosity (%)	Void ratio	Notes
338-C0002K-						
1H-1, 113.0	201.13	1.756	2.683	55.87	1.2661	
1H-2, 74.0	202.075	1.684	2.760	61.98	1.6299	Carbonate rich
1H-4, 4.0	202.925	1.664	2.668	61.04	1.5668	Cluster
1H-4, 75.0	203.635	2.002	2.756	43.51	0.7702	Sand
1H-5, 0.0	204.29	1.704	2.718	59.86	1.4912	
1H-6, 35.0	205.015	1.733	2.668	56.89	1.3196	
2H-1, 22.0	204.72	1.609	2.699	65.06	1.862	
2H-1, 58.0	205.08	1.796	2.542	49.16	0.9668	
3T-1, 14.0	205.64	1.761	2.739	57.02	1.3267	
3T-1, 56.0	206.06	1.823	2.757	53.91	1.1694	Sand
3T-2, 35.0	206.75	1.828	2.695	51.85	1.0769	Sand
3T-2, 60.0	207	1.740	2.683	56.83	1.3165	
3T-3, 59.0	207.86	1.920	2.692	46.3	0.8621	
3T-3, 60.0	207.87	1.993	2.767	44.4	0.7986	Sand
3T-4, 25.0	208.725	1.836	2.757	53.12	1.1331	
3T-4, 134.0	209.815	1.886	2.774	50.73	1.0296	
3T-6, 13.0	210.425	1.897	2.763	49.8	0.9919	
3T-6, 126.0	211.555	1.996	2.763	44.12	0.7895	
3T-7, 31.0	211.995	1.988	2.721	43.16	0.7595	
4T-1, 9.0	215.09	1.977	2.800	46.37	0.8648	Sand
4T-1, 36.0	215.36	1.858	2.789	52.75	1.1164	
4T-3, 0.0	215.715	1.890	2.740	49.56	0.9827	
4T-4, 80.0	216.915	2.004	2.714	42	0.7242	Sand
4T-4, 101.0	217.125	2.044	2.747	40.81	0.6896	
5T-1, 14.0	220.14	1.739	2.762	58.86	1.4304	
5T-1, 42.0	220.42	1.913	2.733	48.02	0.9237	Sand
5T-2, 23.0	220.965	2.084	2.714	37.27	0.5941	Sand
5T-3, 73.0	222.445	2.004	2.962	49.44	0.9777	
5T-4, 8.0	222.69	1.866	2.671	48.91	0.9572	Sand
5T-7, 0.0	224.515	1.756	2.715	56.7	1.3093	
5T-8, 50.0	226.005	1.990	2.689	41.98	0.7234	Sand
6T-1, 20.0	229.7	1.594	2.717	66.35	1.9717	
6T-2, 3.0	230.53	1.631	2.687	63.51	1.7406	
6T-2, 73.0	231.23	1.652	2.744	63.49	1.7392	
6T-4, 17.0	231.815	1.967	2.788	46.57	0.8717	
6T-4, 64.0	232.285	1.777	2.659	53.96	1.1719	
6T-4, 95.0	232.595	1.956	2.695	44.27	0.7943	
7X-1, 46.0	239.46	1.777	2.691	54.83	1.2138	
7X-2, 38.0	239.98	1.887	2.694	48.35	0.9363	

Table T39 (continued). (Continued on next page.)

Core, section, interval (cm)	Depth (mbsf)	Density (g/cm³)		Porosity (%)	Void ratio	Notes
		Bulk	Grain			
7X-3, 20.0	240.41	1.941	2.722	46.01	0.8521	Sand
7X-3, 45.0	240.66	1.849	2.781	53.02	1.1284	
7X-4, 63.0	241.43	1.892	2.771	50.33	1.0132	
7X-4, 87.0	241.67	1.959	2.726	45.06	0.8201	Sand
7X-4, 106.0	241.86	1.892	2.688	47.88	0.9185	Cluster
7X-6, 16.0	242.365	1.848	2.695	50.72	1.0292	
7X-6, 77.0	242.975	1.980	2.888	48.73	0.9503	
7X-7, 20.0	243.7	1.816	2.705	52.89	1.1227	
8X-1, 20.0	248.7	1.674	2.696	61.15	1.5737	
8X-1, 110.0	249.6	1.728	2.702	58.02	1.3823	
8X-3, 0.0	250.395	1.811	2.697	52.97	1.1261	
8X-3, 107.0	251.465	1.820	2.693	52.28	1.0954	
8X-4, 20.0	251.85	1.851	2.702	50.69	1.0279	
8X-4, 116.0	252.81	1.753	2.691	56.28	1.2872	
8X-5, 15.0	253.205	1.788	2.707	54.63	1.2041	
8X-5, 116.0	254.215	1.832	2.744	53.01	1.1282	
9X-1, 30.0	258.3	1.841	2.682	50.72	1.0293	
9X-1, 96.0	258.96	1.892	2.696	48.08	0.9259	Sand
9X-2, 11.0	259.115	1.879	2.649	47.37	0.9	Soupy
9X-2, 81.0	259.815	1.891	2.719	48.82	0.954	
9X-4, 0.0	260.385	1.768	2.687	55.24	1.2339	
9X-4, 43.0	260.815	1.954	2.707	44.76	0.8104	Sand
9X-5, 20.0	261.99	1.868	2.811	52.78	1.1176	
9X-5, 120.0	262.99	1.931	2.676	45.07	0.8206	
9X-6, 19.0	263.38	1.936	2.783	48.16	0.9291	Sand
9X-6, 122.0	264.41	1.818	2.720	53.2	1.1368	
9X-7, 7.0	264.67	1.834	2.650	50.17	1.0069	
9X-7, 121.0	265.81	1.945	2.697	44.93	0.8158	Sandy
9X-8, 7.0	266.07	1.775	2.647	53.71	1.1603	
9X-8, 89.0	266.89	1.949	2.649	43.09	0.757	Sandy
10X-1, 14.0	267.64	1.914	2.694	46.67	0.8752	Sandy
10X-3, 0.0	268.185	1.919	2.724	47.36	0.8999	
10X-4, 0.0	269.075	1.931	2.705	46.04	0.8531	Sandy
10X-4, 80.0	269.875	1.797	2.667	52.93	1.1243	
10X-5, 50.0	270.82	1.867	2.725	50.45	1.0182	
10X-5, 135.0	271.67	1.806	2.741	54.46	1.1957	
10X-6, 70.0	272.44	1.797	2.743	55.02	1.223	
10X-7, 93.0	274.08	1.963	2.668	42.88	0.7508	Sand
11X-1, 26.0	277.26	1.790	2.763	55.99	1.2721	
11X-3, 2.0	277.75	2.017	2.798	44.02	0.7864	
11X-3, 140.0	279.13	2.004	2.746	43.1	0.7576	
11X-4, 63.0	279.85	1.798	2.715	54.21	1.1841	
11X-4, 86.0	280.08	1.874	2.834	53.06	1.1304	
338-C0002L-						
1X-1, 30.0	277.3	1.879	2.721	49.58	0.9835	
1X-1, 105.0	278.05	1.766	2.705	55.86	1.2655	
1X-2, 6.0	278.25	1.868	2.700	49.67	0.9867	Sand
1X-2, 81.0	279	1.807	2.711	53.61	1.1555	
1X-3, 21.0	279.435	1.910	2.852	51.52	1.0627	
1X-3, 127.0	280.495	1.709	2.720	59.58	1.4742	
1X-5, 31.0	281.14	1.925	2.677	45.48	0.8341	Sand
1X-5, 98.0	281.81	1.827	2.708	52.32	1.0972	
1X-6, 16.0	282.405	1.926	2.731	47.15	0.892	
1X-6, 103.0	283.275	1.874	2.726	50.06	1.0023	
1X-7, 74.0	284.335	1.910	2.724	47.86	0.9178	Sand
1X-7, 129.0	284.885	1.951	2.688	44.31	0.7957	
2X-1, 27.0	286.77	1.874	2.679	48.63	0.9466	
2X-2, 0.0	286.98	1.797	2.669	53.04	1.1296	
3X-1, 20.0	296.2	1.706	2.602	56.78	1.3138	
3X-1, 103.0	297.03	1.813	2.462	45.15	0.823	
3X-3, 110.0	298.49	1.799	2.510	47.84	0.9174	
3X-4, 58.0	299.27	1.959	2.715	44.73	0.8092	
4X-1, 25.0	305.75	1.762	2.712	56.29	1.2878	
4X-3, 0.0	307.05	1.691	2.718	60.59	1.5376	
4X-3, 80.0	307.85	1.751	2.773	58.44	1.4063	
4X-4, 44.0	308.74	1.654	2.641	61.06	1.5682	
4X-4, 78.0	309.08	1.802	2.692	53.35	1.1436	Sand
4X-5, 60.0	310.11	1.739	2.774	59.12	1.4464	

Table T39 (continued). (Continued on next page.)

Core, section, interval (cm)	Depth (mbsf)	Density (g/cm³)		Porosity (%)	Void ratio	Notes
		Bulk	Grain			
4X-5, 120.0	310.71	1.685	2.624	58.68	1.4204	
4X-6, 20.0	311.105	1.728	2.670	57.25	1.3394	
4X-6, 73.0	311.635	1.774	2.759	56.77	1.3134	
4X-7, 18.0	312.46	1.765	2.690	55.55	1.2496	
4X-8, 70.0	313.845	1.779	2.602	52.12	1.0888	
5X-1, 15.0	315.15	1.749	2.716	57.16	1.3344	
5X-1, 120.0	316.2	1.795	2.710	54.23	1.185	
5X-2, 60.0	317	1.892	2.844	52.33	1.0979	
5X-4, 50.0	318.195	1.879	2.714	49.38	0.9756	
5X-4, 76.0	318.455	1.894	2.729	49.02	0.9614	
5X-5, 13.0	318.88	1.883	2.721	49.41	0.9769	
5X-6, 15.0	320.135	1.950	2.681	44.08	0.7882	
5X-6, 75.0	320.735	1.941	2.697	45.18	0.824	
5X-8, 10.0	321.945	2.011	2.776	43.67	0.7752	
5X-8, 80.0	322.645	1.900	2.685	47.27	0.8964	
5X-9, 55.0	323.375	1.950	2.725	45.59	0.8377	
6X-1, 16.0	324.66	1.806	2.740	54.45	1.1952	
6X-1, 66.0	325.16	1.945	2.692	44.8	0.8116	
6X-2, 15.0	325.465	1.892	2.675	47.42	0.9017	
6X-2, 121.0	326.525	1.846	2.662	49.85	0.9938	
6X-3, 20.0	326.93	1.943	2.719	45.81	0.8453	
6X-5, 103.0	328.475	1.793	2.709	54.34	1.19	Sand
6X-6, 11.0	328.78	1.923	2.778	48.78	0.9524	
6X-6, 57.0	329.24	1.846	2.688	50.6	1.0241	Sandy
6X-7, 17.0	330.07	1.829	2.753	53.45	1.1482	
6X-7, 98.0	330.88	1.854	2.722	51.1	1.0452	
6X-8, 12.0	331.42	1.947	2.736	46.07	0.8544	
6X-8, 109.0	332.39	1.807	2.835	56.74	1.3116	
6X-9, 13.0	332.55	1.813	2.748	54.26	1.1861	
6X-9, 78.0	333.2	1.850	2.747	52.06	1.0861	
7X-1, 23.0	334.23	1.746	2.788	59.1	1.4448	
7X-1, 71.0	334.71	1.878	2.734	50.05	1.0021	
7X-3, 0.0	335.36	1.843	2.723	51.78	1.0738	
7X-3, 90.0	336.26	1.942	2.713	45.67	0.8407	
8X-1, 4.0	343.54	1.887	2.747	49.93	0.9971	
8X-2, 28.0	344.085	1.867	2.710	50.02	1.0009	Sand
8X-2, 105.0	344.855	1.875	2.726	49.98	0.9991	
8X-3, 20.0	345.18	1.985	2.741	44.06	0.7875	Sand
8X-3, 91.0	345.89	1.899	2.732	48.78	0.9524	
8X-5, 0.0	346.7	1.839	2.723	52	1.0832	
8X-5, 75.0	347.45	1.904	2.793	50.28	1.0112	Sand
8X-6, 53.0	348.635	1.889	2.685	47.94	0.9208	Sand
8X-6, 113.0	349.235	1.901	2.743	48.99	0.9604	
8X-7, 43.0	349.945	1.894	2.678	47.43	0.9021	Sand
8X-7, 73.0	350.245	1.823	2.652	50.92	1.0375	
8X-8, 11.0	351.03	1.812	2.691	52.73	1.1157	
8X-9, 6.0	351.68	1.953	2.739	45.79	0.8448	
8X-9, 71.0	352.33	1.938	2.729	46.43	0.8666	
9X-1, 9.0	353.09	1.976	2.800	46.37	0.8646	
9X-1, 40.0	353.4	1.863	2.723	50.65	1.0263	
9X-2, 36.0	353.98	1.896	2.739	49.14	0.966	
9X-3, 25.0	354.53	1.897	2.746	49.32	0.9731	Sand
9X-3, 80.0	355.08	1.859	2.733	51.14	1.0465	
9X-4, 20.0	355.405	1.958	2.745	45.75	0.8432	
9X-4, 70.0	355.905	1.953	2.726	45.41	0.8318	
9X-6, 0.0	356.725	1.939	2.761	47.31	0.8977	
9X-6, 34.5	357.07	1.899	2.750	49.29	0.9719	
9X-7, 20.0	357.92	1.936	2.714	46.02	0.8525	
9X-7, 81.0	358.53	1.988	2.728	43.4	0.7668	Sand
9X-8, 70.0	359.405	1.770	2.711	55.78	1.2616	Sand
9X-8, 95.0	359.655	1.987	2.764	44.66	0.8071	
10X-1, 34.0	362.84	1.836	2.719	52.1	1.0878	
10X-1, 100.0	363.5	1.705	2.734	60.17	1.5106	Soupy clay
10X-2, 99.0	364.625	1.965	2.756	45.67	0.8406	
10X-4, 32.0	365.36	1.838	2.736	52.45	1.1032	
10X-5, 25.0	365.65	1.913	2.707	47.16	0.8925	
10X-5, 87.0	366.27	1.821	2.615	49.89	0.9957	Sand
10X-6, 43.0	367.05	1.886	2.742	49.79	0.9917	Sand
10X-7, 14.0	367.58	1.918	2.755	48.39	0.9374	

Table T39 (continued). (Continued on next page.)

Core, section, interval (cm)	Depth (mbsf)	Density (g/cm³) Bulk	Density (g/cm³) Grain	Porosity (%)	Void ratio	Notes
10X-7, 111.0	368.55	1.933	2.749	47.31	0.8978	Sand
10X-8, 54.0	369.225	1.859	2.736	51.25	1.0515	
11X-1, 63.0	372.63	1.867	2.776	51.87	1.0776	Sand
11X-1, 80.0	372.8	1.836	2.721	52.14	1.0893	
11X-2, 80.0	373.995	1.871	2.684	48.95	0.9589	
11X-3, 20.0	374.83	1.741	2.661	56.18	1.2822	Soupy
11X-3, 62.0	375.25	1.830	2.744	53.12	1.1332	
11X-6, 13.0	376.345	1.727	2.612	55.71	1.2577	
12X-1, 14.0	381.64	1.949	2.796	47.77	0.9147	
12X-1, 103.0	382.53	1.843	2.645	49.48	0.9794	
12X-2, 60.0	383.33	1.947	2.763	46.95	0.8849	
12X-3, 70.0	384.44	1.873	2.695	49.16	0.967	
12X-4, 10.0	384.94	1.874	2.696	49.15	0.9664	
12X-4, 104.0	385.88	1.881	2.681	48.26	0.9326	
12X-5, 25.0	386.5	1.879	2.707	49.17	0.9673	
12X-6, 15.0	387.25	1.902	2.710	47.93	0.9205	
12X-7, 32.0	388.27	1.938	2.750	47.07	0.8891	
12X-8, 73.0	389.095	1.941	2.765	47.31	0.898	
13X-1, 47.0	391.47	1.895	2.748	49.5	0.9801	
13X-2, 80.0	392.92	1.857	2.732	51.24	1.0508	
13X-3, 81.0	394.345	1.838	2.716	51.91	1.0794	
13X-4, 45.0	395.255	1.813	2.751	54.28	1.1873	
13X-5, 37.0	396.505	1.809	2.684	52.7	1.1139	
13X-6, 27.0	397.005	1.803	2.697	53.45	1.148	
13X-6, 95.0	397.685	1.790	2.683	53.82	1.1652	
13X-7, 30.0	398.455	1.723	2.732	59.04	1.4415	
14X-1, 32.0	400.82	1.787	2.700	54.46	1.1959	
14X-1, 105.0	401.55	1.844	2.724	51.75	1.0726	
14X-2, 12.0	402.02	1.843	2.703	51.22	1.0501	
14X-2, 42.0	402.32	1.928	2.759	47.91	0.9196	Sand
14X-2, 100.0	402.9	1.759	2.780	58.12	1.3878	
14X-4, 28.0	403.735	1.812	2.823	56.18	1.2823	
14X-4, 120.0	404.655	1.771	2.707	55.59	1.2518	
14X-5, 3.0	404.885	1.804	2.705	53.61	1.1555	
14X-5, 116.0	406.015	1.850	2.711	51.02	1.0417	
14X-6, 13.0	406.395	1.887	2.761	50.32	1.0129	
14X-6, 123.0	407.495	1.916	2.742	48.05	0.9251	
14X-7, 86.0	408.525	1.965	2.763	45.9	0.8483	Sand
14X-7, 137.0	409.035	1.906	2.740	48.57	0.9445	
14X-8, 29.0	409.37	1.890	2.739	49.48	0.9795	
15X-1, 23.0	410.23	1.941	2.720	45.96	0.8504	
15X-2, 9.0	410.945	1.945	2.786	47.72	0.9126	
15X-3, 7.0	411.855	1.929	2.831	49.94	0.9974	Sand
15X-5, 0.0	412.575	1.874	2.805	52.29	1.0962	
15X-6, 15.0	413.515	1.926	2.738	47.36	0.8996	
15X-6, 137.0	414.735	1.836	2.754	53.09	1.1315	Sand
15X-7, 70.0	415.465	1.764	2.871	59.92	1.4951	Sand/Soupy mud
15X-7, 118.0	415.945	1.927	2.760	47.99	0.9226	
15X-8, 12.0	416.285	1.938	2.761	47.4	0.9012	
15X-8, 129.0	417.455	2.001	2.926	48.65	0.9473	Soupy sand
15X-9, 12.0	417.605	1.928	2.786	48.68	0.9486	
15X-9, 74.0	418.225	1.951	2.751	46.34	0.8635	
15X-10, 47.0	418.945	1.925	2.782	48.72	0.95	
16X-1, 50.0	420	1.842	2.734	52.18	1.0911	
16X-2, 65.0	421.125	1.851	2.745	51.94	1.0806	
16X-2, 135.0	421.825	1.866	2.794	52.42	1.1017	
16X-4, 33.0	422.71	1.909	2.715	47.65	0.9104	
16X-4, 94.0	423.32	1.925	2.761	48.12	0.9275	
16X-5, 20.0	423.98	1.918	2.700	46.64	0.874	
16X-5, 64.0	424.42	1.938	2.691	45.18	0.8241	Sand
16X-6, 19.0	425.175	1.871	2.703	49.58	0.9831	
16X-6, 110.0	426.085	1.871	2.705	49.63	0.9854	
16X-7, 40.0	426.805	1.996	2.711	42.41	0.7364	Sand
16X-7, 95.0	427.355	1.884	2.669	47.76	0.9142	
16X-8, 81.0	428.385	1.943	2.713	45.59	0.8379	
17X-1, 25.0	429.25	1.962	2.762	46.02	0.8524	
17X-1, 107.0	430.07	1.913	2.755	48.65	0.9472	Sand
17X-2, 10.0	430.25	1.826	2.767	53.98	1.1729	
17X-3, 43.0	431.355	1.881	2.699	48.81	0.9535	

Table T39 (continued). (Continued on next page.)

Core, section, interval (cm)	Depth (mbsf)	Density (g/cm^3) Bulk	Density (g/cm^3) Grain	Porosity (%)	Void ratio	Notes
17X-3, 76.0	431.685	1.979	2.758	44.92	0.8156	
17X-5, 49.0	432.745	1.844	2.752	52.52	1.1061	
17X-5, 104.0	433.295	1.943	2.714	45.6	0.8381	Sand
17X-6, 65.0	434.175	2.034	2.822	43.8	0.7795	
17X-6, 133.0	434.855	1.950	2.754	46.5	0.869	
17X-7, 47.0	435.375	1.882	2.720	49.42	0.9769	
17X-8, 6.0	435.875	1.942	2.772	47.51	0.9052	
17X-8, 59.0	436.405	2.035	2.764	41.92	0.7218	Sand
17X-9, 60.0	437.605	1.944	2.773	47.43	0.9024	
18X-1, 64.0	439.14	1.896	2.747	49.39	0.9758	
18X-2, 63.0	440.03	1.919	2.733	47.6	0.9085	
18X-4, 0.0	440.7	1.916	2.779	49.16	0.9671	
18X-4, 92.0	441.62	1.926	2.747	47.66	0.9105	
18X-5, 90.0	443	1.953	2.738	45.81	0.8455	
18X-5, 122.0	443.32	2.056	2.708	38.74	0.6324	Sand
18X-6, 20.0	443.705	1.963	2.780	46.54	0.8707	
18X-6, 86.0	444.365	2.051	2.672	37.67	0.6043	Sand
18X-7, 55.0	445.465	1.882	2.722	49.44	0.9779	
18X-7, 104.0	445.955	2.042	2.743	40.75	0.6878	Sandy
18X-8, 57.0	446.895	1.943	2.785	47.84	0.9173	
19X-1, 52.0	448.52	1.925	2.750	47.8	0.9155	
19X-1, 110.0	449.1	1.937	2.818	49.12	0.9654	
19X-2, 30.0	449.515	1.891	2.738	49.41	0.9768	
19X-4, 5.0	450.95	1.939	2.735	46.52	0.8699	
19X-4, 114.0	452.04	1.735	2.479	51.11	1.0456	
19X-5, 10.0	452.265	1.777	2.405	45.47	0.8339	
19X-5, 99.0	453.155	2.023	2.736	41.63	0.7131	Sand
19X-6, 10.0	453.52	1.903	2.741	48.8	0.9531	
19X-6, 122.0	454.64	1.959	2.792	47.09	0.8899	
19X-7, 2.0	454.77	1.973	2.722	44.12	0.7894	Sand
19X-7, 80.0	455.55	1.938	2.725	46.25	0.8604	
20X-1, 16.0	457.66	1.938	2.742	46.82	0.8805	
20X-1, 102.0	458.52	2.031	2.761	42.01	0.7245	Sandy
20X-3, 32.0	459.365	1.942	2.748	46.75	0.8778	
20X-3, 119.0	460.235	1.935	2.763	47.61	0.9089	
20X-4, 9.0	460.545	1.937	2.778	47.95	0.9213	
20X-4, 103.0	461.485	1.928	2.734	47.16	0.8923	
20X-5, 15.0	462.015	1.901	2.696	47.56	0.9068	
20X-5, 131.0	463.175	1.907	2.729	48.22	0.9314	
20X-6, 8.0	463.355	1.912	2.731	48	0.9232	
20X-6, 112.0	464.395	1.896	2.695	47.8	0.9157	
20X-7, 14.0	464.665	1.925	2.778	48.65	0.9475	
20X-7, 130.0	465.825	1.954	2.769	46.72	0.8768	
20X-8, 3.0	465.88	1.945	2.791	47.86	0.9179	
21X-1, 31.0	467.31	1.893	2.781	50.53	1.0214	
21X-1, 132.0	468.32	1.873	2.707	49.59	0.9837	
21X-2, 20.0	468.615	1.845	2.708	51.24	1.0509	
21X-2, 109.0	469.505	1.894	2.701	48.14	0.9282	
21X-3, 10.0	469.715	1.886	2.661	47.37	0.9001	
21X-5, 0.0	471.065	1.815	2.706	52.94	1.1248	
21X-5, 102.0	472.085	1.852	2.778	52.78	1.1178	
21X-6, 33.0	472.8	1.825	2.670	51.36	1.0561	
21X-6, 129.0	473.76	1.824	2.778	54.38	1.1922	
21X-7, 66.0	474.445	1.784	2.728	55.38	1.2411	
21X-7, 127.0	475.055	1.826	2.720	52.7	1.1141	
21X-8, 61.0	475.735	1.896	2.744	49.28	0.9718	
22X-1, 10.0	476.6	1.915	2.702	46.89	0.8828	
22X-2, 31.0	477.47	1.873	2.696	49.22	0.9692	
22X-4, 8.0	478.07	1.894	2.687	47.66	0.9107	
22X-4, 90.0	478.89	1.818	2.680	52.06	1.086	Sand
22X-5, 18.0	479.4	1.819	2.731	53.42	1.147	
22X-5, 98.0	480.2	1.799	2.684	53.3	1.1415	Sand
22X-7, 19.0	480.995	1.747	2.621	54.74	1.2094	Soup
22X-8, 10.0	481.33	1.888	2.697	48.34	0.9359	
22X-8, 136.0	482.59	1.921	2.757	48.31	0.9345	
24X-1, 14.0	495.64	1.897	2.728	48.79	0.9528	
24X-1, 129.0	496.79	1.977	2.758	45.04	0.8193	
24X-2, 40.0	497.295	1.890	2.672	47.49	0.9043	Sand
24X-2, 101.0	497.905	1.835	2.726	52.37	1.0995	

Table T39 (continued).

Core, section, interval (cm)	Depth (mbsf)	Density (g/cm³)		Porosity (%)	Void ratio	Notes
		Bulk	Grain			
24X-3, 55.0	498.81	1.874	2.710	49.58	0.9833	Sand
24X-3, 115.0	499.41	1.919	2.686	46.12	0.8559	
24X-4, 77.0	500.43	1.891	2.716	48.74	0.9508	
24X-6, 33.0	501.305	1.999	2.726	42.72	0.7458	Sand
24X-7, 33.0	502.005	1.943	2.727	46.02	0.8525	
338-C0002J-						
1R-1, 72.0	902.72	1.989	2.727	43.33	0.7646	
1R-4, 0.0	903.15	2.017	2.755	42.67	0.7444	
1R-6, 0.0	903.565	2.012	2.685	40.52	0.6813	Partially dried before wet mass measurement
1R-7, 45.0	904.255	1.879	2.537	43.52	0.7704	
1R-7, 109.0	904.895	2.040	2.711	39.77	0.6602	
1R-8, 47.0	905.46	2.040	2.706	39.59	0.6552	
2R-1, 23.5	907.235	2.025	2.721	41	0.695	
3R-1, 75.0	912.75	1.929	2.697	45.9	0.8484	
3R-2, 69.0	913.47	1.927	2.749	47.63	0.9093	
3R-5, 1.0	913.85	1.854	2.666	49.47	0.9789	
3R-5, 138.0	915.22	1.865	2.641	47.99	0.9227	
3R-6, 85.0	916.095	1.865	2.666	48.79	0.9527	
4R-1, 37.0	917.37	1.913	2.759	48.75	0.9514	
4R-3, 0.0	917.76	1.827	2.696	51.99	1.0828	
4R-3, 122.0	918.98	1.911	2.683	46.58	0.8718	
4R-4, 22.0	919.36	1.879	2.722	49.63	0.9855	
4R-4, 80.0	919.94	1.837	2.629	49.31	0.9729	
4R-5, 38.0	920.905	1.905	2.681	46.82	0.8806	
4R-5, 80.0	921.325	1.996	2.842	46.54	0.8705	
5R-3, 7.0	922.835	1.954	2.733	45.57	0.8372	
5R-5, 13.5	923.12	1.934	2.653	44.11	0.7893	
5R-6, 48.0	923.66	1.935	2.705	45.81	0.8455	
5R-6, 110.0	924.28	1.966	2.731	44.8	0.8114	
5R-7, 45.0	924.825	1.976	2.805	46.58	0.872	
5R-8, 0.0	925.68	2.009	2.744	42.74	0.7463	
5R-8, 30.0	925.98	2.028	2.737	41.39	0.7063	
6R-1, 39.0	927.39	1.940	2.726	46.15	0.857	Sandy
6R-1, 94.0	927.94	1.966	2.676	42.95	0.7529	Sand
7R-1, 58.0	932.58	2.030	2.760	42.05	0.7256	Sand
7R-2, 27.0	933.27	2.039	2.719	40.12	0.67	
338-C0002H-						
1R-1, 29.0	1100.79	2.047	2.727	39.93	0.6646	
1R-1, 129.0	1101.79	2.125	2.714	34.87	0.5355	
1R-2, 36.0	1102.27	2.101	2.685	35.18	0.5426	
2R-1, 15.0	1110.65	2.136	2.758	35.88	0.5596	
2R-3, 2.0	1111.195	2.112	2.691	34.71	0.5315	Sand
2R-3, 63.0	1111.805	2.148	2.761	35.27	0.5449	

Table T40. Resistivity results from cubic core samples, Holes C0002H and C0002J.

Core, section, interval (cm)	Depth (mbsf)	R_x (Ωm)	R_y (Ωm)	R_z (Ωm)	α_l (%)	α_T (%)	Notes
338-C0002J-							
1R-1, 12.0	902.12	1.42	2.02	2.19	–34.9	–24.1	
1R-1, 45.0	902.45	2.26	2.23	2.01	1.3	10.7	
1R-7, 87.0	904.675	1.73	2.50	2.93	–36.5	–32.2	
1R-8, 0.0	904.99	1.66	2.78	3.32	–50.3	–39.7	Cracked normal to the *x*-*y* plane
2R-1, 53.0	907.53	2.64	3.27	1.80	–21.1	48.6	
3R-1, 0.0	912	1.39	1.35	2.10	2.9	–41.8	Bad parallel face along *z*-axis
4R-3, 85.0	918.61	1.28	1.28	1.43	–0.2	–11.1	
5R-6, 91.0	924.09	2.38	1.76	3.14	29.7	–41.0	Broken chip along *x*-*y* plane
5R-8, 75.0	926.43	1.54	1.66	1.89	–7.2	–16.7	
338-C0002H-							
1R-1, 13.0	1100.63	1.95	1.54	1.64	23.5	6.6	
2R-1, 26.0	1110.76	1.71	1.51	2.18	12.6	–30.3	

Table T41. *P*-wave velocity results from cubic core samples, Holes C0002H and C0002J.

Core, section, interval (cm)	Depth (mbsf)	Resonant frequency of transducers (kHz)	V_{Px} (m/s)	V_{Py} (m/s)	V_{Pz} (m/s)	α_I (%)	α_T (%)	Notes
338-C0002J-								
1R-1, 12.0	902.12	230	2111	2142.7	1966.7	−1.49	7.82	
1R-1, 45.0	902.45	230	2016.7	2082.7	1927.3	−3.22	6.16	
1R-7, 87.0	904.675	230	2074	2076	2051.3	−0.10	1.15	
1R-8, 0.0	904.99	230	2040	2059.3	1922.7	−0.94	6.39	
2R-1, 53.0	907.53	230	2115	2175.3	2059.3	−2.81	4.08	
3R-1, 0.0	912	230	2143	2034	2100	5.22	−0.55	
4R-3, 85.0	918.61	230	2004	2079	1963	−3.67	3.92	
5R-6, 91.0	924.067	230	2277	2290	2116	−0.57	7.61	Broken along *x*-*y* plane
5R-8, 75.0	926.382	230	2291	2196	2207	4.23	1.64	
338-C0002H-								
1R-1, 13.0	1100.63	230	2122	2225	2302	−4.74	−5.74	
2R-1, 26.0	1110.76	230	2271	2307	2081	−1.57	9.52	

Table T42. Electrical resistivity measurements, Holes C0002K and C0002L. (Continued on next six pages.)

Core, section, interval (cm)	Depth (mbsf)	Electrical resistivity* (Ωm)	Formation factor*	MAD porosity (%)	MAD porosity depth (mbsf)	Archie *m* exponent	Archie tortuosity	Notes
338-C0002K-								
1H-1, 15.0	200.15	0.764	3.745	55.87	201.13	2.27	6.70	Silty mud
1H-1, 129.0	201.29	1.153	5.652	55.87	201.13	2.98	10.12	Sandy mud
1H-2, 23.0	201.565	0.544	2.667	55.87	201.13	1.69	4.77	Biscuit silty mud
1H-4, 18.0	203.065	0.793	3.887	61.98	202.075	2.84	6.27	Silty mud
1H-4, 64.0	203.525	3.516	17.235	43.51	203.635	3.42	39.61	Dark sand
1H-4, 110.0	203.985	0.528	2.588	59.86	204.29	1.85	4.32	Silty mud
1H-CC, 16.0	205.44	0.539	2.642	56.89	205.015	1.72	4.64	Dark sandy mud
1H-CC, 20.0	205.48	0.448	2.196	57.02	205.64	1.40	3.85	Clay-rich mud
1H-CC, 27.0	205.55	0.542	2.657	49.16	205.08	1.38	5.40	Silty mud
2H-1, 10.0	204.6	0.6	2.941	65.06	204.72	2.51	4.52	Liquid mud
2H-1, 40.0	204.9	0.319	1.564	56.89	205.015	0.79	2.75	Silty mud
2H-1, 57.0	205.07	0.937	4.593	49.16	205.08	2.15	9.34	Dark silty mud
2H-1, 68.0	205.18	0.756	3.706	49.16	205.08	1.84	7.54	Light clay-rich mud
3T-1, 18.0	205.68	0.705	3.456	57.02	205.64	2.21	6.06	Mud
3T-1, 56.0	206.06	0.73	3.578	53.91	206.06	2.06	6.64	Silty mud
3T-1, 75.0	206.25	0.634	3.108	53.91	206.06	1.84	5.77	Mud
3T-2, 50.0	206.9	0.58	2.843	51.85	206.75	1.59	5.48	Mud
3T-3, 20.0	207.47	0.553	2.711	56.83	207	1.76	4.77	Mud
3T-3, 27.0	207.54	0.852	4.176	46.3	207.86	1.86	9.02	Dark sandy mud
3T-4, 45.0	208.925	0.686	3.363	53.12	208.725	1.92	6.33	Mud
3T-4, 100.0	209.475	0.758	3.716	50.73	209.815	1.93	7.33	Clay-rich mud
3T-5, 18.0	210.055	0.752	3.686	49.8	210.425	1.87	7.40	Sandy mud
3T-6, 50.0	210.795	0.761	3.73	49.8	210.425	1.89	7.49	Mud
3T-7, 20.0	211.885	0.692	3.392	43.16	211.995	1.45	7.86	Mud
4T-1, 5.0	215.05	0.443	2.172	46.37	215.09	1.01	4.68	Liquid silty mud
4T-1, 23.0	215.23	0.583	2.858	52.75	215.36	1.64	5.42	Silty mud
4T-4, 107.0	217.185	0.597	2.926	40.81	217.125	1.20	7.17	Silty mud
5T-1, 7.0	220.07	0.46	2.255	58.86	220.14	1.53	3.83	Clay-rich mud
5T-1, 40.0	220.4	0.92	4.51	48.02	220.42	2.05	9.39	Sandy mud
5T-2, 15.0	220.885	0.451	2.211	37.27	220.965	0.80	5.93	Silty mud
5T-2, 60.0	221.335	0.457	2.24	37.27	220.965	0.82	6.01	Clay-rich mud
5T-4, 50.0	223.11	0.462	2.265	48.91	222.69	1.14	4.63	Dark silty mud
5T-7, 30.0	224.815	0.449	2.201	56.7	224.515	1.39	3.88	Silty mud
5T-8, 35.0	225.855	0.494	2.422	41.98	226.005	1.02	5.77	Sandy mud
6T-1, 40.0	229.9	0.215	1.054	66.35	229.7	0.13	1.59	Liquid mud
6T-2, 25.0	230.75	0.27	1.324	63.51	230.53	0.62	2.08	Dark liquid mud
6T-4, 40.0	232.045	0.687	3.368	53.96	232.285	1.97	6.24	Mud
7X-1, 10.0	239.1	0.574	2.814	54.83	239.46	1.72	5.13	Silty mud
7X-1, 42.0	239.42	1.777	8.711	48.35	239.98	2.98	18.02	Clay-rich mud
7X-3, 10.0	240.31	0.613	3.005	46.01	240.41	1.42	6.53	Sand

Table T42 (continued). (Continued on next page.)

Core, section, interval (cm)	Depth (mbsf)	Electrical resistivity* (Ωm)	Formation factor*	MAD porosity (%)	MAD porosity depth (mbsf)	Archie *m* exponent	Archie tortuosity	Notes
7X-3, 50.0	240.71	0.615	3.015	53.02	240.66	1.74	5.69	Silty mud
7X-4, 8.0	240.88	0.592	2.902	53.02	240.66	1.68	5.47	Dark sandy mud
7X-4, 34.0	241.14	0.313	1.534	50.33	241.43	0.62	3.05	Liquid mud
7X-4, 80.0	241.6	0.633	3.103	45.06	241.67	1.42	6.89	Silty mud
7X-4, 91.0	241.71	0.998	4.892	47.88	241.86	2.16	10.22	Sand
7X-4, 104.0	241.84	0.757	3.711	47.88	241.86	1.78	7.75	Clay-rich mud
7X-6, 10.0	242.305	0.554	2.716	50.72	242.365	1.47	5.35	Dark sandy mud
7X-6, 40.0	242.605	0.583	2.858	48.73	242.975	1.46	5.86	Silty mud
7X-7, 10.0	243.6	0.608	2.98	52.89	243.7	1.71	5.63	Sandy mud
7X-7, 66.0	244.16	0.627	3.074	52.89	243.7	1.76	5.81	Clay-rich mud
8X-1, 40.0	248.9	0.553	2.711	61.15	248.7	2.03	4.43	Mud
8X-1, 125.0	249.75	0.495	2.426	58.02	249.6	1.63	4.18	Mud
8X-3, 118.0	251.575	0.499	2.446	52.28	251.465	1.38	4.68	Liquid silty mud
8X-4, 82.0	252.47	0.678	3.324	56.28	252.81	2.09	5.91	Mud
8X-5, 89.0	253.945	0.835	4.093	53.01	254.215	2.22	7.72	Mud
9X-1, 8.0	258.08	0.391	1.917	50.72	258.3	0.96	3.78	Liquid mud
9X-1, 70.0	258.7	0.666	3.265	48.08	258.96	1.62	6.79	Mud
9X-2, 10.0	259.105	0.561	2.75	47.37	259.115	1.35	5.81	Liquid mud
9X-2, 80.0	259.805	0.777	3.809	48.82	259.815	1.87	7.80	Mud
9X-4, 44.0	260.825	0.862	4.225	44.76	260.815	1.79	9.44	Sand
9X-4, 70.0	261.085	0.745	3.652	44.76	260.815	1.61	8.16	Mud
9X-4, 95.0	261.335	0.869	4.26	52.78	261.99	2.27	8.07	Sand
9X-4, 120.0	261.585	0.747	3.662	52.78	261.99	2.03	6.94	Mud
9X-6, 20.0	263.39	1.094	5.363	48.16	263.38	2.30	11.14	Sand
9X-6, 50.0	263.69	0.747	3.662	48.16	263.38	1.78	7.60	Mud
9X-6, 79.0	263.98	0.983	4.819	48.16	263.38	2.15	10.01	Sand
9X-7, 27.0	264.87	0.92	4.51	50.17	264.67	2.18	8.99	Sand
9X-7, 50.0	265.1	0.697	3.417	44.93	265.81	1.54	7.61	Mud
9X-7, 81.0	265.41	1.025	5.025	44.93	265.81	2.02	11.18	Sand
9X-8, 26.0	266.26	0.865	4.24	53.71	266.07	2.32	7.89	Sand
9X-8, 70.0	266.7	0.666	3.265	43.09	266.89	1.41	7.58	Mud
9X-8, 94.0	266.94	0.755	3.701	43.09	266.89	1.55	8.59	Sand
9X-8, 100.0	267	0.723	3.544	43.09	266.89	1.50	8.22	Mud
10X-1, 15.0	267.65	0.564	2.765	46.67	267.64	1.33	5.92	Dark sandy mud
10X-3, 40.0	268.585	0.675	3.309	47.36	268.185	1.60	6.99	Mud
10X-4, 10.0	269.175	1.273	6.24	46.04	269.075	2.36	13.55	Sand
10X-4, 54.0	269.615	0.669	3.279	52.93	269.875	1.87	6.19	Silty mud
10X-5, 50.0	270.82	0.574	2.814	50.45	270.82	1.51	5.58	Clay-rich mud
10X-5, 104.0	271.36	0.724	3.549	54.46	271.67	2.08	6.52	Dark sand
10X-5, 135.0	271.67	0.528	2.588	54.46	271.67	1.56	4.75	Clay-rich mud
10X-6, 30.0	272.04	0.78	3.824	55.02	272.44	2.24	6.95	Sandy mud
10X-6, 70.0	272.44	0.548	2.686	55.02	272.44	1.65	4.88	Clay-rich mud
10X-6, 100.0	272.74	1.013	4.966	55.02	272.44	2.68	9.03	Dark sand
10X-6, 120.0	272.94	0.543	2.662	55.02	272.44	1.64	4.84	Silty mud
10X-7, 30.0	273.45	0.549	2.691	55.02	272.44	1.66	4.89	Clay-rich mud
10X-7, 38.0	273.53	0.706	3.461	55.02	272.44	2.08	6.29	Dark sand
10X-7, 65.0	273.8	0.532	2.608	42.88	274.08	1.13	6.08	Mud
10X-7, 93.0	274.08	1.221	5.985	42.88	274.08	2.11	13.96	Dark sand
10X-7, 100.0	274.15	0.7	3.431	42.88	274.08	1.46	8.00	Mud
11X-1, 4.0	277.04	0.444	2.176	55.99	277.26	1.34	3.89	Liquid mud
11X-3, 27.0	278	0.961	4.711	55.86	278.05	2.66	8.43	Dark sand
11X-3, 50.0	278.23	0.649	3.181	49.67	278.25	1.65	6.40	Silty mud
11X-4, 7.0	279.29	0.868	4.255	43.1	279.13	1.72	9.87	Dark sand
11X-4, 70.0	279.92	0.569	2.789	54.21	279.85	1.68	5.14	Silty mud
11X-4, 80.0	280.02	0.566	2.775	53.06	280.08	1.61	5.23	Liquid dark mud
11X-4, 90.0	280.12	0.63	3.088	53.06	280.08	1.78	5.82	Silty mud
11X-4, 96.0	280.18	0.792	3.882	53.06	280.08	2.14	7.32	Liquid dark mud
338-C0002L-								
1X-1, 30.0	277.3	0.698	2.576	49.58	277.3	1.35	5.20	Mud
1X-2, 7.0	278.26	0.663	2.446	49.67	278.25	1.28	4.92	Sand
1X-2, 70.0	278.89	0.8	2.952	53.61	279	1.74	5.51	Mud
1X-3, 90.0	280.125	0.788	2.908	59.58	280.495	2.06	4.88	Mud
1X-5, 48.0	281.31	0.801	2.956	45.48	281.14	1.38	6.50	Mud
1X-6, 104.0	283.285	0.837	3.089	50.06	283.275	1.63	6.17	Mud
1X-7, 71.0	284.305	0.94	3.469	47.86	284.335	1.69	7.25	Sand
1X-7, 110.0	284.695	0.914	3.373	44.31	284.885	1.49	7.61	Mud
2X-1, 3.0	286.53	0.577	2.129	48.63	286.77	1.05	4.38	Soupy mud

Table T42 (continued). (Continued on next page.)

Core, section, interval (cm)	Depth (mbsf)	Electrical resistivity* (Ωm)	Formation factor*	MAD porosity (%)	MAD porosity depth (mbsf)	Archie *m* exponent	Archie tortuosity	Notes
2X-1, 19.0	286.69	1.198	4.421	48.63	286.77	2.06	9.09	Dark sand
2X-1, 23.0	286.73	1.011	3.731	48.63	286.77	1.83	7.67	Silty mud
2X-2, 43.0	287.41	0.855	3.155	53.04	286.98	1.81	5.95	Silty mud
3X-1, 3.0	296.03	0.558	2.059	56.78	296.2	1.28	3.63	Silty mud
3X-1, 32.0	296.32	0.742	2.738	56.78	296.2	1.78	4.82	Soupy silty mud
3X-1, 72.0	296.72	0.743	2.742	45.15	297.03	1.27	6.07	Dark clay-rich mud
3X-3, 25.0	297.64	0.772	2.849	45.15	297.03	1.32	6.31	Silty mud
3X-3, 120.0	298.59	0.906	3.343	47.84	298.49	1.64	6.99	Ash
3X-4, 35.0	299.04	1.196	4.413	44.73	299.27	1.85	9.87	Ash
3X-4, 58.0	299.27	1.022	3.771	44.73	299.27	1.65	8.43	Silty mud
4X-1, 25.0	305.75	0.867	3.199	56.29	305.75	2.02	5.68	Mud
4X-3, 80.0	307.85	0.707	2.609	58.44	307.85	1.79	4.46	Mud
4X-4, 44.0	308.74	0.74	2.731	61.06	308.74	2.04	4.47	Mudstone
4X-6, 100.0	311.905	0.774	2.856	56.77	311.635	1.85	5.03	Mudstone
4X-7, 29.0	312.57	0.913	3.369	55.55	312.46	2.07	6.06	Mudstone
5X-1, 35.0	315.35	0.868	3.203	57.16	315.15	2.08	5.60	Mud
5X-1, 79.0	315.79	0.718	2.649	54.23	316.2	1.59	4.88	Soupy silty mud
5X-2, 15.0	316.55	0.926	3.417	54.23	316.2	2.01	6.30	Silty mud
5X-2, 32.0	316.72	0.921	3.399	52.33	317	1.89	6.50	Dark silty mud
5X-4, 7.0	317.765	0.87	3.21	49.38	318.195	1.65	6.50	Dark silty mud
5X-4, 20.0	317.895	0.995	3.672	49.38	318.195	1.84	7.44	Mud
5X-4, 73.0	318.425	0.966	3.565	49.02	318.455	1.78	7.27	Dark soupy sand
5X-5, 45.0	319.2	1.078	3.978	49.41	318.88	1.96	8.05	Mud
5X-5, 56.0	319.31	1.366	5.041	49.41	318.88	2.29	10.20	Dark soupy sand
5X-5, 70.0	319.45	0.952	3.513	44.08	320.135	1.53	7.97	Silty mud
5X-5, 81.0	319.56	1.071	3.952	44.08	320.135	1.68	8.97	Dark soupy sand
5X-5, 95.0	319.7	1.02	3.764	44.08	320.135	1.62	8.54	Mud
5X-5, 108.0	319.83	1.177	4.343	44.08	320.135	1.79	9.85	Dark sand
5X-5, 122.0	319.97	0.942	3.476	44.08	320.135	1.52	7.89	Silty mud
5X-6, 25.0	320.235	0.95	3.506	44.08	320.135	1.53	7.95	Silty mud
5X-6, 50.0	320.485	1.053	3.886	45.18	320.735	1.71	8.60	Dark soupy sand
5X-6, 60.0	320.585	0.937	3.458	45.18	320.735	1.56	7.65	Mud
5X-7, 21.0	321.305	1.086	4.007	43.67	321.945	1.68	9.18	Dark soupy sand
5X-7, 40.0	321.495	0.898	3.314	43.67	321.945	1.45	7.59	Mud
5X-7, 53.0	321.625	0.927	3.421	43.67	321.945	1.48	7.83	Dark soupy silty mud
5X-7, 65.0	321.745	1.005	3.708	43.67	321.945	1.58	8.49	Mud
5X-8, 68.0	322.525	1.14	4.207	47.27	322.645	1.92	8.90	Dark soupy sand
5X-9, 50.0	323.325	1.183	4.365	45.59	323.375	1.88	9.57	Mud
6X-1, 11.0	324.61	0.972	3.696	54.45	324.66	2.15	6.79	Mud
6X-1, 65.0	325.15	0.843	3.205	44.8	325.16	1.45	7.15	Soupy silty mud
6X-2, 68.0	325.995	1.358	5.163	49.85	326.525	2.36	10.36	Soupy silty mud
6X-2, 105.0	326.365	1.095	4.163	49.85	326.525	2.05	8.35	Mud
6X-5, 103.0	328.475	1.199	4.559	54.34	328.475	2.49	8.39	Soupy silty mud
6X-6, 12.0	328.79	0.987	3.753	48.78	328.78	1.84	7.69	Mud
6X-7, 16.0	330.06	0.866	3.293	53.45	330.07	1.90	6.16	Ash
6X-7, 46.0	330.36	1.183	4.498	53.45	330.07	2.40	8.42	Mud
6X-8, 56.0	331.86	0.854	3.247	46.07	331.42	1.52	7.05	Mud
6X-9, 100.0	333.42	1.15	4.373	52.06	333.2	2.26	8.40	Mud
7X-1, 23.0	334.23	0.877	3.335	59.1	334.23	2.29	5.64	Silty mud
7X-3, 37.0	335.73	1.119	4.255	51.78	335.36	2.20	8.22	Silty mud mess partially consolidated
7X-CC, 20.0	336.67	1.226	4.662	45.67	336.26	1.96	10.21	Silty mud
8X-1, 11.0	343.61	0.876	3.318	49.93	343.54	1.73	6.65	Mud consolidated
8X-2, 8.0	343.885	0.804	3.045	50.02	344.085	1.61	6.09	Mud consolidated
8X-2, 28.0	344.085	1.392	5.273	50.02	344.085	2.40	10.54	Soupy dark sand
8X-2, 95.0	344.755	0.82	3.106	49.98	344.855	1.63	6.21	Mud consolidated
8X-3, 54.0	345.52	0.81	3.068	48.78	345.89	1.56	6.29	Mud consolidated
8X-5, 24.0	346.94	0.875	3.314	52	346.7	1.83	6.37	Mud consolidated
8X-5, 73.0	347.43	1.603	6.072	50.28	347.45	2.62	12.08	Soupy dark sand
8X-5, 100.0	347.7	0.917	3.473	50.28	347.45	1.81	6.91	Mud consolidated
8X-5, 113.0	347.83	1.559	5.905	50.28	347.45	2.58	11.74	Dark sand
8X-6, 125.0	349.355	0.923	3.496	48.99	349.235	1.75	7.14	Mud consolidated
8X-7, 50.0	350.015	0.766	2.902	47.43	349.945	1.43	6.12	Mud consolidated
8X-8, 49.0	351.41	0.76	2.879	45.79	351.68	1.35	6.29	Mud consolidated
8X-9, 25.0	351.87	4.235	16.042	45.79	351.68	3.55	35.03	Dark sand
8X-9, 67.0	352.29	0.837	3.17	46.43	352.33	1.50	6.83	Mud consolidated
8X-CC, 15.0	352.75	0.925	3.504	46.37	353.09	1.63	7.56	Mud consolidated
9X-1, 10.0	353.1	0.83	3.132	46.37	353.09	1.49	6.75	Soupy mud

Table T42 (continued). (Continued on next page.)

Core, section, interval (cm)	Depth (mbsf)	Electrical resistivity* (Ωm)	Formation factor*	MAD porosity (%)	MAD porosity depth (mbsf)	Archie *m* exponent	Archie tortuosity	Notes
9X-1, 25.0	353.25	0.738	2.785	50.65	353.4	1.51	5.50	Mud consolidated
9X-3, 25.0	354.53	0.762	2.875	49.32	354.53	1.49	5.83	Soupy mud
9X-3, 55.0	354.83	0.68	2.566	51.14	355.08	1.41	5.02	Soupy mud
9X-3, 80.0	355.08	0.736	2.777	51.14	355.08	1.52	5.43	Mud consolidated
9X-6, 10.0	356.825	0.916	3.457	47.31	356.725	1.66	7.31	Mud consolidated
9X-7, 82.0	358.54	4.078	15.389	43.4	358.53	3.27	35.46	Dark sand
9X-7, 95.0	358.67	0.856	3.23	43.4	358.53	1.40	7.44	Mud consolidated
9X-8, 75.0	359.455	0.67	2.528	55.78	359.405	1.59	4.53	Soupy mud
9X-8, 95.0	359.655	0.96	3.623	44.66	359.655	1.60	8.11	Soupy silty mud
9X-8, 120.0	359.905	0.836	3.155	44.66	359.655	1.43	7.06	Mud consolidated
9X-CC, 40.0	360.325	1.275	4.811	44.66	359.655	1.95	10.77	Mud consolidated
10X-1, 28.0	362.78	0.887	3.335	52.1	362.84	1.85	6.40	Silt
10X-1, 32.0	362.82	0.824	3.098	52.1	362.84	1.73	5.95	Sand
10X-1, 49.0	362.99	0.782	2.94	52.1	362.84	1.65	5.64	Clay
10X-1, 99.0	363.49	0.381	1.432	60.17	363.5	0.71	2.38	Soupy mud
10X-2, 15.0	363.785	0.991	3.726	60.17	363.5	2.59	6.19	Clay
10X-4, 9.0	365.13	0.786	2.955	52.45	365.36	1.68	5.63	Soupy sand
10X-4, 32.0	365.36	0.705	2.65	52.45	365.36	1.51	5.05	Clay
10X-5, 57.0	365.97	0.925	3.477	47.16	365.65	1.66	7.37	Clay
10X-5, 87.0	366.27	0.885	3.327	49.89	366.27	1.73	6.67	Sand
10X-6, 45.0	367.07	0.808	3.038	49.79	367.05	1.59	6.10	Sand
10X-6, 72.0	367.34	0.993	3.733	48.39	367.58	1.81	7.71	Clay
10X-7, 15.0	367.59	1.005	3.778	48.39	367.58	1.83	7.81	Clay
10X-7, 122.0	368.66	0.645	2.425	47.31	368.55	1.18	5.13	Soupy sand
10X-8, 56.0	369.245	0.86	3.233	51.25	369.225	1.76	6.31	Clay
10X-CC, 8.0	369.635	0.952	3.579	51.25	369.225	1.91	6.98	Sandy silt
10X-CC, 15.0	369.705	1.173	4.41	74.43	372.09	5.02	5.93	Clay
11X-1, 20.0	372.2	0.805	3.004	74.43	372.09	3.72	4.04	Mud consolidated
11X-1, 83.0	372.83	0.828	3.09	52.14	372.8	1.73	5.93	Soupy dark sand
11X-2, 63.0	373.825	0.587	2.19	52.14	372.8	1.20	4.20	Sand
11X-2, 80.0	373.995	1.243	4.638	48.95	373.995	2.15	9.47	Mud consolidated
11X-3, 20.0	374.83	0.455	1.698	56.18	374.83	0.92	3.02	Soupy silty mud
11X-6, 13.0	376.345	0.705	2.631	55.71	376.345	1.65	4.72	Soupy sand
11X-CC, 16.0	377.44	1.146	4.276	55.71	376.345	2.48	7.68	Mud consolidated
12X-1, 13.0	381.63	1.141	4.257	47.77	381.64	1.96	8.91	Mud
12X-1, 103.0	382.53	0.641	2.392	49.48	382.53	1.24	4.83	Soupy
12X-2, 19.0	382.92	1.618	6.037	49.48	382.53	2.56	12.20	Sand
12X-2, 60.0	383.33	0.899	3.354	46.95	383.33	1.60	7.14	Mud
12X-2, 86.0	383.59	1.291	4.817	46.95	383.33	2.08	10.26	Sand
12X-3, 70.0	384.44	0.971	3.623	49.16	384.44	1.81	7.37	Mud
12X-4, 25.0	385.09	0.931	3.474	49.15	384.94	1.75	7.07	Sand
12X-4, 104.0	385.88	0.928	3.463	48.26	385.88	1.70	7.18	Mud
12X-6, 82.0	387.92	1.778	6.634	47.07	388.27	2.51	14.09	Sandy
12X-8, 23.0	388.595	0.946	3.53	47.07	388.27	1.67	7.50	Mud
12X-8, 63.0	388.995	1.247	4.653	47.31	389.095	2.05	9.84	Sand
13X-1, 18.0	391.18	7.56	28.209	47.31	389.095	4.46	59.63	Sand
13X-1, 47.0	391.47	1.056	3.94	49.5	391.47	1.95	7.96	Mud consolidated
13X-2, 60.0	392.72	1.027	3.832	51.24	392.92	2.01	7.48	Sand
13X-2, 80.0	392.92	0.949	3.541	51.24	392.92	1.89	6.91	Mud consolidated
13X-3, 81.0	394.345	0.9	3.358	51.91	394.345	1.85	6.47	Glauconized mud
13X-3, 100.0	394.535	0.818	3.052	51.91	394.345	1.70	5.88	Mud consolidated
13X-4, 45.0	395.255	0.728	2.716	54.28	395.255	1.64	5.00	Mud consolidated
13X-5, 32.0	396.455	0.801	2.989	52.7	396.505	1.71	5.67	Soupy sand
13X-6, 28.0	397.015	0.717	2.675	53.45	397.005	1.57	5.00	Mud consolidated
13X-7, 30.0	398.455	0.745	2.78	59.04	398.455	1.94	4.71	Mud consolidated
13X-7, 75.0	398.905	1.188	4.433	59.04	398.455	2.83	7.51	Ash
13X-CC, 61.0	399.745	0.927	3.459	54.46	400.82	2.04	6.35	Mud consolidated
14X-1, 33.0	400.83	0.79	2.959	54.46	400.82	1.79	5.43	Mud consolidated
14X-2, 13.0	402.03	1.072	4.015	51.22	402.02	2.08	7.84	Mud consolidated
14X-2, 43.0	402.33	1	3.745	47.91	402.32	1.79	7.82	Sand
14X-4, 21.0	403.665	1.072	4.015	58.12	402.9	2.56	6.91	Mud consolidated
14X-5, 61.0	405.465	1.098	4.112	53.61	404.885	2.27	7.67	Mud consolidated
14X-5, 90.0	405.755	0.926	3.468	51.02	406.015	1.85	6.80	Sand
14X-6, 14.0	406.405	1.293	4.843	50.32	406.395	2.30	9.62	Mud consolidated
14X-6, 59.0	406.855	1.188	4.449	50.32	406.395	2.17	8.84	Sand
14X-7, 30.0	407.965	1.46	5.468	48.05	407.495	2.32	11.38	Mud consolidated
14X-7, 63.0	408.295	1.206	4.517	45.9	408.525	1.94	9.84	Silty mud
14X-7, 80.0	408.465	1.085	4.064	45.9	408.525	1.80	8.85	Sand

Table T42 (continued). (Continued on next page.)

Core, section, interval (cm)	Depth (mbsf)	Electrical resistivity* (Ωm)	Formation factor*	MAD porosity (%)	MAD porosity depth (mbsf)	Archie *m* exponent	Archie tortuosity	Notes
14X-8, 30.0	409.38	1.283	4.805	49.48	409.37	2.23	9.71	Mud consolidated
14X-8, 88.0	409.96	1.241	4.648	45.96	410.23	1.98	10.11	Sand
14X-CC, 14.0	410.2	1.515	5.674	45.96	410.23	2.23	12.35	Mud consolidated
15X-1, 64.0	410.64	0.994	3.723	47.72	410.945	1.78	7.80	Mud consolidated
15X-2, 9.0	410.945	0.986	3.693	47.72	410.945	1.77	7.74	Mud consolidated
15X-3, 10.0	411.885	0.545	2.041	49.94	411.855	1.03	4.09	Mud consolidated
15X-3, 27.0	412.055	0.993	3.719	49.94	411.855	1.89	7.45	Mud consolidated
15X-5, 12.0	412.695	1.03	3.858	52.29	412.575	2.08	7.38	Mud consolidated
15X-5, 31.0	412.885	0.829	3.105	52.29	412.575	1.75	5.94	Sand
15X-6, 21.0	413.575	1.011	3.787	47.36	413.515	1.78	8.00	Mud consolidated
15X-7, 8.0	414.845	1.213	4.543	53.09	414.735	2.39	8.56	Sand
15X-7, 26.0	415.025	0.859	3.217	53.09	414.735	1.85	6.06	Mud consolidated
15X-7, 44.0	415.205	0.686	2.569	59.92	415.465	1.84	4.29	Soupy sand
15X-7, 62.0	415.385	0.958	3.588	59.92	415.465	2.49	5.99	Mud consolidated
15X-7, 70.0	415.465	0.616	2.307	59.92	415.465	1.63	3.85	Soupy sand
15X-7, 116.0	415.925	0.94	3.521	47.99	415.945	1.71	7.34	Mud consolidated
15X-7, 137.0	416.135	1.012	3.79	47.4	416.285	1.78	8.00	Sand
15X-8, 30.0	416.465	1.04	3.895	47.4	416.285	1.82	8.22	Mud consolidated
15X-8, 68.0	416.845	1.063	3.981	47.4	416.285	1.85	8.40	Silty sand
15X-8, 108.0	417.245	0.943	3.532	48.65	417.455	1.75	7.26	Mud consolidated
15X-8, 130.0	417.465	0.946	3.543	48.65	417.455	1.76	7.28	Soupy sand
15X-9, 20.0	417.685	1.122	4.202	48.68	417.605	1.99	8.63	Mud consolidated
15X-9, 46.0	417.945	1.272	4.764	48.68	417.605	2.17	9.79	Sand
15X-9, 82.0	418.305	1.027	3.846	46.34	418.225	1.75	8.30	Mud consolidated
15X-10, 7.0	418.545	1.172	4.39	46.34	418.225	1.92	9.47	Mud consolidated
15X-10, 36.0	418.835	2.573	9.637	48.72	418.945	3.15	19.78	Black sand
15X-CC, 20.0	419.465	1.298	4.861	48.72	418.945	2.20	9.98	
16X-1, 50.0	420	0.924	3.448	52.18	420	1.90	6.61	Mud consolidated
16X-2, 44.0	420.915	0.959	3.578	51.94	421.125	1.95	6.89	Soupy sand
16X-2, 65.0	421.125	0.801	2.989	51.94	421.125	1.67	5.75	Mud consolidated
16X-2, 114.0	421.615	1.048	3.91	52.42	421.825	2.11	7.46	Dark thin sand layers
16X-3, 42.0	422.29	0.985	3.675	52.42	421.825	2.02	7.01	Silty mud
16X-3, 47.0	422.34	1.057	3.944	47.65	422.71	1.85	8.28	Sand
16X-4, 33.0	422.71	0.972	3.627	47.65	422.71	1.74	7.61	Mud consolidated
16X-4, 49.0	422.87	1.222	4.56	47.65	422.71	2.05	9.57	Silty mud
16X-4, 54.0	422.92	1.436	5.358	47.65	422.71	2.26	11.24	Dark sand
16X-4, 76.0	423.14	1.262	4.709	48.12	423.32	2.12	9.79	Dark sand
16X-4, 94.0	423.32	1.061	3.959	48.12	423.32	1.88	8.23	Mud consolidated
16X-4, 108.0	423.46	1.086	4.052	48.12	423.32	1.91	8.42	Sand
16X-5, 20.0	423.98	0.841	3.138	46.64	423.98	1.50	6.73	Silty mud
16X-5, 26.0	424.04	1.004	3.746	46.64	423.98	1.73	8.03	Sandy mud
16X-5, 64.0	424.42	0.989	3.69	45.18	424.42	1.64	8.17	Sand
16X-5, 75.0	424.53	0.781	2.914	45.18	424.42	1.35	6.45	Mud consolidated
16X-5, 85.0	424.63	0.818	3.052	45.18	424.42	1.40	6.76	Sandy mud
16X-5, 88.0	424.66	0.699	2.608	45.18	424.42	1.21	5.77	Ash
16X-5, 89.0	424.67	0.607	2.265	45.18	424.42	1.03	5.01	Base of mud white
16X-6, 12.0	425.105	0.765	2.854	49.58	425.175	1.49	5.76	Sandy mud
16X-6, 20.0	425.185	1.061	3.959	49.58	425.175	1.96	7.99	Mud consolidated
16X-6, 110.0	426.085	1.184	4.418	49.63	426.085	2.12	8.90	Mud consolidated
16X-7, 38.0	426.785			42.41	426.805			Soupy mud
16X-7, 96.0	427.365	0.76	2.836	47.76	427.355	1.41	5.94	Mud consolidated
16X-7, 105.0	427.455			47.76	427.355			Soupy mud
16X-8, 18.0	427.755	1.026	3.828	47.76	427.355	1.82	8.02	Mud consolidated
16X-8, 22.0	427.795	1.21	4.515	47.76	427.355	2.04	9.45	Sandy mud
16X-8, 69.0	428.265	1.024	3.821	45.59	428.385	1.71	8.38	Sandy mud
16X-8, 80.0	428.375	1.105	4.123	45.59	428.385	1.80	9.04	Mud consolidated
17X-1, 25.0	429.25	0.938	3.5	46.02	429.25	1.61	7.61	Mud consolidated
17X-1, 107.0	430.07	0.631	2.354	48.65	430.07	1.19	4.84	Soupy mud
17X-2, 10.0	430.25	0.86	3.209	53.98	430.25	1.89	5.94	Mud consolidated
17X-2, 61.0	430.76	0.854	3.187	53.98	430.25	1.88	5.90	Sandy mud
17X-3, 44.0	431.365	0.998	3.724	48.81	431.355	1.83	7.63	Mud consolidated
17X-5, 105.0	433.305	0.88	3.284	45.6	433.295	1.51	7.20	Sandy mud
17X-5, 120.0	433.455	0.838	3.127	45.6	433.295	1.45	6.86	Mud consolidated
17X-6, 25.0	433.775	0.872	3.254	45.6	433.295	1.50	7.14	Soupy mud
17X-6, 65.0	434.175	1.05	3.918	43.8	434.175	1.65	8.95	Mud consolidated
17X-7, 25.0	435.155	0.988	3.687	49.42	435.375	1.85	7.46	Soupy mud
17X-7, 68.0	435.585	0.936	3.493	47.51	435.875	1.68	7.35	Soupy mud

Table T42 (continued). (Continued on next page.)

Core, section, interval (cm)	Depth (mbsf)	Electrical resistivity* (Ωm)	Formation factor*	MAD porosity (%)	MAD porosity depth (mbsf)	Archie *m* exponent	Archie tortuosity	Notes
17X-8, 7.0	435.885	1.152	4.299	47.51	435.875	1.96	9.05	Mud consolidated
17X-8, 59.0	436.405	1.327	4.951	41.92	436.405	1.84	11.81	Sandy mud
17X-9, 10.0	437.105	0.974	3.634	47.43	437.605	1.73	7.66	Mud consolidated
17X-9, 43.0	437.435	1.256	4.687	47.43	437.605	2.07	9.88	Sandy mud
17X-9, 60.0	437.605	1.358	5.067	47.43	437.605	2.18	10.68	Mud consolidated
18X-1, 64.0	439.14	1.29	4.76	49.39	439.14	2.21	9.64	Mud consolidated
18X-4, 27.0	440.97	1.079	3.982	47.6	440.03	1.86	8.37	Thin black layers
18X-4, 74.0	441.44	1.064	3.926	47.66	441.62	1.85	8.24	Black silty mud
18X-4, 93.0	441.63	1.179	4.351	47.66	441.62	1.98	9.13	Mud consolidated
18X-4, 111.0	441.81	1.071	3.952	47.66	441.62	1.85	8.29	Black silty mud
18X-5, 90.0	443	1.112	4.103	45.81	443	1.81	8.96	Mud consolidated
18X-5, 123.0	443.33	1.566	5.779	38.74	443.32	1.85	14.92	Soupy sandy laminae
18X-6, 86.0	444.365	1.356	5.004	37.67	444.365	1.65	13.28	Sandy laminae
18X-7, 80.0	445.715	1.08	3.985	40.75	445.955	1.54	9.78	Mud consolidated
18X-8, 18.0	446.505	1.074	3.963	47.84	446.895	1.87	8.28	Sandy laminae
18X-8, 57.0	446.895	1.317	4.86	47.84	446.895	2.14	10.16	Mud consolidated
19X-1, 65.0	448.65	1.226	4.524	47.8	448.52	2.04	9.46	Mud consolidated
19X-2, 80.0	450.015	1.177	4.343	49.41	449.515	2.08	8.79	Black sandy mud
19X-2, 95.0	450.165	1.172	4.325	46.52	450.95	1.91	9.30	Mud consolidated
19X-4, 60.0	451.5	1.047	3.863	51.11	452.04	2.01	7.56	Mud consolidated
19X-4, 115.0	452.05	0.783	2.889	51.11	452.04	1.58	5.65	Light mud
19X-5, 6.0	452.225	0.942	3.476	45.47	452.265	1.58	7.64	Soupy mud and ash
19X-5, 13.0	452.295	0.854	3.151	45.47	452.265	1.46	6.93	Ash
19X-5, 18.0	452.345	1.311	4.838	45.47	452.265	2.00	10.64	Base of ash
19X-5, 20.0	452.365	1.177	4.343	45.47	452.265	1.86	9.55	Base of ash in mud
19X-5, 80.0	452.965	1.382	5.1	41.63	453.155	1.86	12.25	Mud consolidated
19X-5, 100.0	453.165	1.376	5.077	41.63	453.155	1.85	12.20	Black sandy mud
19X-6, 70.0	454.12	2.268	8.369	48.8	453.52	2.96	17.15	Mud consolidated
19X-7, 5.0	454.8	0.67	2.472	44.12	454.77	1.11	5.60	Soupy black sandy laminae
19X-7, 48.0	455.23	0.67	2.472	46.25	455.55	1.17	5.34	Soupy mud
19X-7, 80.0	455.55	1.036	3.823	46.25	455.55	1.74	8.27	Mud consolidated
19X-CC, 5.0	456.15	1.39	5.129	46.25	455.55	2.12	11.09	Mud consolidated
19X-CC, 13.0	456.23	2.596	9.579	46.25	455.55	2.93	20.71	Sandy laminae
20X-1, 17.0	457.67	1.125	4.167	46.82	457.66	1.88	8.90	Mud consolidated
20X-1, 34.0	457.84	0.906	3.356	46.82	457.66	1.60	7.17	Soupy mud
20X-3, 42.0	459.465	1.197	4.433	46.75	459.365	1.96	9.48	Mud consolidated
20X-3, 49.0	459.535	1.293	4.789	46.75	459.365	2.06	10.24	Silty mud laminae
20X-3, 80.0	459.845	1.372	5.081	47.61	460.235	2.19	10.67	Mud consolidated
20X-3, 101.0	460.055	1.09	4.037	47.61	460.235	1.88	8.48	Silty mud laminae
20X-4, 10.0	460.555	1.199	4.441	47.95	460.545	2.03	9.26	Mud consolidated
20X-4, 22.0	460.675	0.875	3.241	47.95	460.545	1.60	6.76	Dark mud
20X-4, 70.0	461.155	1.448	5.363	47.16	461.485	2.23	11.37	Mud consolidated
20X-4, 76.0	461.215	0.935	3.463	47.16	461.485	1.65	7.34	Dark mud
20X-4, 110.0	461.555	0.973	3.604	47.16	461.485	1.71	7.64	Mud consolidated
20X-5, 50.0	462.365	1.045	3.87	47.56	462.015	1.82	8.14	Mud consolidated
20X-6, 40.0	463.675	0.992	3.674	48	463.355	1.77	7.65	Mud consolidated
20X-6, 47.0	463.745	1.289	4.774	48	463.355	2.13	9.95	Sandy mud laminae
20X-6, 105.0	464.325	1.107	4.1	47.8	464.395	1.91	8.58	Mud consolidated
20X-7, 13.0	464.655	1.66	6.148	48.65	464.665	2.52	12.64	Sand
20X-7, 105.0	465.575	0.916	3.393	46.72	465.825	1.61	7.26	Silty mud laminae
20X-7, 110.0	465.625	0.631	2.337	46.72	465.825	1.12	5.00	Mud consolidated
20X-8, 55.0	466.4	1.194	4.422	47.86	465.88	2.02	9.24	Mud consolidated
20X-8, 80.0	466.65	0.961	3.559	50.53	467.31	1.86	7.04	Sandy mud laminae
20X-CC, 35.0	467.06	1.454	5.385	50.53	467.31	2.47	10.66	Mud consolidated
20X-CC, 44.0	467.15	1.772	6.563	50.53	467.31	2.76	12.99	Sand and mica ?
21X-1, 19.0	467.19	0.375	1.404	50.53	467.31	0.50	2.78	Soupy mud
21X-1, 31.0	467.31	0.954	3.573	50.53	467.31	1.87	7.07	Mud consolidated
21X-1, 54.0	467.54	0.72	2.697	50.53	467.31	1.45	5.34	Soupy mud
21X-1, 71.0	467.71	0.945	3.539	50.53	467.31	1.85	7.00	Mud
21X-1, 88.0	467.88	0.738	2.764	50.53	467.31	1.49	5.47	Soupy silt
21X-1, 104.0	468.04	0.678	2.539	49.59	468.32	1.33	5.12	Soupy sand
21X-1, 107.0	468.07	0.944	3.536	49.59	468.32	1.80	7.13	Mud
21X-1, 112.0	468.12	0.65	2.434	49.59	468.32	1.27	4.91	Soupy sand
21X-1, 134.0	468.34	1.007	3.772	49.59	468.32	1.89	7.61	Mud
21X-2, 11.0	468.525	0.96	3.596	51.24	468.615	1.91	7.02	Black layer in mud
21X-2, 14.0	468.555	0.815	3.052	51.24	468.615	1.67	5.96	Soupy sand
21X-2, 21.0	468.625	0.736	2.757	51.24	468.615	1.52	5.38	Mud
21X-2, 28.0	468.695	0.672	2.517	51.24	468.615	1.38	4.91	Sand

Table T42 (continued).

Core, section, interval (cm)	Depth (mbsf)	Electrical resistivity* (Ωm)	Formation factor*	MAD porosity (%)	MAD porosity depth (mbsf)	Archie *m* exponent	Archie tortuosity	Notes
21X-2, 30.0	468.715	0.608	2.277	51.24	468.615	1.23	4.44	Soupy sand
21X-2, 34.0	468.755	0.988	3.7	51.24	468.615	1.96	7.22	Mud
21X-2, 36.0	468.775	0.689	2.581	51.24	468.615	1.42	5.04	Soupy sand
21X-2, 45.0	468.865	0.575	2.154	51.24	468.615	1.15	4.20	Mud
21X-2, 54.0	468.955	0.997	3.734	51.24	468.615	1.97	7.29	Mud
21X-2, 78.0	469.195	0.563	2.109	48.14	469.505	1.02	4.38	Soupy sand
21X-2, 86.0	469.275	1.038	3.888	48.14	469.505	1.86	8.08	Mud
21X-2, 95.0	469.365	0.597	2.236	48.14	469.505	1.10	4.64	Soupy sand
21X-2, 99.0	469.405	0.991	3.712	48.14	469.505	1.79	7.71	Mud
21X-3, 16.0	469.775	1.129	4.228	47.37	469.715	1.93	8.93	Mud
21X-3, 28.0	469.895	0.688	2.577	47.37	469.715	1.27	5.44	Soupy mud
21X-3, 41.0	470.025	0.777	2.91	47.37	469.715	1.43	6.14	Mud
21X-5, 18.0	471.245	0.75	2.809	52.94	471.065	1.62	5.31	Mud
21X-7, 7.0	473.855	0.826	3.094	54.38	473.76	1.85	5.69	Mud
21X-7, 13.0	473.915	0.599	2.243	54.38	473.76	1.33	4.12	Soupy mud
21X-7, 33.0	474.115	0.692	2.592	55.38	474.445	1.61	4.68	Ash
21X-7, 42.0	474.205	0.778	2.914	55.38	474.445	1.81	5.26	Mud
21X-7, 44.0	474.225	0.558	2.09	55.38	474.445	1.25	3.77	Soupy mud
21X-7, 63.0	474.415	0.857	3.21	55.38	474.445	1.97	5.80	Mud
21X-7, 116.0	474.945	0.869	3.255	52.7	475.055	1.84	6.18	Mud
21X-8, 99.0	476.115	0.854	3.199	46.89	476.6	1.54	6.82	Mud
22X-1, 10.0	476.6	1.02	3.835	46.89	476.6	1.77	8.18	Mud
22X-1, 37.0	476.87	0.758	2.85	46.89	476.6	1.38	6.08	Black layer in mud
22X-2, 22.0	477.38	0.722	2.714	49.22	477.47	1.41	5.51	Soupy sand
22X-2, 30.0	477.46	0.881	3.312	49.22	477.47	1.69	6.73	Mud
22X-3, 14.0	477.725	0.65	2.444	49.22	477.47	1.26	4.97	Soupy sand
22X-3, 26.0	477.845	0.831	3.124	47.66	478.07	1.54	6.55	Mud
22X-4, 9.0	478.08	0.92	3.459	47.66	478.07	1.67	7.26	Mud
22X-4, 15.0	478.14			47.66	478.07			Sand
22X-4, 63.0	478.62	0.703	2.643	52.06	478.89	1.49	5.08	Sand
22X-4, 81.0	478.8	0.863	3.244	52.06	478.89	1.80	6.23	Mud
22X-4, 90.0	478.89	0.485	1.823	52.06	478.89	0.92	3.50	Sand
22X-5, 18.0	479.4	0.939	3.53	53.42	479.4	2.01	6.61	Mud
22X-5, 52.0	479.74	0.619	2.327	53.3	480.2	1.34	4.37	Soupy sand
22X-5, 97.0	480.19	0.49	1.842	53.3	480.2	0.97	3.46	Soupy sand
22X-5, 115.0	480.37	0.882	3.316	53.3	480.2	1.91	6.22	Greenish mud
22X-7, 3.0	480.835	0.945	3.553	54.74	480.995	2.10	6.49	Mud
22X-8, 11.0	481.34	0.88	3.308	48.34	481.33	1.65	6.84	Mud
22X-8, 16.0	481.39	0.579	2.177	48.34	481.33	1.07	4.50	Soupy sand
23X-CC, 16.0	486.16	0.901	3.387	0				Mud
23X-CC, 25.0	486.25	1.228	4.617	0				Sand
24X-1, 35.0	495.85	0.59	2.177	48.79	495.64	1.08	4.46	Soupy mud
24X-1, 100.0	496.5	0.351	1.295	45.04	496.79	0.32	2.88	Soupy mud
24X-2, 20.0	497.095	0.483	1.782	47.49	497.295	0.78	3.75	Mud consolidated
24X-2, 85.0	497.745	0.41	1.513	52.37	497.905	0.64	2.89	Soupy mud
24X-3, 30.0	498.56	0.421	1.554	49.58	498.81	0.63	3.13	Soupy mud
24X-3, 75.0	499.01	0.779	2.875	49.58	498.81	1.51	5.80	Mud consolidated
24X-4, 10.0	499.76	0.369	1.362	46.12	499.41	0.40	2.95	Soupy mud
24X-4, 68.0	500.34	0.479	1.768	48.74	500.43	0.79	3.63	Mud consolidated
24X-6, 25.0	501.225	0.501	1.849	42.72	501.305	0.72	4.33	Silty mud laminae
24X-7, 15.0	501.825	0.577	2.129	46.02	502.005	0.97	4.63	Silty mud laminae
24X-7, 38.0	502.055	0.817	3.015	46.02	502.005	1.42	6.55	Mud consolidated

* = measured on *x*-axis. MAD = moisture and density.

Table T43. Unconfined compressive strength (UCS) tests on core samples, Holes C0002H and C0002J.

Core, section, interval (cm)	Depth (mbsf)	Sample number	*x* (mm)	*y* (mm)	*z* (mm)	Area (mm^2)	Peak load (kN)	UCS (MPa)	Sample quality
338-C0002H-									
2R-1 W, 26.0–28.0	1110.76	1	8.85	8.75	17.7	77.44	0.38	4.91	Not good, fractured
		2	8.5	9.2	17.55	78.20	0.42	5.37	Good
		3	8.2	8.7	17.55	71.34	0.56	7.85	Not good
		4	8.5	9.2	17.7	78.20	0.76	9.72	Good
338-C0002J-									
1R-1 W, 45.0–52.0	902.45	1	9.95	9.95	20.4	99.00	0.91	9.19	
	902.45	2	10	9.5	20.03	95.00	0.89	9.37	
	902.45	3	20.5	21	19.5	430.50	3.68	8.55	
	902.45	4	20.35	20.35	40.4	414.12	2.46	5.94	
2R-1 W, 16.0–21.0	907.16	1	21	21.2	51	445.20	0.68	1.53	Fractured
	907.16	2	10.5	10.9	21	114.45	0.33	2.88	
3R-1 W, 3.0–6.0	912.03	1	10	11.45	25.8	114.50	0.78	6.81	
	912.03	2	10	10.4	25.75	104.00	0.88	8.46	
	912.03	3	10.9	14.1	21.2	153.69	1.4	9.11	

Table T44. Results of gray values from each photograph acquired on cuttings, Hole C0002F. (Continued on next page.)

Cuttings sample	Top depth MSF (m)	Gray value		
		Minimum	Maximum	Mean
338-C0002F-				
22-SMW	930.5	64	110	90
25-SMW	940.5	25	140	66
27-SMW	950.5	26	202	71
29-SMW	960.5	31	177	71
31-SMW	970.5	27	118	70
34-SMW	980.5	24	143	68
36-SMW	990.5	26	106	67
40-SMW	1000.5	20	111	58
42-SMW	1010.5	22	116	54
44-SMW	1020.5	22	129	60
46-SMW	1030.5	20	216	58
48-SMW	1040.5	25	126	69
50-SMW	1050.5	29	151	68
52-SMW	1060.5	38	169	75
54-SMW	1070.5	26	137	57
56-SMW	1080.5	24	87	54
58-SMW	1090.5	28	117	58
62-SMW	1100.5	30	131	60
64-SMW	1110.5	27	159	69
66-SMW	1120.5	32	101	69
68-SMW	1130.5	30	128	71
71-SMW	1140.5	27	82	53
73-SMW	1150.5	36	131	80
75-SMW	1160.5	21	99	58
77-SMW	1170.5	32	137	76
80-SMW	1180.5	28	127	78
82-SMW	1190.5	25	96	64
84-SMW	1200.5	28	125	64
86-SMW	1210.5	29	131	63
90-SMW	1220.5	26	106	63
92-SMW	1230.5	25	92	55
94-SMW	1240.5	17	101	51
96-SMW	1250.5	24	151	64
98-SMW	1260.5	25	93	54
100-SMW	1270.5	25	202	55
102-SMW	1280.5	23	89	55
104-SMW	1290.5	22	96	58
106-SMW	1300.5	27	107	59
108-SMW	1310.5	20	91	53
110-SMW	1320.5	25	98	58
112-SMW	1330.5	33	99	67

Table T44 (continued).

Cuttings sample	Top depth MSF (m)	Gray value Minimum	Maximum	Mean
114-SMW	1340.5	25	149	71
116-SMW	1350.5	21	111	58
120-SMW	1360.5	17	97	47
122-SMW	1370.5	26	116	60
124-SMW	1380.5	30	93	64
126-SMW	1390.5	20	112	64
130-SMW	1400.5	29	127	73
132-SMW	1410.5	27	114	61
134-SMW	1420.5	23	106	63
136-SMW	1430.5	30	137	64
138-SMW	1440.5	21	91	52
140-SMW	1450.5	19	120	53
142-SMW	1460.5	24	143	67
144-SMW	1470.5	27	129	74
148-SMW	1480.5	22	114	62
150-SMW	1490.5	32	118	69
153-SMW	1500.5	14	97	51
155-SMW	1510.5	27	94	57
158-SMW	1520.5	26	111	62
161-SMW	1530.5	19	129	63
163-SMW	1540.5	26	131	64
167-SMW	1550.5	25	121	64
169-SMW	1560.5	32	116	66
172-SMW	1570.5	23	110	55
174-SMW	1580.5	22	117	59
177-SMW	1590.5	25	99	60
182-SMW	1600.5	28	103	60
184-SMW	1610.5	23	61	40
187-SMW	1620.5	27	100	56
189-SMW	1630.5	50	86	70
193-SMW	1640.5	27	119	74
195-SMW	1650.5	24	130	57
199-SMW	1660.5	33	64	47
201-SMW	1670.5	17	160	60
203-SMW	1680.5	17	124	53
205-SMW	1690.5	29	112	61
207-SMW	1700.5	19	104	53
209-SMW	1710.5	32	141	66
211-SMW	1720.5	30	161	65
213-SMW	1730.5	22	80	55
215-SMW	1740.5	27	180	59
217-SMW	1750.5	23	119	65
219-SMW	1760.5	29	100	63
223-SMW	1770.5	33	97	60
227-SMW	1780.5	22	124	58
229-SMW	1790.5	31	127	76
231-SMW	1800.5	29	115	74
233-SMW	1810.5	33	136	75
235-SMW	1820.5	32	117	72
238-SMW	1830.5	30	143	66
240-SMW	1840.5	32	98	66
250-SMW	1850.5	27	117	59
253-SMW	1860.5	27	103	62
255-SMW	1870.5	22	109	60
258-SMW	1880.5	24	115	62
260-SMW	1890.5	26	177	71
263-SMW	1900.5	28	127	71
265-SMW	1910.5	27	137	66
267-SMW	1920.5	28	125	64
269-SMW	1930.5	24	121	65
272-SMW	1940.5	17	101	57
274-SMW	1950.5	21	102	60
280-SMW	1960.5	22	122	64
311-SMW, coarse	1970.0	53	113	69
282-SMW	1970.5	24	119	70
284-SMW	1980.5	34	127	73
286-SMW	1990.5	27	160	69
289-SMW	2000.5	24	102	62

Values in 8 bits (0–256). Gray values extracted from the grayscale histogram using Adobe Photoshop on a circular area of 11 pixels diameter.

Table T45. Dielectric measurements and salinity index extracted from paste preparation on cuttings in Hole C0002F from 930.5 to 2005.5 mbsf. This table is available in an **oversized format.**

Table T46. List of key data from the second cycle of the leak-off test, Site C0002.

Parameter	Pressure (MPa)
Hydrostatic pressure	28.26
Static mud pressure	30.68
Leak-off pressure	32.0
Instantaneous shut in pressure	32.0